
Development and Characterization of new Inhibitors for Protein Kinase Nek1



TECHNISCHE
UNIVERSITÄT
DARMSTADT

Vom Fachbereich Chemie
der Technischen Universität Darmstadt

zur Erlangung des Grades

Doctor rerum naturalium

(Dr. rer. nat.)

Dissertation

von

Georg Baumann, M.Sc.

aus Darmstadt

Erstgutachter:

Prof. Dr. Boris Schmidt

Zweitgutachterin:

Prof. Dr. Katja Schmitz

Darmstadt 2021

Baumann, Georg: Development and Characterization of new Inhibitors for Potein Kinase Nek1

Darmstadt, Technische Universität Darmstadt,

Jahr der Veröffentlichung der Dissertation auf TUPrints: 2021


Tag der mündlichen Prüfung: 31. Mai 2021

Veröffentlicht unter CC BY-SA 4.0 International – Creative Commons, Attribution Sharealike

<https://creativecommons.org/licenses>

“I don’t have talent, I have tenacity.”

Henry Rollins



The present work was carried out under the direction of Prof. Dr. Boris Schmidt from May 2017 to May 2021 at the Clemens Schoepf Institute for Organic Chemistry and Biochemistry at the Technical University of Darmstadt.

Die vorliegende Arbeit wurde unter der Leitung von Herrn Prof. Dr. Boris Schmidt in der Zeit von Mai 2017 bis Mai 2021 am Clemens-Schöpf-Institut für Organische Chemie und Biochemie der Technischen Universität Darmstadt angefertigt.

Acknowledgments

Zuallererst möchte ich mich bei meinem Doktorvater Herrn Prof. Dr. Boris Schmidt für die hervorragende Zusammenarbeit während meiner Promotion bedanken. Insbesondere für die anregenden fachlichen Diskussionen, das mir entgegengebrachte Vertrauen sowie die stete Bereitschaft sich meinen Fragen und Anliegen zu widmen.

Ich richte meinen herzlichen Dank an PD Dr. Tobias Meckel für die kompetente und freundliche Unterstützung bei der Durchführung der mikroskopischen Aufnahmen sowie für die wertvollen Ratschläge und Hinweise. Frau Prof. Dr. Katja Schmitz danke ich für die Übernahme des Korreferats.

Darüber hinaus möchte ich mich bei der Deutschen Forschungsgemeinschaft für die Bereitstellung eines Stipendiums bedanken. Herrn Prof. Dr. Markus Löbrich, Frau Kastenholz und allen weiteren Mitgliedern des DFG Graduiertenkollegs 1657 danke ich für die wertvollen Erfahrungen und Ihre weitreichende Unterstützung.

Großer Dank gilt den aktiven und ehemaligen Mitgliedern der Arbeitskreise Schmidt und Schmitz, insbesondere Daniel, Dennis, Johanna, Johannes und Chris, Steffi und Vicky, für das freundliche und angenehme Arbeitsklima sowie für die schönen Zeiten außerhalb des Laboralltags. Zudem danke ich allen Studenten die mich während meiner Promotion begleitet haben. Ich habe viel von Euch gelernt und danke Euch für Euren unermüdlichen Einsatz. Kevin Böhm, Mirco Dickhaut, Jana Anton und Torben Reichardt danke ich für die tatkräftige Unterstützung bei der Synthese ausgewählter Substanzen und Yung-Hsin Shih, Michelle Kilb und Jessica Kondol danke ich für Ihre Beiträge zur Etablierung der fluoreszenzmikroskopischen Experimente. Ebenfalls gilt mein Dank Holger Hermann Merschroth und Dr. Dieter Spiehl, für die Bereitstellung der 3D-Drucker und die wertvollen Vorschläge und Anregungen. Dr. Andree Blaukat, Dr. Frank Zenke, Dr. Mireille Krier, Dr. Markus Klein und insbesondere Herrn Dr. Ulrich Pehl von *Merck KGaA* danke ich für die anregenden Gespräche und die Unterstützung bei der Evaluation ausgewählter Substanzen.

Ein besonderer Dank gilt meiner Familie, die mich bereits mein ganzes Leben in all meinen Entscheidungen unterstützt. Meiner Mutter Barbara danke ich für einfach Alles. Paul, Du bist der Beste Bruder den man sich nur wünschen kann.

Zu guter Letzt danke ich meiner unvergleichlichen Frau. Du hast mir das größte Glück der Welt geschenkt und Dein unermüdlicher Glaube an mich hat mich zu einem besseren Menschen und diese Arbeit erst möglich gemacht. Danke! Dir widme ich diese Arbeit.

Publications

Partial results of this work were presented, published or submitted for publication at the following instances:

Journal Articles

- **Illuminating a Dark Kinase: Structure-Guided Design, Synthesis, and Evaluation of a Potent Nek1 Inhibitor and Its Effects on the Embryonic Zebrafish Pronephros**

Georg Baumann, Tobias Meckel, Kevin Böhm, Yung-Hsin Shih, Mirco Dickhaut, Torben Reichardt, Johannes Pilakowski, Ulrich Pehl, Boris Schmidt, *Journal of Medicinal Chemistry*, (in press), DOI: 10.1021/acs.jmedchem.0c02118.

To be published in the “Journal of Medicinal Chemistry” special issue: “New Horizons in Drug Discovery – Understanding and Advancing Kinase Inhibitors” in January 2022.

- **Design, synthesis and evaluation of 7-azaindoles as Nek1 kinase inhibitors**

Johannes Pilakowski, Georg Baumann, Yung-Hsin Shih and Boris Schmidt.

Expected to be submitted to “Bioorganic & Medicinal Chemistry Letters” in June 2021.

Poster

- **Development and Characterization of New Inhibitors for Protein Kinase Nek1**

Georg Baumann, Johannes Pilakowski, Kevin Böhm, Yung-Hsin Shih, Mirco Dickhaut, Michael Ensminger, Linda Tillert, Markus Löbrich and Boris Schmidt, GRK1657-GRK1739 Network Meeting, Deutsche Forschungsgemeinschaft, Höchst, Germany, 22 January 2019.

Table of Contents

Acknowledgments	v
Publications	vi
Table of Contents	vii
Table of Abbreviations	xiii
List of Amino Acid Abbreviations	xviii
1.Introduction	1
1.1. Protein Kinases as Drug Targets	1
1.1.1. Protein Kinase Structure and Function	3
1.1.2. Strategies for Small Molecule Inhibition of Protein Kinases	9
1.2. The Nek-Family of Protein Kinases	14
1.2.1. Functional and Disease Roles of Nek-Family Kinases	16
1.3. Protein Kinase Nek1	20
1.3.1. The Role of Nek1 in Polycystic Kidney Disease (PKD)	23
1.3.2. Roles of Nek1 in DNA repair, Apoptosis and Cancer	31
2.Aims and Objectives	40
3.Results and Discussion	41
3.1. Structure-guided Design and Synthesis of Nek1 Inhibitors	41
3.1.1. Identification of new Nek1 Inhibitor Scaffolds	41
3.1.2. Nek1 Crystal Structure Analysis and Molecular Scaffold Docking	46
3.1.3. Design and Synthesis of 4-Phenyl-7-Azaindole Nek1 inhibitors	53
3.1.4. Design and Synthesis of 3,4-Disubstituted 7-Azaindole Nek1 Inhibitors	69
3.1.5. Design and Synthesis of 4,6-Disubstituted 7-Azaindole Nek1 Inhibitors	75
3.2. Structure-Activity-Relationship Studies and Pharmacological Evaluation	83
3.2.1. Structure-Activity-Relationship for 4-Phenyl-7-Azaindole Nek1 Inhibitors	83
3.2.2. Structure-Activity-Relationship for Back Pocket-Targeting Nek1 Inhibitors	88
3.2.3. Structure-Activity-Relationship for <i>In Silico</i> -Screening Hit Compounds	91
3.2.4. Structure-Activity-Relationship for 3,4-Disubstituted 7-Azaindole Nek1 Inhibitors	96
3.2.5. Kinase Selectivity Profile for Lead Compound 19f	98
3.2.6. Shake-Flask Solubility Assay for Lead Compound 19f	101
3.2.7. Caco-2 Cell Permeability Assay for Lead Compound 19f	103

3.3.	<i>In Vivo</i> Profiling of Lead Compound 19f in Wild-Type Zebrafish	106
3.3.1.	Zebrafish Developmental Toxicity Assay for lead compound 19f	106
3.3.2.	<i>In Vivo</i> Efficacy Assay for Lead Compound 19f	108
4.....	Summary and Outlook	123
5.....	Experimental Section	128
5.1.	General Information	128
5.1.1.	Column and Thin-layer Chromatography	128
5.1.2.	Infrared spectroscopy	129
5.1.3.	Nuclear Magnetic Resonance Spectroscopy	129
5.1.4.	Mass Spectrometry	130
5.1.5.	High Performance Liquid Chromatography	130
5.1.6.	Microwave-assisted Synthesis	130
5.1.7.	Sonochemical synthesis	131
5.1.8.	Lyophilization	131
5.2.	Synthetic Procedures	132
5.2.1.	General Procedures	132
5.2.2.	4-bromo- <i>N</i> -(2-(dimethylamino)ethyl)benzenesulfonamide (2a)	133
5.2.3.	4-bromo- <i>N</i> -(2-(diethylamino)ethyl)benzenesulfonamide (2b)	134
5.2.4.	4-bromo- <i>N</i> -(2-(piperidin-1-yl)ethyl)benzenesulfonamide (2c)	135
5.2.5.	4-bromo- <i>N</i> -(2-morpholinoethyl)benzenesulfonamide (2d)	136
5.2.6.	<i>tert</i> -butyl (2-(4-bromophenyl)sulfonamido)ethyl)carbamate (2e)	137
5.2.7.	4-bromo- <i>N</i> -(2-hydroxyethyl)benzenesulfonamide (2f)	138
5.2.8.	4-bromo- <i>N</i> -(2-methoxyethyl)benzenesulfonamide (2g)	139
5.2.9.	4-bromo- <i>N</i> -(2-hydroxyethyl)- <i>N</i> -methylbenzenesulfonamide (2h)	140
5.2.10.	2-((4-bromophenyl)sulfonamido)ethyl acetate (2i)	141
5.2.11.	4-bromo- <i>N</i> -(2-hydroxy-2-methylpropyl)benzenesulfonamide (2j)	142
5.2.12.	1-((4-bromophenyl)sulfonyl)-4-methylpiperazine (2k)	143
5.2.13.	((4-bromophenyl)sulfonyl)- <i>L</i> -phenylalanine (2l)	144
5.2.14.	4-bromo- <i>N</i> -(3-hydroxypropyl)benzenesulfonamide (2m)	145
5.2.15.	<i>N</i> -(2-((4-bromophenyl)sulfonamido)ethyl)acetamide (2n)	146
5.2.16.	4-bromo- <i>N</i> -(3-hydroxypropyl)- <i>N</i> -methylbenzenesulfonamide (2o)	147

5.2.17.	<i>N</i> -(2-((4-bromo- <i>N</i> -methylphenyl)sulfonamido)ethyl)acetamide (2p)	148
5.2.18.	<i>N</i> -(2-(dimethylamino)ethyl)-4-(1 <i>H</i> -pyrrolo[2,3- <i>b</i>]pyridin-4-yl)benzenesulfonamide (3a)	149
5.2.19.	<i>N</i> -(2-(diethylamino)ethyl)-4-(1 <i>H</i> -pyrrolo[2,3- <i>b</i>]pyridin-4-yl)benzenesulfonamide (3b)	151
5.2.20.	<i>N</i> -(2-(piperidin-1-yl)ethyl)-4-(1 <i>H</i> -pyrrolo[2,3- <i>b</i>]pyridin-4-yl)benzenesulfonamide (3c)	152
5.2.21.	<i>N</i> -(2-morpholinoethyl)-4-(1 <i>H</i> -pyrrolo[2,3- <i>b</i>]pyridin-4-yl)benzenesulfonamide (3d)	153
5.2.22.	<i>tert</i> -butyl(2-((4-(1 <i>H</i> -pyrrolo[2,3- <i>b</i>]pyridin-4-yl)phenyl)-sulfonamido)ethyl)-carbamate (3e)	154
5.2.23.	<i>N</i> -(2-hydroxyethyl)-4-(1 <i>H</i> -pyrrolo[2,3- <i>b</i>]pyridin-4-yl)benzenesulfonamide (3f)	155
5.2.24.	<i>N</i> -(2-methoxyethyl)-4-(1 <i>H</i> -pyrrolo[2,3- <i>b</i>]pyridin-4-yl)benzenesulfonamide (3g)	156
5.2.25.	<i>N</i> -(2-hydroxyethyl)- <i>N</i> -methyl-4-(1 <i>H</i> -pyrrolo[2,3- <i>b</i>]pyridin-4-yl)benzenesulfonamide (3h)	157
5.2.26.	2-((4-(1 <i>H</i> -pyrrolo[2,3- <i>b</i>]pyridin-4-yl)phenyl)sulfonamido)ethyl acetate (3i)	158
5.2.27.	<i>N</i> -(2-hydroxy-2-methylpropyl)-4-(1 <i>H</i> -pyrrolo[2,3- <i>b</i>]pyridin-4-yl)benzenesulfonamide (3j)	159
5.2.28.	4-(4-((4-methylpiperazin-1-yl)sulfonyl)phenyl)-1 <i>H</i> -pyrrolo[2,3- <i>b</i>]pyridine (3k)	160
5.2.29.	((4-(1 <i>H</i> -pyrrolo[2,3- <i>b</i>]pyridin-4-yl)phenyl)sulfonyl)- <i>L</i> -phenylalanine (3l)	161
5.2.30.	<i>N</i> -(3-hydroxypropyl)-4-(1 <i>H</i> -pyrrolo[2,3- <i>b</i>]pyridin-4-yl)benzenesulfonamide (3m)	163
5.2.31.	<i>N</i> -(2-((4-(1 <i>H</i> -pyrrolo[2,3- <i>b</i>]pyridin-4-yl)phenyl)sulfonamido)ethyl)acetamide (3n)	164
5.2.32.	<i>N</i> -(3-hydroxypropyl)- <i>N</i> -methyl-4-(1 <i>H</i> -pyrrolo[2,3- <i>b</i>]pyridin-4-yl)benzenesulfonamide (3o)	165
5.2.33.	<i>N</i> -(2-((<i>N</i> -methyl-4-(1 <i>H</i> -pyrrolo[2,3- <i>b</i>]pyridin-4-yl)phenyl)sulfonamido)ethyl)acetamide (3p)	166
5.2.34.	2-(4-bromobenzamido)ethyl 4-bromobenzoate (5)	167
5.2.35.	4-bromo- <i>N</i> -(2-hydroxyethyl)benzamide (6)	168
5.2.36.	<i>N</i> -(2-hydroxyethyl)-4-(1 <i>H</i> -pyrrolo[2,3- <i>b</i>]pyridin-4-yl)benzamide (7)	169
5.2.37.	4-bromo-3-methoxyaniline (10)	170
5.2.38.	4-bromo-3-methoxybenzenesulfonyl chloride (11)	171

5.2.39.	4-bromo- <i>N</i> -(2-hydroxyethyl)-3-methoxybenzenesulfonamide (12)	172
5.2.40.	4-(4,4,5,5-tetramethyl-1,3,2-dioxaborolan-2-yl)-1 <i>H</i> -pyrrolo[2,3- <i>b</i>]pyridine (14)	173
5.2.41.	<i>N</i> -(2-hydroxyethyl)-3-methoxy-4-(1 <i>H</i> -pyrrolo[2,3- <i>b</i>]pyridin-4-yl)benzenesulfonamide (15)	174
5.2.42.	(<i>R</i>)-4-(2-amino-3-hydroxypropyl)phenol (17d)	175
5.2.43.	(<i>S</i>)-2-amino-3-(1 <i>H</i> -indol-3-yl)propan-1-ol (17e)	176
5.2.44.	(<i>R</i>)-2-amino-3-(1 <i>H</i> -indol-3-yl)propan-1-ol (17f)	177
5.2.45.	(<i>S</i>)-4-bromo- <i>N</i> -(1-hydroxy-3-phenylpropan-2-yl)benzenesulfonamide (18a)	178
5.2.46.	(<i>R</i>)-4-bromo- <i>N</i> -(1-hydroxy-3-phenylpropan-2-yl)benzenesulfonamide (18b)	179
5.2.47.	(<i>S</i>)-4-bromo- <i>N</i> -(1-hydroxy-3-(4-hydroxyphenyl)propan-2-yl)benzenesulfonamide (18c)	180
5.2.48.	(<i>R</i>)-4-bromo- <i>N</i> -(1-hydroxy-3-(4-hydroxyphenyl)propan-2-yl)benzenesulfonamide (18d)	181
5.2.49.	(<i>S</i>)-4-bromo- <i>N</i> -(1-hydroxy-3-(1 <i>H</i> -indol-3-yl)propan-2-yl)-benzenesulfonamide (18e)	182
5.2.50.	(<i>R</i>)-4-bromo- <i>N</i> -(1-hydroxy-3-(1 <i>H</i> -indol-3-yl)propan-2-yl)benzenesulfonamide (18f)	183
5.2.51.	(<i>S</i>)- <i>N</i> -(1-hydroxy-3-phenylpropan-2-yl)-4-(1 <i>H</i> -pyrrolo[2,3- <i>b</i>]pyridin-4-yl)benzenesulfonamide (19a)	184
5.2.52.	(<i>R</i>)- <i>N</i> -(1-hydroxy-3-phenylpropan-2-yl)-4-(1 <i>H</i> -pyrrolo[2,3- <i>b</i>]pyridin-4-yl)-benzenesulfonamide (19b)	185
5.2.53.	(<i>S</i>)- <i>N</i> -(1-hydroxy-3-(4-hydroxyphenyl)propan-2-yl)-4-(1 <i>H</i> -pyrrolo[2,3- <i>b</i>]pyridin-4-yl)benzenesulfonamide (19c)	186
5.2.54.	(<i>R</i>)- <i>N</i> -(1-hydroxy-3-(4-hydroxyphenyl)propan-2-yl)-4-(1 <i>H</i> -pyrrolo[2,3- <i>b</i>]-pyridin-4-yl)benzenesulfonamide (19d)	187
5.2.55.	(<i>S</i>)- <i>N</i> -(1-hydroxy-3-(1 <i>H</i> -indol-3-yl)propan-2-yl)-4-(1 <i>H</i> -pyrrolo[2,3- <i>b</i>]pyridin-4-yl)benzenesulfonamide (19e)	188
5.2.56.	(<i>R</i>)- <i>N</i> -(1-hydroxy-3-(1 <i>H</i> -indol-3-yl)propan-2-yl)-4-(1 <i>H</i> -pyrrolo[2,3- <i>b</i>]pyridin-4-yl)benzenesulfonamide (19f)	189
5.2.57.	4-chloro-3-iodo-1 <i>H</i> -pyrrolo[2,3- <i>b</i>]pyridine (21)	190
5.2.58.	4-chloro-3-iodo-1-tosyl-1 <i>H</i> -pyrrolo[2,3- <i>b</i>]pyridine (22)	191
5.2.59.	4-chloro-3-phenyl-1-tosyl-1 <i>H</i> -pyrrolo[2,3- <i>b</i>]pyridine (23a)	192

5.2.60.	4-chloro-3-(pyridin-3-yl)-1-tosyl-1 <i>H</i> -pyrrolo[2,3- <i>b</i>]pyridine (23b)	193
5.2.61.	<i>N</i> -(2-hydroxyethyl)-4-(3-phenyl-1-tosyl-1 <i>H</i> -pyrrolo[2,3- <i>b</i>]pyridin-4-yl)benzene sulfonamide (24a)	195
5.2.62.	<i>N</i> -(2-hydroxyethyl)-4-(3-(pyridin-3-yl)-1-tosyl-1 <i>H</i> -pyrrolo[2,3- <i>b</i>]pyridin-4-yl)benzene sulfonamide (24b)	197
5.2.63.	<i>N</i> -(2-hydroxyethyl)-4-(3-phenyl-1 <i>H</i> -pyrrolo[2,3- <i>b</i>]pyridin-4-yl)benzenesulfonamide (25a)	199
5.2.64.	<i>N</i> -(2-hydroxyethyl)-4-(3-(pyridin-3-yl)-1 <i>H</i> -pyrrolo[2,3- <i>b</i>]pyridin-4-yl)benzene sulfonamide (25b)	200
5.2.65.	<i>N</i> -(2-hydroxyethyl)-4-(4,4,5,5-tetramethyl-1,3,2-dioxaborolan-2-yl)-benzene sulfonamide (26)	202
5.2.66.	1 <i>H</i> -pyrrolo[2,3- <i>b</i>]pyridine 7-oxide 3-chlorobenzoic acid salt (29)	203
5.2.67.	1 <i>H</i> -pyrrolo[2,3- <i>b</i>]pyridine 7-oxide (30)	204
5.2.68.	Methyl 6-chloro-1 <i>H</i> -pyrrolo[2,3- <i>b</i>]pyridine-1-carboxylate (31)	205
5.2.69.	6-chloro-1 <i>H</i> -pyrrolo[2,3- <i>b</i>]pyridine (32)	206
5.2.70.	6-chloro-1 <i>H</i> -pyrrolo[2,3- <i>b</i>]pyridine 7-oxide (33)	207
5.2.71.	4-bromo-6-chloro-1 <i>H</i> -pyrrolo[2,3- <i>b</i>]pyridine (34)	208
5.2.72.	4-bromo-1 <i>H</i> -pyrrolo[2,3- <i>b</i>]pyridine 7-oxide (36)	209
5.2.73.	6-chloro- <i>N</i> -phenyl-1 <i>H</i> -pyrrolo[2,3- <i>b</i>]pyridin-4-amine (39)	210
5.2.74.	4-chloro-1 <i>H</i> -pyrrolo[2,3- <i>b</i>]pyridine 7-oxide (41)	211
5.2.75.	4-chloro-1 <i>H</i> -pyrrolo[2,3- <i>b</i>]pyridin-6-amine (42)	212
5.2.76.	4-chloro- <i>N</i> -phenyl-1 <i>H</i> -pyrrolo[2,3- <i>b</i>]pyridin-6-amine (43)	213
5.3.	Molecular Modeling	215
5.3.1.	General Information	215
5.3.2.	Preparation of Nek1 Crystal Structures	215
5.3.3.	Preparation of a Nek1 Kinase Domain Homology Model	216
5.3.4.	Computational Protein-Ligand Docking	216
5.3.5.	Sequence Homology Analysis of the Zebrafish Nek1 Kinase Domain	217
5.4.	Pharmacological Evaluation	218
5.4.1.	<i>In Vitro</i> Kinase Activity Assays	218
5.4.2.	Shake-Flask Solubility Assay	220

5.4.3.	Caco-2 Cell Permeability Assay	220
5.4.4.	Zebrafish Developmental Toxicity Assay	221
5.4.5.	Stability-indicating HPLC Assay	221
5.5.	Zebrafish Maintenance and Husbandry	222
5.6.	Fluorescence Microscopy Imaging of Zebrafish Pronephroi	224
5.6.1.	Preparation of Agarose Molds and the 96-Well Plate Molding tool	224
5.6.2.	Embryo selection and compound treatment	225
5.6.3.	Image Acquisition	226
5.6.4.	Image Processing and Deconvolution	226
	References	229
	Appendix	272
A.	<i>In silico</i> screening data for the molecular docking of the virtual compound library	272
B.	Kinase selectivity profile for compound 19f	274
C.	Fluorescence-Microscopy Imaging of 19f-treated Wild-Type Zebrafish Embryos	275
D.	Journal Article (<i>Journal of Medicinal Chemistry</i>) “Illuminating a Dark Kinase: Structure-Guided Design, Synthesis, and Evaluation of a Potent Nek1 Inhibitor and Its Effects on the Embryonic Zebrafish Pronephros” with adapted Supporting Information	278
E.	Erklärung laut Promotionsordnung	356
F.	Abstract	357
G.	Alternative Abstract (German)	358

Table of Abbreviations

a.u.	arbitrary unit
aa	amino acid
ADPKD	autosomal-dominant polycystic kidney disease
APCI	atmospheric pressure chemical ionization
ARPKD	autosomal-recessive polycystic kidney disease
ATM	<i>ataxia telangiectasia</i> mutated
ATP	adenosine triphosphate
ATR	<i>ataxia telangiectasia</i> mutated and Rad3-related
ATR-IR	attenuated total reflection infrared spectroscopy
ATRIP	<i>ataxia telangiectasia</i> mutated and Rad3-related-interacting protein
BCR/Abl	breakpoint cluster region-Abelson kinase
BCS	biopharmaceutical drug classification system
BEI	binding efficiency index
c-SRC	proto-oncogene tyrosine-protein kinase
CAMK	calmodulin/calcium regulated kinase
cAMP	cyclic adenosine monophosphate
CDK	cyclin-dependent kinase
CHF	congenital hepatic fibrosis
Chk1	checkpoint kinase 1
Chk2	checkpoint kinase 2
CI	confidence interval
CKD	chronic kidney disease
CLKs	cdc-like kinase (CLKs)
CLogP	calculated n-octanol-water partition coefficient
CML	chronic myelogenous leukemia
COSY	correlated spectroscopy
COX	cyclooxygenase

CRPC	castration-resistant prostate cancer
DAD	diode-array detector
dba	dibenzylidenacetone
DCE	1,2-dichloroethane
DCM	dichloromethane
DHJ	double Holliday junction
DIPA	diisopropylamine
DMS	dimethyl sulfate
DNA-PK	DNA-dependent protein kinase
dpf	days post fertilization
dppf	1,1'-Bis(diphenyl-phosphino)ferrocene
DSBR	double-strand break repair
DSBs	DNA double-strand breaks
DSF	differential scanning fluorimetry
dtbpf	1,1'-Bis(di-tert-butylphosphino)ferrocene
DZIP1L	DAZ-interacting protein 1-like
EDTA	ethylenediaminetetraacetic acid
EGFP	enhanced green fluorescent protein
EGFR	endothelial growth factor receptor
EI	electron ionization
EMA	European Medicines Agency
ePK	eukaryotic protein kinases
ER	endoplasmatic reticulum
ErbB2	erb-b2 receptor tyrosine kinase 2
ESI	electrospray ionization
ESRD	end-stage renal disease
FDA	U.S. Food and Drug Administration
FDM	fused deposition modeling
FLK1	fetal liver kinase 1

FTIR	fourier-transform infrared spectroscopy
GK	gatekeeper
GPCR	G protein-coupled receptor
GSK3	glycogen synthase kinase 3
HAN	heavy atom number
HMBC	heteronuclear multiple bond correlation
hpf	hours post fertilization
HPLC	high-performance liquid chromatography
HR	homologous recombination
HR1	hydrophobic region 1
HR2	hydrophobic region 2
HRR	homology-directed recombination-mediated repair
HSQC	heteronuclear single quantum coherence
INN	international nonproprietary names
JNK	c-Jun N-terminal kinase
KIF3A	kinesin-like protein
KOtBu	potassium tert-butoxide
LE	ligand efficiency
LFU	low frequency ultrasound
LogP	n-Octanol-water partition coefficient
mAbs	monoclonal antibodies
MAPK	mitogen-activated protein kinase
mCBA	meta-chlorobenzoic acid
MCF	methyl chloroformate
mCPBA	meta-chloroperoxybenzoic acid
MOE	Molecular Operating Environment
mRNA	messenger RNA
MS	mass spectrometry
MsCl	mesyl chloride

mTOR	mechanistic target of rapamycin
mw	microwave
MW	molecular weight
n.d.	not determined
n.e.	no effect at maximum concentration
NaN	not a number
NaOtBu	sodium tert-butoxide
NCEs	new chemical entities
Nek	never in mitosis-gene A (NIMA)-related kinase
NHEJ	non-homologous end joining
NIMA	never in mitosis-gene A
NMR	nuclear magnetic resonance spectroscopy
pADPr	poly(adenosine diphosphate-ribose)
PARP	poly(adenosine diphosphate -ribose)-polymerase
PCT	proximal convoluted tubule
PDB	Protein Database
PKIS2	<i>Published Kinase Inhibitor Set 2</i>
PSF	point spread function
PTU	<i>N</i> -Phenylthiourea
RCC1	regulator of chromosome condensation 1
RMSD	root-mean-square deviation
SARs	structure-activity relationship
SD	standard deviation
SDSA	synthesis-dependent strand annealing
SIADH	syndrome of inappropriate antidiuretic hormone secretion
SL2	<i>SuperLooper2</i>
SSBs	single-strand DNA breaks
ssDNA	single-strand DNA
TAZ	transcriptional coactivator with PDZ- binding motif

TBAB	tetrabutylammonium bromide
TFA	trifluoroacetic acid
THF	tetrahydrofuran
TK	tyrosine kinase
TLC	thin-layer chromatography
Tlk1	tousled-like kinase 1
TMS	tetramethylsilane
TOF	time-of-flight
tPSA	topological surface area
TSA	thermal shift assay
U/S	ultrasonic irradiation
UV	ultraviolet
VDAC1	voltage-dependent anion channel 1
VWD	variable wavelength detector
Wee1	Wee1 G2 checkpoint kinase

List of Amino Acid Abbreviations

Alanine	A	Ala
Arginine	R	Arg
Asparagine	N	Asn
Aspartic acid	D	Asp
Cysteine	C	Cys
Glutamic acid	E	Glu
Glutamine	Q	Gln
Glycine	G	Gly
Histidine	H	His
Isoleucine	I	Ile
Leucine	L	Leu
Lysine	K	Lys
Methionine	M	Met
Phenylalanine	F	Phe
Proline	P	Pro
Serine	S	Ser
Threonine	T	Thr
Tryptophan	W	Trp
Tyrosine	Y	Tyr
Valine	V	Val

1. Introduction

1.1. Protein Kinases as Drug Targets

Kinases are a group of enzymes that catalyze the transfer of γ -phosphate of adenosine triphosphate (ATP) onto various hydroxyl-bearing substrates, such as proteins, polysaccharides, nucleic acids and lipids. They are primarily responsible for mediating cellular signal transduction and play a crucial role in the regulation of most aspects of cell life.

The first scientific description of cell function regulation by reversible phosphorylation dates back to the 1930s, when Carl and Gerty Cori reported on the discovery of two forms of glycogen phosphorylase that catalyze the rate-determining step of glycogenolysis.¹ They were awarded a Nobel prize for their findings in 1947, but it took a long time for the general significance of their discovery to be fully appreciated. Even though the intricate interplay between several phosphotransferases and their dependency on second messengers was slowly being unraveled over the course of several decades, their function was still thought to be confined to glycogen metabolism. Today, it is estimated that around one third of the human proteome contains covalently bound phosphate and dysregulation of phosphorylation and mutations of protein kinases are now recognized as key factors in many human diseases.² As a consequence, kinases are now a primary drug target class with over 50 U.S. food and drug administration (FDA)-approved drugs and over 200 other international nonproprietary names (INNs) in clinical development, as of today.³

Historically, kinase activity has been modulated for therapeutic applications since the 1930s. However, directed medicinal chemistry efforts toward targeted kinase inhibitors were not undertaken before the 1980s.⁴ Fasudil, the first small molecule kinase inhibitor approved for clinical use, was greenlighted for the treatment of cerebral vasospasms in 1995 in Japan (Figure 1). Several years later, the first natural product kinase inhibitor (Sirolimus, 1999, Figure 1), targeting mechanistic target of rapamycin (mTOR) for prevention of organ transplant rejection, and the first monoclonal antibody kinase drug (Trastuzumab, 1998), targeting erb-b2 receptor tyrosine kinase 2 (ErbB2) for the treatment of ErbB2-positive breast cancer, followed.⁵⁻⁶ In 2001, the approval of Imatinib, the first-in-class tyrosine kinase inhibitor for the treatment of chronic myelogenous leukemia (CML), marked a revolution in kinase inhibitor development and antineoplastic chemotherapy (Figure 1).

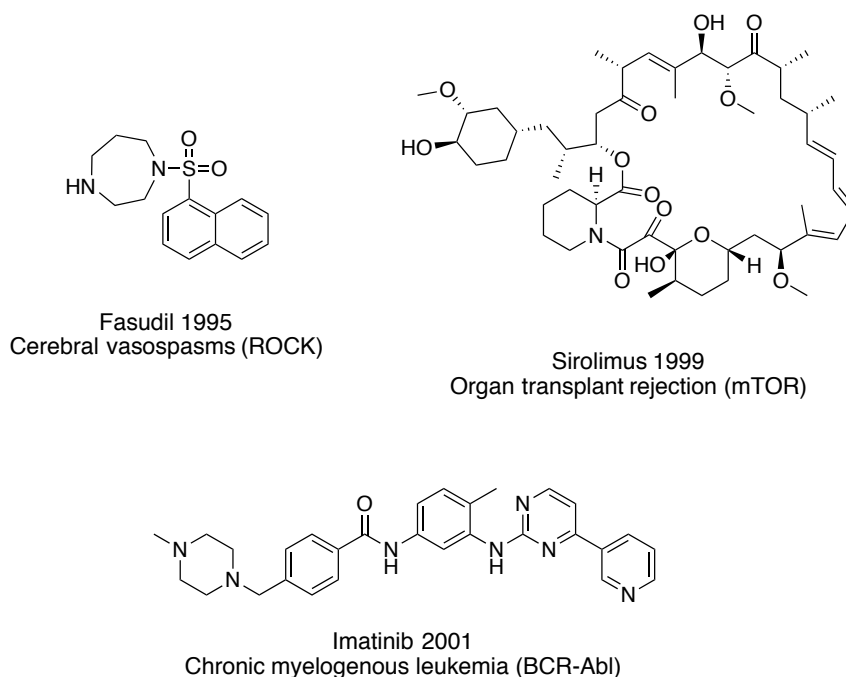


Figure 1: Hallmark small molecule kinase drugs.⁵⁻⁷

This landmark drug shifted the chemotherapeutic paradigm, from highly toxic and unspecific cancer drugs, toward a targeted therapeutical approach by selectively inhibiting the sole oncogenic driver of CML, breakpoint cluster region-Abelson kinase (BCR/Abl). Furthermore, the development of Imatinib had a sustained and powerful impact on the research field, being the first approved small molecule inhibitor to induce a distinct inactive kinase conformation in addition to displacing ATP.⁷

Since then, the focus of kinase drugs has expanded from non-receptor tyrosine kinases to other protein kinase classes, such as serine/threonine and receptor tyrosine kinases, as well as lipid and carbohydrate kinases. Although most kinase drug research is still dedicated to cancer treatment, new therapeutic indications like inflammation, autoimmunity, tropical diseases and neurodegenerative diseases are on the rise.⁸ In the face of the current coronavirus crisis, protein kinase inhibitors moved into the spotlight in an attempt to repurpose approved drugs in terms of their antiviral potential, due to reported potencies against key kinases involved in viral entry, metabolism and reproduction.⁹

1.1.1. Protein Kinase Structure and Function

Despite their diverse substrates, functions, and primary sequences, protein kinases share a great deal of similarity in their structures, especially in the catalytically active ATP-binding domains. The human genome encodes over 500 kinases of which the majority still remains to be investigated for their structure and function. Thanks to rapid advances in protein structure elucidation techniques, mainly X-ray crystallography and nuclear magnetic resonance (NMR), a large number of three-dimensional protein structures have already been solved and deposited in databases. The number of entries in the Protein Data Bank (PDB),¹⁰ for example, has increased from 54,000 protein structures in 2008 to 160,000 in 2020.¹¹ In addition to protein structures, the PDB also contains structures of protein-ligand complexes, providing an even deeper pool of information to be exploited for drug-design purposes.

Most protein kinases contain a conserved catalytic domain and are thereupon grouped into the superfamily of eukaryotic protein kinases (ePKs). All other kinases make up the atypical protein kinase (aPK) family, which is characterized by altered regulatory and catalytic structure-motifs that come along with a limited number of binding modes when compared to the ePKs.¹² Within their superfamily, the ePKs are classified into seven major groups, based on the sequence similarity of their respective kinase domains. Some unique kinases as well as several families that by definition belong to the ePKs but do not fit into the major groups, are classified as the so-called “Other”-kinases (Figure 2).

Furthermore, protein kinases can also be divided into two major classes, based on their cellular location: a) Membrane-bound protein kinases that comprise an extracellular ligand-binding domain linked to an intracellular kinase domain by a transmembrane region and b) soluble kinases that are localized in either the cytoplasm or the nucleus and constitute a large variety of functional domains in addition to the conserved kinase domain. While the specific function of membrane-bound kinases is limited by their location and the specificity of the ligand-receptor interaction, the activity and specific physiological function of soluble protein kinases critically depends on their tightly regulated subcellular localization.¹³⁻¹⁵

The conserved protein kinase domain of the ePK superfamily generally features two subdomains, called the N-terminal and C-terminal lobe that are linked by a short polypeptide chain, commonly referred to as the hinge region. The N-terminal lobe is composed of a series of β -strands and contains at least one globally conserved α -helical element, the structurally important C-helix (Figure 3).¹⁶

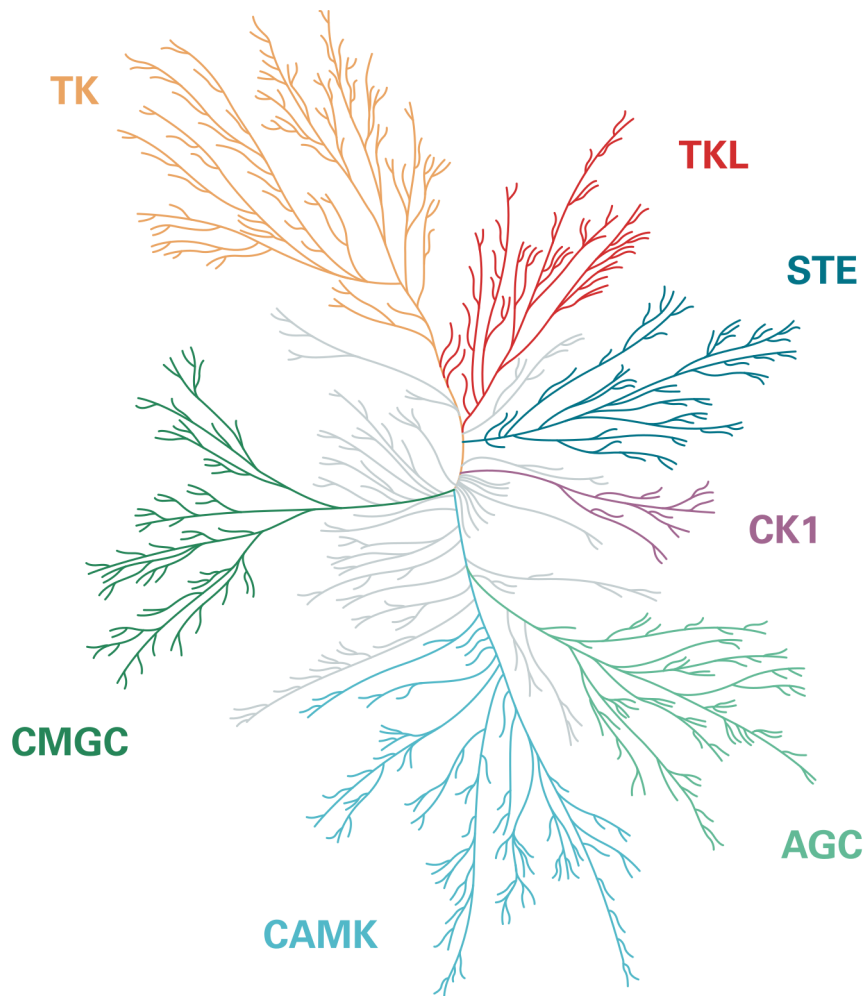


Figure 2: Phylogenetic tree of the human eukaryotic kinome. Seven major groups are classified on the basis of structural similarity, known function and evolutionary conservation: tyrosine kinases (TK, orange); tyrosine kinase-like group (TKL, red) with high similarity to tyrosine kinases but general activity toward serine/threonine; homologs of yeast sterile kinases (STE, cyan); cell kinase 1 group (CK1, purple); group named after protein kinase A, G, and C families (AGC, light green); group of calmodulin/calcium regulated kinase (CAMK, light blue) families that also contains non-calcium regulated kinases; functionally diverse group named after contained kinase families: CDK, MAPK, GSK3 and CLK (CMGC, dark green); “Other” kinases group that contains unique kinases and several families that do not fit into the major groups (grey). Figure adapted with permission from *Kinase Investigations open new Doors in Oncology and Neuroscience* by D. Maelle, 2019, <https://www.cisbio.eu/content/kinase-investigations-open-new-doors-in-oncology-and-neuroscience/>.

Sitting at the interface of the subdomains, the C-helix interacts with many different parts of the molecule and serves as a dynamic regulatory element in the kinase molecule.¹⁶ The predominantly α -helical C-lobe is more diverse in terms of size, topology and sequence but generally larger than its N-terminal equivalent. Being responsible for substrate binding, the C-terminal subdomains’ diversity allows for the accommodation of a broad range of kinase substrates.¹⁷ Some kinases also feature a C-terminal tail, which wraps itself around the outside of the kinase and interacts with hydrophobic regions of the N-lobe.¹⁸

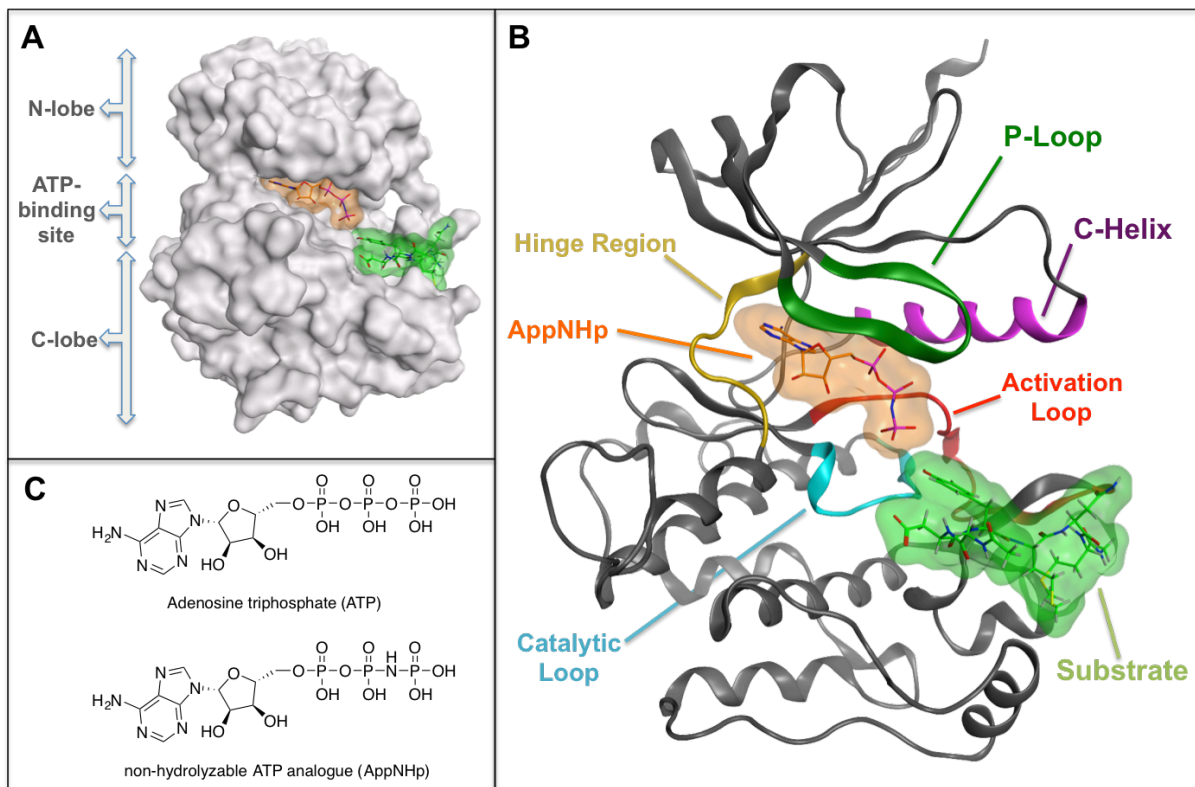


Figure 3: Structure of a typical eukaryotic protein kinase domain (insulin receptor kinase domain crystal structure, PDB code: 1IR3). (A) Crystal structure based protein surface model of activated insulin receptor tyrosine kinase domain in complex with peptide substrate and β,γ non-hydrolyzable ATP analogue (AppNHp), displaying the N-terminal lobe, the ATP-binding site and the C-terminal lobe. (B) Conserved structural elements of ePKs displayed in the crystal structure of phosphorylated insulin receptor kinase domain, featuring the C-helix (purple), the P-loop (dark green), the hinge region (yellow), the activation loop (red), the catalytic loop (cyan), the ATP analogue (orange) and the peptide substrate (lime green). (C) Chemical structures of ATP and the β,γ non-hydrolyzable ATP analogue AppNHp.

The ATP-binding site, on the other hand, is located in a cleft at the interface between the two lobes. In general, the adenosine moiety of ATP forms two hydrogen bonds with the hinge region backbone, while the core of ATP interacts with the backbone of a glycine-rich phosphate binding loop (P-loop) that bridges the outermost N-terminal β -strands.¹⁷ As a consequence of its central role in binding and orienting ATP, the hinge region backbone conformation is nearly identical in almost all structurally solved kinases.

Located immediately N-terminal to the hinge region's linker sequence is an important amino acid (aa) residue, generally referred to as the "gatekeeper" (GK, Figure 4). This amino acid has a major influence on the size of the ATP-binding site and is of particular importance for the design of small molecule kinase inhibitors. Its size varies between kinases, but it is almost always a bulky residue.¹⁹

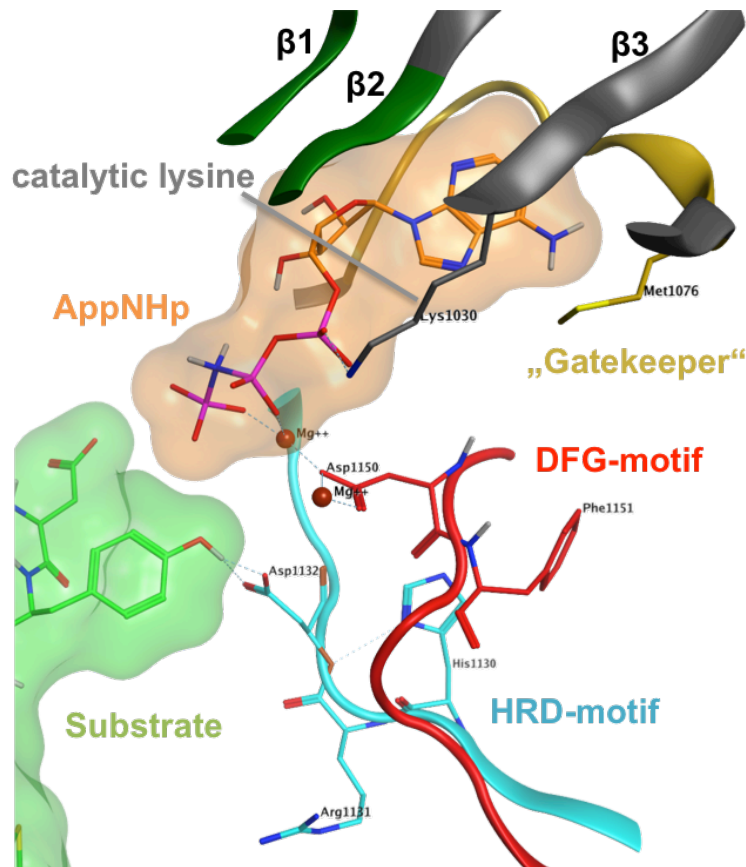


Figure 4: Key amino acid residues and their interactions in the active kinase core domain (PDB code: 1IR3). The GK (yellow) has a major influence on the size and shape of the ATP-binding site. The DFG-motif (red) aspartate coordinates the divalent ATP-bound magnesium in the active conformation. The HRD-motif (cyan) contains the catalytic aspartate, which abstracts the proton from the hydroxyl group of the substrate (lime green) threonine. The catalytic lysine (grey) originates from β -strand 3 (β 3) and interacts with the α - and β -phosphates of the ATP analogue (orange).

The glycine rich loop, also termed P-loop, is responsible for localizing the phosphates of ATP. It features a typical GxGxxG sequence motif in which the polypeptide backbone coordinates the γ -phosphate and the small glycine side chains provide extra flexibility.²⁰ In some kinases, the catalytic lysine, which interacts with the α - and β -phosphates of ATP, is located in immediate C-terminal proximity of the P-loop on β -strand 2. For most kinases though, the catalytic lysine originates from β -strand 3.²¹ Bordering the ATP-binding-site from the C-lobe, the catalytic loop contains the catalytic aspartate, which abstracts the proton from the hydroxyl group of the substrate amino acid. While some protein kinases are capable of utilizing non-metal-bound ATP as the phosphoryl-donor substrate, the large majority is dependent on Mg-bound ATP and requires at least one additional divalent metal ion (Mg^{2+} or Mn^{2+}) for catalysis. This results from the fact that the high affinity of magnesium ions for ATP leaves only a low concentration of non-Mg-bound ATP in cells.²²

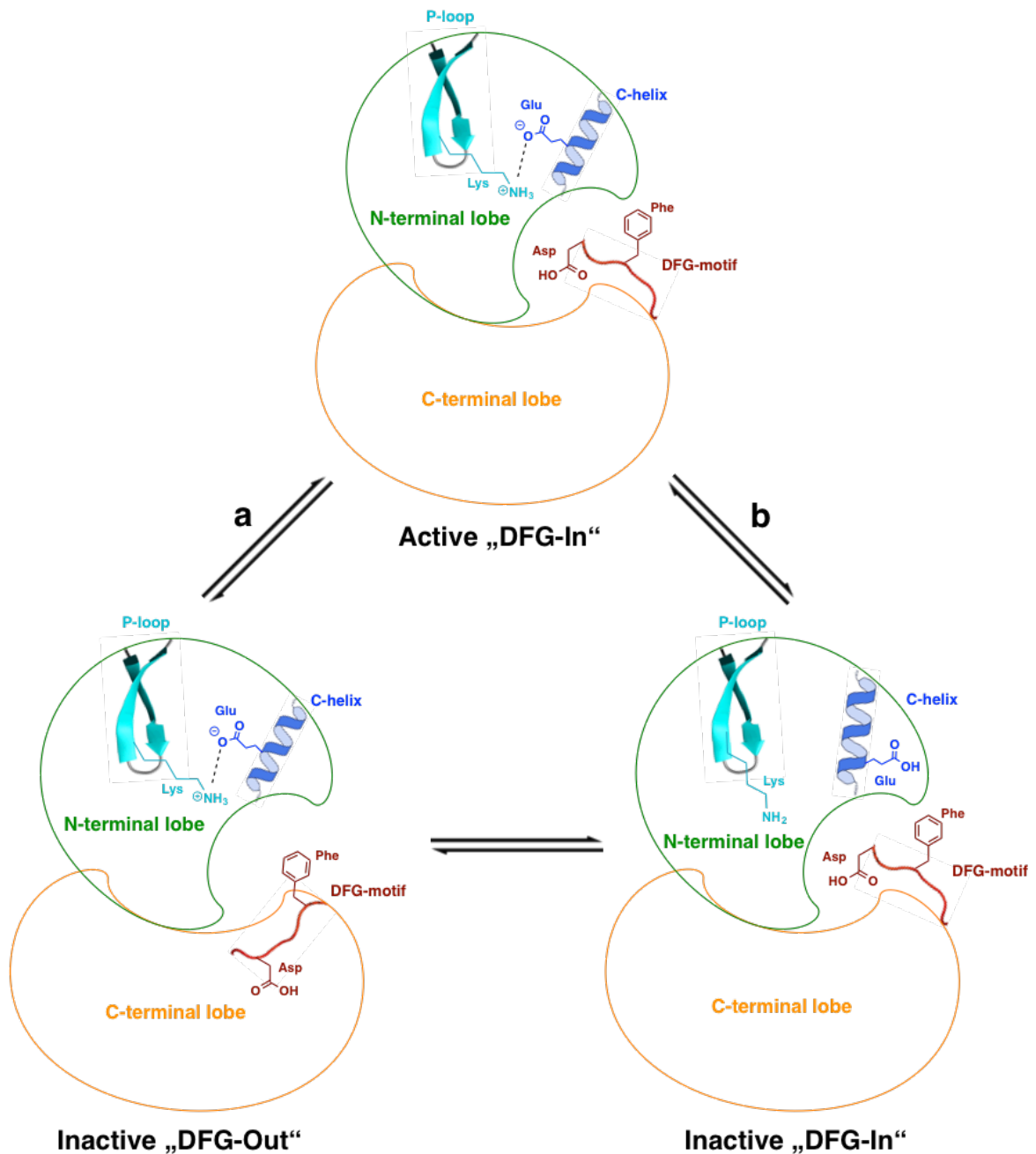


Figure 5: Schematic representation of the conformational differences between the active “DFG-In”, inactive “DFG-Out” and inactive “DFG-In” conformations of eukaryotic protein kinases (ePKs). (a) A 180° rotation of the DFG motif results in the inactive “DFG-out” conformation, where the DFG-aspartate can no longer coordinate Mg-bound ATP. (b) An outward rotation of the C-helix disrupts the salt bridge between the conserved C-helix glutamate and the catalytic lysine, resulting in the inactive “DFG-In” conformation.²⁴⁻²⁵

Additionally, ePKs possess a flexible activation loop close to their rather static catalytic loop. Most ePKs are activated by site-specific phosphorylation of residues in the activation loop, that cause a drastic change in the activation loop’s conformation by counteracting the positive charge of the arginine, located in the conserved HRD-motif of the catalytic loop (Figure 4).²³

This structural plasticity is paramount for kinase regulation and enzymatic activity and different conformations have been shown to reflect distinct functional states. Two essential structural features characterize the active kinase conformation: (a) Orientation of the conserved DFG-motif-aspartate toward the active site and (b) a salt bridge between a conserved C-helix glutamate and the catalytic lysine, that is formed upon inward rotation of the C-helix (“C-helix-In”, Figure 5). The relative stability of the active and inactive kinase conformations determines the overall activity of a kinase and can be altered by regulatory proteins, post-translational modifications, substrates and ligands.²⁴⁻²⁵

Comparative studies of the active and inactive conformations of several protein kinases by Kornev *et al.* led to the description of two other structural skeletons, important for the characterization of active and dormant states.²⁶⁻²⁷ The catalytic spine (C-spine) consists of eight hydrophobic residues, spanning across the adenine base of ATP from the N-terminal to the C-terminal lobe and positions ATP to enable catalysis. In contrast, the regulatory spine (R-spine) is made up of only four hydrophobic residues, located in the C-helix and the activation segment and positions the substrate in a similar manner. Proper alignment of these hydrophobic spines is a crucial prerequisite for the assembly of an active protein kinase domain.²⁸

1.1.2. Strategies for Small Molecule Inhibition of Protein Kinases

Over the years, a growing number of strategies for the purposeful alteration of protein kinase activity has been developed. Most often, membrane-permeable small molecule inhibitors that bind tightly to either the active site or an allosteric binding site are used to alter protein kinases activity, due to the fact that the vast majority kinases are located intracellularly and can thus not be targeted by non-cell-permeable monoclonal antibodies (mAbs). Nonetheless, mAbs are generally more target-specific than small molecule inhibitors and are widely used for indirect kinase inhibition and to induce immune responses through receptor-bound kinases, by binding to extracellular domains prevalent in these kinases.²⁹

In the case of small molecules, the structure of the enzyme-bound antagonist complex is commonly used as the basis for categorization, based on a classification system that was first introduced by Dar and Shokat and later extended by others.^{28, 30} Originally, inhibitors that bind to the ATP pocket in any active kinase conformation were termed Type I inhibitors, those that bind to an inactive conformation as Type II inhibitors and allosteric inhibitors that do not compete with ATP-binding were classified as Type III inhibitors. Ongoing discoveries led to the introduction of several subtypes that further specify the structure of kinase inhibitor drug-enzyme complexes. Today, it is generally accepted that only inhibitors binding to an active conformation with DFG-Asp in, the α C-helix in, and with the regulatory spine in its active linear configuration count as the Type I. For inhibitors that target the “DFG-in”-conformation but extend into the ATP back cavity formed by the outward rotation of the C-helix (“ α C-helix out”), the Type I^{1/2} subclass was defined by Zucotto *et al.*³¹

Type I inhibitor binding is typically described by a commonly accepted pharmacophore, in which the inhibitors bind to the kinase hinge region by the formation of one to three hydrogen bonds, while additional hydrophobic interactions are formed with the adenine ring region (Figure 6).³² As a consequence of high degrees of sequence and structural similarity among kinase family ATP pockets, Type I inhibitors often display promiscuous activity that can lead to adverse side effects, and extensive optimization is often needed to achieve clean selectivity profiles.³³

Type I^{1/2} and Type II inhibitors provide opportunities for the development kinase inhibitors with increased potency and selectivity by extending the Type I pharmacophore into an additional back pocket, accessible as a result of the defining conformational changes of the

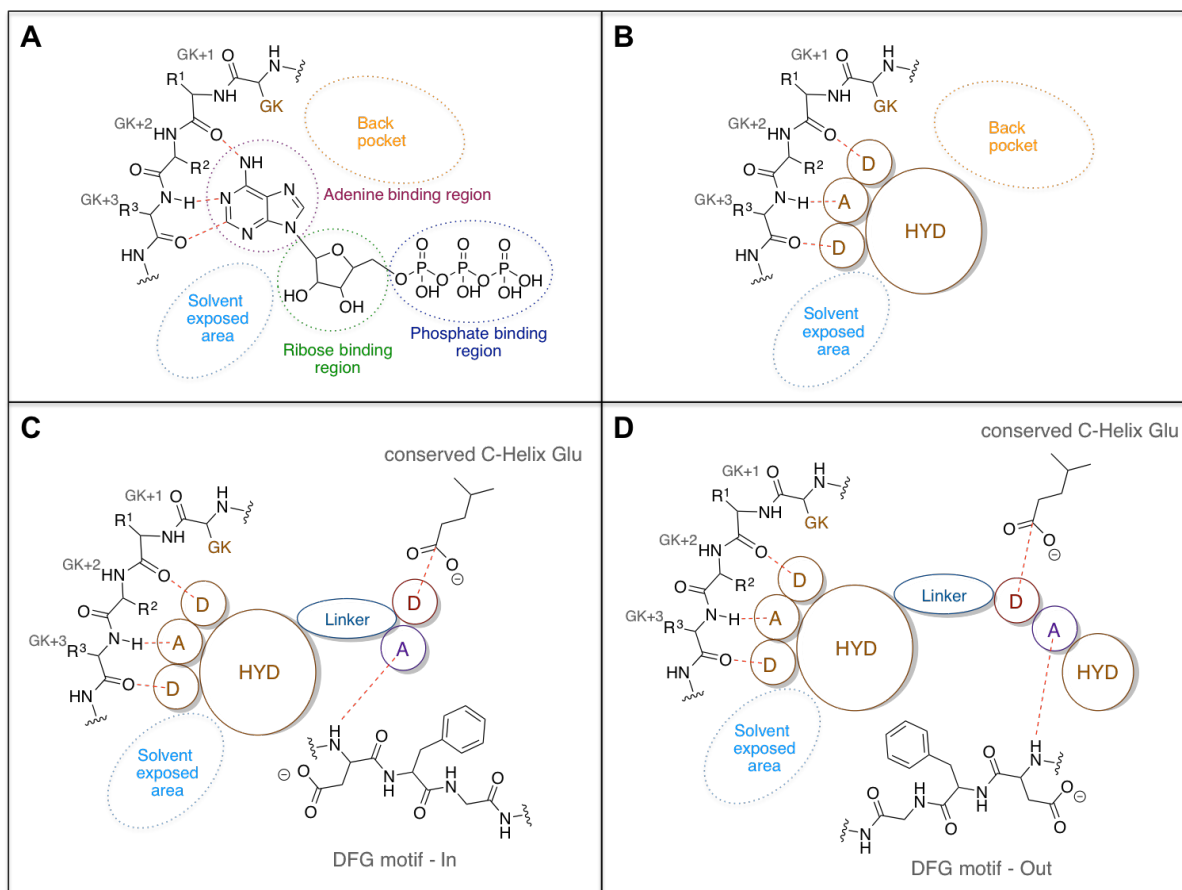


Figure 6: Pharmacophore interaction maps for ATP-binding and Type I, Type I^{1/2} and Type II kinase inhibitors. (A) ATP interactions with the hinge residues and location of ATP-binding site regions. (B) Type I kinase inhibitor pharmacophore with three potential hydrogen bond interactions at the hinge region and no occupation of the back pocket. (C) Type I^{1/2} pharmacophore with three potential hydrogen bond interactions at the hinge region and occupation of the back pocket, accessible by outward rotation of the C-helix. (D) Type II kinase inhibitor pharmacophore with three potential hydrogen bond interactions at the hinge region, occupation of the back pocket and access to the second hydrophobic pocket, present in the inactive „DFG-out“-conformation. A, hydrogen bond acceptors; D, hydrogen bond donors; GK, gatekeeper; HYD, hydrophobic moieties. Hydrogen bonds are shown as dashed red lines. Redrawn in parts from Zuccotto *et al.*³⁴

α C-helix (Figure 6, Figure 7). Additional hydrogen bond interactions with the conserved C-helix Glu are consequently available to the Type I^{1/2} and Type II pharmacophores. The characteristic “DFG-Out” conformation allows the Type II pharmacophore to extend even further, giving access to a second hydrophobic pocket. As a consequence of the variability of those conformational changes across the kinome and the lower level of sequence similarity in the second hydrophobic pocket, Type II inhibitors are often much more selective than their Type I counterparts. Furthermore, targeting an inactive conformation, normally characterized

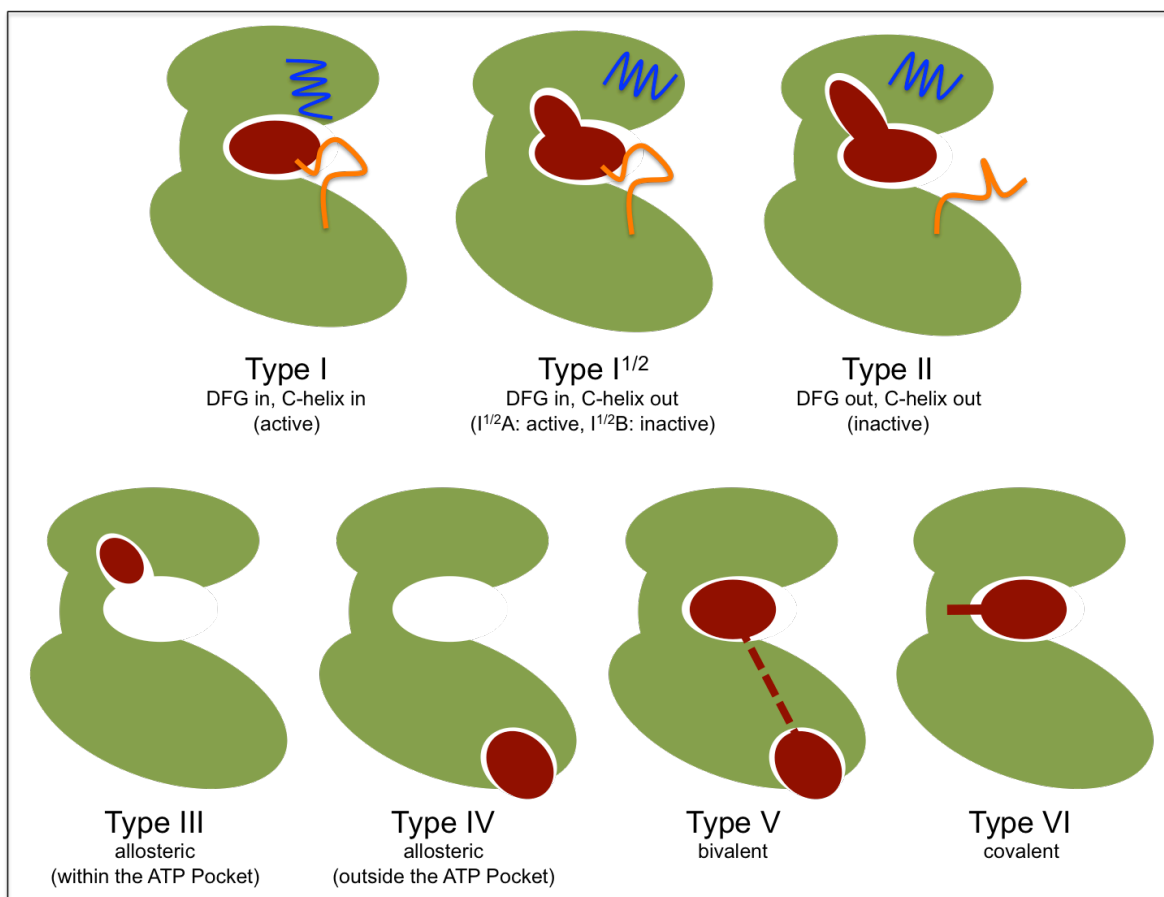


Figure 7: Classification of small molecule protein kinase inhibitors. The protein kinase is shown in green, the inhibitor in red, the DFG motif in orange and the C-helix in blue. Redrawn in parts from Martinez III *et al.*³⁵

by higher $K_{M,ATP}$ values compared to the active conformation, dampens ATP competition and thus enhances *in vivo* activity.³⁴ However, a recent data mining study by Miljković *et al.* revealed that differences in selectivity between Type I and II inhibitors are not as clear cut as generally perceived and that there is no simple relationship between clinical performance and selectivity versus promiscuity of kinase-targeting compounds.³⁶ Nonetheless, achieving selectivity tends to be more challenging and resource intensive for Type I inhibitors.

Despite the fact that Type I^{1/2} and Type II kinase inhibitors offer distinct advantages over Type I inhibitors, there are also downsides associated with the extension of the Type I pharmacophore. For one, Type I^{1/2} and Type II inhibitors are more vulnerable to persistent drug resistance-conferring mutations outside the ATP pocket that can result in reduction or complete loss of inhibitory activity, while the kinase remains functional. In contrast, mutations that would interfere with Type I inhibitor binding inside the ATP pocket would likely also render the targeted kinase dysfunctional and lead to cell death eventually.³⁴

One of the most frequent causes of Type II kinase inhibitor drug-resistance is a mutation of the gatekeeper residue, which mainly determines the size and shape of the back cavity.³⁷ This resistance-conferring mechanism was first unveiled for the T315I gatekeeper mutation in BCR/Abl that leads to resistance against virtually all ATP competitors and can result in full relapse in late-stage leukemia patients that previously experienced remission by Type II BCR/Abl-inhibitor treatment.³⁸ Furthermore, Type II compounds often display reduced cellular membrane penetration and lower ligand efficiencies as a consequence of their greater molecular weight.³⁹⁻⁴⁰

In recent years, a new class of protein kinase inhibitors emerged that targets allosteric binding sites with no direct interaction with the hinge region of the ATP-binding pocket. Allosteric kinase inhibitors are divided into Type III inhibitors that bind to an allosteric binding site directly adjacent to the ATP-binding pocket and Type IV inhibitors that bind to a remote allosteric site in the kinase domain (Figure 7). The majority of developed Type III and Type IV inhibitors exhibit excellent kinome selectivity but often lack selectivity against members of the targeted kinase subfamily.⁴¹ Furthermore, the purely allosteric Type IV inhibitors are generally characterized by reduced potency, when compared to active site-directed inhibitors. This is likely to result from the fact that they bind to much flatter protein-protein interaction regions, which remain difficult to inhibit with small molecule inhibitors.⁴²

Bivalent kinase inhibitors that can target two different sites simultaneously are classified as Type V inhibitors. Joining any combination of the previously described Type I-IV with an optimized linker can generate Type V inhibitors. By combination of an allosteric inhibitor with an active site-directed inhibitor in this manner, one would theoretically be able to reinforce the affinity of Type IV compounds while retaining their selectivity.⁴²

Most recently, covalent kinase inhibitors, also termed Type VI inhibitors, have experienced a renaissance in drug discovery. In covalent inhibition, small molecules are designed to undergo a bond-forming event after being properly oriented under equilibrium binding conditions by classical non-covalent molecular interactions. The bond-forming event can result in covalent linkage, durable enough to be irreversible within the target proteins half-life, which theoretically allows for complete target inactivation not achievable by reversible inhibition.⁴³ In almost all cases, covalent bond formation is achieved by means of reactive electrophilic groups, the so-called “warheads”, that target poorly conserved nucleophilic residues like cysteine, lysine, threonine, serine and in some recent examples also methionine.⁴⁴⁻⁴⁵ Drugs that covalently bind to target proteins have a long history that dates back to the late 1800s when *Bayer* started manufacturing acetylsalicylic acid (Aspirin) for the treatment of

inflammation and pain. Interestingly, the irreversible mechanism with which Aspirin inhibits cyclooxygenase (COX)-1 and 2 was not discovered until the 1970s.⁴³ In the same vein, several other covalent drugs were developed serendipitously, including famous examples, such as the penicillin and cephalosporin antibiotics,⁴⁶ the proton pump inhibitors omeprazole and lansoprazole⁴⁷ and the antiplatelet agent clopidogrel.⁴⁸ Nonetheless, the intentional development of covalent kinase modifiers was for a long time approached with caution, due to safety concerns regarding the formation of non-specific highly reactive electrophilic metabolites that were hypothesized to cause drug-induced idiosyncratic toxicities and immunogenic responses.⁴⁹⁻⁵⁰ Today, these concerns have been mitigated by the development of covalent kinase inhibitors with less reactive warheads, such as acrylamide- and nitrile-containing drugs that are generally safe and are used clinically with impressive success. As of today, seven of the 62 protein kinase inhibitors approved by the FDA are irreversible covalent modifiers.⁵¹

1.2. The Nek-Family of Protein Kinases

The never in mitosis-gene A (NIMA) related kinase (Nek)-family, originally discovered by genetic studies of the fungus *Aspergillus nidulans*, represents a fourth important family of mitotic kinases, alongside the well known cyclin-dependent kinase (CDK), Polo and Aurora kinase families.⁵² While the filamentous fungus *Aspergillus nidulans* possesses only a single NIMA-gene, the number, complexity and range of functions of NIMA-related kinases have significantly expanded in numerous higher eukaryotes over the course of evolution. Originally, the fungal serine/threonine kinase NIMA is required for the active nuclear transport of the cyclin-dependent kinase 1 (CDK1) coding CDC2-gene, which is essential for functional mitotic regulation.⁵³⁻⁵⁴ Furthermore, NIMA is crucially involved in chromosome condensation by phosphorylation of histone H3 and regulates the separation of the nuclear envelope during mitosis.⁵⁵⁻⁵⁶

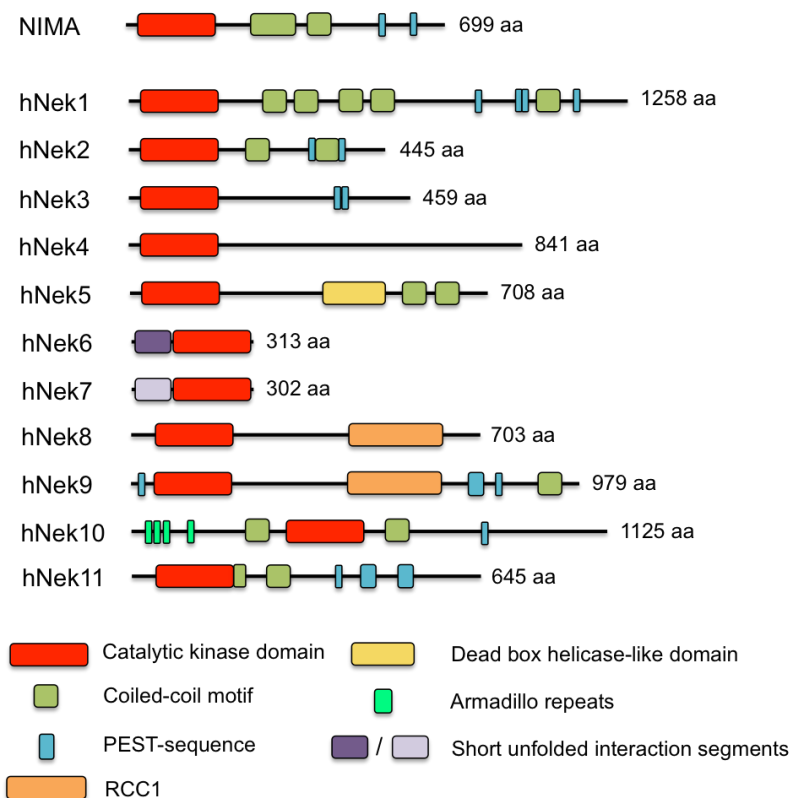


Figure 8: Schematic representation of the structural alignment of human Nek kinase family key features with the fungal *Aspergillus nidulans* NIMA kinase.⁵⁷ Colored bars indicate the relative positions of significant motifs and regions. The lengths of the full proteins are indicated by number of amino acids at the C-terminus of the proteins. For Nek11, only the 74 kDa-Nek11L isoform is shown. aa, amino acids; NIMA, never in mitosis-gene A kinase; RCC1, Regulator of chromosome condensation 1.

In humans, a total number of 11 Nek-family members are present, whose functions are no longer limited to cell cycle regulation but have broadly extended to fulfil crucial roles in ciliogenesis, the DNA-damage response (DDR) and apoptosis as well. Despite the fact that the human Nek kinases display low overall sequence homology with NIMA, many structural features remain highly conserved (Figure 8).⁵⁸ For example, all human Nek kinases possess a conserved kinase domain, which is N-terminally located in most members. Nevertheless, the human homologs have vastly different lengths and vary significantly with regard to their regulatory domains. With the exception of Nek3, 4, 5 and 6, all Nek-family members feature coiled-coil domains that act as classical protein-protein-interaction modules mediating oligomerization with a wide range of interactors.⁵⁷

Like NIMA, 6 of the 11 human Neks feature potential PEST-sequences, rich in proline (P), glutamate (E), serine (S) and threonine (T) residues, which are primed for proteasomal degradation that is thought to be regulated by fine-tuned phosphorylation events inside the PEST-sequence or in neighbouring domains.⁵⁹⁻⁶⁰ Despite these similarities, some of the Nek kinases feature domains with unique functionalities, such as regulator of chromosome condensation (RCC1) repeats in Nek8 and 9, a predicted DEAD-box helicase-like domain in Nek5 and several armadillo repeats in Nek10.⁵³ Once more, this structural diversity points to the acquisition of new functions by evolutionary diversification.

1.2.1. Functional and Disease Roles of Nek-Family Kinases

In general, the Nek family members participate in more than one functional context, with the exception of Nek3, which until today has only been attributed to cell cycle and mitosis regulation (Figure 9). In particular, three major functions, namely primary cilia formation, cell cycle regulation and the DDR, stand out as being frequently represented. Deregulations in these functions are known characteristics of several severe diseases like ciliopathies, neuronal and bone diseases and various cancers.⁵² Despite the fact that information about the involvement of Nek kinases in the development and progression of several diseases has accumulated in recent years, there is still a great lack of knowledge regarding most members of this important kinase family, spanning from missing structural information and interactome studies to lacking pharmacological approaches.^{57, 61-63}

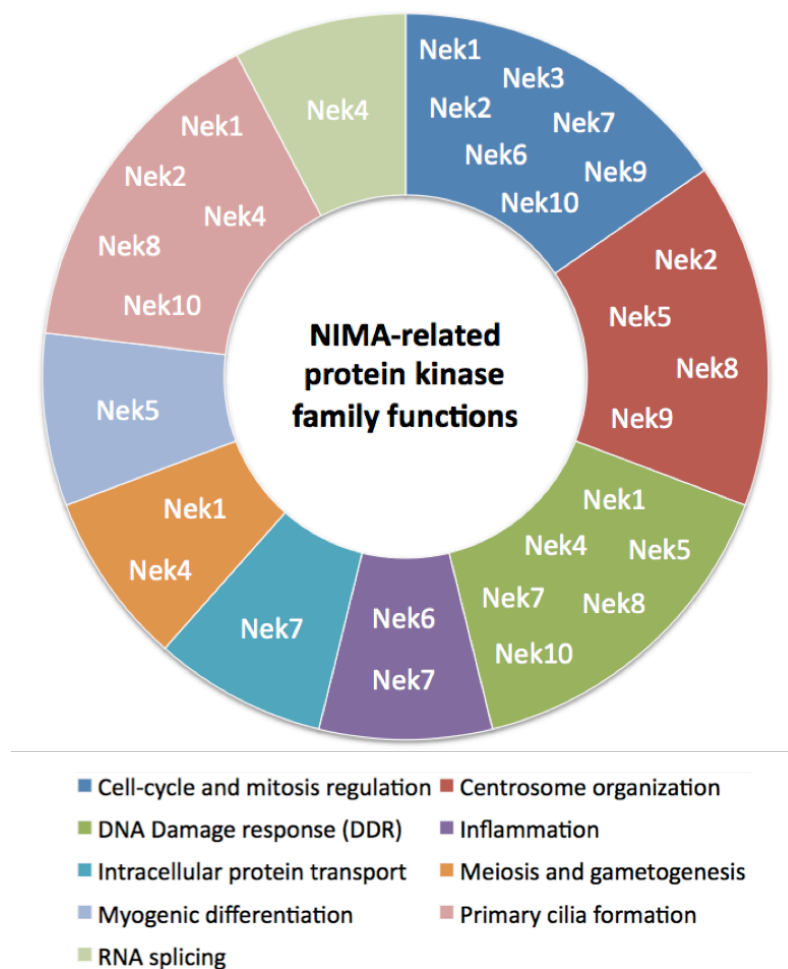


Figure 9: Schematic overview of the functions of Nek (Never in Mitosis A (NIMA)-related kinase) family members. Functions are color-coded according to the subtitles shown at the bottom.⁵²

Nek1, Nek2 and Nek7 are among the better-studied representatives of the family and their atomic structures have been deposited in the PDB.⁶⁴⁻⁶⁶ A detailed introduction to Nek1 will be given in the following chapter (see chapter 1.3.).

Human *NEK2* presents the best-studied human homolog and is the only Nek family member that has been extensively targeted by directed medicinal chemistry efforts. In recent years, several focused small molecule Nek2-inhibitors have been published.⁶⁷⁻⁶⁸ As Nek2 is the mammalian Nek family member most closely related to the parent NIMA, it is no surprise that its functions have been most prominently identified in the framework of cell cycle regulation and chromosomal integrity.⁶⁹⁻⁷⁰ In addition, a considerable number of studies have linked Nek2 to a high variety of cancer types, among them multiple myeloma, colorectal and hepatocellular carcinoma and malignant glioma, making Nek2 a much sought after oncology target.⁵² Furthermore, Nek2 has been linked to ciliary function in a study by Endicott *et al.* that identified a causative relationship between reduced motile cilia counts and abnormally looped hearts in *NEK2* overexpressor and *NEK2* morphant xenopus embryos.⁷¹

NEK3 is one of the least-studied homologs, which has, as previously mentioned, only been marginally linked to function in cell cycle regulation. Despite the fact that elevated Nek3 levels were identified during the G0-arrested cell cycle, no cell cycle dependent changes in Nek3 activity and no effects on cell cycle progression were observed upon antibody-mediated Nek3 activity inhibition in mice and in murine *NEK3* overexpression mutants.⁷² Nonetheless, Nek3 has been shown to be involved in breast cancer development and *NEK3* overexpression was detected in tissues of thyroid cancer and gastric cancer patients, where it was linked to poor disease progression and poor overall survival.^{63, 73-74}

Similarly to Nek3, the cellular functions of Nek4 and Nek5 have not been fully elucidated yet. While functional relevance in primary cilium assembly,⁵² regulation of microtubule stabilization,⁷⁵ the DDR⁷⁶⁻⁷⁷ and RNA splicing⁷⁷ has been suggested for Nek4, Nek5 is implied to function in myogenic differentiation,⁷⁸ centrosome integrity⁷⁹ and the DDR.⁸⁰ An association of Nek4 and Nek5 with human cancers is likely, given the suggested involvement of Nek4 and Nek5 in the DDR, but there is little supporting data in the literature and further studies are needed to confirm implied connections.⁵²

Nek6 and Nek7 are the shortest representatives of the NIMA-related kinase family and bear high structural similarity (Figure 8). Moreover, Nek9 was shown to activate both Nek6 and Nek7 in a mitotic cascade by phosphorylation of equivalent serine residues.⁸¹ Furthermore, Nek6 and Nek7 share redundant functions in mitosis and cytokinesis,⁸² and have both been

linked inflammatory disorders.⁸³⁻⁸⁴ However, substantial differences in their short unfolded N-terminal segments lead to varying interaction partners and divergent cellular functions. Nek7, unlike Nek6, also participates in RNA processing, intracellular protein transport, mitochondrial regulation and DNA repair.⁸⁵ In addition to their potential as cancer drug targets, a feature commonly shared across Nek family kinases, Nek6 and Nek7 might be established as future targets or biomarkers for inflammatory disorders, such as ulcerative colitis in the case of Nek6,⁸³ or diabetes and systemic lupus erythematosus in the case of Nek7.^{84,86} Only recently, de Donato *et al.* identified a Nek6-inhibitor with promising inhibitory activity, which showed antiproliferative activity against a panel of human cancer cell lines and displayed a synergistic effect with cisplatin and paclitaxel in a BRCA2 mutated ovarian cancer cell line. Interestingly, the developed small molecule inhibitor was selective against the more closely related Nek7 kinase domain, although it decreased Nek1 activity to a comparable degree.⁸⁷

The functions of Nek8 are poorly described in the literature. *NEK8* was first mentioned as the causal mutated gene in juvenile autosomal recessive cystic kidney mice, which was also confirmed by cross-species analysis in zebrafish.⁸⁸ Later, an *in vivo* study by Sohara *et al.* provided evidence for the localization of Nek8 in primary cilia and linked Nek8 to polycystic kidney disease (PKD)-causative glycoprotein polycystin-2 (PC2) by co-immunoprecipitation analysis.⁸⁹ The mutation is located in the Nek8 C-terminal RCC1-domain, whose precise function remains unclear.⁵⁷ More recently, it was shown that *NEK8* mutant mice and Nek8-lacking cells accumulate DNA double-strand breaks (DSBs), highlighting Nek8 as a critical component of the DDR.⁹⁰

Nek9, also termed Nercc1, is one of the larger Nek-family representatives and features an extensive C-terminal regulatory domain that contains an RCC1-motif, a coiled-coil oligomerization motif and several PEST-sequences.⁵⁷ *In vivo*, Nek9 is only partially activated during early mitosis and localizes to spindle poles and centrosomes, implying important functions in microtubular organization during cell division. *In vitro*, Nek9 was shown to autoactivate and bind to γ -tubulin, a crucial player in microtubule nucleation and orientation.⁹¹ Moreover, Nek9 was recently identified as a potential biomarker for head and neck cancer, in a quantitative chemical proteomics study.⁹²

Being the most structurally divergent, the less-studied Nek10 holds a special role in the Nek-family. Unlike in the other Nek kinases, the Nek10 catalytic kinase domain centrally located and flanked by two regulatory coiled-coil motifs. Furthermore, four repetitions of an armadillo repeat motif are present at the N-terminus, which have in other serine/threonine

kinases been shown to recruit interaction partners that influence substrate recognition, regulate phosphorylation or enhance function by non-phosphorylating mechanisms.⁹³⁻⁹⁵ At the C-terminus, Nek10 also features a PEST-sequence, which manifests the hypothesis that Nek10 levels and activity are finely regulated by several mechanisms and interaction partners.⁵⁷ Despite the intriguing nature of these features, there is a large gap in knowledge regarding the functions of Nek10. However, involvement in the cell cycle, more specifically in maintenance of the G2/M checkpoint, has been identified for Nek10 in post UV-irradiation events.⁹⁶ Moreover, Nek10 has been associated with melanoma and the development of breast cancer, where it may serve as a diagnostic precision-biomarker in the future.⁹⁷⁻⁹⁸

The lesser-studied Nek11 appears in two different isoforms, more specifically, a long 645 amino acid residue variant termed 74 KDa-Nek11L and a short 470 amino acid residue variant named 54 KDa-Nek11S. The N-terminally-located kinase domain bears high similarity with the catalytic domains of Nek3 and Nek4, while Nek11 features two C-terminal coiled-coil motifs, in contrast to Nek3 and Nek4.⁵² Nek11 was first discovered in the context of DNA replication, where its upregulation in response to genotoxic stress was demonstrated by cellular treatment with various DNA-damaging agents and replication inhibitors.⁹⁹ Furthermore, the association of *NEK11* downregulation with drug-resistance in ovarian cancer cells was suggested in a recent bioinformatics study.¹⁰⁰

1.3. Protein Kinase Nek1

The more widely studied Nek1 is a dual serine/threonine protein kinase that also possesses some tyrosine kinase activity, albeit to a lesser degree.¹⁰¹ Nek1 is the single largest member of the Nek family of protein kinases and also features the highest number of coiled-coil motifs and PEST-sequences in its C-terminal regulatory domain (Figure 8).

Since its discovery in a murine cDNA expression library screen, this mammalian homolog of the fungal NIMA cell cycle regulator has attracted widespread attention due to its pleiotropic function and its association with a number of diseases in humans.^{52, 57, 102} The ever-growing interest in this remarkable kinase was first sparked by findings that linked NEK1 to two independent mutant alleles (*kat* and *kat^{2J}*), which spontaneously arose from two inbred mouse strains, causing various defects, such as male sterility, dwarfing, facial dysmorphism, anemia and a progressive PKD.¹⁰³⁻¹⁰⁴ PKD is the most common genetic cause for renal failure in humans and is characterized by the relentless growth of large fluid-filled cysts and the accompanying destruction of the adjacent renal parenchyma.¹⁰⁵ The role of Nek1 in the onset and progression of PKD is described in the following subchapter (see chapter 1.3.1.).

As suggested by the pleiotropic nature of the phenotypes observed in Nek1 deficient mice, Nek1 participates in a large variety of basic cellular functions. In addition to its function in primary cilium formation, Nek1 plays a crucial role in cell cycle control and in particular the DDR.⁵⁸ Eventually, Nek1-deficient cells accumulate unrepaired DSBs leading to genomic instability, chromosomal damage and finally cell death.¹⁰⁶⁻¹⁰⁷ A remarkable feature of Nek1, which has only recently been revealed, is its ability to limit apoptotic cell death even after severe damage has occurred already.¹⁰⁸ Taken together, these functions highlight Nek1 as an outstanding target for novel anticancer therapeutics.¹⁰⁹ A description of the functional roles of Nek1 in cell cycle regulation, the DDR and apoptosis and the resulting implications for human cancer treatment are provided in a later subchapter (see chapter 1.3.2.).

Interestingly, NEK1 mutations have not only been linked to defects of ciliogenesis, like PKD, short-rib polydactyly syndrome (SRPS) type Majewski and Mohr-Laussen syndrome but also to other inheritable diseases, such as amyotrophic lateral sclerosis (ALS). SRPS is a rare lethal skeletal dysplasia, characterized by severe intrauterine growth restrictions that cause peculiar features like characteristic facial dysmorphism, polydactyly and drastically shortened ribs and lungs in infants.¹¹⁰ *NEK1* mutations have been identified as the cause for disturbed cilia formation that can negatively affect signal transduction in various pathways, leading to the

pleiotropic clinical defects observed in SRPSs.¹¹¹⁻¹¹² To give an example, molecular analysis of fetal tissue revealed a paternal-origin heterozygous splice site mutation in *NEK1*-gene intron 7 that caused an alteration of the splice acceptor site (IVS7-1 G>A).¹¹³

Mohr-Laussen syndrome, also oral-facial-digital syndrome type II, is part of a group of related disorders with a combination of oral, facial and digital anomalies, linked to mutated variants in several ciliary genes. With the use of whole-exome sequencing, a novel heterozygous *NEK1* variant (464G>C) was identified in two siblings with Mohr syndrome, which disturbs normal splicing in an essential region of the kinase domain.¹¹⁴

ALS, on the other hand, is a fatal neurodegenerative disorder that causes the selective death of motor neurons and is associated with an altered DDR.¹¹⁵ Approximately 90 to 95% of all ALS cases appear sporadically without any known cause, while the rest are familial cases linked to over 20 causative genes.¹¹⁶ The discovery of the *NEK1*-genes association with ALS was accompanied by an unprecedented attention by mainstream media, as the corresponding study was made possible by funds raised in the so-called “ice-bucket challenge” that went viral on social media.¹¹⁷ Two independent *NEK1* variants, more specifically a loss-of-function variant and a p.Arg261His mutant, were identified by whole-exome screening analysis.¹¹⁸ In total, these two *NEK1* variations are present in 3.1% (95% CI 2.5–3.8%) of all sporadic and familial ALS cases in European and North American populations, ranking them among the most common genetic causes of the disease.¹¹⁹⁻¹²⁰

Despite the crucial role of Nek1 in a broad variety of diseases and its outstanding potential as a target for anticancer therapeutics, no directed medicinal chemistry efforts toward potent and selective Nek1 inhibitors have been published in the past.^{52, 109} Nevertheless, finding suitable inhibitors for Nek1 is not trivial, as indicated by the low hit rates of previously reported screenings. In the first attempt to pinpoint structural elements that influence Nek family inhibitor specificity, Moraes *et al.* screened a commercial 80 compound library (Inhibitor Select™ 96-Well Protein Kinase Inhibitor Library II, *Calbiochem*), against truncated Nek1 and Nek2 activation loop mutants, five recombinant Nek6 variants and wild-type Nek7 in a thermal shift assay (TSA).¹²¹ A significant thermal shift ($T_m \geq 4.0$ °C) against Nek1 was observed for only one compound, the rather promiscuous c-Jun N-terminal kinase (JNK) inhibitor *SP600125*.¹²² In contrast, 10 and 5 hit compounds were identified for wild-type Nek7 and the Nek2 mutant respectively.¹²¹ Melo-Hanchuk *et al.*, who screened the purified Nek1 kinase domain against a library of protein kinase inhibitors using differential scanning fluorimetry (DSF),¹²³ described a similar situation in a published report.⁶⁴ According to the

authors, this screening had a low hit rate compared to other protein kinases that were previously tested against this compound library. In the authors' opinion, the low hit-rate may be related to specific features of the unusual ATP-binding site of Nek1. Unfortunately, the authors did not provide any information on library size and composition. A kinome-wide selectivity screen of over 20000 compounds, performed by Posy *et al.*, provided further substantial evidence for the modest tractability of the Nek-family kinases and Nek1 in particular. Low hit rates (calculation based on <13% of control) were determined for six Nek kinases (Nek1, Nek2, Nek5, Nek6, Nek7, Nek9), between 0.1% for Nek1 and 3.2% for Nek7. For comparison purposes, the commonly referenced FMS-like receptor tyrosine kinase-3 (FLT3) had a hit rate of 15% in the same selectivity screen.^{61, 124}

1.3.1. The Role of Nek1 in Polycystic Kidney Disease (PKD)

PKD, the most common inherited nephropathy in humans, is characterized by the growth of fluid-filled intrarenal cysts, which causes severe kidney enlargement and damage.¹⁰⁵ In humans, PKD comes in two forms, termed autosomal-dominant PKD (ADPKD) and autosomal-recessive PKD (ARPKD), which differ significantly with regards to age of onset, prevalence, cyst localization and causative gene mutations. Interestingly, both forms are in themselves genetically and phenotypically heterogeneous, despite their monogenetic inheritance.¹²⁵

Autosomal-Dominant Polycystic Kidney Disease (ADPKD)

ADPKD is the more common form, with a reported prevalence between 1 in 400 and 1 in 1000 live births, according to early studies from Denmark (1958)¹²⁶ and Minnesota, USA (1983)¹²⁷. More recently, an annual incidence of 0.62 per 10000 was determined in an US nationwide epidemiologic study between the years 2013 and 2015. Strikingly, young females are diagnosed with ADPKD at nearly twice the rate of young men in this study, although a reverse trend is visible at ages 65 and older, which is hypothesized to result from more frequent ultrasound scans in females during child-bearing years.¹²⁸ Determining characteristics of ADPKD are the adult onset of gradual cystic growth throughout all kidney areas and other accompanying abnormalities outside the kidneys, such as hepatobiliary changes and intracranial arterial aneurysms.¹²⁹⁻¹³⁰

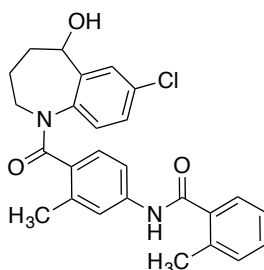
In ADPKD patients, approximately 1% of nephrons develop cysts, which are fluid-filled outgrowths from the renal epithelium, that induce stress in adjacent nephrons, thus promoting apoptotic events that in turn increase the likelihood of cyst formation. This feedback loop accumulates severe renal damage that leads to chronic kidney disease (CKD) and finally end-stage renal disease (ESRD) (Figure 10).¹³¹

Until today, there is no cure for ADPKD, but a new treatment is available that has been shown to slow the progression of ADPKD and to delay the onset of CKD and ESRD. The selective vasopressin V2 receptor antagonist Tolvaptan, marketed by *Otsuka Pharmaceutical Co., Ltd.* under the brand name *Jinarc*[®], was originally developed for the treatment of syndrome of



Figure 10: A photograph illustrating the gross pathologic changes in a human case of polycystic kidney disease (PKD). This image is in the public domain and comes from the Centers for Disease Control and Prevention's Public Health Image Library (PHIL, identification number #861, CDC/ Dr. Edwin P. Ewing, Jr.).

inappropriate antidiuretic hormone secretion (SIADH) patients but received European approval for treatment of ADPKD by the European Medicines Agency (EMA) in 2015 (Figure 11). Although Tolvaptan was also approved in Canada and Japan, the FDA delayed approval in the USA until 2018, due to persisting concerns regarding therapeutic effectiveness and potential hepatic injury.¹³² Tolvaptan is the first specific drug available on the market to delay the progression of ADPKD for patients with fast progression of the disease in early CKD stages.¹³³ For patients with ESRD, which is associated with an increased mortality and occurs



Tolvaptan

Figure 11: Chemical structure of the selective vasopressin V2 receptor antagonist Tolvaptan, marketed by *Otsuka Pharmaceutical Co., Ltd.* under the brand name *Jinarc*[®]. *Jinarc*[®] received approval for treatment of ADPKD patients with fast progression of the disease in early CKD stages by the EMA in 2015.¹³³

as a result of ADPKD in up to 75% of patients by 70 years of age, dialysis or kidney transplantation are the only treatment options.¹³⁴⁻¹³⁵

Most commonly, ADPKD is caused by mutations in the polycystin 1 (PC1) and 2 (PC2) coding genes *PKD1* and *PKD2*, with ~85% of patients carrying their mutation in the *PKD1* gene, ~15% in the *PKD2* gene and ~5-10% carry genetically unresolved or rare mutations in other loci.¹³⁶⁻¹³⁷ PC1 and PC2 are ciliary membrane glycoproteins that function independently, or as a heterodimeric complex that is formed by interaction of C-terminal coiled-coil motifs present in both proteins. Trafficking of PC1 to membranes of primary cilia is essential for tubulogenesis and was shown to rely on PC2, and thus formation of the PC1/PC2-complex, in a dose-dependent manner.¹³⁸ Upon enrichment in the ciliary membrane, the PC1/PC2-complex is thought to enable PC2 to function as an ion channel (Figure 12).

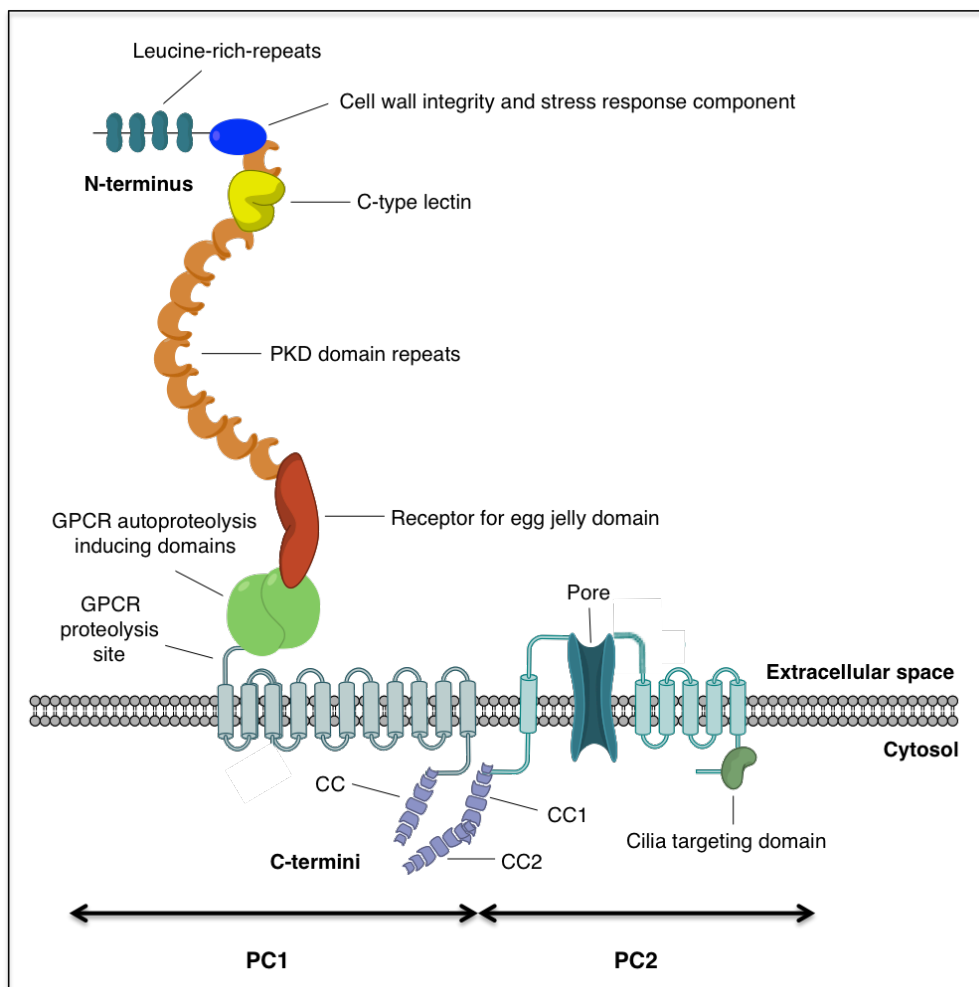


Figure 12: Schematic representation of domain organization for proteins implicated in autosomal-dominant polycystic kidney disease (ADPKD). The structures of polycystin 1 (PC1), polycystin 2 (PC2) are shown (not to scale). Redrawn from Bergmann *et al.*¹²⁵ CC, coiled coil; GPCR, G protein-coupled receptor, PKD, polycystic kidney disease.

However, technical hurdles in channel-activity measuring methods have until recently hampered exact understandings of the underlying molecular mechanisms. As described in a recent report by Ha *et al.*, the artificial reconstruction of the PC1/PC2-complex, in the plasma membranes of HEK293 and mIMCD3 cells, allowed for the elucidation of an outward-directed rectifying channel function. Furthermore, it was proposed that autoproteolytic cleavage of the PC-1 N-terminus releases a soluble protein fragment that acts as an intrinsic agonist *in vivo*, sufficient for activation of the complex.¹³⁹ In addition, PC2 also localizes in the endoplasmic reticulum (ER), mediating Ca²⁺ efflux from this organelle,¹⁴⁰ and the multimeric PC1/PC2-complexes modulate several growth-related signaling pathways.¹⁴¹ Alterations in these pathways trigger secondary events that further change cellular growth signaling, planar cell polarity and cellular metabolism, thus impairing healthy fluid transportation and cell adhesion while also mediating increased proliferation, differentiation and apoptosis.¹⁴²⁻¹⁴⁴

Autosomal-Recessive Polycystic Kidney Disease (ARPKD)

ARPKD is the less common form of PKD, with a reported incidence of 1 in 26500 live births, in North, Central and South America.¹⁴⁵ Generally, data on ARPKD prevalence is more scarcely available and varies significantly between populations. For example, a much higher prevalence of 1 in 8000 live births was reported for Finland, which is suggested to result from the finnish populations genetic isolation.¹⁴⁶ Characteristic for ARPKD are the early, often perinatal onset of cystic growth, which is mainly restricted to the collecting ducts and leads to greatly enlarged kidneys.¹²⁵

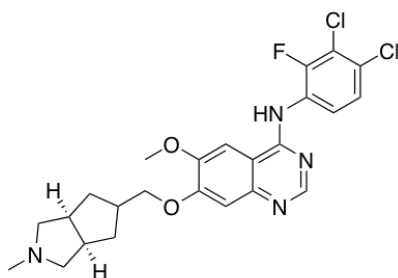
The clinical course in ARPKD patients is usually much more severe than in ADPKD patients and often accompanied by additional complications like heart failure, pulmonary hypoplasia and arterial hypertension in perinatal cases.¹⁴⁷ High mortality rates of up to 40%, mainly a consequence of the impaired pulmonary status of neonatal ARPKD infants, have been reported.¹⁴⁸ Although survival rates improve drastically after the perinatal period (one-year survival: ~85%; 10-year survival: ~82%), an accompanying congenital hepatic fibrosis (CHF) manifests in many infantile and juvenile cases.¹⁴⁹ CHF, a pathological condition resulting in the abnormal proliferation and accumulation of scar tissue in the liver, often leads to life threatening complications like cholangitis, an infection of the bile ducts, and hepatocellular carcinoma (HCC).¹⁵⁰ In patients who survive into adulthood, renal size in relation to body mass often decreases and renal function remains stable over many years. However, the risk

for renal failure at a higher age, mainly due to development of macroscopic cysts and interstitial fibrosis, remains elevated.¹⁵¹

Currently, there is no cure for ARPKD and treatment options are limited to the management of specific symptoms, apparent in each individual. In severe cases in newborns, invasive procedures can assist the maintenance of kidney, liver, and lung functions. Peritoneal dialysis is required during the first days of life, for patients with reduced urine production or no passage of urine, while mechanical ventilation can assist breathing in pulmonary hypoplasia cases and a portacaval shunt can relieve high blood pressure off the portal vein.¹²⁵ Alternatively, arterial hypertension can be treated by medication with angiotensin-converting enzyme (ACE) inhibitors and nitrous oxide is used to provide oxygen to the lungs.¹⁵²⁻¹⁵³

Furthermore, the unique multi-kinase inhibitor Tesevatinib was investigated for its therapeutic potential in pediatric ARPKD patients (age 5-12) in a phase I clinical trial, but results are not yet available (Figure 13).¹⁵⁴ Tesevatinib is also under current investigation in an active phase II study for ADPKD.¹⁵⁵ Interestingly, Tesevatinib targets multiple kinases that are involved in abnormal signal transduction events in both ADPKD and ARPKD, as cyst formation not only requires a PKD mutation but also simultaneous cell proliferation.

More specifically, Tesevatinib inhibits proto-oncogene tyrosine-protein kinase (c-SRC), which decreases activity of both the cyclic adenosine monophosphate (cAMP) and endothelial growth factor receptor (EGFR) pathways, as well as fetal liver kinase 1 (FLK1), an angiogenesis-driving kinase that promotes cystic growth.¹⁵⁶⁻¹⁵⁷ In a recent study by Sweeney *et al.*, Tesevatinib stunted the progression of renal cystic disease in two well characterized rodent ARPKD models without obvious evidence for toxicity or detrimental effects.¹⁵⁸



Tesevatinib

Figure 13: Chemical structure of multi-kinase inhibitor Tesevatinib, which is currently under investigation for its therapeutic potential in ARPKD (phase I) and ADPKD (phase II).

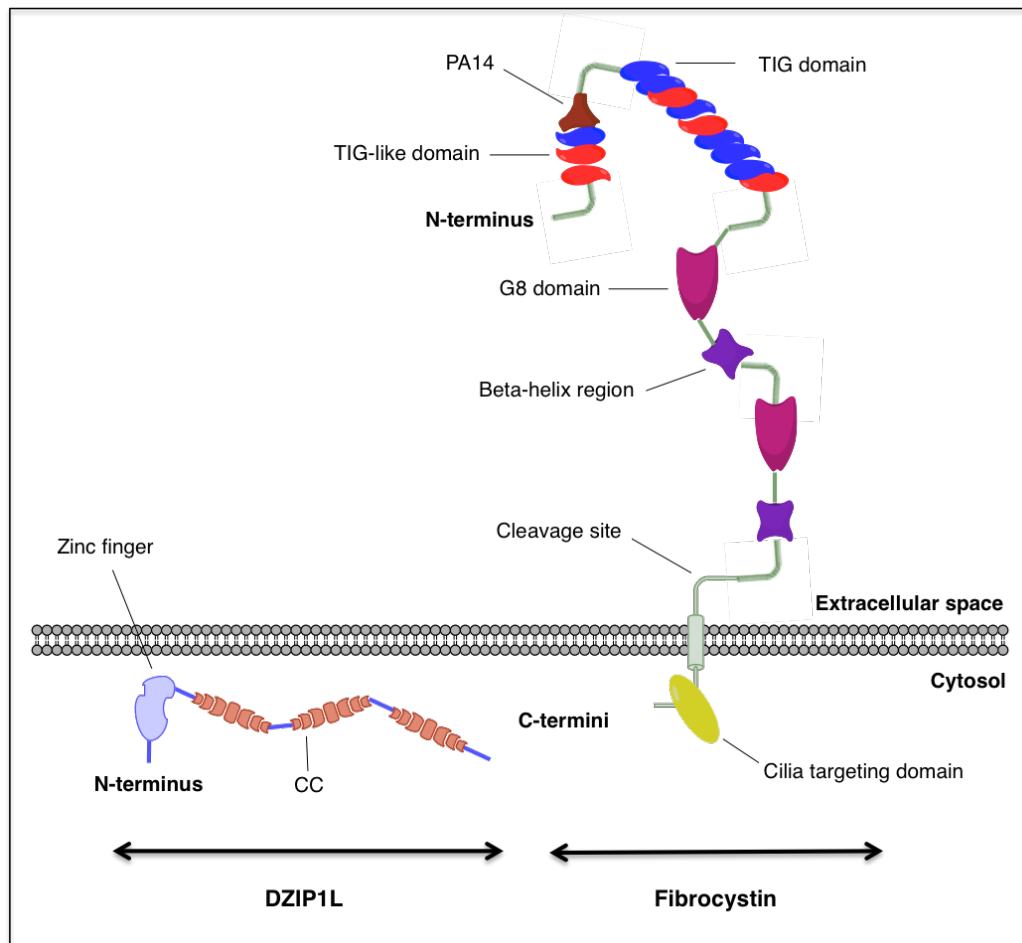


Figure 14: Schematic representation of domain organization for proteins implicated in autosomal-recessive polycystic kidney disease (ARPKD). The structures DAZ-interacting protein 1-like protein (DZIP1L) and membrane-bound fibrocystin are shown (not to scale). Redrawn from Bergmann *et al.*¹²⁵ CC, coiled coil; PKD, polycystic kidney disease.

ARPKD is mostly caused by mutations in *PKHD1*, which codes for fibrocystin, a transmembrane receptor-like protein that localizes mainly to the primary cilium in both the renal tubule and the bile ducts but also to other organelles like the centrosome.¹⁵⁹⁻¹⁶⁰ Several transcripts are produced from the *PKHD1* messenger RNA (mRNA) by alternative splicing, with the longest transcript encoding a 4074-residue protein that features a large N-terminal extracellular domain, a transmembrane domain and a short C-terminal cytoplasmic tail (Figure 14).¹²⁵ The extracellular domain features several functional subdomains as well as a cleavage site for notch-like proteolytic processing that results in release of the carboxy-terminal tail, which can translocate to the nucleus and possibly regulates the expression of cystic-growth related genes.¹⁶¹⁻¹⁶² Fibrocystin functions are not fully elucidated yet; however its early expression suggests an involvement in primary tubule morphogenesis.¹⁶³ The C-terminus of fibrocystin was shown to interact with the N-terminus of PC2 and an absence of

fibrocystin reduced PC2 expression in a rodent model. In the same study, a lack PC2 did not influence fibrocystin levels, suggesting that PC2 may function immediately downstream of fibrocystin *in vivo*.¹⁶⁴ Alongside its involvement in cilia, fibrocystin probably also acts in other subcellular functional roles. In another study, three different splicing variants, with evidence for distinct subcellular localization, were detected by immunostaining, suggesting that PKHD1 encodes membrane-bound and soluble isoforms with alternate functions.¹⁶⁵

In addition to *PKHD1*, *DZIP1L*, which encodes DAZ interacting protein 1-like (DZIP1L) protein, was shown to be a second gene involved in ARPKD pathogenesis. The soluble zinc-finger protein DZIP1L localizes to centrioles and to the distal ends of basal bodies, where it interacts with septin2 and the PKD proteins PC1 and PC2.¹⁶⁶ Septin2 is a cytoskeletal GTPase, implicated to function as part of the periciliary diffusion barrier at the ciliary transition zone and may therefore also contribute to ARPKD severity.¹⁶⁷

Nek1 in the Pathogenesis of Polycystic Kidney Disease (PKD)

Upadhyaya *et al.* identified first evidence for the link between *NEK1* and PKD, by fine-mapping genome analysis and subsequent cloning and expression analysis of transcribed sequences from the mutated gene-region in a previously developed PKD mouse-model (*kat*^{2J}).¹⁰⁴ Mutant *kat*^{2J}-mice exhibit a slowly progressing form of PKD, with latent onset of cystogenesis and similarity of the renal pathology to human ADPKD. Furthermore, these animals show pleiotropic phenotypes, including dwarfing, male sterility, facial dysmorphism, anemia and a cystic choroid plexus.^{103, 168} The link between *NEK1* and PKD was further strengthened by an interactomic study, which indicated strong interactions of the PKD-associated proteins kinesin-like protein (KIF3A), α -catulin and tuberin with the central coiled-coil region of Nek1.¹⁶⁹ Mutations in KIF3A, a component of the intraflagellar transport system, lead to ciliary defects in mice,¹⁷⁰ whereas α -catulin was implicated to affect signalling pathways that regulate cell proliferation, including the canonical Wnt/ β -catenin signalling pathway that has been linked to renal cyst development in a rodent model.¹⁷¹⁻¹⁷² The role of tuberin in PKD has been elucidated in more detail. Intracellular trafficking of PC1 is disrupted in tuberin-deficient polycystic rat renal cells and reexpression of tuberin coding *TSC2* restored PC1 function in the cellular membrane. Tuberin was therefore identified as a key player in the functional localization of PC1, which suggests that tuberin also influences ADPKD severity.¹⁷³

With the involvement of the C-terminal Nek1 regulatory domain established, more evidence regarding the localization and kinase function of Nek1 in the PKD context accumulated over the years. More recently, prominently elevated Nek1 expression levels were identified in embryonic proximal tubule and podocyte precursor cells that decrease with kidney maturation, supporting the observation that Nek1 is of functional importance for healthy kidney development and the etiology of PKD.¹⁷⁴

Furthermore, Yim *et al.* revealed the first direct link between Nek1 kinase activity and PKD in 2011. Nek1 phosphorylates transcriptional coactivator with PDZ-binding motif (TAZ) protein at a site essential for the ubiquitination and proteasomal degradation of PKD-causative PC2. Underphosphorylation of TAZ was shown to create a negative feedback loop that leads to abnormal accumulation of PC2, as TAZ also primes Nek1 for degradation.¹⁷⁵ Based on a previous report by the same group, which showed that phosphorylation of mouse TAZ is crucial for maintaining PC2 levels and an altered PC1/PC2 ratio results in PKD, the authors concluded that the interaction between Nek1 and TAZ maintains PC2 levels at a level needed for healthy ciliogenesis.¹⁷⁶⁻¹⁷⁷

Taken together, the role of Nek1 in the pathogenesis of PKD has been well established. Nek1 is a key player in early ciliogenesis and functions in the PKD context not only through its C-terminal regulatory domain but also its kinase activity.

1.3.2. Roles of Nek1 in DNA repair, Apoptosis and Cancer

In addition to its functions in primary cilia formation, meiosis and gametogenesis, Nek1 has more recently been established as one of the key players in DNA-damage sensing, DNA repair and cell cycle control. A remarkable feature of Nek1 is its ability to also limit apoptotic cell death through non-DDR mechanisms, even after severe damage has occurred already. The involvement of Nek1 in the DDR and apoptosis regulation as well as related implications for Nek1-targeted cancer treatments are discussed in this chapter.

Nek1 in Homology-Directed Recombination-Mediated Repair (HRR) and Checkpoint Control

As previously stated, like most of the 11 members of the human Nek family, Nek1 plays a crucial role in cell cycle control and in particular the DDR.⁵⁸ Nek1 expression is upregulated upon chemical or radiative induction of DSBs and acts as a regulator of DNA repair by homologous recombination (HR).¹⁷⁸⁻¹⁷⁹ HR is a type of genetic recombination conserved in all organisms that plays a pivotal role in facilitating genetic diversity and maintaining genomic stability. During meiosis, paired parental chromosomes are aligned, replicated, crossed-over and finally resolved at the created junctions, to give recombined chromosomes with shuffled genetic information.

In homology-directed recombination-mediated repair (HRR) the same basic mechanism is applied to the accurate repair of complex DNA-damage, like in the form of DSBs, that can be caused by exposure to exogenous factors, such as chemical agents or UV and high-energy radiation.¹⁸⁰ Moreover, HR provides a mechanism that protects and reactivates stalled replication forks to prevent the formation of endogenous DNA-damage upon prolonged fork stalling.¹⁸¹ HRR is active in the S and G2 cell cycle phases, when a homologous template sister chromatid is present and follows one of several homology-mediated DSB repair sub-pathways.

The repair by HRR is initiated by resection of 5' DNA ends by the MRN complex together with the endonuclease Sae2/Ctp1/CtIP (Figure 15, step A). The single-strand DNA (ssDNA) binding replication protein A (RPA) then binds to the resulting 3' overhangs (step B). In the next step, BRCA2 replaces RPA with Rad51, which catalyzes the search of a homologous

sequence in the sister chromatid by invasion of one of the overhanging 3' ssDNA overhangs, thereby creating a "D-loop" (step C).¹⁸⁰ After formation of the synaptic complex of three homologously aligned DNA strands (ssDNA:Rad51:dsDNA), Rad51 is removed by the ATPase Rad54, which is activated by Nek1 through G2 phase specific phosphorylation (step D).¹⁸²⁻¹⁸³ The establishment of the unbound „D-loop“ primes DNA synthesis along the homologous template sequence (step E).

In the synthesis-dependent strand annealing (SDSA) pathway, DNA helicase Srs2 prevents the formation of a double Holliday junction (DHJ) and the extended invading strand anneals to the second 3' ssDNA overhang, dissolving the „D-loop“ (step F). DNA synthesis in the opposing direction, primed by the second overhang, and ligation of the newly synthesized strands completes the repair process without chromosomal crossover (step G).¹⁸⁰

In the double-strand break repair (DSBR) sub-pathway, a second Holliday junction is formed in absence of helicase Srs2, by second end capture of the opposing 5' ssDNA end into the "D-loop" (step H).¹⁸⁴ The DSBR pathway is completed by ligase-mediated recombination of the newly synthesized DNA strands, followed by cleavage of the Holliday junctions (step I). Junction cleavage can occur along the direction of DNA synthesis, resulting in non-crossover double strands, or across it, resulting in chromosomal crossover.¹⁸⁵

The aforementioned cell-cycle phase specific HRR-role of Nek1 was revealed in a key publication by Spies *et al.*, which demonstrated that Rad54 phosphorylation by Nek1 only occurs during G2-phase and not during S-phase. This led the authors to the conclusion that Nek1 orchestrates HRR with replication fork stability by way of permitting HRR by Rad51 removal from chromatin in G2-phase, or ensuring replication fork stability in S-phase.¹⁸²

Despite the fact that HRR is more accurate than its competing DNA repair mechanisms, the intrinsically mutagenic but faster non-homologous end joining (NHEJ), defects in HRR components can cause genomic instability and cancer.¹⁸⁶ As for example, women who inherit loss-of-function mutations in HRR genes, *BRCA1* or *BRCA2*, have a risk of up to 85% of developing breast cancer by the age of 70.¹⁸⁷ In the same vein, Nek1 has been linked to several cancer types and Nek1-deficient cells were shown to accumulate unrepaired DSBs leading to chromosomal damage and finally cell death.¹⁰⁶⁻¹⁰⁷

Interestingly, Nek1 has also been shown to interact with Ku80 in response to replication stress, suggesting an additional role for Nek1 in NHEJ, due to the fact that the Ku70/Ku80 heterodimeric complex is a key player in this alternative recombination mechanism.¹⁸⁸⁻¹⁸⁹

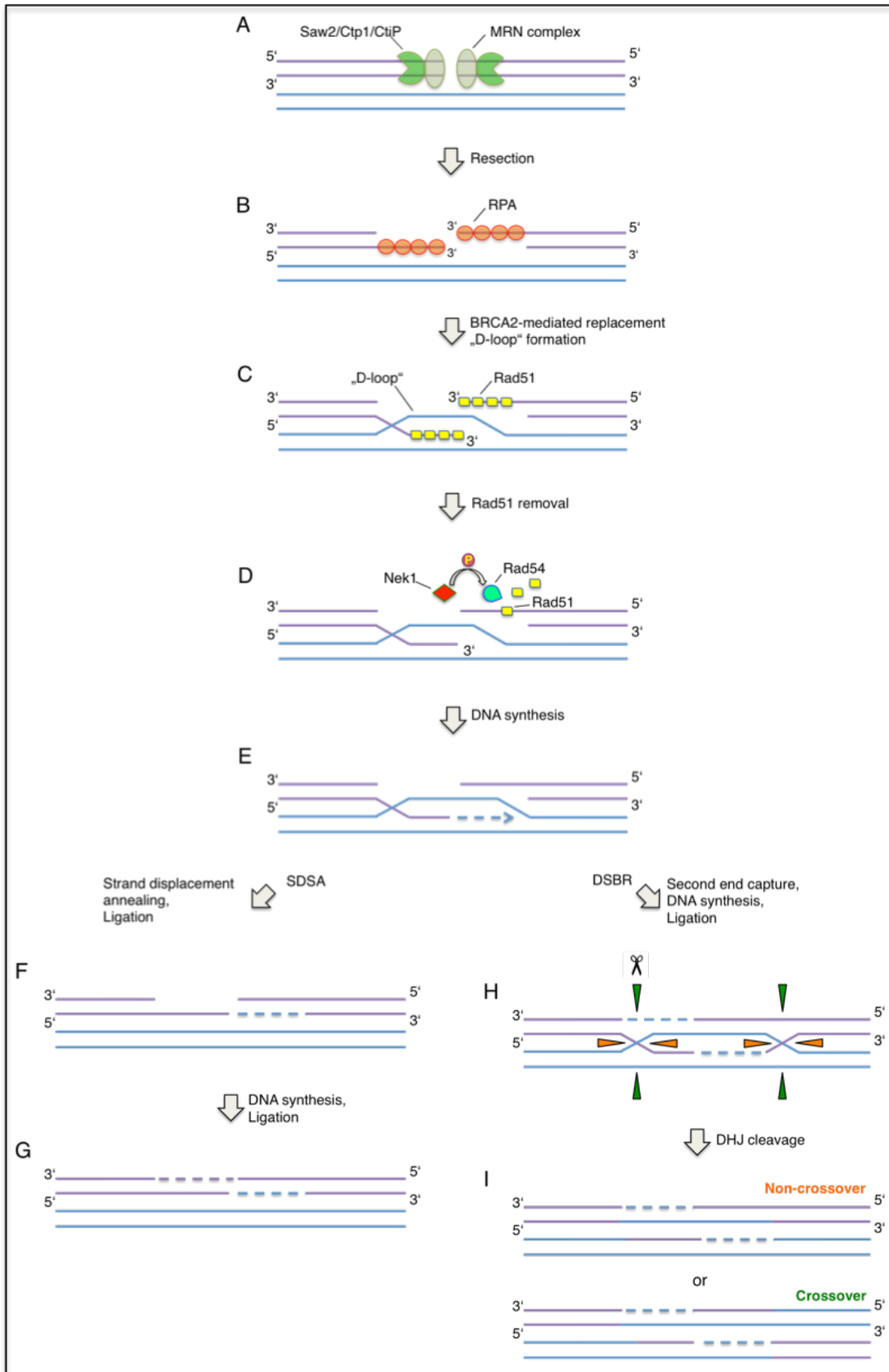


Figure 15: Homology-directed recombination-mediated repair (HRR) by synthesis-dependent strand annealing (SDSA) and double-strand break repair (DSBR). DHJ, double Holliday junction. Partly Redrawn from Cannan *et al.*¹⁸⁰

In addition to its roles in DNA repair, Nek1 is indispensable for proper DNA-damage sensing and cell cycle checkpoint control. As a first indicator, the activation of checkpoint kinases 1 and 2 (Chk1/Chk2) was shown to fail in cells without functional Nek1 in response to radiative stress.¹⁹⁰ First evidence pointed toward an unidentified mechanism, in which Nek1 promotes Chk1 activity independent from the canonical upstream mediators ataxia telangiectasia mutated (ATM) and ATM and Rad3-related (ATR).¹⁹¹ Soon thereafter, a direct link between Nek1 and Chk1 activation was identified by Liu *et al.*, who demonstrated that Nek1 in fact does play a critical role in priming the central DNA-damage sensing ATR/ATR-interacting protein (ATRIP)-kinase complex for a robust DNA-damage response. Once the ATR/ATRIP-complex is activated, ATR phosphorylates and activates its downstream kinase Chk1, which then coordinates a number of proteins involved in replication and repair of DNA as well as in cell cycle transitions, with the goal of suppressing genomic instability.¹⁹²

Taken together, Nek1 has been established as a key player in the DDR and several important cell cycle regulating functions have been attributed to this remarkable kinase. These features, alongside Nek1's involvement in numerous cancer types, designate Nek1 as an attractive new target in the development of DNA repair targeting cancer therapies, which have been successfully applied in the past and are promised a bright future.¹⁹³⁻¹⁹⁴

Nek1 as a Target for Cancer Therapies

A remarkable feature of Nek1 is its ability to also limit apoptotic cell death even after severe damage has occurred already. Direct phosphorylation of voltage-dependent anion channel 1 (VDAC1) by Nek1 closes the channel and prevents the efflux of preapoptotic signaling molecules, such as cytochrome c, thus limiting the caspase-mediated killing of cells (Figure 16).¹⁹⁵⁻¹⁹⁶ More recent evidence suggests that an activating phosphorylation by tousel-like kinase 1 (Tlk1) in the Nek1 kinase domain contributes to the phosphorylation of VDAC1 and that cancer cells can hijack this mechanism for survival through Nek1 overexpression.^{108, 197} Interestingly, the same activating phosphorylation on Nek1 Thr141 was found to also contribute to cell cycle regulation through a proposed Tlk1>Nek1>ATR>Chk1 signaling cascade. Overexpression of the Nek1-T141A mutant, as well as the addition of a Tlk1-inhibitor, hampered ATR and Chk1 activation in response to doxorubicin-induced DNA-damage. In the same study, first evidence for the cell cycle altering effects of this proposed

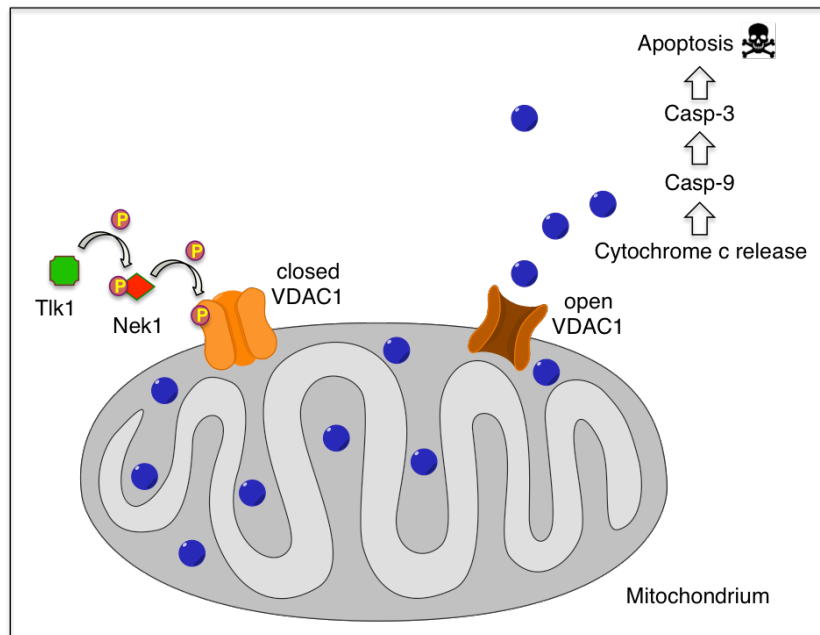


Figure 16: Schematic representation of VDAC1 regulation via the Tlk1>Nek1>VDAC1 axis. Tlk1 activates Nek1 by phosphorylation on Thr141 and direct phosphorylation of VDAC1 by Nek1 closes the ion channel (left). Efflux of cytochrome c through the open channel triggers caspase-mediated killing of cells through apoptosis (right).¹⁹⁵⁻¹⁹⁷

pathway was demonstrated. Tlk1 deprived cells skipped G1-phase arrest and exhibited intra-S-phase checkpoint activation when exposed to oxidative stress.¹⁹⁸

Conclusively, inhibition of Tlk1 or Nek1, either as a monotherapy or in combination with DNA damaging agents, might turn out as an effective way to influence the TLK1>Nek1>VDAC1 or Tlk1>Nek1>ATR>Chk1 axes for therapeutic interventions. As exemplified in a recent study, Tlk1 inhibition in combination with indirect DNA-damage, which was induced in prostate-cancer cells through Bicalutamide-induced androgen deprivation, suppressed the outgrowth of androgen independent prostate tumors in a LNCaP xenograft model.¹⁹⁹ In a related preliminary study, Nek1 expression and Nek1-T141 phosphorylation were shown to increase with prostate cancer progression in primary biopsies of untreated patients, supporting the notion that castration-resistant prostate cancer (CRPC) progression may not only be treated through inhibition of Tlk1 but also Nek1.²⁰⁰

Elevated levels of Nek1 expression have also been identified in other cancer types like thyroid cancer, human gliomas or in renal cell carcinoma (RCC).^{63, 197, 201} In the latter case, a decreased sensitivity to genotoxic treatment and ionizing radiation was associated with high levels of Nek1, emphasizing the importance of Nek1 inhibition as a therapeutic strategy for drug development in the treatment of RCC.^{197, 202}

More recently, Freund *et al.* have shown that high Nek1 expression levels associate with impaired clinical outcome in cervical cancer patients following chemoradiotherapy or brachytherapy and that a Nek1 knockdown impacts the 3D clonogenic survival of HeLa-cervix and HCT-15 colorectal carcinoma cells. Furthermore, the Nek1 knockdown sensitized these cells to ionizing radiation, underlining the potential of Nek1 inhibitors to increase the radiation or chemotherapy response in anti-cancer treatment.²⁰³

Despite the fact that the aforementioned studies provide promising initial results for the therapeutic application of Nek1 inhibitors in combination with DNA damaging agents, the absence of specificity in the sensitization to DNA-damage remains a problem. Traditional chemotherapeutics and chemoradiation techniques lack cancer-cell specificity or precision and are thus prone to also cause severe damage to healthy cells, sensitized by unspecific DNA repair-targeting drugs. However, several therapeutic strategies with the aim to minimize deleterious effects to healthy cells in this context have been developed and successfully implemented in the past.²⁰⁴

With regards to radiotherapy, recent advances in intensity modulation radiotherapy, live image-guidance techniques and software-controlled adaptive patient immobilization devices have reduced radiation-related normal-tissue toxicity to unprecedented levels.²⁰⁵ Furthermore, the emerging use of protons and heavy ions as an alternative to traditional photon-based radiotherapy offers an improved ratio of tumor to healthy tissue dose. The physical properties of ion beams result in the sparing of normal tissue as a consequence of a lower energy deposition rate upon entering the body. Compared to photon beams, ion beams are also characterized by steeply increasing energy deposition at the targeted tissue site, while essentially no energy is being delivered beyond the tumor.²⁰⁶ Nevertheless, these technically advanced methods are expensive and not broadly accessible. Furthermore, radiotherapy is not universally applicable, as it is estimated that only about 50% of all cancer patients receive radiation therapy during their course of illness.²⁰⁷

Alternatively, the concept of synthetic lethality has been applied to cancer therapy, providing a novel mechanism to specifically target cancer cells, thereby reducing the toxicity associated with DNA repair-targeting treatment. In contrast to conventional chemotherapeutic drugs, synthetically lethal therapeutics differentiate cancer cells from normal cells by targeting specific gene products of DNA repair defective phenotypes.¹⁹³ In fact, it is suggested that all cancers display defects in at least one DDR pathway, in order to maintain the genomic instability needed for unbridled growth.^{193, 208} However, this loss of DDR pathways can leave

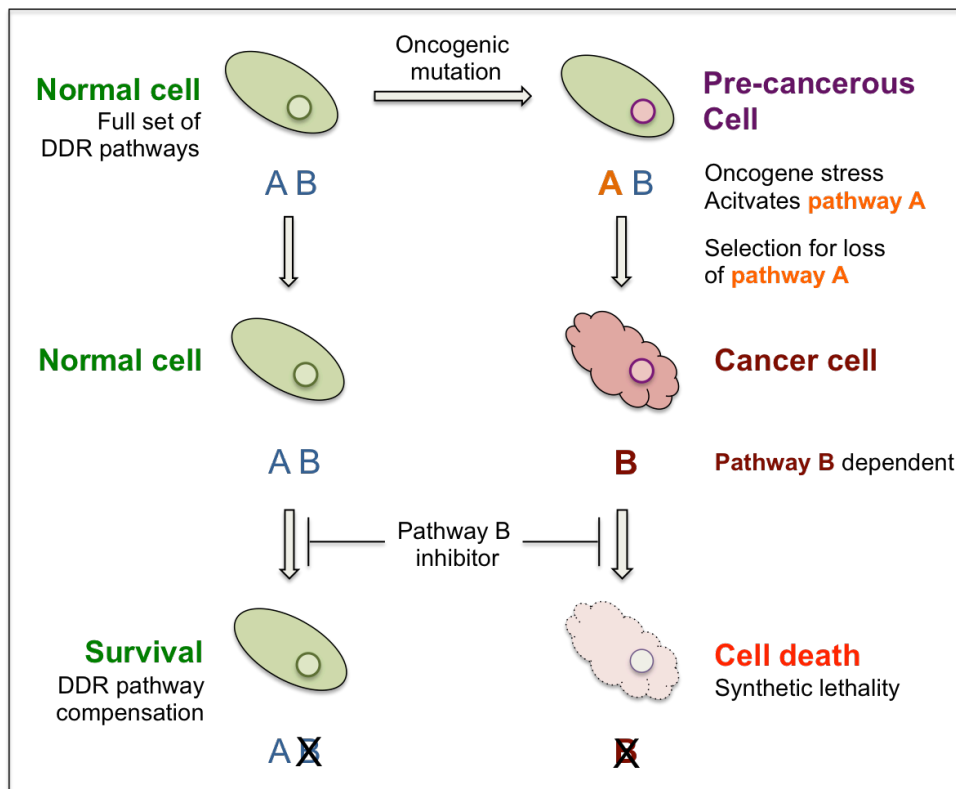
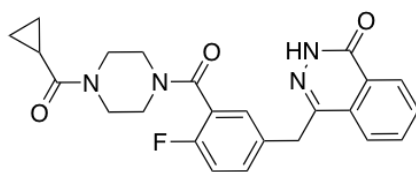


Figure 17: Schematic representation of the synthetic lethality approach in cancer therapy. Loss of DDR Pathways during tumorigenesis results in DDR pathway dependencies that can be targeted by pathway specific DNA repair inhibition. Cancer cell death occurs as a consequence of accumulated and unrepaired DNA-damage or genomic instability overburden. Normal cells, equipped with a full set of repair responses, can compensate for the loss of individual DDR pathways. Redrawn from O'Connor *et al.*²⁰⁹

cancer cells vulnerable to specific inhibition of remaining repair mechanisms, whereas normal cells, equipped with a full set of repair responses, can compensate for the loss of individual DDR pathways (Figure 17).

Clinical validation for this concept has been provided through the regulatory approval of olaparib (Lynparza; EMA, 2014; FDA, 2015), the first poly(ADP-ribose)-polymerase (PARP) inhibitor to hit the market for the treatment of BRCA-mutated advanced ovarian cancer (Figure 18).²¹⁰ Soon thereafter, the approval was extended for BRCA-mutated breast and prostate cancers.²¹¹⁻²¹² Clinical studies demonstrated that olaparib monotherapy was able to selectively target HRR deficient cells, resulting in impressive response rates, especially in patients with BRCA1 or BRCA2 mutated ovarian cancer, where efficacy was increased approximately 1000-fold.^{209, 213} Although PARP is not directly involved in DNA repair, it recognizes and binds to single-strand DNA breaks (SSBs), where it catalyzes the synthesis of



Olaparib

Figure 18: Chemical structure of the NAD⁺ competitive poly(ADP-ribose)-polymerase (PARP)-inhibitor olaparib, sold by AstraZeneca and Merck Sharp & Dohme under the brand name *Lynparza*[®]. *Lynparza*[®] received first approval for the treatment of BRCA-mutated advanced ovarian cancer by the EMA in 2014 (FDA 2015).²¹⁰ Approval was later extended for gBRCAm metastatic breast cancer (FDA 2018, EMA 2019)²¹¹ and BRCA- mutated metastatic castration-resistant prostate cancer (FDA 2020, EMA 2020).^{212, 214}

poly(ADP-ribose) (pADPr) chains on glutamate, aspartate and lysine residues of target proteins. Ultimately, PARP and the pADR chains recruit repair proteins to the damage site and pADR chain formation on histones relaxes chromatin structure to facilitate repair protein access. For efficient repair protein access, PARP has to also be removed from the damage site. PARP removal is mediated by pADR chain formation, which is not functional under the influence of PARP inhibitors like olaparib, thus leaving PARP trapped on the DNA.²¹⁵ The resulting repair inefficiency leads to an accumulation of SSBs that can be converted to single-sided DSBs during replication. The persistence of DSBs is synthetically lethal to BRCA1 or BRCA2 mutated cancer cells that do not possess an intact HRR pathway for efficient DSB repair.²¹⁶ Furthermore, an improved effect of olaparib on progression free survival in ovarian cancer patients was shown for combinatorial treatments with other targeted ovarian cancer drugs as well as non-specific cytotoxic chemotherapeutics.²⁰⁹

The clinical success of olaparib was followed by the development and approval of several other PARP-inhibitors for novel indications and sparked an enormous interest in other DNA repair targets like ATR, ATM, DNA-dependent protein kinase (DNA-PK), Chk1, Chk2, and Wee1 G2 checkpoint kinase (Wee1). There are currently no approved inhibitors of DDR proteins other than PARP, although several inhibitors for the aforementioned targets are currently under clinical investigation.²¹⁷

Considering the clinical success of PARP inhibitors and the promising study results of inhibitors targeting other DNA repair proteins, DNA repair targeted therapies have established their place in the spotlight of personalized cancer drug research. Due to its key functions in the cell cycle as well as the DDR Nek1 holds great potential as a target for future anticancer drug development, especially in the context of DNA repair targeted therapy. Nonetheless, the

complexity of the cellular response to DNA-damage must be considered in every step of the development process and necessitates a detailed understanding of Nek1 biology. Despite the growing body of Nek1 research, a lot of questions remain unanswered and there is a dire need for potent and selective Nek1 inhibitors, which would enable researchers to further clarify the function and pharmacology of this neglected kinase.

2. Aims and Objectives

NIMA-related kinase 1 (Nek1) has lately gained attention for its widespread function in ciliogenesis, apoptosis, and the DNA-damage response. Despite its involvement in various diseases and its potential as a cancer drug target, no inhibitors against Nek1 have been reported in the literature. Therefore, the aim of this thesis is the development of a highly selective and active small molecule inhibitor against the Nek1 kinase domain by medicinal chemistry approaches.

Due to the fact that there are no Nek1-directed medicinal chemistry efforts in the reported literature, this aim incorporates the identification and evaluation of new molecular scaffolds for inhibitors of this dark kinase. Furthermore, this thesis aims to investigate the pharmacological and toxicological *in vivo* effects of Nek1 inhibition in wild-type zebrafish. Fortunately, two Nek1 kinase domain crystal structures have been solved and reported to the literature prior to this work. A structure-guided ligand design process, assisted by state-of-the-art computer-guided ligand design methods, will thus be followed in order to achieve the aforementioned aims.

As a first objective in the *de novo* ligand design process, molecular scaffolds are sought to be identified from established literature scaffolds, by *in silico* docking analyses in the available Nek1 kinase domain crystal structures. With the goal of generating highly active and selective lead structures, structure-activity-relationships (SARs) of the scaffolds and related derivatives are to be investigated in an iterative process of structure modeling and design, compound synthesis and biochemical evaluation. The generation of initial hit structures and their derivatization shall herein be performed by structure-guided design and *in silico* screenings of virtual compound libraries. Inhibitory activities are to be determined in multiple independent *in vitro* kinase activity assays and a focused kinase selectivity panel shall give insight into structure-promiscuity relationships. The developed compounds are ought to be further profiled for their safety, toxicity and bioavailability using established *in vitro* and *in vivo* methods. Assessment of lead structure bioavailability shall be carried out *in vitro*, in a Caco-2 cell permeability assay and by determination of relevant physicochemical parameters, whereas *in vivo* bioavailability, safety and toxicity are to be investigated in a wild-type zebrafish developmental toxicity screen. In addition, the development of a zebrafish PKD model that enables the visualization of Nek1 inhibitor efficacy *in vivo*, is set as an objective. Finally, the efficacy of developed Nek1 inhibitors is to be evaluated in this model with regards to phenotypical alterations, previously reported for Nek1-deficient mutant PKD rodent models.

3. Results and Discussion

3.1. Structure-guided Design and Synthesis of Nek1 Inhibitors

This chapter describes the identification of suitable scaffolds for Nek1 inhibition, as well as the structure-guided design and synthesis of related small molecule Nek1 inhibitors. Their *in vitro* evaluation with regards to activity, selectivity and relevant physicochemical parameters follows in chapter 3.2.

3.1.1. Identification of new Nek1 Inhibitor Scaffolds

The notion of chemical scaffolds is a widely utilized concept in medicinal chemistry, for both screening-based as well as structure-guided drug design approaches. A scaffold is defined as the core structure of a chemical compound and by that plays a crucial role in numerous focused medicinal chemistry efforts such as lead generation in target-based designs, the rationalization of (SARs) and target specific activities, and the estimation of key physicochemical parameters.²¹⁸ Since the first approval of a protein kinase inhibitor by the FDA in 2001, a vast amount of scaffolds have been collected and assessed in the literature. This allowed for the identification of several scaffolds, privileged for binding to specific kinase families.²¹⁹ Recently, the furo[3,2b]pyridine core has for example been identified as a novel scaffold for potent and highly selective inhibitors of the cdc-like kinases (CLKs).²²⁰

Unfortunately, no directed medicinal chemistry efforts toward potent and selective Nek1 inhibitors have been published in the past and there are no privileged scaffolds for the Nek kinase family to build upon.^{52, 109} As previously mentioned, Moraes *et al.* identified a JNK inhibitor¹²² with limited inhibitory activity ($71.5\% \pm 0.1\%$ at $50 \mu\text{M}$) against a truncated Nek1 activation loop mutant in a thermal shift assay, in an attempt to pinpoint structural elements that influence Nek family inhibitor specificity (Figure 19A).¹²¹ As a consequence of this anthrapyrazolone's limited Nek1 activity, and the fact that it is highly active against JNK, this scaffold does not appear as a promising core structure for lead generation. Shortly thereafter, the same group reported the crystal structure analysis of the human Nek1 kinase domain in both its apo form (PDB code: 4APC) and in complex (PDB code: 4B9D) with an ATP-competitive cyclin-dependent kinase (CDK) inhibitor (Figure 19B).⁶⁴

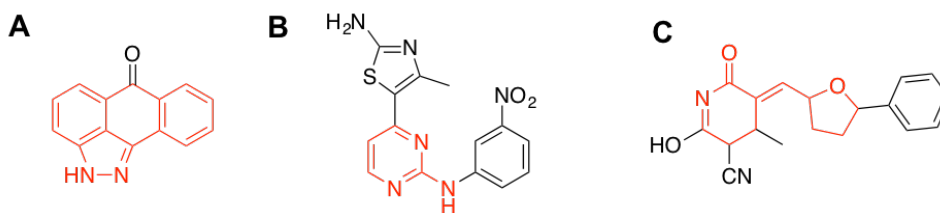


Figure 19: Candidate scaffolds for small molecule Nek1 inhibitors identified from the literature. (A) C-Jun N-terminal kinase (JNK) inhibitor II containing the dibenzo[*cd,g*]-indazole scaffold (red).¹²¹ (B) Cyclin-dependent kinase (CDK) inhibitor CK7 containing the 2-Aminopyrimidine scaffold (red).⁶⁴ (C) Nek6/1 inhibitor 8 containing the tetrahydrofuran-2(3*H*)-one scaffold (red).⁸⁷

Based on the 2-aminopyrimidine scaffold of this ATP mimetic, a number of small molecule inhibitors for Nek1 were developed by the Schmidt group prior to this work. Unfortunately, they generally lacked selectivity and proved to be unstable in solution (DMSO), thus rendering them unattractive for future endeavors.

More recently, a pyridine-2(3*H*)-one based inhibitor with a low micromolar IC_{50} value ($3.4 \pm 1.2 \mu M$) against Nek6 was also shown to decrease Nek1 activity to a comparable degree (47% for Nek6 and 42.5% for Nek1 at 10 μM , Figure 19C).⁸⁷ Despite the more promising activity, the lack of selectivity across the Nek family pleads against the utilization of this scaffold.

As a consequence of the lack of suitable scaffolds in the literature, two new 7-azaindole (1*H*-pyrrolo(2,3-*b*)pyridine) scaffolds for Nek1 inhibition were derived from the 2-aminopyrimidine core of previously mentioned CDK2/CDK9 inhibitor CK 7,²²¹⁻²²² on the basis of unpublished investigations previously conducted by Johannes Pilakowski of the Schmidt group (Figure 20A)

Azaindole scaffolds have lately garnered increasing attention in the development of kinase inhibitors, due to the fact that their target-binding, bioavailability and ADME-tox properties can be easily tuned. Moreover, their commercial availability is steadily increasing and synthetic innovations regarding their modification are continuously being published.²²³⁻²²⁴ Special attention is hereby given to the bioisosteric purine analogue 7-azaindole, as a consequence of its outstanding hinge-binding motif. A recently published investigation of protein kinase X-ray cocrystal structures in complex with 7-azaindole based small molecules, revealed three major binding modes.²²⁵ In the so-called “normal” and “flipped” binding modes, the 7-azaindole core forms two hydrogen bonds with the backbone amides of hinge region

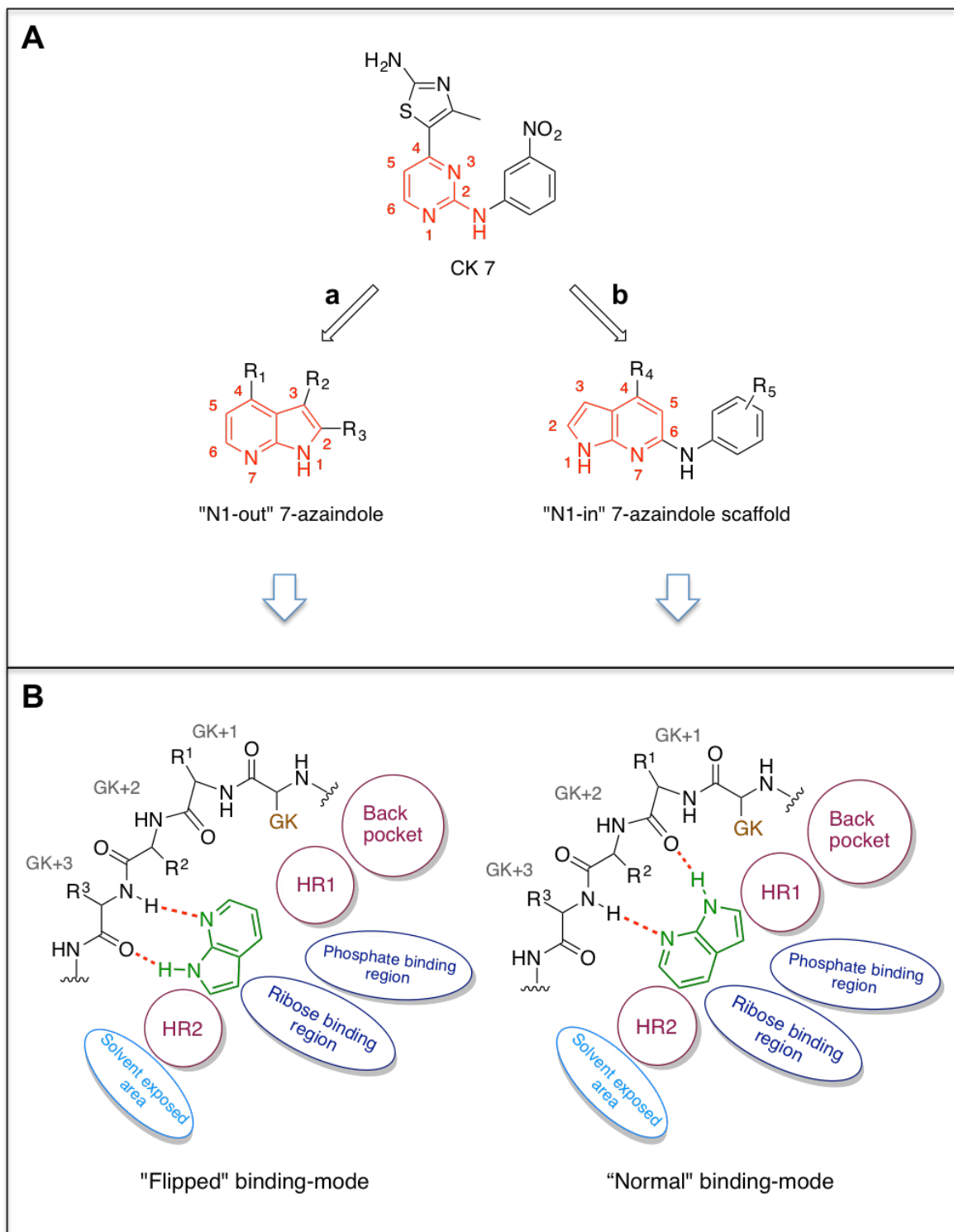


Figure 20: Identification of scaffolds for the structure-guided design of Nek1 inhibitors. (A) Structural scaffold derivation from 2-aminopyrimidine CDK2/CDK9 inhibitor CK 7 for (a) the "N1-Out" 7-azaindole scaffold, focused on adopting the "flipped" binding mode, and (b) the "N1-In" 7-azaindole scaffold, focused on adopting the "normal" binding mode. (B) Schematic representation of the relative position and hinge-binding interactions of the 7-azaindole scaffold in the "flipped" and "normal" binding modes. The "non-hinge" binding mode is not shown. GK, gatekeeper; HR1, hydrophobic region 1; HR2, hydrophobic region 2.

amino acid residues (Figure 20B). More precisely, the backbone NH of GK+3 acts as a hydrogen bond donor, while the carbonyl oxygen of GK+1 accepts a hydrogen bond in the “normal” binding mode. For the “flipped” binding mode, the GK+3 backbone interacts as both a hydrogen bond donor and as an acceptor. In the third binding mode („non-hinge“, not shown), the 7-azaindole moiety binds to non-hinge amino acid residues due to the presence of an alternative hinge-binding motif in the same compound.

For the scaffold derivation from CK7 to 7-azaindole based structures, two main objectives were set. For one, the retention of the acceptor-donor hinge-binding motif of the 2-aminopyrimidine core and for another, the preservation of the attachment points for the nitrophenyl and thiazolyl moieties was focused. This was achieved by (a) the conceptual cyclization of the amino-bearing side-chain and (b) the conceptual annulation of a pyrrole-ring to the opposite side (5,6-face) of the pyrimidine-ring (Figure 20A). In both cases, the second pyrimidine nitrogen was omitted, as no beneficial influence on binding was identified by analysis of the crystal structure (PDB code: 4B9D). Additionally, the substitution from nitrogen to carbon opens up the 5-position for derivatization in case (b).

With the aim of adopting the “flipped” binding mode, the resulting “N1-Out” 7-azaindole scaffold (a) thus retains the attachment point at the 4-position while offering two new substitutable hydrogen atoms at the 2- and 3-positions. 2-position derivatives of the “N1-Out” scaffold are hereby enabled to interact with the hydrophobic region 2 (HR2) for improved affinity and the solvent exposed area for fine-tuning of pharmacokinetic parameters. Derivatization at the 3-position may allow for additional interactions with the ribose-binding region. In contrast, substitutions at the 5- and 6-positions are unpromising, due to potential steric clashes with the gatekeeper and other hinge region residues. Furthermore, a fusion of the nitrophenyl moiety to the 2,3-face is conceivable. The resulting 9*H*-pyrido[2,3-*b*]-indoles are currently under investigation for use as antiparasitic agents.²²⁶⁻²²⁷ Unfortunately, their application as kinase inhibitors is not well researched.²²⁸

In the case of the “N1-In” 7-azaindole scaffold (b), the attachment points for the thiazolyl moiety as well as the nitro group are retained at the 4-position and the 6-aminophenyl moiety respectively. In addition, the 6-amino moiety hereby serves as an additional hinge-binder. This extended hinge-binding motif has been successfully exploited in the structure-guided design of selective purine-based inhibitors for Nek2, a Nek-family kinase that shares high structural similarity with Nek1.²²⁹ As a consequence of this envisaged interaction, the derivatized phenyl moiety is once again correctly positioned to interact with the HR2 and the solvent exposed area.

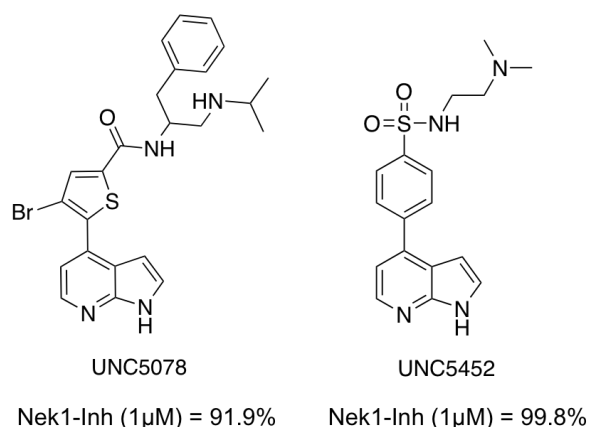


Figure 21: Structures of chemical starting points for the development of Nek1 inhibitors, as identified by Wells *et al.* in an analysis of kinome cross-screening data.⁶¹

The described 7-azaindole-scaffold identification approach is supported by a highly impactful study that was published in the midst of this work. In the framework of developing a comprehensive kinase chemogenomic set, Wells *et al.* compiled chemical starting points for Nek-family inhibitors by performing an intricate analysis of kinome cross-screening data, which share key features with the scaffolds that were identified by the approach described in this thesis.⁶¹ In the case of Nek1, two series of compounds with promising activities were identified from the profiling data of a large inhibitor set (Published Kinase Inhibitor Set 2, PKIS2).²³⁰ The most potent candidate, of a series of 4-thiophene-7-azaindoles (UNC5078), exhibited 91.9% Nek1 inhibition at 1 μ M.^{61, 231} Strikingly, the 4-aryl-7-azaindole derivative UNC5452, which was originally intended as an I κ B kinase β (IKK β) inhibitor, exhibited even higher Nek1 inhibitory activity (99.8% inhibition at 1 μ M) while only inhibiting 18 off-target kinases $\geq 90\%$ at 1 μ M (Figure 21).^{61, 232}

As a next step, the derived scaffolds need to be evaluated in context of the Nek1 kinase domain. This shall be accomplished by the application of *in silico* methods, which set the cornerstone for the structure-guided drug design approach.

3.1.2. Nek1 Crystal Structure Analysis and Molecular Scaffold Docking

In order to generate lead structures for the design of Nek1 inhibitors, an in-depth analysis of the available Nek1 crystal structures, followed by the molecular docking of the derived scaffolds, was performed. The PDB-available Nek1 crystal structures, obtained from the same truncated (aa residues: 1–328) inactivating T162A mutant, expectedly constitute an inactive “DFG-out/C-helix-out” conformation, as reported by Melo-Hanchuk *et al.* (Figure 22).⁶⁴

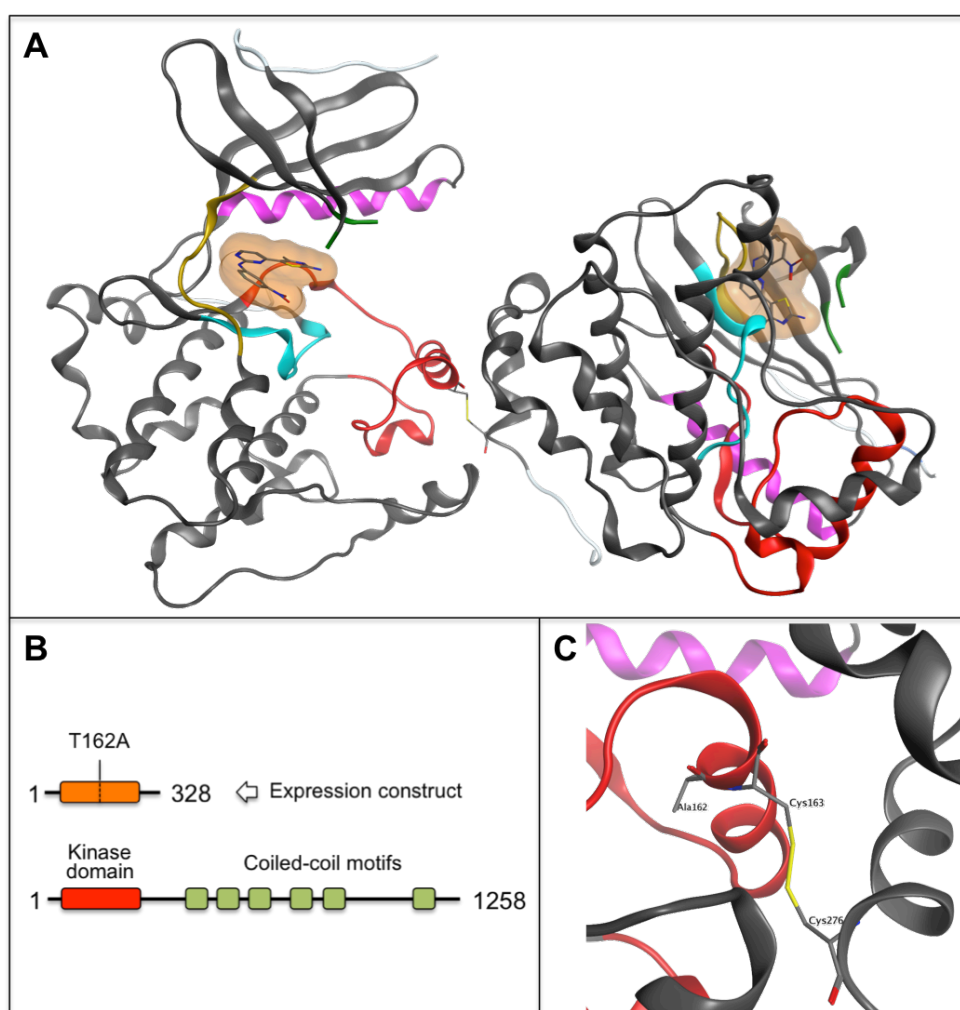


Figure 22: Crystal structure of human Nek1 kinase domain in complex with CDK-inhibitor CK7 (PDB code: 4B9D). (A) Overview of the disulfide-bridged homodimer. The kinase domains feature an inactive “DFG-out/C-helix-out” (red/purple) conformation and an unusually ordered activation loop (red). The P-loop (green) is disordered and not structurally resolved. (B) Schematic comparison of the truncated expression construct, containing an inactivating T162A mutation and an N-terminal hexahistidine tag (not shown), with full-length human Nek1. (C) Detailed view of the unusual α -helical activation loop segment, containing the artificial disulfide bridge between A-chain Cys163.A and Cys276.B as well as the inactivating T162A mutation.

On first glance, it stands out that both the apo (PDB code: 4APC) and the CDK-inhibitor bound 3D-structures (PDB code: 4B9D) were recorded from crystals of disulfide-bridged homodimers (Figure 9A). This non-physiological feature is believed to be an artifact, resulting from the described oxidative crystallization conditions. The disulfide bridges are formed between A-chain Cys163.A, located in the activation loop, and B-chain Cys276.B, located in the C-terminal α -helix. Interestingly, the activation loop forms an unusual α -helix around Cys163 in both chains, which is therefore unlikely to artificially result from the disulfide bond's influence. The partially ordered activation loop is speculated to unfold upon auto-phosphorylation, thus adopting a disordered conformation more commonly found in active kinases.⁶⁴ This activation mechanism might to some degree be conserved in the Nek-family, since a similar α -helical activation loop is present in Nek2 structures, although not in Nek7, which is activated by a different mechanism that involves binding of the non-catalytic C-terminal domain of Nek9.^{65, 233} Moreover, the P-loop is disordered and not structurally resolved (residues 11-16) in both structures. Upon closer analysis of the active site, it is noteworthy that Nek1 features a rather constricted ATP-binding pocket, due to the intrusion of an unusual phenylalanine (Phe135) paired with the large GK (Met80).

The presence of a cysteine residue (Cys83) in the active site suggests that covalent inhibitors may be used to target the Nek1 kinase domain. However, an approach from the ATP pocket appears futile, due to the cysteine's location at the GK+3 hinge-position and the outward orientation of the nucleophilic cysteine side chain. As a consequence, the hinge-binding scaffold, whose reversible interactions are required for the pre-orientation of an electrophilic warhead, would have to be replaced with the reactive warhead itself. Alternatively, the cysteine may be addressable through an unidentified transient allosteric binding site at the backside of the hinge region.

Molecular Docking of 7-Azaindole Scaffolds

In order to confirm the scaffold derivation described in 3.1.1, the “N1-Out” and “N1-In” 7-azaindole scaffolds were docked into the CK7-bound crystal structures B-chain (Figure 23B and C). As expected, the cocrystallized CDK-inhibitor CK7 forms two hydrogen bonds with the GK+3 (Cys83) backbone, while the 4-methyl-thiazole-2-amine is packed tightly against a narrow channel formed between the side chains of Phe135, Val31, Ile10, Ala18 and the

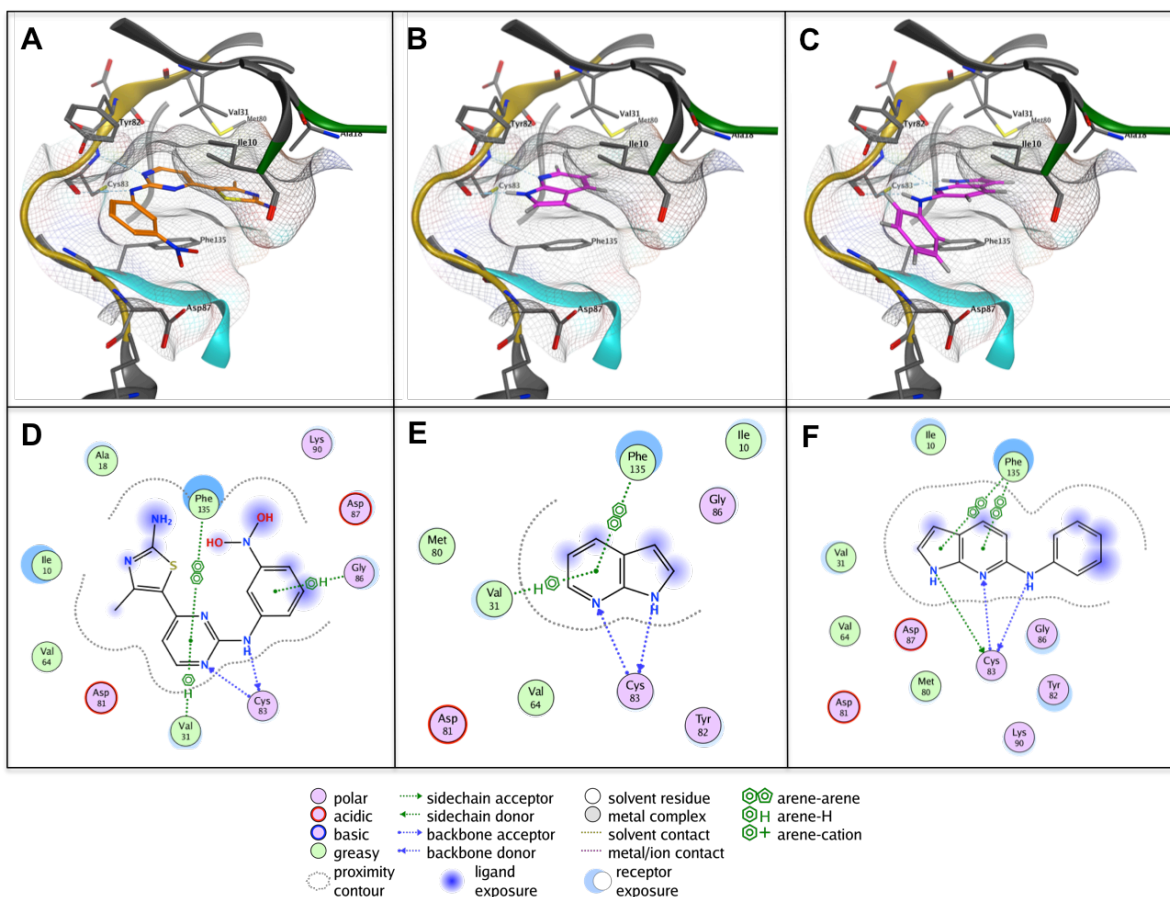


Figure 23: Nek1 binding mode analysis for cocrystallized Inhibitor CK7 (PDB code: 4B9D) and molecular scaffolding. (A) Binding of CDK-inhibitor CK7 to Nek1. (B) Docking of “N1-Out” 7-azaindole scaffold into the Nek1 ATP-binding site (PDB code: 4B9D.B). (C) Docking of “N1-In” *N*-phenyl-7-azaindole-6-amino scaffold into the Nek1 ATP-binding site (PDB code: 4B9D.B). (D) Ligand interaction analysis for the binding of CDK-inhibitor CK7 to Nek1. (E) Ligand interaction analysis for the molecular docking of the “N1-Out” 7-azaindole scaffold into Nek1. (F) Ligand interaction analysis for the molecular docking of the “N1-In” 7-azaindole scaffold into Nek1.

gatekeeper (Figure 23A). The nitrophenyl moiety occupies the HR2, forming a C-H- π interaction with hinge region Gly86, and orients the partial positive charge of the nitro-group toward Asp87, presumably forming favorable interactions.

As predicted, the “N1-Out” scaffold forms the same hydrogen bonds with the GK+3 (Cys83) residue as CK7. More precisely, the pyrrole NH donor interacts with the backbone carbonyl oxygen, while the pyridine nitrogen acceptor interacts with the backbone amide. Interestingly, the orientation of the scaffolds 4-position C-H bond remains virtually identical to the thiazolyl-fusing bond in CK7. In contrast, the “N1-In” *N*-phenyl-7-azaindole-6-amino scaffold adopts an untypical hinge-binding motif, not commonly found in the “normal” binding mode. Here, the scaffold forms all three hydrogen bonds with Cys83, whereas the 7-azaindole core

usually interacts with two separate hinge residues (GK+1 and GK+3).²²⁵ As a consequence of the spatial restrictions, imposed by Met80, Val31 and Phe 135, the 7-azaindole core is reoriented, forming a hydrogen bond interaction between the pyrrole NH and the Cys83 side chain sulfur instead of the GK+1 (Asp81) carbonyl oxygen. This reorientation leads to a misalignment of the pyridine nitrogen toward the Cys83 backbone amide, hypothetically weakening this interaction. Additionally, the 6-amino moiety forms the expected hydrogen bond with the Cys83 carbonyl oxygen and orients the scaffolds phenyl group toward Asp87, in a similar fashion to the nitrophenyl moiety in CK7. Conversely, the 4-position C-H bond is tilted upwards, compared to the thiazolyl-fusing bond in CK7, hypothetically limiting access to the phosphate-binding region.

In an attempt to identify areas of conformational mobility in the active site, the monomeric kinase domains were isolated and superimposed using the *Molecular Operating Environment* (MOE) software platform (Figure 24). Interestingly, the DFG-motif aspartate (Asp146) and the gatekeeper (Met80) formed hydrogen bonds with an internal water molecule in the ATP-binding site in all but one of the isolated chains (PDB code: 4APC.A). In this particular case, the side chains of Asp146 and Met80 extend outwards in absence of the water molecule, thus extending a back pocket toward the DFG-motif (Figure 24D). This conformational mobility may be exploited by locking Nek1 in an inactive conformation with a small molecule inhibitor.

The back pocket in Nek1 arises through the combination of a small Ala56, at the end of the C-helix, and the large gatekeeper (Met80) that allows Tyr66 to adopt a “Tyr66-up”-conformation, not found in other structurally solved Nek kinases (Nek2, Nek7). Furthermore, Nek3 is the only other Nek-family member that features this small alanine in combination with a methionine gatekeeper.⁶⁴ This suggests that targeting the inactive „Tyr66-up/DFG-out“ conformation might allow for good specificity within the Nek-Family.

In order to explore its binding mode and to assess the amenability of the back pocket, chemical starting point UNC5452 was also docked into the Nek1 ATP-binding site (PDB code: 4APC.A, Figure 25). As expected, the 7-azaindole moiety positions itself between the Val31 and Phe135 side chains and forms two hydrogen bonds with the backbone heteroatoms of the hinge region Cys83, thus adopting the “flipped” binding mode. The pyrrole-ring is packed tightly against the side chain of Tyr82 and directed toward the solvent exposed area. From the hinge-binding motif, the phenyl-ring of UNC5452 protrudes toward the phosphate-binding region of Nek1 through a narrow channel formed by the side chains of Phe135, Ala18, Ile10 and the catalytic lysine (Lys33). Unfortunately, the terminal nitrogen atom of Lys33 is not

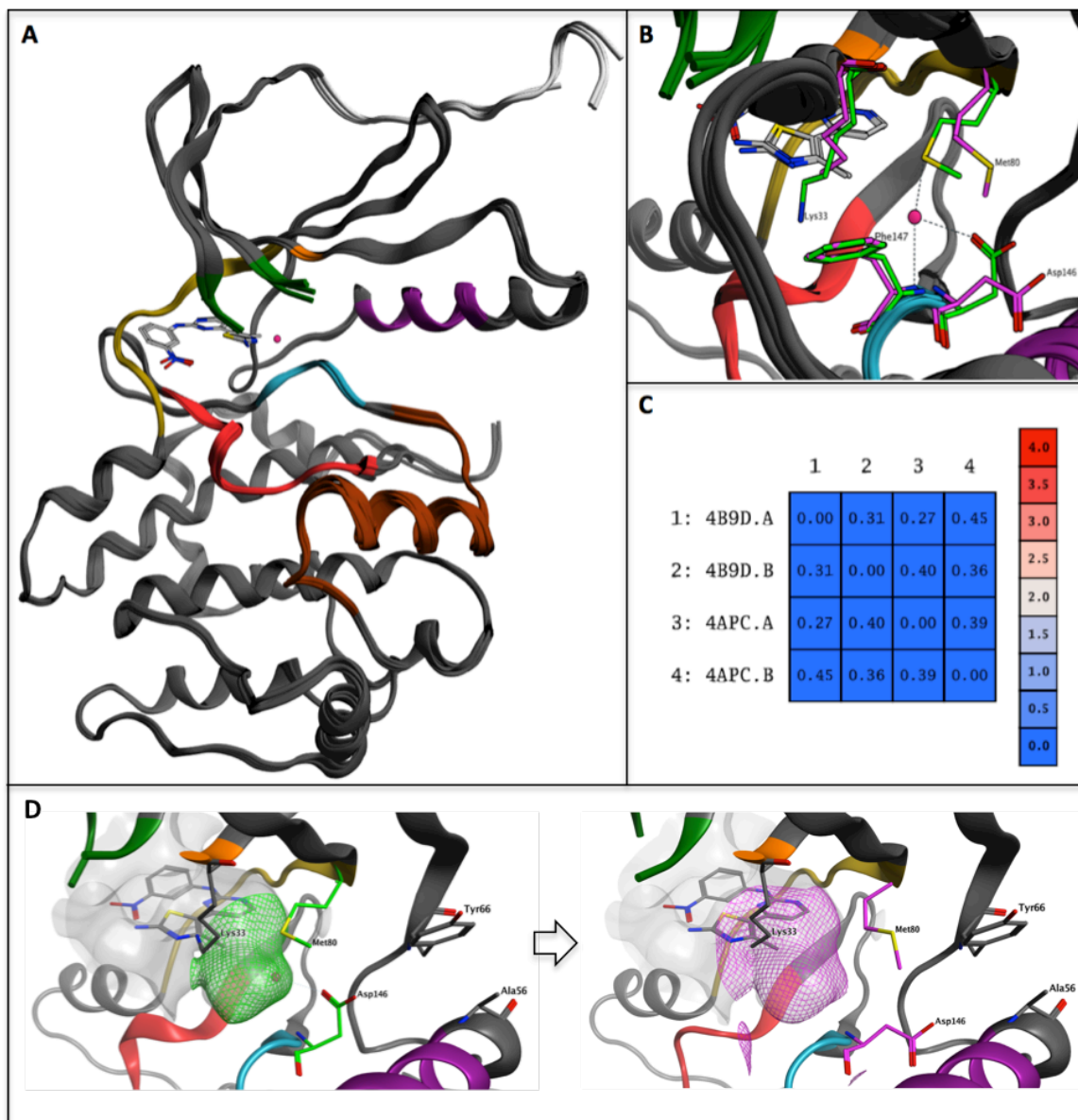


Figure 24: Comparison of Nek1 kinase domain crystal structures; (A) Superposition of the isolated monomeric Nek1 kinase domains (PDB codes: 4APC, 4B9D). The protein backbone is shown in dark and the ligand in light grey. The hinge region is shown in yellow. The P-loop is shown in green and the catalytic lysine in orange. The C-Helix is shown in purple. The DFG-motif is shown in cyan and the catalytic loop is shown in red. The activation loop is shown in brown. The internal water molecule in the ATP-binding site is shown in pink; (B) Detailed comparison of the DFG-motif side chains (Asp 146, Phe147), gatekeeper (Met80) and catalytic lysine (Lys33) in the 4APC A-chain (*fuchsia*) and the 4B9D B-chain (*lime green*); (C) Root-mean-square deviation of atomic positions for the isolated monomeric Nek1 kinase domains. (D) Conformational mobility of the DFG-motif Asp146 and Met80 extends the Nek1 back pocket upon absence of the internal water molecule.

structurally resolved, but it appears that its side-chain flexibility and the close proximity to the sulfonamide oxygen allow for hydrogen bonding. Consequently, the sulfonamide nitrogen is positioned downward, toward the catalytic loop. As expected, the highly flexible

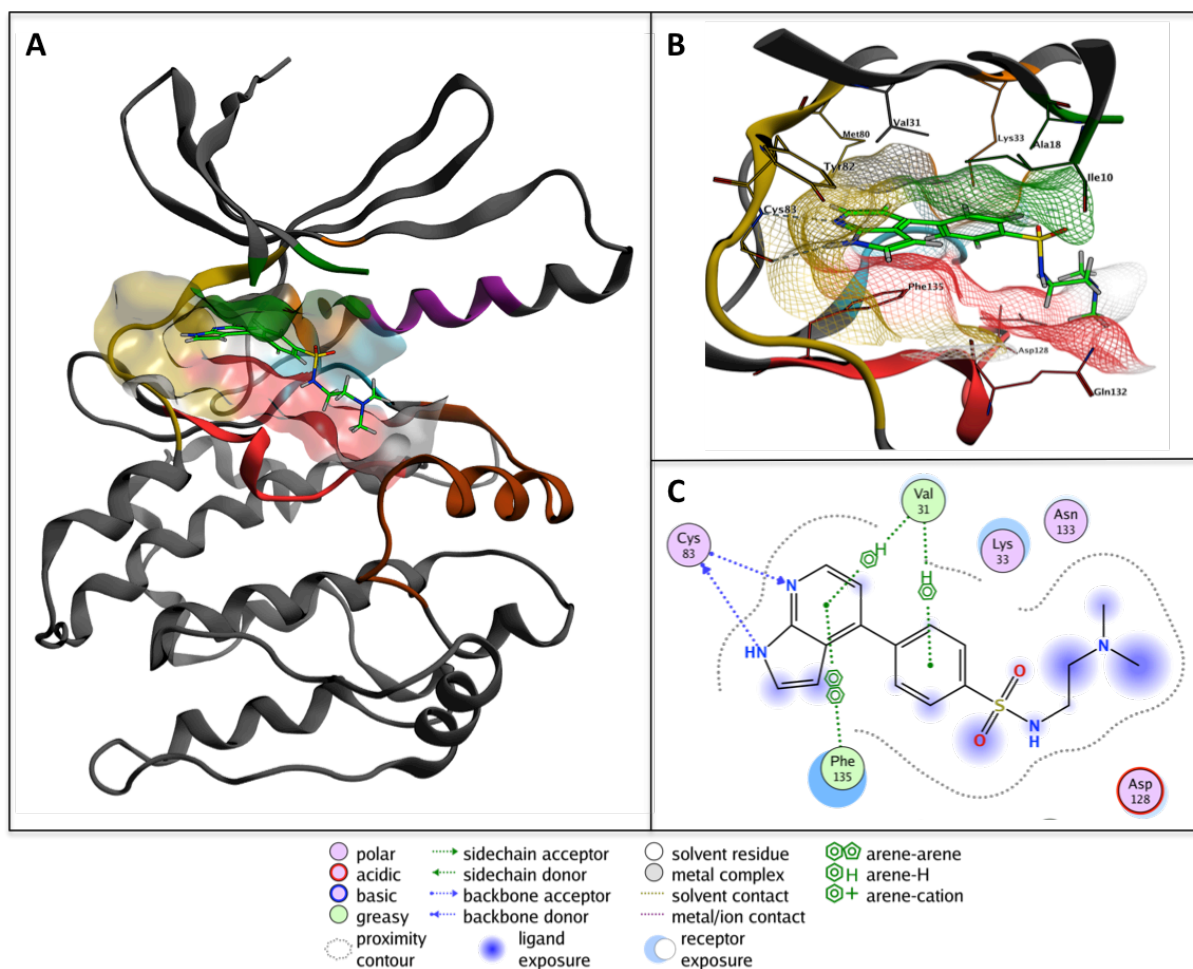


Figure 25: Molecular docking of UNC5452 into the Nek1 ATP-binding site (PDB code: 4APC.A). (A) Localization of UNC5452 in the Nek1 kinase domain. (B) Putative binding mode of UNC5452. The protein backbone is shown in dark grey and the ligand in lime green. The hinge region is shown in yellow. The glycine-rich loop is shown in green and the catalytic lysine in orange. The C-helix is shown in purple. The DFG-motif is shown in cyan and the catalytic loop is shown in red. The activation loop is shown in brown. Hydrogen bond interactions are shown as dotted lines.

dimethylaminoethyl fragment was able to adopt multiple conformations. Depending on the tertiary amine's protonation state, interactions with the side chains of the catalytic loop residues Asp128, Gln132 or the unresolved side chains of P-Loop residues Asp12 and Ser14 are conceivable. The adoption of the “normal” binding mode is also conceivable for UNC5452 but was not favored in the performed docking experiments.

Unfortunately, our experiments led to the conclusion that an entrance into the back pocket from the 4-phenyl-7-azaindole scaffold is not trivial. Due to the intrusion of the Phe135 and Tyr82 side chains into the hinge-binding region, the 7-azaindole moiety is angled in a way that prevents access to from the 5-position in the “flipped” binding mode. In the disfavored “normal” binding mode, the same problem arises for the 3-position, while an entry from the

2-position is blocked by the gatekeeper. Nevertheless, the docking results make an approach from the phenyl ring of UNC5452 plausible, which will be examined in greater detail in chapter 3.1.3.

In summary, the Nek1 kinase domain offers distinctive features that can potentially be exploited by carefully designed small molecule inhibitors, in order to achieve high selectivity. Nevertheless, the unusual shape of the ATP-binding site suggests that finding suitable inhibitors for Nek1 is not trivial. This hypothesis is supported by the low hit rates of several kinase inhibitor library screenings, reported in the literature.^{61, 64, 121, 124} *In silico* superposition of four kinase domain structures, which were isolated from the two disulfide-bridged homodimer crystal structures available in the PDB, revealed conformational mobility of the DFG-motif within the inactive “DFG-out”-conformation. In combination with a unique “Tyr66”-up conformation, this mobility opens a distinct back pocket in Nek1. Molecular docking of the 4-phenyl-7-azaindole UNC5452 identified a potential point of attack for this pocket that might allow for improved selectivity over other Nek-family members as well as the human kinome in general. Overall, the performed docking experiments demonstrated the suitability of the previously derived 7-azaindole scaffolds and puts further emphasis on the UNC5452-derived 4-phenyl-7-azaindole scaffold. Furthermore, it was identified that the unresolved P-loop is of critical importance and demands the application of a reconstruction model. This problem is going to be addressed at later stages of the work (Chapter 3.1.3).

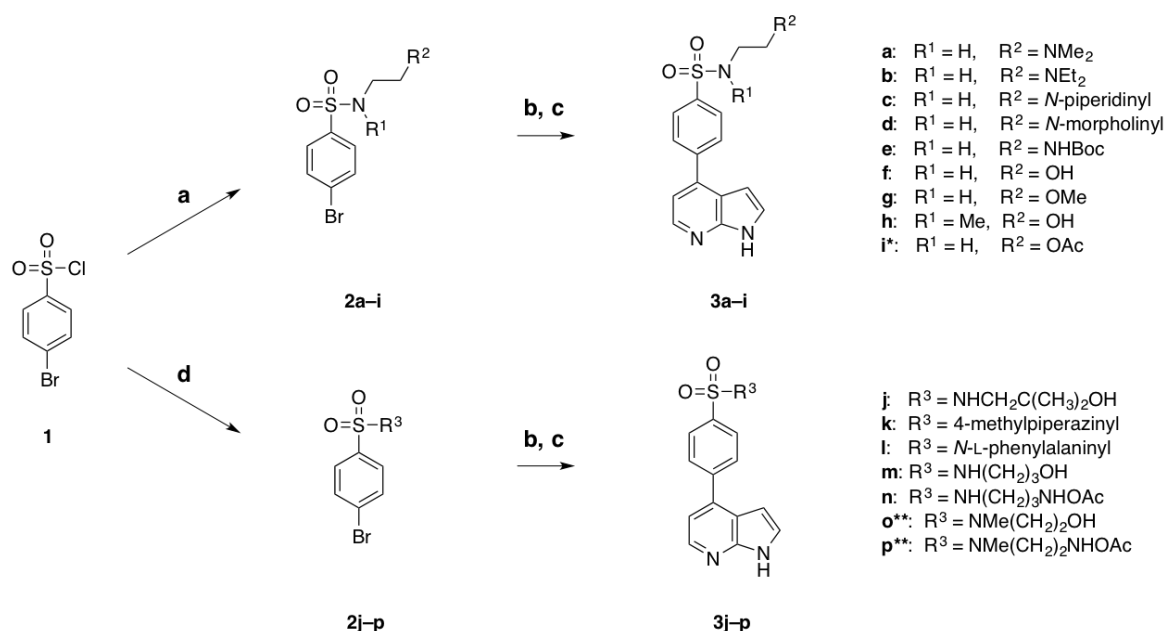
The following chapter deals with the generation of lead structures, based on the promising UNC5452-derived 4-phenyl-7-azaindole scaffold. The design and synthesis of 3,4-disubstituted 7-azaindole Nek1 Inhibitors, derived from the molecular docking analysis of the “N1-Out”-scaffold, follows in chapter 3.1.4., while chapter 3.1.5. describes initial steps toward 4,6-disubstituted 7-azaindole Nek1 Inhibitors that are based on the “N1-In”-scaffold.

3.1.3. Design and Synthesis of 4-Phenyl-7-Azaindole Nek1 inhibitors

As a result of the promising inhibitory activity of UNC5452 against Nek1, a focus was set on the 4-phenylsulfonamide-7-azaindole scaffold. While this chapter describes the structure-guided design as well as the synthetic routes toward the UNC5452-derived Nek1 inhibitors, the biochemical evaluation and the corresponding SARs are discussed in a later chapter (see 3.2).

Derivatization of the Dimethylaminoethyl Fragment

Building upon the findings of the *in silico* analysis, the attention was first centered on the derivatization of the dimethylaminoethyl fragment, with means to optimize existing and to establish new interactions in the P-loop and phosphate-binding regions. In order to establish a



Scheme 1: Synthesis of UNC5452-derived Nek1 inhibitors. **a)** **2a–h:** DCM, amine, NEt₃, 0 °C–rt, 74–95%; **b)** DMF, bis(pinacolato)diboron, KOAc, PdCl₂(dppf), 100 °C, not isolated; **c)** DMF, 4-bromo-7-azaindole, NaHCO₃ (aq), Pd(PPh)₃, 100 °C, 11–89%; **d)** **2j:** DCM, amine, NEt₃, 0 °C–rt, 64%; **2k:** THF, 1-methylpiperazine, rt, 75%; **2l:** H₂O/acetone, L-phenylalanine, NaHCO₃, rt, 49%; **2m–p:** DCM, amine, NEt₃, 0 °C–rt, 24–92%. *Compound **2i** was prepared from **2f** by acetylation with acetic anhydride and NEt₃ in DCM, 82%; **Compounds **2o** and **2p** were prepared from **2m** and **2n** by methylation with NaH and CH₃I in DMF, 24–72%; see Table 1 and experimental section for more details.

SAR for the dimethylaminoethyl fragment, a series of compounds (**3a–p**), with a range of steric demands as well as varying basicity and hydrogen bond capabilities, was designed and synthesized (Scheme 1).

The synthesis of UNC5452 (**3a**) and its derivatives was based on a method described by Liddle *et al.*²³⁴ and commenced with the amide formation between commercially available 4-bromobenzenesulfonyl chloride (**1**) and the respective primary or secondary amines to afford sulfonamides **2a–h** and **2j–n** in 49–95% yield. Acetyloxyester **2i** was prepared from alcohol **2f** by acetylation with acetic anhydride in 82% yield. Tertiary sulfonamides **2o** and **2p** were prepared by methylation of **2m** or **2n** with sodium hydride and methyl iodide in poor to good yields of 24% and 72% respectively. MIYAJI-BORYLATION of aryl halides **2a–p** gave the corresponding pinacol boronic acid esters, which were fused with commercially available

Table 1: Compilation of yields for synthesized UNC5452-derivatives. Compounds **2a–h** were prepared by method a), compounds **2j–o** by method d), and compounds **3a–p** were prepared by methods b), and c) (Scheme 1). ^aCompound **2i** was prepared from **2f** by acetylation with acetic anhydride and NEt₃ in DCM. Compounds **2o** and **2p** were prepared from **2m** and **2n** by methylation with NaH and CH₃I in DMF. *HPLC purity was determined by the method described in 5.1.5.

Compound	Yield of 1st step [%]	Compound	Yield of 2nd step [%]	HPLC purity* [%]	Combined yield [%]
2a	95	3a	42	95.8	40
2b	74	3b	41	97.3	30
2c	91	3c	58	97.2	53
2d	87	3d	69	96.7	60
2e	74	3e	15	96.6	11
2f	81	3f	66	95.7	53
2g	74	3g	65	97.7	48
2h	75	3h	58	97.3	44
2i	82 ^a	3i	23	95.4	19
2j	64	3j	11	96.2	7
2k	75	3k	58	97.0	44
2l	49	3l	25	97.8	12
2m	67	3m	89	97.7	60
2n	92	3n	55	97.8	51
2o	72 ^b	3o	55	95.1	40
2p	24 ^b	3p	52	90.7	12

4-bromo-7-azaindole by palladium catalyzed SUZUKI CROSS-COUPLING. This gave access to 4-phenyl-7-azaindoles **3a–p** in 7–60% combined yield over 2 steps. With the exception of compound **3p**, which was only isolated in 91% purity, all compounds were obtained in $\geq 95\%$ purity, as determined in the HPLC-method described in chapter 5.1.5 (Table 1). TUDA students Kevin Böhm (**3b–e**), Mirco Dickhaut (**3g, 3i**), Torben Reichardt (**3j**) and Jana Anton (**3m–p**) assisted in the synthesis of selected compounds during supervised internships.

In contrast to the method described by Liddle *et al.*²³⁴, the isolation of the boronic ester intermediates was hereby omitted (see 5.2.18). In an exemplary experiment, the pinacol boronic ester intermediate of compound **3f** was isolated by column chromatography before conversion to the final SUZUKI-COUPLING product, in order to evaluate the influence of the additional purification step on the overall yield. The intermediate was successfully isolated in 29% yield (see 3.1.4. and 5.2.65) and converted to azaindole **3f** in 70% yield, giving an overall yield of 20%. In comparison, the direct conversion of alcohol **2f** yielded **3f** in 66% yield. This experiment shows that the modified method is capable of providing higher overall yields, in addition to being more time and resource efficient. However, this result must be interpreted with caution, as it cannot easily be transferred to other related reaction sequences without restrictions. Overall, the applied method provided azaindoles **3a–p** in a highly efficient manner and in good yields. Confirmation of the structural identities was performed by nuclear magnetic resonance (NMR) spectroscopy and mass spectrometry (MS). In the case of **3p**, the desired methylation at the sulfonamide nitrogen was confirmed in a heteronuclear multiple bond correlation (HMBC) NMR-experiment (Figure 26).

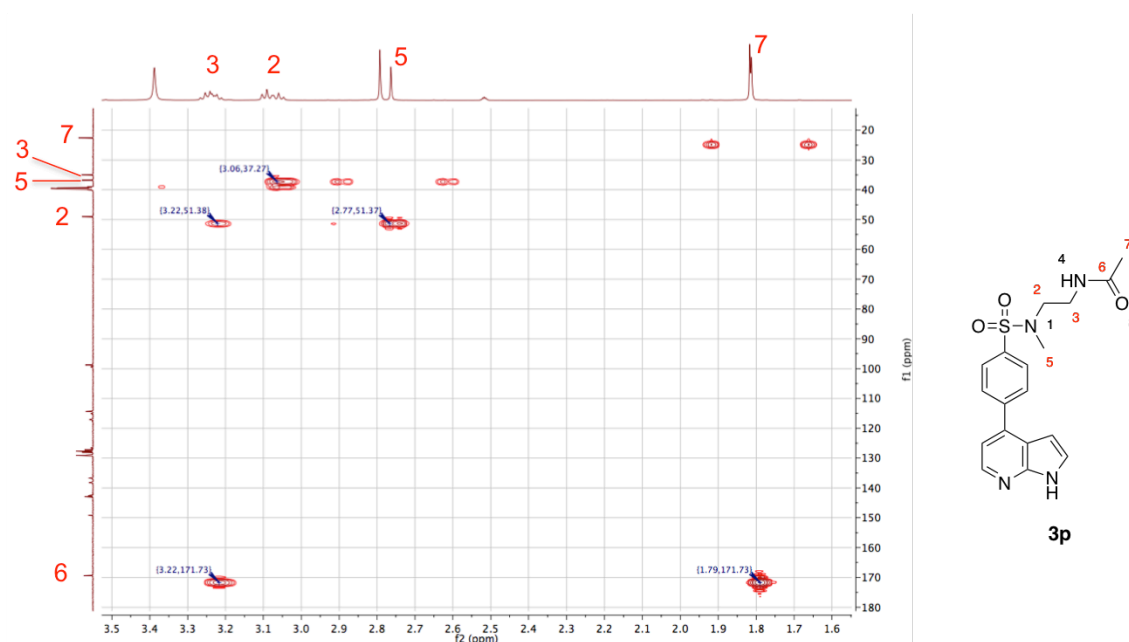
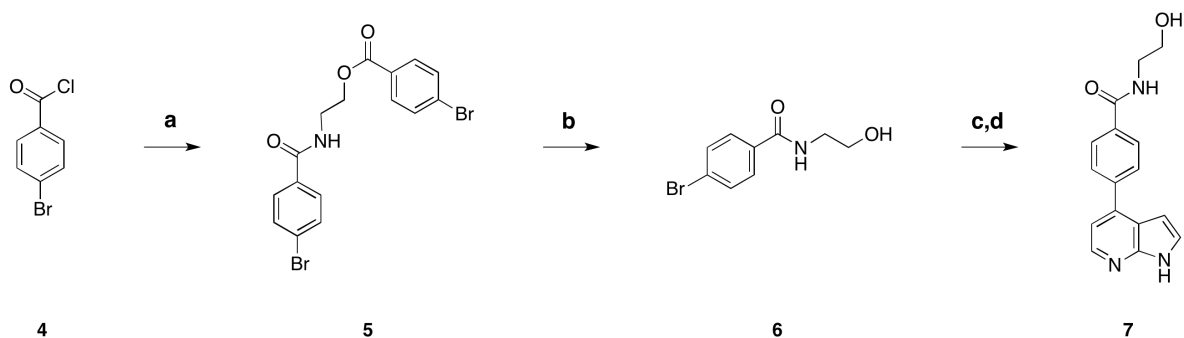


Figure 26: Cropped region of interest of the HMBC-spectrum of compound **3p**, measured at 500 MHz in DMSO-*d*₆.



Scheme 2: Synthesis of carboxylic acid derivative **7**. (a) DCM, monoethanolamine, NEt_3 , 0 °C–rt, 48%; (b) THF, 50% w/v KOH (aq), 60 °C, 92%; (c) DMF, bis(pinacolato)diboron, KOAc, $\text{PdCl}_2(\text{dppf})$, 100 °C, not isolated; (d) DMF, 4-bromo-7-azaindole, NaHCO_3 (aq), $\text{Pd}(\text{PPh})_3$, 100 °C, 43%; see experimental section for more details.

Strong evidence for the desired methylation was found, since the NMR experiment allows correlation of the *N*-methyl (C-5) protons of **3p** with C-2 and not C-3. Furthermore, the carbonyl carbon (C-6) does not correlate with the *N*-methyl protons (C-5) but only the methyl protons of C-7. Unfortunately, **3p** was only isolated in 91% HPLC purity, insufficient for biochemical evaluation.

With the aim to investigate the importance of the sulfonamide's tetrahedral geometry for Nek1 binding, the synthesis of the carboxylic amide analogue **6** of sulfonamide **2f** was attempted under identical conditions. However, 4-bromobenzoyl chloride (**4**) was unexpectedly transformed to the undesired ester **5** in 48% yield. Nonetheless, alkaline hydrolysis of **5** provided the desired benzamide **6** in excellent yield (92%), which was coupled to 4-bromo-7-azaindole, giving azaindole **7** in the final SUZUKI CROSS-COUPLING step (43% yield, Scheme 2). Overall, the carboxamide analogue **7** of 4-phenylsulfonamide-7-azaindole **3f** was made available, in 19% combined yield over three steps and 96% HPLC purity.

To sum up, the designed 4-phenyl-7-azaindole derivatives **3a–p** and **7** were synthesized in good overall yields, following an optimized literature procedure. With the exception of compound **3p**, which was only isolated in 91% purity, all compounds were obtained in $\geq 95\%$ purity and are hence all set for biochemical evaluation. The inhibitory activities and derived SARs for compounds **3a–o** are discussed in chapter 3.2.1.

Design and Synthesis of 3'-Substituted 4-Phenyl-7-azaindoles Targeting the Nek1 Back Pocket

As described in chapter 3.1.2, the inactive Nek1 kinase domain conformation features a distinct back pocket, which can potentially be targeted by carefully designed small molecule inhibitors, in order to improve potency and selectivity. The acquired docking results made an approach from the phenyl ring of the 4-phenyl-7-azaindole scaffold plausible and a series of compounds was designed for the occupation of the back pocket (Figure 27).

The most potent compound of the previously described series of UNC5452 derivatives, alcohol **3f** (see chapter 3.2.), served as the starting point for the *in silico* design, which resulted in a series of 3'-substituted **3f** derivatives that either displace, or in the case of **8f** interact with, the internal water molecule of the back pocket. Targeting the water networks of kinases, which are generally poorly understood, is a promising approach for many facets of inhibitor design, including selectivity and potency.²³⁵ The free energy change for water displacement is under current investigation and was shown to result in a net change of up to $\Delta\Delta G = -2,5$ kcal/mol in a recent experimental study.²³⁶ While the enthalpic component is unfavorable in most cases where bonding interactions are not replaced, the entropic

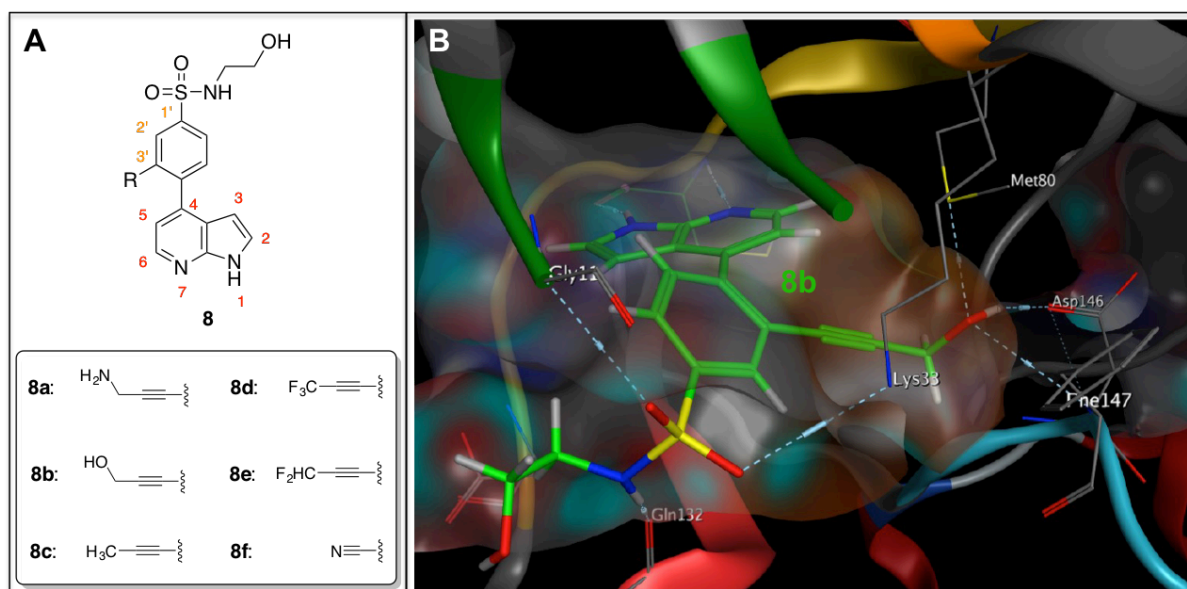
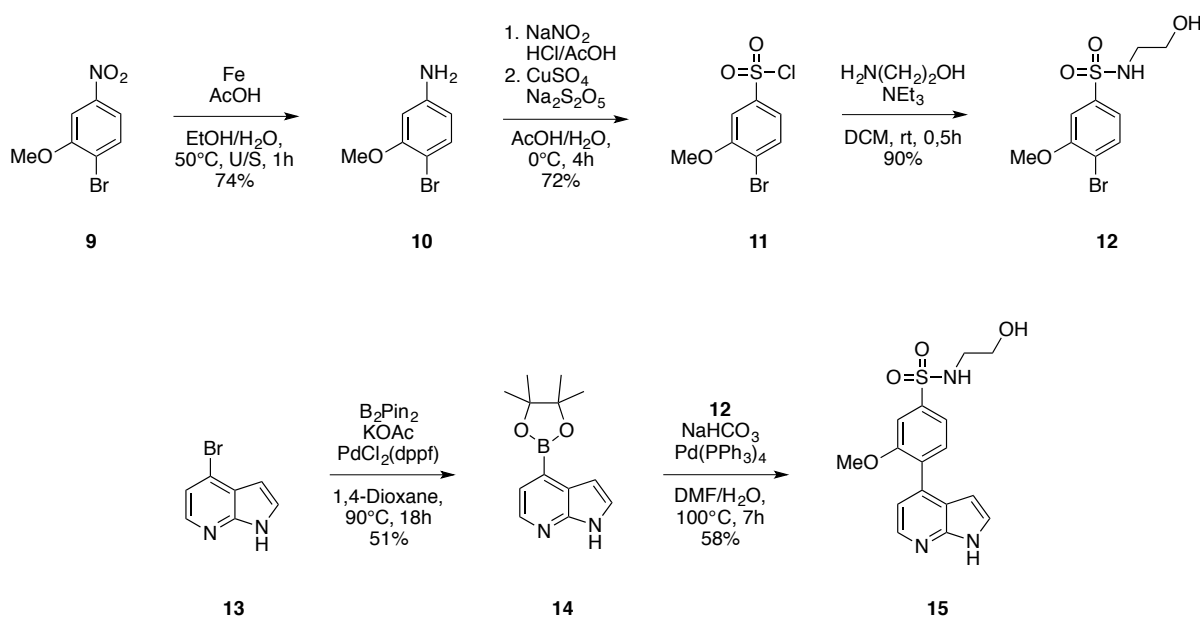


Figure 27: (A) Design of 3'-substituted 4-phenyl-7-azaindoles targeting the Nek1 back pocket. (B) Exemplary docking for compound **8b** (lime green), displacing the internal water molecule in the Nek1 kinase domain back pocket (PDB code: 4B9D.B). The P-loop is shown in dark green, the hinge region in yellow, the DFG-motif in cyan and the catalytic loop in red. Hydrogen bond interactions are indicated by dotted lines.

contribution is generally beneficial to inhibitor binding, mainly due to the increased number of hydrogen-bonding orientations available to the released water molecule in bulk.²³⁷⁻²³⁸ For compounds **3a–b**, a compensation of the unfavorable enthalpic contribution was intended by surrogate hydrogen bond interactions of the inhibitor.

Strikingly, only 3'-cyano derivative **8f** favored the “normal” binding mode, while compounds **8a–e** adopted the “flipped” binding mode in the performed docking experiments (Figure 27). Generally, one of the sulfonamide oxygens accepted a hydrogen bond from the catalytic lysine (Lys33) and the sulfonamide NH acted as a hydrogen donor toward the backbone carbonyl oxygen of Gln132. The associated synthesis of compounds **8a–f** was attempted in a supervised master's thesis (Böhm, K.; 2019: *Entwicklung eines Typ-II-Inhibitors für Nek1: Design, Synthese und Charakterisierung von 4-Arylsulfonamid-7-Azaindolen als potente DFG-out Inhibitoren*. Master's thesis; Technische Universität Darmstadt; Darmstadt, Germany; Retrievable from <https://tubama.ulb.tu-darmstadt.de/>). Unfortunately, the synthetic approach remained unsuccessful, due to the inaccessibility of a key intermediate product.

With the aim of circumventing the numerous protection steps necessary for the orthogonal introduction of the terminal alkynes in **8a–e** by palladium catalyzed SONOGASHIRA or CACCHI CROSS-COUPLING, surrogate compound **15** was devised, in order to evaluate the prospects of the designed inhibitors (Scheme 3). The synthesis of 3'-methoxy derivative **15** commenced with the iron catalyzed reduction of the commercially available nitroaryl **9** under ultrasonic



Scheme 3: Synthesis of 3'-methoxy-4-phenyl-7-azaindole **15** (14% combined yield). U/S, ultrasonic irradiation; B₂Pin₂, bis(pinacolato)diboron, dppf, 1,1'-Bis(diphenylphosphino)ferrocene.

Table 2: Reaction conditions and associated yields for the reduction of 1-bromo-2-methoxy-4-nitrobenzene (**9**) to 4-bromo-3-methoxyaniline (**10**). U/S, ultrasonic irradiation.

Reagents	Solvents	Temperature [°C]	Reaction time [h]	Yield [%]
Fe (powder), AcOH	EtOH/H ₂ O	80	1 (under U/S)	74
SnCl ₂	EtOH	reflux	24	0
Fe (powder), NH ₄ Cl	EtOH/H ₂ O	50	96	57

irradiation, as described by Gamble *et al.* (74% yield).²³⁹ The iron catalyzed reduction of nitroaryl **9** with iron-ammonium chloride, following a modified procedure by Ramadas *et al.*, proceeded only sluggishly under absence of ultrasonic irradiation.²⁴⁰ In an attempt to reduce compound **9** with stannous chloride, only the protodeboronation product was isolated (Table 2).

Sonication has been applied to numerous metal-catalyzed reactions, with the potential to improve yields, suppress side product formation or to drastically increase the catalytic activity of metal particles.²⁴¹ The acceleration of reaction rates is hypothesized to result from the repeated activation of the metal surface. Ultrasonic irradiation creates high-pressure microjets in the liquid transmission medium, through the formation and implosive collapse of bubbles, which fragmentize the metal surface to remove impurities and to increase the surface area. Furthermore, the high temperatures and pressures in the microscopic region around the sonicated hot spots lead to chemical excitation of the reagents.²⁴²

As a next step, sulfonylchloride **11** was prepared from aniline **10** in a two step, one-pot synthesis that was modified from a patented procedure (72% yield).²⁴³ First, the amino function of **10** was diazotated, with nitrous acid generated *in situ* from sodium nitrite and hydrochloric acid, followed by the copper-catalyzed chlorosulfonylation of the diazonium salt with sulfur dioxide, in the second step. The sulfur dioxide was generated *in situ* from sodium metabisulfite upon decay under aqueous acidic conditions.²⁴⁴ This method presents a convenient lab-scale alternative to the patented method,²⁴⁵ as it circumvents the difficulties associated with the handling and use of gaseous sulfur dioxide, a toxic and expensive reagent.^{244, 246}

The following amide formation between arylsulfonyl chloride **11** and ethanolamine was performed under the previously described conditions and provided sulfonamide **12** in excellent yield (90%).

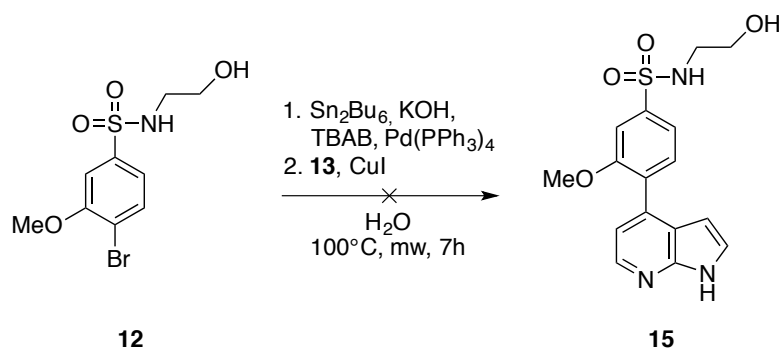
Table 3: Reaction conditions and associated yields for the MIYAUURA-BORYLATION of 4-bromo-*N*-(2-hydroxyethyl)-3-methoxybenzenesulfonamide (**12**) with bis(pinacolato)diboron, dppf, 1,1'-Bis(diphenylphosphino)ferrocene.

Base	Catalyst	Ligand	Solvent	Temperature [°C]	Reaction time [h]	Yield [%]
KOAc	PdCl ₂ (dppf)	–	DMF	100	9	0
KOAc	PdCl ₂ (dppf)	–	1,4-Dioxane	100	1.5	0
K ₂ CO ₃	PdCl ₂ (dppf)	–	1,4-Dioxane	100	4	0
K ₂ CO ₃	PdCl ₂ (dppf)	–	1,4-Dioxane	80	2	0
K ₂ CO ₃	PdCl ₂ (dppf)	–	1,4-Dioxane	80	72	0
NEt ₃	PdCl ₂ (MeCN) ₂	XPhos	1,4-Dioxane	80	67	0
NEt ₃	PdCl ₂ (PPh ₃) ₂	XPhos	1,4-Dioxane	80	22	0

As the final step, the aryl halides **12** and commercially available 4-bromo-7-azaindole (**13**) were linked by SUZUKI CROSS-COUPLING chemistry, which requires the transformation of either aryl halide to the respective organoboron compound.

In a first attempt, sulfonamide (**12**) was treated with bis(pinacolato)diboron under several MIYAUURA-BORYLATION conditions (Table 3). Unfortunately, only the protodeboronation product was isolated under the tested conditions, despite the use of different bases and solvents.²⁴⁷ It is hypothesized that the combination of the electronic effects of the sulfonamide and methoxy substituents plays a major role in promoting the decomposition, since a single methoxy ortho substituent does not result in protodeboronation in the reported literature and protodeboronation was not previously observed in related 4-bromo-phenylsulfonamides.²⁴⁸ As a consequence of these findings, the reaction temperature was lowered and the catalytic system was adapted (PdCl₂(MeCN)₂/XPhos), in order to form the catalytically active species under conditions where organoboronic decomposition is slowed down.²⁴⁹

Due to the fact that this approach also remained unsuccessful, the STILLE-COUPLING of aryl halides **12** and **13** moved into focus as an alternative method. On the one hand, this coupling method benefits from the increased stability and functional group tolerance of the intermediary organostannides, on the other hand, it suffers from the major drawback of their high toxicity and the difficulties associated with the separation of organostannic residues in the synthesis process.²⁵⁰ In order to minimize exposure and to bypass the often-difficult isolation of the organostannic intermediate, the coupling was first attempted in a microwave assisted one-pot procedure by Tan *et al.* (Scheme 4).²⁵¹

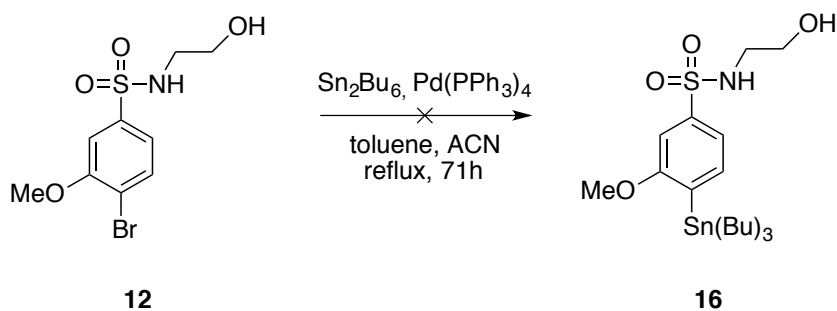


Scheme 4: Attempted microwave assisted one-pot STILLE-COUPLING of 4-bromo-N-(2-hydroxyethyl)-3-methoxybenzenesulfonamide (**12**) and 4-bromo-7-azaindole (**13**) following a procedure by Tan *et al.*²⁵¹ TBAB, tetrabutylammonium bromide.

The sequential reaction of **12** with hexabutylditin under $\text{Pd}(\text{PPh}_3)_4$ catalysis, followed by the addition of **13** and copper(I) iodide, was performed in water, using KOH as the base and tetrabutylammonium bromide (TBAB) as a phase transfer catalyst. Unfortunately, the desired product was not isolated (Scheme 4).

In order to rule out solubility issues in water, arylhalide **12** was treated with hexabutylditin and $\text{Pd}(\text{PPh}_3)_4$ under archetypal STILLE-conditions in a mixture of toluene and acetonitrile, in a second stannylation attempt. Nevertheless, no reaction was observed (Scheme 5).

At last, the synthesis of target compound **15** was achieved by MIYAUURA-BORYLATION of 4-bromo-7-azaindole (**13**) to boronic ester **14**, following a procedure by Adams *et al.*, and the subsequent SUZUKI-COUPLING with aryl halide **12** under the previously established routine conditions (Scheme 3). Both the borylation (51%) and the coupling product (58%) resulted in fair yields.



Scheme 5: Attempted stannylation of 4-bromo-N-(2-hydroxyethyl)-3-methoxybenzenesulfonamide (**12**) with hexabutylditin under $\text{Pd}(\text{PPh}_3)_4$ catalysis.

To sum up, the 3'-substituted 4-phenyl-7-azaindole **15** was synthesized in good overall yield (14% combined over 5 steps) and in HPLC purity of 98% (see 5.1.5), adequate for biochemical evaluation. The inhibitory activity of **15** and its relevance for the Nek1 back pocket-targeting approach are discussed in chapter 3.2.2.

In Silico Chemical Library Screening for the Identification of Lead Compounds

In order to explore the potential of additional interactions with the Nek1 P-loop and phosphate-binding region, an *in silico* chemical library screening was devised. Herein, the most potent compound of the 4-phenyl-7-azaindole series, alcohol **3f** (see chapter 3.2.1.), served as the starting point for a virtual library docking experiment to identify hit compounds (Figure 28).

It was reasoned, that the structural relation of the sulfonamide-linked side chain to *N*-substituted α -amino acids, and their corresponding alcohols, allows for the utilization of nature's own toolkit for protein binding. Moreover, this strategy ensured the convenient access to stereoisomerically pure starting materials and a straightforward synthetic approach.

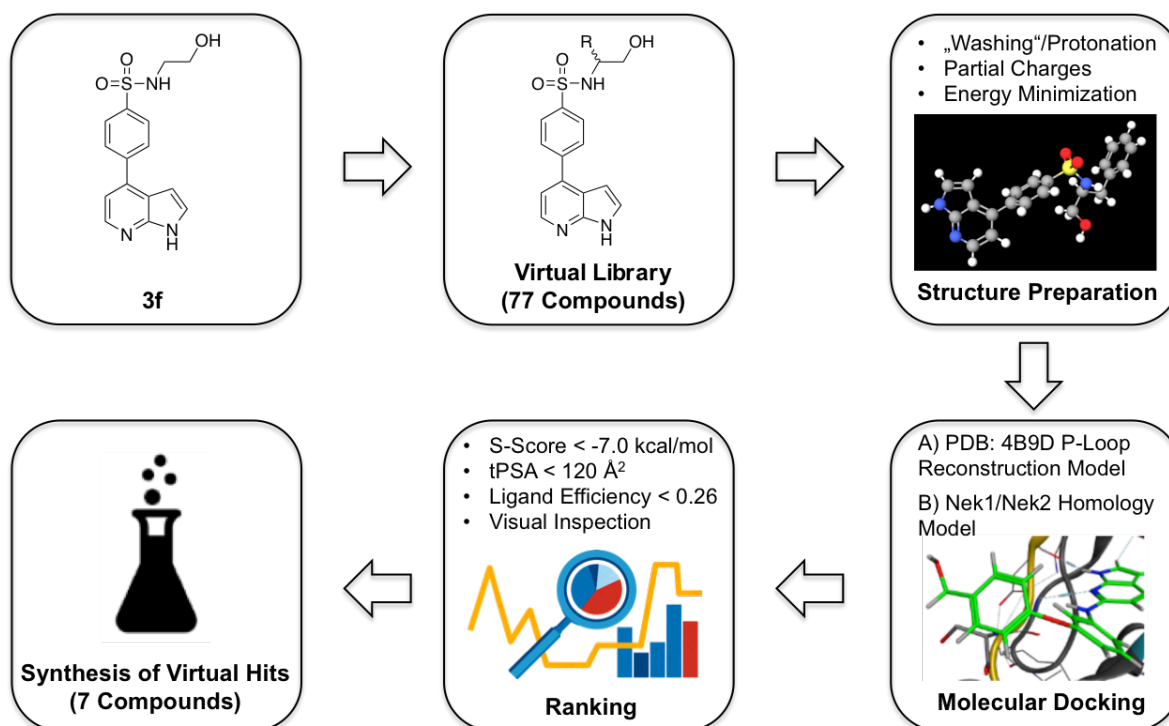
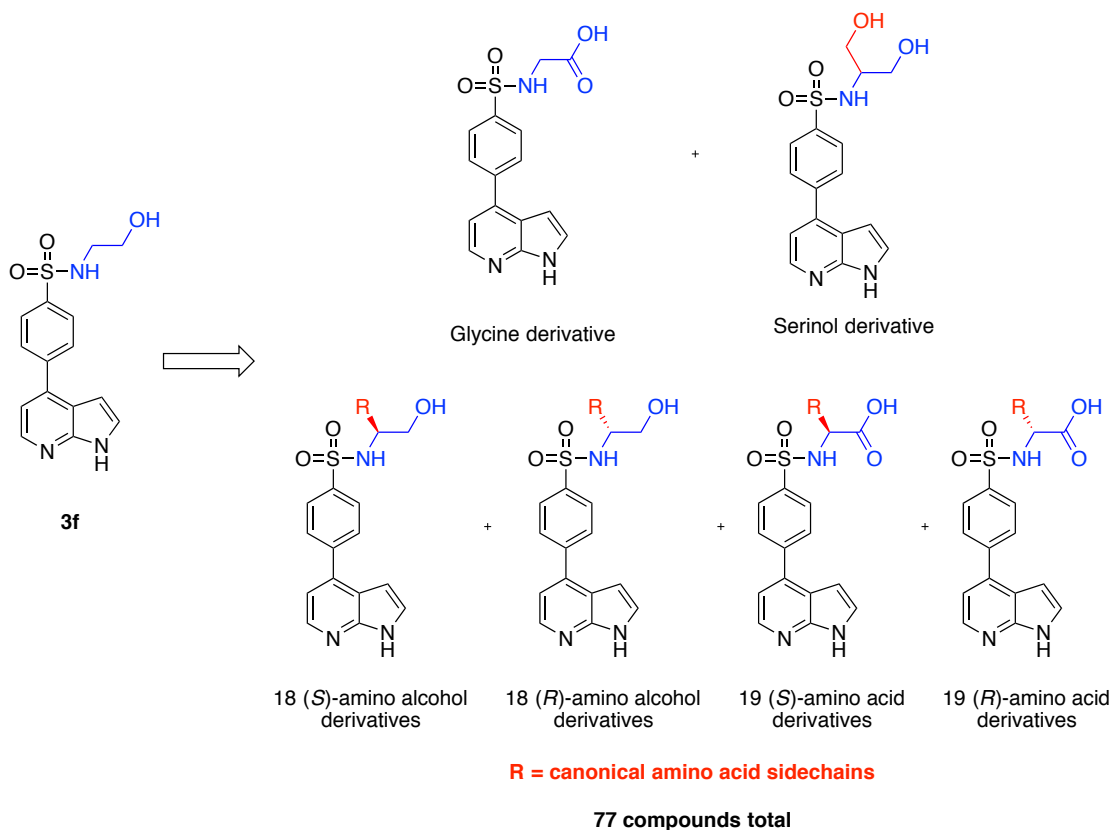


Figure 28: *In silico* chemical library screening to identify hit compounds (see experimental section 5.3 for more details).



Scheme 6: Structure derivation of the virtual compound library from 4-phenyl-7-azaindole Nck1 inhibitor **3f** (77 compounds). The sulfonamide-linked α -amino acid/alcohol motif is shown in blue. The R-groups are derived from the 20 canonical amino acid side-chains (red).

The virtual library included a total of 77 compounds that correspond to both stereoisomers of the 20 canonical amino acids and their respective amino alcohols, with the exception of the glycine-, glycinol-, and Serinol-derivatives that do not contain a stereocenter (Scheme 6).

As a means to ensure proper molecular mechanics parameters and atom types, the compound library underwent several structure preparation steps, generally accepted as a prerequisite in the field.²⁵²⁻²⁵⁴ This so-called “ligand washing” included the addition of explicit hydrogen atoms, the replacement of atomic coordinates with an aesthetic 2D depiction layout, the regeneration of 3D-coordinates via 3D-embedding, the enumeration of tautomers and protonation states, the recalculation of partial charges and finally energy minimization (see experimental section 5.3.4 for more details).

With the ligands prepared, molecular docking of the virtual library into the Nck1 kinase domain required reconstruction of the P-loop, which was performed using two independent methods. Firstly, the P-loop was reconstructed using the *SuperLooper2* (SL2) web application, a fragment-based tool for the prediction and interactive placement of loop structures.²⁵⁵

Starting from the ligand-bound B-chain (PDB code: 4B9D.B), which was chosen because of its shorter unresolved gap, the missing loop sequence EGSFG between G11 and K17 was reconstructed by using the AGPAG loop (between P311 and R317) of the *Mycobacterium tuberculosis* probable periplasmic sugar-binding lipoprotein UspC (PDB code: 5K2Y) crystal structure as a template.

Secondly, a homology model of the Nek1 kinase domain was created, using the ‘homology model’ function of the *Molecular Operating Environment* (MOE) software suite and the X-ray structure of Nek2 bound to an aminopurine inhibitor (PDB code: 5M53) as the template (Figure 29A).²²⁹ The quality of the homology model was validated by phi-psi-plot analysis of the homology models protein geometry and a root-mean-square deviation (RMSD)-plot of atomic positions, comparing the Nek1 kinase domains crystal structure to the homology model (Figure 29).

The phi-psi plot serves as an important indicator for the quality of a three-dimensional protein structure, by providing an overview of allowed and disallowed regions of torsion-angle values.²⁵⁶ The homology model was found to be of high quality, with 94.7% of the 263 residues in most favored regions, 3.8% in additional allowed regions and only 1.5% in disallowed regions. Remarkably, the RMSD-plot revealed that nearly all of the significant conformational differences are located outside of the active site (Figure 29). Most prominently, the activation loop rotated upwards into close proximity of the C-helix, presumably forming additional interactions. However, the structurally important DFG-motif deviated only moderately.

As a next step, the “washed” virtual compound library was docked into the prepared P-loop reconstructed model structures (see 5.3.4) and virtual hit compounds were identified by analysis of the docking results. The selection was based on docking score (S-score), topological polar surface area (TPSA), ligand efficiency and visual inspection of the docked conformations. S-scores are predicted values of the free energy of protein-ligand binding that are not all by themselves suited for the ranking of docking results, as a consequence of their inability to account for hydrophobic effects and important receptor conformations in the unbound state.²⁵⁷⁻²⁵⁸ In addition, S-scores are known to poorly scale with molecular mass and the number of rotatable bonds in compounds, due to the increased number of hypothetical interactions in the binding site.²⁵⁹ Therefore, S-scores rather de-select inappropriate compounds to provide an enriched shortlist of compounds with high probability of being active, a feat more easily achieved within the accuracy limitations, and must be complemented with appropriate selection strategies.

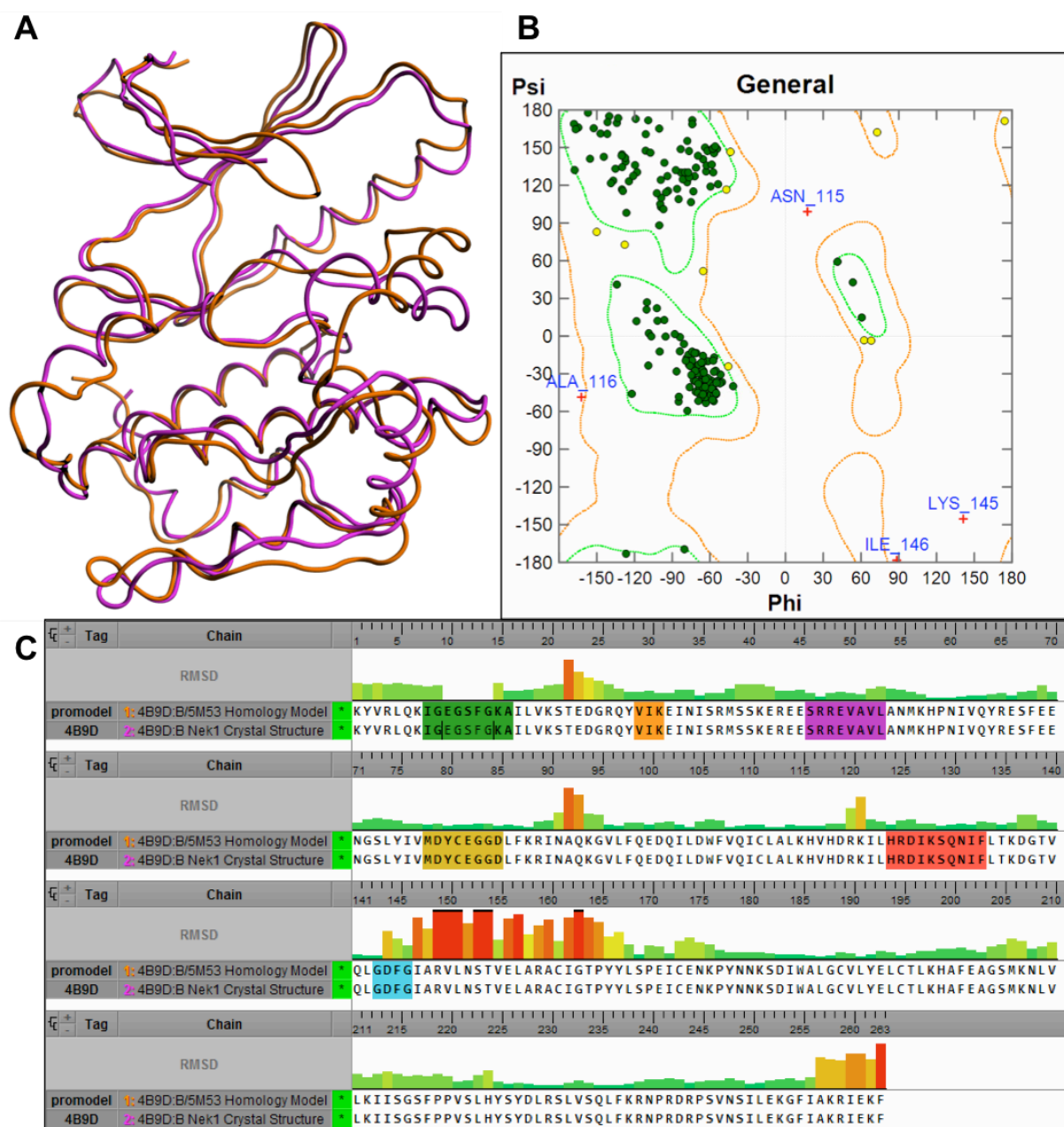


Figure 29: Evaluation of the Nek1 kinase domain homology model. The model was created using the ‘homology model’ function of the *molecular operating environment* (MOE) software suite, using the crystal structure of Nek2 bound to an aminopurine inhibitor (PDB code: 5M53) as the template. A) Superposition of the homology model with the Nek1 crystal structure (PDB code: 4B9D:B). The homology model is shown in orange and the Nek1 crystal structure in magenta. B) Phi-Psi-plot analysis of the homology models protein geometry. Favored torsion-angle regions are shown in green, with residues as green dots, and additional allowed regions in orange, with residues as yellow dots. Outliers are marked as red crosses. C) Root-mean-square deviation (RMSD)-plot of atomic positions for the Nek1 kinase domains crystal structure and the homology model. The glycine-rich loop is marked in green and the catalytic lysine motif in orange. The C-helix is marked in purple. The DFG-motif is marked in cyan, the hinge region in yellow and the catalytic loop in red.

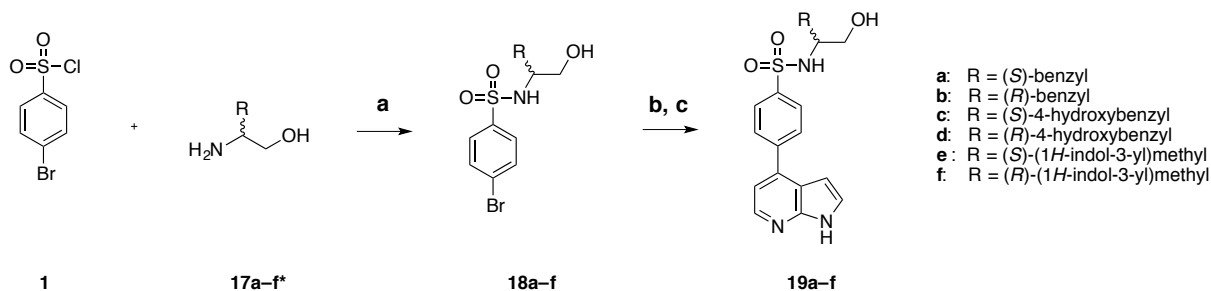
Most importantly, this entailed visual inspection of the pre-selected docking poses, thereby adding chemical intuition knowledge and experience to the selection process. Moreover, solubility and permeability influencing parameters were taken into account. Poor absorption and permeation are more likely when the calculated n-octanol-water partition coefficient (CLogP) is greater than 5, the molecular weight is greater than 500 and when there are more than 5 hydrogen bond donors or 10 acceptors.²⁶⁰ In this case, none of the library compounds exceeded these restrictions. In addition, a topological surface area (tPSA) limit of 120 Å² was defined. The tPSA is defined as the amount of molecular surface arising from heteroatoms together with their attached hydrogen atoms.²⁶¹ tPSA values over 140 Å² are generally considered to be poor at permeating cell membranes, while a tPSA under 90 Å² is usually required to cross the blood-brain-barrier.²⁶² Ligand efficiency (LE) and the binding efficiency index (BEI), defined as the binding energy per heavy atom or the molecular weight, were also included in the selection process, as a means of indirectly minimizing the focus on non-specific potency gains.²⁶³

Selection and Synthesis of *In Silico* Chemical Library Screening Hits

Both the homology and the SL2-model provided similar results, favoring aromatic amino alcohol side chains (see Appendix: Table A 1 and Table A 2). Interestingly, the structurally related Nek1 kinase cross screening hit UNC5078 also possesses an equivalent benzyl group, although the stereoinformation is missing (Figure 21).⁶¹

Based on the aforementioned criteria, six virtual hit compounds were selected and synthesized (Scheme 7). Compounds **20a** and **20b** were selected for synthesis despite their moderate S-scores, as a means of evaluating the structure models, given their significant scoring differences. Moreover, they structurally complement the top-five scoring compounds **20c-f** for the envisioned SAR-studies. It should be noted that two of the library compounds, namely glycinol derivative **3f** and phenylalanine derivative **3l**, were already made available for pharmacological evaluation (Scheme 1). Interestingly, compound **3f** scored lowest in both models, while hit compound **3l** was among the top scorers only in the SL2-model.

Amino alcohols **17a-f** were converted to final compounds **19a-f** through a similar sequence described in Scheme 1. **17a-c** were obtained commercially, while **17d** was prepared by reduction of D-tyrosine methyl ester with sodium borohydride. In contrast, amino alcohols **17e-f** were obtained by reduction of L-tryptophan and D-tryptophan following a procedure by



Scheme 7: Synthesis of six virtual hit compounds, identified in the in silico chemical library screening. **a)** **18a–b**: DCM, amine, NEt₃, 0 °C–rt, 98–99%; **18c–d**: H₂O/acetone, L-phenylalanine, NaHCO₃, rt, 60–70%; **18e–f**: DCM/acetonitrile, *N,N*-diisopropylethylamine, 0 °C–rt, 30–43%, **b)** **19a–f**: DMF, bis(pinacolato)diboron, KOAc, PdCl₂(dppf), 100 °C, not isolated; **c)** **19a–f**: DMF, 4-bromo-7-azaindole, NaHCO₃ (aq), Pd(PPh₃)₄, 100 °C, 26–62%. *Compounds **17a–c** were obtained commercially; Compound **17d** was prepared from D-tyrosine methyl ester hydrochloride by freeing the amine with KOAc in acetonitrile and subsequent reduction with NaBH₄ in methanol, 61%; Compounds **17e–f** were prepared by reduction of the corresponding tryptophan isomer using the method described by Meyers *et al.*, 72–84%;²⁶⁴ see experimental section for more details.

Meyers *et al.*²⁶⁴⁻²⁶⁵ Amide formation between 4-bromosulfonyl chloride (**1**) and amino alcohols **17a–f** provided aryl halides **9a–f**, which again underwent MIYAURO-BORYLATION and subsequent SUZUKI CROSS-COUPLING to afford azaindoles **19a–f** (Scheme 7).

A compilation of yields and HPLC purities for the synthesis of the six virtual hit compounds **19a–f**, are given in Table 4. The reduction of D-tyrosine methyl ester to **17d** was achieved in fair yield (61%) and the reductions of L-tryptophan and D-tryptophan gave **17e** and **17f** in good to very good yields (72% and 84%) that are comparable to the literature yields.²⁶⁴

Amide formation was achieved in excellent yields for the phenylalaninol-derivatives **18a** (98%) and **18b** (99%), using the previously described method (chapter 3.1.3). However, yields dropped significantly for tyrosinol-derivatives **18c** (60%) and **18d** (70%) as well as tryptophanol-derivatives **18e** (30%) and **18f** (43%). Solubility issues arose for amino alcohols **17a** and **17b** in dichloromethane, and the solvent system was thus changed to a mixture of acetone and water and sodium bicarbonate was used as the base instead of triethylamine. Moreover, the reaction time was increased to 17 h to ensure ample conversion in the case of **18a**. In order to address the long reaction time, the reaction temperature was increased to 40 °C for the synthesis of **18b**, resulting in a significantly decreased reaction time of 4h.

It has to be noted that both **18a** and **18b** were obtained as crude products with acceptable HPLC purity (85%) for further use without additional purification. In the case of **18e/f**, amide

Table 4: Compilation of yields and HPLC purities for synthesis of six virtual hit compounds, identified in the *in silico* chemical library screening. (a) **18a–b**: DCM, amine, NEt₃, 0 °C–rt, 98–99%; **18c–d**: H₂O/acetone, L-phenylalanine, NaHCO₃, rt, 60–70%; **18e–f**: DCM/acetonitrile, *N,N*-diisopropylethylamine, 0 °C–rt, 30–43%, (b) **19a–f**: DMF, bis(pinacolato)diboron, KOAc, PdCl₂(dppf), 100 °C, not isolated; (c) **19a–f**: DMF, 4-bromo-7-azaindole, NaHCO₃ (aq), Pd(PPh₃)₄, 100 °C, 26–62%. *Compounds **17a–c** were obtained commercially; Compound **17d** was prepared from D-tyrosine methyl ester hydrochloride by freeing the amine with KOAc in acetonitrile and subsequent reduction with NaBH₄ in methanol, 61%; Compounds **17e–f** were prepared by reduction of the corresponding tryptophan isomer using the method described by Meyers *et al.*, 72–84%;²⁶⁴ *HPLC purity was determined by the method described in 5.1.5. Cpd., compound.

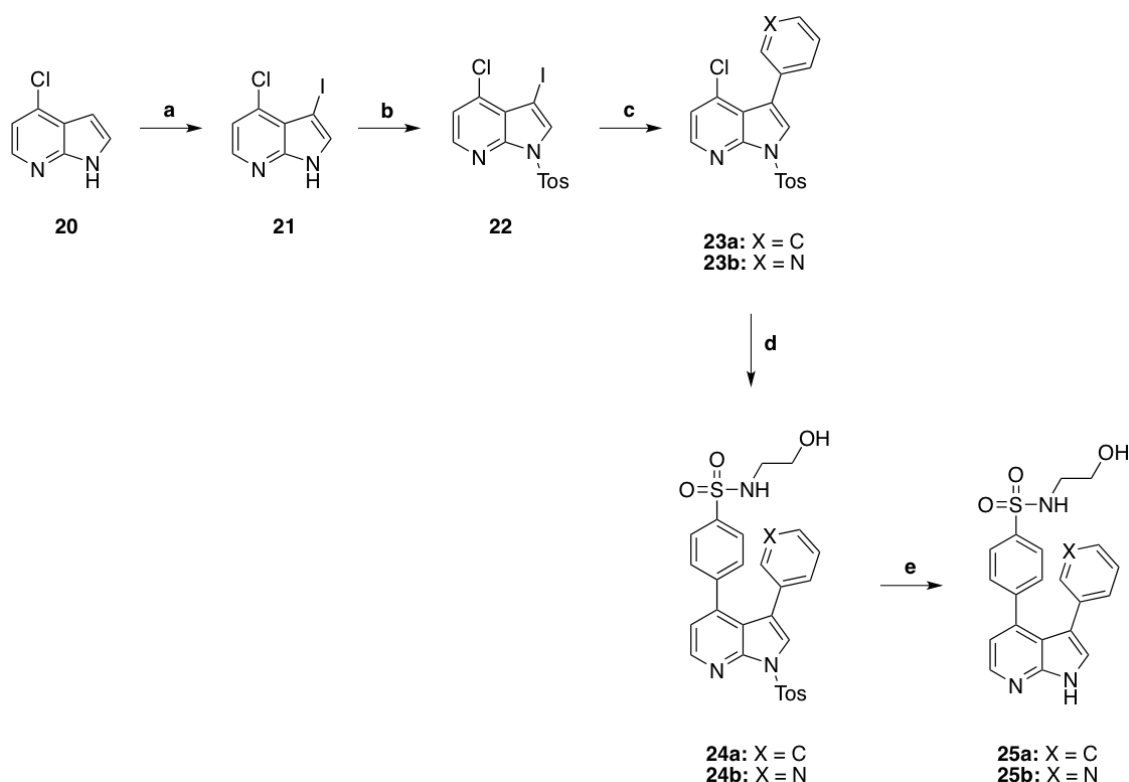
Cpd.	Yield [%]	Cpd.	Yield of 1st step [%]	Cpd.	Yield of 2nd step [%]	HPLC purity* [%]	Combined yield [%]
17a	-	18a	98	19a	42	98.1	37
17b	-	18b	99	19b	56	95.1	55
17c	-	18c	60	19c	51	95.0	31
17d	61	18d	70	19d	26	95.3	11
17e	72	18e	30	19e	60	96.5	13
17f	84	18f	43	19f	62	98.3	22

formation was performed at ambient temperature in a mixture of acetonitrile and dichloromethane using diisopropylethylamine as the base. Here, significant side product formation made chromatographic purification necessary, resulting in the low yields. The following MIYAUURA-BORYLATION/SUZUKI CROSS-COUPLING cascade step was achieved in yields comparable to previously described syntheses, giving 4-phenyl-7-azaindoles **19a–f** in 26–62% yield. This resulted in fair to very good combined yields of 11–55% over 3 steps, for **19a–c**, and 4 steps, for **19d–f**, respectively.

All six compounds were obtained in ≥95% purity, as determined in the HPLC method described in 5.1.5, and are thus poised for biochemical evaluation and related SAR studies that follow in chapter 3.2, alongside a comparison of the employed docking models and a discussion regarding their goodness.

3.1.4. Design and Synthesis of 3,4-Disubstituted 7-Azaindole Nek1 Inhibitors

Based on the *in silico* scaffold analysis described in chapter 3.1.1, 3-substitution in the “N1-Out”-7-azaindole scaffold was hypothesized to enable the establishment of additional interactions with the Nek1 kinase domains hydrophilic ribose-binding region. The performed docking studies revealed that a linker moiety has to be introduced in order to reach the ribose-binding residues and that the linker would have to traverse over the Phe135 residue that intrudes the Nek1 ATP pocket from the catalytic loop. Location and orientation of this hydrophobic residue led to the hypothesis that Phe135 may also be targetable for hydrophobic and/or aromatic π -stacking interactions through an appropriate linker moiety. Furthermore, interactions with Phe135 may potentially contribute to Nek1-selectivity, as a consequence of the peculiar nature of this residue. In order to test this hypothesis, two derivatives of the previously established 4-phenyl-7-azaindole **3f**, more specifically 3-phenyl derivative **25a** and 3-pyridinyl derivative **25b**, were designed and synthesized in five steps (Scheme 8).

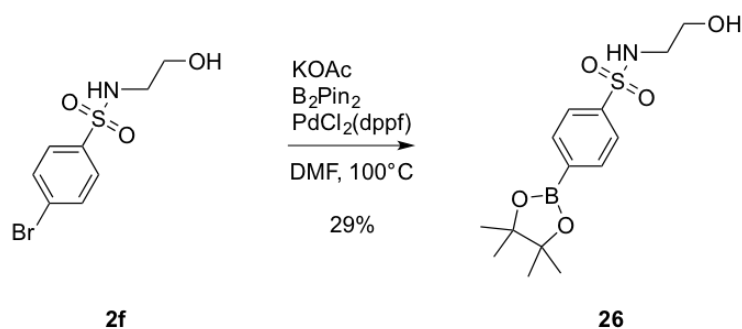


Scheme 8: Synthesis of 3,4-disubstituted 7-azaindoles **25a** and **25b**. a) DMF, *N*-Iodosuccinimide, rt, 99%; b) DCM, TosCl, *n*-Bu₄NCl, 4N NaOH, rt, 98%; c) **23a**: 1,4-Dioxane/H₂O (4:1), Pd[PPh₃]₄, Cs₂CO₃, PhB(OH)₂, 120 °C, 77%; **23b**: 1,4-Dioxane/H₂O (4:1), Pd[PPh₃]₄, Cs₂CO₃, 4-pyridinylboronic acid, 120 °C, 23%; d) 1,4-Dioxane/H₂O (100:1), PdCl₂[dtbpf], Cs₂CO₃, *N*-(2-hydroxyethyl)-4-(Bpin)benzenesulfonamide, 120 °C, **24a**: 41%, **24b**: 48%; e) THF, *n*-Bu₄NF trihydrate, 60 °C, mw, **25a**: 14%, **25b**: 21% (contaminated).

The synthesis commenced with the regioselective iodination of commercially available 4-chloro-7-azaindole (**20**) with *N*-Iodosuccinimide in DMF, which was performed according to a published procedure by Cardenas *et al.* and provided 4-chloro-3-iodo-7-azaindole (**21**) in almost quantitative yield.²⁶⁶ In the following step, the azaindole NH was tosylated with *p*-toluenesulfonyl chloride in excellent yield (98%) by a standard procedure that utilizes a biphasic system (DCM/4N NaOH, 7:3) and tetrabutylammonium chloride as a phase transfer catalyst. The tosyl-group is not introduced to protect the nitrogen but to reduce the electron density of the electron-rich pyrrole moiety that is prone to dehalogenation at the 3-position under SUZUKI-conditions.²⁶⁷⁻²⁶⁸

With the tosyl-group in place, site-selective SUZUKI-COUPILING to the 3-position was performed following a patented procedure by Galatsis *et al.*,²⁶⁹ which was followed by a second SUZUKI-COUPILING step that introduced the phenyl-sulfonamide moiety at the 4-position. Site-selectivity of the first coupling step was achieved through the differing C-Hal bond dissociation energies that mainly determine the rate of the rate-determining and irreversible oxidative addition of the catalytic palladium species.²⁷⁰ As expected, no dehalogenation and no reactions at the chlorinated 4-position were observed for the couplings of diaryl-7-azaindole **22** with phenylboronic acid and 4-pyridinylboronic acid. The reactions provided 3-aryl-7-azaindoles **23a** and **23b** in poor to good yields of 77% and 23% respectively. The poor yield for the synthesis of **23b** is attributed to major formation of the detosylated product species, which nonetheless may still serve as a suitable reactant in the following steps, albeit this was not further investigated.

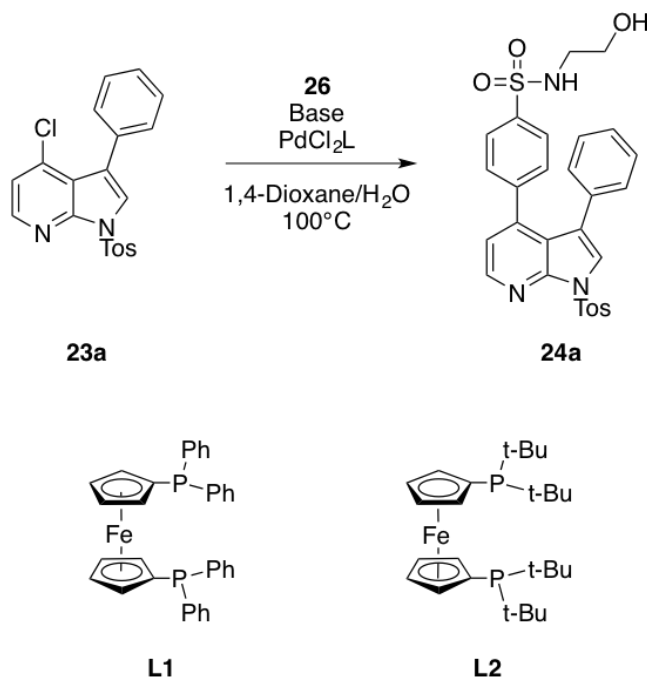
The second SUZUKI-COUPILING step required the synthesis of boronic ester **26** from previously described 4-bromo-*N*-(2-hydroxyethyl)benzenesulfonamide (**2f**), which was achieved in 29% yield under standard MIYAUURA-BORYLATION conditions (Scheme 9).



Scheme 9: MIYAUURA-BORYLATION of 4-bromo-*N*-(2-hydroxyethyl)benzenesulfonamide (**2f**) to boronic ester **26**. KOAc, potassium acetate; B₂Pin₂, Bis(pinacolato)diboron; dppf, 1,1'-Bis(diphenylphosphino)ferrocene.

In a first attempt, the SUZUKI-REACTION between boronic ester **26** and aryl chloride **23a** failed under the conditions described in the aforementioned patent (Table 5, entry 1).²⁶⁹ Since no conversion was observed over 16 hours, the 1,1'-bis(diphenyl-phosphino)ferrocene (dppf) ligand in the utilized catalytic palladium complex was substituted with an alternative bidentate ligand, 1,1'-bis(di-tert-butylphosphino)ferrocene (dtbpf), which was shown to increase palladium complex activity for the conversion of unactivated and sterically challenged aryl chlorides in a report by Colacot *et al.*²⁷¹ However, the desired product was only identified in traces by HPLC/MS analysis and the protodeboronation product of **26** was isolated as the major side product alongside the recovered starting material (Table 5, entry 2).

Table 5: Screening of conditions for the Pd-catalyzed SUZUKI-COUPPING of aryl chloride **23a** and arylboronic acid **26** to 3,4-disubstituted 7-azaindole **24a**. ^[a]Determined by HPLC-MS analysis.



Entry	Ligand	Base	Solvent ratio (1,4-Dioxane/H ₂ O)	Reaction time [h]	Yield
1	L1	Cs ₂ CO ₃	10:1	16	-
2	L2	Cs ₂ CO ₃	10:1	16	Traces ^[a]
3	L2	KOtBu	1:0	15	-
4	L2	Cs₂CO₃	100:1	6.5	41%

Reaction conditions: **23a** (1.0 eq.; 0.4 mmol), **26** (1.5 eq.), Base (2 eq.), Pd catalyst (0.03 eq.), Solvent mixture (5 mL) degassed under argon. Note: The bold entry highlights the best result.

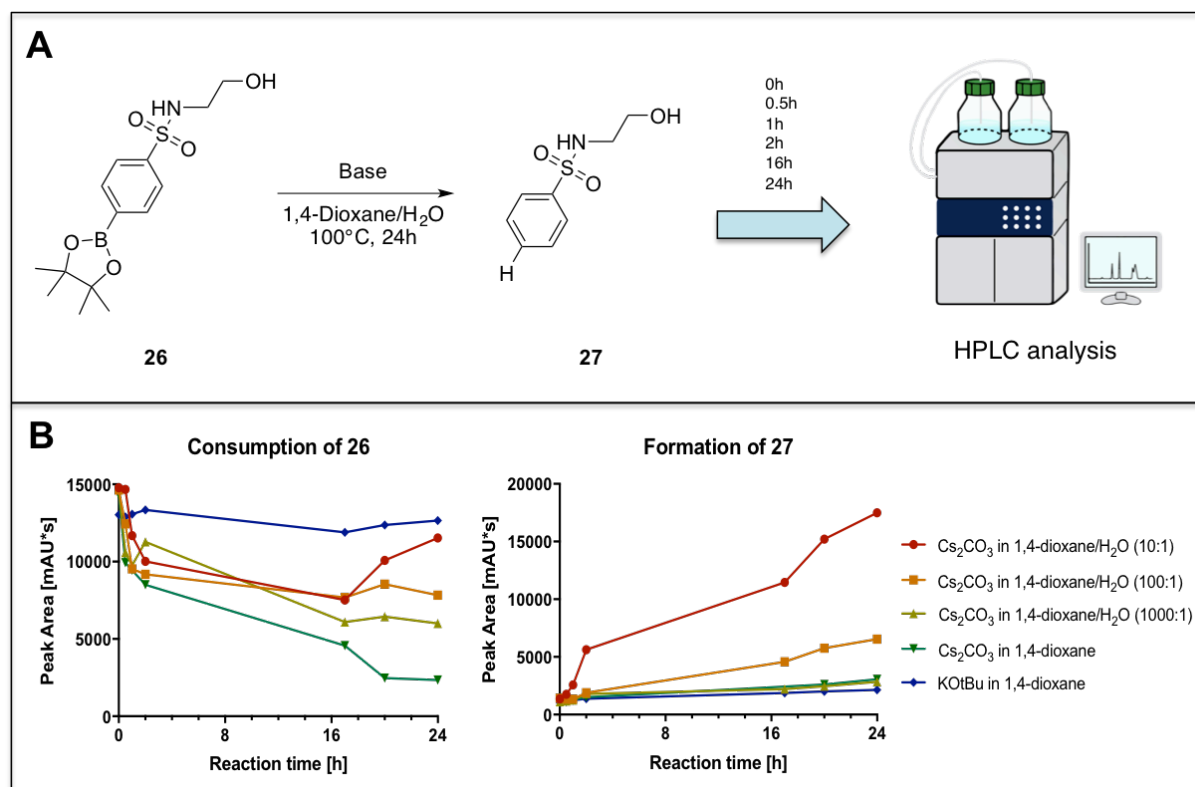


Figure 30: Investigation of the influences of differing water-to-solvent ratios and bases on the protodeboronation of arylboronic ester **26**. (A) Reaction conditions and experimental setup. All solvents were degassed prior to use. Aliquots of the reaction mixture were analyzed by HPLC directly after addition of the base and after 0.5h, 1h, 2h, 16h and 24h, using a diode array detector at a wavelength of 230 nm. $t_R(\mathbf{26}, 230\text{nm}) = 2.8$ min; $t_R(\mathbf{27}, 230\text{nm}) = 3.2$ min, as identified by previous HPLC/MS-analysis. (B) Consumption of arylboronic ester **26** and formation of protodeboronation product **27**, as determined by HPLC analysis and plotting of peak area [mAU*s] versus reaction time [h]. The HPLC clipart is licensed under the Creative Commons Attribution 4.0 International license (<https://creativecommons.org/licenses/by/4.0/deed.en>).

On the basis of a proposed mechanism for the base-catalyzed protodeboronation of areneboronic acids, which involves the ipso-protonation of an arylboronate intermediate by water, the influences of differing water-to-solvent ratios and bases on the protodeboronation of **26** were investigated.²⁷²⁻²⁷³ Arylboronic ester **26** was hence treated at 100 °C with caesium carbonate in several 1,4-dioxane/water ratios (10:1, 100:1, 1000:1, 1:0). As an alternative, the use of the organic base potassium tert-butoxide (KOtBu) was investigated in 1,4-dioxane. The consumption of **26** as well as the formation of the protodeboronation product **27** were monitored by HPLC over 24h (Figure 30, see experimental section 5.1.5 for more details, DAD).

The experiment revealed that the accelerated formation of **27**, under caesium carbonate treatment, is indeed positively correlated to the water content and that protodeboronation

of **26** is already significantly suppressed at a 1,4-dioxane/water ratio of 100:1. Furthermore, it appears that the protodeboronation of **26** is almost fully repressed at a 1,4-dioxane/water ratio of 1000:1 and under water free conditions. Conversely, the consumption of arylboronic ester **26** is accelerated with reduced water content at the presence of caesium carbonate. However, almost no consumption of **26** was observed at the presence of KOtBu. It is important to note here that several unidentified decomposition products were visible in the HPLC spectrograms

As a consequence of these findings, the SUZUKI-COUPPING of aryl chloride **23a** and arylboronic acid **26** to 3,4-disubstituted 7-azaindole **24a** was again attempted under modified conditions using PdCl₂(dtbpf) as the catalyst. No conversion of **23a** was observed over 15 hours at 100 °C using KOtBu as the base under water-free conditions (Table 5, entry 3). This is likely to result from the fact that water plays an important role in SUZUKI-COUPPING reactions, which has been emphasized in many studies that for example suggest that a water phase aids in dissolving and providing polar reactants.²⁷⁴⁻²⁷⁵

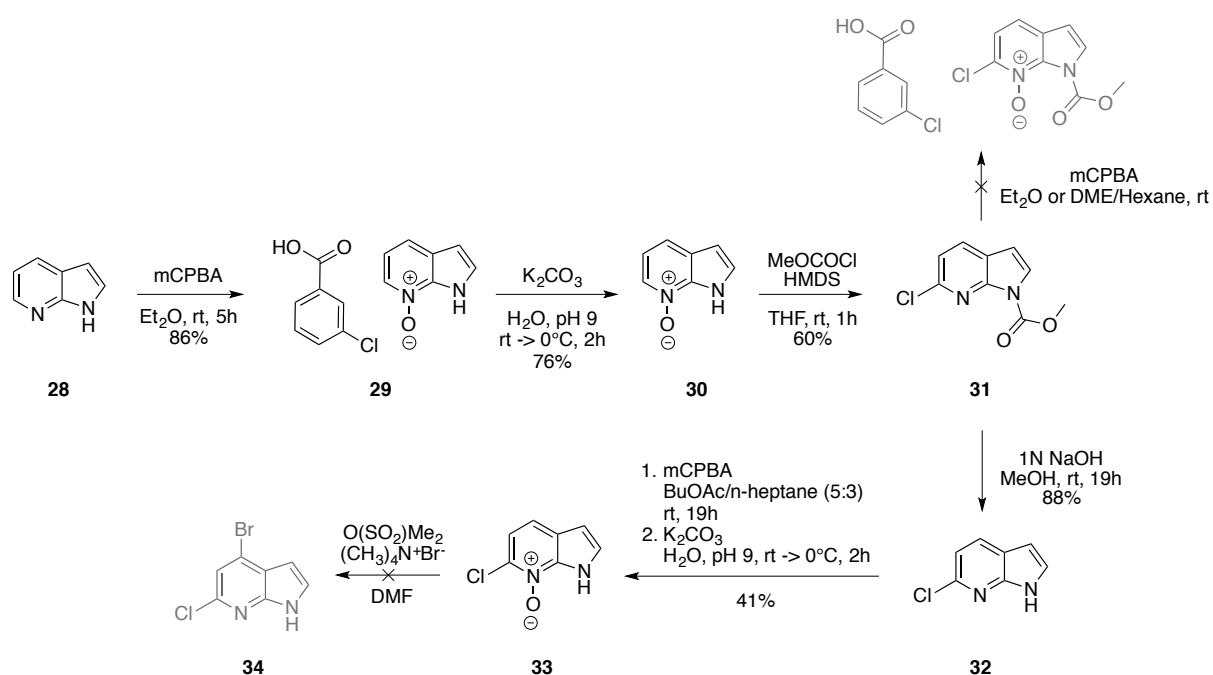
At last, 3,4-disubstituted 7-azaindole **24a** was successfully synthesized in 41% yield, using caesium carbonate as the base in a 100:1 mixture of 1,4-dioxane and water in combination with the PdCl₂(dtbpf) catalyst system (Table 5, entry 4). The pyridinyl analogue **24b** was obtained under equivalent conditions in 48% yield. Based on the results of the screened conditions, it appears that finely-tuned amounts of water and an appropriate catalyst system are required for the efficient coupling of arylboronic esters to the chlorinated 4-position in sterically challenged 3-aryl-7-azaindoles.

In the final step, detosylation of **24a** and **24b** was performed with tetrabutylammonium trihydrate under microwave irradiation in THF, following a modified procedure by Yasuhara *et al.*²⁷⁶ The purification of target compounds **25a** and **25b** was attempted by normal-phase flash chromatography, but neither **25a** nor **25b** were isolated as a consequence of insufficient separation in several eluent systems. Eventually, isolation of **25a** was achieved by automated reversed-phase gradient chromatography using a *Combiflash R_f 4x-system (Teledyne ISCO)*, which required subsequent lyophilization, and **25a** was hence isolated in poor yields of 14% (96% HPLC-purity). Unfortunately, the isolation of target compound **25b** was not achieved in sufficient HPLC purity of >95% for biochemical evaluation, following the same chromatography approach. The low yields of the final step may be attributed to material loss during lyophilization, although comparably low yields have been reported for the detosylation of 3,5-disubstituted 7-azaindoles under alkaline conditions before.^{223, 277}

Nonetheless, a synthetic route to 3,4-disubstituted 7-azaindoles was successfully established and **25a** was investigated for its inhibitory activity against Nek1, in order to test the aforementioned hypothesis (see chapters 3.2.1 and 3.2.4).

3.1.5. Design and Synthesis of 4,6-Disubstituted 7-Azaindole Nek1 Inhibitors

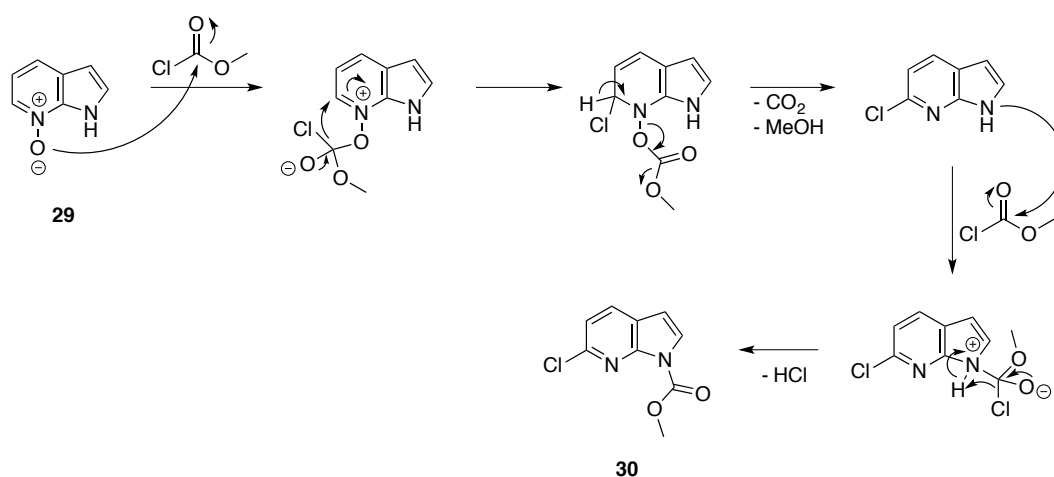
Based on the identification of the “N1-In” 7-azaindole scaffold and the related molecular docking studies, 4,6-disubstituted 7-azaindoles were identified as promising structures for Nek1 inhibition (see chapters 3.1.1 and 3.1.2). Generally, the synthesis of 7-azaindole derivatives can be approached by *de novo* assembly of the substituted 1*H*-pyrrolo[2,3-*b*]-pyridine ring system or by site-selective derivatization of the parent core structure. Due to its more modular nature, a site-selective approach was favored in this thesis, which was ought to facilitate the synthesis of a broader variety of derivatives, once a synthetic route was established. While several strategies for the *de novo* synthesis of 7-azaindole and its derivatives are reported in the literature, the available methods for site-selective derivatization of the parent molecule are mostly focused on the pyrrole nitrogen or the 3-position.²⁷⁸ However, L'Heureux *et al.* have described the synthesis of 4-bromo-7-azaindole from 7-azaindole in one step²⁷⁹ and Minakata *et al.* have published a selective chlorination at the 6-position.²⁸⁰ Hence, the appropriate sequence of these methods, in combination with selected transition metal-catalyzed cross-coupling reactions was envisioned to produce a robust synthetic route that allows convenient access to a broad variety of 4,6-disubstituted 7-azaindoles, in similar fashion to the previously described route to 3,4-disubstituted 7-azaindole derivatives (see 3.1.4).



Scheme 10: Attempted synthesis of key compound 4-bromo-6-chloro-7-azaindole (**34**) from 7-azaindole (**28**).

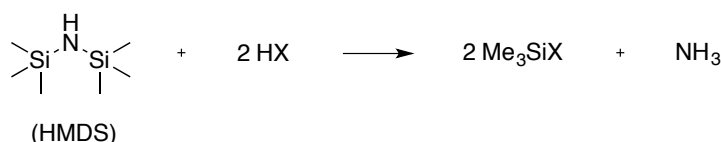
In a first attempt, the synthesis of key compound 4-bromo-6-chloro-7-azaindole (**34**) was approached by starting from commercially available 7-azaindole (**28**). The synthesis foresaw the site-selective 6-chlorination of 7-azaindole (**28**), which was to be performed via a REISSERT-HENZE type reaction from related *N*7-oxide **29**. 7-Azaindole *N*-oxide (**29**) was obtained as the stable meta-chlorobenzoic acid (mCBA)-salt (86% yield), through the reaction of 7-azaindole (**28**) with meta-chloroperbenzoic acid (mCPBA), and subsequently freed by basic treatment in 76% yield, following a published procedure by Sreenivasachry *et al.* (Scheme 10).²⁸¹

In similar fashion to the BOEKELHEIDE-REARRANGEMENT, acyl transfer of methyl chloroformate to the *N*-oxide oxygen, in the following REISSERT-HENZE type reaction, facilitates cleavage of the N-O bond during rearomatization while simultaneously positioning the chlorine leaving group for nucleophilic attack on the 6-position. The required methyl chloroformate excess ultimately leads to *N*-acylation of the pyrrole nitrogen (Scheme 11).



Scheme 11: Proposed mechanism for the site-selective 6-chlorination of 7-azaindole *N*-oxide (**29**) with methyl chloroformate in a REISSERT-HENZE type reaction.

Since unreacted *N*-oxides are prone to form unreactive hydrogen halide salts, the method described by Minakata *et al.* utilizes hexamethyldisilazane (HMDS) as the base, which showed improved yields over other organic bases in a comparative study.²⁸⁰ This comes from the fact that HMDS traps the proton released upon *N*-Acylation, resulting in the formation of ammonia that hence does not serve as a proton donor in contrast to otherwise obtained ammonium salts (Scheme 12). By following this method, *N*-acylated 6-chloro 7-azaindole **30** was isolated in 60% yield after purification by column chromatography (Scheme 10).²⁸⁰



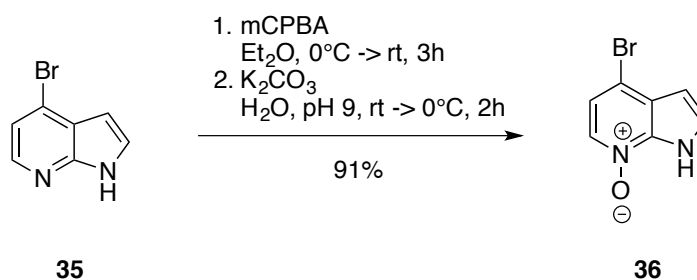
Scheme 12: Reaction of HMDS with hydrogen halides to trimethylsilyl halides and ammonia.

The site-selective 4-bromination of resulting azaindole **30** once again required *N*-oxidation with mCPBA, which was attempted in diethylether and dimethoxyethane/n-hexane, and repeatedly failed due to solubility issues, incomplete conversion, and problematic product isolation. As a consequence, the acyl group on N1 of compound **30** was readily removed by basic treatment, to give 6-chloro-7-azaindole **32** in 88% yield, and the following *N*-oxidation was achieved with MCPBA in a 5:3 mixture of n-butyl acetate/n-heptane in 41% yield, using a modified procedure by Storz *et al.* (Scheme 10).²⁷⁸

Unfortunately, no product formation was observed in the subsequent 4-bromination with methanesulfonic anhydride and tetrabutylammonium bromide, following the method described by L'Heureux *et al.*, in several attempts.²⁸²

As a consequence, the synthesis of key compound 4-bromo-6-chloro-7-azaindole (**34**) was attempted in an alternative three-step-synthesis, using commercially available 4-bromo-7-azaindole (**35**) as the starting point. Again, *N*-oxidation of starting compound **35** was performed with mCPBA and *N*-oxide **36** was freed from the corresponding *N*-oxide mCBA salt by basic precipitation with potassium carbonate in water, following a modified version of the previously described method by Sreenivasachry *et al.* (Scheme 13).²⁸¹

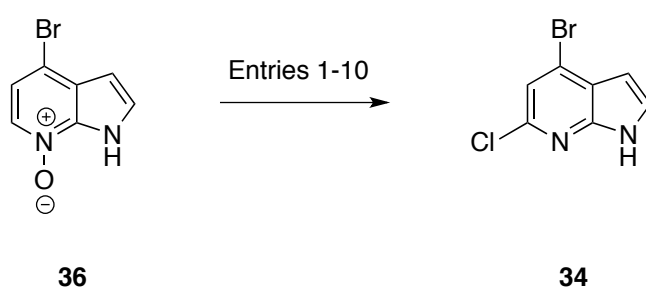
For the following site-selective modification on C6, several chlorinating agents and conditions were screened. Initially, adapted versions of the previously described methods by



Scheme 13: *N*-Oxidation of 4-bromo-7-azaindole (**35**) with mCPBA in Et₂O to corresponding *N*-oxide mCBA salt, which was freed by basic precipitation with potassium carbonate in water, following a modified method by Sreenivasachry *et al.*²⁸¹

L'Heureux *et al.*,²⁸² using mesyl chloride (MsCl), and Minakata *et al.*,²⁸⁰ using methyl chloroformate (MCF) and HMDS, were investigated alongside methods employing thionyl chloride (SOCl₂) and phosphoryl chloride (POCl₃)²⁸³ as chlorinating agents (Table 6). Treatment of compound **36** with MsCl in DMF and 1,2-dichloroethane (DCE) at 75 °C resulted in an inseparable mixture of products, among them the 4-chloro substitution product and the 4,6-dichloro product (Table 6, entries 1 and 2).

Table 6: Screening of chlorinating agents and conditions for the site-selective 6-chlorination of 4-bromo-7-azaindole *N*-oxide (**36**) to 4-bromo-6-chloro-7-azaindole (**34**).



Entry	Chlorinating agent	Base	Solvent	Temperature	Reaction time	Yield
1	MsCl	-	DMF	75 °C	72 h	-
2	MsCl	-	DCE	75 °C	72 h	-
3	MCF	HMDS	THF	rt	3 h	-
4	MCF	HMDS	THF	0 °C → rt	3 h	16%
5	SOCl ₂	Pyridine	neat	75 °C	5 h	-
6	POCl ₃	-	DCM	0 °C → rt	17h	No conversion
7	POCl ₃	DIPA	DCM	0 °C → rt	17 h	No conversion
8	POCl ₃	-	neat	110 °C (reflux)	3 h	24%
9	POCl ₃	-	neat	110 °C (reflux)	17 h	-
10	POCl₃	-	neat	55 °C → 80 °C	30 h	42%

Reaction conditions: **Entries 1, 2, 3 and 4:** **36** (1.0 eq.; 0.47 mmol), chlorinating agent (2.5 eq.), base (1.0 eq.), dry Solvent (5 mL). **Entry 5:** **36** (1.0 equiv; 0.47 mmol), chlorinating agent (100.0 eq.), base (1.0 eq.). **Entries 6 and 7:** **36** (1.0 eq.; 0.47 mmol), chlorinating agent (11.0 eq.), dry Solvent (1 mL). **Entries 8, 9 and 10:** **36** (1.0 eq.; 0.47 mmol), chlorinating agent (100.0 eq.) Note: The bold entry highlights the best result. DCE, 1,2-dichloro-ethane; DCM, dichloromethane; DIPA, diisopropylamine; eq., equivalents; MCF, methyl chloroformate; MsCl, mesyl chloride; THF, tetrahydrofuran; rt, room temperature.

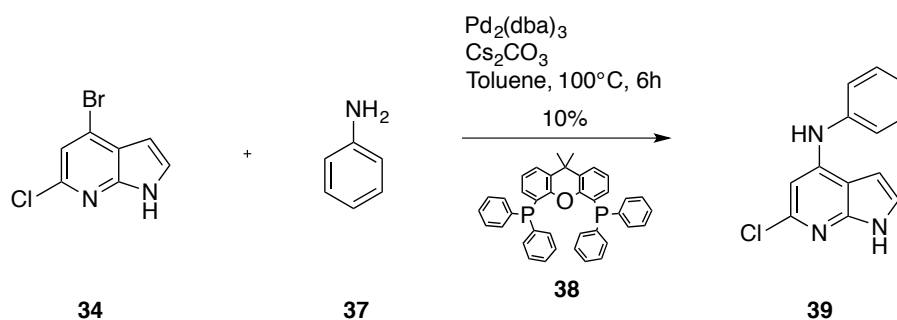
However, HPLC-MS analysis revealed formation of a species with the expected m/z value and the predicted isotopic distribution, although no evidence for the desired regioselectivity can be deduced from the acquired data.

Similar problems arose for the conversion of compound **36** with thionyl chloride (Table 6, entry 5), and by following the method by Minakata *et al.* with MCF and HMDS at room temperature (Table 6, entry 3).²⁸⁰ Side product formation was partially suppressed through modification of the latter procedure, more specifically by slow addition of MCF under ice cooling, and target compound **34** was hence isolated in 16% yield and characterized by a combination of MS and 2D-NMR methods (Table 6, entry 4). Nevertheless, the method suffered from lacking site-selectivity, since the undesired 3-chlorinated regioisomer was identified as the main product. Furthermore, undesired substitution at the 4-position prevailed.

Alternatively, the synthesis of compound **34** was attempted by treatment of *N*-oxide **36** with phosphoryl chloride, on the basis of a reported site-selective short-path chloride transfer on (-)-nicotine pyridine *N*-oxide via the BOEKELHEIDE REACTION by Schmidt *et al.*²⁸³ Schmidt and colleagues achieved regiocontrol by addition of a sterically demanding base, which overrides the intramolecular steering effects of the neighbouring amine, present in the (-)-nicotine derived substrate.

Due to the fact that no regiocompetition of that sort is present in the case of 7-azaindole *N*-oxide **36**, the conversion with phosphoryl chloride was attempted at the presence and absence of diisopropylamine in dichloromethane at low temperatures (Table 6, entries 6 and 7). Unfortunately, no conversion of compound **36** was herein observed.

In order to study the reaction at higher temperatures, the use of a solvent was omitted and **36** was heated to reflux in neat phosphoryl chloride. Early abortion of the reaction (3 h) came with a much-improved product distribution, when compared to the previously employed methods, and allowed for the isolation of desired product **34** in 24% yield (Table 6, entry 8). Interestingly, no substitution at the 4-position was observed, but prolonged reaction times at elevated temperatures, as well as removal of phosphoryl chloride by distillation during work-up, increased the formation of undesired 3-chloro and 5-chloro regioisomers (Table 6, entry 9). At last, 4-bromo-6-chloro-7-azaindole (**34**) was obtained in improved yield of 42% by reaction of 4-bromo-7-azaindole *N*-oxide (**36**) in neat phosphoryl chloride at reduced temperatures over 30 h, followed by aqueous work-up (Table 6, entry 10).



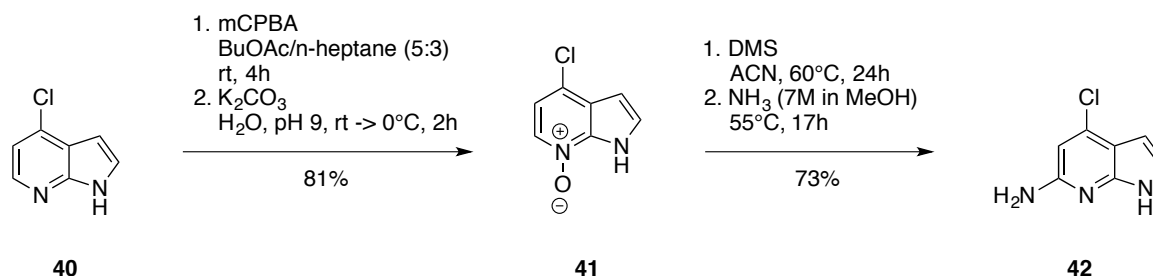
Scheme 14: BUCHWALD-HARTWIG AMINATION of 4-bromo-6-chloro-7-azaindole (**34**) with aniline (**37**) to arylamine **39**, following a modified procedure by Surasani *et al.*²⁸⁴

With key compound **34** in hand, first studies toward its selective modification via palladium catalyzed BUCHWALD-HARTWIG AMINATION were undertaken.

Following a modified procedure by Surasani *et al.*, which uses $\text{Pd}_2(\text{dba})_3$ as the palladium source in combination with bidentate phosphine ligand Xantphos (**38**) and caesium carbonate as the base, compound **34** was successfully aminated with aniline (**37**) at the 4-position, giving arylamine **39** in 10% yield (Scheme 14).²⁸⁴

The low yield results from significant side-product formation, which may be mitigated by the use of appropriate BUCHWALD-HARTWIG precatalyst systems.²⁸⁵

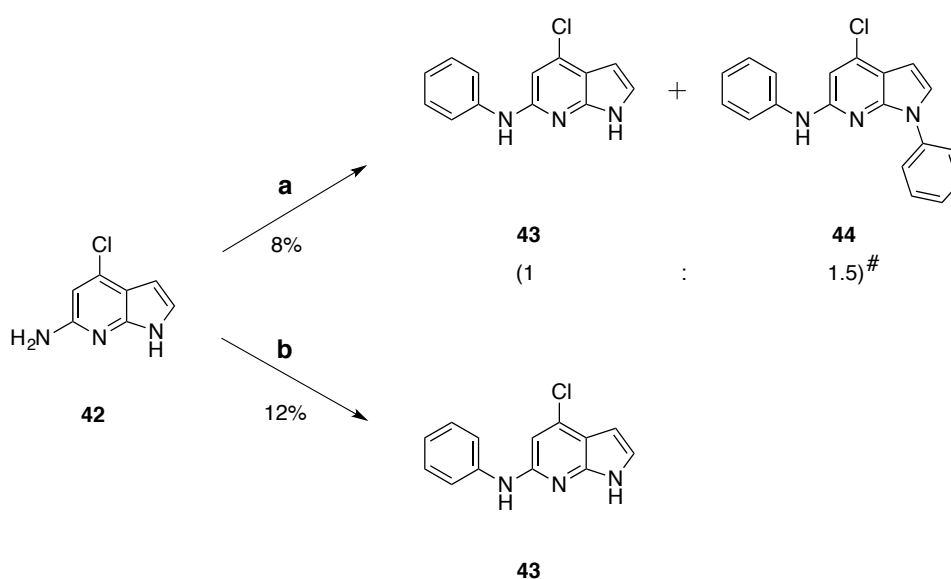
As an alternative route to 4,6-disubstituted 7-azaindoles, commercially available 4-chloro-7-azaindole (**40**) was transformed to its *N*-oxide **41** in the previously described manner (81% yield) and smoothly aminated at the 6-position via a REISSERT-HENZE type reaction with dimethyl sulfate (DMS) and ammonia, to give 6-amino-4-chloro-7-azaindole (**42**, 73% yield) in a modified procedure by Storz *et al.* (Scheme 15).²⁷⁸



Scheme 15: Synthesis of 6-amino-4-chloro-7-azaindole (**42**) from 4-chloro-7-azaindole (**40**) by *N*-oxide formation and subsequent REISSERT-HENZE type amination, following a modified procedure by Storz *et al.*²⁷⁸ DMS, dimethyl sulfate; ACN, acetonitrile.

In similar fashion to the previously described REISSERT-HENZE type reaction (Scheme 11), methylation of the *N*-oxide oxygen by DMS herein primes the N-O bond for cleavage upon nucleophilic attack by ammonia on the 6-position.

As a next step, first studies toward the selective modification of 6-amino-4-chloro-7-azaindole (**42**) via two transition-metal-catalyzed cross-coupling reactions were undertaken. BUCHWALD-HARTWIG AMINATION of bromobenzene with compound **42** was performed with a palladium(II) acetate/XPhos catalyst system, in a published procedure by Sreenivasachry *et al.*, giving desired 6-phenylaminated product **43** in 8% yield (Scheme 16).²⁸¹



Scheme 16: Synthesis of 4-chloro-6-phenylamino-7-azaindole (**43**) from 6-amino-4-chloro-7-azaindole (**42**) via (a) BUCHWALD-HARTWIG AMINATION and (b) CHAN-LAM COUPLING. a) Toluene, bromobenzene (1.0 eq.), NaOtBu (3.0 eq.), Pd(OAc)₂ (0.1 eq.), XPhos (0.3 eq.), 110 °C, 5 h, 8%; b) DCM, phenylboronic acid (2.0 eq.), copper(II) acetate (1.0 eq.), NEt₃ (2.0 eq.), reflux (40 °C), 42 h, 12%.# Product ratio estimated by ¹H-NMR.

Unfortunately, the reaction suffered from long reaction times, incomplete conversion and the significant formation of undesired diarylated product **44**.

As an alternative method, CHAN-LAM COUPLING between phenylboronic acid and 6-amino-4-chloro-7-azaindole (**42**) was investigated. Copper-catalyzed CHAN-LAM REACTIONS between arylboronic acids and varying nucleophilic groups have recently emerged as an efficient and environmentally friendly alternative to traditional carbon-heteroatom coupling methods, by combining the advantages of mild reaction conditions with lower toxicity and stability under air.²⁸⁶

On the basis of a published procedure by Vantourout *et al.*, compound **42** was selectively *N*-phenylated to 4-chloro-6-phenylamino-7-azaindole (**43**), using copper(II) acetate as the catalyst and triethylamine as the base (Scheme 16).²⁸⁷

Unfortunately, conversion of the starting material remained incomplete over prolonged reaction times (42 h) and compound **43** was only obtained in 12% yield. However, no undesired phenylation on the pyrrole nitrogen was observed, likely due to the milder reaction conditions. Despite the promising results of the CHAN-LAM COUPLING, the reaction conditions need to be optimized in order to maximize the yield.

To sum up, two promising synthetic routes toward 4,6-disubstituted 7-azaindole Nck1 inhibitors have successfully been established. Key intermediary compounds **34** and **42** were made available from affordable starting materials, in good overall yields of 38 and 59% over two steps respectively, which allow for modular diversification by appropriate transition-metal-catalyzed cross-coupling reactions. Furthermore, first studies toward the selective modification of these compounds were successfully undertaken, although reaction conditions need to be further optimized, in order to maximize yields.

As a consequence of the more promising docking results for the 4-phenyl-7-azaindoles, as well as their facile synthetic accessibility, the main focus of this work was set on the development of Nck1 inhibitors based on the “N1-Out”-scaffold, and no further studies toward Nck1 inhibitors of the “N1-In”-scaffold were undertaken.

3.2. Structure-Activity-Relationship Studies and Pharmacological Evaluation

This chapter deals with the performed structure-activity-relationship studies for the developed 4-phenyl-7-azaindole (3.2.1.), back pocket-targeting (3.2.2.), *in silico*-screening based (3.2.3.) and 3,4-disubstituted 7-azaindole Nek1 Inhibitors as well as with the pharmacological evaluation of therein identified lead compounds (3.2.5. to 3.2.7.).

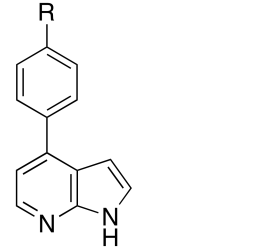
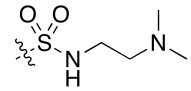
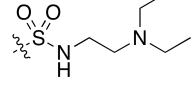
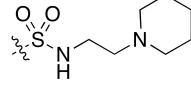
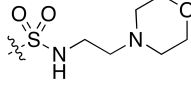
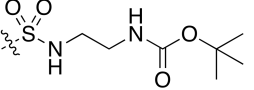
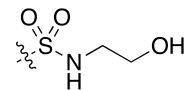
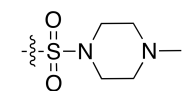
3.2.1. Structure-Activity-Relationship for 4-Phenyl-7-Azaindole Nek1 Inhibitors

Initially, a commercial *in vitro* Nek1 activity assay by Eurofins Discovery (*KinaseProfiler*TM Item 15-020KP10) was benchmarked with previously described Nek1-inhibitor UNC5452 (**3a**). Compound **3a** inhibited Nek1 activity by only 63% at 1 μ M in this ATP-dependent radiometric assay, compared to the 99.8% inhibitory activity reported by Wells *et al.*⁶¹ It is hypothesized that this difference results from the fact that screening of the parent PKIS2 dataset was performed using an ATP-independent competition-binding assay (*DiscoverX* KINOME-scan[®]) that instead measures the ability of a small molecule to compete for the active site with an immobilized inhibitor.²³⁰

The molecular modeling suggested interactions of **3a** with the Nek1 hinge Cys83, catalytic Lys33, and the catalytic loop residues Asp128 and Gln132 to be essential for potent inhibition. With the primary aim of optimizing the dimethylaminoethyl fragment in mind, an improvement of inhibitory activity was initially attempted by derivatization of the terminal dimethylamino group, as described in chapter 3.1.3. In the light of the performed docking experiments and the significant drop in activity upon removal of the two methyl groups from UNC5452 (**3a**) to primary amine UNC5023 in the PKIS2 dataset,⁶¹ the influence of the amine pKa was evaluated by testing compounds **3b–e** in the aforementioned radiometric kinase activity assay (Table 7).

Overall, the radiometric Nek1 assay revealed no clear trend between amine basicity and kinase binding. Compounds **3b**, **3d** and **3e** displayed decreased activity in comparison to **3a**, while **3c** showed comparable activity. Hence, the results were confirmed by the determination of IC₅₀ values for **3a–e** in a *LANCE*[®] *Ultra TR-FRET* Nek1 activity assay at K_{M,ATP} (60 μ M), with kind help from Dr. Ulrich Pehl (*Merck Healthcare KGaA*, Biopharma R&D, Darmstadt, Germany) (Table 7, see experimental section 5.4.1 for more details).

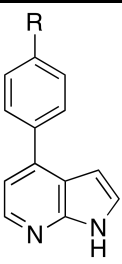
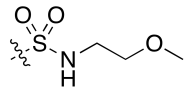
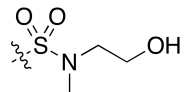
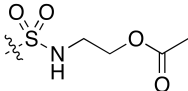
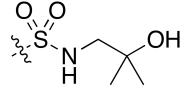
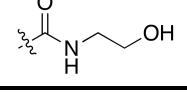
Table 7: Inhibitory activity of compounds **3a–f** and **3k** against Nek1 and Nek2. ^[a]Eurofins Discovery KinaseProfiler™ service at 10 μ M ATP; ^[b]LANCE® Ultra TR-FRET kinase assay at $K_{m,ATP}$ (60 μ M); ^[c]Eurofins Discovery IC50Profiler™ service at $K_{m,ATP}$ (90 μ M). #A relative IC₅₀ value was provided as the determined IC₅₀ value exceeded the employed maximum test concentration (10 μ M). See experimental section for more details. See appendix D for raw data. CI, confidence interval; n.d., not determined; n.e., no effect at maximum concentration (30 μ M).

		Residual kinase activity (1 μ M) ^[a]		IC ₅₀ [μ M] ^[b]	
Cpd.	R	Nek1	Nek1	95% CI	Nek2
3a		37%	7.1 (4.6) ^[c]	6.4 – 7.8 (4.0 – 5.4) ^[c]	n. e.
3b		68%	10	9.6 - 11	n. e.
3c		37%	6.6	6.3 – 6.9	n. e.
3d		51%	25	23 - 29	n. e.
3e		49%	n.e.	n.d.	n. e.
3f		12%	3.2 (2.1) ^[c]	2.9 – 3.5 (1.6 – 2.8) ^[c]	n. e.
3k		45%	>10 [#]	n.d.	n. e.

Strikingly, no effect on Nek1 activity was herein observed for **3e**, which reduced Nek1 activity to 49% in the radiometric assay. Furthermore, compound **3d** displayed a ~2.5-fold decrease in inhibitory activity compared to **3b**, in contrast to the previous findings. Apart from these discrepancies, the results confirm that a variation of the terminal amine's basicity did not improve inhibitory activity against Nek1. Rigidification of the flexible dimethylaminoethyl fragment in compound **3k** also significantly decreased inhibitory activity against Nek1 to over 10 μ M from 7.1 μ M for **3a**. As a result, it was reasoned that the attempted optimization of interactions of **3a** with the catalytic loop residues Asp128 and Gln132, as suggested by the docking experiment, is elusive, and that the introduction of an alternative hydrogen bond

donor might improve inhibitory activity. Synthesis and evaluation of alcohol **3f** revealed a significant decrease in residual Nek1 activity to 12% as well as a more than 2-fold decreased IC_{50} value of $3.2 \mu\text{M}$, compared to **3a**. In order to evaluate the hydrogen bond characteristics of the hydroxy group in **3f**, methyl ether **3g** and acetyl ester **3i** analogues were prepared and tested (Table 8).

Table 8: Inhibitory activity of compounds **3g–j** and **7** against Nek1 and Nek2. ^[a]Eurofins Discovery KinaseProfiler™ service at $10 \mu\text{M}$ ATP; ^[b]LANCE® Ultra TR-FRET kinase assay at $K_{m,ATP}$ ($60 \mu\text{M}$). #A relative IC_{50} value was provided as the determined IC_{50} value exceeded the employed maximum test concentration ($30 \mu\text{M}$). See experimental section for more details. See appendix D for raw data. CI, confidence interval; n.d., not determined; n.e., no effect at maximum concentration ($30 \mu\text{M}$).

		Residual kinase activity ^[a] ($1 \mu\text{M}$)		IC_{50} [μM] ^[b]	
Cpd.	R	Nek1	Nek1	95% CI	Nek2
3g		44%	>30 [#]	n.d.	n. e.
3h		46%	2.7	2.5 – 3.0	n. e.
3i		49%	8.8	7.0 - 11	n. e.
3j		32%	5.8	4.7 – 7.2	n. e.
7		89%	29	25 - 35	n. e.

Both analogues showed decreased inhibitory activities compared to **3f**, with an IC_{50} value greater than $30 \mu\text{M}$ for ether **3g** and an IC_{50} value of $8.8 \mu\text{M}$ for ester **3i**. The results clearly indicate that the hydroxy group in **3f** does indeed act as a hydrogen bond donor and not as an acceptor, as the reduced acceptor capability in **3i** did not further reduce inhibitory activity. It remains unclear if the carbonyl oxygen in **3i** acts as an alternative hydrogen bond acceptor, but it is unlikely to interact with the same region, due to its different position relative to the rest of the molecule. Moreover, the introduction of a bulky tertiary alcohol in **3j** led to a significantly decreased IC_{50} value of $5.8 \mu\text{M}$.

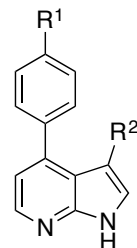
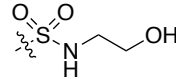
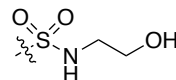
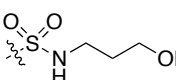
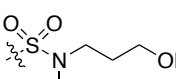
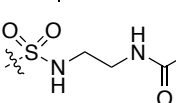
With the improved inhibitory activity of **3f** in hand, the focus was switched to the sulfonamide moiety (Table 8). As previously suggested, by docking of UNC5452 (**3a**) into the Nek1 ATP binding-site, the methyl replacement of the secondary sulfonamide hydrogen from **3f** to **3h** did not influence Nek1 inhibition significantly. However, substitution of the tetrahedral sulfonamide group with a planar carboxamide in **7** led to a 9-fold increased IC₅₀ value compared to **3f**, providing evidence for the proposed importance of the sulfonamide's geometry in hydrogen bonding to Lys33.

In addition, compounds **3a–k** and **7** were profiled for their Nek2 inhibitory activity using the same TR-FRET based assay platform. In concordance with the Nek-family selectivity data for UNC5452 (**3a**) reported by Wells *et al.*,⁶¹ none of the tested compounds exerted an observable effect on the kinase activity of Nek2.

Based on the fact that the most active compounds of the series, alcohols **3f** and **3h**, bear structural resemblance to published IKK β inhibitors (reference 232: compound **16**; reference 234: compound **16**),^{232, 234} compound **3f** and related compounds **3m–o** and **25a** were evaluated for their inhibitory activity against Nek1 and IKK β in a single-concentration (1 μ M) experiment, in order to identify structural elements that improve selectivity over IKK β (Table 9).

Residual kinase activity for both Nek1 and IKK β was determined in the *Eurofins Discovery KinaseProfiler*[™] service at K_{M,ATP} (see experimental section 5.4.1, Table 13), so that the resulting selectivity profile directly reflects the intrinsic affinities of the tested compounds.²⁸⁸ Unfortunately, only one of the tested compounds showed improved inhibitory activity against Nek1. 3-Phenyl derivative **25a** significantly reduced residual Nek1 activity to 32%, compared to 58% for parent compound **3f**, under the tested conditions, while IKK β activity was equally reduced to 13% by both **3f** and **25a**. The SAR of compound **25a** will be discussed in greater detail in chapter 3.2.4. With the goal of optimizing the hydrogen bond donor interaction with Nek1, while possibly also discriminating against IKK β , the carbon-chain of the 3-amino-ethan-1-ol moiety in **3f** was extended to a 3-amino-propan-1-ol moiety in **3m**. This extension resulted in beneficially increased residual activity for IKK β (20%) but also significantly increased Nek1 residual activity (75%). The same trend was followed for *N*-methyl-3-amino-propan-1-ol derivative **3n**, which increased residual activities for Nek1 (72%) and IKK β (28%) to similar degrees. *N*-acetyl derivative **3o** was designed to combine the hydrogen bond donor capability of **3f** with an additional hydrogen bond acceptor, based on the previous observation that the activity loss upon removal of the hydrogen bond donor capability was partially

Table 9: Residual kinase activity of Nek1 and IKK β against compounds **3f**, **3m–o** and **25a** (1 μ M) at $K_{M,ATP}$. ^[a]Eurofins Discovery KinaseProfiler™ service at 90 μ M ATP; ^[b] Eurofins Discovery KinaseProfiler™ service against IKK β at 10 μ M ATP;. See experimental section for more details. n.e., no effect at tested concentration (1 μ M).

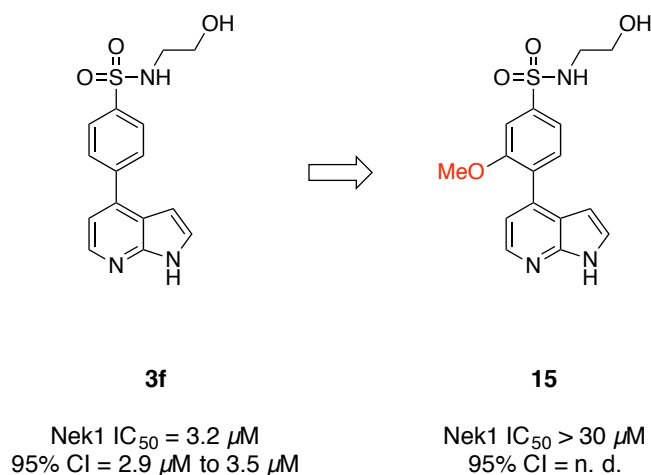
			Residual kinase activity (1 μ M)	
Cpd.	R ¹	R ²	Nek1 ^[a]	IKK β ^[b]
3f		H	58%	13%
25a		Ph	32%	13%
3m		H	75%	20%
3n		H	72%	18%
3o		H	72%	33%

rescued in the case of *O*-acetyl derivative **3i**, but not in methyl ether **3g**. Unfortunately, no beneficial effect on Nek1 inhibition was observed for compound **3o** (72%), although IKK β inhibition was significantly hampered in comparison to parent compound **3f**.

To sum up, the dimethylaminoethyl fragment of the developmental starting point UNC5452 (**3a**) was successfully optimized for its inhibitory activity against Nek1 and culminated in the identification of Nek1-inhibitors **3f** and **3h**, which exhibited improved Nek1 IC₅₀ values in low micromolar range. Unfortunately, the modulation of the dimethylaminoethyl fragment did not result in improved selectivity against the known off-target IKK β without compromising on-target potency. However, 3-aryl-substituted 4-phenylsulfonamide-7-azaindole **25a** showed improved Nek1 inhibition and selectivity and will be discussed in greater detail in chapter 3.2.4.

3.2.2. Structure-Activity-Relationship for Back Pocket-Targeting Nek1 Inhibitors

In order to evaluate the feasibility of the back pocket-targeting approach, 3'-methoxy-4-phenyl-7-azaindole **15** was designed and synthesized, as described in chapter 3.1.3. The IC_{50} value for the inhibition of Nek1 by compound **15** was determined in the aforementioned TR-FRET based activity assay. Unfortunately, compound **15** displayed only negligible inhibition on Nek1 activity with a relative IC_{50} value $> 30 \mu M$. No meaningful absolute IC_{50} value is deducible from the acquired data, due to the fact that the determined value exceeds the employed maximum test concentration of $30 \mu M$. Hence, no meaningful 95% confidence interval can be given as well. However, the assay reveals that the addition of the methoxy-group to the 3'-position of phenyl ring in parent compound **3f** reduces Nek1 inhibition by at least 10-fold (Scheme 17).



Scheme 17: IC_{50} values for parent compound **3f** and 3'-methoxy derivative **15**, as determined in the TR-FRET based Nek1 kinase activity assay at $K_{m,ATP}$ ($60 \mu M$). A relative IC_{50} value was provided for **15**, as the determined IC_{50} value exceeded the employed maximum test concentration ($30 \mu M$). CI, confidence interval; n. d., not determined.

Unfortunately, the results lead to the conclusion that an entrance into the hydrophobic back pocket from the 3'-position of the scaffolds phenyl ring is not feasible. As a possible explanation, it is hypothesized that pre-coordination of the sulfonamide moiety to catalytic Lys33 tightens the entrance to the back pocket. This issue was not taken into consideration in the molecular docking approach, as a consequence of the unresolved Lys33 amino group in

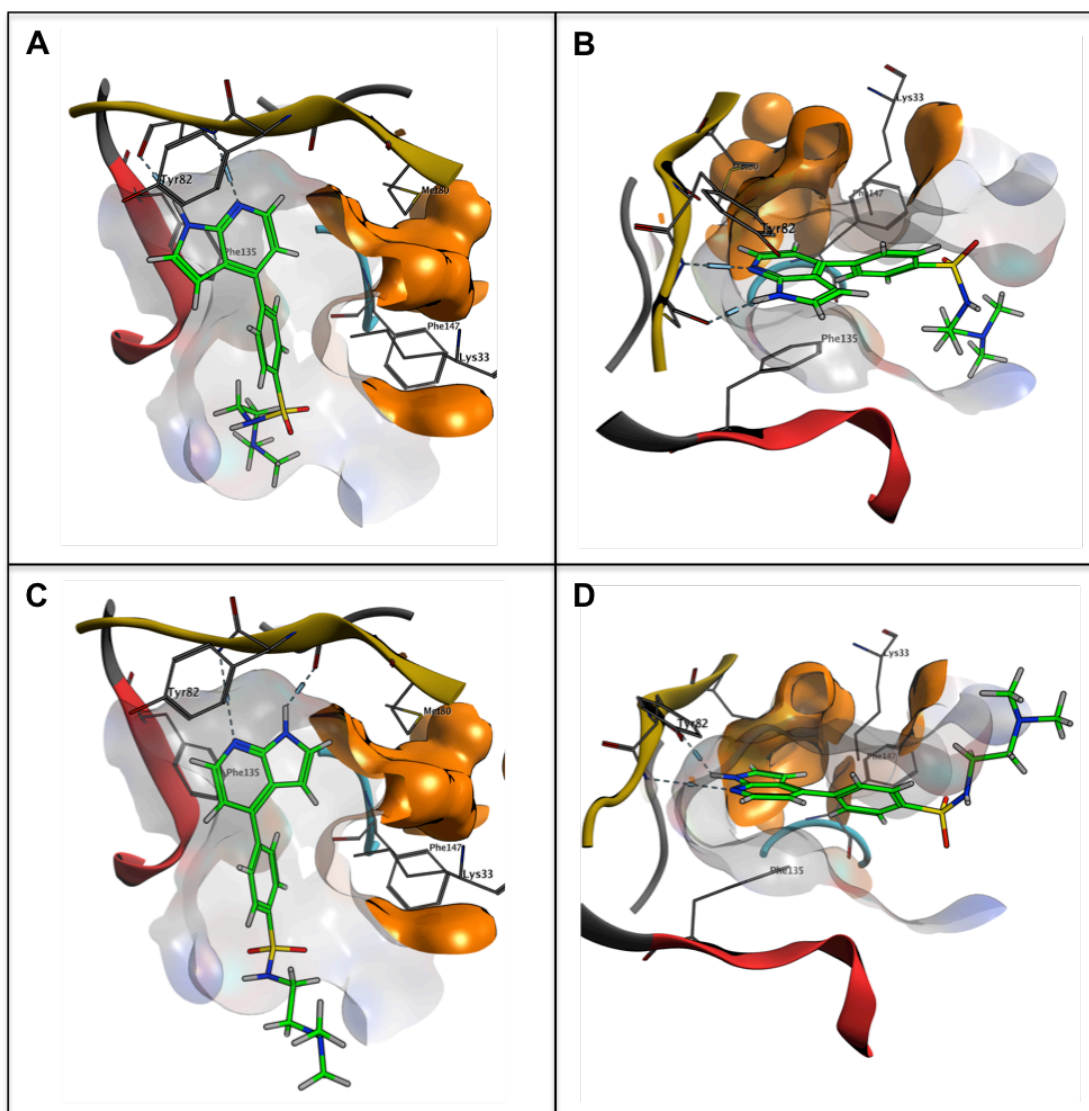


Figure 31: Evaluation of access to the Nek1 kinase domain back pocket (orange) by molecular docking of UNC5452 (**3a**) into the Nek1 ATP-binding site (PDB code: 4APC.A); A) Top-view of UNC5452 (**3a**) in the “flipped” binding pose; B) Side-view of UNC5452 (**3a**) in the “flipped” binding pose; C) Top-view of UNC5452 (**3a**) in the “normal” binding pose; D) Side-view of UNC5452 (**3a**) in the “normal” binding pose. The protein backbone is shown in dark grey and the ligand in lime green. The hinge region is shown in yellow. The DFG-motif is shown in cyan and parts of the catalytic loop are shown in red. Hydrogen bond interactions are shown as dotted lines. The receptor surface is shown in grey with the back pocket colored in orange.

the underlying X-ray structure. Alternatively, the introduction of an ortho-substituent to the phenyl ring, relative to the 7-azaindole moiety, could stabilize an unfavorable ligand conformation that significantly hampers the shape complementarity to the active site of Nek1 in the bound state, thus increasing the conformational reordering required upon binding. Similar effects have been repeatedly described in the reported literature, where a torsional twist, induced by the introduction of an even smaller methyl group, can alter activity more than thousandfold.²⁸⁹

It is also possible that an approach from the ortho-position of the scaffold's phenyl ring is simply blocked by the gatekeeper (Met80, Figure 31). It remains unclear if scaffold hopping to a five membered aromatic ring, as in UNC5078 (Figure 21), would sufficiently widen the C-C-C bond angle to allow bypassing of the gatekeeper. Laufer and colleagues have successfully applied this strategy in the development of inhibitors for EGFR Met gatekeeper mutants in the past.²⁹⁰

Furthermore, a reevaluation of the molecular docking of parent structure UNC5452 (**3a**) into the Nek1 kinase domain, with a focus on alternative points of attack toward the back pocket, led to unpromising conclusions. Due to the intrusion of the Phe135 and Tyr82 side chains into the hinge-binding region, the 7-azaindole moiety is angled in a way that hypothetically prevents access to the back pocket from the 5-position in the "flipped" binding mode. In the disfavored "normal" binding mode, the same problem arises for the 3-position and an entry from the 2-position is likely also blocked by the gatekeeper (Figure 31).

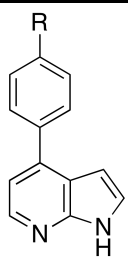
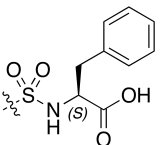
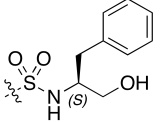
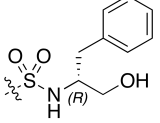
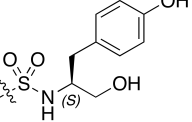
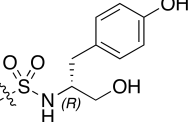
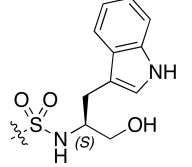
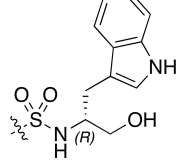
Taken together, the back pocket-targeting approach remained unsuccessful. 3'-methoxy derivative **15** did not decrease Nek1 activity substantially, rendering an approach from the phenyl ring of the 4-phenyl-7-azaindole unpromising. Furthermore, the related molecular docking studies revealed difficulties with alternative approaches from the 7-azaindole moiety. Therefore, the focus of this work was set on further derivatization of the dimethylaminoethyl fragment, with the aim to establish new interactions with the P-loop and the phosphate-binding region.

3.2.3. Structure-Activity-Relationship for *In Silico*-Screening Hit Compounds

As described in chapter 3.1.3, seven virtual hit compounds (**31** and **19a–f**) were identified in an *in silico* screening from a library of *N*-substituted canonical α -amino acid derivatives, and their corresponding alcohols, structurally based on **3f**. Accordingly, phenylalanine derivative **31** and phenylalaninol, tyrosinol and tryptophanol derivatives **19a–f** were evaluated for their inhibitory activity (Table 10). The L-phenylalanine derivative **31** did not notably decrease Nek1 activity, while the corresponding phenylalaninol derived enantiomers **19a** and **19b** displayed decreased Nek1 IC₅₀ values of 1.9 μ M and 1.3 μ M respectively. The tyrosinol derivatives **19c** and **10d** performed slightly worse, while the L-tryptophanol derivative **19e** exhibited a decreased IC₅₀ value compared to **19a** (0.99 μ M). Strikingly, the D-tryptophanol derivative **19f** showed a 6-fold decreased IC₅₀ value of 0.33 μ M against Nek1, compared to **3f**.

The putative binding mode of **19f** was thus determined by molecular docking into the P-loop reconstructed X-ray structure of the Nek1 kinase domain (Figure 32). The docking experiment suggests that the improved activity results from the generally favored orientation of the D-enantiomers, which in this particular case gives rise to an additional hydrogen bond interaction of the indole-NH with the Asp128 side chain, as well as an additional C-H- π -interaction of the aromatic system with the Thr166 backbone NH. In similar fashion to UNC5452 (**3a**), the 7-azaindole moiety adopts the “flipped” binding mode, is tightly packed between Val31 and Phe135 and forms two hydrogen bonds with the hinge region Cys83. Furthermore, the docking experiment indicates C-H- π -interactions of the heterocyclic rings with the Gly86 and Val31 side chains as well as a contingent parallel-displaced π - π -stacking interaction with Phe135. The phenyl ring of **19f** once again protrudes toward the phosphate-binding region and positions the sulfonamide moiety in close proximity to the catalytic lysine (Lys33), forming a hydrogen bond. Resulting from this interaction, the hydroxyl group of **19f** acts as a hydrogen donor toward the backbone carbonyl oxygen of Ile10 while the indole moiety fits tightly between Lys17, Gln132 and Arg161. From here, the indole-NH forms the aforementioned hydrogen bond with the side chain of Asp128, while the aromatic system establishes a C-H- π -interaction with the Thr166 backbone-NH. Judging by these results, **19f** can be classified as a Type-IIB inhibitor that binds to an inactive DFG-out conformation without occupying the back cleft.²⁸ In an attempt to confirm the ATP-competitiveness of **19f**, the IC₅₀ value against Nek1 was also determined at 10 μ M ATP in the same radiometric assay, and compared to the IC₅₀ value at KmATP (90 μ M) (Table 10).

Table 10: Inhibitory activity of compounds **3l** and **19a–f** against Nek1. ^[a]*Eurofins Discovery KinaseProfiler™* service at 10 μM ATP; ^[b]*Eurofins Discovery IC50Profiler™* service at $K_{m,\text{ATP}}$ (90 μM) ^[c]*Eurofins Discovery IC50Profiler™* service at 10 μM ATP. See experimental section for more details. See appendix for raw data. CI, confidence interval; n.d., not determined; n.e., no effect at maximum concentration (10 μM).

		Residual kinase activity ^[a] (1 μM)		IC ₅₀ [μM] ^[b]	
Cpd.	R	Nek1	Nek1	95% CI	
3l		94%	n.e.	n.d.	
19a		19%	1.9	1.4 - 2.6	
19b		16%	1.3	0.95 - 1.7	
19c		33%	2.0	1.2 - 3.0	
19d		25%	1.6	1.1 - 2.2	
19e		19%	1.1	0.81 - 1.4	
19f		4%	0.33 (0.33) ^[c]	0.22 - 0.52 (0.19 - 0.51) ^[c]	

No significant difference was herein observed with IC₅₀ values of 0.33 μM for both ATP-concentrations. This does not constitute the fact that **19f** is not ATP-competitive, only that the employed functional assay is not suited as a consequence of the conditions changing too

rapidly as soon as a reaction takes place. Therefore, a designated ATP-competition assay, a biophysical binding assay or a cocrystallized X-ray structure is needed to provide proof for this hypothesis.²⁹¹

With the inhibitory activities and IC₅₀-values of the virtual hit compounds in hand, the goodness of the employed P-loop reconstructed Nek1 kinase domain models can now be evaluated.

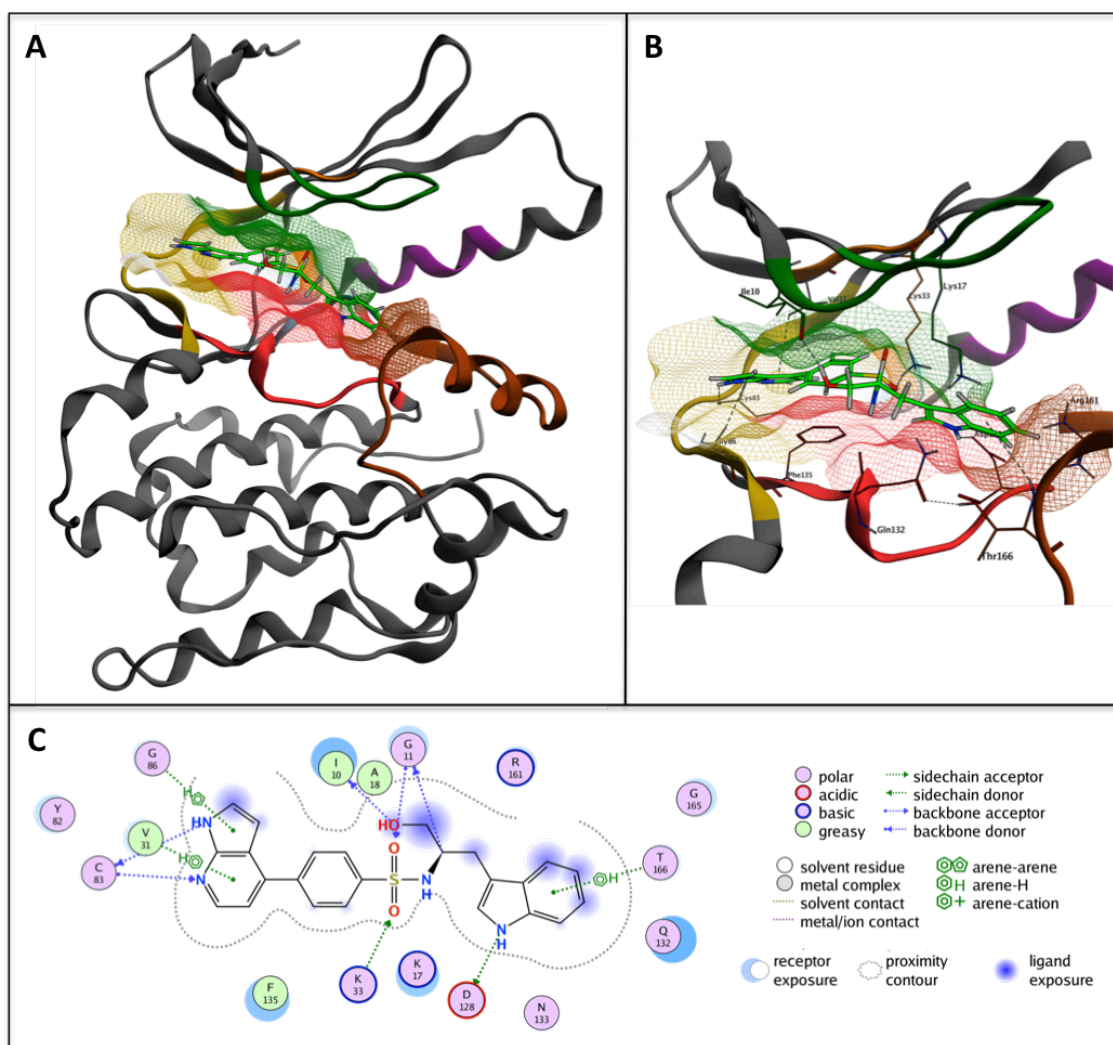


Figure 32: Molecular docking of **19f** into the Nek1 ATP-binding site (PDB code: 4B9D.B). The glycine-rich loop was reconstructed using the Super Looper 2 web application (<http://proteininformatics.charite.de/sl2>).²⁵⁵ See experimental section for more details. A) Localization of **19f** in the Nek1 kinase domain. B) Putative binding mode of **19f**. The protein backbone is shown in dark grey and the ligand in lime green. C) Ligand interaction analysis (bottom view) for molecular docking of **19f** into the Nek1 ATP-binding site. The hinge region is shown in yellow. The glycine-rich loop is shown in green and the catalytic lysine in orange. The alpha-C-Helix is shown in purple. The DFG-motif is shown in cyan and the catalytic loop is shown in red. The activation loop is shown in brown. Hydrogen bond interactions and C-H- π intercalations are shown as dotted lines.

Strikingly, both models ranked one of the phenylalanine-derived enantiomers as “Top-5” compounds (see appendix Table A 1 Table A 2), while the L-phenylalanine derivative **31** showed no inhibitory effect in the performed assays. This false positive hit can likely be attributed to an incorrect prediction of the protonation state in **31**. Protein-ligand complex formation usually involves titratable groups with unusual pKa’s, whose protonation states frequently change from unbound to bound states. Accurate predictions are available when provided with the structures of the unbound proteins and their complex, but modeling becomes far more complicated if the bound state has to be predicted *in silico*.²⁹²

Furthermore, both models ranked the phenylalaninol derivatives **19a** and **19b** substantially lower than the tyrosinol derivatives **19c** and **19d**, in contrast to the results of the *in vitro* kinase activity assays. Here, a trend favoring the D-enantiomers **19b** and **19d** was observed and the respective phenylalaninol derivatives slightly outperformed their tyrosinol counterparts. This discrepancy is likely to arise from an overestimation of potential hydrogen bond capabilities and of the hydroxy groups electronic influence on the aromatic system. Interestingly, the *SuperLooper2*-model strongly favored **19a** (rank: 7) over **19b** (rank: 21), while this order was reversed in the homology model (rank: 11 for **19b**; rank: 22 for **19a**). In addition, only the homology model was able to predict the increased inhibitory activity for the D-enantiomers in the other enantiomeric pairs.

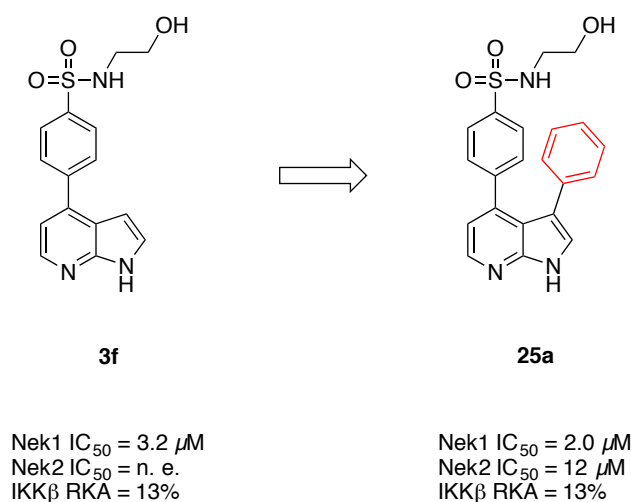
Surprisingly, the evaluation of the underlying Nek1 kinase domain P-loop reconstruction models thus revealed superiority of the Nek1/Nek2 homology model, despite the fact that the underlying X-ray structure was herein remodeled as a whole, in contrast to the SL2 model that merely reconstructed the missing P-loop segment. This finding is hypothesized to result from the fact that the homology models virtual conformation of the highly flexible P-loop more strongly resembles the *de facto* Nek1 P-loop conformation upon ligand binding, despite the higher SL2-ranking of the template employed in the SL2 model. The SL2-score is based on a geometrical fingerprint database that matches the sterical fit of the stem atoms of the N- and C-termini of each database fragment to the C- and N-terminal stem atoms of a gap in the protein structure.²⁵⁵ While this method is reasonable, the employed rigid receptor docking approach does not take ligand induced conformational changes of the loop structure into account. It should be noted that induced fit docking was intentionally left out, as the additional side-chain flexibility significantly increases the necessary computer time of docking and often results in false positive hits.²⁹³⁻²⁹⁴

In summary, seven virtual hit compounds, identified in the previously described *in silico* chemical library screening (Chapter 3.1.3), were synthesized and evaluated for their

inhibitory activity. Lead compound **19f** emerged as a potent Nek1-inhibitor with an IC₅₀ value in the low to medium micromolar range (0.33 μ M) and its putative binding mode in the Nek1 kinase domain was determined by molecular docking. Furthermore, a comparison of the acquired IC₅₀ values to the S-Score rankings of the P-loop reconstruction models revealed a superior goodness of fit for the homology model. Nonetheless, both the homology model and the SL2 model provided results that allowed for the successful selection of virtual screening hits that culminated in the identification of lead compound **19f**. Lead compound **19f** was further evaluated regarding its kinase selectivity, solubility, cell-permeability, and its *in vivo* efficacy and toxicity, as described in later chapters.

3.2.4. Structure-Activity-Relationship for 3,4-Disubstituted 7-Azaindoles Nek1 Inhibitors

As described in chapter 3.1.4, two 3,4-disubstituted 7-azaindoles, more specifically 3-phenyl derivative **25a** and 3-pyridinyl derivative **25b** of 4-phenylsulfonamide-7-azaindole **3f**, were designed in order to investigate possible attractive interactions between 3-aryl substituents with the unusual Phe135 residue in the Nek1 ATP pocket. Ultimately, these substituents may serve as a linker structure that enables additional hydrophilic interactions with the Nek1 ribose-binding region. However, only 3-phenyl derivative **25a** was acquired in adequate HPLC purity for biochemical evaluation and its inhibitory activity against Nek1 and Nek2 was hence determined in the aforementioned TR-FRET based kinase activity assay platform (Scheme 18). As previously described, compound **25a** was furthermore profiled for its inhibitory activity on IKK β in a single-concentration (1 μ M) kinase inhibition experiment, using the *Eurofins Discovery KinaseProfiler*[™] service (Chapter 3.2.1, Table 9, Scheme 18).



Scheme 18: Inhibitory activities for parent compound **3f** and 3-phenyl derivative **25a** against Nek1, Nek2 and IKK β . IC₅₀ values against Nek1 and Nek2 were determined in the TR-FRET based kinase activity assay platform at K_{M,ATP} (60 μ M for both Nek1 and Nek2). Residual kinase activity (RKA) of IKK β against 1 μ M **3a** and **25a** was determined in the *Eurofins Discovery KinaseProfiler*[™] service at K_{M,ATP} (10 μ M). See experimental section for more details. n. e., no effect at maximum concentration (30 μ M); RKA, Residual kinase activity.

In concordance with the hypothesis, the introduction of the phenyl substituent in compound **25a** led to a 1.6-fold decreased IC₅₀ value against Nek1, when compared with the parent structure **3f**. Despite the peculiar nature of the Nek1 Phe135 residue, the established

interaction is not selective for Nek1 over Nek2, due to the fact that Nek2 activity was also substantially reduced by **25a** in the TR-FRET assay. In contrast, **3f** had no measurable effect on Nek2 activity at the maximum concentration (30 μ M). However, the newly established interaction is selective for Nek1 over IKK β (Table 9, Scheme 18).

Taken together, first evidence for the beneficial influence of 3-aryl substitutions, in 4-phenylsulfonamide-7-azaindole based inhibitors, on Nek1 inhibition and selectivity over IKK β was provided. Furthermore, the improved potency supports the molecular docking studies, which suggest that the underlying “N1-Out” scaffold binds to the Nek1 hinge region in the “flipped” binding mode. However, further studies are needed in order to elucidate the usefulness of the phenyl-moieties as a linker toward the ribose-binding region. As a consequence of the unselective nature of the newly established interaction over Nek2, this was not pursued further and the main focus was set on the in-depth profiling of lead compound **19f**.

3.2.5. Kinase Selectivity Profile for Lead Compound 19f

Kinase selectivity profiling of **19f** was carried out against 50 kinases with ATP-concentrations set within 15 μM of the apparent K_m for ATP for each kinase tested, so that the resulting selectivity profile directly reflects the intrinsic affinities of **19f**.²⁸⁸ In order to preserve comparability, the selectivity profile was determined with the *KinaseProfiler*[™] service by *Eurofins Discovery Services*. The panel size was based on findings by Bembenek *et al.* that link panel size to the average error that comes along with the use of a smaller sized panel in comparison to full kinome data. For one, it was found that most of the improvements, obtained by the use of a larger kinase panel, quickly tail off at a panel size of around 50 kinases. Furthermore, it was demonstrated that the described average error can be further diminished by selecting a focused combination of kinases instead of making selections at random.²⁹⁵ Based on these findings, a focused kinase selectivity panel was designed for lead compound **19f** that incorporates 50 kinases from all major kinase families, predicated on the focused 20 kinase panel reported by Bembenek *et al.* and the *Eurofins Kinase Profiler*[™] Diversity Panel (Figure 33, Appendix Table A3).²⁹⁵⁻²⁹⁶

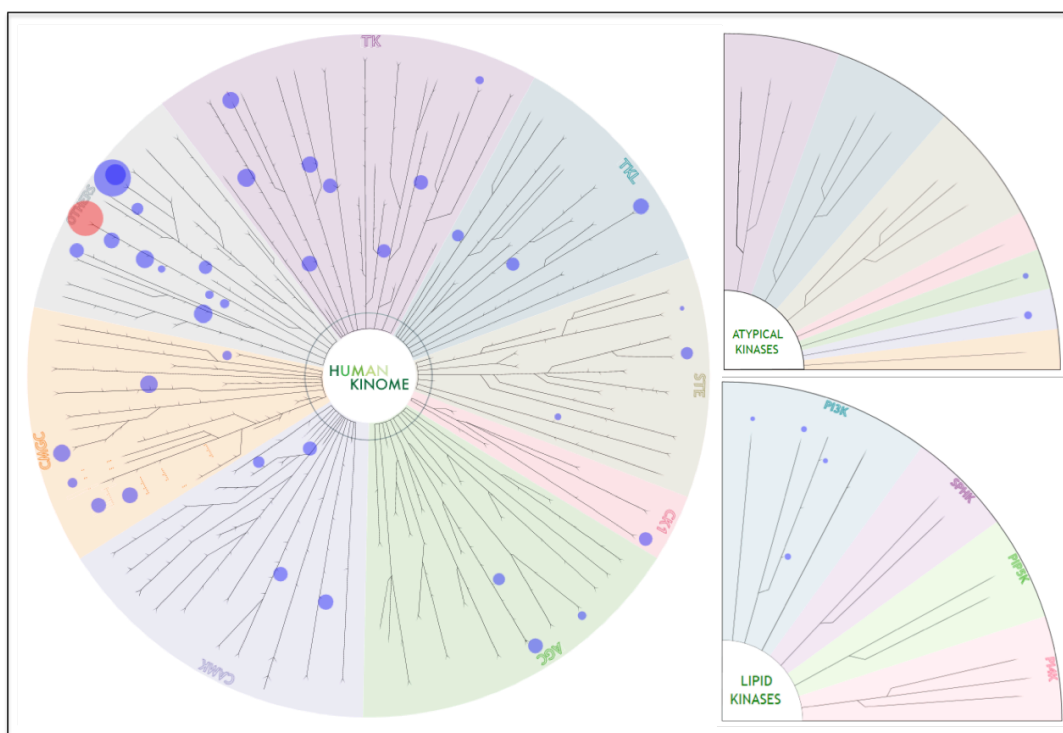


Figure 33: *KinaseProfiler*[™] screening of compound **19f** (1 μM) against a focused panel of 50 human protein kinases. cATP was set to the approximate $K_{m,ATP}$ for each kinase tested. Each dot represents the inhibitory activity against one protein kinase. Nek1 inhibitory activity is shown as the red dot. See experimental section and appendix for more details.

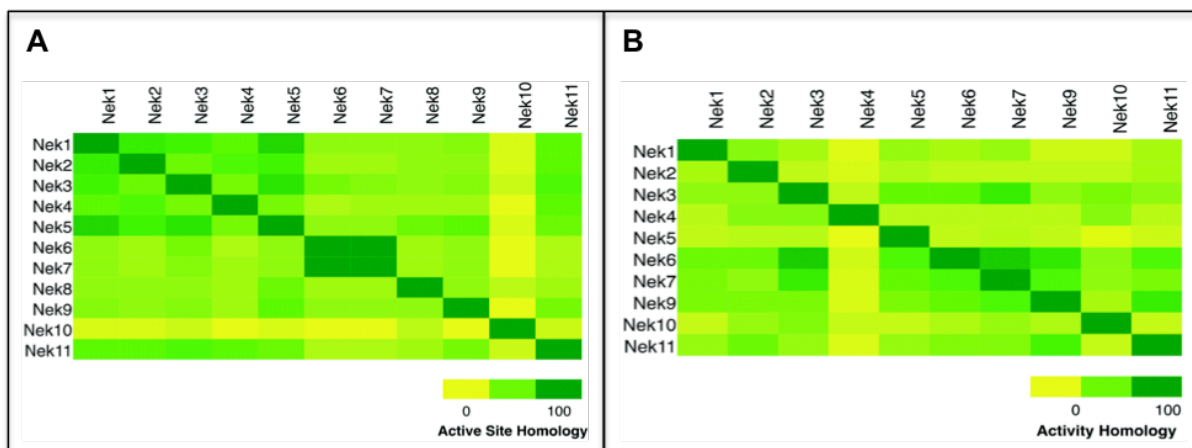


Figure 34: Active site homology (A) and activity homology (B) for the Nek family of protein kinases as determined by Wells *et al.*⁶¹ Adapted with permission from "In depth analysis of kinase cross screening data to identify chemical starting points for inhibition of the Nek family of kinases" by C. I. Wells, N. R. Kapadia, R. M. Couñago and D. H. Drewry, *Med. Chem. Commun.*, **2018**, *9*, 44-66. Copyright 2018, The Royal Society of Chemistry.

Furthermore, several members of the Nek-family were included, based on their availability in the *Kinase Profiler*[™] service as well as their active site and activity homologies, as described by Wells *et al.* (Figure 34).⁶¹

Employing a cutoff at 80% inhibitory activity, Wells and colleagues compiled all compounds from a number of underlying datasets that inhibit a particular Nek kinase and identified the percentages of those compounds that inhibit each other Nek kinase.⁶¹ Protein kinases Nek5, Nek8 and Nek9 were not available from *Kinase Profiler*[™] and Nek4, and Nek10 were excluded due to their low activity homology, as reported by Wells *et al.* Interestingly, Nek1 and Nek5 share rather high active site homology with 24/28 shared residues. However, only 5 of the 29 tested compounds that showed $\geq 80\%$ inhibition for Nek5 also inhibited Nek1 $\geq 80\%$. Furthermore, very broad kinase inhibition profiles were reported for several of these compounds. A similar picture is drawn for Nek4, with 21/28 shared residues in the active site and an Nek1 activity homology comparable to Nek5. Unfortunately, no activity homology data is available for Nek8, as a consequence of missing commercial assays.²³⁰ Nek10 is the most structurally divergent and shares only 9/28 active site residues with Nek1, which is also reflected in the low activity homology.⁶¹ Taken together, the employed selectivity panel is well equipped to give insight into the kinase selectivity of **19f** over all kinase families and the Nek-family of kinases in particular. 47 out of the 50 kinases in this focused panel showed an activity higher than 75%, whereas Nek1 displayed a residual activity of only 49.7%. The only kinase that was also significantly inhibited by **19f** was IKK β with a residual activity of 36.1% (Figure Figure 35, see Appendix Table A3 for more details).

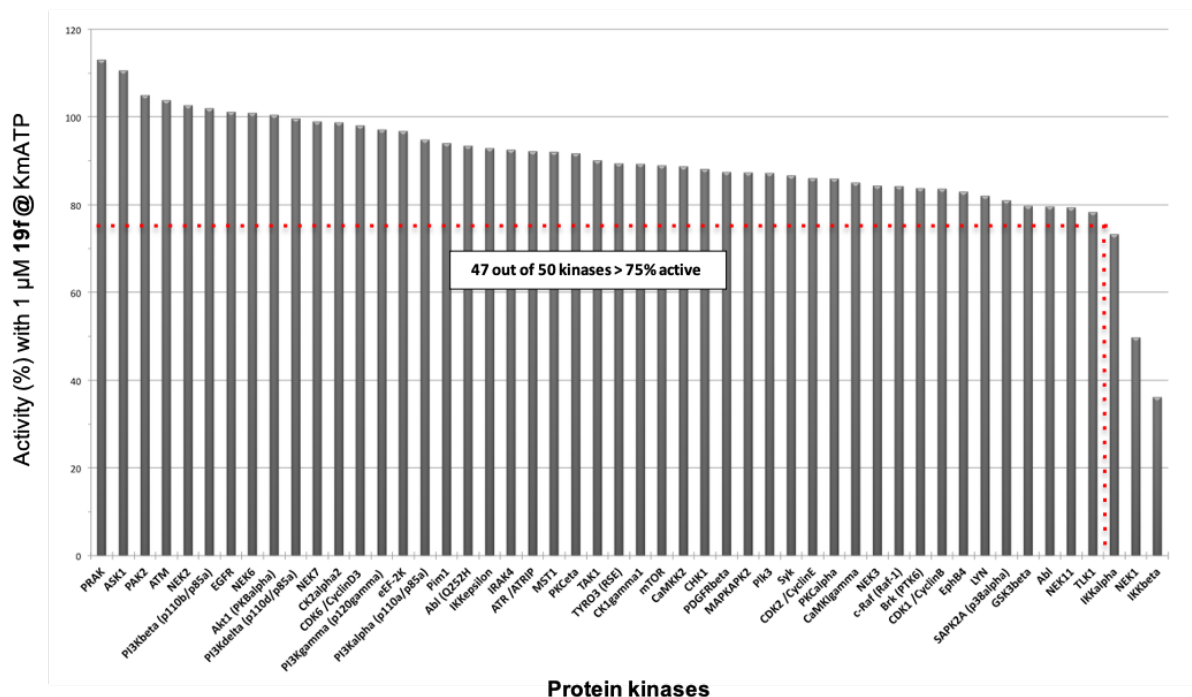


Figure 35: *KinaseProfiler*TM screening of compound **19f** (1 μ M) against a focused panel of 50 human protein kinases. The ATP concentration was set to the approximate $K_{M,ATP}$ for each kinase tested. Each bar represents the activity of one individual protein kinase. Nek1 inhibitory activity is shown as the red dot. See experimental section and appendix for more details.

IKK cross-reactivity was expected, as the 4-phenyl-7-azaindole scaffold in **19f** was derived from the chemical starting point UNC5452 (**3a**), which was originally developed as an IKK β inhibitor.^{232, 234}

To sum up, lead compound **19f** displayed good selectivity over a broad range of kinases, including several members of the Nek kinase family, in a focused kinase selectivity panel. However, given that the selectivity profile is based on a limited number of kinases (approx. 10% of the kinome) and does not extend to enzymes beyond the kinome, caution must still be exercised in deducing general selectivity from the data.

3.2.6. Shake-Flask Solubility Assay for Lead Compound 19f

With the promising activity and selectivity profile of **19f** in hand, studies toward a zebrafish *in vivo* efficacy model were undertaken. As a first step, a bioavailability profile of compound **19f** was established.

The aqueous solubility of pharmaceutically active compounds and its precise determination play a pivotal role in the discovery and development of drugs and research associated tool compounds. It is estimated that around 90% of all molecules in the discovery pipeline and nearly 40% of new chemical entities (NCEs) suffer from poor aqueous solubility, resulting in low oral bioavailability and suboptimal drug delivery.²⁹⁷⁻²⁹⁸ Hence, poor solubility is on top of the list of undesired compound properties and one of the main reasons for the failure of drug candidates. Until today, the shake-flask method constitutes the ‘gold-standard’ in determining the aqueous solubility of pharmaceutical compounds.²⁹⁹

Aqueous solubility of **19f** was determined in a shake-flask HPLC solubility assay using the HPLC system described in the experimental section (see 5.1.5) connected to a diode array detector (DAD). A calibration curve (peak area [mAu*s] against concentration [μ M]) was created by dilution of a 10 mM compound stock solution in DMSO to 1, 5, 10, 50, and 100 μ M solutions in acetonitrile. At equilibrium, the absorption was measured at 280 nm and all measurements were performed in triplicates. With the aforementioned zebrafish *in vivo* efficacy model in mind, a saturated solution of **19f** in E3-medium (with 2 v/v% DMSO), was prepared by shaking for 24h at 25 °C. Finally, the aqueous solubility was determined by linear regression of the calibration line and subsequent interpolation using *GraphPad Prism 8* (see 0, Figure 36).

E3-medium is the accepted standard medium for the work with developing zebrafish embryos and contains several salts that supply the embryos with minerals, like calcium and magnesium, which are necessary for healthy development. Furthermore, methylene blue is added as an antifungal agent.³⁰⁰ E3-medium was prepared according to the *Cold Spring Harbor Protocols* recipe for E3-medium for zebrafish embryos (see 5.5).³⁰¹

The aqueous solubility of lead compound **19f** in E3-medium was determined as $31.07 \pm 0.35 \mu\text{M}$ ($13.87 \pm 0.16 \mu\text{g/mL}$), with the linear regression of the calibration line showing excellent goodness-of-fit with a coefficient of determination of 99.7% (Figure 36).

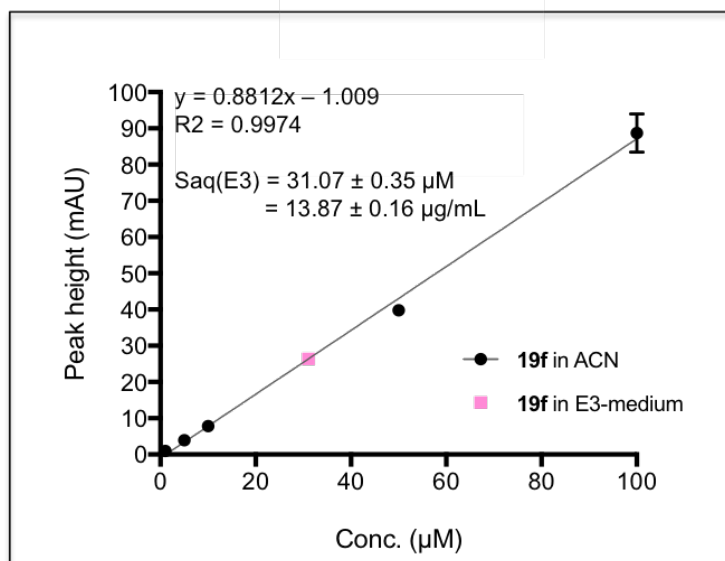


Figure 36: Determination of the aqueous solubility (E3-medium) of lead compound **19f** in a HPLC shake-flask solubility assay. Data is presented as mean \pm SD; $n = 3$. Error bars that are shorter than the size of the symbol are not shown. See experimental section 5.4.2. for more details.

In order to meaningfully discuss the correlation between the *in vitro* dissolution of **19f** and its *in vivo* bioavailability, the intestinal permeability of **19f** was evaluated in the following chapter.

3.2.7. Caco-2 Cell Permeability Assay for Lead Compound 19f

As a next step toward a zebrafish *in vivo* efficacy model, the intestinal permeability of **19f** was estimated in a Caco-2 permeability assay. The determination of permeability coefficients across monolayers of the human colon carcinoma cell line Caco-2, cultured on permeable supports, is nowadays considered to be the *in vitro* 'gold standard' for assessing the uptake efficiency of drugs and pharmaceutical tool compounds (Figure 37).³⁰²⁻³⁰³

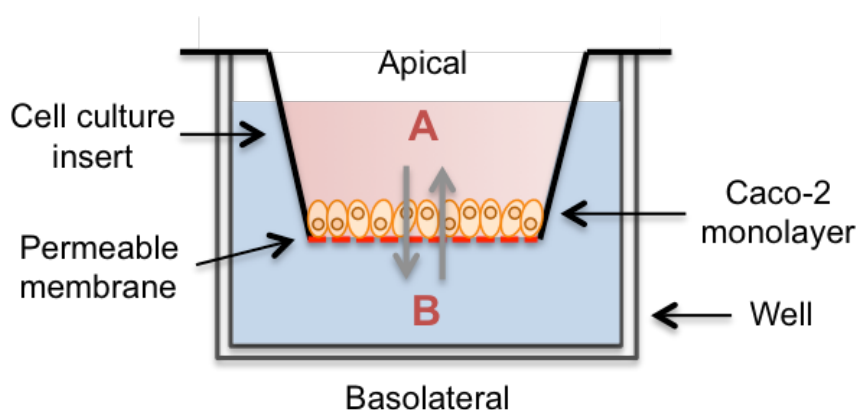


Figure 37: Schematic representation of the Caco-2 permeability assays experimental setup. Apical to basolateral (A-B) permeability is determined by adding the drug to the apical chamber and measuring its appearance in the basolateral chamber, using time-resolved HPLC/MS-MS detection. The percent recovery is defined as the sum of the compound recovered from the apical and basolateral chambers at the end of the experiment, divided by the initial compound amount.

Despite the fact that Caco-2 cells are derived from colon carcinoma cells, they differentiate into a phenotype that functionally and morphologically resembles the enterocytic lining of the small intestine, when cultured under specific conditions.³⁰⁴⁻³⁰⁵ When cultured on a cell culture insert filter as a confluent monolayer, the cells form a polarized barrier that hinders the free crossing of small molecules and ions between the apical and basolateral chambers. The rate-of-passage of small molecules through the monolayer, by passive diffusion or active transport, is expressed in the permeability coefficient (in 10^{-6} cm/s) that is used to predict the absorption of orally administered xenobiotics.³⁰⁶⁻³⁰⁷ Apical to basolateral (A-B) permeability is determined by adding the small molecule to the apical chamber and measuring its appearance in the basolateral chamber in a time-resolved manner.³⁰² Moreover, the determination of an endpoint recovery percentage can be used to indicate heightened uptake and/or metabolic conversions.^{302, 308}

A-B permeability and percent recovery of **19f** were determined by HPLC-MS/MS detection of the peak area response in a commercial assay by *Eurofins Discovery Services* (Item 3318), at pH 6.5 for the apical and pH 7.4 for the basolateral chamber. Propranolol, labetalol, colchicine and ranitidine were concurrently tested as reference compounds (Table 11).

Table 11: A-B permeability (Caco-2, pH 6.5/7.4), and percent recovery of selected compounds at a test concentration of 10 μ M. All measurements were performed in duplicates. Aqueous solubilities at pH 7.0 - 7.5 and 25 °C were included from the reported literature for colchicine³⁰⁹, labetalol³¹⁰, propranolol³¹¹ and ranitidine³¹². [†]See chapter 3.2.6 [∗]Aqueous solubility and BCS-class refer to the corresponding hydrochloride salts. [‡]Aqueous solubility at pH 4.0 – 6.5 and 25 °C. BCS, *Biopharmaceutical Drug Classification System*.

Compound	Aq. Solubility (mg/mL)	Permeability (10 ⁻⁶ cm/s)			Percent Recovery (%)			BCS-class
		1st	2nd	Mean	1st	2nd	Mean	
19f	0.031 ^[‡]	3,41	3,44	3,4	42	48	45	-
Colchicine	16.7 ^[309]	0,56	0,58	0,6	70	71	70	3
Labetalol	10.1 ^[310]	7,64	7,93	7,8	88	93	90	1
Propranolol	0.13 (319.8) ^[∗, 311]	28,69	27,34	27,5	77	77	77	1*
Ranitidine	24,7 ^[∗, ‡, 312]	0,91	0,94	0,9	85	85	85	3*

The permeability coefficient of **19f** was determined as 3.4 x 10⁻⁶ cm/s and the percent recovery as 45%. In comparison to the reference compounds, this test reveals that the intestinal permeability of **19f** lies between the values of marketed highly permeable drugs labetalol and propranolol and low permeability drugs colchicine and ranitidine. Interestingly, the recovery percentage is significantly reduced in comparison to the reference compounds. It is well reported that lipophilic compounds have a tendency to non-specifically bind to the Caco-2 cell surface or to plastic devices used in his permeability assay.³¹³⁻³¹⁴ In a recently published report by Cai *et al.* nonspecific binding to various plastic surfaces was identified as

the major cause of limited compound recovery.³¹⁵ Alternatively, it is possible that **19f** accumulates in the Caco-2 cells, or is partially metabolized over the course of the experiment.

In order to correlate the intestinal permeability and *in vitro* drug dissolution pharmaceutical compounds with its *in vivo* bioavailability, the Biopharmaceutical Drug Classification System (BCS), was introduced by Amidon *et al.* in 1995.³¹⁶ Although a classification of **19f**, according to the BCS, would require a dosing regimen, the comparison to classified market drugs is a useful guideline for the estimation of a new compound's *in vivo* bioavailability.

In the BCS, drug substances are classified as follows: Class 1: High solubility – high permeability; Class 2: Low solubility – high permeability; Class 3: High solubility – low permeability; Class 4: Low solubility – low permeability.

As a consequence of its low aqueous solubility, lead compound **19f** would most likely be classified as a BCS-class 2 or class 4 compound and further development toward improved solubility or adequate formulation strategies would have to be considered, if **19f** were to be intended for use as a drug. Nonetheless, the determined aqueous solubility and permeability of **19f** are sufficient for the intended use as a research tool compound, more particularly when its low to mid nanomolar Nek1-potency ($IC_{50(Nek1)} = 330$ nM) and its good selectivity profile are taken into account.

With the bioavailability profile in hand, lead compound **19f** was further profiled for its safety, toxicity and *in vivo* efficacy, as described in the following chapter.

3.3. *In Vivo* Profiling of Lead Compound **19f** in Wild-Type Zebrafish

In order to evaluate whether its *in vitro* inhibitory activity translates into predictable effects *in vivo*, lead compound **19f** was further profiled for its efficacy, safety and toxicity in wild-type zebrafish (*Danio rerio*).

3.3.1. Zebrafish Developmental Toxicity Assay for lead compound **19f**

Safety and toxicity of lead compound **19f** were investigated in a wild-type zebrafish developmental toxicity screen that was performed in accordance with guidelines published by M. Haldi *et al.* in *Zebrafish: Methods for Assessing Drug Safety and Toxicity* (see 5.4.4).³¹⁷

4 hours post fertilization (hpf) embryos with intact chorion membranes were selected according to the referenced guidelines, grouped in E3-medium and at 6 hpf test compound **19f** was added in a range of concentrations (0.05 μM to 30 μM). Survival was monitored every 24 h over five days, by observation of the heartbeat (Figure 38).

All survival rates were determined at least in triplicate, with the controls and the survival rate at 30 μM being determined in 5 replicates. Furthermore, all groups were kept in the dark in between observations.

Strikingly, none of the treated groups displayed mortality that significantly exceeded the natural early mortality, which was also observed in the control groups, up to a concentration of 15 μM **19f**, over the course of 5 days. For a concentration of 20 μM **19f**, the survival rate significantly decreased from day 1 to day 3 and then stabilized at around 60%. Full mortality was only observed close to the previously determined solubility limit, for a concentration of 30 μM **19f**, after 3 days. Treatment with **19f** did not induce obvious phenotypes visible to the eye. The treated embryos exhibited normal eye development, body curvature and an inconspicuous heartbeat.

Overall, lead compound **19f** is well tolerated in zebrafish, up to a test concentration of 20 μM . Furthermore, no gross morphological changes were exhibited even at high concentrations and this toxicity profile thus allows for the planned efficacy studies, which are presented in the following chapters, to be conducted over an adequate concentration range.

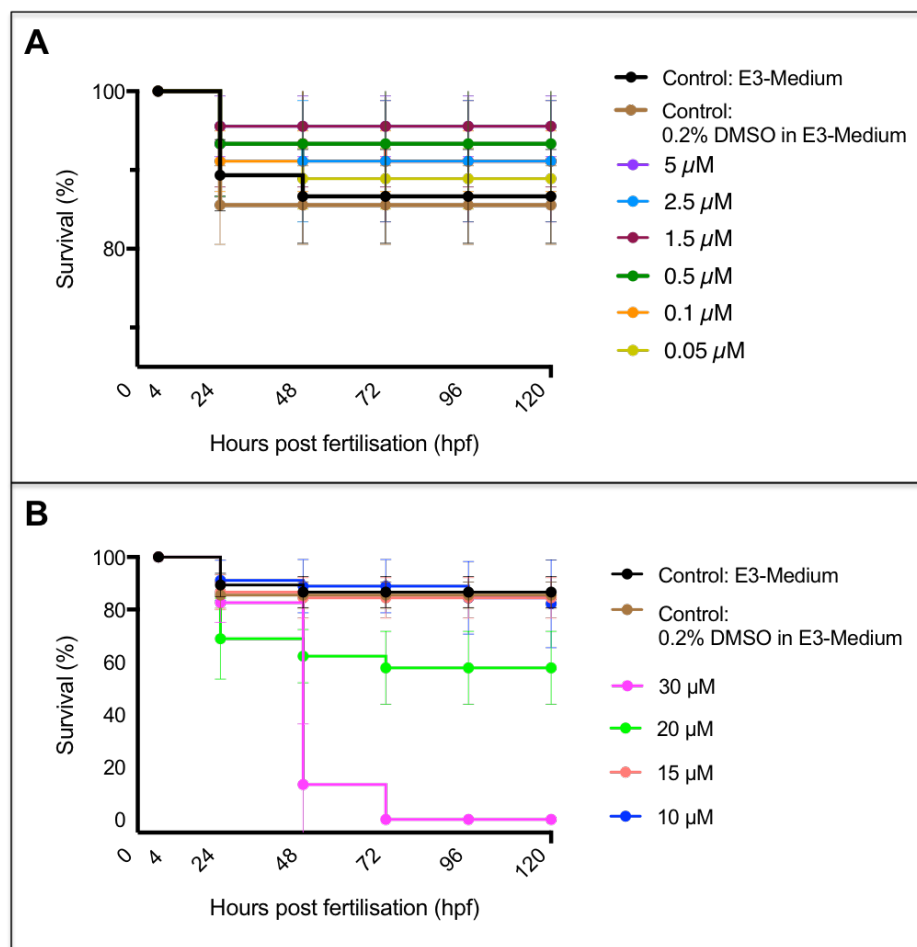


Figure 38 Zebrafish developmental toxicity assay for compound **19f**. (A) Survival rates for lower concentrations (y-axis cropped at 65%). (B) Survival rates for higher concentrations. Survival rates were determined in triplicate with the controls and the survival rates at 30 μM being determined in 5 replicates. Error bars represent the SD and were clipped at the axis limits. Error bars that are shorter than the size of the symbol are not shown. See experimental section 5.4.4. for more details.

3.3.2. *In Vivo* Efficacy Assay for Lead Compound 19f

Development of a Zebrafish Polycystic Kidney disease (PKD) model

In order to evaluate, whether the *in vitro* inhibitory activity of lead compound **19f** translates into predictable effects *in vivo*, a zebrafish PKD model was established. The model was based on a previously mentioned report by Chen *et al.*, which indicates that Nek1 deficiency results in renal cyst formation as a consequence of disordered kidney maturation in *kat2j* mice.¹⁷⁴ It was therefore hypothesized that treatment with **19f**, during early stages of embryonic organ development, leads to the formation of renal cysts, thus indicating the efficient absorption and *in vivo* efficacy of **19f**. Indeed, the zebrafish has proven itself as an established model system for the evaluation of mammalian kidney morphology, because of its simple pronephric structure, which consists of two nephroi that share major anatomical and functional features with the mammalian metanephros. Its usefulness as a model for cystic kidney diseases has recently been reviewed.³¹⁸⁻³¹⁹

It is important to note here that the model is based on the necessary assumption that Nek1 inhibition results in the same phenotype that is associated with its depletion, as the correlation between small molecule inhibition and loss-of-function phenotypes is not always straightforward.³²⁰ However, the approach is substantiated by the observation that a reduction in cilia number is linked to the absence of Nek1, as well as to its overexpression, as reported by Shalom *et al.*³²¹ Hence, the authors conclude that healthy ciliogenesis requires a delicate spatiotemporal activity of Nek1, which is likely to be substantially disturbed by inhibition and depletion alike.³²¹

This assumption is further backed by findings that describe phosphorylation of the E3 ubiquitin ligase complex adaptor protein TAZ by Nek1, at a site essential for the ubiquitination and proteasomal degradation of PKD-causative PC2. Underphosphorylation of TAZ was shown to create a negative feedback loop that leads to abnormal accumulation of PC2, as TAZ also primes Nek1 for degradation.^{175, 177}

It is furthermore important to take differences between the Nek1-coding human and zebrafish orthologs into account. This aspect is of major importance and all-too-often glossed over or omitted from consideration.

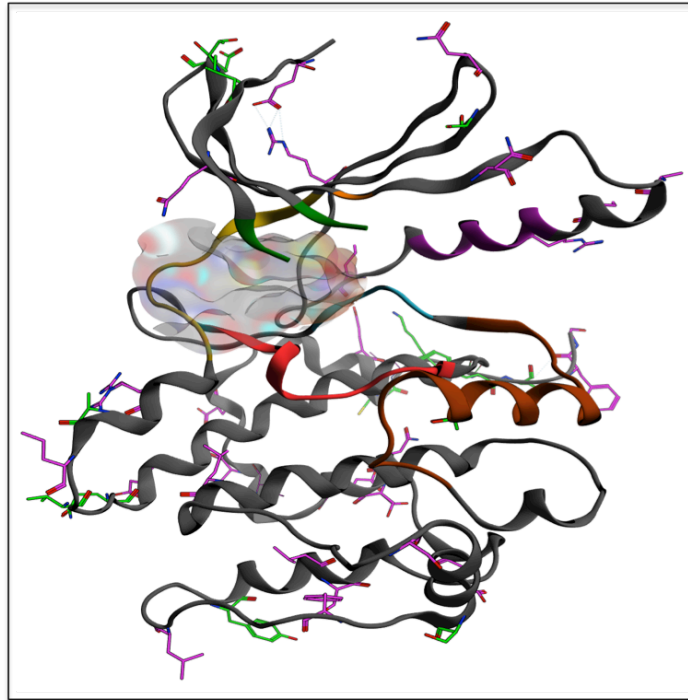


Figure 39: Comparison of human and zebrafish (*Danio rerio*) Nek1 kinase domains. Human Nek1 kinase domain (PDB code: 4B9D.B) with similar/non-identical amino acid residues shown in fuchsia and non-similar residues shown in lime green. The ATP-binding site is shown as a multicolored surface. The protein backbone is shown in dark grey and the hinge region in yellow. The P-loop is shown in green, the catalytic lysine in orange and the α -C-Helix in violet. The DFG-motif is shown in cyan, the catalytic loop in red, and the activation loop in brown.

Similarity	5	10	15	20	25	30	35	40	45																																								
NEK1 HUMAN	M	E	K	Y	V	R	L	Q	K	I	G	E	G	S	F	G	K	A	I	L	V	K	S	T	E	D	G	R	Q	Y	V	I	K	E	I	N	I	S	R	M	S	S	K	E	R	E	E	S	R
NEK1 DANIO RERIO	M	D	K	Y	E	R	L	K	K	I	G	E	G	S	F	G	K	A	I	L	V	K	S	R	T	D	G	R	Q	Y	V	I	K	E	I	G	I	S	R	M	S	N	K	E	R	Q	E	S	R
Similarity	54	59	64	69	74	79	84	89	94																																								
NEK1 HUMAN	R	E	V	A	V	L	A	N	M	K	H	P	N	I	V	Q	Y	R	E	S	F	E	E	N	G	S	L	Y	I	V	M	D	Y	C	E	G	G	D	L	F	K	R	I	N	A	Q	K	G	V
NEK1 DANIO RERIO	K	E	V	A	V	L	A	N	M	S	H	P	N	I	V	Q	Y	K	E	S	F	E	E	S	G	C	L	Y	I	V	M	D	Y	C	E	G	G	D	L	F	K	K	I	N	N	Q	R	G	S
Similarity	103	108	113	118	123	128	133	138	143																																								
NEK1 HUMAN	L	F	Q	E	D	Q	I	L	D	W	F	V	Q	I	C	L	A	L	K	H	V	H	D	R	K	I	L	H	R	D	I	K	S	Q	N	I	F	L	T	K	D	G	T	V	Q	L	G	D	F
NEK1 DANIO RERIO	L	F	P	E	E	Q	I	L	D	W	F	V	Q	I	C	L	A	L	K	H	V	H	D	R	K	I	L	H	R	D	I	K	S	Q	N	I	F	L	T	K	D	G	T	V	Q	L	G	D	F
Similarity	152	157	162	167	172	177	182	187	192																																								
NEK1 HUMAN	G	I	A	R	V	L	N	S	T	V	E	L	A	R	A	C	I	G	T	P	Y	L	S	P	E	I	C	E	N	K	P	Y	N	N	K	S	D	I	W	A	L	G	C	V	L	Y	E	L	
NEK1 DANIO RERIO	G	I	A	R	V	L	N	S	T	V	E	L	A	R	T	C	I	G	T	P	Y	L	S	P	E	I	C	E	N	K	P	Y	N	N	K	S	D	I	W	A	L	G	C	V	L	Y	E	M	
Similarity	201	206	211	216	221	226	231	236	241																																								
NEK1 HUMAN	C	T	L	K	H	A	F	E	A	G	S	M	K	N	L	V	L	K	I	I	S	G	S	F	P	P	V	S	L	H	Y	S	D	L	R	S	L	S	Q	L	F	K	R	N	P	R	D		
NEK1 DANIO RERIO	C	T	L	K	H	A	F	E	A	G	N	M	K	N	L	V	L	K	I	I	R	G	S	Y	P	P	V	S	I	H	Y	S	P	D	L	R	S	L	L	A	Q	L	F	K	R	N	P	R	E
Similarity	250	255	260	265	270	275	280	285	290																																								
NEK1 HUMAN	R	P	S	V	N	S	I	L	E	K	G	F	I	A	K	R	I	E	K	F	L	S	P	Q	L	I	A	E	E	F	C	L	K	T	F	S	K	F	G										
NEK1 DANIO RERIO	R	P	S	V	S	T	I	L	D	K	P	F	L	A	R	R	I	H	K	F	L	S	P	Q	L	I	A	Q	E	F	S	H	S	I	H	L	Q	P	K	M	S								

Figure 40: Comparison of human and zebrafish (*Danio rerio*) Nek1 kinase domains; Human (PDB code: 4B9D.B) and Zebrafish Nek1 kinase domain sequence (UniProtKB - F1RC73) identity (84.2%) and similarity analysis (92.6%). Identity and similarity values are equal to the number of matches divided by the number of amino acids in the chain corresponding to the cell column. Residues are considered similar if their BLOSUM62 scores are greater than zero.³²²

Generally, it has been shown that the majority of the human kinases display high degrees of identity with their zebrafish homologs. Human Nek1 for example shares 89% identity to zebrafish Nek1 for the catalytically active kinase domain, according to a study by Wlodarchak *et al.*³²³ Moreover, a sequence analysis was performed, showing that all residues of the active site are conserved across the two species (Figure 39 and Figure 40).

Due to the fact that this analysis is focused only on primary sequences, it cannot be safely excluded that subtle conformational differences may still disrupt or strengthen certain inhibitor interactions. Moreover, differences in quaternary interactions across species cannot be evaluated, due to the fact that studies on the zebrafish Nek1 interactome are missing.^{64, 169}

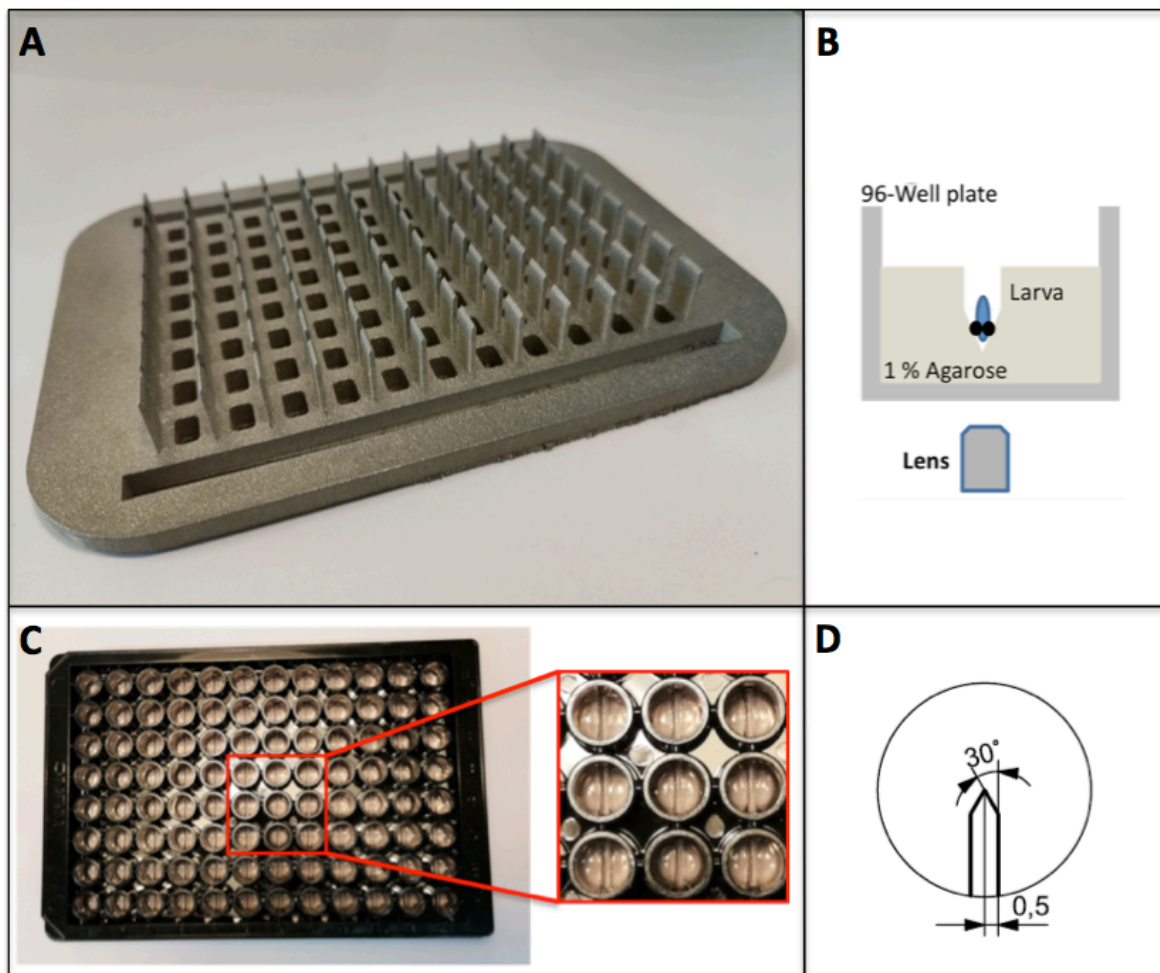


Figure 41: Experimental setup of the adapted pipeline for the fluorescence-microscopy based imaging of embryonic zebrafish pronephroi.³²⁴ A) A 96-well plate molding tool was remodeled and manufactured from stainless steel by selective laser melting on a metal 3D-printing system. B) Schematic representation of dorsal zebrafish embryo orientation in the molded agarose-coated well, relative to the lens of an inverted widefield microscope. C) Detailed view of a molded, agarose-coated 96-well plate, prepared with the molding-tool. D) Technical drawing of the pin geometry. For detailed specifications see the experimental section 5.6.1. Figure 52.

In order to visualize the influence of **19f** on larval zebrafish nephrogenesis, a fluorescence-microscopy based imaging pipeline, developed by Westhoff *et al.*, was modified and implemented.³²⁴ In the original method, highlighting of the larval pronephroi is achieved via localized enhanced green fluorescent protein (EGFP) expression and the transgenic Tg(wt1b:EGFP) zebrafish embryos are accurately oriented for microscopy in agarose coated microtiter plates that are created with a custom-made brass molding-tool. The tool consists of a base plate with 96 perpendicular pins that match the positions of the wells of a microtiter plate (Figure 41).

First attempts to recreate the molding tool via fused deposition modeling (FDM) 3D-printing from polylactic acid were conducted by TUDA students Michelle Kilb and Jessica Kondol in a supervised practical course, with kind help from Dr. Dieter Spiehl (TU Darmstadt Institute for Printing Science Technology). Unfortunately, the FDM-printed molding tool provided lack-luster results, due to inadequate accuracy and structural integrity of the pins. At last, the molding tool was manufactured by selective laser melting on an EOS M290 (*EOS GmbH Electro Optical Systems*, Krailing, Germany) metal 3D-printing system using EOS StainlessSteel 316L as the material, with kind help from Holger Hermann Merschroth of the TU Darmstadt Institute of Production Management, Technology and Machine Tools (Figure 41A).

In order to save material and to reduce the cost and time of production, slight modifications were introduced into the baseplate, while the geometry of the pins remained unaltered, as to preserve the functionality of the original tool.³²⁴

Fluorescent Labeling of Zebrafish Pronephroi with PT-Yellow

As a means of avoiding dependence on the transgenic Tg(wt1b:EGFP) zebrafish line, the fluorescent probe PT-Yellow (BDNCA3-D2), which selectively labels the renal proximal tubules in wild-type zebrafish, was used for fluorescent highlighting instead of GFP expression.³²⁵ The use of PT-Yellow thus allowed for zebrafish maintenance and husbandry in a standard laboratory and it was furthermore reasoned that the ingestion of an external probe is better suited to indicate the impaired renal clearance associated with fluid-filled cysts.³²⁶

It should be noted here that in contrast to the transgenic zebrafish line, the glomerulus is not highlighted in PT-Yellow treated animals. However, this difference is of minor importance for

the visualization of cystic malformations but should be taken into account for investigations regarding glomerular diseases and drug-induced acute kidney injury.³²⁷

It is hypothesized that the localized accumulation of PT-Yellow results from selective and irreversible thioether formation between its electrophilic chloroacetamide moiety and cysteine residues in specific renal tubular proteins. The reactivity and specificity of electrophilic chloroacetamides toward thiol groups, over other nucleophilic amino-acid side chains, is well studied.³²⁸⁻³³⁰

In order to evaluate the adequate ingestion and accumulation of PT-Yellow, a preliminary fluorescence microscopy experiment was performed by TUDA students Michelle Kilb and Jessica Kondol as part of a supervised practical course. 3 days post fertilization (dpf) wild-type zebrafish embryos were incubated in a 100 nM solution of PT-Yellow (BDNCA3-D2) in E3-medium for an incubation time of 20 min (Figure 42).

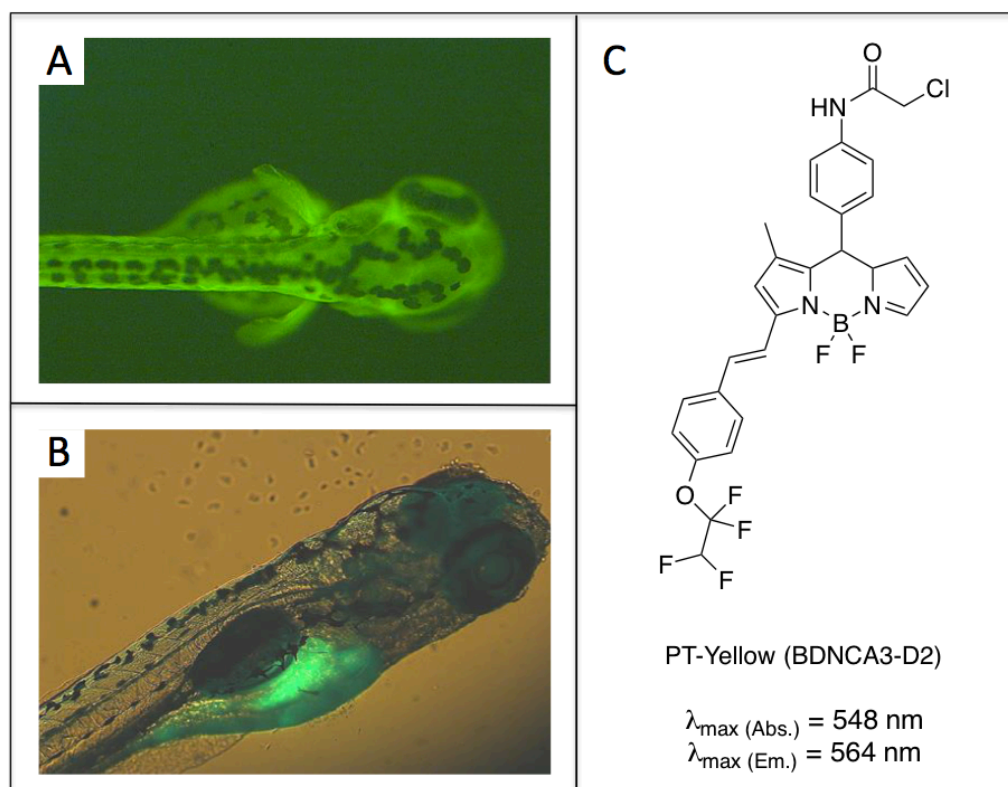


Figure 42: Fluorescent labeling of wild-type zebrafish pronephric ducts. Wild-type zebrafish embryos were at 3 days post fertilization (dpf) incubated in a 100 nM solution of PT-Yellow (BDNCA3-D2) in E3-medium (incubation time = 20 min). Fluorescence-microscopy imaging was performed, after anaesthization in tricaine mesylate solution (0.02%) and mounting in methylcellulose, using an AF 546 narrow-band excitation filter. A) Fluorescence microscopy image of 4 dpf wild-type zebrafish embryo, 24 h post incubation. B) Fluorescence microscopy image of 5 dpf wild-type zebrafish embryo, 48 h post incubation.

Fluorescence-microscopy imaging was performed after 24 and 48 h respectively, after anaesthization in tricaine mesylate solution (0.02%) and mounting in methylcellulose, using an AF546 narrow-band excitation filter. The distinct renal localization of PT-Yellow, which has a maximum absorbance at 548 nm and a fluorescence emission peak at 564 nm, was only observed after 48 h, while no accumulation was observed after 24 h.

The experiment furthermore emphasizes that the zebrafish's pigmentation hampers visibility of the fluorescently labeled structures. This is especially problematic considering the embryos dorsal orientation in the molded agarose cavity, which is necessary as a consequence of the swim bladders tendency to turn upwards, once the embryo is anaesthetized (Figure 41).

As a means to avoid this problem, the effects of the melanogenesis inhibitor *N*-phenylthiourea (PTU) on pigmentation were investigated in the same supervised practical course (Figure 43).

It is important to note that the timepoint of PTU treatment initiation was carefully chosen to lie in between the 28 somite and prim 5 developmental stages, which corresponds to around 24 hpf for embryos developing at 28.5 °C (see experimental section 5.5).³³¹

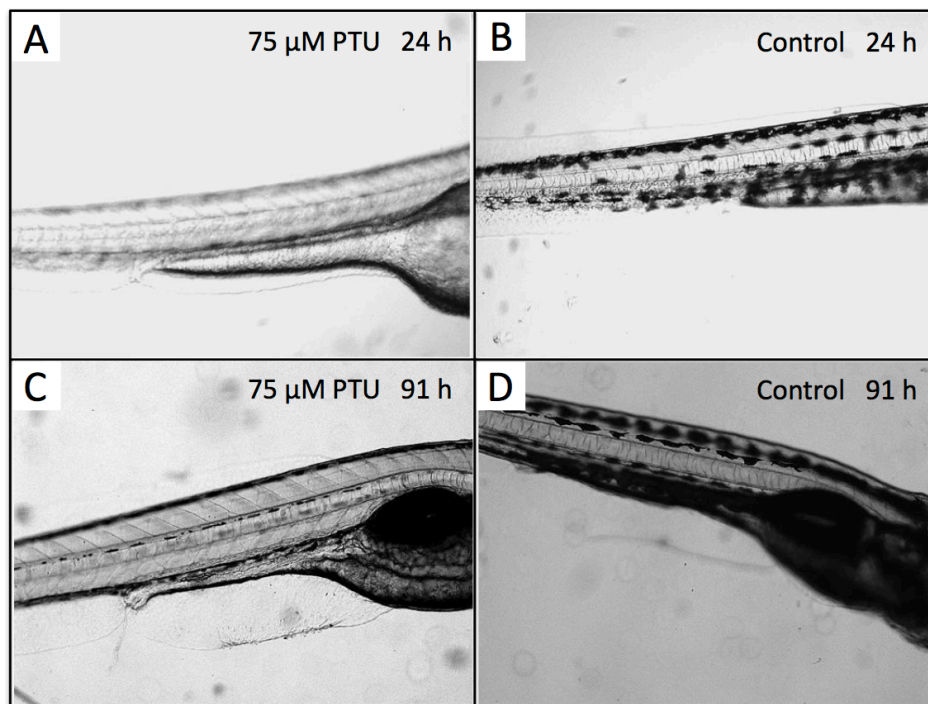


Figure 43: Effects of *N*-phenylthiourea (PTU) on pigmentation in developing wild-type zebrafish embryos. At 24 hours post fertilization (hpf), treated embryos were incubated in a 75 μM solution of PTU in E3-medium over the duration of the experiment. Controls were left untreated in E3-medium. Microscopy imaging was performed after anaesthization in tricaine mesylate solution (0.02%) and mounting in methylcellulose. A) PTU (75 μM) treated embryo after 24h. B) Control embryo after 24h. C) PTU (75 μM) treated embryo after 91h. D) Control embryo after 91h.

Treatment with PTU must be initiated before the onset of pigmentation, at around the prim 5 developmental stage, as PTU inhibits melanogenesis by blocking all tyrosinase-dependent steps in the melanin pathway and does therefore not remove already formed pigment.³³² For the same reason, embryos must be treated with PTU over the entire duration of the experiment, due to the fact that depigmented embryos will again produce pigmentation on discontinuation of treatment. Moreover, the PTU concentration must be set accordingly, as embryos treated with PTU concentrations up to 70 μM still produced pigmentation in a study by Karlsson *et al.*³³³ High concentrations of PTU, on the other hand, have been shown to disrupt thyroid function and produce numerous embryotoxic effects, such as increased embryonic mortality or teratogenesis.³³³⁻³³⁴ Hence, the PTU concentration was set to 75 μM , in order to sufficiently suppress pigmentation while keeping adverse effects to a minimum.

For the aforementioned reasons, 24 hours post fertilization (hpf) wild-type zebrafish embryos were incubated at 28.5 °C in a 75 μM solution of PTU in E3-medium over 24 and 91 h respectively and analyzed by microscopy imaging after anaesthization in tricaine mesylate solution (0.02%) and mounting in methylcellulose (Figure 43).

Full depigmentation was observed for treated embryos after 24 h, while insubstantial pigmentation arose after 91 h. Furthermore, no unusual phenotypes were observed in treated embryos, which exhibited normal eye development, body curvature and an inconspicuous heartbeat. The control embryos showed normal pigmentation.

Alternatively, a fully transparent zebrafish mutant has recently been developed.³³⁵ As a consequence of the sufficient depigmentation observed in the preliminary experiment, and to avoid the strict regulations associated with the experimental use of transgenic animals, it was decided to employ PTU depigmentation, at a concentration of 75 μM , for the *in vivo* efficacy study of **19f**.

Stability-indicating HPLC-Assay for Lead Compound 19f

In order to rule out any cross-reactivity related interferences in the planned *in vivo* efficacy study, a stability-indicating HPLC-assay was performed for lead compound **19f** against PTU and PT-Yellow in E3-medium (Figure 44).

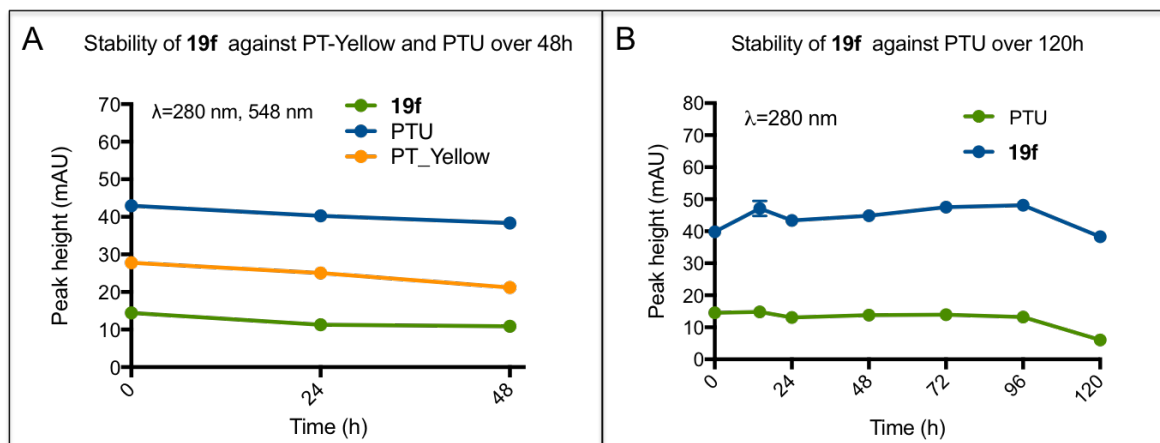


Figure 44: Stability-indicating HPLC-assay for lead compound **19f**. Absorption was measured at 280 nm for **19f** and PTU and at 548 nm for PT-Yellow (BDNCA3-D2). A) Stability of **19f** against PTU and PT-Yellow over 48 h. B) Stability of **19f** against PTU over 120 h. All measurements were performed in triplicates. Error bars represent SD and are not shown if shorter than the size of the symbol. See experimental section for more details.

From a theoretical standpoint, no chemical reactions should occur between the compounds at the employed standard conditions in pH neutral aqueous solution. The moderately reactive chloroacetamide group in PT-Yellow is well known to chemoselectively react with sulfhydryls under physiological conditions, giving stable thioethers by nucleophilic substitution but not with less nucleophilic hydroxyl groups, such as in **19f**.³²⁹

Stability against PT-Yellow was examined over 48 h at the presence of PTU, to match the previously determined incubation time, necessary for adequate renal accumulation of the fluorescent probe in zebrafish embryos. As previously stated, embryos must be treated with PTU over the entire duration of the experiment. According to EU Directive 2010/63/EU on the protection of animals used for scientific purposes, independent food uptake is considered as the stage from which animals are defined as protected by respective laws.³³⁶ Based on criteria such as yolk consumption, feeding and swimming behavior, it is generally accepted

that zebrafish embryos are regarded as independently feeding from 120 hpf onwards.³³⁷ Therefore, a maximum incubation time of 120 h was defined for the planned *in vivo* efficacy studies and this endpoint was hence also set for the stability-indicating HPLC-assay of compound **19f** against PTU.

The stability-indicating HPLC assay was performed using the HPLC system described in the experimental section (see 5.1.5), connected to a diode array detector (DAD). A 15 μM solution of **19f** in E3-medium, containing 75 μM PTU and a 15 μM solution of **19f** containing 75 μM PTU and 2.5 μM PT-Yellow (BDNCA3-D2)³²⁵ were prepared for HPLC injection. Absorptions were measured every 24 hours at 280 nm for compound **19f** and PTU and 548 nm for PT-Yellow over 48h or 120h respectively.

The experiment verified that **19f** is stable against PTU in E3-medium over the duration of 120 h and no reaction between **19f**, PTU and PT-yellow was observed over 48 h. The minor drop-off at the 120 h timepoint is likely an artifact resulting from HPLC-injection inaccuracy, due to the fact that all determined stability curves generally follow the same trends.

Fluorescence-Microscopy Imaging of 19f-treated Wild-Type Zebrafish Embryos

With the goal of studying the dose-dependent *in vivo* effects of Nek1-inhibitor **19f** on the embryonic zebrafish pronephros during early development, a workflow for the fluorescence microscopy imaging of PT-Yellow-labeled zebrafish kidneys was established in preliminary experiments over the course of a supervised internship, with kind assistance from TUDA student Yung-Hsin Shih.

On basis of the acquired results, the established workflow entails the selection of suitable wild-type zebrafish embryos, which is followed by a compound treatment regimen that leads to the final image acquisition step. As a last step, the acquired images were analyzed by qualitative visual inspection and quantitative image analysis.

For the first step, 4 hpf embryos that exhibited intact chorion membranes were selected and reexamined after 2 hrs in accordance to guidelines published by M. Haldi *et al.* in *Zebrafish: Methods for Assessing Drug Safety and Toxicity*.³¹⁷

In the following step, the zebrafish embryos at 6 hpf were incubated with (i) the negative control (E3-medium), (ii) 0.2% DMSO, (iii) 10 μM **19f** and (iv) 20 μM **19f** in E3-medium,

containing 75 μM PTU. After 48 h, all embryos were treated with 100 nM PT-Yellow for 20 min, thoroughly washed with E3-medium and returned to the respective compound solution for a total incubation time of 96 h. Finally, the embryos were anesthetized with tricaine methylsulfonate³³⁸ (0.02%) and transferred to agarose molds, which were prepared in 96-well plates using the previously described molding-tool for fluorescent imaging in a widefield microscope (see 5.6.1 and 5.6.2).³²⁴

For the image acquisition step, 33 Z-slices with a Z-distance of 15 μM were recorded per embryo at 15x magnification, after careful manual orientation in the agarose molds. In order to visually assess the acquired images, several image-processing steps were necessary. Images in fluorescence microscopy are inherently blurred, due to the limits of light diffraction. Deconvolution is a standard technique in fluorescence microscopy imaging that improves contrast and allows for the detection of small and dim-lighted details, otherwise obscured in the sample. This step is especially necessary for enhancement of the low-contrast, high-background image data, often acquired from widefield microscopes.³³⁹ In practice, special restoration algorithms are used to calculate the shape of a fluorescent object that would produce the acquired image data, when convolved with the specific point-spread function of the imaging setup.³⁴⁰ With the planned quantitative image analysis in mind, the restoration algorithm was carefully calibrated to specimen properties, sample setup and the microscopes specifications, in order to preserve the relative fluorescence intensities needed for accurate analysis (Figure 45 and Table 12).

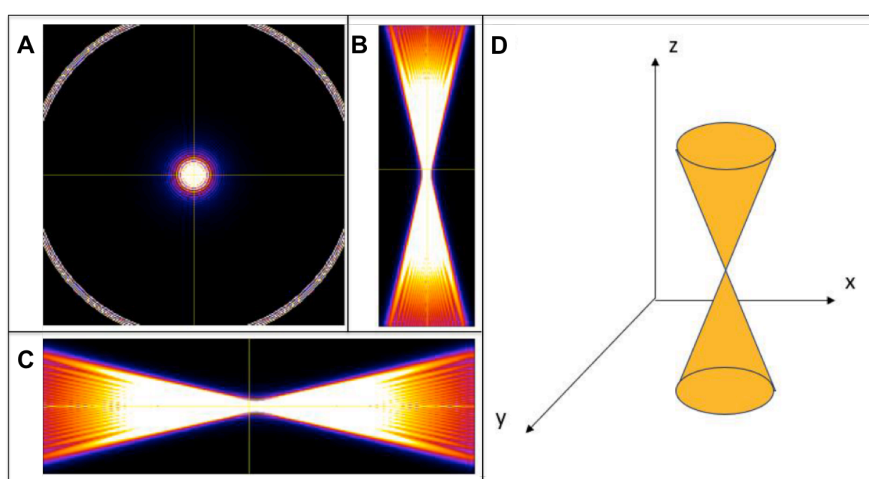


Figure 45: Visual representation of the simulated point-spread function in *ImageJ*, using the calibration parameters for the *Gibson-Lanni* modeled point-spread function simulation in the *PSFGenerator* plug-in.³⁴¹⁻³⁴² (A) Z-Axis view. (B) XZ-Plane view. (C) YZ-Plane view. (D) Scheme of a two-coned point-square function in a three-dimensional cartesian coordinate system.

Table 12: Calibration parameters for the *Gibson-Lanni* modeled point-spread function simulation in the *PSFGenerator* plugin of the *ImageJ* software package.³⁴¹⁻³⁴² See experimental section for more details.

Parameter	Value	Comment
Refractive index immersion	1.000273	Air at standard temperature and pressure ³⁴³
Refractive index sample	1.34	Agarose (similar to biological tissue) ³⁴⁴
Working distance	9500 μM	Distance between 96-wellplate and lens
Particle position Z	1000 nm	Distance between well-bottom and embryo
Accuracy computation	Good	Richardson-Lucy-Algorithm accuracy setting
Wavelength	564 nm	Maximum emission of PT-Yellow
Pixelsize XY	433.34 nm	Camera: PCO Edge 5.5 with Pixelsize: 6.5 x 6.5 μM (6500 nm/15 = 433.34 nm)
Numerical aperture	0.3	Olympus CPlanFL N, 10x, NA 0.3 objective with a 1.5x tube lens magnification, 15x total magnification.
Z-step	15000 nM	Z-step distance
Size XYZ	256, 256, 65	Image size of the simulated PSF
Display	Linear, 32-bit	Visualization properties

Simulation of the point-spread function, which is required for the deconvolution process, was performed using *ImageJ* plugin *PSF Generator*, employing *Gibson-Lanni* modelling.³⁴¹⁻³⁴² Deconvolution was performed using the *DeconvolutionLab2* plugin.³⁴⁵ The commonly used *Richardson-Lucy-Algorithm* was chosen as the mathematical basis of the deconvolution, which iteratively calculates maximum likelihood estimations based on Poisson statistics.³⁴⁶⁻³⁴⁷

As a consequence of related parameter setting limitations, the necessary assumption was made that the refractive indices of the imaged embryos and agarose are identical. The assumption is reasonable, due to the fact the refractive indices of agarose and biological tissues are closely similar.³⁴⁴

For the final step of the fluorescence microscopy imaging workflow, maximum Z-projections were generated from the deconvolved Z-stacks and color-coded for fluorescence intensity, in order to facilitate the qualitative visual inspection (Figure 46).

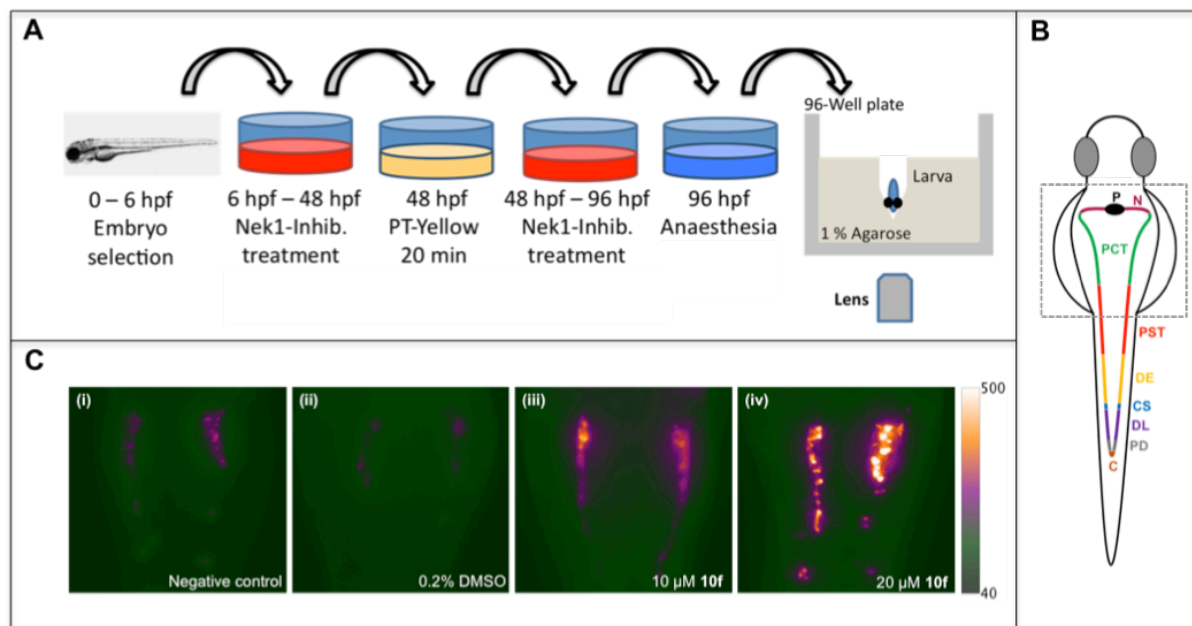


Figure 46: Microscopic imaging of fluorescence-labeled (PT-Yellow) zebrafish pronephroi after treatment with Nek1-inhibitor **19f**. (A) Schematic representation of the workflow, entailing embryo selection, compound treatment and image acquisition. (B) Schematic representation of the pronephros in the developing zebrafish (28-somite stage). Adapted from Gehrig *et al.*³¹⁹ (C) Exemplary maximum intensity projections of deconvolved Z-stacks (15x magnification; 33 Z-slices; $dZ=15\ \mu\text{m}$). The dotted line indicates the cropped region of interest. (C, i) negative control E3-medium, (C, ii) negative control 0.2% DMSO, (C, iii) $10\ \mu\text{M}$ **19f** and (C, iv) $20\ \mu\text{M}$ **19f**. For images of biological replicates see appendix C. Abbreviations: a.u., arbitrary unit; C, Cloaca; CS, corpuscles of Stannius; DE, distal early tubule; DL, distal late tubule; hpf, hours post fertilization; N, neck region; P, Podocytes of the glomerulus; PCT, Proximal convoluted tubule; PD, Pronephric duct; PST, Proximal straight tubule.

Administration of **19f** caused a substantial increase in fluorescence intensity and expansion of the proximal convoluted tubules, thus indicating pronephric swelling alongside an impaired renal clearance of the fluorescent marker. Strikingly, the fluorescent marker is more homogeneously distributed in control embryos and in embryos subjected to $10\ \mu\text{M}$ **19f**, compared to the $20\ \mu\text{M}$ **19f** group, thus indicating the growth of fluid-filled cysts (see appendix C for images of all biological replicates). Furthermore, the findings provide further evidence for the adequate absorption and bioavailability of **19f**.

While pronephric enlargement and increased fluorescence intensity over the controls are visually evident for the $20\ \mu\text{M}$ **19f**-treated group, a clear effect is not unambiguously obvious to the naked eye for the $10\ \mu\text{M}$ **19f**-treated group. Therefore, a quantitative image analysis was performed over all biological replicates, with the goal to confirm the conclusions drawn from the qualitative visual inspection and to clarify a potential dose dependency.

Quantitative Image Analysis

Quantitative image analysis was performed over two independent measures, namely total fluorescence intensity and pronephroi size. The fluorescence intensity measurement gauges the increased fluid uptake and impaired renal clearance associated with fluid-filled cysts. Quantification of the pronephroi size, by determination of the fluorescent pixel area, provides information on the extent of pronephric swelling and thus kidney enlargement.

Since it was not possible to remove all out of focus blur with the deconvolution procedure, the sharpest 5 consecutive Z-slices of the acquired image stacks were manually selected in each stack for the quantitative analysis (see appendix C). Subsequently, the following image analysis steps were applied using *ImageJ*.

As a first step, background subtraction was performed for the individual slices, using a 150 pixel-rolling ball, and the slices were summed into a single image. A fluorescence intensity threshold was set (above 100) and the background was converted to an 8-bit mask for the intensity quantification (see Appendix C, Figure A 2). The integrated density in the summed stacks was used as the quantity to express the fluorescence intensity.

For the determination of pronephric size, the same background subtraction was used, but the background was converted to “Not a Number” (NaN) pixels for the quantification of the pronephron areas (see Appendix C, Figure A 3). The summed pixel area in μM^2 in the summed stacks was used as the quantity to estimate the size of the pronephroi.

The quantitative analysis provided statistically relevant evidence for the dose-dependent increase in both fluorescence intensity as well as pronephric size in **19f**-treated PT-Yellow labeled zebrafish pronephroi (Figure 47).

As expected, no significant difference was observed between the controls in both measures. While the fluorescence intensity in the treated groups increased linearly with **19f** concentration, the pronephric size was nearly doubled for the $10\mu\text{M}$ **19f**-treated group and increased 2.5-fold for the $20\mu\text{M}$ **19f**-treated group, when compared to the controls. As hypothesized, the experiment thus demonstrates that Nek1-inhibition by **19f**, during early organ development, causes cystic kidney growth in zebrafish embryos, in a dose-dependent manner.

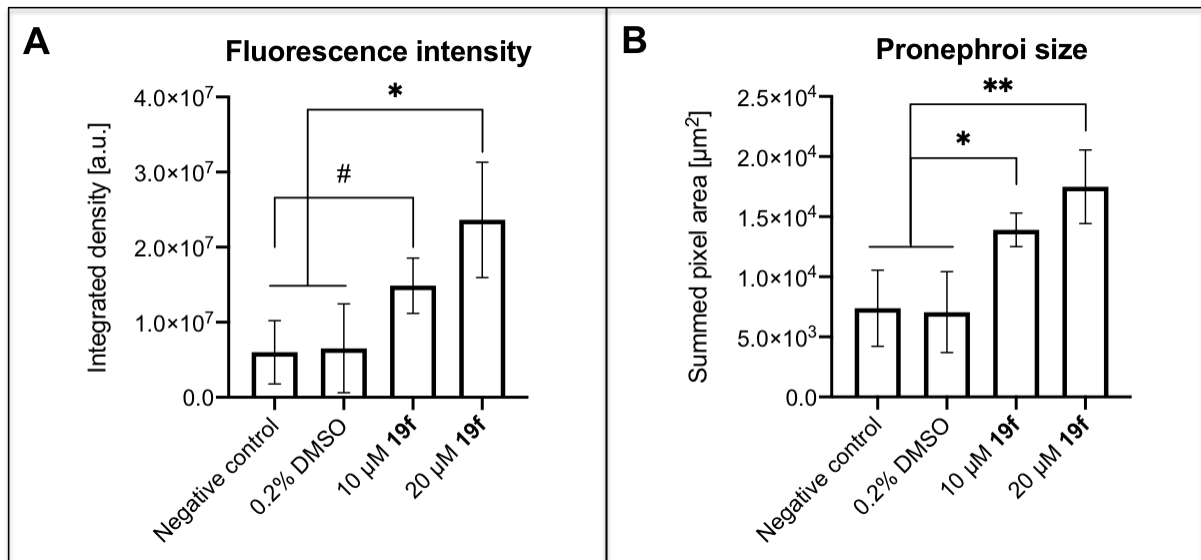


Figure 47: Quantitative image analysis for acquired fluorescence microscopy images of PT-Yellow labeled zebrafish pronephroi. Column heights represent the mean and error bars represent the SD. (A) Quantification of fluorescence intensity based on summed image projections of deconvolved Z-stacks using *ImageJ*. n=3 for negative control, 0.2% DMSO and 10 μM **19f**; n=5 for 20 μM **19f** (#*P*=0.0516; **P*<0.05). (B) Quantification of pronephroi size by summed pixel area determination based on summed image projections of deconvolved Z-stacks using *ImageJ*. n=3 for negative control, 0.2% DMSO and 10 μM **19f**; n=5 for 20 μM **19f** (**P*<0.05; ***P*<0.01).

These conclusions were drawn despite the fact that **19f** was found to be unselective against IKKβ. Park *et al.* have shown that levels of phosphorylated-IKKα/β and its downstream factor NF-κB are upregulated in the renal tissue of transgenic *PKD2*-overexpressing mice that show the cystic phenotype, when compared to wild-type controls.³⁴⁸ Moreover, Booij *et al.* demonstrated that cystic growth was in fact reduced by IKKα/β-inhibitors in a murine 3D cell culture-based screening platform.³⁴⁹ It therefore appears that Nek1 inhibition overturns any presumed protective effects of IKKβ-inhibition on cystogenesis, in the performed experiment. It should be noted here that, unlike in murine models, zebrafish IKKα is suspected to negatively regulate NF-κB activity and IKKα^{-/-} zebrafish embryos displayed severe head and tail malformations, as well as an upregulated NF-κB-response and increased NF-κB-dependent apoptosis, in a study by Correa *et al.*³⁵⁰ In accordance with the low IKKα-activity of **19f** (see Appendix B), this phenotype was not observed in the experiments conducted in this thesis. Overall, this leads to the conclusion that the aberrant cystic growth in **19f**-treated zebrafish embryos is unlikely to be mediated by IKK cross-reactivity. However, a causative relation to hitherto unidentified cross-reactivity cannot be ruled out entirely, due to the aforementioned limitations of the selectivity test panel and the fact that the complex PKD-related molecular pathways and regulatory networks are not yet fully understood.³⁵¹⁻³⁵³

It was, for example, shown that *in vitro* expression of mutated Nek8 in murine autosomal recessive juvenile cystic kidney (*jck*) mice cells results in a multinucleated and enlarged cell morphology that also displays an abnormal actin cytoskeleton. Furthermore, injection of zebrafish embryos with a morpholino anti-sense oligonucleotide corresponding to the ortholog of Nek8 resulted in the formation of pronephric cysts.⁸⁸

Unfortunately, cross-reactivity of **19f** with Nek8 was not ruled out, since commercial assays are missing, and no activity homology data from the aforementioned kinase cross-screening study by Wells *et al.* is available for Nek8 for the same reason (see chapter 3.2.5.). However, the reported low active site homology between Nek1 and Nek8 (15/28 shared residues) speaks against the assumption that **19f** may also inhibit Nek8.²³⁰

4. Summary and Outlook

Despite the impressive accomplishments in the development of small molecule kinase inhibitors over the past 25 years, the majority of human kinases still lack high-quality inhibitors that can be used as chemical probes to investigate their biological function and pharmacology. Many members of the untargeted kinome are known to play a crucial role in the cell cycle and thus represent unexploited cancer drug targets. Nek1 is one such example, as it has been shown to be involved in numerous cancers, as well as in several ciliopathies and neurodegenerative diseases. However, no directed medicinal chemistry efforts toward potent and selective Nek1 inhibitors have been made publicly available, prior to this work.

To address this issue, this doctoral thesis discloses the structure-guided design of a potent, selective and bioavailable small molecule inhibitor for Nek1, using state-of-the-art computer-guided drug design methods. Lead compound **19f** (BSc5452) displayed Nek1 activity *in vitro*, with IC₅₀ values in the mid to low nanomolar range in two independent kinase activity assays, and good kinase selectivity. Furthermore, ample bioavailability, excellent tolerability and dose-dependent *in vivo* efficacy were demonstrated for **19f** in a wild-type zebrafish polycystic kidney disease model. In order to visualize the influence of **19f** on larval zebrafish nephrogenesis, a fluorescence-microscopy imaging pipeline was established, which makes use of an external fluorescent probe, thereby overcoming the prevalent need for transgenic zebrafish lines. This work thus provides the first directed tool compound for a mostly neglected kinase that has been shown to be a key player in numerous forms of cancer and other illnesses, thereby helping to establish Nek1 as a therapeutic target and providing a powerful tool to further elucidate its biological function.

The structure-guided inhibitor design process commenced with the identification of suitable molecular scaffolds, which was initially approached by analysis of literature-reported screening data. Due to the scarce number of published structures associated with Nek1-binding, as well as their lack of suitability for inhibitor development, two novel scaffolds were derived from a reported Nek1 X-ray structure cocrystallized ligand (CK7), by computer-assisted structure-guided design. Both scaffolds were based on the versatile bioisosteric purine analogue 7-azaindole, with each of the scaffolds targeting one of two distinct binding modes associated with this heterocycle's reported ability to interact with kinase active sites. Molecular docking studies for the "normal" binding mode-targeting "N1-In"-scaffold, into PDB-deposited Nek1 crystal structures, revealed promising interaction potential for 4- and 6-position derivatives and two synthetic routes toward 4,6-disubstituted 7-azaindoles were

hence explored. Starting from affordable, commercially available materials, both routes delivered key synthetic intermediates, which are poised for modular diversification by a range of synthetic methods. Furthermore, initial studies on the site-selective modification of these synthetic intermediates, by transition-metal-catalyzed cross-coupling reactions, were successfully undertaken. Nonetheless, more compounds need to be synthesized and evaluated, in order to investigate the potential of 4,6-disubstituted 7-azaindoles for Nek1 inhibition.

Despite the successful advances toward inhibitors of the “N1-In”-scaffold, the publication of a highly impactful kinase cross-screening study in the midst of this work shifted attention to the “flipped” binding mode-targeting “N1-Out”-scaffold. The published report not only confirmed the preceding scaffold identification process but also provided an advanced chemical starting point (UNC5452, **3a**) with close structural relation. Extending upon this starting point, hypotheses for improved interactions with the Nek1 ATP-binding site were generated by molecular docking of UNC5452 (**3a**) into PDB-available crystal structures. These hypotheses were challenged by a series of structurally related inhibitors, based on the same 4-phenylsulfonamide-7-azaindole scaffold.

Initial focus was set on modifications of the dimethylaminoethyl fragment in UNC5452 (**3a**) and a SAR for this fragment was established through design, synthesis and evaluation of a series of related compounds. The most potent analogue of this series, compound **3f**, displayed low micromolar IC₅₀ values against Nek1 in two independent *in vitro* kinase activity assays and served as the structural basis for further SAR studies.

In silico isolation and superposition of available Nek1 kinase domain crystal structures revealed conformational mobility of the functionally important DFG-motif through interaction with a water molecule, located in a back pocket behind the gatekeeper residue. It was hypothesized that occupation of this pocket may substantially decrease Nek1 kinase activity, by locking the enzyme in an inactive “DFG-out”-conformation. Furthermore, the unconserved nature of this unique back pocket provided opportunities for the development of Nek1 inhibitors with increased selectivity. In order to test this hypothesis, a series of back pocket-targeting 3'-substituted 4-phenylsulfonamide-7-azaindoles was designed *in silico*. The synthesis of this compound series was attempted in a supervised master thesis but ultimately remained unsuccessful. With the aim to gain information on the feasibility of this approach, surrogate 3'-methoxy 4-phenylsulfonamide-7-azaindole **15** was designed, synthesized, and evaluated for its Nek1 activity *in vitro*. Unfortunately, compound **15** did not substantially influence Nek1 activity, which speaks against the feasibility of approaching the back pocket from the 3'-position in UNC5452 derivatives. As demonstrated by presented molecular

docking studies, an entry from the 3'-position is likely blocked by the gatekeeper. Furthermore, an approach from the 7-azaindole core appears to be unpromising from both the "normal" and the "flipped" binding mode. Nonetheless, further experiments are needed to fully rule out the possibility of effective Nek1 back pocket-occupation by UNC5452-based structures. It for example remains unclear, if a replacement of the phenyl moiety to a five membered aromatic ring would sufficiently widen the C-C-C bond angle to bypass the gatekeeper. Alternatively, a scaffold hopping strategy can be applied to discover structurally novel compounds that retain their biological activity and facilitate pocket access.

In the next attempt to expand upon Nek1 inhibitor **3f**, for improved potency and selectivity, 3,4-disubstituted 7-azaindole derivatives were designed and successfully obtained in a five-step synthesis. On the basis of preceding molecular docking studies, the introduction of aromatic substituents to the azaindole 3-position was hypothesized to establish additional interactions with the unusual Nek1 Phe135 residue and provide access to the Nek1 ribose-binding region. Starting from affordable and commercially available 4-chloro-7-azaindole (**20**), the key steps in the ultimately successful synthetic route were comprised of two sequential, site-selective and sterically challenging SUZUKI-MIYAJIMA CROSS-COUPLED REACTIONS that required extensive screening of suitable catalyst systems and reaction conditions. One related compound, 3-phenyl derivative **25a**, showed increased inhibitory activity against Nek1 and improved selectivity over the known off-target IKK β . Unfortunately, the excellent Nek2 selectivity of parent compound **3f** was significantly reduced in compound **25a**. As a consequence of the reduced Nek-family binding selectivity and the lengthy synthetic route, the investigation of 3-aryl-4-phenylsulfonamide 7-azaindole Nek1 inhibitors was not further pursued. Nevertheless, this work provides novel insight into the site-selective 3,4-derivatization of the 7-azaindole core structure, which enables further studies toward unexplored interactions with the Nek1 ribose-binding region and can also be applied to structurally related 7-azaindole inhibitors with different protein targets.

In order to explore additional interactions with the Nek1 P-loop and phosphate-binding regions, a virtual structure library was constructed on the basis of parent Nek1 inhibitor **3f**. The natural product-based library encompassed 77 *N*-substituted amino acids and their corresponding alcohols and allowed for the convenient access to enantiomerically pure starting materials, a straightforward synthetic route and provided opportunities to exploit nature's own toolkit for protein binding. Molecular docking of the virtual library into the Nek1 kinase domain required reconstruction of the P-loop, which was performed using two independent methods. First, the P-loop was reconstructed using the *SuperLooper2* web

application, a fragment-based tool for the prediction and interactive placement of loop structures, and second, a homology model of the Nek1 kinase domain was created, using the X-ray structure of Nek2 bound to an aminopurine inhibitor as the template. Seven virtual hits were thereupon identified and a detailed comparative evaluation of the reconstruction models was performed.

The efforts cumulated in Nek1 inhibitor **19f** that displayed much improved potency, with IC_{50} values in the mid to low nanomolar range ($IC_{50, Nek1} = 330$ nM). Moreover, 48 out of 50 kinases were not substantially inhibited by **19f** in a focused kinase selectivity panel and IKK β was identified as an off-target. The putative binding mode of **19f** in the Nek1 kinase domain was elucidated by molecular docking into available X-ray structures and suggests ATP-competitive binding to an inactive conformation without occupation of the back cleft (*Type IIb* inhibition). Future studies should aim to confirm the putative binding mode in suitable co-crystallization experiments, which would also enable further advances through iterative anchored docking calculations and targeted structure design and furthermore confirm the ATP competitive nature of **19f**. It can be envisioned that modifications of the indole, phenyl and 7-azaindole moieties in **19f** may further improve inhibitory activity against Nek1 and selectivity over IKK β . For example, the synthesis protocol for the 3,4-disubstitution of 7-azaindoles developed in this work could also be applied to generate structural derivatives of **19f**. Moreover, a broader selectivity screen may uncover further kinase and non-kinase off-targets and allow for directed efforts toward even more selective Nek1 inhibitors.

In the second part of this doctoral thesis, lead compound **19f** was further profiled *in vitro* and *in vivo*, for its bioavailability, safety and efficacy. Bioavailability of **19f** was estimated *in vitro* by determination of its aqueous solubility in a shake-flask solubility assay and its cell-permeability was investigated in a Caco-2 assay. Lead compound **19f** displayed sufficient aqueous solubility and Caco-2 cell permeability for use as a research tool compound and the planned *in vivo* efficacy studies. As a consequence of the limited recovery rate obtained from the Caco-2 assay, the metabolic stability of **19f** should be further investigated in future studies.

With the ample bioavailability data in hand, safety and toxicity of compound **19f** were investigated in wild-type zebrafish embryos. Treatment with **19f** was well tolerated, as full lethality was only observed close to the solubility limit for a concentration of 30 μ M and no gross morphological changes were observed, even at high concentrations.

With the aim to evaluate the *in vivo* efficacy of **19f**, a zebrafish PKD model was established, predicated on reported morphological changes to rodent renal structures associated with Nek1 depletion. The effects of **19f** on larval zebrafish nephrogenesis were visualized in a fluorescence microscopy imaging pipeline, which revamped a published procedure by incorporating an external fluorescent probe, thereby overcoming the prevalent need for transgenic zebrafish lines. As hypothesized, the performed experiments demonstrated that Nek1-inhibition by **19f**, during early organ development, causes cystic kidney growth in zebrafish embryos. Furthermore, a method for the quantitative analysis of acquired imaging data, with regards to fluorescence intensity and pronephroi size, was devised and provided statistically relevant evidence for the dose-dependent *in vivo* efficacy of lead compound **19f**. In further studies, a Nek8 kinase activity assay should be established, in order to rule out the cross-reactivity of **19f** against this PKD-related kinase, since commercial options are presently not available.

To sum up, the results of the present work are of wide interest among the biomedical research community, as they provide the first high-quality inhibitor against a highly impactful kinase, thus bestowing a much-needed tool upon members of this research field. Furthermore, the methods used provide a blueprint for the fast and resource-efficient development of chemical probes for other dark kinases from widely available chemogenomic kinase data sets.

5. Experimental Section

5.1. General Information

Unless otherwise noted, starting materials and reagents were purchased from *Acros Organics*, *Activate Scientific*, *Alfa Aesar*, *Fluka*, *Merck*, *Carl Roth*, *Sigma-Aldrich*, *TCI*, *Carbolution Chemicals* and *VWR* and were used without further purification. All reactions employing anhydrous conditions were performed in dried glassware with dry solvents under argon atmosphere (5.0 quality), unless otherwise noted. All cross-coupling reactions were performed with degassed solvents.

5.1.1. Column and Thin-layer Chromatography

Thin-layer chromatography was performed on precoated 0.2 mm silica gel 60 F254 aluminum sheets (*Merck KGaA*, Darmstadt, Germany) with detection performed by UV-light (254 and 365 nm) or potassium permanganate staining. Column chromatography was carried out by isocratic elution with solvent systems, specified for each experiment, on 40–63 μm *NORMASIL* 60 silica gel (*VWR International*, Radnor, Pennsylvania, USA). Automated flash column chromatography was performed on a *Combiflash R_f 4x* system (*Teledyne ISCO Inc.*, Thousand Oaks, California, USA) using prepacked *TELOS* Flash-Silica or Reversed-Phase C18(EC) cartridges (*Kinesis GmbH*, Langenfeld, Germany) of specified size and manually programmed elution solvent gradients (Solvent A: Acetonitrile with 0.1% trifluoroacetic acid; Solvent B: Water with 0.1% trifluoroacetic acid) specified for each experiment. All cartridges were conditioned with the initial solvent composition prior to sample loading. Compound detection was performed using the UV-Vis absorption module at 254 and 280 nm for normal-phase or 214 and 254 nm for reversed-phase chromatography.

5.1.2. Infrared spectroscopy

IR spectra were recorded on a *Spectrum Two* (PerkinElmer Inc., Waltham, Massachusetts, USA) attenuated total reflection (ATR) fourier-transform infrared (FTIR)-spectrometer. All solid samples were prepared and measured as KBr pellets. Absorption peaks are reported as wavenumbers (cm^{-1}). Vibrational modes are denoted as symmetric stretching (ν_s), asymmetric stretching (ν_{as}), deformation vibrations (d) and latitudinal scissoring (δ).

5.1.3. Nuclear Magnetic Resonance Spectroscopy

NMR spectra were recorded on an *Avance II* (Bruker Corporation, Billerica, Massachusetts, USA) at 300 MHz for ^1H and 75 MHz for ^{13}C NMR, a *Avance III* (Bruker Corporation, Billerica, Massachusetts, USA) spectrometer at 300 MHz for ^1H - and 75 MHz for ^{13}C -NMR or a *DRX500* (Bruker Corporation, Billerica, Massachusetts, USA) spectrometer at 500 MHz for ^1H - and 126 MHz for ^{13}C -NMR. The measuring frequency and solvent are specified for each experiment. Chemical shifts are reported as ppm by frequency downfield of tetramethylsilane.

The following residual solvent signals were used as internal standards:

$$\delta^1_{\text{H}} (\text{CDCl}_3) = 7.26 \text{ ppm}$$

$$\delta^{13}_{\text{C}} (\text{CDCl}_3) = 77.16 \text{ ppm}$$

$$\delta^1_{\text{H}} (\text{DMSO-}d_6) = 2.50 \text{ ppm}$$

$$\delta^{13}_{\text{C}} (\text{DMSO-}d_6) = 39.52 \text{ ppm}$$

$$\delta^1_{\text{H}} (\text{D}_2\text{O}) = 4.79 \text{ ppm}$$

Coupling constants are reported in Hertz (Hz). Signal multiplicities are denoted as singlet (s), doublet (d), triplet (t), quartet (q) or multiplet (m) or a combination thereof. Processing and analysis of the acquired spectra was performed using *MestReNova 10.0.2* software (Mestrelab Research S.L., Santiago de Compostela, A Coruña, Spain).

5.1.4. Mass Spectrometry

Mass spectrometry was performed on a *ImpactII* quadrupol-TOF spectrometer (*Bruker Corporation*, Billerica, Massachusetts, USA) for atmospheric pressure chemical ionization (APCI) and ESI experiments. EI experiments were performed on either a *MAT95* (*Thermo Finnigan LLC*, San José, Kalifornien, USA) sector field or a *MD 800* (*Fisons plc*, Ipswich, United Kingdom) quadrupol spectrometer.

5.1.5. High Performance Liquid Chromatography

High performance liquid chromatography (HPLC) was carried out on an *Agilent 1100* system (*Agilent Technologies Inc.*, Santa Clara, California, USA) using a *Synergi Polar-RP* (*Phenomenex Inc.*, Torrance, California, USA) reversed-phase column (4 μ m particle size, 150 \times 3.0 mm, pore size 80 Å) connected to a variable wavelength detector (VWD) or a *Synergi Hydro-RP* (*Phenomenex Inc.*, Torrance, California, USA) reversed-phase column (4 μ m particle size, 150 \times 3.0 mm, pore size 80 Å) connected to a diode array detector (DAD). Solvent gradient: 30% A for 1 min, linear gradient to 10% A for 10 min, 10% A for 1 min; solvent A = 0.1% trifluoroacetic acid (TFA) in water; solvent B = acetonitrile; flow rate 1.0 mL/min. All compounds used in biological or biochemical assays had \geq 95% purity as determined in the HPLC method described above, if not explicitly stated otherwise.

5.1.6. Microwave-assisted Synthesis

Microwave-assisted synthesis was performed in an *Initiator+* microwave reactor (*Biotage AB*, Uppsala, Sweden) under conditions specified in each experiment.

5.1.7. Sonochemical synthesis

All sonochemical reactions were performed in an *Bandelin Sonorex Digitec DT 52* (*BANDELIN electronic GmbH & Co. KG*, Berlin, Germany) ultrasonic bath using low frequency ultrasound (LFU) at 35 kHz and deionized water as the transmission medium.

5.1.8. Lyophilization

Lyophilization was performed on an *Alpha 2-4 LDplus* freeze dryer (*Martin Christ Gefriertrocknungsanlagen GmbH*, Osterode am Harz, Germany) in combination with an *ILMVAC Type 109030 Chemvac* combination pump (*ILMVAC GmbH*, Ilmenau, Germany).

5.2. Synthetic Procedures

5.2.1. General Procedures

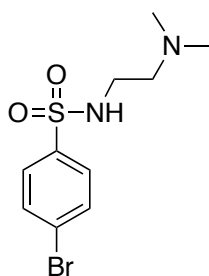
General Procedure A: Synthesis of Phenylsulfonamides.

General Procedure A is exemplified by the triethylamine-mediated sulfonamide formation of compound **2a** from 4-bromo-benzenesulfonyl chloride **1** and *N,N*-dimethylethylenediamine. Compounds **2b–h**, **2j**, **2m–n**, **12** and **18a–b** were prepared in accordance to *General Procedure A* starting from 4-bromobenzene-sulfonyl chloride **1** and the corresponding amine respectively.

General Procedure B: Suzuki-Miyaura Coupling of Aromatic Rings.³⁵⁴

General Procedure B is exemplified by the SUZUKI-MIYAUURA COUPLING of 4-bromo-7-azaindole and 4-bromo-*N*-(2-(dimethylamino)-ethyl)benzenesulfonamide (**2a**) to give target compound **3a**. Compounds **3b–k**, **3m–p**, **19a–f** and **7** were prepared in accordance to *General Procedure B* starting from 4-bromo-7-azaindole and phenylsulfonamides **2b–k**, **2m–p**, **19a–f** and benzamide **6** respectively.

5.2.2. 4-bromo-*N*-(2-(dimethylamino)ethyl)benzenesulfonamide (**2a**)



C₁₀H₁₅BrN₂O₂S: 307.21 g/mol

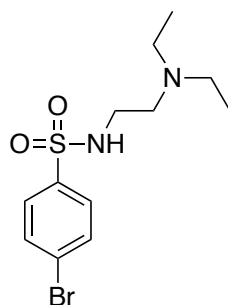
To a stirred solution of 4-bromobenzene-sulfonyl chloride (**1**, 1.00 g, 3.91 mmol) in 10 mL DCM were added *N,N*-dimethylethylenediamine (414 mg, 4.70 mmol) and triethylamine (774 mg, 9.78 mmol) at 0 °C under cooling in an ice bath. The cooling bath was removed and the solution was stirred for 1 h at ambient temperature. The organic layer was washed with water (3 x 5 mL) and brine (5 mL) and dried over MgSO₄. The solvent was removed under reduced pressure to give **2a** (1.14 g, 95%) as a light tan solid.

HPLC (DAD): $t_R = 3.396$ min (94%).

¹H NMR (CDCl₃, 300 MHz): $\delta = 7.78 - 7.71$ (m, 2H), 7.69 – 7.62 (m, 2H), 3.01 – 2.95 (m, 2H), 2.40 – 2.33 (m, 2H), 2.11 (s, 6H).

The acquired spectral data is in line with the published literature.²³⁴

5.2.3. 4-bromo-*N*-(2-(diethylamino)ethyl)benzenesulfonamide (**2b**)



$C_{12}H_{19}BrN_2O_2S$: 335.26 g/mol

Synthesis of **2b** was performed by following *General Procedure A* using *N,N*-dimethylethylenediamine. Yield: 74%, yellow oil.

HPLC (DAD): $t_R = 3.609$ min (98%).

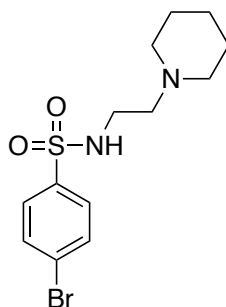
1H NMR ($CDCl_3$, 300 MHz): $\delta = 7.77 - 7.60$ (m, 4H), 4.74 (s, 1H), 2.99 – 2.88 (m, 2H), 2.53 – 2.45 (m, 2H), 2.39 (q, $J = 7.1$ Hz, 4H), 0.92 (t, $J = 7.1$ Hz, 6H).

^{13}C NMR ($CDCl_3$, 75 MHz): $\delta = 139.0, 132.4, 128.8, 127.6, 51.1, 46.5, 40.3, 11.7$.

MS (EI): $m/z = 335$ ($[M + H]^+$).

The acquired spectral data is in line with the published literature.³⁵⁵

5.2.4. 4-bromo-*N*-(2-(piperidin-1-yl)ethyl)benzenesulfonamide (2c)



C₁₃H₁₉BrN₂O₂S: 347.27 g/mol

Synthesis of **2c** was performed by following *General Procedure A* using 1-(2-aminoethyl)-piperidine. Yield: 91%, orange solid.

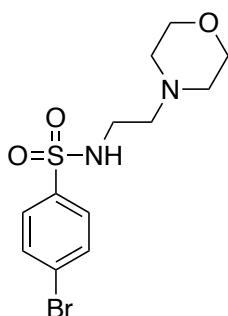
HPLC (VWD): $t_R = 2.390$ min (93%).

¹H NMR (CDCl₃, 300 MHz): $\delta = 7.78 - 7.67$ (m, 2H), $7.69 - 7.58$ (m, 2H), 5.31 (s, 1H), 2.95 (dd, $J = 6.6, 5.1$ Hz, 2H), 2.34 (dd, $J = 6.6, 5.1$ Hz, 2H), 2.19 (t, $J = 5.1$ Hz, 4H), 1.43 (dp, $J = 22.4, 5.7$ Hz, 7H).

¹³C NMR (CDCl₃, 75 MHz): $\delta = 138.9, 132.4, 128.7, 127.5, 56.2, 54.0, 39.4, 25.9, 24.3$.

MS (APCI): $m/z = 347.05$ ($[M + H]^+$).

5.2.5. 4-bromo-N-(2-morpholinoethyl)benzenesulfonamide (2d)



C₁₂H₁₇BrN₂O₃S: 349.24 g/mol

Synthesis of **2d** was performed by following *General Procedure A* using 4-(2-aminoethyl)morpholine. Yield: 87%, colorless solid.

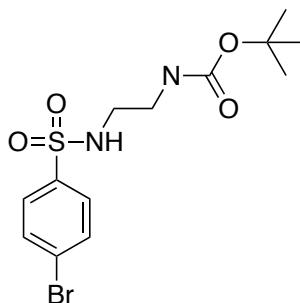
HPLC (VWD): $t_R = 1.730$ min (96%).

¹H NMR (CDCl₃, 300 MHz): $\delta = 7.78 - 7.70$ (m, 2H), $7.70 - 7.62$ (m, 2H), 5.29 (s, 1H), $3.67 - 3.60$ (m, 4H), 3.02 (dd, $J = 6.7, 4.9$ Hz, 2H), $2.46 - 2.40$ (m, 2H), $2.33 - 2.27$ (m, 4H).

¹³C NMR (CDCl₃, 75 MHz): $\delta = 138.8, 132.4, 128.6, 127.6, 66.7, 56.3, 53.0, 38.9$.

MS (APCI): $m/z = 349.02$ ($[M + H]^+$).

5.2.6. *tert*-butyl (2-(4-bromophenyl)sulfonamido)ethylcarbamate (**2e**)



$C_{13}H_{18}BrN_2O_4S$: 378.26 g/mol

Synthesis of **2e** was performed by following *General Procedure A* using *N*-Boc-ethylenediamine. Yield: 78%, colorless solid.

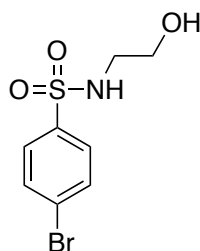
HPLC (DAD): $t_R = 6.297$ min (90%).

1H NMR ($CDCl_3$, 300 MHz): $\delta = 7.76 - 7.59$ (m, 4H), 5.05 (s, 1H), 3.24 – 3.18 (m, 2H), 3.04 (dd, $J = 6.3, 4.8$ Hz, 2H), 1.41 (s, 9H).

^{13}C NMR ($CDCl_3$, 75 MHz): $\delta = 156.8, 139.2, 132.5, 128.7, 127.6, 53.0, 46.3, 43.9, 42.0, 40.4, 28.5, 28.5, 10.7$.

MS (EI): $m/z = 378$ ($[M + H]^+$).

5.2.7. 4-bromo-*N*-(2-hydroxyethyl)benzenesulfonamide (2f)



C₈H₁₀BrNO₃S: 280.14 g/mol

Synthesis of **2f** was performed by following *General Procedure A* using 2-aminoethanol.
Yield: 81%, colorless solid.

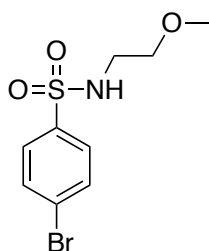
HPLC (DAD): $t_R = 3.737$ min (87%).

¹H NMR (DMSO-*d*₆, 300 MHz): $\delta = 7.84 - 7.70$ (m, 4H), 4.67 (t, $J = 5.5$ Hz, 1H), 3.40 – 3.32 (m, 2H), 2.80 (q, $J = 6.1$ Hz, 2H).

MS (APCI): $m/z = 279.96$ ($[M + H]^+$).

The acquired spectral data is in line with the published literature.²³⁴

5.2.8. 4-bromo-*N*-(2-methoxyethyl)benzenesulfonamide (2g)



C₉H₁₂BrNO₃S: 294.16 g/mol

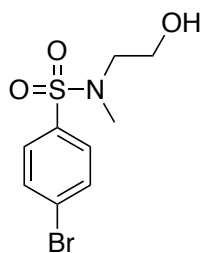
Synthesis of **2g** was performed by following *General Procedure A* using 2-methoxyethylamine.
Yield: 78%, yellow oil.

HPLC (VWD): $t_R = 4.163$ min (94%).

¹H NMR (DMSO-*d*₆, 300 MHz): $\delta = 7.82 - 7.78$ (m, 2H), $7.75 - 7.69$ (m, 2H), 3.32 (s, 3H), 3.29 (t, $J = 5.6$ Hz, 2H), 2.92 (q, $J = 5.8$ Hz, 2H).

The acquired spectral data is in line with the published literature.³⁵⁶

5.2.9. 4-bromo-*N*-(2-hydroxyethyl)-*N*-methylbenzenesulfonamide (2h)



C₉H₁₂BrNO₃S: 294.16 g/mol

Synthesis of **2h** was performed by following *General Procedure A* using *N*-methylethanolamine.
Yield: 90%, colorless oil.

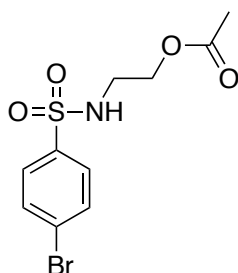
HPLC (VWD): $t_R = 3.482$ min (97%).

¹H NMR (CDCl₃, 300 MHz): $\delta = 7.68$ (s, 4H), 3.78 (dd, $J = 5.6, 4.9$ Hz, 2H), 3.18 (t, $J = 5.3$ Hz, 2H), 2.85 (s, 3H).

MS (APCI): $m/z = 293.98$ ($[M + H]^+$).

The acquired spectral data is in line with the published literature.²³⁴

5.2.10. 2-((4-bromophenyl)sulfonamido)ethyl acetate (**2i**)



C₁₀H₁₂BrNO₄S: 322.17 g/mol

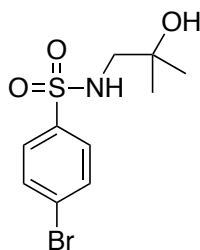
To a stirred solution of **2f** (0.77 g, 2.73 mmol) and triethylamine (0.33 g, 3.28 mmol) in 5 mL DCM, acetic anhydride (0.34 g, 3.28 mmol) was added dropwise at 0 °C under cooling in an ice bath. The cooling bath was removed and the solution was stirred for 72 h at ambient temperature. The reaction mixture was diluted with 20 mL DCM and quenched by bringing the pH to 9 through addition of saturated NaHCO₃ (aq). The organic layer was washed with saturated NaHCO₃ (aq, 3 x 5 mL) and brine (5 mL) and dried over MgSO₄. The solvent was removed under reduced pressure to give **2i** (0.73 g, 82%) as a yellow oil that was used without further purification.

HPLC (DAD): $t_R = 5.268$ min (86%).

¹H NMR (DMSO-*d*₆, 300 MHz): $\delta = 7.85 - 7.80$ (m, 2H), $7.75 - 7.69$ (m, 2H), 3.95 (t, $J = 5.6$ Hz, 2H), 3.03 (q, $J = 5.6$ Hz, 2H), 1.93 (s, 3H).

MS (ESI): $m/z = 343.96$ ([M + Na]⁺).

5.2.11. 4-bromo-*N*-(2-hydroxy-2-methylpropyl)benzenesulfonamide (2j)



C₁₀H₁₄BrNO₃S: 308.19 g/mol

Synthesis of **2j** was performed by following *General Procedure A* using 1-amino-2-methyl-2-propanol. Yield: 64%, yellow solid.

HPLC (VWD): $t_R = 3.026$ min (94%).

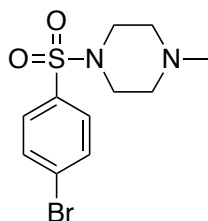
¹H NMR (DMSO-*d*₆, 500 MHz): $\delta = 7.83 - 7.78$ (m, 2H), $7.75 - 7.71$ (m, 2H), 7.59 (t, $J = 6.5$ Hz, 1H), 4.40 (s, 1H), 2.62 (d, $J = 6.5$ Hz, 2H), 1.04 (s, 6H).

¹³C NMR (DMSO-*d*₆, 126 MHz): $\delta = 140.1, 132.1, 128.5, 125.9, 68.7, 53.6, 27.0$.

¹³C NMR (DMSO-*d*₆, 126 MHz, DEPT): $\delta = 132.1, 128.6, 53.6, 45.5, 27.1, 8.5$.

MS (APCI): $m/z = 307.98$ ($[M + H]^+$).

5.2.12. 1-((4-bromophenyl)sulfonyl)-4-methylpiperazine (2k)



C₁₁H₁₅BrN₂O₂S: 319.22 g/mol

To a solution of 4-bromobenzene-sulfonyl chloride (**1**) (0.40 g, 1.47 mmol) in 9 mL dry THF, 1-Methyl-piperazin (1.41 g, 14.09 mmol) was added and the mixture was stirred for 16 h at ambient temperature. The solvent was removed under reduced pressure and the resulting residue was dissolved in 10 mL DCM. The organic layer was washed with saturated NaHCO₃ (aq, 3 x 2,5 mL) and dried over MgSO₄. The solvent was removed under reduced pressure to give **2k** (0.37 g, 75%) as a yellow solid.

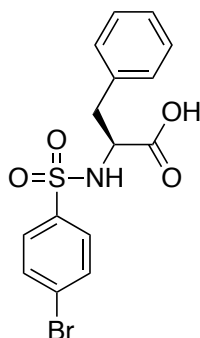
HPLC (DAD): $t_R = 3.713$ min (96%).

¹H NMR (CDCl₃, 500 MHz): $\delta = 7.69 - 7.63$ (m, 2H), $7.62 - 7.58$ (m, 2H), 3.03 (t, $J = 4.9$ Hz, 4H), 2.47 (t, $J = 5.0$ Hz, 4H), 2.26 (s, 3H).

¹³C NMR (CDCl₃, 126 MHz): $\delta = 134.7, 132.4, 129.4, 128.0, 54.1, 46.0, 45.8$.

MS (ESI): $m/z = 380$ ([M]⁺).

5.2.13. ((4-bromophenyl)sulfonyl)-L-phenylalanine (**2l**)



C₁₅H₁₄BrNO₄S: 384.24 g/mol

To a stirred solution of L-Phenylalanine (194 mg, 1.17mmol) in 4 mL of water was added sodium bicarbonate (296 mg, 3.52 mmol). The mixture was stirred at ambient temperature for 15 min and a solution of 4-bromobenzene-sulfonyl chloride (**1**, 300 mg, 1.17 mmol) in 4 mL acetone was added at 0 °C under cooling in an ice bath. The cooling bath was removed and the solution was stirred at ambient temperature for 20 h. After evaporation of the volatile solvent under reduced pressure, the product was precipitated by setting the pH to 7 using hydrochloric acid (1 N). Filtration and drying under reduced pressure gave **2l** (220 mg, 49%) as a yellow solid.

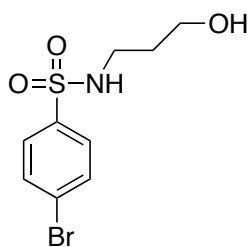
HPLC (DAD): $t_R = 6.179$ min (90%).

¹H NMR (DMSO-*d*₆, 500 MHz): $\delta = 7.72 - 7.69$ (m, 2H), 7.65 – 7.61 (m, 2H), 7.18 – 7.11 (m, 5H), 3.35 (t, $J = 5.1$ Hz, 1H), 2.98 (dd, $J = 13.4, 5.0$ Hz, 1H), 2.90 (dd, $J = 13.4, 5.2$ Hz, 1H).

¹³C NMR (DMSO-*d*₆, 126 MHz): $\delta = 170.8, 139.7, 138.7, 132.0, 129.9, 128.7, 127.5, 125.9, 125.55, 58.3, 38.5$.

MS (ESI): $m/z = 788.95$ ([2M + Na]⁺), 405.97 ([M + Na]⁺), 383.99 ([M + H]⁺).

5.2.14. 4-bromo-*N*-(3-hydroxypropyl)benzenesulfonamide (**2m**)



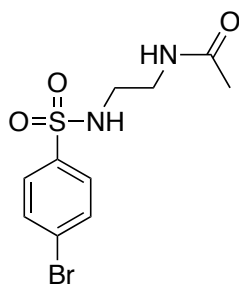
C₉H₁₂BrNO₃S: 294.16 g/mol

Synthesis of **2m** was performed by following *General Procedure A* using 3-aminopropan-1-ol. Yield: 67%, colorless solid.

HPLC (DAD): $t_R = 3.991$ min (96%).

¹H NMR (CDCl₃, 300 MHz): $\delta = 7.81 - 7.73$ (m, 2H), $7.71 - 7.62$ (m, 2H), 5.59 (d, $J = 12.6$ Hz, 1H), $3.80 - 3.70$ (m, 2H), 3.39 (q, $J = 7.3$ Hz, 1H), 3.13 (t, $J = 6.1$ Hz, 2H), $1.81 - 1.66$ (m, 2H), $1.46 - 1.30$ (m, 2H).

5.2.15. *N*-(2-((4-bromophenyl)sulfonamido)ethyl)acetamide (**2n**)



C₁₀H₁₃BrN₂O₃S: 321.19 g/mol

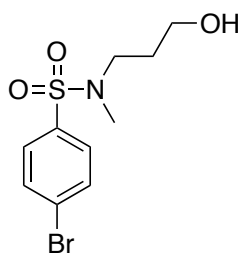
Synthesis of **2n** was performed by following *General Procedure A* using *N*-(2-aminoethyl)-acetamide. Yield: 92%, colorless solid.

HPLC (DAD): $t_R = 3.963$ min (97%).

¹H NMR (CDCl₃, 500 MHz): $\delta = 7.76 - 7.71$ (m, 2H), $7.69 - 7.62$ (m, 2H), 6.17 (s, 1H), 5.77 (s, 1H), 3.35 (q, $J = 5.7$ Hz, 2H), 3.09 (t, $J = 5.7$ Hz, 2H), 1.97 (s, 3H).

¹³C NMR (CDCl₃, 126 MHz): $\delta = 171.4, 132.4, 128.6, 127.7, 76.8, 46.0, 43.5, 39.4, 23.1$.

5.2.16. 4-bromo-*N*-(3-hydroxypropyl)-*N*-methylbenzenesulfonamide (**2o**)



C₁₀H₁₄BrNO₃S: 308.19 g/mol

4-bromo-*N*-(3-hydroxypropyl)benzenesulfonamide (**2m**, 0.35 g, 1.19 mmol) was dissolved in 6 mL dry DMF in an oven-dried vessel under argon atmosphere. After the addition of sodium hydride (0.05 g, 2.08 mmol), the mixture was stirred at room temperature until the gas formation ceased and methyl iodide (0.17 g, 1.25 mmol) was added dropwise over 15 min. The mixture was stirred for 17 h at ambient temperature. Upon completion, the reaction was quenched with 6 mL sat. aq. NH₄Cl-solution, diluted with 20 mL EtOAc and washed with 20 mL 7.5% LiCl-solution five times. After washing with 10 mL brine, the solvent was removed under reduced pressure and the resulting residue was purified by column chromatography using a 1:1 mixture of petrol ether/ethyl acetate to give **2o** (259 mg, 72%) as a colorless solid.

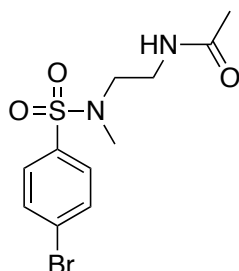
HPLC (DAD): $t_R = 4.750$ min (99%).

¹H NMR (CDCl₃, 500 MHz): $\delta = 7.64 - 7.55$ (m, 4H), 3.65 (t, $J = 5.8$ Hz, 2H), 3.06 (t, $J = 6.7$ Hz, 2H), 2.69 (s, 3H), 1.69 (tt, $J = 6.6, 5.7$ Hz, 2H).

¹³C NMR (CDCl₃, 126 MHz): $\delta = 136.5, 132.4, 128.8, 127.6, 58.8, 46.9, 34.9, 30.1$.

¹³C NMR (126 MHz, DMSO-*d*₆, DEPT): $\delta = 132.4, 128.8, 58.8, 46.9, 34.9, 30.1$.

5.2.17. *N*-(2-((4-bromo-*N*-methylphenyl)sulfonamido)ethyl)acetamide (**2p**)



C₁₁H₁₅BrN₂O₃S: 335.22 g/mol

N-(2-((4-bromophenyl)sulfonamido)ethyl)acetamide (**2n**, 0.35 g, 1.04 mmol) was dissolved in 6 mL dry DMF in an oven-dried vessel under argon atmosphere. After the addition of sodium hydride (0.05 g, 2.08 mmol), the mixture was stirred at room temperature until the gas formation ceased and methyl iodide (0.18 g, 1.27 mmol) was added dropwise over 15 min. The mixture was stirred for 15 h at ambient temperature. Upon completion, the reaction was quenched with 6 mL sat. aq. NH₄Cl-solution, diluted with 20 mL EtOAc and washed with 20 mL 7.5% LiCl-solution five times. After washing with 10 mL brine, the solvent was removed under reduced pressure and the resulting residue was purified by column chromatography using a 45:1:0.1 mixture of DCM/MeOH/NH₃ in MeOH (7 N) to give **2p** (100 mg, 24%) as a colorless solid.

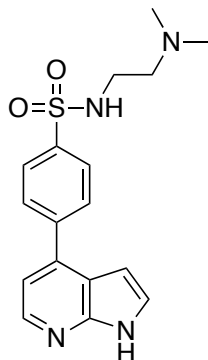
HPLC (DAD): $t_R = 4.750$ min (99%).

¹H NMR (CDCl₃, 500 MHz): $\delta = 7.64 - 7.55$ (m, 4H), 3.65 (t, $J = 5.8$ Hz, 2H), 3.06 (t, $J = 6.7$ Hz, 2H), 2.69 (s, 3H), 1.69 (tt, $J = 6.6, 5.7$ Hz, 2H).

¹³C NMR (CDCl₃, 126 MHz): $\delta = 136.5, 132.4, 128.8, 127.6, 58.8, 46.9, 34.9, 30.1$.

¹³C NMR (126 MHz, DMSO-*d*₆, DEPT): $\delta = 132.4, 128.8, 58.8, 46.9, 34.9, 30.1$.

5.2.18. *N*-(2-(dimethylamino)ethyl)-4-(1*H*-pyrrolo[2,3-*b*]pyridin-4-yl)benzenesulfonamide
(3a)



C₁₇H₂₀N₄O₂S: 344.43 g/mol

To a solution of sulfonamide **2a** (100 mg, 0.33 mmol) in 1.5 mL DMF were added potassium acetate (97 mg, 0.99 mmol), bis(pinacolato)diboron (100 mg, 0.40 mmol) and PdCl₂(dppf) (7 mg, 10 μmol), under argon atmosphere. The reaction mixture was stirred at 100 °C for 3 h. After cooling to ambient temperature 15 mL of ethyl acetate were added, the solution was filtered through Celite and the organic layer was washed with brine (5 x 15 mL) before drying over Na₂SO₄. The solvent was removed under reduced pressure to give the corresponding boronic acid pinacolester as a crude solid that was dissolved in 1.5 mL DMF and treated with 4-bromo-7-azaindole (65 mg, 0.33 mmol), 0.5 mL saturated NaHCO₃ (aq) and Pd(PPh₃)₄ (38 mg, 36 μmol) under argon atmosphere. The mixture was stirred at 100 °C for 18 h, cooled to ambient temperature and diluted with 20 mL EtOAc. After filtration through Celite, the organic layer was washed with brine (5 x 20 mL), dried over MgSO₄ and the solvent was removed under reduced pressure. Purification was performed by column chromatography using a 10:1:0.1 mixture of DCM/MeOH/NH₃ in MeOH (7 N) to give **3a** (47 mg, 42%) as a colorless solid.

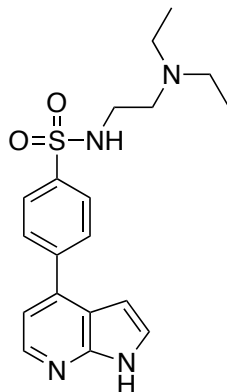
HPLC (DAD): t_R = 2.899 min (96%).

¹H NMR (DMSO-*d*₆, 300 MHz): δ = 11.89 (s, 1H), 8.33 (d, *J* = 4.9 Hz, 1H), 7.98 (s, 4H), 7.60 (d, *J* = 3.5 Hz, 1H), 7.25 (d, *J* = 4.9 Hz, 1H), 6.64 (d, *J* = 3.5 Hz, 1H), 2.91 (t, *J* = 6.8 Hz, 2H), 2.28 (t, *J* = 6.8 Hz, 2H), 2.07 (s, 6H).

¹³C NMR (DMSO-*d*₆, 75 MHz): $\delta = 149.2, 142.92, 142.2, 140.3, 138.5, 128.9, 127.2, 127.2, 117.13, 114.4, 98.8, 58.1, 45.0, 40.7.$

MS (APCI): $m/z = 345.13$ ($[M + H]^+$).

5.2.19. *N*-(2-(diethylamino)ethyl)-4-(1*H*-pyrrolo[2,3-*b*]pyridin-4-yl)benzenesulfonamide
(3b)



C₁₉H₂₄N₄O₂S: 372.49 g/mol

Starting from **2b**, the synthesis of **3b** was performed by following *General Procedure B*. Purification was performed by column chromatography using a 10:1:0.1 mixture of DCM/MeOH/NH₃ in MeOH (7 N). Yield: 41%, beige semisolid.

HPLC (DAD): $t_R = 3.033$ min (97%).

¹H NMR (DMSO-*d*₆, 500 MHz): $\delta = 11.88$ (s, 1H), 8.33 (d, $J = 4.9$ Hz, 1H), 8.04 – 7.90 (m, 4H), 7.60 (d, $J = 3.5$ Hz, 1H), 7.25 (d, $J = 4.9$ Hz, 1H), 6.63 (d, $J = 3.5$ Hz, 1H), 2.88 (dd, $J = 8.1, 6.3$ Hz, 2H), 2.43 (t, $J = 7.2$ Hz, 2H), 2.39 (q, $J = 7.1$ Hz, 4H), 0.86 (t, $J = 7.1$ Hz, 6H).

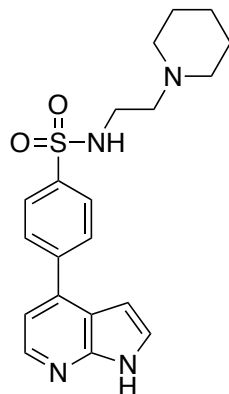
¹³C NMR (DMSO-*d*₆, 126 MHz): $\delta = 149.2, 142.9, 142.2, 140.3, 138.45, 128.9, 127.2, 127.1, 117.1, 114.3, 98.7, 51.8, 46.5, 41.0, 11.6$.

¹³C NMR (126 MHz, DMSO-*d*₆, DEPT): $\delta = 142.9, 128.9, 127.1, 114.4, 98.7, 51.8, 46.5, 41.0, 11.6$.

MS (ESI): $m/z = 373.18$ ([M + H]⁺), 187.09 ([M + 2H]²⁺).

Melting point: 143 °C.

**5.2.20. *N*-(2-(piperidin-1-yl)ethyl)-4-(1*H*-pyrrolo[2,3-*b*]pyridin-4-yl)benzenesulfonamide
(3c)**



C₂₀H₂₄N₄O₂S: 384.50 g/mol

Starting from **2c**, the synthesis of **3c** was performed by following *General Procedure B*. Purification was performed by column chromatography using a 15:1:0.1 mixture of DCM/MeOH/NH₃ in MeOH (7 N). Yield: 58%, beige solid.

HPLC (DAD): $t_R = 3.052$ min (97%).

¹H NMR (DMSO-*d*₆, 300 MHz): $\delta = 11.88$ (s, 1H), 8.32 (d, $J = 4.8$ Hz, 1H), 7.97 (s, 4H), 7.60 (d, $J = 3.4$ Hz, 1H), 7.25 (d, $J = 4.8$ Hz, 1H), 6.63 (d, $J = 3.4$ Hz, 1H), 2.92 (t, $J = 6.9$ Hz, 2H), 2.29 (t, $J = 6.9$ Hz, 2H), 2.23 (t, $J = 5.0$ Hz, 4H), 1.45 – 1.21 (m, 6H).

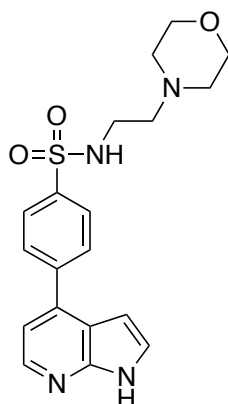
¹³C NMR (DMSO-*d*₆, 75 MHz,): $\delta = 149.2, 142.9, 142.1, 140.3, 138.5, 128.9, 127.2, 127.1, 117.1, 114.4, 98.7, 57.6, 53.9, 40.3, 25.4, 23.9$.

¹³C NMR (DMSO-*d*₆, 75 MHz, DEPT): $\delta = 142.9, 128.9, 127.2, 127.1, 114.4, 98.7, 57.6, 53.9, 40.2, 25.4, 23.9$.

MS (APCI): $m/z = 385.18$ ($[M + H]^+$).

Melting point: 204 °C.

5.2.21. *N*-(2-morpholinoethyl)-4-(1*H*-pyrrolo[2,3-*b*]pyridin-4-yl)benzenesulfonamide (**3d**)



C₁₉H₂₂N₄O₃S: 386.43 g/mol

Starting from **2d**, the synthesis of **3d** was performed by following *General Procedure B*. Purification was performed by column chromatography using a 50:1:0.5 mixture of DCM/MeOH/NH₃ in MeOH (7 N). Yield: 69%, beige solid.

HPLC (DAD): $t_R = 2.942$ min (97%).

¹H NMR (DMSO-*d*₆, 500 MHz): $\delta = 11.88$ (s, 1H), 8.33 (d, $J = 4.9$ Hz, 1H), 7.98 (s, 4H), 7.65 (t, $J = 5.9$ Hz, 1H), 7.60 (dd, $J = 3.5, 2.5$ Hz, 1H), 7.25 (d, $J = 4.9$ Hz, 1H), 6.64 (dd, $J = 3.5, 1.8$ Hz, 1H), 3.52 – 3.46 (m, 4H), 2.95 (q, $J = 6.3$ Hz, 2H), 2.33 (t, $J = 6.8$ Hz, 2H), 2.27 (t, $J = 4.7$ Hz, 4H).

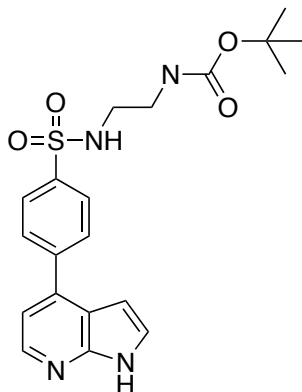
¹³C NMR (DMSO-*d*₆, 126 MHz) $\delta = 149.2, 142.9, 142.1, 140.3, 138.5, 128.9, 127.2, 127.1, 117.1, 114.4, 98.7, 66.0, 57.2, 53.1, 39.9$.

¹³C NMR (DMSO-*d*₆, 126 MHz, DEPT): $\delta = 142.9, 128.9, 127.2, 127.1, 114.4, 98.7, 66.0, 57.2, 53.1, 39.8$.

MS (APCI): $m/z = 387.16$ ([M + H]⁺).

Melting point: 201 °C.

5.2.22. *tert*-butyl(2-((4-(1*H*-pyrrolo[2,3-*b*]pyridin-4-yl)phenyl)-sulfonamido)ethyl)-carbamate (3e)



C₂₀H₂₃N₄O₄S: 415.49 g/mol

Starting from **2e**, the synthesis of **3e** was performed by following *General Procedure B*. Purification was performed by column chromatography using a 20:1:0.1 mixture of DCM/MeOH/NH₃ in MeOH (7 N). Yield: 60%, colorless solid.

HPLC (DAD): $t_R = 4.202$ min (97%).

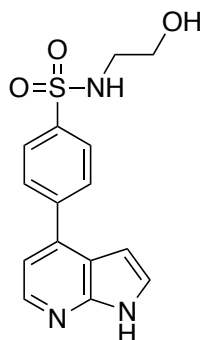
¹H NMR (DMSO-*d*₆, 500 MHz): $\delta = 11.88$ (s, 1H), 8.33 (d, $J = 4.9$ Hz, 1H), 8.01 – 7.93 (m, 4H), 7.76 (t, $J = 6.0$ Hz, 1H), 7.60 (dd, $J = 3.5, 2.6$ Hz, 1H), 7.26 (d, $J = 4.9$ Hz, 1H), 6.78 (t, $J = 5.9$ Hz, 1H), 6.66 (dd, $J = 3.5, 1.8$ Hz, 1H), 3.01 (q, $J = 6.6$ Hz, 2H), 2.84 (q, $J = 6.4$ Hz, 2H), 1.34 (s, 9H).

¹³C NMR (DMSO-*d*₆, 126 MHz): $\delta = 155.4, 149.12, 142.9, 142.2, 140.0, 138.4, 129.0, 127.2, 127.1, 117.1, 114.4, 98.8, 77.8, 42.3, 28.1$.

¹³C NMR (DMSO-*d*₆, 126 MHz, DEPT): $\delta = 142.9, 128.8, 127.2, 127.1, 114.4, 98.8, 42.3, 39.8, 28.2$.

MS (APCI): $m/z = 417.16$ ([M + H]⁺).

5.2.23. *N*-(2-hydroxyethyl)-4-(1*H*-pyrrolo[2,3-*b*]pyridin-4-yl)benzenesulfonamide (**3f**)



C₁₅H₁₅N₃O₃S: 317.36 g/mol

Starting from **2f**, the synthesis of **3f** was performed by following *General Procedure B*. Purification was performed by column chromatography using a 10:1:0.1 mixture of DCM/MeOH/NH₃ in MeOH (7 N). Yield: 66%, colorless solid.

HPLC (DAD): $t_R = 2.852$ min (96%).

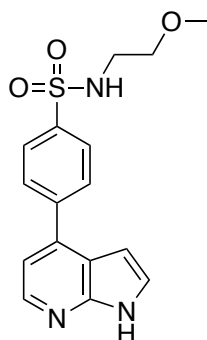
¹H NMR (DMSO-*d*₆, 500 MHz): $\delta = 11.88$ (s, 1H), 8.33 (d, $J = 4.9$ Hz, 1H), 8.01 – 7.94 (m, 4H), 7.71 (t, $J = 5.9$ Hz, 1H), 7.60 (t, $J = 3.0$ Hz, 1H), 7.26 (d, $J = 5.0$ Hz, 1H), 6.65 (dd, $J = 3.5, 1.8$ Hz, 1H), 4.70 (t, $J = 5.6$ Hz, 1H), 3.42 (q, $J = 6.0$ Hz, 2H), 2.88 (q, $J = 6.2$ Hz, 2H).

¹³C NMR (DMSO-*d*₆, 126 MHz): $\delta = 149.2, 142.9, 142.1, 140.2, 138.5, 128.9, 127.2, 127.1, 117.1, 114.4, 98.8, 59.9, 45.1$.

¹³C NMR (DMSO-*d*₆, 126 MHz, DEPT): $\delta = 142.9, 128.9, 127.2, 127.1, 114.4, 98.8, 56.0, 45.1$.

MS (APCI): $m/z = 318.09$ ([M + H]⁺).

5.2.24. *N*-(2-methoxyethyl)-4-(1*H*-pyrrolo[2,3-*b*]pyridin-4-yl)benzenesulfonamide (**3g**)



C₁₆H₁₇N₃O₃S: 331.39 g/mol

Starting from **2g**, the synthesis of **3g** was performed by following *General Procedure B*. Purification was performed by column chromatography using a 20:1:0.1 mixture of DCM/MeOH/NH₃ in MeOH (7 N). Yield: 65%, colorless solid.

HPLC (VWD): $t_R = 1.737$ min (98%).

¹H NMR (DMSO-*d*₆, 500 MHz): $\delta = 11.88$ (s, 1H), 8.33 (d, $J = 4.9$ Hz, 1H), 8.02 – 7.91 (m, 4H), 7.83 (t, $J = 6.0$ Hz, 1H), 7.60 (dd, $J = 3.5, 2.5$ Hz, 1H), 7.25 (d, $J = 4.9$ Hz, 1H), 6.65 (dd, $J = 3.6, 1.8$ Hz, 1H), 3.34 (t, $J = 5.7$ Hz, 2H), 2.99 (q, $J = 5.8$ Hz, 2H).

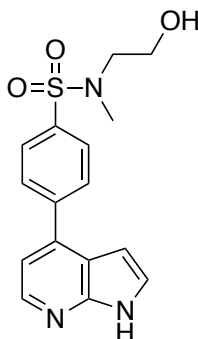
¹³C NMR (DMSO-*d*₆, 126 MHz): $\delta = 149.2, 142.9, 142.2, 140.4, 138.5, 128.9, 127.2, 127.1, 117.1, 114.4, 98.8, 70.6, 57.8, 42.2$.

¹³C NMR (DMSO-*d*₆, 126 MHz, DEPT): $\delta = 142.9, 128.9, 127.2, 127.1, 114.4, 98.8, 70.6, 57.8, 42.2$.

MS (APCI): $m/z = 332.10$ ($[M + H]^+$).

Melting point: 215 °C.

5.2.25. *N*-(2-hydroxyethyl)-*N*-methyl-4-(1*H*-pyrrolo[2,3-*b*]pyridin-4-yl)benzenesulfonamide
(3h)



C₁₆H₁₇N₃O₃S: 331.39 g/mol

Starting from **2h**, the synthesis of **3h** was performed by following *General Procedure B*. Purification was performed by column chromatography using a 20:1:0.1 mixture of DCM/MeOH/NH₃ in MeOH (7 N). Yield: 42%, colorless solid.

HPLC (DAD): $t_R = 3.260$ min (97%).

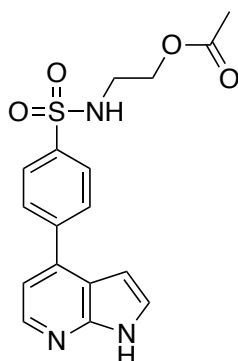
¹H NMR (DMSO-*d*₆, 500 MHz): $\delta = 11.89$ (s, 1H), 8.33 (d, $J = 4.9$ Hz, 1H), 8.01 (d, $J = 8.4$ Hz, 2H), 7.93 (d, $J = 8.4$ Hz, 2H), 7.60 (t, $J = 3.0$ Hz, 1H), 7.27 (d, $J = 5.0$ Hz, 1H), 6.66 (dd, $J = 3.6, 1.8$ Hz, 1H), 4.81 (td, $J = 5.5, 1.3$ Hz, 1H), 3.56 (q, $J = 5.8$ Hz, 2H), 3.10 (t, $J = 6.1$ Hz, 2H), 2.80 (s, 3H).

¹³C NMR (DMSO-*d*₆, 126 MHz): $\delta = 149.2, 142.9, 142.6, 138.3, 136.8, 129.0, 127.7, 127.2, 117.1, 114.4, 98.7, 59.1, 51.9, 35.6$.

¹³C NMR (DMSO-*d*₆, 126 MHz, DEPT): $\delta = 142.9, 142.7, 129.0, 127.7, 127.2, 114.4, 98.73, 59.1, 51.9, 35.6$.

MS (APCI): $m/z = 332.11$ ([M + H]⁺).

5.2.26. 2-((4-(1*H*-pyrrolo[2,3-*b*]pyridin-4-yl)phenyl)sulfonamido)ethyl acetate (**3i**)



C₁₇H₁₇N₃O₄S: 359.40 g/mol

Starting from **2i**, the synthesis of **3i** was performed by following *General Procedure B*. Purification was performed by column chromatography using a 15:1:0.1 mixture of DCM/MeOH/NH₃ in MeOH (7 N). Yield: 23%, colorless solid.

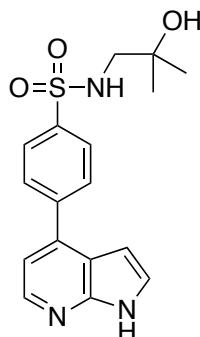
HPLC (VWD): $t_R = 1.956$ min (95%).

¹H NMR (DMSO-*d*₆, 500 MHz): $\delta = 11.90$ (s, 1H), 8.35 (d, $J = 5.0$ Hz, 1H), 8.03 – 7.96 (m, 5H), 7.62 (dd, $J = 3.5, 2.5$ Hz, 1H), 7.28 (d, $J = 5.0$ Hz, 1H), 6.67 (dd, $J = 3.5, 1.9$ Hz, 1H), 4.02 (t, $J = 5.6$ Hz, 2H), 3.12 (q, $J = 5.7$ Hz, 2H), 1.96 (s, 3H).

¹³C NMR (DMSO-*d*₆, 126 MHz): $\delta = 170.2, 149.2, 142.9, 142.3, 140.2, 138.5, 129.0, 127.2, 127.1, 117.1, 114.4, 98.8, 62.5, 41.4, 20.6$.

MS (APCI): $m/z = 360.10$ ($[M + H]^+$).

5.2.27. N-(2-hydroxy-2-methylpropyl)-4-(1H-pyrrolo[2,3-b]pyridin-4-yl)benzenesulfonamide (3j)



C₁₇H₁₉N₃O₃S: 345.42 g/mol

Starting from **2j**, the synthesis of **3j** was performed by following *General Procedure B*. Purification was performed by column chromatography using a 13:1:0.1 mixture of DCM/MeOH/NH₃ in MeOH (7 N). Yield: 11%, colorless solid.

HPLC (VWD): $t_R = 1.444$ min (97%).

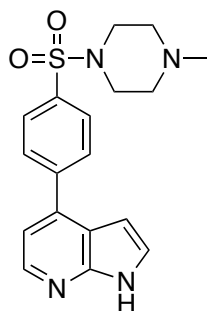
¹H NMR (DMSO-*d*₆, 500 MHz): $\delta = 11.87$ (s, 1H), 8.33 (d, $J = 4.9$ Hz, 1H), 8.01 – 7.94 (m, 4H), 7.62 – 7.54 (m, 2H), 7.26 (d, $J = 4.9$ Hz, 1H), 6.65 (dd, $J = 3.5, 1.9$ Hz, 1H), 4.42 (s, 1H), 2.70 (d, $J = 6.6$ Hz, 2H), 1.08 (s, 6H).

¹³C NMR (DMSO-*d*₆, 126 MHz): $\delta = 149.2, 142.9, 142.1, 140.4, 138.5, 129.0, 127.2, 127.2, 117.1, 114.4, 98.8, 68.8, 53.8, 27.1$.

¹³C NMR (DMSO-*d*₆, 126 MHz, DEPT): $\delta = 142.9, 128.9, 127.2, 127.2, 114.4, 98.8, 53.7, 27.1$.

MS (EI): $m/z = 345$ ([M]⁺).

5.2.28. 4-(4-((4-methylpiperazin-1-yl)sulfonyl)phenyl)-1H-pyrrolo[2,3-b]pyridine (3k)



C₁₈H₂₀N₄O₂S: 356.42 g/mol

Starting from **2k**, the synthesis of **3k** was performed by following *General Procedure B*. Purification was performed by column chromatography using a 20:1:0.1 mixture of DCM/MeOH/NH₃ in MeOH (7 N). Yield: 58%, colorless solid.

HPLC (DAD): $t_R = 2.817$ min (97%).

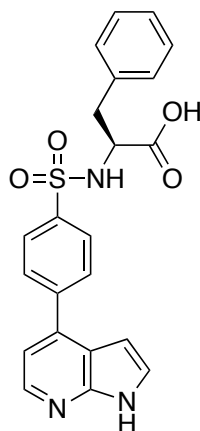
¹H NMR (D₂O, as a TFA salt, 500 MHz): $\delta = 8.39$ (d, $J = 6.0$ Hz, 1H), 8.00 – 7.87 (m, 4H), 7.72 (d, $J = 3.6$ Hz, 1H), 7.54 (d, $J = 6.0$ Hz, 1H), 6.82 (d, $J = 3.6$ Hz, 1H), 4.02 (d, $J = 13.5$ Hz, 2H), 3.68 (d, $J = 12.7$ Hz, 2H), 3.33 (td, $J = 12.5, 3.3$ Hz, 2H), 2.98 (s, 3H), 2.95 – 2.86 (m, 2H).

¹³C NMR (D₂O, as a TFA salt, 126 MHz): $\delta = 146.8, 141.2, 139.6, 135.1, 133.6, 130.2, 130.0, 128.1, 122.9, 114.9, 101.7, 52.7, 43.2, 42.8$.

¹³C NMR (D₂O, as a TFA salt, 126 MHz, DEPT): $\delta = 133.5, 130.2, 130.0, 128.1, 114.9, 101.7, 52.7, 43.3, 42.8$.

MS (APCI): $m/z = 357.15$ ([M + H]⁺).

5.2.29. ((4-(1*H*-pyrrolo[2,3-*b*]pyridin-4-yl)phenyl)sulfonyl)-*L*-phenylalanine (**3l**)



C₂₂H₁₉N₃O₄S: 421.47 g/mol

To a solution of sulfonamide **2l** (200 mg, 0.52 mmol) in 3 mL DMF were added potassium acetate (153 mg, 1.56 mmol) bis(pinacolato)diboron (159 mg, 0.62 mmol) and PdCl₂(dppf) (13 mg, 15 μmol), under argon atmosphere. The reaction mixture was stirred at 100 °C for 3 h. After cooling to ambient temperature 20 mL of EtOAc were added, the solution was filtered through Celite and the organic layer was washed with brine (5 x 20 mL) before drying over NaSO₄. The solvent was removed under reduced pressure to give the corresponding boronic acid pinacolester as a crude solid that was dissolved in 3 mL DMF and treated with 4-bromo-7-azaindole (103 mg, 0.52 mmol), 1 mL saturated NaHCO₃ (aq) and Pd(PPh₃)₄ (60 mg, 52 μmol) under argon atmosphere. The mixture was stirred at 100 °C for 17 h, cooled to ambient temperature and diluted with 20 mL EtOAc. After filtration through Celite the organic layer was washed with brine (5 x 20 mL) and the product was precipitated by setting the pH to 4 using hydrochloric acid (0.1 N). Filtration and drying under reduced pressure gave **3l** (55 mg, 25%) as a colorless solid.

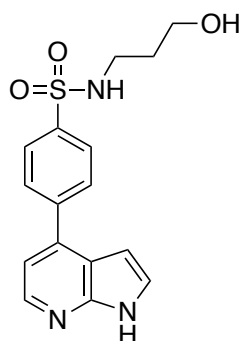
HPLC (VWD): *t_R* = 5.418 min (98%).

¹H NMR (DMSO-*d*₆, 500 MHz): δ = 11.89 (s, 1H), 8.41 (d, *J* = 9.0 Hz, 1H), 8.33 (d, *J* = 4.9 Hz, 1H), 7.80 (d, *J* = 8.1 Hz, 2H), 7.70 (d, *J* = 8.3 Hz, 2H), 7.61 (t, *J* = 3.0 Hz, 1H), 7.22 (d, *J* = 4.9 Hz, 1H), 7.20 – 7.10 (m, 5H), 6.62 (dd, *J* = 3.5, 1.7 Hz, 1H), 3.95 (dt, *J* = 8.8, 4.0 Hz, 1H), 2.99 (dd, *J* = 13.8, 5.5 Hz, 1H), 2.79 – 2.72 (m, 1H).

¹³C NMR (DMSO-*d*₆, 126 MHz): δ = 172.4, 149.2, 142.9, 141.9, 140.6, 138.6, 136.8, 129.2, 128.54, 128.1, 127.2, 126.8, 126.4, 117.1, 114.3, 98.8, 57.5, 57.5, 37.8.

MS (APCI): m/z = 422.12 ([M + H]⁺).

5.2.30. *N*-(3-hydroxypropyl)-4-(1*H*-pyrrolo[2,3-*b*]pyridin-4-yl)benzenesulfonamide (**3m**)



C₁₆H₁₇N₃O₃S: 331.39 g/mol

Starting from **2m**, the synthesis of **3m** was performed by following *General Procedure B*. Purification was performed by column chromatography using a 15:1:0.1 mixture of DCM/MeOH/NH₃ in MeOH (7 N). Yield: 89%, beige solid.

HPLC (DAD): $t_R = 3.101$ min (98%).

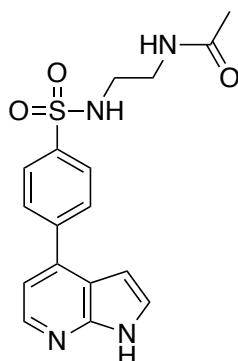
¹H NMR (DMSO-*d*₆, 500 MHz): $\delta = 11.90$ (s, 1H), 8.34 (dd, $J = 4.9, 1.5$ Hz, 1H), 8.05 – 7.93 (m, 4H), 7.66 (t, $J = 5.8$ Hz, 1H), 7.62 (dd, $J = 3.6, 2.3$ Hz, 1H), 7.28 (dd, $J = 4.9, 1.4$ Hz, 1H), 6.67 (dt, $J = 3.3, 1.6$ Hz, 1H), 4.44 (td, $J = 5.2, 1.5$ Hz, 1H), 3.45 – 3.37 (m, 2H), 2.88 (td, $J = 7.4, 5.7$ Hz, 2H), 1.63 – 1.54 (m, 2H).

¹³C NMR (DMSO-*d*₆, 126 MHz): $\delta = 149.1, 142.9, 142.1, 140.0, 138.5, 128.9, 127.2, 127.2, 117.1, 114.4, 98.8, 58.1, 40.0, 32.3$.

¹³C NMR (DMSO-*d*₆, 126 MHz, DEPT): $\delta = 142.9, 128.9, 127.2, 127.2, 114.4, 98.8, 58.1, 40.0, 32.3$.

HRMS (ESI): calcd. 331.10, found 332.1066 ($[M + H]^+$).

5.2.31. *N*-(2-((4-(1*H*-pyrrolo[2,3-*b*]pyridin-4-yl)phenyl)sulfonamido)ethyl)acetamide (**3n**)



C₁₇H₁₈N₄O₃S: 358.42 g/mol

Starting from **2n**, the synthesis of **3n** was performed by following *General Procedure B*. Purification was performed by column chromatography using a 15:1:0.1 mixture of DCM/MeOH/NH₃ in MeOH (7 N). Yield: 55%, colorless solid.

HPLC (DAD): $t_R = 2.997$ min (98%).

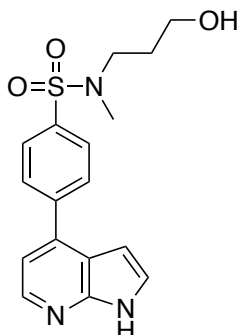
¹H NMR (DMSO-*d*₆, 500 MHz): $\delta = 11.91$ (s, 1H), 8.35 (d, $J = 4.9$ Hz, 1H), 8.04 – 7.94 (m, 4H), 7.90 (t, $J = 5.8$ Hz, 1H), 7.81 (t, $J = 6.0$ Hz, 1H), 7.62 (dd, $J = 3.5, 2.5$ Hz, 1H), 7.27 (d, $J = 4.9$ Hz, 1H), 6.67 (dd, $J = 3.6, 1.7$ Hz, 1H), 3.13 (q, $J = 6.5$ Hz, 2H), 2.88 (q, $J = 6.5$ Hz, 2H), 1.78 (s, 3H).

¹³C NMR (DMSO-*d*₆, 126 MHz): $\delta = 169.4, 149.2, 142.9, 142.3, 139.9, 138.4, 128.1, 127.2, 127.15, 117.1, 114.4, 98.8, 42.1, 38.6, 22.5$.

¹³C NMR (DMSO-*d*₆, 126 MHz, DEPT): $\delta = 142.9, 129.0, 127.2, 127.2, 114.4, 98.8, 42.1, 38.6, 22.5$.

MS (ESI): $m/z = 358.42$ ([M + H]⁺).

5.2.32. *N*-(3-hydroxypropyl)-*N*-methyl-4-(1*H*-pyrrolo[2,3-*b*]pyridin-4-yl)benzenesulfonamide (3o)



C₁₇H₁₉N₃O₃S: 345.42 g/mol

Starting from **2o** the synthesis of **3o** was performed by following *General Procedure B*. Purification was performed by column chromatography using a 30:1:0.1 mixture of DCM/MeOH/NH₃ in MeOH (7 N). Yield: 55%, beige solid.

HPLC (DAD): $t_R = 3.387$ min (98%).

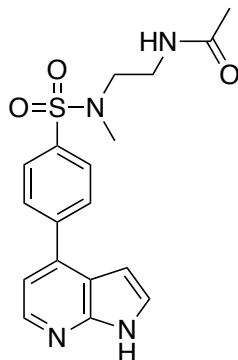
¹H NMR (DMSO-*d*₆, 500 MHz): $\delta = 11.93$ (s, 1H), 8.35 (d, $J = 4.9$ Hz, 1H), 8.06 – 8.01 (m, 2H), 7.97 – 7.91 (m, 2H), 7.62 (dd, $J = 3.5, 2.5$ Hz, 1H), 7.28 (d, $J = 5.1$ Hz, 1H), 6.68 (dd, $J = 3.5, 1.7$ Hz, 1H), 4.53 (t, $J = 5.1$ Hz, 1H), 3.46 (q, $J = 5.8$ Hz, 3H), 3.10 (dd, $J = 8.1, 6.6$ Hz, 2H), 2.74 (d, $J = 13.2$ Hz, 3H), 1.72 – 1.64 (m, 2H).

¹³C NMR (DMSO-*d*₆, 126 MHz): $\delta = 149.2, 142.9, 142.6, 138.3, 136.6, 129.1, 127.8, 127.3, 117.1, 114.4, 98.8, 58.1, 47.2, 34.8, 30.6$.

¹³C NMR (DMSO-*d*₆, 126 MHz, DEPT): $\delta = 142.9, 129.1, 127.8, 127.3, 114.4, 98.8, 58.1, 47.2, 34.8, 30.6$.

HRMS (ESI): calcd. 345.11, found 346.1222 ([M + H]⁺).

5.2.33. N-(2-((N-methyl-4-(1H-pyrrolo[2,3-b]pyridin-4-yl)phenyl)sulfonamido)ethyl)acetamide (3p)



C₁₈H₂₀N₄O₃S: 372.44 g/mol

Starting from **2p** the synthesis of **3p** was performed by following *General Procedure B*. Purification was performed by column chromatography using a 15:1:0.1 mixture of DCM/MeOH/NH₃ in MeOH (7 N). Yield: 52%, colorless solid.

HPLC (DAD): $t_R = 3.159$ min (98%).

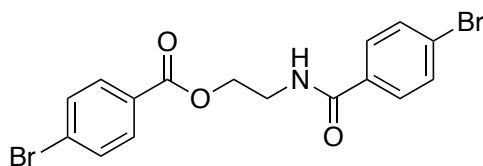
¹H NMR (DMSO-*d*₆, 500 MHz): $\delta = 11.93$ (s, 1H), 8.35 (d, $J = 4.9$ Hz, 1H), 7.99 (td, $J = 6.0, 3.0$ Hz, 2H), 7.97 – 7.87 (m, 2H), 7.62 (dd, $J = 3.5, 2.5$ Hz, 1H), 7.27 (d, $J = 4.9$ Hz, 1H), 6.67 (dd, $J = 3.6, 1.7$ Hz, 1H), 3.27 – 3.20 (m, 2H), 3.15 – 3.01 (m, 2H), 2.78 (d, $J = 14.4$ Hz, 3H), 1.81. (d, $J = 3.0$ Hz, 3H).

¹³C NMR (DMSO-*d*₆, 126 MHz): $\delta = 169.4, 149.2, 142.9, 142.7, 138.2, 136.7, 129.1, 127.7, 127.3, 117.1, 114.4, 98.8, 49.1, 36.8, 35.0, 22.6$.

¹³C NMR (DMSO-*d*₆, 126 MHz, DEPT): $\delta = 142.9, 129.1, 127.7, 127.3, 114.4, 98.8, 49.1, 36.7, 35.0, 22.6$.

MS (ESI): $m/z = 373.1330$ ([M + H]⁺).

5.2.34. 2-(4-bromobenzamido)ethyl 4-bromobenzoate (5)



C₁₆H₁₃Br₂NO₃: 427.09 g/mol

A solution of 4-bromobenzoyl chloride (**4**, 2.00 g, 9.11 mmol) in 10 mL DCM was dropwise added to a solution of monoethanolamine (0.67 g, 10.94 mmol) and triethylamine (1.08 g, 6.78 mmol) in 10 mL DCM over the course of 20 min. The mixture was stirred at ambient temperature for 24 h, diluted with 10 mL DCM and washed with saturated aqueous NaHCO₃-solution (3 x 5 mL). The organic layer was dried over MgSO₄ and the solvent was removed to give a colorless residue that was recrystallized from EtOH to give **5** (0.60 g, 48%) as a colorless solid.

HPLC (VWD): $t_R = 6.898$ min (94%).

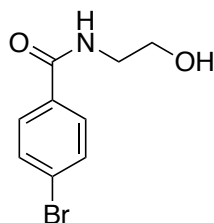
¹H NMR (DMSO-*d*₆, 500 MHz): $\delta = 8.76$ (t, $J = 5.6$ Hz, 1H), 7.92 – 7.87 (m, 2H), 7.81 – 7.76 (m, 2H), 7.75 – 7.70 (m, 2H), 7.70 – 7.64 (m, 2H), 4.40 (t, $J = 5.5$ Hz, 2H), 3.64 (q, $J = 5.6$ Hz, 2H).

¹³C NMR (DMSO-*d*₆, 126 MHz): $\delta = 165.7, 165.1, 133.4, 131.8, 131.3, 131.2, 129.3, 128.9, 127.3, 124.9, 63.6, 38.4$.

¹³C NMR (DMSO-*d*₆, 126 MHz, DEPT): $\delta = 131.8, 131.3, 131.2, 129.3, 63.6, 38.4$.

MS (ESI): $m/z = 425.93$ ([M + H]⁺).

5.2.35. 4-bromo-*N*-(2-hydroxyethyl)benzamide (**6**)



$C_9H_{10}BrNO_2$: 244.09 g/mol

To a solution of ester **5** (0.50 g, 1.17 mmol) in 20 mL THF were added 2 mL of 50% w/v aq. KOH solution and the mixture was stirred at 60 °C for 16 h. The solvent was removed under reduced pressure and the resulting white residue was taken up in 20 mL EtOAc and washed with water (3 x 5 mL) and brine (5 mL). Purification was performed by column chromatography using a 15:1 mixture of DCM/MeOH to give **6** (262 mg, 92%) as a colorless solid.

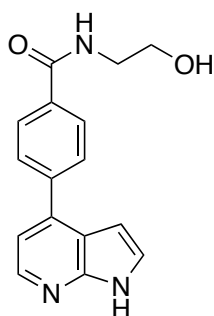
HPLC (DAD): $t_R = 3.693$ min (93%).

1H NMR (DMSO- d_6 , 500 MHz): $\delta = 8.49$ (t, $J = 5.7$ Hz, 1H), 7.82 – 7.77 (m, 2H), 7.68 – 7.65 (m, 2H), 4.70 (t, $J = 5.6$ Hz, 1H), 3.51 (q, $J = 5.9$ Hz, 2H), 3.32 (q, $J = 6.1$ Hz, 2H).

^{13}C NMR (DMSO- d_6 , 126 MHz): $\delta = 165.4, 133.7, 131.2, 129.3, 124.7, 59.6, 42.2$.

MS (ESI): $m/z = 243$ ($[M]^+$).

5.2.36. *N*-(2-hydroxyethyl)-4-(1*H*-pyrrolo[2,3-*b*]pyridin-4-yl)benzamide (7)



C₁₆H₁₅N₃O₂: 281.32 g/mol

Starting from **6**, the synthesis of **7** was performed by following *General Procedure B*. Purification was performed by column chromatography using a stepwise gradient from a 15:1:0.1 to a 10:1:0.1 mixture of DCM/MeOH/10% aq. NH₄OH (25%) in MeOH. Yield: 43%, colorless solid.

HPLC (DAD): $t_R = 2.860$ min (96%).

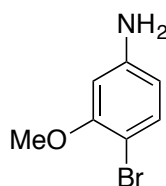
¹H NMR (DMSO-*d*₆, 500 MHz): $\delta = 11.83$ (s, 1H), 8.53 (t, $J = 5.6$ Hz, 1H), 8.31 (d, $J = 4.9$ Hz, 1H), 8.07 – 8.00 (m, 2H), 7.89 – 7.82 (m, 2H), 7.60 – 7.55 (m, 1H), 7.23 (d, $J = 4.9$ Hz, 1H), 6.63 (dd, $J = 3.6, 1.8$ Hz, 1H), 4.75 (t, $J = 5.6$ Hz, 1H), 3.56 (q, $J = 6.0$ Hz, 2H), 3.39 (q, $J = 6.1$ Hz, 2H).

¹³C NMR (DMSO-*d*₆, 126 MHz): $\delta = 165.9, 149.2, 142.9, 141.0, 139.3, 134.2, 128.0, 127.8, 126.9, 117.2, 114.3, 98.9, 59.8, 42.2$.

¹³C NMR (DMSO-*d*₆, 126 MHz, DEPT): $\delta = 142.9, 128.0, 127.9, 126.9, 114.3, 98.9, 59.8, 42.3$.

MS (ESI): $m/z = 282.12$ ([M + H]⁺).

5.2.37. 4-bromo-3-methoxyaniline (**10**)



C₇H₈BrNO: 202.05 g/mol

To a solution of 1-bromo-2-methoxy-4-nitrobenzene (**9**, 2.20 g, 9.48 mmol) in 30 mL ethanol/water (2:1) were added 20 mL glacial acetic acid and powdered iron (2.65 g, 47.41 mmol). The suspension was heated to 50 °C under LFU (35 kHz) in an ultrasonic bath for 1 h. The reaction mixture was diluted with 150 mL ethyl acetate and the layers were separated. The organic layer was washed with 2N KOH-solution (2 x 100 mL), water (3 x 100 mL) and brine (100 mL). The organic layer was dried over MgSO₄ and the solvent was removed to give a red residue. Purification was performed by column chromatography using a 1:1 mixture of ethylacetate/cyclohexane to give **10** (1.56 g, 74%) as a reddish solid.

HPLC (VWD): $t_R = 1.280$ min; 5.816 min.

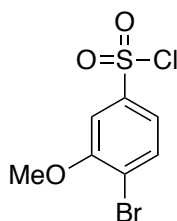
¹H-NMR (500 MHz, CDCl₃): $\delta = 7.24$ (d, $J = 8.4$ Hz, 1H), 6.25 (d, $J = 2.5$ Hz, 1H), 6.18 (dd, $J = 8.4, 2.5$ Hz, 1H), 3.83 (s, 3H), 3.69 (s, 2H).

¹³C-NMR (126 MHz, CDCl₃): $\delta = 156.6, 147.3, 133.55, 108.7, 99.9, 56.1$.

MS (EI): $m/z = 201$ ([M]⁺).

IR (ATR): 3404.20 cm⁻¹ (NH₂, ν_{as}); 3329.78 cm⁻¹ (NH₂, ν_s); 1591.62 cm⁻¹ (aromatic =C-H and C=C; ν_s); 1484.82 cm⁻¹ (aromatic =C-H and C=C, ν_{as}); 1448.05 cm⁻¹ (O-CH₃, δ); 1205.25 cm⁻¹ (=C-O, ν_{as}); ~1100 cm⁻¹ (C-O, ν_s); 615.33 cm⁻¹ (C-Br, ν_s).

5.2.38. 4-bromo-3-methoxybenzenesulfonyl chloride (**11**)



C₇H₆BrClO₃S: 285.54 g/mol

A solution of sodium nitrite (1.60 g, 23.16 mmol) in 5.5 mL water was dropwise added to a solution of 4-bromo-3-methoxyaniline (**10**, 1.56 g, 7.72 mmol) in 10 mL conc. HCl and 10 mL glacial acetic acid at -10 °C. The reaction mixture was stirred for 1 h while the temperature is maintained between -15 and -5 °C. Upon completion of the diazotation, copper(II) sulfate (1.93 g, 7.72 mmol) was added as a solution in 10 mL conc. HCl under ice cooling and a solution of sodium metabisulfite (7.93 g, 41.69 mmol) in 16 mL water was added dropwise, not exceeding a reaction temperature of 10 °C. After stirring at for 2 h under ice cooling, the reaction mixture was allowed to reach room temperature and was stirred for an additional 1 h. The reaction mixture was extracted with 80 mL ethyl acetate three times and the combined organic layers were washed with sat. sodium bicarbonate solution until neutral. After washing with water (3x 100 mL) and brine (1x 100 mL). The organic layer was dried over MgSO₄ and the solvent was removed to give **11** (1.60 g, 72%) as a red oil.

HPLC (VWD): $t_R = 6.940$ min (91%).

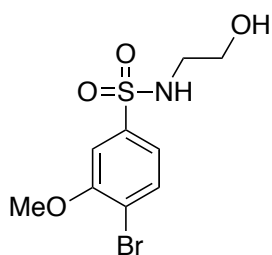
¹H-NMR (500 MHz, CDCl₃): $\delta = 7.80$ (d, $J = 8.3$ Hz, 1H), 7.52 (dd, $J = 8.2, 2.1$ Hz, 1H), 7.46 (d, $J = 2.1$ Hz, 1H), 4.01 (s, 3H).

¹³C-NMR (126 MHz, CDCl₃): $\delta = 156.9, 134.5, 125.6, 123.2, 120.2, 109.5, 57.0$.

MS (EI): $m/z = 284$ ($[M]^+$).

IR (ATR): 1581,84 cm⁻¹ (aromatic =C-H and C=C; ν_s); 1475,23 cm⁻¹ (aromatic =C-H and C=C, ν_{as}); 1450,07 cm⁻¹ (O-CH₃, δ); 1205,25 cm⁻¹ (=C-O, ν_{as}); 1376.62 cm⁻¹ (Ar-SO₂Cl ν_{as}); 1172.99 cm⁻¹ (Ar-SO₂Cl ν_s); 1039.36 cm⁻¹ (C-O, ν_s); 615,33 cm⁻¹ (C-Br, ν_s).

5.2.39. 4-bromo-N-(2-hydroxyethyl)-3-methoxybenzenesulfonamide (12)



C₉H₁₂BrNO₄S: 310.16 g/mol

Synthesis of **12** was performed by following *General Procedure A* using 2-aminoethan-1-ol.
Yield: 90%, colorless solid.

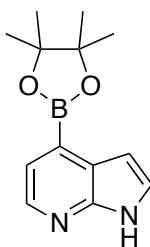
HPLC (VWD): $t_R = 2.868$ min.

¹H-NMR (500 MHz, CDCl₃): $\delta = 7.68$ (d, $J = 8.2$ Hz, 1H), 7.37 (d, $J = 2.0$ Hz, 1H), 7.33 (dd, $J = 8.2, 2.0$ Hz, 1H), 5.27 (t, $J = 6.1$ Hz, 1H), 3.95 (s, 3H), 3.74 – 3.67 (m, 2H), 3.15 – 3.09 (m, 2H), 2.20 (s, 1H).

¹³C-NMR (126 MHz, CDCl₃): $\delta = 1156.6, 140.2, 134.1, 120.3, 117.5, 110.2, 61.4, 56.8, 45.4, 56.9, 134.5, 125.6, 123.2, 120.2, 109.5, 57.0$.

MS (ESI): $m/z = 311.97$ ([M + H]⁺).

5.2.40. 4-(4,4,5,5-tetramethyl-1,3,2-dioxaborolan-2-yl)-1H-pyrrolo[2,3-b]pyridine (14)



C₁₃H₁₇BN₂O₂: 244.10 g/mol

To a solution of 4-bromo-7-azaindole (**13**, 500 mg, 2.54 mmol) in 17 mL dry 1,4-dioxane were added potassium acetate (747 mg, 5.08 mmol), bis(pinacolato)diboron (1.29 g, 5.08 mmol) and PdCl₂(dppf) (85 mg, 102 μmol), under argon atmosphere. The reaction mixture was stirred at 90 °C for 18 h. After cooling to ambient temperature, 20 mL of ethyl acetate were added, the solution was filtered through Celite and the organic layer was washed with brine (5 x 20 mL), before drying over NaSO₄. The solvent was removed under reduced pressure to give the crude product. Purification was performed by column chromatography using a 30:1:0.1 mixture of DCM/MeOH/10% aq. NH₄OH (25%) in MeOH to give **14** (318 mg, 51%) as a beige solid.

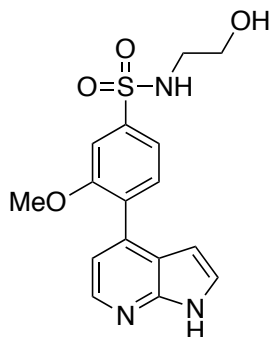
HPLC (DAD): $t_R = 2.628$ min.

¹H-NMR (500 MHz, CDCl₃): $\delta = 10.48$ (s, 1H), 8.51 (s, 1H), 7.53 (d, $J = 4.0$ Hz, 1H), 7.41 (d, $J = 3.5$ Hz, 1H), 6.94 (d, $J = 3.4$ Hz, 1H), 1.41 (s, 12H).

¹³C-NMR (126 MHz, CDCl₃): $\delta = 148.4, 141.8, 125.7, 125.5, 122.4, 116.2, 103.0, 84.3, 25.2$.

MS (ESI): $m/z = 244$ ([M]⁺).

5.2.41. *N*-(2-hydroxyethyl)-3-methoxy-4-(1*H*-pyrrolo[2,3-*b*]pyridin-4-yl)benzenesulfonamide (15)



C₁₆H₁₇N₃O₄S: 347.39 g/mol

To a solution of sulfonamide **12** (237 mg, 0.77 mmol), in 12 mL DMF, were added boronic ester **14** (187 mg, 0.77 mmol), Pd(PPh₃)₄ (88 mg, 76 μmol) and 2.2 mL saturated aq. NaHCO₃-solution under argon atmosphere. The mixture was stirred at 100 °C for 5 h, cooled to ambient temperature and diluted with 20 mL EtOAc. After filtration through Celite the organic layer was washed with brine (5 x 20 mL), dried over MgSO₄ and the solvent was removed under reduced pressure to give the crude product. Purification was performed by column chromatography using a 20:1:0.1 mixture of DCM/MeOH/10% aq. NH₄OH (25%) in MeOH to give **15** (154 mg, 58%) as a beige solid.

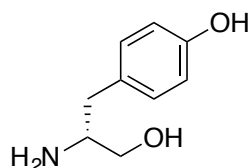
HPLC (DAD): *t_R* = 3.101 min. (98%).

¹H-NMR (500 MHz, CDCl₃): δ = 11.70 (s, 1H), 8.26 (d, *J* = 4.9 Hz, 1H), 7.69 (d, *J* = 5.6 Hz, 1H), 7.60 (d, *J* = 7.9 Hz, 1H), 7.56 (d, *J* = 1.7 Hz, 1H), 7.52 (dd, *J* = 7.8, 1.7 Hz, 1H), 7.48 (dd, *J* = 3.5, 2.4 Hz, 1H), 7.10 (d, *J* = 4.9 Hz, 1H), 6.25 (dd, *J* = 3.5, 1.8 Hz, 1H), 4.72 (t, *J* = 5.6 Hz, 1H), 3.83 (s, 3H), 3.44 (q, *J* = 6.1 Hz, 2H), 2.90 (q, *J* = 6.0 Hz, 2H).

¹³C-NMR (126 MHz, CDCl₃): δ = 156.5, 148.7, 142.2, 141.6, 136.6, 131.2, 131.0, 126.3, 118.7, 118.5, 116.0, 109.5, 99.5, 60.0, 55.8, 45.2.

MS (ESI): *m/z* = 348,1 ([M+H]⁺).

5.2.42. (R)-4-(2-amino-3-hydroxypropyl)phenol (**17d**)



C₉H₁₃NO₂: 167.21 g/mol

To a stirred solution of D-Tyrosine methyl ester hydrochloride (2.00 g, 8.63 mmol) in 20 mL acetonitrile was added potassium carbonate (2.98 g, 21.6 mmol) and the solution was heated to 50 °C for 16 h. Filtration of the formed salt and evaporation of the solvent under reduced pressure gave an orange oil that was taken up in 20 mL methanol. Under cooling to 0 °C in an ice bath NaBH₄ (491 mg, 12.99 mmol) was added in small portions over 30 min. The cooling bath was removed and the solution was stirred at ambient temperature for 5 h. The solvent was removed under reduced pressure, the resulting residue taken up in 50 mL water and the aqueous layer was extracted with ethyl acetate (5x 50 mL). The combined organic layers were dried over MgSO₄, filtered and concentrated *in vacuo* to give **17d** (878 mg, 61%) as a crude yellow solid that was used for the next step without further purification.

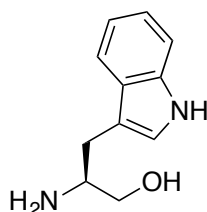
HPLC (DAD): $t_R = 0.889$ min (66%).

¹H NMR (DMSO-*d*₆, 500 MHz): $\delta = 6.68 - 6.65$ (m, 2H), 6.37 - 6.34 (m, 2H), 2.97 (dd, $J = 10.3, 4.5$ Hz, 1H), 2.87 - 2.83 (m, 1H), 2.24 (dd, $J = 13.4, 6.0$ Hz, 1H), 2.20 - 2.09 (m, 1H), 2.02 (dd, $J = 13.4, 7.5$ Hz, 1H), 1.44 (s, 1H).

¹³C NMR (DMSO-*d*₆, 500 MHz): $\delta = 155.5, 130.0, 129.5, 115.0, 65.5, 54.6, 39.0$.

MS (EI): $m/z = 167$ ([M]⁺).

5.2.43. (S)-2-amino-3-(1H-indol-3-yl)propan-1-ol (**17e**)



C₁₁H₁₄N₂O: 190.25 g/mol

An oven-dried three-neck flask was charged with L-tryptophan (2.04 g, 10.0 mmol) sodium borohydride (757 mg, 20.0 mmol) and 20 mL dry THF and equipped with a dropping funnel and a reflux condenser under argon atmosphere. A solution of iodine (2.54 g, 10.0 mmol) in 10 mL dry THF was added dropwise over the course of 30 min at 0 °C under cooling in an ice bath. Once the evolution of gas had stopped the ice bath was removed and the mixture was heated to reflux for 20 h. After cooling to ambient temperature methanol was slowly added under vigorous stirring until the solution became clear. After stirring for another 15 min removal of the solvents under reduced pressure gave a white residue that was dissolved in 25 mL aq. KOH solution (20% w/v) and stirred for 16 h at ambient temperature. Adjustment to pH 11 by addition of hydrochloric acid (2 M) was followed by extraction of the aqueous layer with DCM (3 x 25 mL) and a 1:4 mixture of ethanol/chloroform (5 x 25 mL). The combined organic layers were washed with water (3 x 25 mL) and brine (25 mL) and dried over MgSO₄. The solvent was removed under reduced pressure to give **17e** (1.36 g, 72%) as a crude yellow oil that was used without further purification.

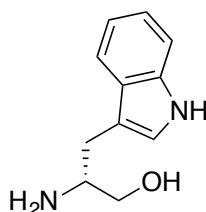
HPLC (DAD): $t_R = 3.047$ min (77%).

¹H NMR (DMSO-*d*₆, 500 MHz): $\delta = 10.82$ (s, 1H), 7.54 (d, $J = 7.8$ Hz, 1H), 7.32 (d, $J = 7.8$ Hz, 1H), 7.17 (d, $J = 1.9$ Hz, 1H), 7.05 (ddt, $J = 8.2, 5.0, 1.4$ Hz, 1H), 6.99 – 6.94 (m, 1H), 3.39 – 3.37 (m, 1H), 3.24 (m, 1H), 3.01 (q, $J = 6.0$ Hz, 1H), 2.81 (dd, $J = 14.0, 6.1$ Hz, 1H), 2.60 (dd, $J = 14.0, 7.1$ Hz, 1H).

¹³C NMR (75 MHz, CDCl₃): $\delta = 136.5, 127.7, 122.9, 122.01, 119.4, 118.9, 112.4, 111.4, 66.6, 53.1, 30.1$.

MS (ESI): $m/z = 191.12$ ([M + H]⁺).

5.2.44. (*R*)-2-amino-3-(1*H*-indol-3-yl)propan-1-ol (**17f**)



C₁₁H₁₄N₂O: 190.25 g/mol

An oven-dried three-neck flask was charged with D-tryptophan (1.57 g, 7.69 mmol) sodium borohydride (640 mg, 16.91 mmol) and 15 mL dry THF and equipped with a dropping funnel and a reflux condenser under argon atmosphere. A solution of iodine (1.95 g, 7.69 mmol) in 8 mL dry THF was added dropwise over the course of 30 min at 0 °C under cooling in an ice bath. Once the evolution of gas had stopped the ice bath was removed and the mixture was heated to reflux for 19 h. After cooling to ambient temperature methanol was slowly added under vigorous stirring until the solution became clear. After stirring for another 15 min removal of the solvents under reduced pressure gave a white residue that was dissolved in 20 mL aq. KOH solution (20% w/v) and stirred for 15 h at ambient temperature. Adjustment to pH 11 by addition of hydrochloric acid (2 M) was followed by extraction of the aqueous layer with DCM (3 x 25 mL) and a 1:4 mixture of ethanol/chloroform (5 x 25 mL). The combined organic layers were washed with water (3 x 25 mL) and brine (25 mL) and dried over MgSO₄. The solvent was removed under reduced pressure to give **17f** (1.22 g, 84%) as a crude yellow oil that was used for the next step without further purification.

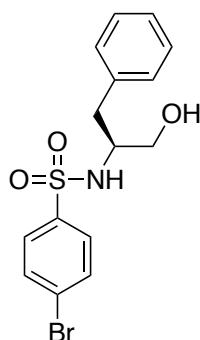
HPLC (DAD): $t_R = 2.886$ min (65%).

¹H NMR (DMSO-*d*₆, 500 MHz): $\delta = 10.83$ (s, 1H), 7.54 (d, $J = 7.9$ Hz, 1H), 7.34 (d, $J = 8.0$ Hz, 1H), 7.15 (d, $J = 1.8$ Hz, 1H), 7.06 (ddt, $J = 8.2, 5.0, 1.4$ Hz, 1H), 6.99 – 6.94 (m, 1H), 3.41 – 3.35 (m, 1H), 3.24 (m, 1H), 3.01 (q, $J = 6.1$ Hz, 1H), 2.81 (dd, $J = 14.2, 6.1$ Hz, 1H), 2.60 (dd, $J = 14.2, 7.1$ Hz, 1H).

¹³C NMR (DMSO-*d*₆, 126 MHz): $\delta = 136.3, 127.6, 123.3, 120.8, 118.4, 118.1, 111.6, 111.3, 65.7, 53.6, 29.4$.

MS (ESI): $m/z = 191.12$ ([M + H]⁺).

5.2.45. (S)-4-bromo-N-(1-hydroxy-3-phenylpropan-2-yl)benzenesulfonamide (18a)



C₁₅H₁₆BrNO₃S: 370.26 g/mol

Synthesis of **18a** was performed by following *General Procedure A* using L-phenylalaninol (**17a**). Yield: 98%, colorless solid.

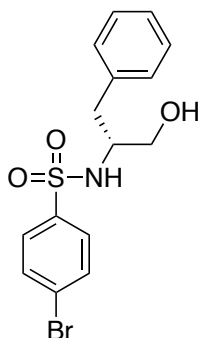
HPLC (DAD): $t_r = 5.908$ min (98%).

¹H NMR (DMSO-*d*₆, 500 MHz): $\delta = 7.60 - 7.56$ (m, 2H), $7.50 - 7.46$ (m, 2H), 7.12 (dd, $J = 5.2, 1.9$ Hz, 3H), $7.06 - 7.00$ (m, 2H), 4.80 (s, 1H), 3.33 (dd, $J = 10.1, 4.2$ Hz, 1H), $3.30 - 3.24$ (m, 1H), 3.21 (dd, $J = 9.9, 6.6$ Hz, 1H), 2.83 (dd, $J = 13.7, 5.3$ Hz, 1H), 2.46 (dd, $J = 13.7, 8.0$ Hz, 1H).

¹³C NMR (DMSO-*d*₆, 126 MHz): $\delta = 140.9, 138.3, 131.8, 129.1, 128.0, 128.0, 125.7, 125.5, 63.2, 57.3, 37.0$.

MS (APCI): $m/z = 370.01$ ($[M + H]^+$).

5.2.46. (*R*)-4-bromo-*N*-(1-hydroxy-3-phenylpropan-2-yl)benzenesulfonamide (**18b**)



C₁₅H₁₆BrNO₃S: 370.26 g/mol

Synthesis of **18b** was performed by following *General Procedure A* using D-phenylalaninol (**17b**). Yield: 99%, colorless solid.

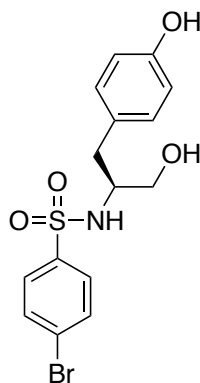
HPLC (VWD): $t_R = 5.310$ min (96%).

¹H NMR (CDCl₃, 300 MHz): $\delta = 7.48$ (s, 4H), 7.21 – 7.13 (m, 3H), 7.00 – 6.93 (m, 2H), 3.69 (dd, $J = 11.1, 4.1$ Hz, 1H), 3.59 (dd, $J = 11.1, 4.6$ Hz, 1H), 3.53 – 3.39 (m, 1H), 2.83 (dd, $J = 13.9, 6.3$ Hz, 1H), 2.68 (dd, $J = 14.0, 8.2$ Hz, 1H).

¹³C NMR (DMSO-*d*₆, 126 MHz): $\delta = 140.8, 138.3, 131.78, 129.0, 128.0, 127.9, 125.7, 125.5, 63.1, 57.2, 37.1$.

MS (ESI): $m/z = 370.01$ ([M + H]⁺).

**5.2.47. (S)-4-bromo-N-(1-hydroxy-3-(4-hydroxyphenyl)propan-2-yl)benzenesulfonamide
(18c)**



C₁₅H₁₆BrNO₄S: 386.26 g/mol

To a solution of L-tyrosinol (**17c**, 469 mg, 2.15 mmol) in 10 mL of a 1:1 mixture of water/acetone was added sodium bicarbonate (658 mg, 7.83 mmol) and the mixture was stirred at ambient temperature for 15 min. 4-bromobenzene-sulfonyl chloride (**1**, 500 mg, 1.96 mmol) was added and stirring was continued for 17 h. After evaporation of the volatile solvent under reduced pressure, 10 mL ethyl acetate were added and layers were separated. The aq. layer was extracted with ethyl acetate (3x 5 mL) and the combined organic layers were washed with saturated NaHCO₃ (aq, 3 x 5 mL) and dried over MgSO₄. The solvent was removed under reduced pressure to give crude crystals that were recrystallized from methanol to give **18c** (455 mg, 60%) as colorless crystals.

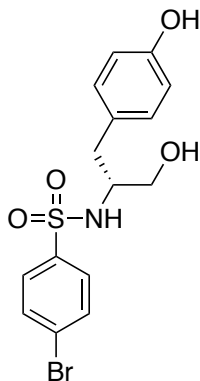
HPLC (DAD): $t_R = 3.929$ min (85%).

¹H NMR (DMSO-*d*₆, 500 MHz): $\delta = 9.09$ (s, 1H), 7.67 (d, $J = 7.3$ Hz, 2H), 7.67 – 7.60 (m, 3H), 7.55 – 7.49 (m, 2H), 6.87 – 6.80 (m, 2H), 6.59 – 6.52 (m, 2H), 4.69 (t, $J = 5.1$ Hz, 1H), 3.30 – 3.25 (m, 2H), 3.22 – 3.14 (m, 2H), 2.69 (dd, $J = 13.8, 5.4$ Hz, 1H), 2.35 (dd, $J = 13.8, 6.9$ Hz, 1H).

¹³C NMR (DMSO-*d*₆, 75 MHz): $\delta = 155.5, 141.1, 132.9, 131.8, 130.1, 130.0, 128.2, 114.9, 62.8, 57.5, 36.3$.

MS (ESI): $m/z = 386.01$ ([M + H]⁺).

**5.2.48. (R)-4-bromo-N-(1-hydroxy-3-(4-hydroxyphenyl)propan-2-yl)benzenesulfonamide
(18d)**



C₁₅H₁₆BrNO₄S: 386.26 g/mol

To a solution of D-tyrosinol (**17d**, 229 mg, 1.37 mmol) in 7 mL of a 1:1 mixture of water/acetone was added sodium bicarbonate (460 mg, 5.48 mmol) and the mixture was stirred at ambient temperature for 15 min. 4-Bromobenzenesulfonyl chloride (**1**, 350 mg, 1.37 mmol) was added and the solution was heated to 40 °C for 4 h. After evaporation of the volatile solvent under reduced pressure, 7 mL ethyl acetate were added and the layers were separated. The aq. layer was extracted with ethyl acetate (3x 5 mL) and the combined organic layers were washed with saturated NaHCO₃ (aq, 3 x 5 mL) and dried over MgSO₄. The solvent was removed under reduced pressure to give **18d** (371 mg, 70%) as a crude yellow solid that was used in the next step without further purification.

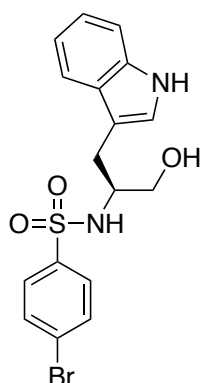
HPLC (DAD): $t_R = 3.880$ min (85%).

¹H NMR (DMSO-*d*₆, 300 MHz): $\delta = 7.68 - 7.58$ (m, 2H), 7.52 (d, $J = 8.5$ Hz, 2H), 6.88 – 6.78 (m, 2H), 6.60 – 6.51 (m, 2H), 4.71 (s, 1H), 3.25 – 3.12 (m, 4H), 2.69 (dd, $J = 13.7, 5.5$ Hz, 1H), 2.35 (dd, $J = 13.9, 6.9$ Hz, 1H).

¹³C NMR (DMSO-*d*₆, 75 MHz): $\delta = 155.6, 141.0, 132.9, 131.8, 130.1, 130.0, 128.2, 114.8, 62.8, 57.4, 36.2$.

MS (ESI): $m/z = 386.01$ ([M + H]⁺).

5.2.49. (S)-4-bromo-N-(1-hydroxy-3-(1H-indol-3-yl)propan-2-yl)benzenesulfonamide (18e)



C₁₇H₁₇BrN₂O₃S: 409.30 g/mol

To a stirred solution of L-Tryptophanol (**17e**, 400 mg, 2.10 mmol) in 40 mL of a 1:2 mixture of DCM/acetonitrile was added *N,N'*-diisopropylethylamine (326 mg, 2.52 mmol). The mixture was stirred at ambient temperature for 1 h and 4-bromobenzene-sulfonyl chloride (**1**, 537 mg, 2.10 mmol) was added in small portions over 30 min at 0 °C under cooling in an ice bath. The cooling bath was removed and the solution was stirred at ambient temperature for 24 h. Removal of the solvent under reduced pressure gave a brown residue that was taken up in 30 mL DCM, washed with hydrochloric acid (1N, 3 x 5 mL), water (3 x 5 mL) and brine (5mL) and dried over MgSO₄. The solvent was removed under reduced pressure to give a crude brown oil that was purified by column chromatography using a 1:1 mixture of ethyl acetate/cyclohexane yielding **18e** (257 mg, 30%) as a yellow oil.

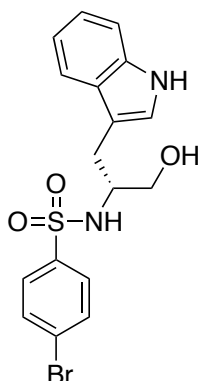
HPLC (DAD): $t_R = 5.227$ min (92%).

¹H NMR (DMSO-*d*₆, 500 MHz): $\delta = 10.70$ (s, 1H), 7.73 (d, $J = 6.9$ Hz, 1H), 7.50 – 7.43 (m, 4H), 7.28 (dt, $J = 7.8, 1.0$ Hz, 2H), 7.07 – 7.01 (m, 2H), 6.91 (tt, $J = 6.9, 0.9$ Hz, 1H), 4.79 (t, $J = 5.3$ Hz, 1H), 3.42 – 3.39 (m, 1H), 3.33 – 3.25 (m, 2H), 2.95 (dd, $J = 14.3, 6.0$ Hz, 1H), 2.61 (dd, $J = 14.3, 7.0$ Hz, 1H).

¹³C NMR (DMSO-*d*₆, 126 MHz): $\delta = 140.6, 136.1, 131.4, 127.9, 127.0, 125.4, 123.7, 120.6, 118.1, 117.9, 111.4, 110.3, 63.2, 56.1, 27.0$.

MS (ESI): $m/z = 409.02$ ([M + H]⁺).

5.2.50. (R)-4-bromo-N-(1-hydroxy-3-(1H-indol-3-yl)propan-2-yl)benzenesulfonamide (18f)



C₁₇H₁₇BrN₂O₃S: 409.30 g/mol

To a stirred solution of D-tryptophanol (**17f**, 625 mg, 3.29 mmol) in 60 mL of a 1:2 mixture of DCM/acetonitrile was added *N,N'*-diisopropylethylamine (510 mg, 3.94 mmol). The mixture was stirred at ambient temperature for 1 h and 4-bromobenzene-sulfonyl chloride (**1**, 839 mg, 3.29 mmol) was added in small portions over 30 min at 0 °C under cooling in an ice bath. The cooling bath was removed and the solution was stirred at ambient temperature for 24 h. Removal of the solvent under reduced pressure gave a brown residue that was taken up in 40 mL DCM, washed with hydrochloric acid (1N, 3 x 7 mL), water (3 x 7 mL) and brine (7 mL) and dried over MgSO₄. The solvent was removed under reduced pressure to give a crude brown oil that was purified by column chromatography using a 1:1 mixture of ethyl acetate/cyclohexane yielding **18f** (579mg, 43%) as a yellow oil.

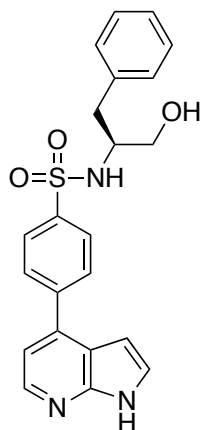
HPLC (DAD): $t_R = 5.229$ min (95%).

¹H NMR (DMSO-*d*₆, 500 MHz): $\delta = 10.66$ (s, 1H), 7.69 (d, $J = 7.0$ Hz, 1H), 7.50 – 7.41 (m, 4H), 7.30 – 7.23 (m, 2H), 7.05 – 6.98 (m, 2H), 6.93 – 6.85 (m, 1H), 4.75 (t, $J = 5.4$ Hz, 1H), 3.40 – 3.36 (m, 1H), 3.33 – 3.24 (m, 2H), 2.94 (dd, $J = 14.4, 6.0$ Hz, 1H), 2.60 (dd, $J = 14.3, 7.0$ Hz, 1H).

¹³C NMR (DMSO-*d*₆, 126 MHz): $\delta = 140.6, 136.1, 131.4, 127.9, 127.0, 125.4, 123.7, 120.6, 118.1, 117.9, 111.4, 110.3, 63.2, 56.1, 27.0$.

MS (ESI): $m/z = 409.02$ ([M + H]⁺).

5.2.51. (S)-N-(1-hydroxy-3-phenylpropan-2-yl)-4-(1H-pyrrolo[2,3-b]pyridin-4-yl)benzene sulfonamide (19a)



$C_{22}H_{21}N_3O_3S$: 407.49 g/mol

Starting from **18a**, the synthesis of **19a** was performed by following *General Procedure B*. Purification was performed by column chromatography using a 20:1:0.1 mixture of DCM/MeOH/10% aq. NH_4OH (25%) in MeOH. Yield: 42%, beige solid.

HPLC (DAD): $t_R = 4.036$ min (98%).

1H NMR (DMSO- d_6 , 500 MHz): $\delta = 11.90$ (s, 1H), 8.35 (d, $J = 14.7, 5.0$ Hz, 1H), 7.86 – 7.67 (m, 4H), 7.59 (t, $J = 22.3, 3.1$ Hz, 1H), 7.28 (d, $J = 50.0, 4.9$ Hz, 1H), 7.16 – 6.99 (m, 4H), 6.58 (t, 1H), 4.87 (t, $J = 5.5$ Hz, 1H), 3.46 – 3.40 (m, 1H), 3.35 – 3.31 (m, 1H), 3.31 – 3.20 (m, 1H), 2.87 (dd, $J = 13.6, 5.5$ Hz, 1H), 2.47 (d, $J = 8.4$ Hz, 1H).

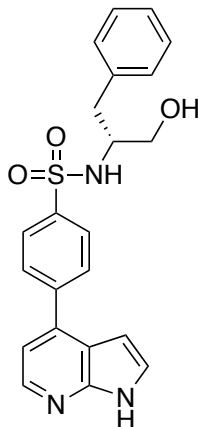
^{13}C NMR (DMSO- d_6 , 126 MHz): $\delta = 149.2, 142.9, 141.6, 141.2, 138.6, 138.4, 129.1, 128.59, 128.0, 127.2, 126.8, 125.9, 117.1, 114.3, 98.8, 63.3, 57.3, 37.0$.

^{13}C NMR (DMSO- d_6 , 126 MHz, DEPT): $\delta = 142.9, 129.1, 128.6, 128.0, 127.1, 126.8, 125.8, 114.3, 98.8, 63.3, 57.3, 37.1$.

MS (ESI): $m/z = 408.14$ ($[M + H]^+$).

HRMS (ESI): calcd. 407.13, found 408.1378 ($[M + H]^+$).

5.2.52. (R)-N-(1-hydroxy-3-phenylpropan-2-yl)-4-(1H-pyrrolo[2,3-b]pyridin-4-yl)-benzene sulfonamide (19b)



C₂₂H₂₁N₃O₃S: 407.49 g/mol

Starting from **18b**, the synthesis of **19b** was performed by following *General Procedure B*. Purification was performed by column chromatography using a 20:1:0.1 mixture of DCM/MeOH/10% aq. NH₄OH (25%) in MeOH. Yield: 56%, beige solid.

HPLC (VWD): $t_R = 2.369$ min (95%).

¹H NMR (DMSO-*d*₆, 500 MHz): $\delta = 11.88$ (s, 1H), 8.34 (d, $J = 4.9$ Hz, 1H), 7.80 – 7.72 (m, 4H), 7.60 (t, $J = 2.9$ Hz, 1H), 7.22 (dd, $J = 4.9, 1.1$ Hz, 1H), 7.15 – 6.98 (m, 5H), 6.72 – 6.54 (m, 1H), 4.86 (t, $J = 5.4$ Hz, 1H), 3.44 – 3.40 (m, 1H), 3.37 – 3.32 (m, 1H), 3.28 (dt, $J = 11.1, 6.1$ Hz, 1H), 2.88 (dd, $J = 13.7, 5.4$ Hz, 1H), 2.50 (dd, 1H).

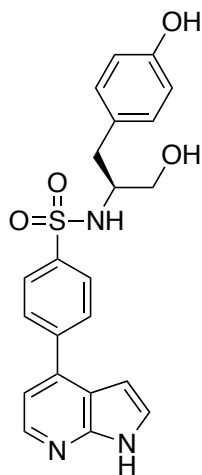
¹³C NMR (DMSO-*d*₆, 126 MHz): $\delta = 149.2, 143.0, 141.6, 141.2, 138.6, 138.4, 129.1, 128.6, 127.97, 127.1, 126.8, 125.9, 117.1, 114.3, 98.8, 63.3, 57.3, 37.1$.

¹³C NMR (DMSO-*d*₆, 126 MHz, DEPT): $\delta = 143.0, 129.2, 128.6, 128.0, 127.2, 126.8, 125.89, 114.4, 98.8, 63.3, 57.3, 37.1$.

MS (ESI): $m/z = 815.09$ ($[2M + H]^+$), 408.14 ($[M + H]^+$).

HRMS (ESI): calcd. 407.13, found 408.1374 ($[M + H]^+$).

5.2.53. (S)-N-(1-hydroxy-3-(4-hydroxyphenyl)propan-2-yl)-4-(1H-pyrrolo[2,3-b]pyridin-4-yl)benzenesulfonamide (19c)



C₂₂H₂₁N₃O₄S: 423.49 g/mol

Starting from **18c**, the synthesis of **19c** was performed by following *General Procedure B*. Purification was performed by column chromatography using a 10:1:0.1 mixture of DCM/MeOH/10% aq. NH₄OH (25%) in MeOH. Yield: 51%, colorless solid.

HPLC (DAD): $t_R = 3.210$ min (95%).

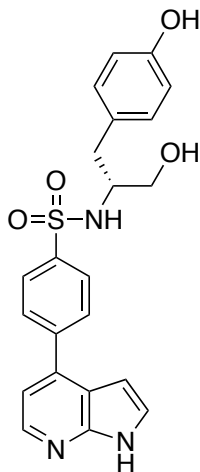
¹H NMR (DMSO-*d*₆, 500 MHz): $\delta = 11.88$ (s, 1H), 9.14 (s, 1H), 8.33 (d, $J = 4.9$ Hz, 1H), 7.86 – 7.74 (m, 4H), 7.71 (d, $J = 7.3$ Hz, 1H), 7.59 (t, $J = 3.0$ Hz, 1H), 7.26 (d, $J = 4.9$ Hz, 1H), 6.88 (d, $J = 8.5$ Hz, 2H), 6.63 (dd, $J = 3.6, 1.8$ Hz, 1H), 6.58 (d, $J = 8.4$ Hz, 2H), 4.79 (t, $J = 5.3$ Hz, 1H), 3.38 – 3.33 (m, 1H), 3.25 (p, $J = 6.1$ Hz, 2H), 2.75 (dd, $J = 13.7, 5.5$ Hz, 1H), 2.40 (dd, $J = 13.7, 6.9$ Hz, 1H).

¹³C NMR (DMSO-*d*₆, 126 MHz): $\delta = 155.7, 149.2, 143.0, 141.8, 141.4, 138.7, 130.1, 128.6, 128.4, 127.2, 126.9, 117.2, 114.9, 114.5, 98.9, 62.9, 57.5, 36.3$.

MS (ESI): $m/z = 424.13$ ([M + H]⁺).

HRMS (ESI): calcd. 423.13, found 424.1326 ([M + H]⁺).

5.2.54. (*R*)-*N*-(1-hydroxy-3-(4-hydroxyphenyl)propan-2-yl)-4-(1*H*-pyrrolo[2,3-*b*]-pyridin-4-yl)benzenesulfonamide (**19d**)



$C_{22}H_{21}N_3O_4S$: 423.49 g/mol

Starting from **18d**, the synthesis of **19d** was performed by following *General Procedure B*. Purification was performed by column chromatography using a 10:1:0.1 mixture of DCM/MeOH/10% aq. NH_4OH (25%) in MeOH. Yield: 26%, colorless solid.

HPLC (VWD): $t_R = 1.566$ min (95%).

1H NMR (DMSO- d_6 , 500 MHz): $\delta = 11.87$ (s, 1H), 9.10 (d, $J = 1.3$ Hz, 1H), 8.33 (d, $J = 4.9$ Hz, 1H), 7.86 – 7.80 (m, 2H), 7.79 – 7.73 (m, 2H), 7.67 (d, $J = 7.0$ Hz, 1H), 7.59 (t, $J = 2.9$ Hz, 1H), 7.26 (dd, $J = 5.0, 1.4$ Hz, 1H), 6.87 (d, $J = 7.1$ Hz, 2H), 6.63 (q, $J = 3.5, 1.6$ Hz, 1H), 6.57 (d, $J = 8.4$ Hz, 2H), 4.75 (t, $J = 5.2$ Hz, 1H), 3.31 – 3.15 (m, 3H), 2.74 (dd, $J = 13.7, 5.4$ Hz, 1H), 2.40 (dd, $J = 13.8, 6.8$ Hz, 1H).

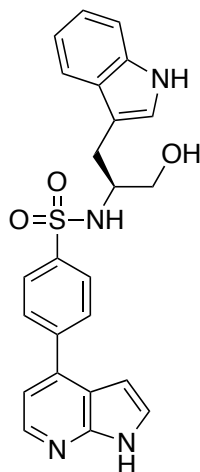
^{13}C NMR (DMSO- d_6 , 126 MHz): $\delta = 155.6, 149.1, 142.9, 141.7, 141.3, 138.6, 130.1, 128.6, 128.4, 127.1, 126.9, 117.2, 114.9, 114.4, 98.8, 62.8, 57.4, 36.3$.

^{13}C NMR (DMSO- d_6 , 126 MHz, DEPT): $\delta = 142.9, 130.1, 128.6, 127.1, 126.9, 114.9, 114.4, 98.8, 62.8, 36.3$.

MS (ESI): $m/z = 424.13$ ($[M + H]^+$).

HRMS (ESI): calcd. 423.13, found 424.1328 ($[M + H]^+$).

5.2.55. (S)-N-(1-hydroxy-3-(1H-indol-3-yl)propan-2-yl)-4-(1H-pyrrolo[2,3-b]pyridin-4-yl)benzenesulfonamide (19e)



$C_{24}H_{22}N_4O_3S$: 446.53 g/mol

Starting from **18e**, the synthesis of **19e** was performed by following *General Procedure B*. Purification was performed by column chromatography using a 20:1:0.1 mixture of DCM/MeOH/10% aq. NH_4OH (25%) in MeOH. Yield: 60%, beige solid.

HPLC (DAD): $t_R = 3.450$ min (96%).

1H NMR (DMSO- d_6 , 500 MHz): $\delta = 11.85$ (s, 1H), 10.69 (s, 1H), 8.32 (d, $J = 4.9$ Hz, 1H), 7.79 – 7.73 (m, 4H), 7.70 (d, $J = 6.5$ Hz, 1H), 7.57 (t, $J = 2.9$ Hz, 1H), 7.31 (d, $J = 7.9$ Hz, 1H), 7.20 (dd, $J = 7.0, 5.3$ Hz, 2H), 7.07 (d, $J = 1.8$ Hz, 1H), 6.93 (td, $J = 8.1, 1.3$ Hz, 1H), 6.86 (t, $J = 7.4$ Hz, 1H), 6.59 (dd, $J = 3.4, 1.7$ Hz, 1H), 4.74 (s, 1H), 3.42 – 3.38 (m, 2H), 3.37 – 3.26 (m, 2H), 2.97 (dd, $J = 14.3, 6.4$ Hz, 1H), 2.67 (dd, $J = 14.3, 6.0$ Hz, 1H).

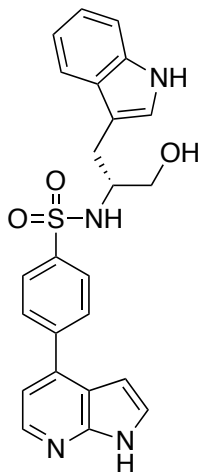
^{13}C NMR (DMSO- d_6 , 126 MHz): $\delta = 149.1, 142.8, 141.6, 141.2, 138.6, 136.1, 128.4, 127.2, 127.1, 126.8, 123.8, 120.7, 118.1, 118.0, 117.1, 114.4, 111.3, 110.4, 98.9, 62.9, 56.2, 27.06$.

^{13}C NMR (DMSO- d_6 , 126 MHz, DEPT): $\delta = 142.9, 128.4, 127.1, 126.8, 123.8, 120.7, 118.1, 118.0, 114.4, 111.3, 98.9, 62.9, 56.2, 27.1$.

MS (ESI): $m/z = 447.15$ ($[M + H]^+$).

HRMS (ESI): calcd. 446.14, found 447.1484 ($[M + H]^+$).

5.2.56. (R)-N-(1-hydroxy-3-(1H-indol-3-yl)propan-2-yl)-4-(1H-pyrrolo[2,3-b]pyridin-4-yl)benzenesulfonamide (19f)



C₂₄H₂₂N₄O₃S: 446.53 g/mol

Starting from **18f**, the synthesis of **19f** was performed by following *General Procedure B*. Purification was performed by column chromatography using a 20:1:0.1 mixture of DCM/MeOH/10% aq. NH₄OH (25%) in MeOH. Yield: 62%, beige solid.

HPLC (VWD): $t_R = 2.539$ min (98%).

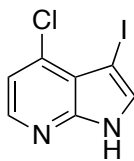
¹H NMR (DMSO-*d*₆, 500 MHz): $\delta = 11.86$ (s, 1H), 10.71 (s, 1H), 8.33 (d, $J = 4.9$ Hz, 1H), 7.79 – 7.74 (m, 4H), 7.71 (d, $J = 7.0$ Hz, 1H), 7.58 (dd, $J = 3.5, 2.6$ Hz, 1H), 7.32 (d, $J = 7.0$ Hz, 1H), 7.22 (d, $J = 4.9$ Hz, 1H), 7.20 (d, $J = 8.2$ Hz, 1H), 7.08 (d, $J = 2.3$ Hz, 1H), 6.94 (ddd, $J = 8.1, 7.0, 1.1$ Hz, 1H), 6.87 (ddd, $J = 7.9, 7.0, 1.0$ Hz, 1H), 6.60 (dd, $J = 3.5, 1.9$ Hz, 1H), 4.76 (t, $J = 5.4$ Hz, 1H), 3.41 – 3.37 (m, 2H), 3.32 – 3.29 (m, 1H), 2.98 (dd, $J = 14.3, 6.5$ Hz, 1H), 2.67 (dd, $J = 14.3, 6.2$ Hz, 1H).

¹³C NMR (DMSO-*d*₆, 126 MHz): $\delta = 149.2, 142.9, 141.6, 141.2, 138.6, 136.1, 128.4, 127.2, 127.1, 126.8, 123.8, 120.7, 118.1, 118.0, 117.1, 114.4, 111.3, 110.4, 98.9, 62.9, 56.2, 27.0$.

MS (ESI): $m/z = 893.29$ ([2M + H]⁺), 447.15 ([M + H]⁺).

HRMS (ESI): calcd. 446.14, found 447.1485 ([M + H]⁺).

5.2.57. 4-chloro-3-iodo-1*H*-pyrrolo[2,3-*b*]pyridine (**21**)



C₇H₄ClIN₂: 278.48 g/mol

To 4-chloro-1*H*-pyrrolo[2,3-*b*]pyridine (**20**, 1.00 g, 6.55 mmol) in 2.5 mL DMF, was added *N*-iodosuccinimide (1.62 g, 7.21 mmol) and the mixture was stirred for 30 minutes at ambient temperature. The product was recrystallized from DMF through the addition of 100 mL of ice-cold water to yield **21** (1.55 g, 98%) as a beige solid.

HPLC (DAD): $t_R = 9.486$ min (94%).

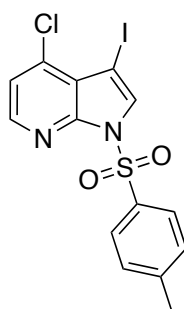
¹H NMR (DMSO-*d*₆, 500 MHz): $\delta = 12.43$ (s, 1H), 8.18 (d, $J = 5.1$ Hz, 1H), 7.80 (d, $J = 1.8$ Hz, 1H), 7.18 (d, $J = 5.1$ Hz, 1H).

¹³C NMR (DMSO-*d*₆, 126 MHz): $\delta = 148.4, 143.7, 134.8, 133.0, 116.9, 116.3, 49.6$.

¹³C NMR (DMSO-*d*₆, 126 MHz, DEPT): $\delta = 143.67, 133.0, 116.9$.

MS (EI): $m/z = 278.92$ ([M + H]⁺).

5.2.58. 4-chloro-3-iodo-1-tosyl-1*H*-pyrrolo[2,3-*b*]pyridine (**22**)



C₁₄H₁₀ClIN₂O₂S: 432.66 g/mol

To a solution of **21** (1.00 g, 3.59 mmol) in 70 mL DCM were added tetrabutylammonium chloride (29.9 mg, 0.10 mmol) and 30 mL 4N NaOH and the biphasic mixture was stirred for 14 h at room temperature. After dilution with 30 mL DCM, 30 mL of water were added and the phases were separated. The organic layer was washed with 10% HCl (20 mL), water (3 x 20 mL) and brine (20 mL) and dried over NaSO₄. The solvent was removed under reduced pressure to give **3a** (47 mg, 42%) as a colorless solid.

HPLC (DAD): $t_R = 6.748$ min (95%).

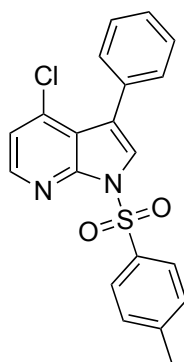
¹H NMR (DMSO-*d*₆, 500 MHz): $\delta = 8.33$ (d, $J = 5.2$ Hz, 1H), 8.21 (s, 1H), 8.04 – 8.00 (m, 2H), 7.43 – 7.40 (m, 3H), 2.33 (s, 3H).

¹³C NMR (DMSO-*d*₆, 126 MHz): $\delta = 146.1, 145.9, 145.7, 136.6, 133.8, 132.2, 130.1, 127.9, 120.6, 118.9, 21.1$.

¹³C NMR (DMSO-*d*₆, 126 MHz, DEPT): $\delta = 145.7, 132.2, 130.1, 127.9, 120.6, 21.1$.

MS (ESI): $m/z = 432$ ([M]⁺), 277 ([M-Tos]⁺).

5.2.59. 4-chloro-3-phenyl-1-tosyl-1*H*-pyrrolo[2,3-*b*]pyridine (**23a**)



C₂₀H₁₅ClN₂O₂S: 382.86 g/mol

To a solution of **22** (130 mg, 0.30 mmol) in 5 mL 1,4-dioxane were added 1.2 mL water, caesium carbonate (293 mg, 0.90 mmol), phenylboronic acid (37 mg, 0.30 mmol) and tetrakis(triphenylphosphine)palladium (17 mg, 15 μ mol), under argon atmosphere. The reaction mixture was heated to 120 °C for 20 min under stirring in a microwave reactor. After cooling to ambient temperature 15 mL of ethyl acetate and were added, the suspension was filtered through Celite and the organic layer was washed with water (3 x 15 mL) and brine (15 mL) before drying over Na₂SO₄. The solvent was removed under reduced pressure to give the crude product as reddish-brown oil. Purification was performed by column chromatography using a 10:1 mixture of cyclohexane/EtOAc to give **23a** (88 mg, 77%) as a reddish brown solid.

HPLC (DAD): $t_R = 9.878$ min.

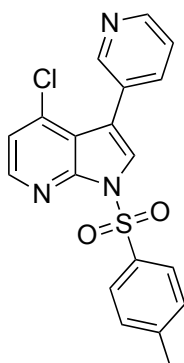
¹H NMR (CDCl₃, 500 MHz): $\delta = 8.24$ (d, $J = 5.2$ Hz, 1H), 8.06 – 8.01 (m, 2H), 7.66 (s, 1H), 7.41 – 7.36 (m, 2H), 7.35 – 7.28 (m, 3H), 7.25 – 7.20 (m, 2H), 7.10 (d, $J = 5.2$ Hz, 1H), 2.31 (s, 3H).

¹³C NMR (CDCl₃, 126 MHz): $\delta =$ ¹³C NMR (126 MHz, CDCl₃) $\delta = 145.55, 145.05, 137.23, 135.11, 132.28, 130.38, 129.73, 129.00, 128.33, 127.84, 127.57, 125.00, 120.31, 21.67.$

¹³C NMR (CDCl₃, 126 MHz, DEPT): $\delta = 145.1, 130.34, 129.7, 129.0, 128.3, 127.8, 125.0, 120.3, 21.7.$

MS (EI): $m/z = 382$ ([M]⁺), 227 ([M-Tos]⁺).

5.2.60. 4-chloro-3-(pyridin-3-yl)-1-tosyl-1*H*-pyrrolo[2,3-*b*]pyridine (**23b**)



C₁₉H₁₅ClN₃O₂S: 383.85 g/mol

To a solution of **22** (433 mg, 1.00 mmol) in 15 mL 1,4-dioxane were added 3.8 mL water, caesium carbonate (977 mg, 3.00 mmol), 4-pyridinylboronic acid (123 mg, 1.00 mmol) and tetrakis(triphenylphosphine)palladium (58 mg, 50 μ mol), under argon atmosphere. The reaction mixture was heated to 120 °C for 40 min under stirring in a microwave reactor and then for 16h at 120 °C under stirring using conventional heating. After cooling to ambient temperature 45 mL of ethyl acetate were added, the suspension was filtered through Celite and the organic layer was washed with water (3 x 45 mL) and brine (45 mL) before drying over Na₂SO₄. The solvent was removed under reduced pressure to give the crude product as orange brown oil. Purification was performed by column chromatography using a 1:1 mixture of cyclohexane/EtOAc to give **23b** (88 mg, 23%) as a reddish-brown solid.

HPLC (DAD): $t_R = 4.489$ min.

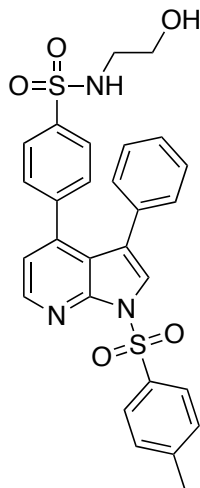
¹H NMR (CDCl₃, 500 MHz): $\delta = 8.73$ (dd, $J = 2.2, 0.9$ Hz, 1H), 8.63 (dd, $J = 4.9, 1.7$ Hz, 1H), 8.35 (d, $J = 5.2$ Hz, 1H), 8.18 (d, $J = 5.2$ Hz, 1H), 8.13 (d, $J = 8.4$ Hz, 2H), 7.80 (s, 1H), 7.35 (ddd, $J = 7.8, 4.9, 0.9$ Hz, 1H), 7.31 (d, $J = 8.0$ Hz, 2H), 7.20 (d, $J = 5.2$ Hz, 1H), 2.39 (s, 3H).

¹³C NMR (CDCl₃, 126 MHz): $\delta = 150.4, 148.9, 147.7, 145.5, 142.6, 137.8, 137.1, 134.8, 129.8, 128.4, 125.5, 122.8, 120.4, 116.1, 21.7$.

¹³C NMR (CDCl₃, 126 MHz, DEPT): δ = 150.4, 148.9, 145.5, 137.8, 129.8, 128.4, 122.8, 120.4, 116.0, 21.7.

MS (ESI): m/z = 384.06 ([M+H]⁺).

5.2.61. *N*-(2-hydroxyethyl)-4-(3-phenyl-1-tosyl-1*H*-pyrrolo[2,3-*b*]pyridin-4-yl)benzenesulfonamide (**24a**)



$C_{28}H_{25}N_3O_5S_2$: 547.64 g/mol

To a solution of **23a** (153 mg, 0.40 mmol) in 4.95 mL 1,4-dioxane were added 50 μ L water, caesium carbonate (261 mg, 0.80 mmol), boronic ester **26** (196 mg, 0.60 mmol) and $PdCl_2(dtbpf)$ (5.2 mg, 8 μ mol), under argon atmosphere. The reaction mixture was heated to 100 $^{\circ}C$ for 6.5 h under stirring and 15 mL of ethyl acetate and were added after the solution was cooled to ambient temperature. The reaction mixture was filtered through Celite and the organic layer was washed with water (3 x 10 mL) and brine (10 mL) before drying over Na_2SO_4 . The solvent was removed under reduced pressure to give the crude product as a brown solid. Purification was performed by column chromatography using a 25:1 mixture of DCM/MeOH/10% aq. NH_4OH (25%) in MeOH to give **23b** (90 mg, 41%) as a beige solid.

HPLC (DAD): $t_R = 7.316$ min (96%).

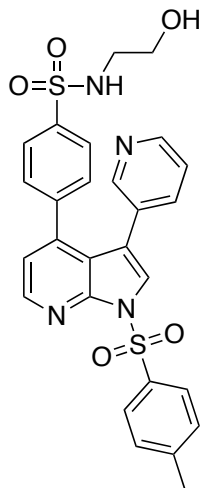
1H NMR ($CDCl_3$, 500 MHz): $\delta = 8.51$ (d, $J = 4.9$ Hz, 1H), 8.16 (d, $J = 8.4$ Hz, 2H), 7.78 (s, 1H), 7.53 (d, $J = 8.0$ Hz, 2H), 7.32 (d, $J = 8.2$ Hz, 2H), 7.16 – 7.08 (m, 4H), 7.01 (t, $J = 7.6$ Hz, 2H), 6.87 – 6.82 (m, 2H), 5.49 (s, 1H), 3.74 (t, $J = 4.9$ Hz, 2H), 3.08 – 3.00 (m, 2H), 2.39 (s, 3H).

¹³C NMR (CDCl₃, 126 MHz): δ = 147.8, 145.6, 145.0, 142.7, 141.6, 139.1, 135.3, 133.0, 129.9, 129.7, 129.1, 128.4, 127.9, 127.3, 126.4, 124.8, 120.9, 120.0, 118.9, 61.4, 45.4, 21.8.

¹³C NMR (CDCl₃, 126 MHz, DEPT): δ = 145.0, 129.9, 129.7, 129.1, 128.4, 127.9, 127.3, 126.4, 124.8, 119.9, 61.4, 45.4, 21.8.

MS (ESI): m/z = 548.13 ([M+H]⁺).

5.2.62. *N*-(2-hydroxyethyl)-4-(3-(pyridin-3-yl)-1-tosyl-1H-pyrrolo[2,3-*b*]pyridin-4-yl)benzene sulfonamide (**24b**)



$C_{27}H_{25}N_4O_5S_2$: 548.63 g/mol

To a solution of **23b** (170 mg, 0.44 mmol) in 4.95 mL 1,4-dioxane were added 50 μ L water, caesium carbonate (289 mg, 0.89 mmol), boronic ester **26** (217 mg, 0.66 mmol) and $PdCl_2(dtbpf)$ (8.6 mg, 13 μ mol), under argon atmosphere. The reaction mixture was heated to 100 $^{\circ}C$ for 24 h under stirring and 15 mL of ethyl acetate and were added after the solution was cooled to ambient temperature. The reaction mixture was filtered through Celite and the organic layer was washed with water (3 x 10 mL) and brine (10 mL) before drying over Na_2SO_4 . The solvent was removed under reduced pressure to give the crude product as a brown solid. Purification was performed by column chromatography using a step gradient from a 30:1 to a 15:1 mixture of DCM/MeOH/10% aq. NH_4OH (25%) in MeOH to give **23b** (116 mg, 48%) as a beige solid.

HPLC (DAD): $t_R = 4.746$ min (95%).

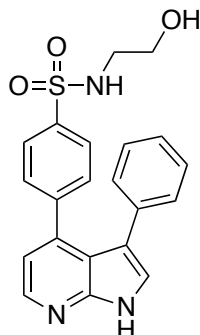
1H NMR ($CDCl_3$, 500 MHz): $\delta = 8.55$ (d, $J = 4.9$ Hz, 1H), 8.30 – 8.25 (m, 1H), 8.17 (d, $J = 8.4$ Hz, 2H), 7.87 (s, 1H), 7.66 (dt, $J = 7.9, 1.7$ Hz, 1H), 7.63 (s, 1H), 7.61 (d, $J = 4.0$ Hz, 2H), 7.32 (d, $J = 8.2$ Hz, 2H), 7.28 (dd, $J = 7.9, 4.8$ Hz, 1H), 7.19 (d, $J = 4.9$ Hz, 1H), 7.14 (d, $J = 8.1$ Hz, 2H), 5.54 (t, $J = 5.5$ Hz, 1H), 3.64 (t, $J = 5.0$ Hz, 2H), 3.12 (q, $J = 5.2$ Hz, 2H), 2.39 (s, 3H).

¹³C NMR (CDCl₃, 126 MHz): δ = 149.3, 147.6, 147.0, 145.9, 145.5, 142.5, 141.2, 140.3, 136.6, 135.5, 135.0, 129.9, 129.8, 128.6, 126.8, 125.9, 124.0, 120.2, 118.1, 116.5, 60.2, 46.0, 21.8.

¹³C NMR (CDCl₃, 126 MHz, DEPT): δ = 149.3, 147.0, 145.5, 136.6, 129.9, 129.8, 128.6, 126.8, 125.9, 124.0, 120.2, 60.2, 46.0, 21.8.

MS (ESI): *m/z* = 549.13 ([M+H]⁺).

5.2.63. *N*-(2-hydroxyethyl)-4-(3-phenyl-1H-pyrrolo[2,3-*b*]pyridin-4-yl)benzenesulfonamide
(25a)



C₂₁H₁₉N₃O₃S: 393.46 g/mol

To a solution of **24a** (88 mg, 0.16 mmol) in 4 mL THF was added tetrabutylammonium fluoride trihydrate (203 mg, 0.64 mmol) and the reaction mixture was heated to 60 °C for 1 h under stirring in a microwave reactor. 15 mL of ethyl acetate were added after the solution was cooled to ambient temperature and the reaction mixture was washed with water (5 x 10 mL) and brine (10 mL) before drying over MgSO₄. The solvent was removed under reduced pressure to give the crude product as a brown solid. Purification was performed by automated reversed-phase flash chromatography using a prepacked 13 g *TELOS Reversed-Phase C18(EC)* cartridge (*Kinesis GmbH*) and employing a linear gradient of 25% acetonitrile (0.1% trifluoroacetic acid), 75% water (0.1% trifluoroacetic acid) to 100% acetonitrile (0.1% trifluoroacetic acid) over 0.5 h at 30 mL/min. Product containing fractions were lyophilized to give **25a** (9 mg, 14%) as a yellow solid.

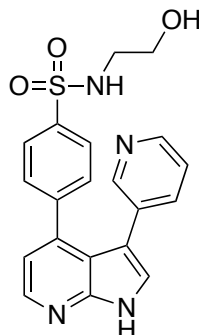
HPLC (DAD): $t_R = 3.744$ min (96%).

¹H NMR (DMSO-*d*₆, 500 MHz): $\delta = 12.11$ (s, 1H), 8.37 (d, $J = 4.8$ Hz, 1H), 7.65 (d, $J = 2.6$ Hz, 1H), 7.57 (t, $J = 6.0$ Hz, 1H), 7.50 (d, $J = 8.0$ Hz, 2H), 7.31 (d, $J = 7.9$ Hz, 2H), 7.12 (d, $J = 4.8$ Hz, 1H), 7.04 (d, $J = 7.2$ Hz, 1H), 7.00 (t, $J = 7.4$ Hz, 1H), 6.88 (d, $J = 7.4$ Hz, 2H), 3.44 (t, $J = 6.5$ Hz, 2H), 2.75 (q, $J = 6.3$ Hz, 2H).

¹³C NMR (DMSO-*d*₆, 126 MHz): $\delta = 149.3, 142.7, 142.1, 140.5, 139.1, 134.9, 129.4, 128.8, 127.3, 125.7, 125.6, 125.5, 116.6, 115.6, 114.5, 97.8, 59.9, 45.0$.

MS (ESI): $m/z = 394.12$ ([M+H]⁺).

5.2.64. *N*-(2-hydroxyethyl)-4-(3-(pyridin-3-yl)-1H-pyrrolo[2,3-*b*]pyridin-4-yl)benzenesulfonamide (**25b**)



C₂₁H₁₉N₃O₃S: 393.46 g/mol

To a solution of **24b** (144 mg, 0.26 mmol) in 6 mL THF was added tetrabutylammonium fluoride trihydrate (331 mg, 1.05 mmol) and the reaction mixture was heated to 60 °C for 1 h under stirring in a microwave reactor. 20 mL of ethyl acetate were added after the solution was cooled to ambient temperature and the reaction mixture was washed with water (5 x 15 mL) and brine (15 mL) before drying over MgSO₄. The solvent was removed under reduced pressure to give the crude product as a brown solid. Purification was performed by automated reversed-phase flash chromatography using a prepacked 13 g *TELOS Reversed-Phase C18(EC)* cartridge (*Kinesis GmbH*) and employing a linear gradient of 15% acetonitrile (0.1% trifluoroacetic acid), 75% water (0.1% trifluoroacetic acid) to 80% acetonitrile (0.1% trifluoroacetic acid), 20% water (0.1% trifluoroacetic acid) over 0.5 h at 30 mL/min. Product containing fractions were lyophilized to give **25b** (22 mg, 21%) as a beige solid that contained uncharacterized impurities.

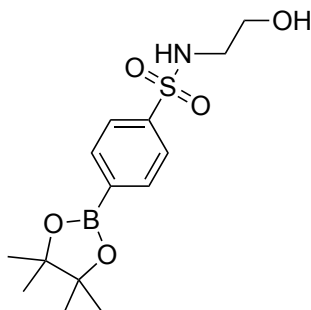
HPLC (DAD): $t_R = 2.895$ min (87%).

¹H NMR (DMSO-*d*₆, 500 MHz): $\delta = 12.26$ (s, 1H), 8.39 (d, $J = 4.9$ Hz, 1H), 8.24 (d, $J = 4.8$ Hz, 1H), 8.15 (s, 1H), 7.78 (d, $J = 2.7$ Hz, 1H), 7.58 (t, $J = 6.0$ Hz, 1H), 7.54 (d, $J = 7.9$ Hz, 2H), 7.48 (d, $J = 7.7$ Hz, 1H), 7.33 (d, $J = 7.9$ Hz, 2H), 7.18 (d, $J = 7.8$ Hz, 1H), 7.14 (d, $J = 4.7$ Hz, 1H), 7.11 (d, $J = 7.7$ Hz, 1H), 7.00 (dd, $J = 7.8, 4.8$ Hz, 1H), 4.78 (s, 1H), 3.45 (d, $J = 6.5$ Hz, 2H), 2.78 (q, $J = 6.2$ Hz, 2H).

¹³C NMR (DMSO-*d*₆, 126 MHz): δ = 149.4, 149.1, 146.4, 143.1, 141.8, 140.4, 139.5, 135.7, 130.8, 129.5, 126.0, 125.5, 122.3, 116.8, 114.6, 111.9, 59.9, 45.1.

MS (ESI): m/z = 395.12 ([M+H]⁺).

5.2.65. *N*-(2-hydroxyethyl)-4-(4,4,5,5-tetramethyl-1,3,2-dioxaborolan-2-yl)-benzenesulfonamide (26)



C₁₄H₂₂BNO₅S: 327.20 g/mol

To a solution of sulfonamide **2f** (500 mg, 1.78 mmol) in 3.5 mL DMF were added potassium acetate (526 mg, 5.35 mmol), bis(pinacolato)diboron (544mg, 2.14 mmol) and PdCl₂(dppf) (39 mg, 54 μmol), under argon atmosphere. The reaction mixture was stirred at 100 °C for 2 h. After cooling to ambient temperature 50 mL of ethyl acetate were added, the solution was filtered through Celite and the organic layer was washed with brine (5 x 15 mL) before drying over Na₂SO₄. The solvent was removed under reduced pressure to give the corresponding boronic acid pinacolester as a crude solid that was purified by column chromatography using a 20:1:0.1 mixture of DCM/MeOH/10% aq. NH₄OH (25%) in MeOH to give **26** (169 mg, 29%) as a colorless solid.

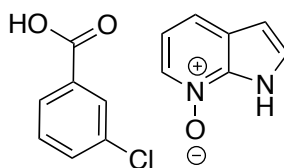
HPLC (DAD): t_R = 2.797 min.

¹H NMR (DMSO-*d*₆, 500 MHz): δ = 7.88 – 7.83 (m, 2H), 7.83 – 7.78 (m, 2H), 7.64 (t, *J* = 5.9 Hz, 1H), 3.35 (q, *J* = 6.2 Hz, 2H), 2.78 (q, *J* = 6.2 Hz, 2H), 1.31 (s, 12H).

¹³C NMR (DMSO-*d*₆, 126 MHz): δ = 143.1, 134.9, 125.7, 84.2, 73.5, 59.8, 45.0, 39.5, 24.91.

MS (ESI): *m/z* = 328.14 ([M+H]⁺).

5.2.66. 1*H*-pyrrolo[2,3-*b*]pyridine 7-oxide 3-chlorobenzoic acid salt (**29**)



C₁₄H₁₁ClN₂O₃: 290.70 g/mol

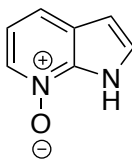
To a solution of 7-azaindole (**28**, 316 mg, 2.54 mmol) in 32 mL diethylether were added mCPBA (1.00 g, 4.06 mmol) and the reaction mixture was stirred at ambient temperature for 5 h. A yellowish solid precipitated, which was filtrated and washed with cold diethylether (3x 5 mL). After drying, target compound **29** (634 mg, 86%) was obtained as a yellowish solid.

HPLC (VWD): $t_R = 1.055$ min (*N*-oxide); $t_R = 3.284$ min (mCBA).

¹H NMR (DMSO-*d*₆, 300 MHz): $\delta = 13.34$ (s, 1H), 8.13 (d, $J = 6.1$ Hz, 1H), 7.79 (m, 2H), 7.70 (m, 1H), 7.64 (d, $J = 7.8$ Hz, 1H), 7.55 (t, $J = 8.1$ Hz, 1H), 7.45 (d, $J = 3.2$ Hz, 1H), 7.06 (t, $J = 7.8$ Hz, 1H), 6.58 (d, $J = 3.2$ Hz, 1H).

The acquired spectral data is in line with the published literature.²⁸¹

5.2.67. 1*H*-pyrrolo[2,3-*b*]pyridine 7-oxide (30)



C₇H₆N₂O: 134.14 g/mol

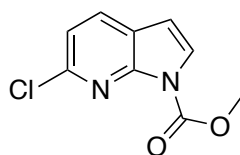
A suspension of 7-azaindole *N*-oxide mCBA salt (**29**, 634 mg, 2.18 mmol) in 15 mL water was charged with saturated potassium carbonate solution until the pH was set to 9 and the suspension was stirred at 0 °C for 2h. A colorless solid precipitated, which was filtrated and washed with ice-cold water (3 mL). After drying under vacuum, target compound **30** (221 mg, 76%) was obtained as a colorless solid.

HPLC (VWD): $t_R = 1.045$ min (96%).

¹H NMR (DMSO-*d*₆, 300 MHz): $\delta = 8.12$ (d, $J = 6.2$ Hz, 1H), 7.64 (d, $J = 8.0$ Hz, 1H), 7.44 (d, $J = 3.3$ Hz, 1H), 7.06 (t, $J = 7.1$ Hz, 1H), 6.58 (d, $J = 3.2$ Hz, 1H).

The acquired spectral data is in line with the published literature.²⁸¹

5.2.68. Methyl 6-chloro-1*H*-pyrrolo[2,3-*b*]pyridine-1-carboxylate (**31**)



C₉H₇ClN₂O₂: 210.62 g/mol

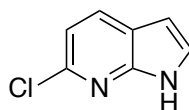
A solution of 7-azaindole *N*-oxide (**30**, 202 mg, 1.49 mmol) in 15 mL freshly distilled THF was charged with hexamethyldisilazane (HMDS) (246 mg, 1.49 mmol) under argon atmosphere and methyl chloroformate (356 mg, 3.73 mmol) was added dropwise under stirring over 30 min at ambient temperature. The solution was stirred for an additional hour at ambient temperature and the solvent was removed *in vacuo*. The crude product was taken up in 20 mL ethyl acetate, washed with water (3 x 10 mL) and brine (10 mL) and dried over MgSO₄, to give target compound **31** as crude off-white platelets that were purified by column chromatography using an 8:1 mixture of cyclohexane/ethyl acetate. Target compound **31** (185 mg, 60%) was obtained as a colorless solid.

HPLC (VWD): $t_R = 4.049$ min (95%).

¹H NMR (CDCl₃, 500 MHz): $\delta = 7.76$ (d, $J = 8.2$ Hz, 1H), 7.66 (d, $J = 4.0$ Hz, 1H), 7.17 (d, $J = 8.2$ Hz, 1H), 6.49 (d, $J = 4.1$ Hz, 1H), 4.04 (s, 3H).

The acquired spectral data is in line with the published literature.²⁸⁰

5.2.69. 6-chloro-1*H*-pyrrolo[2,3-*b*]pyridine (**32**)



C₇H₅ClN₂: 152.58 g/mol

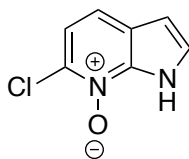
A solution of compound **31** (193 mg, 0.89 mmol) in 30 mL methanol was charged with 10 mL 1N NaOH-solution and the reaction mixture was stirred at ambient temperature for 19 h. Methanol was removed *in vacuo*, the resulting residue was diluted with 20 mL water and extracted with chloroform (3x 20 mL). The combined organic layers were washed with 10 mL brine and dried over MgSO₄, to give target compound **32** (120mg, 88%) as colorless needles.

HPLC (VWD): $t_R = 3.466$ min (96%).

¹H NMR (CDCl₃, 500 MHz): $\delta = 10.44$ (s, 1H), 7.90 (dd, $J = 8.2, 0.8$ Hz, 1H), 7.37 (dd, $J = 3.5, 2.4$ Hz, 1H), 7.11 (d, $J = 8.1$ Hz, 1H), 6.52 (dd, $J = 3.5, 2.0$ Hz, 1H).

The acquired spectral data is in line with the published literature.²⁸⁰

5.2.70. 6-chloro-1*H*-pyrrolo[2,3-*b*]pyridine 7-oxide (**33**)



C₇H₅ClN₂O: 168.58 g/mol

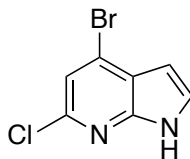
To a solution of 6-chloro-7-azaindole (**32**, 300 mg, 1.97 mmol) in 25 mL *n*-butyl acetate and 15 mL *n*-heptane was added mCPBA (773 mg, 3.15 mmol) and the reaction mixture was stirred at ambient temperature for 19 h. A brown solid precipitated, which was filtrated and washed with cold *n*-heptane (3x 5 mL). The precipitated 6-chloro-7-azaindole *N*-oxide mCBA salt was suspended in 10 mL water, charged with saturated potassium carbonate solution until the pH was set to 9 and the suspension was stirred at 0 °C for 2h. A beige solid precipitated, which was filtrated and washed with ice-cold water (3 mL). After drying under vacuum, target compound **33** (136 mg, 41%) was obtained as a beige solid.

HPLC (VWD): $t_R = 1.233$ min (93%).

¹H NMR (DMSO-*d*₆, 500 MHz): $\delta = 8.65$ (s, 1H), 7.78 (d, $J = 7.8$ Hz, 1H), 6.76 (d, $J = 7.8$ Hz, 1H), 6.64 – 6.53 (m, 1H), 4.95 (s, 1H).

MS (ESI): $m/z = 169.02$ ([M+H]⁺); 152.01 ([M-O]⁺).

5.2.71. 4-bromo-6-chloro-1*H*-pyrrolo[2,3-*b*]pyridine (**34**)



C₇H₄BrClN₂: 231.48 g/mol

A solution of 4-bromo-7-azaindole *N*-oxide (**36**, 255 mg, 1.17 mmol) in phosphoryl chloride (6.30 g, 41.1 mmol) was stirred at 55 °C for 30 min. The heating source was removed and the resulting suspension was stirred for 30 min before being heated to 85 °C under stirring for an additional 2 h, whereupon the suspension turned clear. After being allowed to cool to ambient temperature, the reaction mixture was quenched by addition of 300 mL ice-cold water and the pH was set to 9 by careful addition of sodium carbonate. The resulting biphasic mixture was extracted with dichloromethane (3 x 100 mL). The combined organic layers were washed with brine (1 x 50 mL), dried over MgSO₄ and the solvent was removed under reduced pressure to give the crude product. Purification was performed by column chromatography using a 200:1 mixture of cyclohexane/ethyl acetate to give **34** (109 mg, 42%) as a beige solid.

HPLC (VWD): $t_R = 5.281$ min (94%).

¹H NMR (DMSO-*d*₆, 500 MHz): $\delta =$ ¹H NMR (500 MHz, DMSO-*d*₆) δ 12.24 (s, 1H), 7.62 (dd, $J = 3.5, 1.4$ Hz, 1H), 7.45 (s, 1H), 6.46 (d, $J = 3.4$ Hz, 1H).

¹³C NMR (DMSO-*d*₆, 126 MHz): $\delta = 146.5, 142.7, 127.9, 125.3, 119.9, 117.5, 100.0$.

¹³C NMR (DMSO-*d*₆, 126 MHz, DEPT): $\delta = 127.9, 117.5, 100.0$.

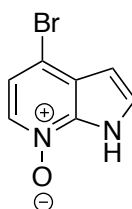
IR (ATR): 1560.11 cm⁻¹ (N-H, *d*); 1405.72 cm⁻¹ (C=C and C=N in-plane vibrations); 1235.56 cm⁻¹ (Ar-Cl, ring and C-Cl *d*); 1103.64 cm⁻¹ (pyrrole, N-H and C-H *d*); 827.77 cm⁻¹ (4-subst. pyridine C-H, *d*); 600.23 cm⁻¹ (Ar-Br, ν_s and ring *d*).

MS (ESI): $m/z = 230.93$ ([M+H]⁺).

Melting point: 186 - 189 °C.

The characterization was supported by 2D-NMR analysis (COSY, HMBC, HSQC) and the acquired spectral data is in line with the published literature.³⁵⁷

5.2.72. 4-bromo-1*H*-pyrrolo[2,3-*b*]pyridine 7-oxide (36)



C₇H₅BrN₂O: 213.03 g/mol

To a solution of 4-bromo-7-azaindole (**35**, 500 mg, 2.54 mmol) in 40 mL diethyl ether mCPBA (1.00 g, 4.06 mmol) was added in portions under cooling in an ice-bath and the reaction mixture was allowed to warm to ambient temperature. The reaction mixture was stirred at ambient temperature for 3 h, whereupon a yellowish solid precipitated. The precipitate was filtrated, washed with cold diethylether (3x 5 mL) and dried through an applied air stream. The filtered 4-bromo-7-azaindole *N*-oxide mCBA salt was suspended in 20 mL water, charged with saturated potassium carbonate solution until the pH was set to 9 and the suspension was stirred at 0 °C for 2h. An off-white solid precipitated, which was filtrated and washed with ice-cold water (3 mL). After drying under vacuum, target compound **36** (502 mg, 91%) was obtained as an off-white solid.

HPLC (VWD): $t_R = 1.660$ min (98%).

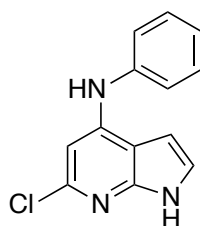
¹H NMR (DMSO-*d*₆, 500 MHz): $\delta = 12.88$ (s, 1H), 8.08 (d, $J = 6.6$ Hz, 1H), 7.56 (d, $J = 3.3$ Hz, 1H), 7.32 (d, $J = 6.6$ Hz, 1H), 6.50 (d, $J = 3.3$ Hz, 1H).

¹³C NMR (DMSO-*d*₆, 126 MHz): $\delta = 138.1, 131.9, 127.4, 124.2, 118.9, 111.7, 102.1$.

MS (ESI): $m/z = 212.69$ ($[M+H]^+$).

Melting point: 179 °C.

5.2.73. 6-chloro-*N*-phenyl-1*H*-pyrrolo[2,3-*b*]pyridin-4-amine (39)



$C_{13}H_{10}ClN_3$: 243.69 g/mol

A flame-dried 25 mL Schlenk tube was charged with 4-bromo-6-chloro-7-azaindole (**34**, 144 mg, 0.62 mmol), aniline (**37**, 145 mg, 1.56 mmol), caesium carbonate (405 mg, 1.24 mmol), $Pd_2(dba)_3$ (46 mg, 49.8 μ mol), Xanthphos (**38**, 58 mg, 99.5 μ mol) and 5 mL dried and degassed toluene and the reaction mixture was stirred at 100 °C for 6 h. After cooling to ambient temperature 10 mL of toluene were added, the solution was filtered through Celite and the organic layer was washed with water (3 x 10 mL). The organic layer was diluted with 15 mL acetonitrile before drying over Na_2SO_4 and the solvent was removed under reduced pressure to give a crude brown solid. Purification was performed by column chromatography using a 1:1 mixture of cyclohexane/ethyl acetate to give **39** (15 mg, 10%) as a colorless solid.

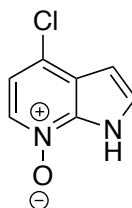
HPLC (VWD): $t_R = 4.701$ min (98%).

1H NMR (DMSO- d_6 , 500 MHz): $\delta = 11.15$ (s, 1H), 8.44 (s, 1H), 8.01 (d, $J = 6.8$ Hz, 1H), 7.39 – 7.42 (m, 2H), 7.35 (d, $J = 6.8$ Hz, 1H), 7.26 – 7.29 (m, 2H), 6.99 (t, $J = 7.4$ Hz, 1H) 6.72 (s, 1H).

^{13}C NMR (DMSO- d_6 , 126 MHz): $\delta = 151.8, 150.1, 145.9, 145.2, 129.5, 127.1, 117.8, 105.9, 102.5, 106.0, 99.2$.

MS (ESI): $m/z = 243.10$ ($[M+H]^+$).

5.2.74. 4-chloro-1*H*-pyrrolo[2,3-*b*]pyridine 7-oxide (41)



C₇H₅ClN₂O: 168.58 g/mol

To a solution of 4-chloro-7-azaindole (**40**, 600 mg, 3.94 mmol) in 25 mL *n*-butyl acetate and 15 mL *n*-heptane was added mCPBA (1.07 g, 4.32 mmol) and the reaction mixture was stirred at ambient temperature for 4 h. A colorless solid precipitated, which was filtrated and washed with cold *n*-heptane (3x 5 mL). The precipitated 4-chloro-7-azaindole *N*-oxide mCBA salt was suspended in 10 mL water, charged with saturated potassium carbonate solution until the pH was set to 9 and the suspension was stirred at 0 °C for 2h. A colorless solid precipitated, which was filtrated and washed with ice-cold water (3 mL). After drying under vacuum, target compound **41** (540 mg, 81%) was obtained as a colorless solid.

HPLC (VWD): $t_R = 1.526$ min (99%).

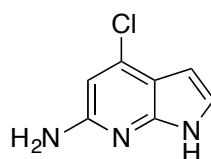
¹H NMR (DMSO-*d*₆, 500 MHz): $\delta = 12.86$ (s, 1H), 8.15 (d, $J = 6.6$ Hz, 1H), 7.98 – 7.80 (m, 1H), 7.52 (d, $J = 8.0$ Hz, 1H), 7.20 (d, $J = 6.6$ Hz, 1H).

¹³C NMR (DMSO-*d*₆, 126 MHz): $\delta = 132.6, 131.8, 130.6, 127.9, 127.4, 116.0, 100.6$.

MS (ESI): $m/z = 169.02$ ([M+H]⁺).

Melting point: 158 °C.

5.2.75. 4-chloro-1*H*-pyrrolo[2,3-*b*]pyridin-6-amine (**42**)



C₇H₆ClN₃: 167.60 g/mol

A stream of argon was passed through a solution of 4-chloro-7-azaindole *N*-oxide (**41**, 410 mg, 1.26 mmol) in 10 mL dry acetonitrile for 10 min, dimethyl sulfate (175 mg, 1.39 mmol) was dropwise added over the course of 20 min and the reaction mixture was stirred at 60 °C for 24 h. The reaction mixture was allowed to cool to ambient temperature and 3 mL of a 7M ammonia-solution in MeOH (354 mg, 20.81 mmol) were added dropwise under ice-cooling. The reaction mixture was stirred at 55 °C for 17 h and the solvent was removed under reduced pressure. The resulting crude residue was taken up in dichloromethane (30 mL) and the organic layer was washed with water (3 x 10 mL) and saturated NaHCO₃-solution (3 x 10 mL) and dried over MgSO₄. Removal of the solvent under reduced pressure gave target compound **42** as a crude amber solid, which was purified by column chromatography using a 1:3 mixture of toluene/ethyl acetate to give **42** (155 mg, 73%) as an amber solid.

HPLC (VWD): $t_R = 1.324$ min (96%).

¹H NMR (DMSO-*d*₆, 500 MHz): $\delta = 11.11$ (s, 1H), 7.00 (dd, $J = 3.5, 2.4$ Hz, 1H), 6.36 (s, 1H), 6.21 (dd, $J = 3.5, 2.0$ Hz, 1H), 5.82 (s, 2H).

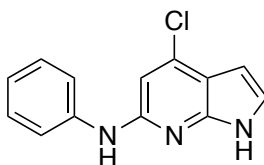
¹³C NMR (DMSO-*d*₆, 126 MHz): $\delta = 156.4, 148.3, 135.1, 121.0, 109.9, 101.7, 98.0$.

¹³C NMR (DMSO-*d*₆, 126 MHz, DEPT): $\delta = 120.7, 101.5, 97.8$.

MS (ESI): $m/z = 168.03$ ([M+H]⁺).

Melting point: 140 °C.

5.2.76. 4-chloro-N-phenyl-1H-pyrrolo[2,3-b]pyridin-6-amine (43)



$C_{13}H_{10}ClN_3$: 243.69g/mol

BUCHWALD-HARTWIG AMINATION

A flame-dried 5 mL Schlenk tube was charged with palladium(II) acetate (13 mg, 0.06 mmol), Xphos (9 mg, 0.18 mmol) and 5 mL dried and degassed toluene and the mixture was stirred at 110 °C for 15 min under argon. 6-amino-4-chloro-7-azaindole (**42**, 100 mg, 0.6 mmol), bromobenzene (94 mg, 0.6 mmol) and sodium tert-butoxide (172 mg, 1.79 mmol) were added and the reaction mixture was stirred at 110 °C under reflux for 5 h. The reaction mixture was allowed to cool to ambient temperature, 10 mL of toluene were added and the reaction mixture was filtered through Celite. The filtrate was washed with water (3 x 5 mL) and brine (1 x 5 mL) and dried over Na_2SO_4 . The solvent was removed under reduced pressure to give a crude brown semi-solid, which was purified by column chromatography using a 97:3 mixture of dichloromethane/methanol to give **43** (12 mg, 8%) as a beige solid.

CHAN-LAM-COUPLING

A flame-dried 5 mL Schlenk tube was charged with 6-amino-4-chloro-7-azaindole (**42**, 87 mg, 0.52 mmol), phenylboronic acid (127 mg, 1.04 mmol), triethylamine (105 mg, 1.04 mmol), copper(II) acetate (94 mg, 0.52 mmol), pulverized activated 4 Å molecular sieves (200 mg) and 5 mL dried dichloromethane and the reaction mixture was stirred at 40 °C under reflux for 42 h. The reaction mixture was allowed to cool to ambient temperature, 10 mL of dichloromethane were added and the reaction mixture was filtered through Celite. The filtrate was washed with 0.05 M EDTA-solution (2 x 5 mL) and sat. $NaHCO_3$ solution (3 x 5 mL) and dried over $MgSO_4$. The solvent was removed under reduced pressure to give a crude brown solid, which was purified by column chromatography using a 2:1 mixture of cyclohexane/ethyl acetate to give **43** (15 mg, 12%) as a beige solid.

HPLC (VWD): $t_R = 5.390$ min (96%).

^1H NMR (DMSO- d_6 , 500 MHz): $\delta = 11.52$ (s, 1H), 9.01 (s, 1H), 7.75 (dd, $J = 8.7, 1.1$ Hz, 2H), 7.27 (dd, $J = 8.6, 7.3$ Hz, 2H), 7.17 (dd, $J = 3.5, 2.4$ Hz, 1H), 6.88 (t, $J = 7.3$ Hz, 1H), 6.71 (s, 1H), 6.32 (dd, $J = 3.4, 2.0$ Hz, 1H).

^{13}C NMR (DMSO- d_6 , 126 MHz): $\delta = 151.9, 147.2, 141.8, 135.0, 128.5, 122.4, 120.2, 117.7, 111.2, 103.9, 98.2$.

^{13}C NMR (DMSO- d_6 , 126 MHz, DEPT): $\delta = 128.3, 122.1, 119.9, 117.4, 103.7, 98.0$.

MS (ESI): $m/z = 244.06$ ($[\text{M}+\text{H}]^+$).

5.3. Molecular Modeling

5.3.1. General Information

Molecular modeling was performed using the *Molecular Operating Environment* (Version 2016.0802, *Chemical Computing Group*, Montreal, Canada) software package, employing an ‘Amber10’ forcefield.

5.3.2. Preparation of Nek1 Crystal Structures

Isolation of the monomeric kinase domains for the Nek1 apo-form (PDB code: 4APC) and inhibitor-bound (PDB code: 4B9D) crystal structures was achieved by manual deletion of the interchain disulfide bonds using the ‘sequence editor’. Superposition of the isolated chains was performed with the “align/superpose” tool of the “sequence editor”.

ID	Dc	S...	PDB	Cl...	Templ...	Se...	Seq position
1	0.21	5k2y	3	AppKg	40.00	312-316:A	
2	0.17	3w38	3	NNSGg	40.00	495-499:A	
3	0.16	3op1	0	EDEKg	40.00	156-160:A	

Figure 48: Settings for the P-loop reconstruction of the Nek1 kinase domain crystal structure (PDB code: 4B9D.B) using the *SuperLooper2* web server (<http://proteininformatics.charite.de/ngl-tools/sl2/start.php>).²⁵⁵

Reconstruction of the glycine-rich loop (P-Loop) was performed using the *SuperLooper2* web server (<http://proteininformatics.charite.de/ngl-tools/sl2/start.php>).²⁵⁵ Starting from the crystal structure of Nek1 (PDB code: 4B9D.B), the missing loop sequence EGSFG between G11 and K17 was reconstructed by using the AGPAG loop (between P311 and R317) of the *Mycobacterium tuberculosis* probable periplasmic sugar-binding lipoprotein UspC (PDB code: 5K2Y) crystal structure as a template (Figure 48).

5.3.3. Preparation of a Nek1 Kinase Domain Homology Model

The Nek1 kinase domain homology model was created using the ‘homology model’ function and the crystal structure of Nek2 bound to an aminopurine inhibitor (PDB code: 5M53) as the template.²²⁹

5.3.4. Computational Protein-Ligand Docking

For all docking experiments, residual water molecules outside the ATP-binding pocket were deleted and the receptors were prepared using the ‘QuickPrep’ function without ‘automated structure preparation’. Using the respective functions of the ‘MOE Database Viewer’, all ligands were ‘washed’ before partial charges were determined and the structures underwent energy minimization. The binding sites were designated from the cocrystallized ligand (PDB code: 4B9D), which was placed in the binding site by superposition in case of the apo structure (PDB code 4APC) and the homology model. Docking poses were placed using the ‘Triangle Matcher’ method and scored by a ‘London dG’ function. Refinements of the poses were performed by using the ‘Rigid Receptor’ method and were finally scored using a ‘GBVI/WSA dG’ function. For the docking of UNC5452 (**3a**) into the apo structure, a hinge-binding pharmacophore was defined, based on the cocrystallized ligand.

All virtual screening hits were filtered for PAINS using the PAINS-remover online application.³⁵⁸ All compounds passed the filter.

5.3.5. Sequence Homology Analysis of the Zebrafish Nek1 Kinase Domain

The sequence homology analysis between the human and zebrafish Nek1 kinase domains was performed using the 'MOE protein similarity monitor'. Identity and similarity values are equal to the number of matches divided by the number of amino acids in the chain corresponding to the cell column. Residues are considered similar if their BLOSUM62 scores are greater than zero.³²²

5.4. Pharmacological Evaluation

5.4.1. *In Vitro* Kinase Activity Assays

Residual Kinase activity was determined with the commercial *Eurofins Discovery KinaseProfiler*[™] service at 1 μM compound concentration and either 10 μM ATP or at an ATP concentration within 15 μM of the apparent K_m for ATP (see Table 13 for $K_{M,ATP}$ values). In the case of Nek1 (*KinaseProfiler*[™] items 15-020KP10 and 15-020KP), recombinant human Nek1 (1-505) was incubated with 8 mM MOPS pH 7.0, 0.2 mM EDTA, 250 μM RLGRDKYKTLRQIRQ, 10 mM magnesium acetate and [γ -³³P-ATP]. The reaction was initiated by the addition of the Mg/ATP mix. After incubation for 40 minutes at room temperature, the reaction was stopped by the addition of phosphoric acid to a concentration of 0.5%. 10 μl of the reaction was then spotted onto a P30 filter mat and washed four times for 4 minutes in 0.425% phosphoric acid and once in methanol prior to drying and scintillation counting. Values are the mean from two independent experiments.

IC_{50} values for Nek1 and Nek2 were determined in a TR-FRET based activity assays (*LANCE® Ultra TR-FRET*, *PerkinElmer Inc.*, Waltham, Massachusetts, USA) with kind help from Dr. Ulrich Pehl (*Merck Healthcare KGaA*, Biopharma R&D, Darmstadt, Germany) at an ATP concentration within 15 μM of the apparent K_m for ATP in the respective assay format (60 μM for both Nek1 and Nek2). The IC_{50} curves consist of 10 test compound concentrations tested at half-log dilutions from 30 μM to 1 nM with vehicle and inhibitory control wells. For compounds **3j** and **3k** the maximum concentration was set to 10 μM as a consequence of solubility issues at 30 μM and the respective IC_{50} curves consist of 9 test compound concentrations tested at half-log dilutions from 10 μM to 1 nM. Values are the mean from two independent experiments. Recombinant human Nek1 (1-505; 0.02 nM) or Nek2 (full length; 0.2 nM) (both *Thermo Fisher Scientific*) was incubated with 50 mM HEPES pH 7.5, 1 mM EGTA, 10 mM MgCl_2 , 0.2mM DTT, 0.01% Tween20, and 50 nM *ULight*[™]-p70 S6K (Thr389) peptide (sequence LGFTYVAP; *PerkinElmer Inc.*, Waltham, Massachusetts, USA). The reaction was initiated by the addition of the p70 S6K peptide/ATP mix. After incubation for 30 min at 22 °C, the reaction was stopped by the addition of 10 mM EDTA and 0.3 nM europium-anti-phospho-p70 S6K (Thr389) antibody in CR97 detection buffer (both *PerkinElmer Inc.*, Waltham, Massachusetts, USA). After incubation for 1 hour at 22 °C for signal development, the plates were analyzed in a *PHERASAR FSX* plate reader

(BMG LABTECH, Ortenberg, Germany). For compounds **3g** and **3k**, relative IC₅₀ values were provided instead of absolute IC₅₀ values, because the determined IC₅₀ values exceeded the employed maximum test concentrations (30 μM for **3g**, 10 μM for **3k**).

Table 13: K_m for ATP values of selected *KinaseProfiler* test panel kinases as determined by *Eurofins Discovery*. All values lie within 15 μM of the apparent K_m for ATP. *K_m for ATP for these kinases has been determined by Eurofins to be greater than 200 μM, this is the maximum ATP concentration currently offered.

Protein Kinase	c[ATP]	Protein Kinase	c[ATP]
Abl(h)	45 μM	MST1(h)	90 μM
Abl(Q252H)(h)	15 μM	mTOR(h)	70 μM
ASK1(h)	200 μM*	NEK1(h)	90 μM
ATM(h)	10 μM	NEK11(h)	200 μM*
ATR/ATRIP(h)	10 μM	NEK2(h)	120 μM
BRK(h)	15 μM	NEK3(h)	120 μM
c-RAF(h)	120 μM	NEK6(h)	45 μM
CaMKIδ(h)	15 μM	NEK7(h)	45 μM
CaMKK2(h)	90 μM	PAK2(h)	90 μM
CDK1/cyclinB(h)	45 μM	PDGFRβ(h)	200 μM
CDK2/cyclinE(h)	120 μM	PI3 Kinase (p110/p85α)(h)	200 μM
CDK6/cyclinD3(h)	200 μM*	PI3 Kinase (p110α/p85α)(h)	200 μM*
CHK1(h)	90 μM	PI3 Kinase (p110δ/p85α)(h)	200 μM*
CK1(γ)	45 μM	PI3KC2γ(h)	200 μM*
CK2α2(h)	10 μM	Pim-1(h)	90 μM
eEF-2K(h)	15 μM	PKBa(h)	155 μM
EGFR(h)	10 μM	PKCh(h)	45 μM
EphB4(h)	10 μM	PKCα(h)	45 μM
GSK3β(h)	15 μM	Plk3(h)	70 μM
IKKα(h)	10 μM	PRAK(h)	15 μM
IKKβ(h)	10 μM	Rse(h)	45 μM
IKKε(h)	15 μM	SAPK2a(h)	90 μM
IRAK4(h)	200 μM*	Syk(h)	15 μM
Lyn(h)	70 μM	TAK1(h)	45 μM
MAPKAP-K2(h)	90 μM	TLK1(h)	10 μM

For compounds **3a**, **3f**, **19a-f**, IC₅₀ values were also determined with the *Eurofins Discovery IC50Profiler*[™] service at either 10 μM (Item 15-020KP10) or at an ATP concentration within 15 μM of the apparent K_m for ATP (90 μM, Item 15-020KP). The IC₅₀ curves consist of 9 test compound concentrations tested at half-log dilutions from 10 μM to 1 nM with vehicle control wells. Values are the mean from two independent experiments.

IC₅₀ values and 95% confidence intervals were determined from the raw data (partially provided in appendix D) by nonlinear regression (log_inhibitor vs. response_variable slope_four parameters) using *GraphPad Prism version 8.4.3 (471) for OS X*, (*GraphPad Software*, San Diego, USA).

5.4.2. Shake-Flask Solubility Assay

Aqueous solubility was determined in a shake-flask HPLC solubility assay using the previously described HPLC system connected to a diode array detector (DAD, see 5.1.5). At equilibrium, the absorption was measured at 280 nm and all measurements were performed in triplicates. A saturated compound solution in E3-medium with 2 v/v% DMSO was prepared by shaking for 24h at 25 °C. For each compound, a calibration curve (peak area [mAu*s] against concentration [μM]) was created by dilution of a 10 mM compound stock solution in DMSO to 1, 5, 10, 50, and 100 μM solutions in acetonitrile. The aqueous solubility was determined by interpolation using *GraphPad Prism version 8.4.3 (471) for OS X*, (*GraphPad Software*, San Diego, California, USA, www.graphpad.com).

5.4.3. Caco-2 Cell Permeability Assay

A-B permeability (Caco-2, pH 6.5/7.4) and percent recovery were determined by HPLC-MS/MS detection of the peak area response in a commercial assay by *Eurofins Discovery Services* (Item 3318). Propranolol, labetalol, colchicine and ranitidine were concurrently tested as reference compounds.

5.4.4. Zebrafish Developmental Toxicity Assay

The zebrafish developmental toxicity screen was performed in accordance to guidelines published by M. Haldi *et al.* in *Zebrafish: Methods for Assessing Drug Safety and Toxicity*.³¹⁷

At 4 hpf, 15 embryos per group (E3-medium control, 0.2% DMSO E3-medium control, 0.05, 0.1, 0.5, 1.5, 2.5, 5, 10, 15, 20, 30 μM) that exhibited intact chorion membranes were selected and reexamined after 2 hrs. Control groups were at 6 hpf sorted into 8-well plates containing 200 μL of E3 medium or a 0.2% solution of DMSO in E3-medium respectively. For the treated groups, a stock solution (10 mM in DMSO) of the test compound was diluted with E3-medium to final concentrations and the embryos were at 6 hpf sorted in 8-well plates containing 200 μL of the compound solution. Survival was monitored every 24 h by observation of the heartbeat and the embryos were kept in the dark in between observations. All survival rates were determined at least in triplicate with the controls and the survival rate at 30 μM being determined in 5 replicates.

5.4.5. Stability-indicating HPLC Assay

The stability-indicating HPLC assay was performed using the previously described HPLC system connected to a diode array detector (DAD, see 5.1.5). A 15 μM solution of **19f** in E3-medium containing 75 μM *N*-Phenylthiourea (PTU) and a 15 μM solution of **19f** containing 75 μM PTU and 2.5 μM PT-Yellow (BDNCA3-D2)³²⁵ were prepared for HPLC injection. Absorptions were measured every 24 hours at 280 nm for compound **19f** and PTU and 548 nm for PT-Yellow over 48h or 120h respectively. All measurements were performed in triplicates.

5.5. Zebrafish Maintenance and Husbandry

Fish maintenance and husbandry protocols were documented and approved by the Darmstadt administrative authority. All animals were treated humanely in accordance with the German animal protection standards and the EU Directive 2010/63/EU of the European parliament and of the council.

All embryos that were used for scientific experiments of any sort were euthanized before developing the ability for independent food intake and at the latest after 120 hpf (5 dpf).

Adult wild-type zebrafish (*Danio rerio*) are maintained in 60 L fish tanks, containing several different aquatic plants, in a laboratory with no daylight and a constant temperature of 28.5 °C (Figure 49).



Figure 49: Exemplary wild-type *Danio rerio* aquarium equipped with two filter pumps, aquarium plants and automated lighting.

Room light is programmed to a 12 h dark/12 h light cycle. The water quality is maintained by regular water change and thorough cleaning of the tanks as well as by two filter pumps per aquarium.

Adult zebrafish are bred in mating containers (3 animals/1 L) or mating tanks (6–8 animals/20 L) that are equipped with plastic grass and a removable sieve at the bottom of the tank (Figure 50).

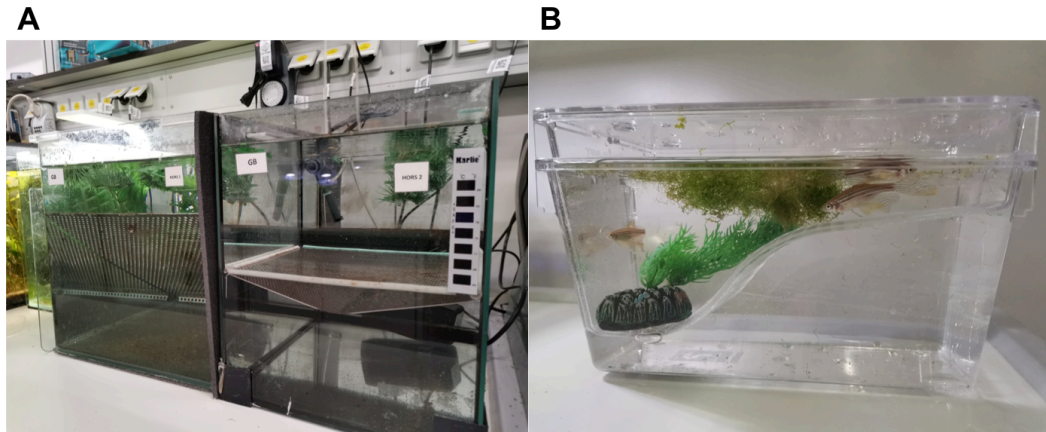


Figure 50: Exemplary wild-type *Danio rerio* mating aquariums. (A) Sieve-bottomed mating tanks for 6-8 animals, each equipped with filter pumps, oxygenators, and plastic plants. (B) Sieve-bottomed mating container for 2-3 animals, equipped with plastic and aquatic plants

Embryos are collected 2 to 3 h after a light cycle started, rinsed with E3-medium, and isolated in Petri dishes containing E3-medium. E3-medium was prepared according to the *Cold Spring Harbor Protocol* recipe for E3-medium for zebrafish embryos (doi:10.1101/pdb.rec066449).³⁰¹

- 34.8 g NaCl
- 1.6 g KCl
- 5.8 g CaCl₂·2H₂O
- 9.78 g MgCl₂·6H₂O

To prepare a 60X stock, the ingredients were dissolved in deionized water to a final volume of 2 l. After adjustment to pH 7.2 with NaOH, the solution was autoclaved. To prepare 1X medium, 16.5 mL of the 60X stock were diluted with deionized water to a final volume of 1 L and 100 μ L of 1% methylene blue (Sigma-Aldrich) were added as an antifungal agent. The 1X medium was freshly prepared for each experiment.

5.6. Fluorescence Microscopy Imaging of Zebrafish Pronephroi

5.6.1. Preparation of Agarose Molds and the 96-Well Plate Molding tool

The 96-well plate molding tool was manufactured by selective laser melting on an EOS M290 (*EOS GmbH Electro Optical Systems, Krailing, Germany*) metal 3D-printing system using EOS StainlessSteel 316L as the material with a layer height of 20 μM . The tool consists of a base plate with 96 perpendicular pins that match the positions of the wells of a microtiter plate. The agarose molds were prepared using NEEO ultra-quality agarose (*Carl Roth, Karlsruhe, Germany, Art. No. 2267.1*) in black-walled 96-well Nunc polymer optical bottom plates (*Thermo Fisher Scientific, Waltham, Massachusetts, USA*) (Figure 51 and 52).

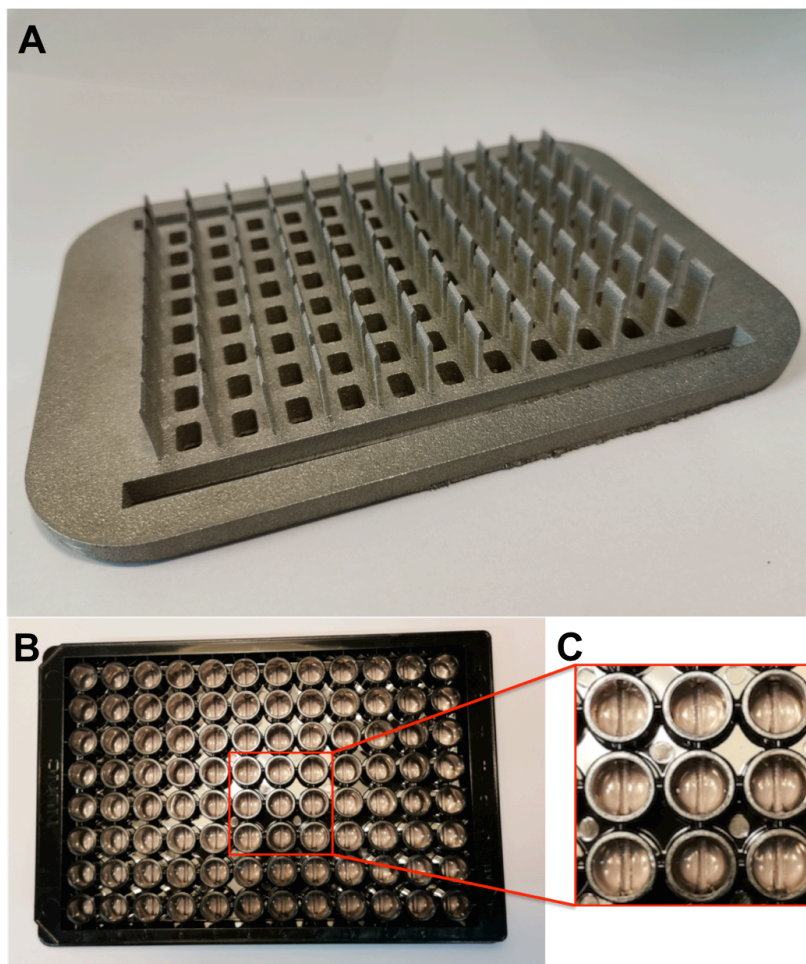


Figure 51: Preparation of agarose molds in 96-well plates. A) The stainless steel 96-well molding tool was manufactured by selective laser melting on a metal 3D-printing system. B) Prepared 96-well plate for Fluorescence microscopy imaging of zebrafish pronephroi. C) Detailed view of agarose mold.

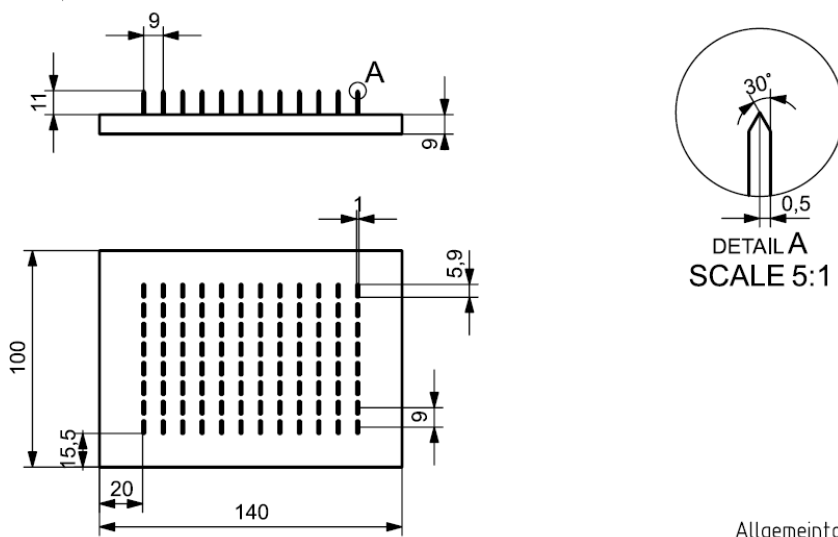


Figure 52: Technical drawing of the 96-well molding tool that was used as the blueprint for the recreation by metal 3d-printing.

40 mL of 1% agarose in E3-medium were heated to boiling for 2 min in a ceramic dish using a household microwave (720 W). The heated agarose solution was stirred and precooled for 30 sec before 70 μ l were added to each well of a 96 well microtiter plate using a multi-channel pipette. The agarose coated well plates were further cooled at room temperature for an additional 30 sec before the molding-tool was carefully inserted. After cooling for 10 min at room temperature the tool was carefully removed and the plates were optionally stored in plastic bags at 4°C.

5.6.2. Embryo selection and compound treatment

Embryo selection was performed in accordance to guidelines published by M. Haldi *et al.* in *Zebrafish: Methods for Assessing Drug Safety and Toxicity*.³¹⁷ At 4 hpf, 20 embryos per group (E3-medium negative control, 0.2% DMSO in E3-medium control, 10 μ M **19f** in E3-medium and 20 μ M **19f** in E3-medium) that exhibited intact chorion membranes were selected and reexamined after 2 hrs. Control groups were at 6 hpf sorted into 8-well plates containing 200 μ L of E3 medium or a 0.2% solution of DMSO in E3-medium respectively. For the treated groups, a stock solution (10 mM in DMSO) of the test compound was diluted with E3-medium to final concentrations and the embryos were at 6 hpf sorted in 8-well plates containing 200 μ L of the compound solution. After 48 h, the embryos were transferred to a 100 nM solution

of PT-Yellow in E3-medium, and after 20 min thoroughly washed with E3-medium and reincubated with the compound solutions for another 48 h. Finally, embryos were transferred to previously prepared agarose-molded 96-well-plates after 96 h of incubation, with each well containing a single embryo, in 100 μ l of a 75 μ M *N*-phenylthiourea (PTU) solution in E3-medium, containing tricaine methanesulfonate (0.02%). The embryos were manually oriented under a stereomicroscope in such a way that all yolk sacs were approximately at the same position within cavities, using features of the well plate as guidelines.

5.6.3. Image Acquisition

Imaging of PTU and PT-Yellow treated zebrafish was performed on an *Axio Scope.A1* microscope (*Carl Zeiss Microimaging GmbH*, Göttingen, Germany) in combination with a *HXP 120 C* lighting module (*Carl Zeiss Microimaging GmbH*, Göttingen, Germany) and either a *AxioCam MRc* mid-range microscopy camera (*Carl Zeiss Microimaging GmbH*, Göttingen, Germany) or a *CRI model Nuance MSI-FX* multispectral imaging system (*Cambridge Research & Instrumentation, Inc.*, Hopkinton, Massachusetts, USA), using appropriate filter sets.

Imaging of fluorescently labeled (PT-Yellow) zebrafish pronephroi was performed on an *Olympus IX-81* widefield microscope, using an *Olympus CPlanFL N*, 10x, NA 0.3 objective (both *Olympus K.K.*, Shinjuku, Tokyo, Japan) in combination with a 1.5x tube lens magnification, resulting in a total magnification of 15x. Fluorescence was excited using a *pE300 Ultra* (*CoolLED Ltd.*, Andover, NY, USA), and detected on an *edge 5.5* (*PCO AG*, Kelheim, Germany) using appropriate filter sets. The whole setup was controlled using *μ Manager 1.4.22* software (open source).³⁵⁹ to record 33 Z-slices, with a Z-distance of 15 μ M per embryo, after previously described manual orientation in the agarose molds.

5.6.4. Image Processing and Deconvolution

Image processing was performed using *ImageJ* version: 2.0.0.–rc-69/1.52p. Deconvolution was performed using the *DeconvolutionLab2* plugin³⁴⁵ and a point-spread function that was simulated in the *PSF Generator* plugin³⁴¹, employing *Gibson-Lanni* modelling³⁴² (see Table 14 and Figure 53). Ten iterations were performed. The image stacks are presented as colored maximum Z-projections using the lookup table *blue orange icb* (Appendix: Figure A 1).

Table 14: Calibration parameters for the *Gibson-Lanni* modeled point-spread function simulation in the *PSFGenerator* plug-in of the *ImageJ* software package.³⁴¹⁻³⁴²

Parameter	Value	Comment
Refractive index immersion	1.000273	Air at standard temperature and pressure ³⁴³
Refractive index sample	1.34	Agarose (similar to biological tissue) ³⁴⁴
Working distance	9500 μM	Distance between 96-wellplate and lens
Particle position Z	1000 nm	Distance between well-bottom and embryo
Accuracy computation	Good	<i>Richardson-Lucy-Algorithm</i> accuracy setting
Wavelength	564 nm	Maximum emission of PT-Yellow
Pixelsize XY	433.34 nm	Camera: PCO Edge 5.5 with Pixelsize: 6.5 x 6.5 μM (6500 nm/15 = 433.34 nm)
Numerical aperture	0.3	Olympus CPlanFL N, 10x, NA 0.3 objective with a 1.5x tube lens magnification, 15x total magnification.
Z-step	15000 nM	Z-step distance
Size XYZ	256, 256, 65	Image size of the simulated PSF
Display	Linear, 32-bit	Visualization properties

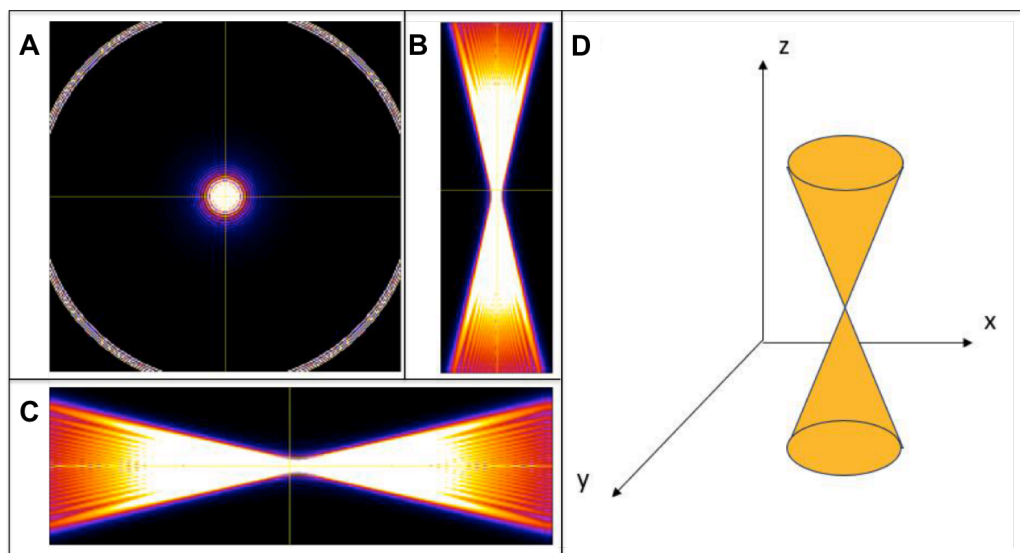


Figure 53: Visual representation of the simulated point-spread function in *ImageJ*, using the calibration parameters for the *Gibson-Lanni* modeled point-spread function simulation in the *PSFGenerator* plug-in.³⁴¹⁻³⁴² (A) Z-Axis view. (B) XZ-Plane view. (C) YZ-Plane view. (D) Scheme of a two-coned point-square function in a three-dimensional cartesian coordinate system.

As it was not possible to remove all out of focus blur with the deconvolution procedure, the sharpest 5 consecutive Z-slices of labeled pronephroi were manually selected in each stack (Appendix: Figure A 2 and Figure A 3).

Subsequently, the following image analysis steps were applied using *ImageJ*: (1) subtract background using a 150 pixel rolling ball, (2) sum all 5 images into one, (3) threshold images above 100, (4) convert background to 8-bit mask for the intensity quantification or convert background to NaN for the quantification of the pronephron areas. The pronephron area in the summed stacks was used as the quantity to estimate the size of the pronephroi.

References

1. Cori, C. F.; Schmidt, G.; Cori, G. T., The Synthesis of a Polysaccharide from Glucose-1-phosphate in Muscle Extract. *Science* **1939**, *89* (2316), 464.
2. Cohen, P., The origins of protein phosphorylation. *Nature Cell Biology* **2002**, *4* (5), E127-E130.
3. Roskoski, R., Properties of FDA-approved small molecule protein kinase inhibitors: A 2020 update. *Pharmacological Research* **2020**, *152*, 104609.
4. Lightfoot, H. L.; Goldberg, F. W.; Sedelmeier, J., Evolution of Small Molecule Kinase Drugs. *ACS Medicinal Chemistry Letters* **2019**, *10* (2), 153-160.
5. Augustine, J. J.; Bodziak, K. A.; Hricik, D. E., Use of Sirolimus in Solid Organ Transplantation. *Drugs* **2007**, *67* (3), 369-391.
6. Nahta, R.; Esteva, F. J., Trastuzumab: triumphs and tribulations. *Oncogene* **2007**, *26* (25), 3637-3643.
7. Iqbal, N.; Iqbal, N., Imatinib: a breakthrough of targeted therapy in cancer. *Chemotherapy Research and Practice* **2014**, *2014*, 357027-357027.
8. Laufer, S.; Briner, K.; Bajorath, J.; Georg, G. I.; Wang, S., New Horizons in Drug Discovery - Understanding and Advancing Kinase Inhibitors. *Journal of Medicinal Chemistry* **2020**, *63* (15), 7921-7922.
9. Weisberg, E.; Parent, A.; Yang, P. L.; Sattler, M.; Liu, Q.; Liu, Q.; Wang, J.; Meng, C.; Buhrlage, S. J.; Gray, N.; Griffin, J. D., Repurposing of Kinase Inhibitors for Treatment of COVID-19. *Pharmaceutical Research* **2020**, *37* (9), 167.
10. Berman, H. M.; Westbrook, J.; Feng, Z.; Gilliland, G.; Bhat, T. N.; Weissig, H.; Shindyalov, I. N.; Bourne, P. E., The Protein Data Bank. *Nucleic Acids Research* **2000**, *28* (1), 235-242.

-
11. Shinada, N.; Schmidtke, P.; de Brevern, A., Accurate Representation of Protein-Ligand Structural Diversity in the Protein Data Bank (PDB). *International Journal of Molecular Sciences* **2020**, *21*, 2243.
 12. Kanev, G. K.; de Graaf, C.; de Esch, I. J. P.; Leurs, R.; Würdinger, T.; Westerman, B. A.; Kooistra, A. J., The Landscape of Atypical and Eukaryotic Protein Kinases. *Trends in Pharmacological Sciences* **2019**, *40* (11), 818-832.
 13. Ilouz, R.; Ram, V. L.; Ellisman, M.; Taylor, S. S., Subcellular Localization and Functional Characterization of cAMP-dependent Protein Kinase A Isoforms: Painting Specificity by Mosaic Brain Mapping. *The FASEB Journal* **2017**, *31* (S1), 770.5-770.5.
 14. Faust, M.; Montenarh, M., Subcellular localization of protein kinase CK2. *Cell and Tissue Research* **2000**, *301* (3), 329-340
 15. Hiromura, K.; Pippin, J. W.; Blonski, M. J.; Roberts, J. M.; Shankland, S. J., The subcellular localization of cyclin dependent kinase 2 determines the fate of mesangial cells: role in apoptosis and proliferation. *Oncogene* **2002**, *21* (11), 1750-1758.
 16. Taylor, S. S.; Kornev, A. P., Protein kinases: evolution of dynamic regulatory proteins. *Trends in Biochemical Sciences* **2011**, *36* (2), 65-77.
 17. Johnson, L. N.; Lowe, E. D.; Noble, M. E. M.; Owen, D. J., The structural basis for substrate recognition and control by protein kinases. *FEBS Letters* **1998**, *430* (1), 1-11.
 18. McClendon, C. L.; Kornev, A. P.; Gilson, M. K.; Taylor, S. S., Dynamic architecture of a protein kinase. *Proceedings of the National Academy of Sciences* **2014**, *111* (43), E4623.
 19. Keyloun, K. R.; Reid, M. C.; Choi, R.; Song, Y.; Fox, A. M. W.; Hillesland, H. K.; Zhang, Z.; Vidadala, R.; Merritt, E. A.; Lau, A. O. T.; Maly, D. J.; Fan, E.; Barrett, L. K.; Van Voorhis, W. C.; Ojo, K. K., The gatekeeper residue and beyond: homologous calcium-dependent protein kinases as drug development targets for veterinarian Apicomplexa parasites. *Parasitology* **2014**, *141* (11), 1499-1509.

-
20. Grant, B. D.; Hemmer, W.; Tsigelny, I.; Adams, J. A.; Taylor, S. S., Kinetic Analyses of Mutations in the Glycine-Rich Loop of cAMP-Dependent Protein Kinase. *Biochemistry* **1998**, *37* (21), 7708-7715.
 21. Knight, J. D. R.; Qian, B.; Baker, D.; Kothary, R., Conservation, variability and the modeling of active protein kinases. *PloS one* **2007**, *2* (10), e982-e982.
 22. Wang, Z.; Cole, P. A., Chapter One - Catalytic Mechanisms and Regulation of Protein Kinases. In *Methods in Enzymology*, Shokat, K. M., Ed. Academic Press: 2014; Vol. 548, pp 1-21.
 23. Scheeff, E. D.; Eswaran, J.; Bunkoczi, G.; Knapp, S.; Manning, G., Structure of the Pseudokinase VRK3 Reveals a Degraded Catalytic Site, a Highly Conserved Kinase Fold, and a Putative Regulatory Binding Site. *Structure* **2009**, *17* (1), 128-138.
 24. Tong, M.; Seeliger, M. A., Targeting Conformational Plasticity of Protein Kinases. *ACS Chemical Biology* **2015**, *10* (1), 190-200.
 25. Treiber, Daniel K.; Shah, Neil P., Ins and Outs of Kinase DFG Motifs. *Chemistry & Biology* **2013**, *20* (6), 745-746.
 26. Kornev, A. P.; Taylor, S. S.; Ten Eyck, L. F., A helix scaffold for the assembly of active protein kinases. *Proceedings of the National Academy of Sciences* **2008**, *105* (38), 14377.
 27. Kornev, A. P.; Haste, N. M.; Taylor, S. S.; Ten Eyck, L. F., Surface comparison of active and inactive protein kinases identifies a conserved activation mechanism. *Proceedings of the National Academy of Sciences* **2006**, *103* (47), 17783.
 28. Roskoski, R., Classification of small molecule protein kinase inhibitors based upon the structures of their drug-enzyme complexes. *Pharmacological Research* **2016**, *103*, 26-48
 29. Gharwan, H.; Groninger, H., Kinase inhibitors and monoclonal antibodies in oncology: clinical implications. *Nature Reviews Clinical Oncology* **2016**, *13* (4), 209-227.

-
-
30. Dar, A. C.; Shokat, K. M., The Evolution of Protein Kinase Inhibitors from Antagonists to Agonists of Cellular Signaling. *Annual Review of Biochemistry* **2011**, *80* (1), 769-795.
 31. Zuccotto, F.; Ardini, E.; Casale, E.; Angiolini, M., Through the "Gatekeeper Door": Exploiting the Active Kinase Conformation. *Journal of Medicinal Chemistry* **2010**, *53* (7), 2681-2694.
 32. Backes, A. C.; Zech, B.; Felber, B.; Klebl, B.; Müller, G., Small-molecule inhibitors binding to protein kinases. Part I: exceptions from the traditional pharmacophore approach of type I inhibition. *Expert Opinion on Drug Discovery* **2008**, *3* (12), 1409-1425.
 33. Knight, Z. A.; Shokat, K. M., Features of Selective Kinase Inhibitors. *Chemistry & Biology* **2005**, *12* (6), 621-637.
 34. Zuccotto, F.; Ardini, E.; Casale, E.; Angiolini, M., Through the "gatekeeper door": exploiting the active kinase conformation. *Journal of medicinal chemistry* **2010**, *53* (7), 2681-2694.
 35. Martinez, R.; Defnet, A.; Shapiro, P., Avoiding or Co-Opting ATP Inhibition: Overview of Type III, IV, V, and VI Kinase Inhibitors. In *Next Generation Kinase Inhibitors: Moving Beyond the ATP Binding/Catalytic Sites*, Shapiro, P., Ed. Springer International Publishing: Cham, 2020; pp 29-59.
 36. Miljković, F.; Bajorath, J., Reconciling Selectivity Trends from a Comprehensive Kinase Inhibitor Profiling Campaign with Known Activity Data. *ACS Omega* **2018**, *3* (3), 3113-3119.
 37. Barouch-Bentov, R.; Sauer, K., Mechanisms of drug resistance in kinases. *Expert Opinions on Investigational Drugs* **2011**, *20* (2), 153-208.
 38. Mian, A. A.; Schüll, M.; Zhao, Z.; Oancea, C.; Hundertmark, A.; Beissert, T.; Ottmann, O. G.; Ruthardt, M., The gatekeeper mutation T315I confers resistance against small

-
- molecules by increasing or restoring the ABL-kinase activity accompanied by aberrant transphosphorylation of endogenous BCR, even in loss-of-function mutants of BCR/ABL. *Leukemia* **2009**, *23* (9), 1614-1621.
39. Matsson, P.; Kihlberg, J., How Big Is Too Big for Cell Permeability? *Journal of Medicinal Chemistry* **2017**, *60* (5), 1662-1664.
40. Hopkins, A. L.; Keserü, G. M.; Leeson, P. D.; Rees, D. C.; Reynolds, C. H., The role of ligand efficiency metrics in drug discovery. *Nature Reviews Drug Discovery* **2014**, *13* (2), 105-121.
41. Lu, X.; Smaill, J. B.; Ding, K., New Promise and Opportunities for Allosteric Kinase Inhibitors. *Angewandte Chemie International Edition* **2020**, *59* (33), 13764-13776
42. Cox, K. J.; Shomin, C. D.; Ghosh, I., Tinkering outside the kinase ATP box: allosteric (type IV) and bivalent (type V) inhibitors of protein kinases. *Future Medicinal Chemistry* **2010**, *3* (1), 29-43.
43. Bauer, R. A., Covalent inhibitors in drug discovery: from accidental discoveries to avoided liabilities and designed therapies. *Drug Discovery Today* **2015**, *20* (9), 1061-1073.
44. Kharenko, O. A.; Patel, R. G.; Brown, S. D.; Calosing, C.; White, A.; Lakshminarasimhan, D.; ...; Young, P. R., Design and Characterization of Novel Covalent Bromodomain and Extra-Terminal Domain (BET) Inhibitors Targeting a Methionine. *Journal of Medicinal Chemistry* **2018**, *61* (18), 8202-8211.
45. Lonsdale, R.; Ward, R. A., Structure-based design of targeted covalent inhibitors. *Chemical Society Reviews* **2018**, *47* (11), 3816-3830.
46. Wright, P. M.; Seiple, I. B.; Myers, A. G., The evolving role of chemical synthesis in antibacterial drug discovery. *Angewandte Chemie International Edition* **2014**, *53* (34), 8840-8869.

-
-
47. Olbe, L.; Carlsson, E.; Lindberg, P., A proton-pump inhibitor expedition: the case histories of omeprazole and esomeprazole. *Nature Reviews Drug Discovery* **2003**, *2* (2), 132-139.
 48. Maffrand, J.-P., The story of clopidogrel and its predecessor, ticlopidine: Could these major antiplatelet and antithrombotic drugs be discovered and developed today? *Comptes Rendus Chimie* **2012**, *15* (8), 737-743.
 49. Miller, J. A., The Metabolism of Xenobiotics to Reactive Electrophiles in Chemical Carcinogenesis and Mutagenesis: A Collaboration with Elizabeth Cavert Miller and our Associates. *Drug Metabolism Reviews* **1998**, *30* (4), 645-674.
 50. Johnson, D. S.; Weerapana, E.; Cravatt, B. F., Strategies for discovering and derisking covalent, irreversible enzyme inhibitors. *Future Medicinal Chemistry* **2010**, *2* (6), 949-964.
 51. Roskoski, R., Orally effective FDA-approved protein kinase targeted covalent inhibitors (TCIs). *Pharmacological Research* **2021**, 105422.
 52. Peres de Oliveira, A.; Kazuo Issayama, L.; Betim Pavan, I. C.; Riback Silva, F.; Diniz Melo-Hanchuk, T.; Moreira Simabuco, F.; Kobarg, J., Checking NEKs: Overcoming a Bottleneck in Human Diseases. *Molecules* **2020**, *25* (8), 1778.
 53. Moniz, L.; Dutt, P.; Haider, N.; Stambolic, V., Nek family of kinases in cell cycle, checkpoint control and cancer. *Cell Division* **2011**, *6*, 18.
 54. Wu, L.; Osmani, S. A.; Mirabito, P. M., A Role for NIMA in the Nuclear Localization of Cyclin B in *Aspergillus nidulans*. *Journal of Cell Biology* **1998**, *141* (7), 1575-1587
 55. De Souza, C. P. C.; Osmani, A. H.; Wu, L.-P.; Spotts, J. L.; Osmani, S. A., Mitotic Histone H3 Phosphorylation by the NIMA Kinase in *Aspergillus nidulans*. *Cell* **2000**, *102* (3), 293-302.

-
56. Davies, J. R.; Osmani, A. H.; De Souza, C. P. C.; Bachewich, C.; Osmani, S. A., Potential Link between the NIMA Mitotic Kinase and Nuclear Membrane Fission during Mitotic Exit in *Aspergillus nidulans*. *Eukaryotic Cell* **2004**, 3 (6), 1433.
57. Meirelles, G. V.; Perez, A. M.; Souza, E. E.; Basei, F. L.; Papa, P. F.; Melo Hanchuk, T. D.; Cardoso, V. B.; Kobarg, J., "Stop Ne(c)king around": How interactomics contributes to functionally characterize Nek family kinases. *World journal of biological chemistry* **2014**, 5 (2), 141–160.
58. Fry, A. M.; Regan, L.; Sabir, S. R.; Bayliss, R., Cell cycle regulation by the NEK family of protein kinases. *Journal of Cell Science* **2012**, 125 (19), 4423.
59. Feige, E.; Shalom, O.; Tsurriel, S.; Yissachar, N.; Motro, B., Nek1 shares structural and functional similarities with NIMA kinase. *Biochimica et Biophysica Acta - Molecular Cell Research* **2006**, 1763 (3), 272-281.
60. García-Alai, M. M.; Gallo, M.; Salame, M.; Wetzler, D. E.; McBride, A. A.; Paci, M.; ...; de Prat-Gay, G., Molecular Basis for Phosphorylation-Dependent, PEST-Mediated Protein Turnover. *Structure* **2006**, 14 (2), 309-319.
61. Wells, C. I.; Kapadia, N. R.; Counago, R. M.; Drewry, D. H., In depth analysis of kinase cross screening data to identify chemical starting points for inhibition of the Nek family of kinases. *MedChemComm* **2018**, 9, 44-46.
62. O'Regan, L.; Blot, J.; Fry, A. M., Mitotic regulation by NIMA-related kinases. *Cell Division* **2007**, 2 (1), 25.
63. Melo-Hanchuk, T. D.; Martins, M. B.; Cunha, L. L.; Soares, F. A.; Ward, L. S.; Vassallo, J.; Kobarg, J., Expression of the NEK family in normal and cancer tissue: an immunohistochemical study. *BMC Cancer* **2020**, 20 (1), 23.
64. Melo-Hanchuk, T. D.; Slepicka, P. F.; Meirelles, G. V.; Basei, F. L.; Lovato, D. V.; Granato, D. C.; ...; Kobarg, J., NEK1 kinase domain structure and its dynamic protein interactome after exposure to Cisplatin. *Scientific Reports* **2017**, 7 (1), 5445.

-
65. Westwood, I.; Cheary, D.-M.; Baxter, J. E.; Richards, M. W.; van Montfort, R. L. M.; Fry, A. M.; Bayliss, R., Insights into the conformational variability and regulation of human Nek2 kinase. *Journal of Molecular Biology* **2009**, *386* (2), 476-485.
66. Richards, M. W.; O'Regan, L.; Mas-Droux, C.; Blot, J. M. Y.; Cheung, J.; Hoelder, S.; ...; Bayliss, R., An Autoinhibitory Tyrosine Motif in the Cell-Cycle-Regulated Nek7 Kinase Is Released through Binding of Nek9. *Molecular Cell* **2009**, *36* (4), 560-570.
67. Khanfar, M. A.; Banat, F.; Alabed, S.; Alqtaishat, S., Discovery of potent NEK2 inhibitors as potential anticancer agents using structure-based exploration of NEK2 pharmacophoric space coupled with QSAR analyses. *Molecular Diversity* **2017**, *21* (1), 187-200.
68. Xi, J.-B.; Fang, Y.-F.; Frett, B.; Zhu, M.-L.; Zhu, T.; Kong, Y.-N.; Guan, F.-J.; Zhao, Y.; Zhang, X.-W.; Li, H.-y.; Ma, M.-L.; Hu, W., Structure-based design and synthesis of imidazo[1,2-a]pyridine derivatives as novel and potent Nek2 inhibitors with in vitro and in vivo antitumor activities. *European Journal of Medicinal Chemistry* **2017**, *126*, 1083-1106.
69. Fry, A. M.; Schultz, S. J.; Bartek, J.; Nigg, E. A., Substrate Specificity and Cell Cycle Regulation of the Nek2 Protein Kinase, a Potential Human Homolog of the Mitotic Regulator NIMA of *Aspergillus nidulans*(*). *Journal of Biological Chemistry* **1995**, *270* (21), 12899-12905.
70. Fry, A. M.; Meraldi, P.; Nigg, E. A., A centrosomal function for the human Nek2 protein kinase, a member of the NIMA family of cell cycle regulators. *The EMBO Journal* **1998**, *17* (2), 470-481.
71. Endicott, S. J.; Basu, B.; Khokha, M.; Brueckner, M., The NIMA-like kinase Nek2 is a key switch balancing cilia biogenesis and resorption in the development of left-right asymmetry. *Development* **2015**, *142* (23), 4068.

-
-
72. Tanaka, K.; Nigg, E. A., Cloning and Characterization of the Murine Nek3 Protein Kinase, a Novel Member of the NIMA Family of Putative Cell Cycle Regulators. *Journal of Biological Chemistry* **1999**, *274* (19), 13491-13497.
73. Miller, S. L.; Antico, G.; Raghunath, P. N.; Tomaszewski, J. E.; Clevenger, C. V., Nek3 kinase regulates prolactin-mediated cytoskeletal reorganization and motility of breast cancer cells. *Oncogene* **2007**, *26* (32), 4668-4678.
74. Cao, Y.; Song, J.; Chen, J.; Xiao, J.; Ni, J.; Wu, C., Overexpression of NEK3 is associated with poor prognosis in patients with gastric cancer. *Medicine* **2018**, *97* (3), e9630-e9630.
75. Doles, J.; Hemann, M. T., Nek4 status differentially alters sensitivity to distinct microtubule poisons. *Cancer research* **2010**, *70* (3), 1033-1041.
76. Nguyen, C. L.; Possemato, R.; Bauerlein, E. L.; Xie, A.; Scully, R.; Hahn, W. C., Nek4 Regulates Entry into Replicative Senescence and the Response to DNA Damage in Human Fibroblasts. *Molecular and Cellular Biology* **2012**, *32* (19), 3963.
77. Basei, F. L.; Meirelles, G. V.; Righetto, G. L.; dos Santos Migueleti, D. L.; Smetana, J. H. C.; Kobarg, J., New interaction partners for Nek4.1 and Nek4.2 isoforms: from the DNA damage response to RNA splicing. *Proteome Science* **2015**, *13* (1), 11.
78. Shimizu, K.; Sawasaki, T., Nek5, a novel substrate for caspase-3, promotes skeletal muscle differentiation by up-regulating caspase activity. *FEBS Letters* **2013**, *587* (14), 2219-2225.
79. Prosser, S. L.; Sahota, N. K.; Pelletier, L.; Morrison, C. G.; Fry, A. M., Nek5 promotes centrosome integrity in interphase and loss of centrosome cohesion in mitosis. *Journal of Cell Biology* **2015**, *209* (3), 339-348.

-
80. Melo-Hanchuk, T. D.; Slepicka, P. F.; Pelegrini, A. L.; Menck, C. F. M.; Kobarg, J., NEK5 interacts with topoisomerase II β and is involved in the DNA damage response induced by etoposide. *Journal of Cellular Biochemistry* **2019**, *120* (10), 16853-16866.
81. Belham, C.; Roig, J.; Caldwell, J. A.; Aoyama, Y.; Kemp, B. E.; Comb, M.; Avruch, J., A Mitotic Cascade of NIMA Family Kinases: Nercc1/Nek9 Activates the Nek6 and Nek7 Kinases. *Journal of Biological Chemistry* **2003**, *278* (37), 34897-34909.
82. Regan, L.; Fry, A. M., The Nek6 and Nek7 Protein Kinases Are Required for Robust Mitotic Spindle Formation and Cytokinesis. *Molecular and Cellular Biology* **2009**, *29* (14), 3975.
83. Gerçeker, E.; Boyacıoğlu, S. O.; Kasap, E.; Baykan, A.; Yuçeyar, H.; Yıldırım, H.; Ayhan, S.; Ellidokuz, E.; Korkmaz, M., Never in mitosis gene A-related kinase 6 and aurora kinase A: New gene biomarkers in the conversion from ulcerative colitis to colorectal cancer. *Oncology Reports* **2015**, *34* (4), 1905-1914.
84. Ma, Z.-Z.; Sun, H.-S.; Lv, J.-C.; Guo, L.; Yang, Q.-R., Expression and clinical significance of the NEK7-NLRP3 inflammasome signaling pathway in patients with systemic lupus erythematosus. *Journal of Inflammation* **2018**, *15* (1), 16.
85. de Souza, E. E.; Meirelles, G. V.; Godoy, B. B.; Perez, A. M.; Smetana, J. H. C.; Doxsey, S. J.; McComb, M. E.; Costello, C. E.; Whelan, S. A.; Kobarg, J., Characterization of the Human NEK7 Interactome Suggests Catalytic and Regulatory Properties Distinct from Those of NEK6. *Journal of Proteome Research* **2014**, *13* (9), 4074-4090.
86. Zhou, X.; Zhang, P.; Wang, Q.; Ji, N.; Xia, S.; Ding, Y.; Wang, Q., Metformin ameliorates experimental diabetic periodontitis independently of mammalian target of rapamycin (mTOR) inhibition by reducing NIMA-related kinase 7 (Nek7) expression. *Journal of Periodontology* **2019**, *90* (9), 1032-1042.
87. De Donato, M.; Righino, B.; Filippetti, F.; Battaglia, A.; Petrillo, M.; Pirolli, D.; Scambia, G.; De Rosa, M. C.; Gallo, D., Identification and antitumor activity of a novel

-
- inhibitor of the NIMA-related kinase NEK6. *Scientific reports* **2018**, *8* (1), 16047-16047.
88. Liu, S.; Lu, W.; Obara, T.; Kuida, S.; Lehoczky, J.; Dewar, K.; Drummond, I. A.; Beier, D. R., A defect in a novel Nek-family kinase causes cystic kidney disease in the mouse and in zebrafish. *Development* **2002**, *129* (24), 5839.
89. Sohara, E.; Luo, Y.; Zhang, J.; Manning, D. K.; Beier, D. R.; Zhou, J., Nek8 Regulates the Expression and Localization of Polycystin-1 and Polycystin-2. *Journal of the American Society of Nephrology* **2008**, *19* (3), 469.
90. Choi, Hyo Jei C.; Lin, J.-R.; Vannier, J.-B.; Slaats, Gisela G.; Kile, Andrew C.; Paulsen, Renee D.;; Cimprich, Karlene A., NEK8 Links the ATR-Regulated Replication Stress Response and S Phase CDK Activity to Renal Ciliopathies. *Molecular Cell* **2013**, *51* (4), 423-439
91. Roig, J.; Groen, A.; Caldwell, J.; Avruch, J., Active Nercc1 Protein Kinase Concentrates at Centrosomes Early in Mitosis and Is Necessary for Proper Spindle Assembly. *Molecular Biology of the Cell* **2005**, *16* (10), 4827-4840.
92. Wu, Z.; Doondeea, J. B.; Gholami, A. M.; Janning, M. C.; Lemeer, S.; Kramer, K.; ...; Kuster, B., Quantitative Chemical Proteomics Reveals New Potential Drug Targets in Head and Neck Cancer. *Molecular & Cellular Proteomics* **2011**, *10* (12), M111.011635.
93. Bustos, V. H.; Ferrarese, A.; Venerando, A.; Marin, O.; Allende, J. E.; Pinna, L. A., The first armadillo repeat is involved in the recognition and regulation of β -catenin phosphorylation by protein kinase CK1. *Proceedings of the National Academy of Sciences* **2006**, *103* (52), 19725.
94. Gu, T.; Mazzurco, M.; Sulaman, W.; Matias, D. D.; Goring, D. R., Binding of an arm repeat protein to the kinase domain of the S-locus receptor kinase. *Proceedings of the National Academy of Sciences* **1998**, *95* (1), 382.

-
-
95. Antoniou, N.; Vlachakis, D.; Memou, A.; Leandrou, E.; Valkimadi, P.-E.; Melachroinou, K.; Re, D. B.; P...; Rideout, H. J., A motif within the armadillo repeat of Parkinson's-linked LRRK2 interacts with FADD to hijack the extrinsic death pathway. *Scientific Reports* **2018**, *8* (1), 3455.
96. Moniz, L. S.; Stambolic, V., Nek10 mediates G2/M cell cycle arrest and MEK autoactivation in response to UV irradiation. *Molecular and cellular biology* **2011**, *31* (1), 30-42.
97. Kaji, T.; Yamasaki, O.; Takata, M.; Otsuka, M.; Hamada, T.; Morizane, S.; ...; Iwatsuki, K., Comparative study on driver mutations in primary and metastatic melanomas at a single Japanese institute: A clue for intra- and inter-tumor heterogeneity. *Journal of Dermatological Science* **2017**, *85* (1), 51-57.
98. Ramirez-Ardila, D. E.; Ruigrok-Ritstier, K.; Helmijr, J. C.; Look, M. P.; van Laere, S.; Dirix, L.; ...; Jansen, M. P. H. M., LRG1 mRNA expression in breast cancer associates with PIK3CA genotype and with aromatase inhibitor therapy outcome. *Molecular Oncology* **2016**, *10* (8), 1363-1373.
99. Noguchi, K.; Fukazawa, H.; Murakami, Y.; Uehara, Y., Nek11, a New Member of the NIMA Family of Kinases, Involved in DNA Replication and Genotoxic Stress Responses. *Journal of Biological Chemistry* **2002**, *277* (42), 39655-39665.
100. Liu, X.; Gao, Y.; Lu, Y.; Zhang, J.; Li, L.; Yin, F., Downregulation of NEK11 is associated with drug resistance in ovarian cancer. *International Journal of Oncology* **2014**, *45* (3), 1266-1274.
101. van de Kooij, B.; Creixell, P.; van Vlimmeren, A.; Joughin, B. A.; Miller, C. J.; Haider, N.; S...; Yaffe, M. B., Comprehensive substrate specificity profiling of the human Nek kinome reveals unexpected signaling outputs. *eLife* **2019**, *8*, e44635.

-
-
102. Letwin, K.; Mizzen, L.; Motro, B.; Ben-David, Y.; Bernstein, A.; Pawson, T., A mammalian dual specificity protein kinase, Nek1, is related to the NIMA cell cycle regulator and highly expressed in meiotic germ cells. *The EMBO Journal* **1992**, *11* (10), 3521-3531.
 103. Janaswami, P. M.; Birkenmeier, E. H.; Cook, S. A.; Rowe, L. B.; Bronson, R. T.; Davisson, M. T., Identification and Genetic Mapping of a New Polycystic Kidney Disease on Mouse Chromosome 8. *Genomics* **1997**, *40* (1), 101-107.
 104. Upadhyaya, P.; Birkenmeier, E. H.; Birkenmeier, C. S.; Barker, J. E., Mutations in a NIMA-related kinase gene, *Nek1* cause pleiotropic effects including a progressive polycystic kidney disease in mice. *Proceedings of the National Academy of Sciences* **2000**, *97* (1), 217.
 105. Chebib, F. T.; Torres, V. E., Recent Advances in the Management of Autosomal Dominant Polycystic Kidney Disease. *Clinical Journal of the American Society of Nephrology* **2018**, *13* (11), 1765.
 106. Chen, Y.; Chen, C.-F.; Riley, D. J.; Chen, P.-L., Nek1 kinase functions in DNA damage response and checkpoint control through a pathway independent of ATM and ATR. *Cell Cycle* **2011**, *10* (4), 655-663.
 107. Chen, Y.; Chen, C.-F.; Chiang, H.-C.; Pena, M.; Polci, R.; Wei, R. L.; ...; Riley, D. J., Mutation of NIMA-related kinase 1 (NEK1) leads to chromosome instability. *Molecular Cancer* **2011**, *10* (1), 5.
 108. Singh, V.; Khalil, M. I.; De Benedetti, A., The TLK1/Nek1 axis contributes to mitochondrial integrity and apoptosis prevention via phosphorylation of VDAC1. *Cell Cycle* **2020**, *19* (3), 363-375.
 109. Chen, Y., NEK1 Protein Kinase as a Target for Anticancer Therapeutics. *Chemotherapy: Open Access* **2012**, *01* (05).

-
-
110. Tonni, G.; Palmisano, M.; Ventura, A.; Grisolia, G.; Baffico, A. M.; Pattacini, P.; ...; De Felice, C., Majewski syndrome (short-rib polydactyly syndrome type II): Prenatal diagnosis and histological features of chondral growth plate, liver and kidneys. *Congenital Anomalies* **2014**, *54* (4), 233-239.
111. Thiel, C.; Kessler, K.; Giessler, A.; Dimmler, A.; Shalev, S. A.; von der Haar, S.; ...; Rauch, A., NEK1 Mutations Cause Short-Rib Polydactyly Syndrome Type Majewski. *The American Journal of Human Genetics* **2011**, *88* (1), 106-114.
112. D'Angelo, A.; Franco, B., The dynamic cilium in human diseases. *PathoGenetics* **2009**, *2* (1), 3.
113. Chen, C.-P.; Chang, T.-Y.; Chen, C.-Y.; Wang, T.-Y.; Tsai, F.-J.; Wu, P.-C.; ...; Wang, W., Short rib-polydactyly syndrome type II (Majewski): Prenatal diagnosis, perinatal imaging findings and molecular analysis of the NEK1 gene. *Taiwanese Journal of Obstetrics and Gynecology* **2012**, *51* (1), 100-105.
114. Monroe, G. R.; Kappen, I. F.; Stokman, M. F.; Terhal, P. A.; van den Boogaard, M.-J. H.; Savelberg, S. M.; ...; van Haaften, G., Compound heterozygous NEK1 variants in two siblings with oral-facial-digital syndrome type II (Mohr syndrome). *European Journal of Human Genetics* **2016**, *24* (12), 1752-1760.
115. Higelin, J.; Catanese, A.; Semelink-Sedlacek, L. L.; Oeztuerk, S.; Lutz, A.-K.; Bausinger, J.; ...; Boeckers, T. M., NEK1 loss-of-function mutation induces DNA damage accumulation in ALS patient-derived motoneurons. *Stem Cell Research* **2018**, *30*, 150-162.
116. Brenner, D.; Müller, K.; Wieland, T.; Weydt, P.; Böhm, S.; Lulé, D.; Hübers, A.; Neuwirth, C.; Weber, M.; Borck, G.; Wahlqvist, M.; Danzer, K. M.; Volk, A. E.; Meitinger, T.; Strom, T. M.; Otto, M.; Kassubek, J.; Ludolph, A. C.; Andersen, P. M.; Weishaupt, J. H., NEK1 mutations in familial amyotrophic lateral sclerosis. *Brain* **2016**, *139* (5), e28-e28.

-
-
117. Sohn, E., Fundraising: The Ice Bucket Challenge delivers. *Nature* **2017**, *550* (7676), S113-S114.
 118. Kenna, K. P.; van Doormaal, P. T. C.; Dekker, A. M.; Ticozzi, N.; Kenna, B. J.; Diekstra, F. P.; ...; Landers, J. E., NEK1 variants confer susceptibility to amyotrophic lateral sclerosis. *Nature Genetics* **2016**, *48* (9), 1037-1042.
 119. Kenna, K. P.; van Doormaal, P. T. C.; Dekker, A. M.; Ticozzi, N.; Kenna, B. J.; Diekstra, F. P.; ...; Landers, J. E., NEK1 variants confer susceptibility to amyotrophic lateral sclerosis. *Nature genetics* **2016**, *48* (9), 1037-1042.
 120. Yao, L.; He, X.; Cui, B.; Zhao, F.; Zhou, C., NEK1 mutations and the risk of amyotrophic lateral sclerosis (ALS): a meta-analysis. *Neurological Sciences* **2021**
 121. Moraes, E. C.; Meirelles, G. V.; Honorato, R. V.; Souza, T. A. C. B.; Souza, E. E.; Murakami, M. T.; ...; Kobarg, J., Kinase inhibitor profile for human nek1, nek6, and nek7 and analysis of the structural basis for inhibitor specificity. *Molecules* **2015**, *20* (1), 1176–1191.
 122. Bennett, B. L.; Sasaki, D. T.; Murray, B. W.; Leary, E. C.; Sakata, S. T.; Xu, W.; ...; Anderson, D. W., SP600125, an anthrapyrazolone inhibitor of Jun N-terminal kinase. *Proceedings of the National Academy of Sciences* **2001**, *98* (24), 13681.
 123. Fedorov, O.; Niesen, F. H.; Knapp, S., Kinase Inhibitor Selectivity Profiling Using Differential Scanning Fluorimetry. In *Kinase Inhibitors: Methods and Protocols*, Kuster, B., Ed. Humana Press: Totowa, NJ, 2012; pp 109-118.
 124. Posy, S. L.; Hermsmeier, M. A.; Vaccaro, W.; Ott, K.-H.; Todderud, G.; Lippy, J. S.; ...; Johnson, S. R., Trends in Kinase Selectivity: Insights for Target Class-Focused Library Screening. *Journal of Medicinal Chemistry* **2011**, *54* (1), 54-66.
 125. Bergmann, C.; Guay-Woodford, L. M.; Harris, P. C.; Horie, S.; Peters, D. J. M.; Torres, V. E., Polycystic kidney disease. *Nature Reviews Disease Primers* **2018**, *4* (1), 50.

-
-
126. McKusick, V. A., Bilateral Polycystic Disease of the Kidneys. A Follow-Up of Two Hundred and Eighty-Four Patients and Their Families. O. Z. Dalgaard. *The Quarterly Review of Biology* **1958**, 33 (3), 223-224.
 127. Garcia Iglesias, C.; Torres, V. E.; Offord, K. P.; Holley, K. E.; Beard, C. M.; Kurland, L. T., Epidemiology of Adult Polycystic Kidney Disease, Olmsted County, Minnesota: 1935–1980. *American Journal of Kidney Diseases* **1983**, 2 (6), 630-639.
 128. Willey, C.; Kamat, S.; Stellhorn, R.; Blais, J., Analysis of Nationwide Data to Determine the Incidence and Diagnosed Prevalence of Autosomal Dominant Polycystic Kidney Disease in the USA: 2013–2015. *Kidney Diseases* **2019**, 5 (2), 107-117.
 129. Torres, V. E.; Harris, P. C.; Pirson, Y., Autosomal dominant polycystic kidney disease. *The Lancet* **2007**, 369 (9569), 1287-1301.
 130. Bergmann, C., ARPKD and early manifestations of ADPKD: the original polycystic kidney disease and phenocopies. *Pediatric Nephrology* **2015**, 30 (1), 15-30.
 131. Leonhard, W. N.; Zandbergen, M.; Veraar, K.; van den Berg, S.; van der Weerd, L.; Breuning, M.; ...; Peters, D. J. M., Scattered Deletion of PKD1 in Kidneys Causes a Cystic Snowball Effect and Recapitulates Polycystic Kidney Disease. *Journal of the American Society of Nephrology* **2015**, 26 (6), 1322.
 132. Sweeney, W. E., Jr.; Avner, E. D., Emerging Therapies for Childhood Polycystic Kidney Disease. *Frontiers in pediatrics* **2017**, 5, 77.
 133. Sans-Atxer, L.; Joly, D., Tolvaptan in the treatment of autosomal dominant polycystic kidney disease: patient selection and special considerations. *International Journal of Nephrology and Renovascular Disease* **2018**, 11, 41-51.
 134. Wakai, K.; Nakai, S.; Kikuchi, K.; Iseki, K.; Miwa, N.; Masakane, I.; ...; Akiba, T., Trends in incidence of end-stage renal disease in Japan, 1983–2000: age-adjusted and age-specific rates by gender and cause. *Nephrology Dialysis Transplantation* **2004**, 19 (8), 2044-2052.

-
-
135. Stengel, B.; Billon, S.; van Dijk, P. C. W.; Jager, K. J.; Dekker, F. W.; Simpson, K.; Briggs, J. D., Trends in the incidence of renal replacement therapy for end-stage renal disease in Europe, 1990–1999. *Nephrology Dialysis Transplantation* **2003**, *18* (9), 1824-1833.
 136. Hoefele, J.; Mayer, K.; Scholz, M.; Klein, H.-G., Novel PKD1 and PKD2 mutations in autosomal dominant polycystic kidney disease (ADPKD). *Nephrology Dialysis Transplantation* **2011**, *26* (7), 2181-2188.
 137. Cornec-Le Gall, E.; Torres, V. E.; Harris, P. C., Genetic Complexity of Autosomal Dominant Polycystic Kidney and Liver Diseases. *Journal of the American Society of Nephrology* **2018**, *29* (1), 13.
 138. Su, X.; Wu, M.; Yao, G.; El-Jouni, W.; Luo, C.; Tabari, A.; Zhou, J., Regulation of polycystin-1 ciliary trafficking by motifs at its C-terminus and polycystin-2 but not by cleavage at the GPS site. *Journal of cell science* **2015**, *128* (22), 4063-4073.
 139. Ha, K.; Nobuhara, M.; Wang, Q.; Walker, R. V.; Qian, F.; Schartner, C.; Cao, E.; Delling, M., The heteromeric PC-1/PC-2 polycystin complex is activated by the PC-1 N-terminus. *eLife* **2020**, *9*, e60684.
 140. Miyakawa, A.; Ibarra, C.; Malmersjö, S.; Aperia, A.; Wiklund, P.; Uhlén, P., Intracellular calcium release modulates polycystin-2 trafficking. *BMC Nephrology* **2013**, *14*, 34-34.
 141. Lee, K.; Battini, L.; Gusella, G. L., Cilium, centrosome and cell cycle regulation in polycystic kidney disease. *Biochimica et Biophysica Acta* **2011**, *1812* (10), 1263-1271.
 142. Fischer, E.; Legue, E.; Doyen, A.; Nato, F.; Nicolas, J.-F.; Torres, V.; ...; Pontoglio, M., Defective planar cell polarity in polycystic kidney disease. *Nature Genetics* **2006**, *38* (1), 21-23.
 143. Yamaguchi, T.; Nagao, S.; Wallace, D. P.; Belibi, F. A.; Cowley, B. D.; Pelling, J. C.; Grantham, J. J., Cyclic AMP activates B-Raf and ERK in cyst epithelial cells from

-
- autosomal-dominant polycystic kidneys. *Kidney International* **2003**, 63 (6), 1983-1994.
144. Rowe, I.; Chiaravalli, M.; Mannella, V.; Ulisse, V.; Quilici, G.; Pema, M.; Song, X. W.; Xu, H.; Mari, S.; Qian, F.; Pei, Y.; Musco, G.; Boletta, A., Defective glucose metabolism in polycystic kidney disease identifies a new therapeutic strategy. *Nature Medicine* **2013**, 19 (4), 488-493.
145. Alzarka, B.; Morizono, H.; Bollman, J. W.; Kim, D.; Guay-Woodford, L. M., Design and Implementation of the Hepatorenal Fibrocystic Disease Core Center Clinical Database: A Centralized Resource for Characterizing Autosomal Recessive Polycystic Kidney Disease and Other Hepatorenal Fibrocystic Diseases. *Frontiers in pediatrics* **2017**, 5, 80-80.
146. Kääriäinen, H., Polycystic kidney disease in children: a genetic and epidemiological study of 82 Finnish patients. *Journal of Medicinal Genetics* **1987**, 24 (8), 474-481.
147. Büscher, R.; Büscher, A. K.; Weber, S.; Mohr, J.; Hegen, B.; Vester, U.; Hoyer, P. F., Clinical manifestations of autosomal recessive polycystic kidney disease (ARPKD): kidney-related and non-kidney-related phenotypes. *Pediatric Nephrology* **2014**, 29 (10), 1915-1925.
148. Guay-Woodford, L. M.; Desmond, R. A., Autosomal Recessive Polycystic Kidney Disease: The Clinical Experience in North America. *Pediatrics* **2003**, 111 (5), 1072.
149. Srinath, A.; Shneider, B. L., Congenital hepatic fibrosis and autosomal recessive polycystic kidney disease. *Journal of Pediatric Gastroenterology and Nutrition* **2012**, 54 (5), 580-587.
150. Khan, K.; Schwarzenberg, S. J.; Sharp, H. L.; Matas, A. J.; Chavers, B. M., Morbidity from Congenital Hepatic Fibrosis after Renal Transplantation for Autosomal Recessive Polycystic Kidney Disease. *American Journal of Transplantation* **2002**, 2 (4), 360-365.

-
-
151. Dell, K. M.; Matheson, M.; Hartung, E. A.; Warady, B. A.; Furth, S. L.; Chronic Kidney Disease in Children, S., Kidney Disease Progression in Autosomal Recessive Polycystic Kidney Disease. *Journal of Pediatrics* **2016**, *171*, 196-201.e1.
 152. Goto, M.; Hoxha, N.; Osman, R.; Dell, K. M., The renin-angiotensin system and hypertension in autosomal recessive polycystic kidney disease. *Pediatric Nephrology* **2010**, *25* (12), 2449-2457.
 153. Harris, P. C. (2019, February 24). Autosomal Recessive Polycystic Kidney Disease. <https://rarediseases.org/rare-diseases/autosomal-recessive-polycystic-kidney-disease/> (Accessed 2021, February 17).
 154. National Library of Medicine (U.S.). (2017, June 14 - 2019 September 30). Safety, Pharmacokinetic, Single Ascending Dose Study of Tesevatinib in Pediatric Subjects With Autosomal Recessive Polycystic Kidney Disease (ARPKD), Identifier: NCT03096080. <https://www.clinicaltrials.gov/ct2/show/NCT03096080>
 155. National Library of Medicine (U.S.). Study of the Efficacy and Safety of Tesevatinib in Subjects With ADPKD. Identifier: NCT03203642. <https://clinicaltrials.gov/ct2/show/NCT03203642>
 156. Sweeney, W. E., Jr.; von Vigier, R. O.; Frost, P.; Avner, E. D., Src inhibition ameliorates polycystic kidney disease. *Journal of the American Society of Nephrology* **2008**, *19* (7), 1331-1341.
 157. Gendreau, S. B.; Ventura, R.; Keast, P.; Laird, A. D.; Yakes, F. M.; Zhang, W.; ...; Joly, A. H., Inhibition of the T790M Gatekeeper Mutant of the Epidermal Growth Factor Receptor by EXEL-7647. *Clinical Cancer Research* **2007**, *13* (12), 3713
 158. Sweeney, W. E.; Frost, P.; Avner, E. D., Tesevatinib ameliorates progression of polycystic kidney disease in rodent models of autosomal recessive polycystic kidney disease. *World Journal of Nephrology* **2017**, *6* (4), 188-200.

-
159. Ward, C. J.; Yuan, D.; Masyuk, T. V.; Wang, X.; Punyashthiti, R.; Whelan, S.; ...; Harris, P. C., Cellular and subcellular localization of the ARPKD protein; fibrocystin is expressed on primary cilia. *Human Molecular Genetics* **2003**, *12* (20), 2703-2710.
160. Zhang, J.; Wu, M.; Wang, S.; Shah, J. V.; Wilson, P. D.; Zhou, J., Polycystic kidney disease protein fibrocystin localizes to the mitotic spindle and regulates spindle bipolarity. *Human Molecular Genetics* **2010**, *19* (17), 3306-3319.
161. Hiesberger, T.; Gourley, E.; Erickson, A.; Koulen, P.; Ward, C. J.; Masyuk, T. V.; ...; Igarashi, P., Proteolytic Cleavage and Nuclear Translocation of Fibrocystin Is Regulated by Intracellular Ca²⁺ and Activation of Protein Kinase C. *Journal of Biological Chemistry* **2006**, *281* (45), 34357-34364.
162. Kaimori, J.-y.; Nagasawa, Y.; Menezes, L. F.; Garcia-Gonzalez, M. A.; Deng, J.; Imai, E.; Onuchic, L. F.; Guay-Woodford, L. M.; Germino, G. G., Polyductin undergoes notch-like processing and regulated release from primary cilia. *Human molecular genetics* **2007**, *16* (8), 942-956.
163. Zhang, M.-Z.; Mai, W.; Li, C.; Cho, S.-y.; Hao, C.; Moeckel, G.; ...; Wu, G., PKHD1 protein encoded by the gene for autosomal recessive polycystic kidney disease associates with basal bodies and primary cilia in renal epithelial cells. *Proceedings of the National Academy of Sciences of the United States of America* **2004**, *101* (8), 2311.
164. Kim, I.; Fu, Y.; Hui, K.; Moeckel, G.; Mai, W.; Li, C.; ...; Wu, G., Fibrocystin/polyductin modulates renal tubular formation by regulating polycystin-2 expression and function. *J Am Soc Nephrol* **2008**, *19* (3), 455-468.
165. Menezes, L. F. C.; Cai, Y.; Nagasawa, Y.; Silva, A. M. G.; Watkins, M. L.; Da Silva, A. M.; ...; Onuchic, L. F., Polyductin, the PKHD1 gene product, comprises isoforms expressed in plasma membrane, primary cilium, and cytoplasm. *Kidney International* **2004**, *66* (4), 1345-1355.

-
-
166. Lu, H.; Galeano, M. C. R.; Ott, E.; Kaeslin, G.; Kausalya, P. J.; Kramer, C.; ...; Bergmann, C., Mutations in DZIP1L, which encodes a ciliary-transition-zone protein, cause autosomal recessive polycystic kidney disease. *Nature Genetics* **2017**, *49* (7), 1025-1034.
167. Hu, Q.; Milenkovic, L.; Jin, H.; Scott, M. P.; Nachury, M. V.; Spiliotis, E. T.; Nelson, W. J., A septin diffusion barrier at the base of the primary cilium maintains ciliary membrane protein distribution. *Science* **2010**, *329* (5990), 436-439
168. Vogler, C.; Homan, S.; Pung, A.; Thorpe, C.; Barker, J.; Birkenmeier, E. H.; Upadhyya, P., Clinical and Pathologic Findings in Two New Allelic Murine Models of Polycystic Kidney Disease. *Journal of the American Society of Nephrology* **1999**, *10* (12), 2534.
169. Surpili, M. J.; Delben, T. M.; Kobarg, J., Identification of Proteins That Interact with the Central Coiled-Coil Region of the Human Protein Kinase NEK1. *Biochemistry* **2003**, *42* (51), 15369-15376.
170. Corbit, K. C.; Shyer, A. E.; Dowdle, W. E.; Gaulden, J.; Singla, V.; Reiter, J. F., Kif3a constrains β -catenin-dependent Wnt signalling through dual ciliary and non-ciliary mechanisms. *Nature Cell Biology* **2008**, *10* (1), 70-76.
171. Merdek, K. D.; Nguyen, N. T.; Toksoz, D., Distinct activities of the alpha-catenin family, alpha-catenin and alpha-catenin, on beta-catenin-mediated signaling. *Molecular and cellular biology* **2004**, *24* (6), 2410-2422.
172. Wuebkens, A.; Schmidt-Ott, K. M., WNT/ β -catenin signaling in polycystic kidney disease. *Kidney International* **2011**, *80* (2), 135-138.
173. Kleymanova, E.; Ibraghimov-Beskrovnaya, O.; Kugoh, H.; Everitt, J.; Xu, H.; Kiguchi, K.; L...; Walker, C., Tuberin-Dependent Membrane Localization of Polycystin-1: A Functional Link between Polycystic Kidney Disease and the TSC2 Tumor Suppressor Gene. *Molecular Cell* **2001**, *7* (4), 823-832.

-
-
174. Chen, Y.; Chiang, H.-C.; Litchfield, P.; Pena, M.; Juang, C.; Riley, D. J., Expression of Nek1 during kidney development and cyst formation in multiple nephron segments in the Nek1-deficient kat2J mouse model of polycystic kidney disease. *Journal of Biomedical Science* **2014**, *21* (1), 63.
175. Yim, H.; Sung, C. K.; You, J.; Tian, Y.; Benjamin, T., Nek1 and TAZ interact to maintain normal levels of polycystin 2. *Journal of the American Society of Nephrology* **2011**, *22* (5), 832-837.
176. Tian, Y.; Kolb, R.; Hong, J.-H.; Carroll, J.; Li, D.; You, J.; ...; Benjamin, T., TAZ Promotes PC2 Degradation through a SCF β -Trcp E3 Ligase Complex. *Molecular and Cellular Biology* **2007**, *27* (18), 6383.
177. Dutcher, S. K.; Lin, H., Tying TAZ and Nek1 into Polycystic Kidney Disease through Polycystin 2 Levels. *Journal of the American Society of Nephrology* **2011**, *22* (5), 791.
178. Polci, R.; Peng, A.; Chen, P.-L.; Riley, D. J.; Chen, Y., NIMA-Related Protein Kinase 1 Is Involved Early in the Ionizing Radiation-Induced DNA Damage Response. *Cancer Research* **2004**, *64* (24), 8800.
179. Grudzenski, S.; Raths, A.; Conrad, S.; Rube, C. E.; Löbrich, M., Inducible response required for repair of low-dose radiation damage in human fibroblasts. *Proceedings of the National Academy of Sciences* **2010**, *107* (32), 14205.
180. Cannan, W. J.; Pederson, D. S., Mechanisms and Consequences of Double-Strand DNA Break Formation in Chromatin. *Journal of Cell Physiology* **2016**, *231* (1), 3-14.
181. Alexander, J. L.; Orr-Weaver, T. L., Replication fork instability and the consequences of fork collisions from rereplication. *Genes & Development* **2016**, *30* (20), 2241-2252.
182. Spies, J.; Waizenegger, A.; Barton, O.; Surder, M.; Wright, W. D.; Heyer, W.-D.; Löbrich, M., Nek1 Regulates Rad54 to Orchestrate Homologous Recombination and Replication Fork Stability. *Molecular cell* **2016**, *62* (6), 903-917.

-
-
183. Spies, J. (2015). *Die Beteiligung von Nek1 an der Homologen Rekombination*. [Doctoral thesis, Technische Universität Darmstadt] TUPrints. <https://tuprints.ulb.tu-darmstadt.de/id/eprint/4423>
184. Blanton, H.; Sekelsky, J., Unique invasions and resolutions: DNA repair proteins in meiotic recombination in *Drosophila melanogaster*. *Cytogenetic and Genome Research* **2004**, *107* (3-4), 172-179.
185. Matos, J.; West, S. C., Holliday junction resolution: Regulation in space and time. *DNA Repair* **2014**, *19*, 176-181.
186. Mao, Z.; Bozzella, M.; Seluanov, A.; Gorbunova, V., Comparison of nonhomologous end joining and homologous recombination in human cells. *DNA repair* **2008**, *7* (10), 1765-1771.
187. Tutt, A.; Ashworth, A., The relationship between the roles of BRCA genes in DNA repair and cancer predisposition. *Trends in Molecular Medicine* **2002**, *8* (12), 571-576.
188. Patil, M.; Pabla, N.; Ding, H.-F.; Dong, Z., Nek1 interacts with Ku80 to assist chromatin loading of replication factors and S-phase progression. *Cell Cycle* **2013**, *12* (16), 2608-2616.
189. Gallego, M. E.; Bleuyard, J. Y.; Daoudal-Cotterell, S.; Jallut, N.; White, C. I., Ku80 plays a role in non-homologous recombination but is not required for T-DNA integration in Arabidopsis. *The Plant Journal* **2003**, *35* (5), 557-565.
190. Chen, Y.; Chen, P.-L.; Chen, C.-F.; Jiang, X.; Riley, D. J., Never-in-mitosis related Kinase 1 functions in DNA damage response and checkpoint control. *Cell Cycle* **2008**, *7* (20), 3194-3201.
191. Chen, Y.; Chen, C.-F.; Riley, D. J.; Chen, P.-L., Nek1 kinase functions in DNA damage response and checkpoint control through a pathway independent of ATM and ATR. *Cell cycle* **2011**, *10* (4), 655-663.

-
-
192. Liu, S.; Ho, C. K.; Ouyang, J.; Zou, L., Nek1 kinase associates with ATR–ATRIP and primes ATR for efficient DNA damage signaling. *Proceedings of the National Academy of Sciences* **2013**, *110* (6), 2175.
193. Gavande, N. S.; VanderVere-Carozza, P. S.; Hinshaw, H. D.; Jalal, S. I.; Sears, C. R.; Pawelczak, K. S.; Turchi, J. J., DNA repair targeted therapy: The past or future of cancer treatment? *Pharmacology & Therapeutics* **2016**, *160*, 65-83
194. Burgess, J. T.; Rose, M.; Boucher, D.; Plowman, J.; Molloy, C.; Fisher, M.; ...; Bolderson, E., The Therapeutic Potential of DNA Damage Repair Pathways and Genomic Stability in Lung Cancer. *Frontiers in Oncology* **2020**, *10*, 1256-1256.
195. Chen, Y.; Craigen, W. J.; Riley, D. J., Nek1 regulates cell death and mitochondrial membrane permeability through phosphorylation of VDAC1. *Cell cycle* **2009**, *8* (2), 257–267.
196. Chen, Y.; Gaczynska, M.; Osmulski, P.; Polci, R.; Riley, D. J., Phosphorylation by Nek1 regulates opening and closing of voltage dependent anion channel 1. *Biochemical and Biophysical Research Communications* **2010**, *394* (3), 798-803.
197. Chen, Y.; Chen, C.-F.; Polci, R.; Wei, R.; Riley, D. J.; Chen, P.-L., Increased Nek1 expression in renal cell carcinoma cells is associated with decreased sensitivity to DNA-damaging treatment. *Oncotarget* **2014**, *5* (12), 4283–4294.
198. Singh, V.; Connelly, Z. M.; Shen, X.; De Benedetti, A., Identification of the proteome complement of humanTLK1 reveals it binds and phosphorylates NEK1 regulating its activity. *Cell Cycle* **2017**, *16* (10), 915-926.
199. Singh, V.; Jaiswal, P. K.; Ghosh, I.; Koul, H. K.; Yu, X.; De Benedetti, A., Targeting the TLK1/NEK1 DDR axis with Thioridazine suppresses outgrowth of androgen independent prostate tumors. *International Journal of Cancer* **2019**, *145* (4), 1055-1067.

-
-
200. Singh, V.; Jaiswal, P. K.; Ghosh, I.; Koul, H. K.; Yu, X.; De Benedetti, A., The TLK1-Nek1 axis promotes prostate cancer progression. *Cancer Letters* **2019**, *453*, 131-141.
201. Zhu, J.; Cai, Y.; Liu, P.; Zhao, W., Frequent Nek1 overexpression in human gliomas. *Biochemical and Biophysical Research Communications* **2016**, *476* (4), 522-527.
202. Wei, R. L.; Chen, Y., Overexpression of Nek1 in Renal Cell Carcinoma Protects against Cell Death from Ionizing Radiation. *International Journal of Radiation Oncology • Biology • Physics* **2011**, *81* (2), S712.
203. Freund, I.; Hehlhans, S.; Martin, D.; Ensminger, M.; Fokas, E.; Rödel, C.; Löbrich, M.; Rödel, F., Fractionation-Dependent Radiosensitization by Molecular Targeting of Nek1. *Cells* **2020**, *9* (5), 1235.
204. Hengel, S. R.; Spies, M. A.; Spies, M., Small-Molecule Inhibitors Targeting DNA Repair and DNA Repair Deficiency in Research and Cancer Therapy. *Cell Chemical Biology* **2017**, *24* (9), 1101-1119.
205. Garibaldi, C.; Jerezek-Fossa, B. A.; Marvaso, G.; Dicuonzo, S.; Rojas, D. P.; Cattani, F.; ...; Ricotti, R., Recent advances in radiation oncology. *Ecancermedicalscience* **2017**, *11*, 785-785.
206. Pompos, A.; Durante, M.; Choy, H., Heavy Ions in Cancer Therapy. *JAMA Oncology* **2016**, *2* (12), 1539-1540.
207. Baskar, R.; Lee, K. A.; Yeo, R.; Yeoh, K.-W., Cancer and radiation therapy: current advances and future directions. *International Journal of Medical Sciences* **2012**, *9* (3), 193-199
208. Jeggo, Penny A.; Löbrich, M., How cancer cells hijack DNA double-strand break repair pathways to gain genomic instability. *Biochemical Journal* **2015**, *471* (1), 1-11.
209. O'Connor, Mark J., Targeting the DNA Damage Response in Cancer. *Molecular Cell* **2015**, *60* (4), 547-560.
210. Deeks, E. D., Olaparib: First Global Approval. *Drugs* **2015**, *75* (2), 231-240.

-
-
211. Kuemmel, S.; Harrach, H.; Schmutzler, R. K.; Kostara, A.; Ziegler-Löhr, K.; Dyson, M. H.; Chiari, O.; Reinisch, M., Olaparib for metastatic breast cancer in a patient with a germline PALB2 variant. *npj Breast Cancer* **2020**, *6* (1), 31.
212. U.S. Food and Drug Administration (2020, May 20). FDA approves olaparib for HRR gene-mutated metastatic castration-resistant prostate cancer. <https://www.fda.gov/drugs/drug-approvals-and-databases/fda-approves-olaparib-hrr-gene-mutated-metastatic-castration-resistant-prostate-cancer> (Accessed 2021, February 26).
213. Lord, C. J.; Tutt, A. N. J.; Ashworth, A., Synthetic Lethality and Cancer Therapy: Lessons Learned from the Development of PARP Inhibitors. *Annual Review of Medicine* **2015**, *66* (1), 455-470.
214. AstraZeneca (2020, Nov 5). Lynparza approved in the EU for the treatment of BRCA-mutated metastatic castration-resistant prostate cancer. <https://www.astrazeneca.com/media-centre/press-releases/2020/lynparza-approved-in-the-eu-for-prostate-cancer.html> (Accessed 2021, February 26).
215. Murai, J.; Huang, S.-y. N.; Das, B. B.; Renaud, A.; Zhang, Y.; Doroshow, ..., Trapping of PARP1 and PARP2 by Clinical PARP Inhibitors. *Cancer Research* **2012**, *72* (21), 5588.
216. Bixel, K.; Hays, J. L., Olaparib in the management of ovarian cancer. *Pharmacogenomics and Personalized Medicine* **2015**, *8*, 127-135.
217. Barnieh, F. M.; Loadman, P. M.; Falconer, R. A., Progress towards a clinically-successful ATR inhibitor for cancer therapy. *Current Research in Pharmacology and Drug Discovery* **2021**, *2*, 100017.
218. Zdrazil, B.; Guha, R., The Rise and Fall of a Scaffold: A Trend Analysis of Scaffolds in the Medicinal Chemistry Literature. *Journal of Medicinal Chemistry* **2018**, *61* (11), 4688-4703.

-
219. Müller, G., Medicinal chemistry of target family-directed masterkeys. *Drug Discovery Today* **2003**, *8* (15), 681-691.
220. Němec, V.; Hylsová, M.; Maier, L.; Flegel, J.; Sievers, S.; Ziegler, S.; S...; Paruch, K., Furo[3,2-b]pyridine: A Privileged Scaffold for Highly Selective Kinase Inhibitors and Effective Modulators of the Hedgehog Pathway. *Angewandte Chemie International Edition* **2019**, *58* (4), 1062-1066
221. Kontopidis, G.; McInnes, C.; Pandalaneni, S. R.; McNae, I.; Gibson, D.; Mezna, M.; ...; Fischer, P. M., Differential Binding of Inhibitors to Active and Inactive CDK2 Provides Insights for Drug Design. *Chemistry & Biology* **2006**, *13* (2), 201-211.
222. Wang, S.; Wood, G.; Meades, C.; Griffiths, G.; Midgley, C.; McNae, I.; McInnes, C.; Anderson, S.; Jackson, W.; Mezna, M.; Yuill, R.; Walkinshaw, M.; Fischer, P. M., Synthesis and biological activity of 2-anilino-4-(1H-pyrrol-3-yl) pyrimidine CDK inhibitors. *Bioorganic & Medicinal Chemistry Letters* **2004**, *14* (16), 4237-4240.
223. Merour, J.-Y.; Buron, F.; Ple, K.; Bonnet, P.; Routier, S., The azaindole framework in the design of kinase inhibitors. *Molecules* **2014**, *19* (12), 19935–19979.
224. Chaudhary, A.; Sharma, N., 7-Azaindole Analogues as Bioactive Agents and Recent Results. *Mini Reviews in Medicinal Chemistry* **2019**, *19*, 727-736.
225. Irie, T.; Sawa, M., 7-Azaindole: A Versatile Scaffold for Developing Kinase Inhibitors. *Chemical and Pharmaceutical Bulletin* **2018**, *66* (1), 29-36.
226. Ashok, P.; Chander, S.; Smith, T. K.; Prakash Singh, R.; Jha, P. N.; Sankaranarayanan, M., Biological evaluation and structure activity relationship of 9-methyl-1-phenyl-9H-pyrido[3,4-b]indole derivatives as anti-leishmanial agents. *Bioorganic Chemistry* **2019**, *84*, 98-105.
227. Srivastava, S. K.; Agarwal, A.; Chauhan, P. M. S.; Agarwal, S. K.; Bhaduri, A. P.; Singh, S. N.; ...; Chatterjee, R. K., Potent 1,3-Disubstituted-9H-pyrido[3,4-b]indoles as New

-
- Lead Compounds in Antifilarial Chemotherapy. *Journal of Medicinal Chemistry* **1999**, *42* (9), 1667-1672.
228. Das, S.; Brown, J. W.; Dong, Q.; Gong, X.; Kaldor, S. W.; Liu, Y.; ...; Wallace, M. B. Preparation of pyridoindoles as kinase inhibiting compounds for treating and preventing kinase-associated diseases. WO2007044779A1, **2007**.
229. Coxon, C. R.; Wong, C.; Bayliss, R.; Boxall, K.; Carr, K. H.; Fry, A. M.; ...; Cano, C., Structure-guided design of purine-based probes for selective Nek2 inhibition. *Oncotarget* **2017**, *8* (12), 19089–19124.
230. Drewry, D. H.; Wells, C. I.; Andrews, D. M.; Angell, R.; Al-Ali, H.; Axtman, A. D.; ...; Willson, T. M., Progress towards a public chemogenomic set for protein kinases and a call for contributions. *PLOS ONE* **2017**, *12* (8), e0181585.
231. Seefeld, M. A.; Rouse, M. B.; McNulty, K. C.; Sun, L.; Wang, J.; Yamashita, D. S.; Luengo, J. I.; ...; Heerding, D. A., Discovery of 5-pyrrolopyridinyl-2-thiophenecarbox amides as potent AKT kinase inhibitors. *Bioorg. Medicinal. Chemistry Letters* **2009**, *19* (8), 2244-2248
232. Liddle, J.; Bamborough, P.; Barker, M. D.; Campos, S.; Cousins, R. P. C.; Cutler, G. J.; ...; Williamson, R. A., 4-Phenyl-7-azaindoles as potent and selective IKK2 inhibitors. *Bioorganic & Medicinal Chemistry Letters* **2009**, *19* (9), 2504-2508.
233. Haq, T.; Richards, M. W.; Burgess, S. G.; Gallego, P.; Yeoh, S.; O'Regan, L.; ...; Bayliss, R., Mechanistic basis of Nek7 activation through Nek9 binding and induced dimerization. *Nature Communications* **2015**, *6* (1), 8771.
234. Liddle, J.; Bamborough, P.; Barker, M. D.; Campos, S.; Chung, C.-W.; Cousins, R. P. C.; ...; Williamson, R. A., 4-Phenyl-7-azaindoles as potent, selective and bioavailable IKK2 inhibitors demonstrating good in vivo efficacy. *Bioorganic & Medicinal Chemistry Letters* **2012**, *22* (16), 5222-5226.

-
235. Asquith, C. R. M.; Tizzard, G. J.; Bennett, J. M.; Wells, C. I.; Elkins, J. M.; Willson, T. M.; ...; Laitinen, T., Targeting the Water Network in Cyclin G-Associated Kinase (GAK) with 4-Anilino-quin(az)oline Inhibitors. *ChemMedChem* **2020**, *15* (13), 1200-1215.
236. Gerogiokas, G.; Southey, M. W. Y.; Mazanetz, M. P.; Hefetz, A.; Bodkin, M.; Law, R. J.; Michel, J., Evaluation of water displacement energetics in protein binding sites with grid cell theory. *Physical Chemistry Chemical Physics* **2015**, *17* (13), 8416-8426.
237. Riniker, S.; Barandun, L. J.; Diederich, F.; Krämer, O.; Steffen, A.; van Gunsteren, W. F., Free enthalpies of replacing water molecules in protein binding pockets. *Journal of Computer-Aided Molecular Design* **2012**, *26* (12), 1293-1309.
238. Abel, R.; Wang, L.; Friesner, R. A.; Berne, B. J., A Displaced-Solvent Functional Analysis of Model Hydrophobic Enclosures. *Journal of Chemical Theory and Computation* **2010**, *6* (9), 2924-2934.
239. Gamble, A. B.; Garner, J.; Gordon, C. P.; O'Conner, S. M. J.; Keller, P. A., Aryl Nitro Reduction with Iron Powder or Stannous Chloride under Ultrasonic Irradiation. *Synthetic Communications* **2007**, *37* (16), 2777-2786.
240. Ramadas, K.; Srinivasan, N., Iron-Ammonium Chloride - A Convenient and Inexpensive Reductant. *Synthetic Communications* **1992**, *22* (22), 3189-3195.
241. Boix, C.; Poliakoff, M., Selective reductions of nitroarenes to anilines using metallic zinc in near-critical water. *Journal of the Chemical Society, Perkin Transactions 1* **1999**, (11), 1487-1490.
242. Suslick, K. S., Sonochemistry. *Science* **1990**, *247* (4949), 1439.
243. Kajino, M.; Hasuoka, A.; Tarui, N.; Takagi, T. Preparation of pyrrole derivatives as proton pump inhibitors. WO2006036024A1, **2006**.
244. Atkinson, D. A.; Sim, T. C.; Grant, J. A., Sodium metabisulfite and SO₂ release: an under-recognized hazard among shrimp fishermen. *Annals of Allergy, Asthma & Immunology* **1993**, *71* (6), 563-6.

-
245. Hoffman, R. V., m-Trifluoromethylbenzenesulfonyl chloride. *Org. Synth.* **1981**, *60*, 121-6.
246. Woolven, H.; González-Rodríguez, C.; Marco, I.; Thompson, A. L.; Willis, M. C., DABCO-Bis(sulfur dioxide), DABSO, as a Convenient Source of Sulfur Dioxide for Organic Synthesis: Utility in Sulfonamide and Sulfamide Preparation. *Organic Letters* **2011**, *13* (18), 4876-4878.
247. Barroso, S.; Joksch, M.; Puylaert, P.; Tin, S.; Bell, S. J.; Donnellan, L.; ...; de Vries, J. G., Improvement in the Palladium-Catalyzed Miyaura Borylation Reaction by Optimization of the Base: Scope and Mechanistic Study. *The Journal of Organic Chemistry* **2020**.
248. Lozada, J.; Liu, Z.; Perrin, D. M., Base-Promoted Protodeboronation of 2,6-Disubstituted Arylboronic Acids. *The Journal of Organic Chemistry* **2014**, *79* (11), 5365-5368.
249. Kinzel, T.; Zhang, Y.; Buchwald, S. L., A New Palladium Precatalyst Allows for the Fast Suzuki–Miyaura Coupling Reactions of Unstable Polyfluorophenyl and 2-Heteroaryl Boronic Acids. *Journal of the American Chemical Society* **2010**, *132* (40), 14073-14075.
250. Cordovilla, C.; Bartolomé, C.; Martínez-Ilarduya, J. M.; Espinet, P., The Stille Reaction, 38 Years Later. *ACS Catalysis* **2015**, *5* (5), 3040-3053.
251. Tan, X.; Zhou, Z. J.; Zhang, J. X.; Duan, X. H., Efficient One-Pot Cross-Coupling of Two Aryl Halides by Stannylation/Stille Reaction in Water under Microwave Irradiation. *European Journal of Organic Chemistry* **2014**, *2014* (24), 5153-5157.
252. Madhavi Sastry, G.; Adzhigirey, M.; Day, T.; Annabhimoju, R.; Sherman, W., Protein and ligand preparation: parameters, protocols, and influence on virtual screening enrichments. *Journal of Computer-Aided Molecular Design* **2013**, *27* (3), 221-234.
253. Feher, M.; Williams, C. I., Numerical Errors and Chaotic Behavior in Docking Simulations. *Journal of Chemical Information and Modeling* **2012**, *52* (3), 724-738.

-
-
254. Oellien, F.; Cramer, J.; Beyer, C.; Ihlenfeldt, W.-D.; Selzer, P. M., The Impact of Tautomer Forms on Pharmacophore-Based Virtual Screening. *Journal of Chemical Information and Modeling* **2006**, *46* (6), 2342-2354.
255. Ismer, J.; Rose, A. S.; Tiemann, Johanna K. S.; Goede, A.; Preissner, R.; Hildebrand, P. W., SL2: an interactive webtool for modeling of missing segments in proteins. *Nucleic Acids Research* **2016**, *44* (W1), W390-W394.
256. Agrawal, P.; Thakur, Z.; Kulharia, M., Homology modeling and structural validation of tissue factor pathway inhibitor. *Bioinformatics* **2013**, *9* (16), 808-812.
257. Park, M.-S.; Gao, C.; Stern, H. A., Estimating binding affinities by docking/scoring methods using variable protonation states. *Proteins: Structure, Function, and Bioinformatics* **2011**, *79* (1), 304-314.
258. Friesner, R. A.; Murphy, R. B.; Repasky, M. P.; Frye, L. L.; Greenwood, J. R.; Halgren, T. A.; ...; Mainz, D. T., Extra Precision Glide: Docking and Scoring Incorporating a Model of Hydrophobic Enclosure for Protein–Ligand Complexes. *Journal of Medicinal Chemistry* **2006**, *49* (21), 6177-6196.
259. Diller, D. J.; Li, R., Kinases, Homology Models, and High Throughput Docking. *Journal of Medicinal Chemistry* **2003**, *46* (22), 4638-4647.
260. Lipinski, C. A.; Lombardo, F.; Dominy, B. W.; Feeney, P. J., Experimental and computational approaches to estimate solubility and permeability in drug discovery and development settings. *Advanced Drug Delivery Reviews* **1997**, *23* (1), 3-25.
261. Gillet, V. J.; Leach, A. R., Chemoinformatics. In *Comprehensive Medicinal Chemistry II*, Taylor, J. B.; Triggle, D. J., Eds. Elsevier: Oxford, 2007; pp 235-264.
262. Pajouhesh, H.; Lenz, G. R., Medicinal chemical properties of successful central nervous system drugs. *NeuroRX* **2005**, *2* (4), 541-553.

-
263. Chen, H.; Zhou, X.; Gao, Y.; Chen, H.; Zhou, J., 2.08 - Fragment-Based Drug Design: Strategic Advances and Lessons Learned. In *Comprehensive Medicinal Chemistry III*, Chackalamannil, S.; Rotella, D.; Ward, S. E., Eds. Elsevier: Oxford, 2017; pp 212-232.
264. McKennon, M. J.; Meyers, A. I.; Drauz, K.; Schwarm, M., A convenient reduction of amino acids and their derivatives. *The Journal of Organic Chemistry* **1993**, *58* (13), 3568-3571.
265. Chong, H.-S.; Song, H. A.; Dadwal, M.; Sun, X.; Sin, I.; Chen, Y., Efficient Synthesis of Functionalized Aziridinium Salts. *The Journal of Organic Chemistry* **2010**, *75* (1), 219-221.
266. Cardenas, M. M.; Toenjes, S. T.; Nalbandian, C. J.; Gustafson, J. L., Enantioselective Synthesis of Pyrrolopyrimidine Scaffolds through Cation-Directed Nucleophilic Aromatic Substitution. *Organic Letters* **2018**, *20* (7), 2037-2041.
267. Handy, S. T.; Bregman, H.; Lewis, J.; Zhang, X.; Zhang, Y., An unusual dehalogenation in the Suzuki coupling of 4-bromopyrrole-2-carboxylates. *Tetrahedron Letters* **2003**, *44* (3), 427-430.
268. Smith, J. A.; Ng, S.; White, J., The regioselective synthesis of aryl pyrroles. *Organic & Biomolecular Chemistry* **2006**, *4* (12), 2477-2482.
269. Paul Galatsis, M. M. H., Bethany Lyn Kormos, Travis T. Wager, Lei Zhang, Jaclyn Louise Henderson, Ravi G. Kurumbail, Patrick Robert Verhoest, Antonia Friederike Stepan, Novel 3,4-disubstituted-1h-pyrrolo[2,3-b]pyridines and 4,5-disubstituted-7h-pyrrolo[2,3-c]pyridazines as lrrk2 inhibitors, WO2015092592A1, **2014**.
270. Almond-Thynne, J.; Blakemore, D. C.; Pryde, D. C.; Spivey, A. C., Site-selective Suzuki-Miyaura coupling of heteroaryl halides - understanding the trends for pharmaceutically important classes. *Chemical Science* **2017**, *8* (1), 40-62.

-
271. Colacot, T. J.; Shea, H. A., Cp₂Fe(PR₂)₂PdCl₂ (R = i-Pr, t-Bu) Complexes as Air-Stable Catalysts for Challenging Suzuki Coupling Reactions. *Organic Letters* **2004**, *6* (21), 3731-3734
272. Kuivila, H. G.; Reuwer Jr, J. F.; Mangravite, J. A., Electrophilic Displacement Reactions: XV. Kinetics and Mechanism of the Base-Catalyzed Protodeboronation of Areneboronic Acids. *Canadian Journal of Chemistry* **1963**, *41* (12), 3081-3090.
273. Cox, P. A.; Reid, M.; Leach, A. G.; Campbell, A. D.; King, E. J.; Lloyd-Jones, G. C., Base-Catalyzed Aryl-B(OH)₂ Protodeboronation Revisited: From Concerted Proton Transfer to Liberation of a Transient Aryl Anion. *Journal of the American Chemical Society* **2017**, *139* (37), 13156-13165.
274. Röhlich, C.; Wirth, A. S.; Köhler, K., Suzuki Coupling Reactions in Neat Water as the Solvent: Where in the Biphasic Reaction Mixture Do the Catalytic Reaction Steps Occur? *Chemistry – A European Journal* **2012**, *18* (48), 15485-15494.
275. Pentsak, E. O.; Ananikov, V. P., Pseudo-Solid-State Suzuki–Miyaura Reaction and the Role of Water Formed by Dehydration of Arylboronic Acids. *European Journal of Organic Chemistry* **2019**, *2019* (26), 4239-4247.
276. Yasuhara, A.; Sakamoto, T., Deprotection of *N*-sulfonyl nitrogen-heteroaromatics with tetrabutylammonium fluoride. *Tetrahedron Letters* **1998**, *39* (7), 595-596.
277. Gummadi, V. R.; Rajagopalan, S.; Looi, C.-Y.; Paydar, M.; Renukappa, G. A.; Ainan, B. R.; ...; Hosahalli, S., Discovery of 7-azaindole based anaplastic lymphoma kinase (ALK) inhibitors: Wild type and mutant (L1196M) active compounds with unique binding mode. *Bioorganic & Medicinal Chemistry Letters* **2013**, *23* (17), 4911-4918.
278. Storz, T.; Bartberger, M. D.; Sukits, S.; Wilde, C.; Soukup, T., The first practical and efficient one-pot synthesis of 6-substituted 7-azaindoles via a Reissert-Henze reaction. *Synthesis* **2008**, (2), 201-214.

-
279. Thibault, C.; L'Heureux, A.; Bhide, R. S.; Ruel, R., Concise and Efficient Synthesis of 4 Fluoro-1H-pyrrolo[2,3-b]pyridine. *Organic Letters* **2003**, *5* (26), 5023-5025.
280. Minakata, S.; Komatsu, M.; Ohshiro, Y., Regioselective Functionalization of 1H-Pyrrolo[2,3-b]pyridine via Its N-Oxide. *Synthesis* **1992**, *1992* (7), 661-663.
281. Sreenivasachary, N.; Kroth, H.; Benderitter, P.; Hamel, A.; Varisco, Y.; Hickman, D. T.; ...; Muhs, A., Discovery and characterization of novel indole and 7-azaindole derivatives as inhibitors of β -amyloid-42 aggregation for the treatment of Alzheimer's disease. *Bioorganic & Medicinal Chemistry Letters* **2017**, *27* (6), 1405-1411.
282. L'Heureux, A.; Thibault, C.; Ruel, R., Synthesis of functionalized 7-azaindoles via directed ortho-metalations. *Tetrahedron Letters* **2004**, *45* (11), 2317-2319.
283. Schmidt, B.; Neitemeier, V., 6-Pyridylnicotine and Bis-6,6'-nicotine – New Chiral 2,2'-Bipyridines. *Synthesis* **1998**, *1998* (1), 42-44.
284. Surasani, R.; Kalita, D.; Rao, A. V. D.; Chandrasekhar, K. B., Palladium-catalyzed C–N and C–O bond formation of N-substituted 4-bromo-7-azaindoles with amides, amines, amino acid esters and phenols. *Beilstein Journal of Organic Chemistry* **2012**, *8*, 2004-2018.
285. Dorel, R.; Grugel, C. P.; Haydl, A. M., The Buchwald–Hartwig Amination After 25 Years. *Angewandte Chemie International Edition* **2019**, *58* (48), 17118-17129.
286. Chen, J.-Q.; Li, J.-H.; Dong, Z.-B., A Review on the Latest Progress of Chan-Lam Coupling Reaction. *Advanced Synthesis & Catalysis* **2020**, *362* (16), 3311-3331.
287. Vantourout, J. C.; Miras, H. N.; Isidro-Llobet, A.; Sproules, S.; Watson, A. J. B., Spectroscopic Studies of the Chan–Lam Amination: A Mechanism-Inspired Solution to Boronic Ester Reactivity. *Journal of the American Chemical Society* **2017**, *139* (13), 4769-4779.
288. Smyth, L. A.; Collins, I., Measuring and interpreting the selectivity of protein kinase inhibitors. *Journal of Chemical Biology* **2009**, *2* (3), 131-151.

-
289. Schönherr, H.; Cernak, T., Profound Methyl Effects in Drug Discovery and a Call for New C-H Methylation Reactions. *Angewandte Chemie International Edition* **2013**, *52*, 12256-12267.
290. Günther, M.; Juchum, M.; Kelter, G.; Fiebig, H.; Laufer, S., Lung Cancer: EGFR Inhibitors with Low Nanomolar Activity against a Therapy-Resistant L858R/T790M/C797S Mutant. *Angewandte Chemie International Edition* **2016**, *55* (36), 10890-10894.
291. Ciulli, A., Biophysical screening for the discovery of small-molecule ligands. *Methods in Molecular Biology* **2013**, *1008*, 357-388.
292. Petukh, M.; Stefl, S.; Alexov, E., The role of protonation states in ligand-receptor recognition and binding. *Current Pharmaceutical Design* **2013**, *19* (23), 4182-4190.
293. Xu, M.; Lill, M. A., Induced fit docking, and the use of QM/MM methods in docking. *Drug Discovery Today: Technologies* **2013**, *10* (3), e411-e418.
294. Lexa, K. W.; Carlson, H. A., Protein flexibility in docking and surface mapping. *Quarterly Reviews of Biophysics* **2012**, *45* (3), 301-343.
295. Bembenek, S. D.; Hirst, G.; Mirzadegan, T., Determination of a Focused Mini Kinase Panel for Early Identification of Selective Kinase Inhibitors. *Journal of Chemical Information and Modeling* **2018**, *58* (7), 1434-1440.
296. EurofinsDiscoveryServices (2020). KinaseProfiler™. <https://www.eurofinsdiscovery.com/services/in-vitro-assays/kinases/kinase-profiler/>. (Accessed 2021, March 3)
297. Savjani, K. T.; Gajjar, A. K.; Savjani, J. K., Drug solubility: importance and enhancement techniques. *ISRN Pharmaceutics* **2012**, *2012*, 195727-195727.
298. Kalepu, S.; Nekkanti, V., Insoluble drug delivery strategies: review of recent advances and business prospects. *Acta Pharmaceutica Sinica B* **2015**, *5* (5), 442-453.

-
-
299. Veseli, A.; Žakelj, S.; Kristl, A., A review of methods for solubility determination in biopharmaceutical drug characterization. *Drug Development and Industrial Pharmacy* **2019**, *45* (11), 1717-1724.
300. Meyers, J. R., Zebrafish: Development of a Vertebrate Model Organism. *Current Protocols Essential Laboratory Techniques* **2018**, *16* (1), e19.
301. Cold Spring Harbor Protocols (2011). E3 medium (for zebrafish embryos). doi:10.1101/pdb.rec066449. (Accessed 2021 March 12)
302. Hubatsch, I.; Ragnarsson, E. G. E.; Artursson, P., Determination of drug permeability and prediction of drug absorption in Caco-2 monolayers. *Nature Protocols* **2007**, *2* (9), 2111-2119.
303. Hilgers, A. R.; Conradi, R. A.; Burton, P. S., Caco-2 Cell Monolayers as a Model for Drug Transport Across the Intestinal Mucosa. *Pharmaceutical Research* **1990**, *7* (9), 902-910.
304. Pinto, M., Enterocyte-like differentiation and polarization of the human colon carcinoma cell line Caco-2 in culture. *Biology of the Cell* **1983**, *47*, 323-330.
305. Hidalgo, I. J.; Raub, T. J.; Borchardt, R. T., Characterization of the human colon carcinoma cell line (Caco-2) as a model system for intestinal epithelial permeability. *Gastroenterology* **1989**, *96* (3), 736-749.
306. Artursson, P., Epithelial Transport Of Drugs In Cell Culture. I: A Model For Studying The Passive Diffusion Of Drugs Over Intestinal Absorbative (Caco-2) Cells. *Journal of Pharmaceutical Sciences* **1990**, *79* (6), 476-482.
307. Wilson, G.; Hassan, I. F.; Dix, C. J.; Williamson, I.; Shah, R.; Mackay, M.; Artursson, P., Transport and permeability properties of human Caco-2 cells: An in vitro model of the intestinal epithelial cell barrier. *Journal of Controlled Release* **1990**, *11* (1), 25-40.
308. Heikkinen, A. T.; Mönkkönen, J.; Korjamo, T., Kinetics of Cellular Retention during Caco-2 Permeation Experiments: Role of Lysosomal Sequestration and Impact on

-
- Permeability Estimates. *Journal of Pharmacology and Experimental Therapeutics* **2009**, 328 (3), 882.
309. Bittner, B.; Guenzi, A.; Fullhardt, P.; Zuercher, G.; González, R. C. B.; Mountfield, R. J., Improvement of the bioavailability of colchicine in rats by co-administration of D-alpha-tocopherol polyethylene glycol 1000 succinate and a polyethoxylated derivative of 12-hydroxy-stearic acid. *Arzneimittelforschung* **2002**, 52 (9), 684-688.
310. Zur, M.; Gasparini, M.; Wolk, O.; Amidon, G. L.; Dahan, A., The Low/High BCS Permeability Class Boundary: Physicochemical Comparison of Metoprolol and Labetalol. *Molecular Pharmaceutics* **2014**, 11 (5), 1707-1714.
311. Stepanovs, D.; Jure, M.; Yanichev, A.; Belyakov, S.; Mishnev, A., Molecular salts of propranolol with dicarboxylic acids: diversity of stoichiometry, supramolecular structures and physicochemical properties. *CrystEngComm* **2015**, 17 (47), 9023-9028.
312. Pavlović, N.; Goločorbin-Kon, S.; Đanić, M.; Stanimirov, B.; Al-Salami, H.; Stankov, K.; Mikov, M., Bile Acids and Their Derivatives as Potential Modifiers of Drug Release and Pharmacokinetic Profiles. *Frontiers in Pharmacology* **2018**, 9, 1283-1283.
313. Awortwe, C.; Fasinu, P. S.; Rosenkranz, B., Application of Caco-2 cell line in herb-drug interaction studies: current approaches and challenges. *Journal of Pharmacy & Pharmaceutical Sciences* **2014**, 17 (1), 1-19.
314. Krishna, G.; Chen, K.-j.; Lin, C.-c.; Nomeir, A. A., Permeability of lipophilic compounds in drug discovery using in-vitro human absorption model, Caco-2. *International Journal of Pharmaceutics* **2001**, 222 (1), 77-89.
315. Cai, X.; Walker, A.; Cheng, C.; Paiva, A.; Li, Y.; Kolb, J.; Herbst, J.; Shou, W.; Weller, H., Approach to Improve Compound Recovery in a High-Throughput Caco-2 Permeability Assay Supported by Liquid Chromatography–Tandem Mass Spectrometry. *Journal of Pharmaceutical Sciences* **2012**, 101 (8), 2755-2762.

-
-
316. Amidon, G. L.; Lennernäs, H.; Shah, V. P.; Crison, J. R., A Theoretical Basis for a Biopharmaceutic Drug Classification: The Correlation of *in Vitro* Drug Product Dissolution and *in Vivo* Bioavailability. *Pharmaceutical Research* **1995**, *12* (3), 413-420.
317. Haldi, M.; Harden, M.; D'Amico, L.; DeLise, A.; Seng, W. L., Developmental Toxicity Assessment in Zebrafish. In *Zebrafish: Methods for Assessing Drug Safety and Toxicity*, P. McGrath, Ed. John Wiley & Sons, Inc.: Hoboken, New Jersey, **2012**; p Ch. 2, pp 15-17.
318. Outtandy, P.; Russell, C.; Kleta, R.; Bockenbauer, D., Zebrafish as a model for kidney function and disease. *Pediatric Nephrology* **2019**, *34* (5), 751-762.
319. Gehrig, J.; Pandey, G.; Westhoff, J. H., Zebrafish as a Model for Drug Screening in Genetic Kidney Diseases. *Frontiers in Pediatrics* **2018**, *6*, 183.
320. Knight, Z. A.; Shokat, K. M., Chemical Genetics: Where Genetics and Pharmacology Meet. *Cell* **2007**, *128* (3), 425-430.
321. Shalom, O.; Shalva, N.; Altschuler, Y.; Motro, B., The mammalian Nek1 kinase is involved in primary cilium formation. *FEBS letters* **2008**, *582* (10), 1465-1470.
322. Karlin, S.; Altschul, S. F., Methods for assessing the statistical significance of molecular sequence features by using general scoring schemes. *Proceedings of the National Academy of Sciences* **1990**, *87* (6), 2264.
323. Wlodarchak, N.; Tariq, R.; Striker, R., Comparative analysis of the human and zebrafish kinomes: focus on the development of kinase inhibitors. *Trends in cell & molecular biology* **2015**, *10*, 49-75.

-
-
324. Westhoff, J. H.; Giselbrecht, S.; Schmidts, M.; Schindler, S.; Beales, P. L.; Tönshoff, B.; ...; Gehrig, J., Development of an Automated Imaging Pipeline for the Analysis of the Zebrafish Larval Kidney. *PLOS ONE* **2013**, *8* (12), e82137.
325. Sander, V.; Patke, S.; Sahu, S.; Teoh, C. L.; Peng, Z.; Chang, Y.-T.; Davidson, A. J., The small molecule probe PT-Yellow labels the renal proximal tubules in zebrafish. *Chemical Communications* **2015**, *51* (2), 395-398.
326. Christou-Savina, S.; Beales, P. L.; Osborn, D. P. S., Evaluation of Zebrafish Kidney Function Using a Fluorescent Clearance Assay. *JoVE (Journal of Visualized Experiments)* **2015**, (96), e52540-e52540.
327. Pouretezadi, S. J.; Wingert, R. A., Little fish, big catch: zebrafish as a model for kidney disease. *Kidney international* **2016**, *89* (6), 1204-1210.
328. Weerapana, E.; Simon, G. M.; Cravatt, B. F., Disparate proteome reactivity profiles of carbon electrophiles. *Nature Chemical Biology* **2008**, *4* (7), 405-407.
329. Hoch, D. G.; Abegg, D.; Adibekian, A., Cysteine-reactive probes and their use in chemical proteomics. *Chemical Communications* **2018**, *54* (36), 4501-4512.
330. Lonsdale, R.; Burgess, J.; Colclough, N.; Davies, N. L.; Lenz, E. M.; Orton, A. L.; Ward, R. A., Expanding the Armory: Predicting and Tuning Covalent Warhead Reactivity. *Journal of Chemical Information and Modeling* **2017**, *57* (12), 3124-3137.
331. Kimmel, C. B.; Ballard, W. W.; Kimmel, S. R.; Ullmann, B.; Schilling, T. F., Stages of embryonic development of the zebrafish. *Developmental Dynamics* **1995**, *203* (3), 253-310.
332. Agalou, A.; Thrapsianiotis, M.; Angelis, A.; Papakyriakou, A.; Skaltsounis, A.-L.; Aligiannis, N.; Beis, D., Identification of Novel Melanin Synthesis Inhibitors From *Crataegus pycnoloba* Using an in Vivo Zebrafish Phenotypic Assay. *Frontiers in Pharmacology* **2018**, *9*, 265.

-
-
333. Karlsson, J.; von Hofsten, J.; Olsson, P.-E., Generating Transparent Zebrafish: A Refined Method to Improve Detection of Gene Expression During Embryonic Development. *Marine Biotechnology* **2001**, 3 (6), 522-527.
334. Elsalini, O. A.; Rohr, K. B., Phenylthiourea disrupts thyroid function in developing zebrafish. *Development Genes and Evolution* **2003**, 212 (12), 593-598.
335. Antinucci, P.; Hindges, R., A crystal-clear zebrafish for in vivo imaging. *Scientific Reports* **2016**, 6 (1), 29490.
336. EUR-Lex (2010, September 20). Horizontal legislation on the protection of animals used for scientific purposes Directive 2010/63/EU. <http://data.europa.eu/eli/dir/2010/63/2019-06-26>. (Accessed 2021, March 20)
337. Strähle, U.; Scholz, S.; Geisler, R.; Greiner, P.; Hollert, H.; Rastegar, S.; Schumacher, A.; Selderslaghs, I.; Weiss, C.; Witters, H.; Braunbeck, T., Zebrafish embryos as an alternative to animal experiments - A commentary on the definition of the onset of protected life stages in animal welfare regulations. *Reproductive Toxicology* **2012**, 33 (2), 128-132.
338. Collymore, C.; Tolwani, A.; Lieggi, C.; Rasmussen, S., Efficacy and safety of 5 anesthetics in adult zebrafish (*Danio rerio*). *Journal of the American Association for Laboratory Animal Science* **2014**, 53 (2), 198-203.
339. Lee, J.-S.; Wee, T.-L. E.; Brown, C. M., Calibration of wide-field deconvolution microscopy for quantitative fluorescence imaging. *Journal of Biomolecular Techniques* **2014**, 25 (1), 31-40.
340. Swedlow, J. R., Chapter 17 - Quantitative Fluorescence Microscopy and Image Deconvolution. In *Methods in Cell Biology*, Sluder, G.; Wolf, D. E., Eds. Academic Press: **2013**; Vol. 114, pp 407-426.

-
-
341. Kirshner, H.; Aguet, F.; Sage, D.; Unser, M., 3-D PSF Fitting for Fluorescence Microscopy: Implementation and Localization Application. *Journal of Microscopy* **2013**, *249* (1), 13-25.
342. Li, J.; Xue, F.; Blu, T., Fast and accurate three-dimensional point spread function computation for fluorescence microscopy. *Journal of the Optical Society of America* **2017**, *34* (6), 1029-1034.
343. Zajac, A.; Hecht, E., *Optics, Fourth Edit.* Pearson Higher Education: Harlow, Essex, **2003**, p 343.
344. Lee, T. M.; Toublan, F. J. J.; Oldenburg, A.; Sitafalwalla, S.; Luo, W.; Daniel, L. M.; Kenneth, S. S.; Stephen, A. B., Optical characterization of contrast agents for optical coherence tomography. *Proceedings of SPIE* **2003**, *4967*.
345. Sage, D.; Donati, L.; Soulez, F.; Fortun, D.; Schmit, G.; Seitz, A.; Guiet, R.; Vonesch, C.; Unser, M., DeconvolutionLab2: An open-source software for deconvolution microscopy. *Methods* **2017**, *115*, 28-41.
346. Laasmaa, M.; Vendelin, M.; Peterson, P., Application of regularized Richardson-Lucy algorithm for deconvolution of confocal microscopy images. *Journal of Microscopy* **2011**, *243* (2), 124-140.
347. Richardson, W. H., Bayesian-Based Iterative Method of Image Restoration. *Journal of the Optical Society of America* **1972**, *62* (1), 55-59.
348. Park, E. Y.; Seo, M. J.; Park, J. H., Effects of Specific Genes Activating RAGE on Polycystic Kidney Disease. *American Journal of Nephrology* **2010**, *32* (2), 169-178.
349. Booiij, T. H.; Bange, H.; Leonhard, W. N.; Yan, K.; Fokkelman, M.; Kunnen, S. J.; ...; Price, L. S., High-Throughput Phenotypic Screening of Kinase Inhibitors to Identify Drug Targets for Polycystic Kidney Disease. *SLAS Discovery* **2017**, *22* (8), 974-984.

-
350. Correa, R. G.; Matsui, T.; Tergaonkar, V.; Rodriguez-Esteban, C.; Izpisua-Belmonte, J. C.; Verma, I. M., Zebrafish IκB Kinase 1 Negatively Regulates NF-κB Activity. *Current Biology* **2005**, *15* (14), 1291-1295.
351. Li, X., Epigenetics and cell cycle regulation in cystogenesis. *Cellular Signalling* **2020**, *68*, 109509.
352. Saigusa, T.; Bell, P. D., Molecular Pathways and Therapies in Autosomal-Dominant Polycystic Kidney Disease. *Physiology* **2015**, *30* (3), 195-207.
353. Song, X.; Di Giovanni, V.; He, N.; Wang, K.; Ingram, A.; Rosenblum, N. D.; Pei, Y., Systems biology of autosomal dominant polycystic kidney disease (ADPKD): computational identification of gene expression pathways and integrated regulatory networks. *Human Molecular Genetics* **2009**, *18* (13), 2328-2343.
354. Bamborough, P.; Barker, M. D.; Campos, S. A.; Cousins, R. P. C.; Faulder, P.; Hobbs, H.; ...; Whitworth, C., Pyrrolo[2,3-b]pyridin-4-yl-benzenesulfonamide compounds as IKK2 inhibitors and their preparation, pharmaceutical compositions and use in the treatment of diseases. WO2008034860A1, **2008**.
355. John, C. S.; Lim, B. B.; Vilner, B. J.; Geyer, B. C.; Bowen, W. D., Substituted Halogenated Arylsulfonamides: A New Class of σ Receptor Binding Tumor Imaging Agents. *Journal of Medicinal Chemistry* **1998**, *41* (14), 2445-2450.
356. Berg, S.; Bergh, M.; Hellberg, S.; Högdin, K.; Lo-Alfredsson, Y.; Söderman, P.; v...; Bhat, R., Discovery of Novel Potent and Highly Selective Glycogen Synthase Kinase-3 β (GSK3 β) Inhibitors for Alzheimer's Disease: Design, Synthesis, and Characterization of Pyrazines. *Journal of Medicinal Chemistry* **2012**, *55* (21), 9107-9119.
357. Khoje, A. D.; Charnock, C.; Wan, B.; Franzblau, S.; Gundersen, L.-L., Synthesis and antimycobacterial activities of non-purine analogs of 6-aryl-9-benzylpurines: Imidazopyridines, pyrrolopyridines, benzimidazoles, and indoles. *Bioorganic & Medicinal Chemistry* **2011**, *19* (11), 3483-3491.

-
358. Baell, J. B.; Holloway, G. A., New Substructure Filters for Removal of Pan Assay Interference Compounds (PAINS) from Screening Libraries and for Their Exclusion in Bioassays. *Journal of Medicinal Chemistry* **2010**, 53 (7), 2719-2740.
359. Edelstein, A. D.; Tsuchida, M. A.; Amodaj, N.; Pinkard, H.; Vale, R. D.; Stuurman, N., Advanced methods of microscope control using μ Manager software. *Journal of Biological Methods; Vol 1, No 2 (2014)* **2014**.

Appendix

A. *In silico* screening data for the molecular docking of the virtual compound library

Table A 1: *In silico* screening data for the molecular docking of the virtual compound library into the P-loop reconstructed SuperLooper2 model. Compounds with TPSA > 120 are not shown. See experimental section for more details. HAN, heavy atom number; LE, ligand efficiency; MW, molecular weight; BEI, binding efficiency index; TPSA, topological polar surface area.

S-Score rank	Cpd.	Corresponding amino acid/alcohol	S-Score	HAN	LE	MW	BEI (x10 ³)	ClogP	TPSA
1	19e	(S)-Tryptophanol	-8,06	32	0,252	446,53	18,0	3,59	110,9
2	19d	(R)-Tyrosinol	-7,80	30	0,260	423,49	18,4	2,82	115,3
3	19f	(R)-Tryptophanol	-7,80	32	0,244	446,53	17,5	3,59	110,9
4	3l	(S)-Phenylalanine	-7,67	30	0,256	420,47	18,3	1,87	115,0
5	19c	(S)-Tyrosinol	-7,59	30	0,253	423,49	17,9	2,82	115,3
6	-	(S)-Methioninol	-7,50	26	0,288	391,52	19,2	2,62	95,1
7	19a	(S)-Phenylalaninol	-7,50	29	0,259	407,49	18,4	3,11	95,1
8	-	(R)-Isoleucinol	-7,50	26	0,288	373,48	20,1	2,92	95,1
9	-	(R)-Isoleucine	-7,48	27	0,277	386,45	19,4	1,67	115,0
10	-	(R)-Phenylalanine	-7,47	30	0,249	420,47	17,8	1,87	115,0
11	-	(S)-Methionine	-7,42	27	0,275	404,49	18,3	1,38	115,0
12	-	(S)-Valinol	-7,40	25	0,296	359,45	20,6	2,53	95,1
13	-	(R)-Methionine	-7,39	27	0,274	404,49	18,3	1,38	115,0
14	-	(S)-Leucinol	-7,36	26	0,283	373,48	19,7	2,92	95,1
15	-	(S)-Threoninol	-7,32	25	0,293	361,42	20,3	1,25	115,3
16	-	(S)-Leucine	-7,32	27	0,271	386,45	19,0	1,67	115,0
17	-	(S)-Isoleucinol	-7,29	26	0,280	373,48	19,5	2,92	95,1
18	-	(R)-Threoninol	-7,27	25	0,291	361,42	20,1	1,25	115,3
19	-	(R)-Methioninol	-7,26	26	0,279	391,52	18,5	2,62	95,1
20	-	(R)-Leucine	-7,25	27	0,268	386,45	18,8	1,67	115,0
21	19b	(R)-Phenylalaninol	-7,24	29	0,250	407,49	17,8	3,11	95,1
22	-	(R)-Leucinol	-7,24	26	0,278	373,48	19,4	2,92	95,1
23	-	(S)-Isoleucine	-7,22	27	0,267	386,45	18,7	1,67	115,0
24	-	(S)-Valine	-7,21	26	0,277	372,42	19,4	1,28	115,0
25	-	(R)-Valine	-7,17	26	0,276	372,42	19,3	1,28	115,0
26	-	(R)-Valinol	-7,15	25	0,286	359,45	19,9	2,53	95,1
27	-	(S)-Proline	-7,05	26	0,271	370,41	19,0	1,13	106,2
28	-	(R)-Prolinol	-7,02	25	0,281	357,43	19,6	2,38	86,3
29	-	(S)-Prolinol	-7,02	25	0,281	357,43	19,6	2,38	86,3
30	-	(R)-Proline	-6,98	26	0,268	370,41	18,8	1,13	106,2
31	-	Serinol	-6,90	24	0,288	347,39	19,9	0,86	115,3
32	-	(R)-Alanine	-6,75	24	0,281	344,37	19,6	0,65	115,0
33	-	(R)-Alaninol	-6,74	23	0,293	331,40	20,4	1,89	95,1
34	-	(S)-Alaninol	-6,70	23	0,291	331,40	20,2	1,89	95,1
35	-	(S)-Alanine	-6,66	24	0,278	344,37	19,3	0,65	115,0
36	-	Glycine	-6,63	23	0,288	330,34	20,1	0,26	115,0
37	3f	Glycinol	-6,54	22	0,297	317,37	20,6	1,50	95,1

Table A 2: *In silico* screening data for the molecular docking of the virtual compound library into the Nek1/Nek2 homology model. Compounds with TPSA > 120 are not shown. See experimental section for more details. HAN, heavy atom number; LE, ligand efficiency; MW, molecular weight; BEI, binding efficiency index; TPSA, topological polar surface area.

S-Score rank	Cpd.	Corresponding amino acid/alcohol	S-Score	HAN	LE	MW	BEI (x10 ³)	ClogP	TPSA
1	19f	(R)-Tryptophanol	-8,36	32	0,261	446,53	18,7	3,59	110,9
2	19e	(S)-Tryptophanol	-8,22	32	0,257	446,53	18,4	3,59	110,9
3	19d	(R)-Tyrosinol	-8,14	30	0,271	423,49	19,2	2,82	115,3
4	19c	(S)-Tyrosinol	-7,99	30	0,266	423,49	18,9	2,82	115,3
5	-	(R)-Phenylalanine	-7,73	30	0,258	420,47	18,4	1,87	115,0
6	-	(S)-Methioninol	-7,63	26	0,293	391,52	19,5	2,62	95,1
7	-	(R)-Methionine	-7,55	27	0,280	404,49	18,7	1,38	115,0
8	-	(R)-Isoleucine	-7,51	27	0,278	386,45	19,4	1,67	115,0
9	-	(S)-Methionine	-7,51	27	0,278	404,49	18,6	1,38	115,0
10	-	(S)-Valinol	-7,46	25	0,298	359,45	20,8	2,53	95,1
11	19b	(R)-Phenylalaninol	-7,45	29	0,257	407,49	18,3	3,11	95,1
12	3l	(S)-Phenylalanine	-7,45	30	0,248	420,47	17,7	1,87	115,0
13	-	(R)-Leucine	-7,45	27	0,276	386,45	19,3	1,67	115,0
14	-	(R)-Valine	-7,44	26	0,286	372,42	20,0	1,28	115,0
15	-	(R)-Valinol	-7,41	25	0,296	359,45	20,6	2,53	95,1
16	-	(R)-Methioninol	-7,40	26	0,285	391,52	18,9	2,62	95,1
17	-	(S)-Threoninol	-7,40	25	0,296	361,42	20,5	1,25	115,3
18	-	Serinol	-7,39	24	0,308	347,39	21,3	0,86	115,3
19	-	(S)-Valine	-7,38	26	0,284	372,42	19,8	1,28	115,0
20	-	(R)-Threoninol	-7,33	25	0,293	361,42	20,3	1,25	115,3
21	-	(S)-Isoleucine	-7,33	27	0,271	386,45	19,0	1,67	115,0
22	19a	(S)-Phenylalaninol	-7,32	29	0,252	407,49	18,0	3,11	95,1
23	-	(R)-Isoleucinol	-7,31	26	0,281	373,48	19,6	2,92	95,1
24	-	(S)-Proline	-7,28	26	0,280	370,41	19,6	1,13	106,2
25	-	(R)-Proline	-7,27	26	0,280	370,41	19,6	1,13	106,2
26	-	(S)-Isoleucinol	-7,25	26	0,279	373,48	19,4	2,92	95,1
27	-	(R)-Leucinol	-7,25	26	0,279	373,48	19,4	2,92	95,1
28	-	(R)-Prolinol	-7,22	25	0,289	357,43	20,2	2,38	86,3
29	-	(S)-Leucine	-7,18	27	0,266	386,45	18,6	1,67	115,0
30	-	(S)-Prolinol	-7,17	25	0,287	357,43	20,1	2,38	86,3
31	-	(S)-Leucinol	-7,15	26	0,275	373,48	19,2	2,92	95,1
32	-	(S)-Alaninol	-6,75	23	0,294	331,40	20,4	1,89	95,1
33	-	(R)-Alanine	-6,75	24	0,281	344,37	19,6	0,65	115,0
34	-	(S)-Alanine	-6,75	24	0,281	344,37	19,6	0,65	115,0
35	-	(R)-Alaninol	-6,70	23	0,291	331,40	20,2	1,89	95,1
36	-	Glycine	-6,54	23	0,284	330,34	19,8	0,26	115,0
37	3f	Glycinol	-6,51	22	0,296	317,37	20,5	1,50	95,1

B. Kinase selectivity profile for compound 19f

Table A 3: The KinaseProfiler™ service is a fast turnaround profile conducted by *Eurofins Discovery Services*. Percentage kinase activities with compound **10f** at one concentration (1 μM) in a panel of human protein kinases are shown. Measurements were performed in duplicate and the average was taken. Assay details are available online at:

<https://www.eurofinsdiscoveryservices.com/>

IKKbeta	36.1	TYRO3 (RSE)	89.3
NEK1	49.7	TAK1	90.1
IKKalpha	73.2	PKCeta	91.7
TLK1	78.3	MST1	92.0
NEK11	79.3	ATR /ATRIP	92.1
Abl	79.6	IRAK4	92.5
GSK3beta	79.6	IKKepsilon	92.9
SAPK2A (p38alpha)	81.0	Abl (Q252H)	93.4
LYN	82.0	Pim1	93.9
EphB4	82.9	PI3Kalpha (p110a/p85a)	94.8
CDK1 /CyclinB	83.6	eEF-2K	96.8
Brk (PTK6)	83.7	PI3Kgamma (p120gamma)	97.1
c-Raf (Raf-1)	84.2	CDK6 /CyclinD3	98.0
NEK3	84.3	CK2alpha2	98.7
CaMKIgamma	84.9	NEK7	99.0
PKCalpha	86.0	PI3Kdelta (p110d/p85a)	99.6
CDK2 /CyclinE	86.0	Akt1 (PKBalphabet)	100.4
Syk	86.6	NEK6	100.9
Plk3	87.1	EGFR	101.1
MAPKAPK2	87.3	PI3Kbeta (p110b/p85a)	101.9
PDGFRbeta	87.4	NEK2	102.6
CHK1	88.1	ATM	103.8
CaMKK2	88.8	PAK2	105.0
mTOR	88.9	ASK1	110.6
CK1gamma1	89.2	PRAK	113.0

C. Fluorescence-Microscopy Imaging of 19f-treated Wild-Type Zebrafish Embryos

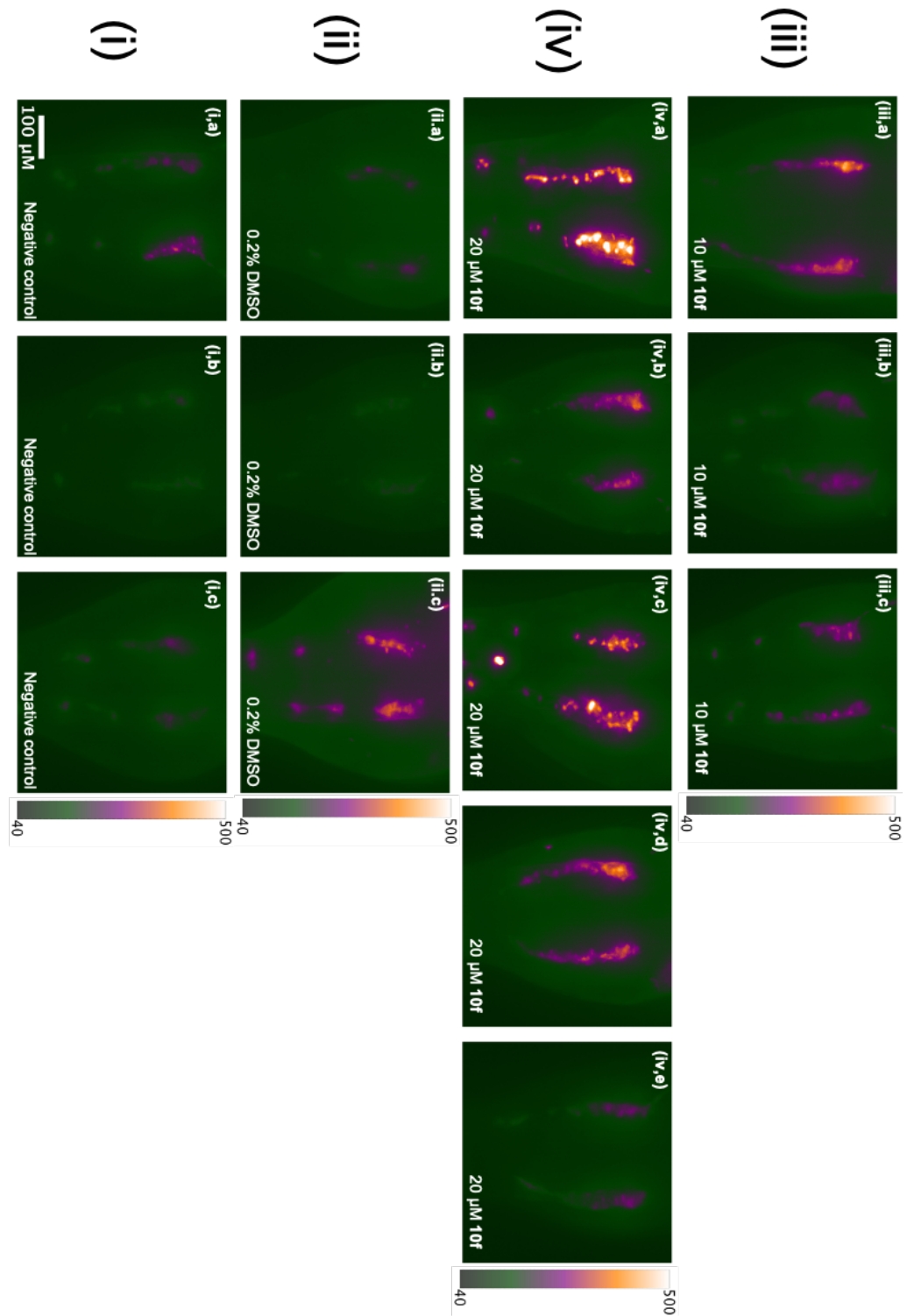


Figure A 1: Microscopic imaging of fluorescence-labeled (PT-Yellow) zebrafish pronephroi after treatment with Nek1-inhibitor **19f**. Maximum intensity projection of deconvolved Z-stacks, colored by lookup table *blue orange icb* (15x magnification; 33 Z-slices; dZ=15 μM): (i) negative control E3-medium, (ii) negative control 0.2% DMSO, (iii) 10 μM **19f** and (iv) 20 μM **19f**.

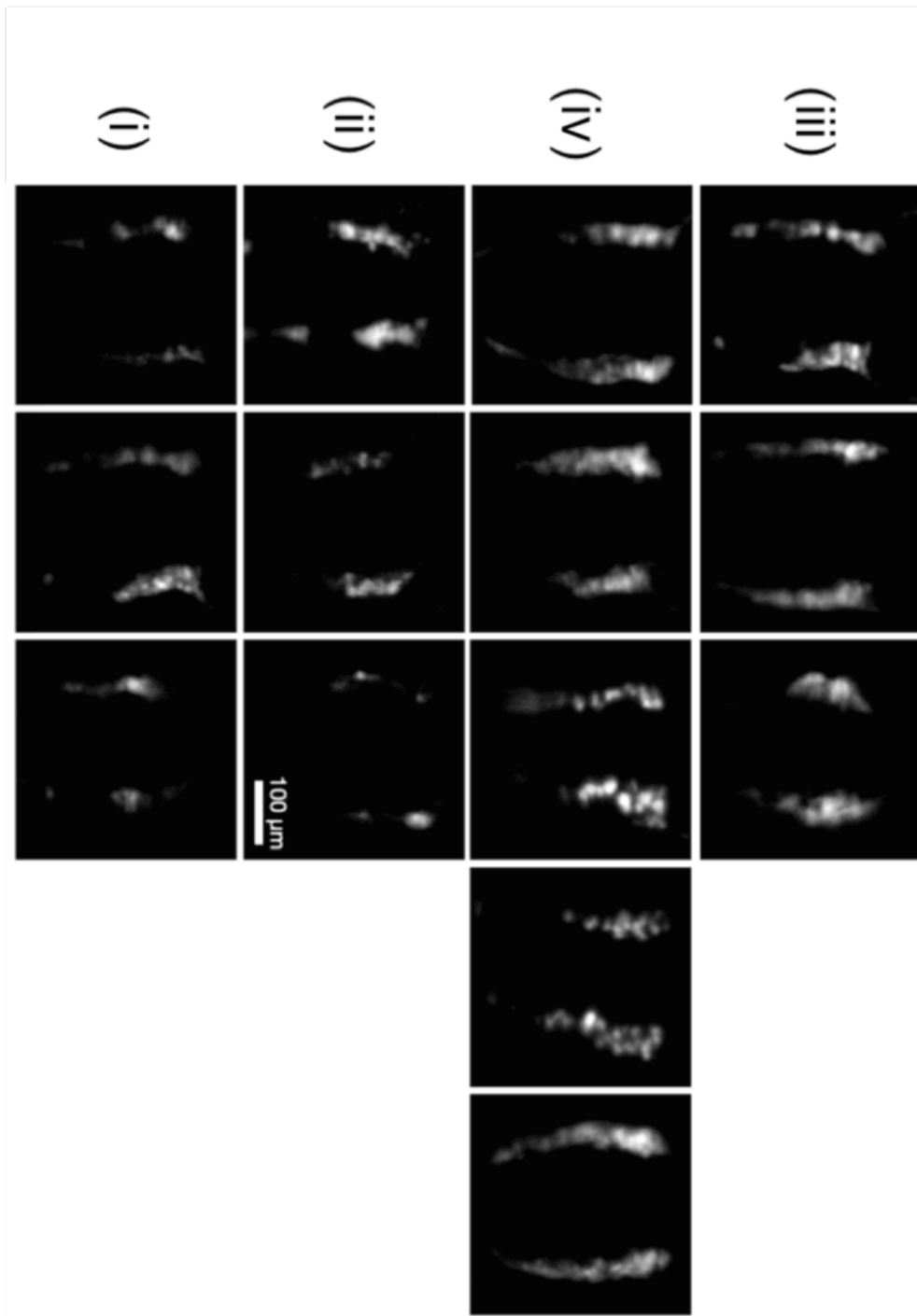


Figure A 2: Microscopic images of fluorescence-labeled (PT-Yellow) zebrafish pronephroi after treatment with Nek1-inhibitor **19f** used for the quantification of fluorescence intensity using *ImageJ*.: (i) negative control E3-medium, (ii) negative control 0.2% DMSO, (iii) 10 μ M **19f** and (iv) 20 μ M **19f** (15x magnification; 33 Z-slices; dZ=15 μ M).

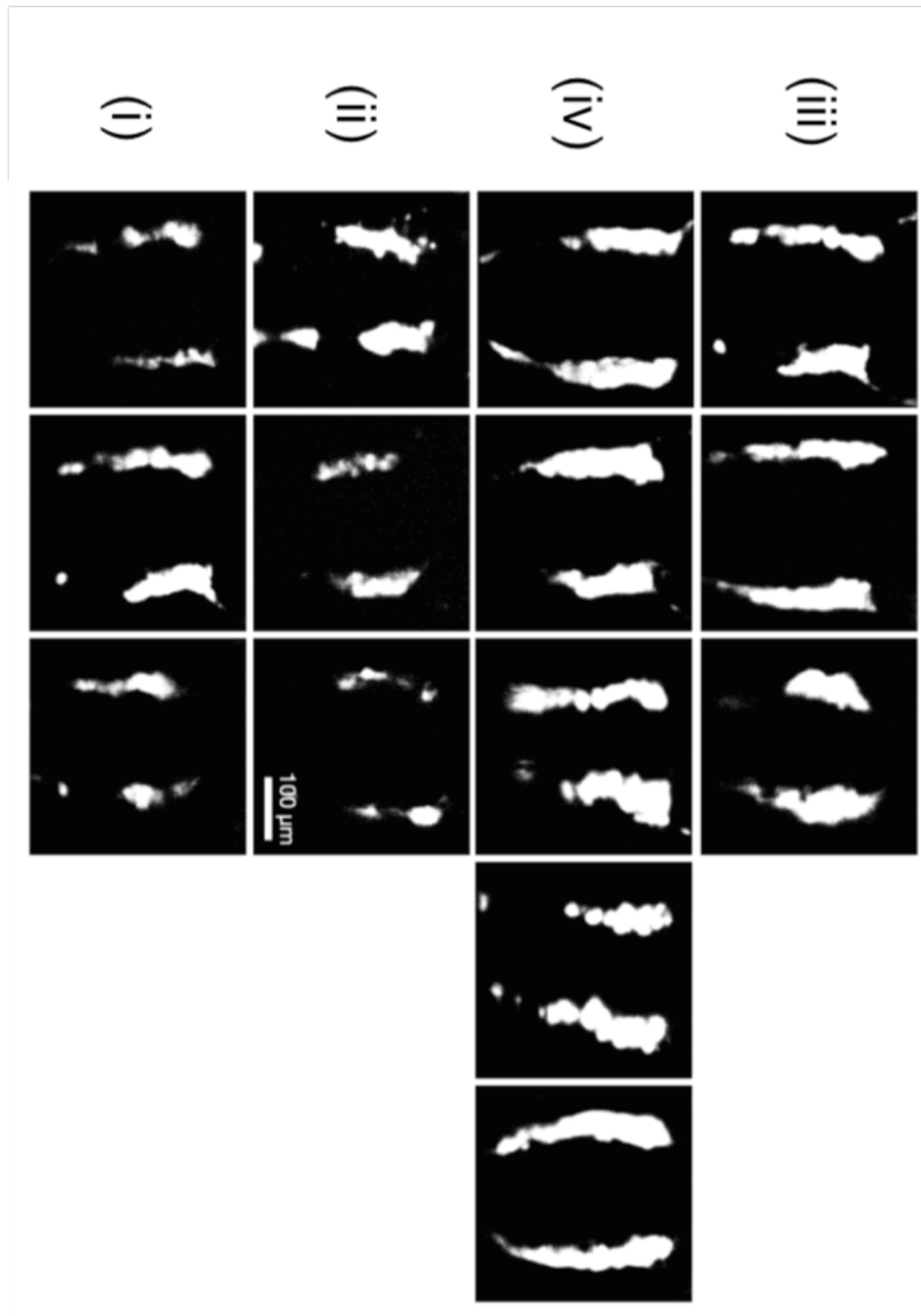


Figure A 3: Microscopic images of fluorescence-labeled (PT-Yellow) zebrafish pronephroi after treatment with Nek1-inhibitor **19f** used for the quantification of pronephroi sizes by summed pixel area determination using *ImageJ*.: (i) negative control E3-medium, (ii) negative control 0.2% DMSO, (iii) 10 μM **19f** and (iv) 20 μM **19f** (15x magnification; 33 Z-slices; $dZ=15 \mu\text{M}$).

D. Journal Article (*Journal of Medicinal Chemistry*) “Illuminating a Dark Kinase: Structure-Guided Design, Synthesis, and Evaluation of a Potent Nek1 Inhibitor and Its Effects on the Embryonic Zebrafish Pronephros” with adapted Supporting Information

Reprinted with permission from:

Baumann, G.; Meckel, T.; Böhm, K.; Shih, Y.-H.; Dickhaut, M.; Reichardt, T.; Pilakowski, J.; Pehl, U.; Schmidt, B., Illuminating a Dark Kinase: Structure-Guided Design, Synthesis, and Evaluation of a Potent Nek1 Inhibitor and Its Effects on the Embryonic Zebrafish Pronephros. *Journal of Medicinal Chemistry* **2021**. (in press) DOI: 10.1021/acs.jmedchem.0c02118.

Copyright 2021 American Chemical Society.

The articles „Supporting Information“ is presented in an adapted version, where redundant information was removed. The full version is available free of charge from the publisher’s website (<https://pubs.acs.org/doi/10.1021/acs.jmedchem.0c02118>).

16.3.2021 Rightslink® by Copyright Clearance Center

Copyright Clearance Center RightsLink® Home ? Email Support Sign in Create Account

Illuminating a Dark Kinase: Structure-Guided Design, Synthesis, and Evaluation of a Potent Nek1 Inhibitor and Its Effects on the Embryonic Zebrafish Pronephros

Author: Georg Baumann, Tobias Meckel, Kevin Böhm, et al
Publication: Journal of Medicinal Chemistry
Publisher: American Chemical Society
Date: Mar 1, 2021
Copyright © 2021, American Chemical Society

PERMISSION/LICENSE IS GRANTED FOR YOUR ORDER AT NO CHARGE

This type of permission/license, instead of the standard Terms & Conditions, is sent to you because no fee is being charged for your order. Please note the following:

- Permission is granted for your request in both print and electronic formats, and translations.
- If figures and/or tables were requested, they may be adapted or used in part.
- Please print this page for your records and send a copy of it to your publisher/graduate school.
- Appropriate credit for the requested material should be given as follows: "Reprinted (adapted) with permission from (COMPLETE REFERENCE CITATION). Copyright (YEAR) American Chemical Society." Insert appropriate information in place of the capitalized words.
- One-time permission is granted only for the use specified in your request. No additional uses are granted (such as derivative works or other editions). For any other uses, please submit a new request.

BACK CLOSE WINDOW

© 2021 Copyright - All Rights Reserved | Copyright Clearance Center, Inc. | Privacy statement | Terms and Conditions
<https://s100.copyright.com/AppDispatchServlet?formTop> 1/2

Figure 54: Permission for other uses was obtained from ACS through request via the RightsLink permission system: <http://pubs.acs.org/page/copyright/permissions.html>.

Illuminating a Dark Kinase: Structure-Guided Design, Synthesis, and Evaluation of a Potent Nek1 Inhibitor and Its Effects on the Embryonic Zebrafish Pronephros

Georg Baumann,* Tobias Meckel, Kevin Böhm, Yung-Hsin Shih, Mirco Dickhaut, Torben Reichardt, Johannes Pilakowski, Ulrich Pehl, and Boris Schmidt*

Cite This: <https://dx.doi.org/10.1021/acs.jmedchem.0c02118>

Read Online

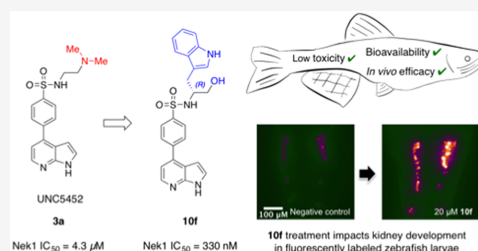
ACCESS |

Metrics & More

Article Recommendations

Supporting Information

ABSTRACT: NIMA-related kinase 1 (Nek1) has lately garnered attention for its widespread function in ciliogenesis, apoptosis, and the DNA-damage response. Despite its involvement in various diseases and its potential as a cancer drug target, no directed medicinal chemistry efforts toward inhibitors against this dark kinase are published. Here, we report the structure-guided design of a potent small-molecule Nek1 inhibitor, starting from a scaffold identified by kinase cross-screening analysis. Seven lead compounds were identified *in silico* and evaluated for their inhibitory activity. The top compound, **10f**, was further profiled for efficacy, toxicity, and bioavailability in a zebrafish polycystic kidney disease model. Administration of **10f** caused the expansion of fluorescence-labeled proximal convoluted tubules, supporting our hypothesis that Nek1-inhibition causes cystic kidneys in zebrafish embryos. Compound **10f** displayed insignificant inhibition in 48 of 50 kinases in a selectivity test panel. The findings provide a powerful tool to further elucidate the function and pharmacology of this neglected kinase.



INTRODUCTION

Nek1 is a dual serine/threonine protein kinase that also possesses tyrosine kinase activity, albeit to a lesser degree.¹ Since its discovery in a murine cDNA expression library screen, this mammalian homologue of the fungal NIMA cell cycle regulator has attracted widespread attention due to its pleiotropic function and its association with a number of diseases in humans.^{2–4} The ever-growing interest in this remarkable kinase was first sparked by findings that linked Nek1 to two independent mutant alleles (*kat* and *kat*²), which spontaneously arose from two inbred mouse strains, causing various effects such as male sterility, dwarfing, facial dysmorphism, anemia, and a progressive polycystic kidney disease (PKD).^{5,6} PKD is the most common genetic cause for renal failure in humans and is characterized by the relentless growth of large fluid-filled cysts and the accompanying destruction of the adjacent renal parenchyma.⁷ The evidence for the causative relation between Nek1 depletion and PKD was further strengthened by an interactomic study, which indicated strong interactions between the PKD-associated proteins KIF3A, tuberin, and α -catulin and the central coiled-coil region of Nek1.⁸ Moreover, Nek1 expression levels are prominently elevated in embryonic proximal tubule and podocyte precursor cells and decrease with kidney maturation, supporting the observation that Nek1 is of functional importance for the etiology of PKD.⁹

Interestingly, NEK1 mutations have been linked not only to defects of ciliogenesis, like PKD and short-rib polydactyly syndrome type Majewski but also to other inheritable diseases such as Mohr–Laussen syndrome or amyotrophic lateral sclerosis (ALS), a neurodegenerative disorder that causes the selective death of motor neurons and is associated with an altered DNA damage response (DDR).^{10–13} Like most of the 11 known members of the human Nek family, Nek1 plays a crucial role in cell cycle control and in particular the DDR.¹⁴ Nek1 expression is upregulated upon chemical or radiative induction of DNA double-strand breaks (DSBs) and acts as a regulator of DNA repair by homologous recombination (HR).^{15,16} Cell cycle phase-specific phosphorylation of Rad54 by Nek1 either permits HR, by way of Rad51 removal from chromatin in G2-phase, or ensures replication fork stability in S-phase.¹⁷ Moreover, functional Nek1 is indispensable for proper cell cycle checkpoint activation through phosphorylation of checkpoint kinases 1 and 2 (Chk1/Chk2)

Special Issue: New Horizons in Drug Discovery - Understanding and Advancing Kinase Inhibitors

Received: December 8, 2020

in response to radiative stress.¹⁸ Eventually, Nek1-deficient cells accumulate unrepaired DSBs leading to genomic instability, chromosomal damage, and finally cell death.¹⁹ A remarkable feature of Nek1 is its ability to also limit apoptotic cell death even after severe damage has occurred already. Direct phosphorylation of voltage-dependent anion channel 1 (VDAC1) by Nek1 stabilizes the mitochondrial membrane potential thus limiting the caspase-mediated killing of cells.^{20,21} More recent evidence suggests that an activating phosphorylation of Nek1 by tousel-like kinase 1 (Tlk1) contributes to the phosphorylation of VDAC1 and that inhibition of the Tlk1/Nek1/VDAC1 axis in combination with DNA damaging agents can sensitize prostate cancer cells to apoptotic killing.^{22–25} Elevated levels of Nek1 expression have also been identified in other cancer types like thyroid cancer, human gliomas, or renal cell carcinoma (RCC).^{26–28} In the latter case, a decreased sensitivity to genotoxic treatment and ionizing radiation was associated with high levels of Nek1, emphasizing the importance of Nek1 inhibition as a therapeutic strategy for drug development in the treatment of RCC.^{28,29} More recently, Freund et al. have shown that high Nek1 expression levels associate with impaired clinical outcome in cervical cancer patients following chemo-radiotherapy or brachytherapy and that a Nek1 knockdown impacts the 3D clonogenic survival of HeLa cervical and HCT-15 colorectal carcinoma cells. Furthermore, the knockdown sensitized those cells to ionizing radiation, underlining the potential of Nek1 inhibitors to increase the radiation or chemotherapy response in anticancer treatment.³⁰

Despite the crucial role of Nek1 in a broad variety of diseases and its outstanding potential as a target for anticancer therapeutics, no directed medicinal chemistry efforts toward potent and selective Nek1 inhibitors have been published in the past.^{4,31} In a first attempt to pinpoint structural elements that influence Nek family inhibitor specificity, Moraes et al. identified a c-Jun N-terminal kinase (JNK) inhibitor with limited inhibitory activity against a truncated Nek1 activation loop mutant in a thermal shift assay.³² Shortly thereafter, the same group reported the crystal structure analysis of the human Nek1 kinase domain both in its apo form and in complex with an ATP-competitive CDK inhibitor.³³ Until today, only three members of the human Nek family, namely, Nek1, -2, and -7, have been structurally solved. More recently, a pyridin-2(5H)-one based inhibitor with a low micromolar IC₅₀ value against Nek6 was also shown to decrease Nek1 activity to a comparable degree.³⁵ In the framework of developing a comprehensive kinase chemogenomic set, Wells et al. compiled chemical starting points for Nek-family inhibitors by performing an intricate analysis of kinome cross-screening data.³⁴ In the case of Nek1, two series of compounds with promising activities were identified from the profiling data of a large inhibitor set (Published Kinase Inhibitor Set 2, PKIS2).³⁶ The most potent candidate (UNC5078) of a series of 4-thiophene-7-azaindoles exhibited 91.9% Nek1 inhibition at 1 μ M.^{34,37} Strikingly, the 4-aryl-7-azaindole derivative UNC5452 (3a), which was originally intended as an I κ B kinase β (IKK β) inhibitor, exhibited even higher Nek1 activity (99.8% inhibition at 1 μ M) while only inhibiting 18 off-target kinases \geq 90% at 1 μ M (Figure 1).^{34,38} Nevertheless, finding suitable inhibitors for Nek1 is not trivial, as indicated by the low hit rates of previously reported screenings.^{33,34}

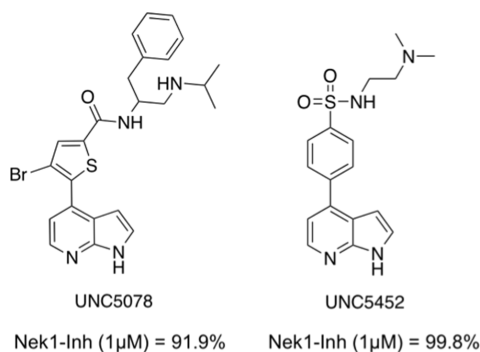


Figure 1. Chemical starting points for the development of Nek1 inhibitors, as identified by Wells et al. in an analysis of kinome cross-screening data.³⁴

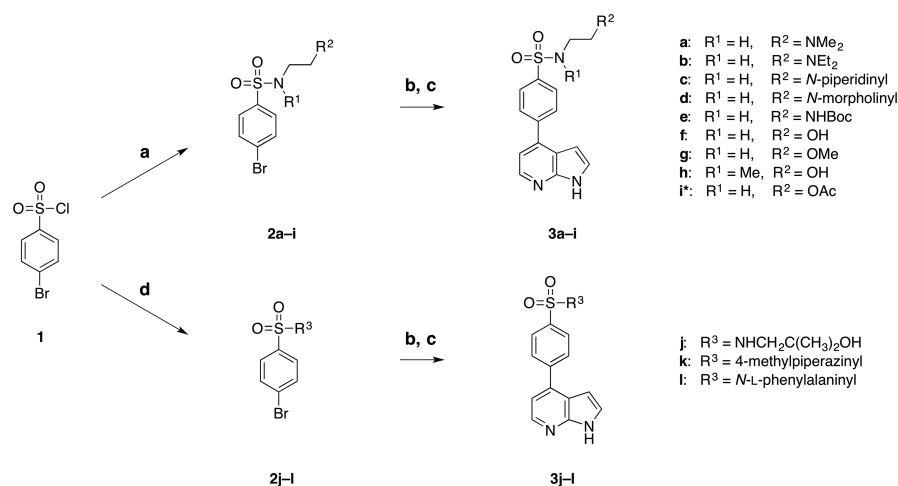
In this work, we report the structure-guided design and synthesis of several novel Nek1 inhibitors. The 4-phenyl-7-azaindole moiety of UNC5452 (3a) served as a starting point and was expanded upon by *in silico* analysis, molecular docking simulations, and a virtual chemical library screen in P-loop reconstructed Nek1 crystal structures (PDB codes 4APC and 4B9D) as well as a Nek1/Nek2 homology model. The most potent compound **10f** was further profiled in a kinase selectivity panel, a Caco-2 permeability assay, and a zebrafish developmental toxicity assay. *In vivo* efficacy of **10f** was evaluated by fluorescence microscopy imaging of zebrafish pronephroi after inhibitor treatment, which is an established model for cystic kidney diseases.³⁹

CHEMISTRY

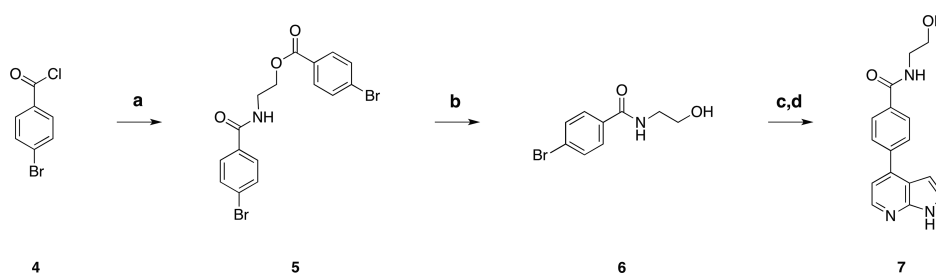
The synthesis of UNC5452 (3a) and its derivatives commenced with the amide formation between sulfonyl chloride **1** and the respective primary or secondary amines to afford sulfonamides **2a–h** and **2j–l**. Acetyloxyster **2i** was prepared from alcohol **2f** by acetylation with acetic anhydride. Miyaura borylation of aryl halides **2a–I** gave the corresponding pinacol boronic acid esters, which were fused with 4-bromo-7-azaindole by palladium catalyzed Suzuki cross-coupling forthwith, yielding 4-phenyl-7-azaindoles **3a–I** (Scheme 1).⁴⁰ In an attempt to synthesize the carboxylic amide analogue **6** of sulfonamide **2f** under identical conditions, 4-bromobenzoyl chloride (**4**) was transformed to the undesired ester **5**. However, alkaline hydrolysis of **5** provided benzamide **6**, which was coupled to 4-bromo-7-azaindole, giving azaindole **7** in the final Suzuki cross-coupling step. (Scheme 2). The amino alcohols **8a–f** were converted to final compounds **10a–f** through a similar sequence described in Scheme 1. Compounds **8a–c** were obtained commercially, while **8d** was prepared by reduction of D-tyrosine methyl ester with sodium borohydride and **8e** and **8f** were prepared by reduction of L-tryptophan and D-tryptophan, following a procedure by Meyers et al.^{41,42} Amide formation between 4-bromosulfonyl chloride (**1**) and amino alcohols **8a–f** provided aryl halides **9a–f**, which again underwent Miyaura borylation and subsequent Suzuki cross-coupling to afford azaindoles **10a–f** (Scheme 3).

B

<https://dx.doi.org/10.1021/acs.jmedchem.0c02118>
J. Med. Chem. XXXX, XXX, XXX–XXX

Scheme 1^{4a}

^{4a}Reagents and conditions: (a) for 2a–h, DCM, amine, NEt₃, 0 °C–rt, 74–95%; (b) DMF, bis(pinacolato)diboron, KOAc, PdCl₂(dppf), 100 °C, not isolated; (c) DMF, 4-bromo-7-azaindole, NaHCO₃ (aq), Pd(PPh₃)₄, 100 °C, 11–69%; (d) for 2j, DCM, amine, NEt₃, 0 °C–rt, 64%; for 2k, THF, 1-methylpiperazine, rt, 75%; for 2l, H₂O/acetone, L-phenylalanine, NaHCO₃, rt, 49%. *Compound 2i was prepared from 2f by acetylation with acetic anhydride and NEt₃ in DCM, 82%; see Experimental Section for more details.

Scheme 2^{4a}

^{4a}Reagents and conditions: (a) DCM, monoethanolamine, NEt₃, 0 °C–rt, 48%; (b) THF, 50% w/v KOH (aq), 60 °C, 92%; (c) DMF, bis(pinacolato)diboron, KOAc, PdCl₂(dppf), 100 °C, not isolated; (d) DMF, 4-bromo-7-azaindole, NaHCO₃ (aq), Pd(PPh₃)₄, 100 °C, 43%; see Experimental Section for more details.

RESULTS AND DISCUSSION

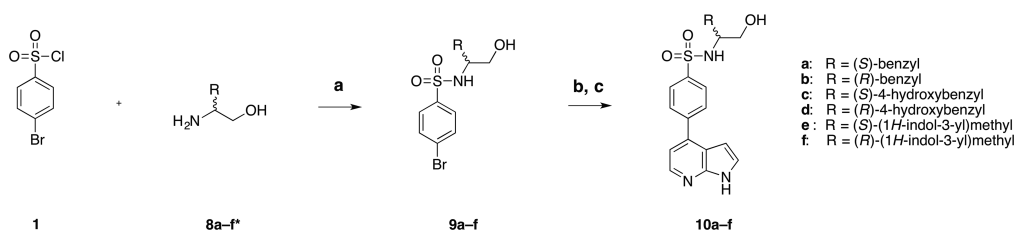
Molecular Modeling. As an initial step of the structure-guided design, the available Nek1 kinase domain crystal structures were analyzed in detail. Both the apo (PDB code 4APC) and the CDK-inhibitor bound 3D structures (PDB code 4B9D) were obtained from the same inactivating T162A activation loop mutant and expectedly constitute an inactive “DFG-out/C-helix-out” conformation. The activation loop forms an ordered α helix, which is speculated to unfold upon autophosphorylation, thus adopting a disordered conformation more commonly found in active kinases.³³ This activation mechanism might to some degree be conserved in the Nek-family, as a similar α -helical activation loop was observed in Nek2 structures but not in Nek7, which is activated through a different mechanism that involves binding of the noncatalytic C-terminal domain of Nek9.^{43,44} Moreover,

the Nek1 structures both crystallized as disulfide bridged dimers.

In an attempt to identify areas of conformational mobility in the active site, we isolated and superimposed the monomeric kinase domains using the Molecular Operating Environment (MOE) software platform (Figure S1). Interestingly, the DFG-motif aspartate (D146) and the gatekeeper (M80) formed hydrogen bonds with an internal water molecule in the ATP binding site in all but one of the isolated chains (PDB code 4APC.A). In this particular case, the side chains of D146 and M80 extend outward in absence of the water molecule, thus opening a hydrophobic back-pocket toward the DFG-motif. This conformational mobility might be exploited by locking Nek1 in an inactive conformation with a small molecule inhibitor. In order to assess the ligand–protein interactions and the amenability of the back-pocket, we docked UNCS452

C

<https://dx.doi.org/10.1021/acs.jmedchem.0c02118>
 J. Med. Chem. XXXX, XXX, XXX–XXX

Scheme 3^a

^aReagents and conditions: (a) for **9a,b**, DCM, amine, NEt₃, 0 °C–rt, 98–99%; for **9c,d**, H₂O/acetone, L-phenylalanine, NaHCO₃, rt, 60–70%; for **9e,f**, DCM/acetonitrile, *N,N*-diisopropylethylamine, 0 °C–rt, 30–43%; (b) DMF, bis(pinacolato)diboron, KOAc, PdCl₂(dppf), 100 °C, not isolated; (c) DMF, 4-bromo-7-azaindole, NaHCO₃ (aq), Pd(PPh₃)₄, 100 °C, 26–62%. *Compounds **8a–c** were obtained commercially; Compound **8d** was prepared from *D*-tyrosine methyl ester hydrochloride by freeing the amine with KOAc in acetonitrile and subsequent reduction with NaBH₄ in methanol, 61%; compounds **8e,f** were prepared by reduction of the corresponding tryptophan isomer using the method described by Meyers et al.,⁴¹ 72–84%; see [Experimental Section](#) for more details.

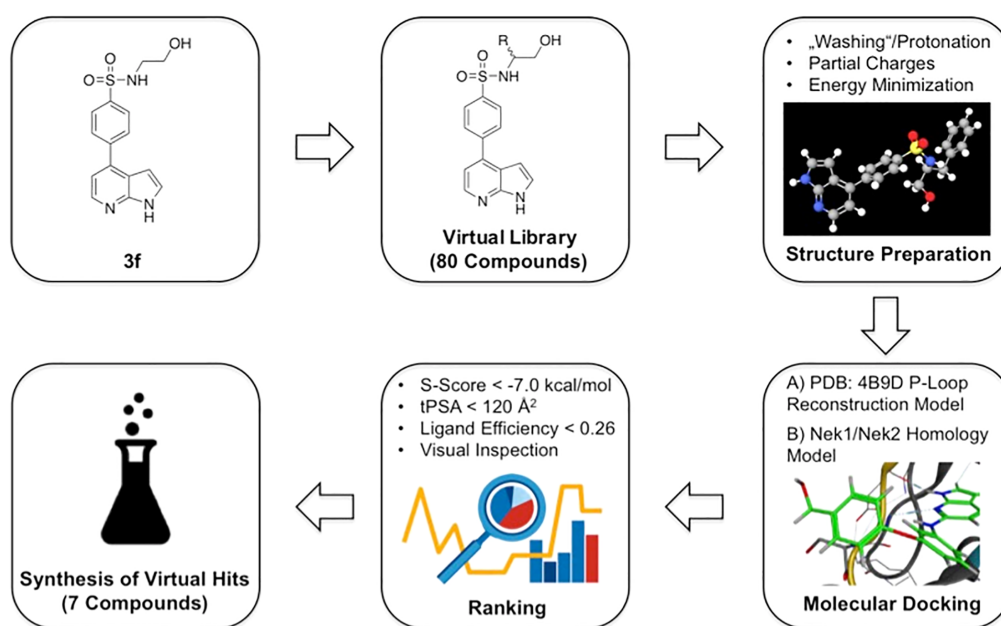


Figure 2. *In silico* chemical library screening to identify hit compounds. See [Experimental Section](#) for more details.

(**3a**) into the Nek1 ATP-binding site (PDB code 4APC.A, [Figures S2 and S3](#)).

The docking experiments suggest that the 7-azaindole moiety positions itself between V31 and F135 side chains and forms two hydrogen bonds with the backbone heteroatoms of the hinge region C83. The pyrrole ring is packed tightly against the side chain of Y82 and directed toward the solvent exposed area of the ATP-binding site, thus adopting the so-called “flipped” binding mode. The “normal” binding mode, where the pyrrole ring points toward the gatekeeper M80, is also conceivable but was not favored in our docking experiments.⁴⁵ From the hinge-binding motif, the phenyl ring of UNC5452 protrudes toward the ribose-binding

region of Nek1 through a narrow channel formed by the side chains of F135, A18, I10, and the catalytic lysine (K33). Unfortunately, the terminal nitrogen atom of K33 is not structurally resolved, but it appears that its side-chain flexibility and the close proximity to the sulfonamide oxygen allow for hydrogen bonding. The proposed binding mode is supported by the 9-fold reduction of activity of carboxylic acid **7** against Nek1, when compared with sulfonamide **3f**. It appears that the tetrahedral geometry of the sulfonamide group is crucial for proper orientation of the ligand. Consequently, the sulfonamide nitrogen is positioned downward, toward the catalytic loop. As proposed by the docking experiment, the sulfonamide NH is not acting as a hydrogen bond donor, as the methyl

D

<https://dx.doi.org/10.1021/acs.jmedchem.0c02118>
J. Med. Chem. XXXX, XXX, XXX–XXX

substitution of the secondary sulfonamide hydrogen from **3f** to **3j** slightly increased potency.

As expected, the highly flexible dimethylaminoethyl fragment was able to adopt multiple conformations. Unfortunately, our experiments led to the conclusion that an entrance into the hydrophobic back pocket from the 4-phenyl-7-azaindole scaffold is not trivial. Due to the intrusion of the F135 and Y82 side chains into the hinge-binding region, the 7-azaindole moiety is angled in a way that hypothetically prevents access to the back-pocket from the 5-position in the “flipped” binding mode. In the disfavored “normal” binding mode, the same problem arises for the 3-position and an entry from the 2-position is presumably blocked by the gatekeeper (M80). Moreover, the docking shows that an approach from the ortho position of the scaffold’s phenyl ring is likely also blocked by M80 (Figure S4). It remains unclear if scaffold hopping to a five membered aromatic ring as in UNC5078 would sufficiently widen the C–C–C bond angle to allow bypassing of the gatekeeper. Laufer and colleagues have successfully applied this strategy in the development of inhibitors for EGFR Met gatekeeper mutants in the past.⁴⁶

As a consequence of these findings, we shifted our attention to the derivatization of the dimethylaminoethyl fragment with means to optimize existing and to establish new interactions in the ribose-binding region. Depending on the protonation state of the tertiary amine, interactions with the side chains of the catalytic loop residues D128 or Q132 or the unresolved side chains of the glycine-rich loop (P-Loop) residues E12 and S14 are conceivable. In order to establish a structure–activity relationship (SAR), we synthesized and evaluated compounds **3b–k**, with a range of steric demands as well as varying basicity and hydrogen bond capabilities. The most potent compound of the series, alcohol **3f**, served as the starting point for an *in silico* virtual library docking experiment to identify virtual hit compounds (Figure 2). We reasoned that the structural relation of the sulfonamide linked side chain to *N*-substituted α -amino acids and their corresponding alcohols allows us to make use of nature’s own toolkit for protein binding. Moreover, this strategy ensured the convenient access to stereochemically pure starting materials and a straightforward synthetic approach.

The virtual library included a total of 80 compounds that correspond to both isomers of the 20 canonical amino acids and their respective amino alcohols. Molecular docking of the virtual library into the Nek1 kinase domain required reconstruction of the P-loop, which was performed using two independent methods. Starting from the ligand-bound B-chain (PDB code 4B9D), which was chosen because of its shorter unresolved gap, we first reconstructed the loop using the SuperLooper2 web application.⁴⁷ Second, a homology model of Nek1 was created using the X-ray structure of Nek2 bound to an aminopurine inhibitor (Figure S7).⁴⁸ Seven virtual hit compounds were identified by analysis of the docking results. The selection was based on docking score (*S*-Score), topological polar surface area (TPSA), ligand efficiency, and visual inspection of the docked conformations. Both methods provided similar results, favoring aromatic amino alcohol side chains (10a–f) and an aromatic amino acid side chain (31).

Interestingly, the structurally related Nek1 kinase cross screening hit UNC5078 also possesses an equivalent benzyl group, although the stereoinformation is missing.³⁴ The putative binding mode of the series most potent compound **10f** was determined from molecular docking into the

reconstructed X-ray structure of Nek1 (Figure 3). In similar fashion to **3a**, the 7-azaindole moiety is tightly packed between

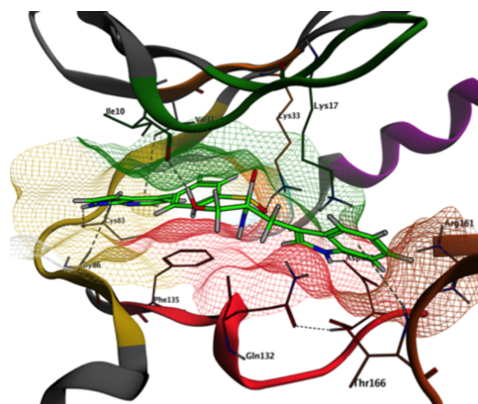


Figure 3. Molecular docking of compound **10f** into X-ray structure of Nek1 (PDB code 4B9D.B). P-loop reconstruction was performed using the SuperLooper2 web application.⁴⁷ See [Experimental Section](#) and [Supporting Information](#) for more details (Figures S5 and S6).

V31 and F135 in the “flipped” binding mode and forms two hydrogen bonds with the hinge region C83. Furthermore, the docking experiment indicates C–H– π interactions of the heterocyclic rings with G86 and V31 side chains as well as a contingent parallel-displaced π – π stacking interaction with F135. The phenyl ring of **10f** once again protrudes toward the ribose binding region and positions the sulfonamide moiety in close proximity to the catalytic lysine (K33), forming a hydrogen bond. Resulting from this interaction, the hydroxyl group of **10f** acts as a hydrogen donor toward the backbone carbonyl oxygen of I10, while the indole moiety fits tightly between K17, Q132, and R161. From here, the indole NH forms a hydrogen bond with the side chain of D128, while the aromatic system establishes a C–H– π interaction with the T166 backbone NH. Judging by these results, **10f** can be classified as a type IIB inhibitor that binds to an inactive DFG-out conformation without occupying the back cleft.⁴⁹

Biological Assays and Structure–Activity Relationship (SAR) Studies. As a first step, we synthesized UNC5452 (**3a**) in order to benchmark a commercial *in vitro* Nek1 activity assay by Eurofins Discovery (KinaseProfiler Item 15-020 KP10). Compound **3a** inhibited Nek1 activity by only 63% at 1 μ M in this ATP-dependent radiometric assay, compared to the 99.8% inhibitory activity reported by Wells et al.³⁴ We hypothesize that this difference results from the fact that screening of the parent PKIS2 data set was performed using an ATP-independent competition-binding assay (DiscoverX KINOME-scan) that instead measures the ability of a small molecule to compete for the active site with an immobilized inhibitor.³⁶

The molecular modeling suggested interactions of **3a** with the Nek1 hinge C83, catalytic K33, and the catalytic loop residues D128 and Q132 to be essential for potent inhibition. Since our primary aim was the optimization of the dimethylaminoethyl fragment, we first opted for the improvement of the terminal dimethylamino group. In the light of our

E

<https://dx.doi.org/10.1021/acs.jmedchem.0c02118>
J. Med. Chem. XXXX, XXX, XXX–XXX

docking experiments and the significant drop in activity upon removal of the two methyl groups, from 3a to primary amine UNCS023 in the PKIS2 data set.³⁴ We investigated the influence of the amine pK_a by synthesis and evaluation of compounds 3b–e (Table 1). Overall, the radiometric Nek1

Table 1. Inhibitory Activity of Compounds 3a–f and 3k against Nek1 and Nek2

Cpd.	R	Residual kinase activity (1 μ M) ^[a]	IC ₅₀ [μ M] ^[b]		
			Nek1	Nek1	Nek2
3a		37%	7.1 (4.3) ^[c]	6.4–7.8 (3.1–5.9) ^[c]	n. e.
3b		68%	10	9.6–11	n. e.
3c		37%	6.6	6.3–6.9	n. e.
3d		51%	27	17–62	n. e.
3e		49%	n.e.	n.d.	n. e.
3f		12%	3.2 (2.0) ^[c]	2.9–3.5 (1.4–2.8) ^[c]	n. e.
3k		45%	>10 ^[e]	n.d.	n. e.

^aEurofins Discovery KinaseProfiler service at 10 μ M ATP. ^bLANCE Ultra TR-FRET kinase assay at $K_{m,ATP}$. ^cA relative IC₅₀ value was provided because the determined IC₅₀ value exceeded the employed maximum test concentration (10 μ M). See Experimental Section for more details. See Supporting Information for raw data. CI, confidence interval; nd, not determined; ne, no effect at maximum concentration (30 μ M). ^eEurofins Discovery IC50Profiler service at $K_{m,ATP}$.

assay revealed no clear trend between the amine basicity and kinase binding. Compounds 3b, 3d, and 3e displayed decreased activity in comparison to 3a, while 3c showed comparable activity. The results were confirmed by the determination of IC₅₀ values for 3a–e in a TR-FRET based Nek1 activity assay (LANCE Ultra TR-FRET, $K_{m,ATP}$; PerkinElmer). Strikingly, no effect on Nek1 activity was herein observed at the maximum concentration (30 μ M) for 3e, which reduced Nek1 activity to 49% in the radiometric assay. Furthermore, compound 3d displayed a significant decrease in inhibitory activity compared to 3b, in contrast to the previous findings. Apart from these discrepancies, the results confirm that a variation of the terminal amine's basicity did not improve inhibitory activity against Nek1. Rigidification of the flexible dimethylamino-ethyl fragment in compound 3k also significantly decreased inhibitory activity against Nek1 to over 10 μ M from 7.1 μ M in 3a. As a result, we reasoned that the attempted optimization of interactions of 3a with the catalytic

loop residues D128 and Q132, as suggested by the docking experiment, is elusive and that the introduction of an alternative hydrogen bond donor might improve inhibitory activity. Synthesis and evaluation of alcohol 3f revealed a significant decrease in residual Nek1 activity to 12% as well as a more than 2-fold decreased IC₅₀ of 3.2 μ M, compared to 3a.

In order to evaluate the hydrogen bond characteristics of the hydroxy group in 3f, methyl ether 3g and acetyl ester 3i analogues were prepared and tested (Table 2). Both analogues

Table 2. Inhibitory Activity of Compounds 3g–j and 7 against Nek1 and Nek2

Cpd.	R	Residual kinase activity ^[a] (1 μ M)	IC ₅₀ [μ M] ^[b]		
			Nek1	95% CI	Nek2
3g		44%	>30 ^[e]	n.d.	n. e.
3h		46%	2.7	2.5–3.0	n. e.
3i		49%	8.8	7.0–11	n. e.
3j		32%	5.8	4.7–7.2	n. e.
7		89%	29	25–35	n. e.

^aEurofins Discovery KinaseProfiler service at 10 μ M ATP. ^bLANCE Ultra TR-FRET kinase assay at $K_{m,ATP}$. ^cA relative IC₅₀ value was provided because the determined IC₅₀ value exceeded the employed maximum test concentration (30 μ M). See Experimental Section for more details. See Supporting Information for raw data. CI, confidence interval; nd, not determined; ne, no effect at maximum concentration (30 μ M).

showed decreased inhibitory activity compared to 3f, with an IC₅₀ larger than 30 μ M for ether 3g and 8.8 μ M for ester 3i. The results clearly indicate that the hydroxy group in 3f does indeed act as a hydrogen bond donor and not as an acceptor, as the reduced acceptor capability in 3i did not further reduce inhibitory activity. It remains unclear if the carbonyl oxygen in 3i acts as an alternative hydrogen bond acceptor but it is unlikely to interact with the same region, due to its different position relative to the rest of the molecule. Moreover, the introduction of a bulky tertiary alcohol in 3j led to a significantly decreased IC₅₀ of 5.8 μ M. With the improved inhibitory activity of 3f in hand, we switched our focus to the sulfonamide moiety (Table 2). As previously suggested by docking of 3a into the Nek1 ATP binding site, the methyl replacement of the secondary sulfonamide hydrogen from 3f to 3h did not influence Nek1 inhibition significantly. However, substitution of the tetrahedral sulfonamide group with a planar carboxamide in 7 led to a 9-fold increased IC₅₀ compared to 3f,

F

<https://dx.doi.org/10.1021/acs.jmedchem.0c02118>
J. Med. Chem. XXXX, XXX, XXX–XXX

providing evidence for the proposed importance of the sulfonamide geometry in hydrogen bonding to K33. In addition, compounds 3a–k and 7 were profiled for their Nek2 inhibitory activity using the same TR-FRET based assay platform. In concordance with the Nek-family selectivity data for 3a reported by Wells et al.,³⁴ none of the tested compounds exerted an observable effect on the kinase activity of Nek2.

As described in the molecular modeling section, seven virtual hit compounds (3l and 10a–f) were identified in an *in silico* screening from a library of canonical *N*-substituted α -amino acid derivatives, and their corresponding alcohols, structurally based on 3f. Accordingly, phenylalanine derivative 3l and phenylalaninol, tyrosinol, and tryptophanol derivatives 10a–f were synthesized and evaluated (Table 3). The *L*-phenylalanine derivative 3l did not notably decrease Nek1 activity, while the corresponding phenylalaninol derived enantiomers 10a and 10b displayed decreased Nek1 IC₅₀ values of 1.9 μ M and 1.3 μ M, respectively. The tyrosinol derivatives 10c and 10d performed slightly worse, while the *L*-tryptophanol derivative 10e exhibited a decreased IC₅₀ compared to 10a (0.99 μ M). Strikingly, the *D*-tryptophanol derivative 10f showed 6-fold decreased IC₅₀ of 0.33 μ M against Nek1 compared to 3f. Our docking experiments suggest that this decrease results from the generally favored orientation of the (*R*)-enantiomers, which in this particular case gives rise to an additional hydrogen bond interaction of the indole NH with the D128 side chain as well as a C–H– π interaction of the aromatic system with the T166 backbone NH (Figure 3).

Kinase selectivity profiling of 10f against 50 kinases was carried out with ATP concentrations set within 15 μ M of the apparent K_m for ATP for each kinase tested, so that the resulting selectivity profile directly reflects the intrinsic affinities of 10f.⁵⁰ Of the 50 kinases in this focused panel, including several members of the Nek family, 47 showed activity higher than 75%, whereas Nek1 displayed a residual activity of only 49.7%. The only kinase that was also significantly inhibited by 10f was IKK β with a residual activity of 36.1% (Figure 4). However, given that the selectivity profile is based on a limited number of kinases (approximately 10% of the kinome) and does not extend to enzymes beyond the kinome, caution must be exercised in deducing general selectivity from the data.

Zebrafish Developmental Toxicity Assay and Fluorescence Microscopy Imaging of Zebrafish Pronephroi.

In order to evaluate whether its *in vitro* inhibitory activity translates into predictable effects *in vivo*, compound 10f was further profiled for its activity, safety, and toxicity in wild-type zebrafish (*Danio rerio*). For this purpose, we established a PKD model based on a previously mentioned report by Chen et al., which indicates that Nek1 deficiency results in renal cyst formation as a consequence of disordered kidney maturation in *kat2b* mice.⁹ Indeed, the zebrafish has proven itself as an established model system for the evaluation of mammalian kidney morphology, because of its simple pronephric structure, which consists of two nephroi that share major anatomical and functional features with the mammalian metanephros. Its usefulness as a model for cystic kidney diseases has recently been reviewed.^{39,51} Furthermore, it has been shown that the majority of human kinases display high degrees of identity with their zebrafish homologues. Human Nek1, for example, shares 89% identity to zebrafish Nek1 for the catalytically active kinase domain, according to a study by Wlodarchak et al.⁵² Moreover, all residues of the active site appear unaltered in

Table 3. Inhibitory Activity of Compounds 3l and 10a–f against Nek1

Cpd.	R	Residual kinase activity ^[a] (1 μ M)			IC ₅₀ [μ M] ^[b]
		Nek1	Nek1	95% CI	
3l		94%	n.e.	n.d.	
10a		19%	1.9	1.4–2.6	
10b		16%	1.3	0.91–1.8	
10c		33%	2.0	1.2–3.0	
10d		25%	1.6	1.1–2.2	
10e		19%	0.99	0.65–1.5	
10f		4%	0.33 (0.33) ^[c]	0.22–0.52 (0.19–0.51) ^[c]	

^aEurofins Discovery KinaseProfiler service at 10 μ M ATP. ^bEurofins Discovery IC50Profiler service at $K_{m,ATP}$. See Experimental Section for more details. See Supporting Information for raw data. CI, confidence interval; nd, not determined; ne, no effect at maximum concentration (10 μ M). ^cEurofins Discovery IC50Profiler service at 10 μ M ATP.

sequence analysis (Figures S8 and S9). We therefore hypothesized that treatment with 10f, during early stages of embryonic organ development, leads to the formation of renal cysts, thus indicating efficient absorption and *in vivo* efficacy of 10f. It is important to note here that our model is based on the necessary assumption that Nek1 inhibition results in the same phenotype that is associated with its depletion, as the correlation between small-molecule inhibition and loss-of-function phenotypes is not always straightforward.⁵³ However, our approach is substantiated by the reported link of aberrant cystic growth to the absence of Nek1, as well as to its overexpression.⁵⁴ Hence, the authors conclude that healthy ciliogenesis requires a delicate spatiotemporal activity of Nek1,

G

<https://dx.doi.org/10.1021/acs.jmedchem.0c02118>
J. Med. Chem. XXXX, XXX, XXX–XXX

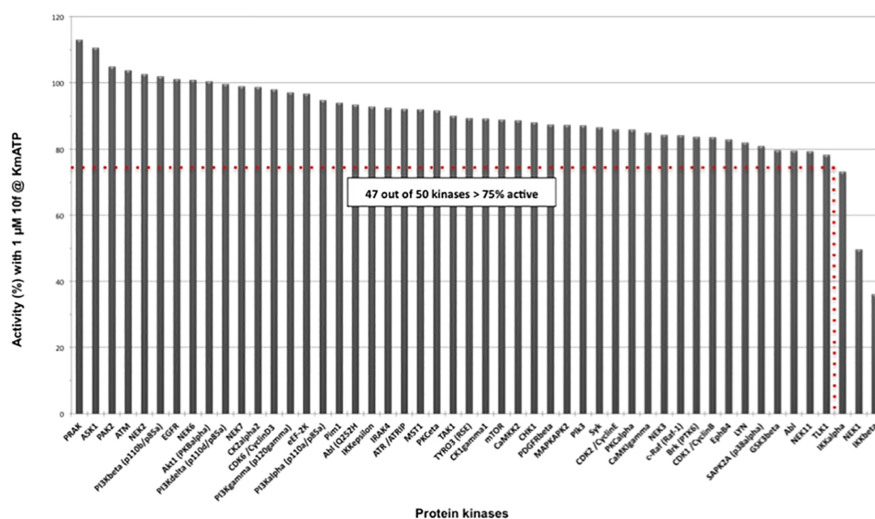


Figure 4. Screening of Compound **10f** against a panel of human protein kinases. Each bar represents the activity of one individual protein kinase. Compound **10f** was tested at a concentration of 1 μM . The ATP concentration was set to the approximate $K_{m,\text{ATP}}$ for each kinase tested. See [Supporting Information](#) for more details.

which is likely to be substantially disturbed by inhibition and depletion alike.

In order to visualize the influence of **10f** on larval zebrafish nephrogenesis, we implemented a fluorescence-microscopy based imaging pipeline developed by Westhoff et al. ([Figure S](#)).⁵⁵ As a means of avoiding dependence on the transgenic *Tg(wt1b:EGFP)* zebrafish line, we instead opted for the use of PT-Yellow (BDNCA3-D2), a fluorescent probe that selectively labels the renal proximal tubules in wild-type zebrafish.⁵⁶ This approach allowed for zebrafish maintenance and husbandry in a standard laboratory, and it was furthermore reasoned that the ingestion of an external probe is better suited to indicate the impaired renal clearance associated with fluid-filled cysts.⁵⁷ As a first step, a bioavailability profile of compound **10f** was evaluated. The aqueous solubility of **10f** in E3-medium ($13.9 \pm 0.1 \mu\text{g/mL}$, [Figure S10](#)) was determined in a shake-flask solubility assay, and apical to basolateral transport was determined in a Caco-2 permeability assay ($3.4 \times 10^{-6} \text{ cm/s}$, 45% recovery, [Table S3](#)). We then determined the minimal lethal concentrations for compound **10f** in a zebrafish developmental toxicity assay over a duration of 120 h. Compound **10f** was added to 6 h postfertilization (hpf) embryos in concentrations ranging from 0.05 μM to 30 μM ([Figure S11](#)). Full lethality was only observed close to the solubility limit for a concentration of 30 μM after 72 h. Treatment with **10f** did not induce obvious phenotypes visible to the eye. The treated embryos exhibited normal eye development and body curvature and an ordinary heartbeat.

Based on these results, zebrafish embryos were incubated with (i) the negative control (E3-medium), (ii) 0.2% DMSO, (iii) 10 μM **10f**, and (iv) 20 μM **10f** in E3-medium containing 75 μM 1-phenyl-2-thiourea (PTU) as a melanogenesis inhibitor at 6 hpf. To ensure the stability of **10f** against PTU and PT-Yellow over the duration of the experiment, a stability-indicating HPLC assay was performed in E3-medium ([Figure](#)

[S12](#)). After 48 h, all embryos were treated with 100 nM PT-Yellow for 20 min, thoroughly washed with E3-medium, and returned to the respective compound solution for a total incubation time of 96 h. Finally, the embryos were anesthetized and transferred to agarose molds, which were prepared in 96-well plates according to a published procedure, for fluorescence imaging in a widefield microscope ([Figure S13](#)).⁵⁵ Administration of **10f** caused a substantial increase in fluorescence intensity ([Figure S5D](#)) and expansion ([Figure S5E](#)) of the proximal convoluted tubules, thus indicating the growth of fluid-filled cysts, alongside an impaired renal clearance. In addition, our findings provide further evidence for the adequate absorption and bioavailability of **10f**. As hypothesized, our experiments thus demonstrate that *Nek1* inhibition by **10f** during early organ development causes cystic kidney growth in zebrafish embryos, despite our findings that **10f** is unselective against *IKK β* . Park et al. have shown that levels of phosphorylated-*IKK α/β* and its downstream factor *NF- κ B* are upregulated in the renal tissue of *PKD2* transgenic mice compared to wild-type controls.⁵⁸

Moreover, Boojj et al. demonstrated that cystic growth was in fact reduced by *IKK α/β* -inhibitors in a murine 3D cell culture based screening platform.⁵⁹ It therefore appears that *Nek1* inhibition overturns any presumed protective effects of *IKK β* inhibition on cystogenesis in our experiments. It should be noted here that, unlike in murine models, zebrafish *IKK α* is suspected to negatively regulate *NF- κ B* activity. *IKK α* ^{-/-} zebrafish embryos displayed severe head and tail malformations, as well as an upregulated *NF- κ B* response and increased *NF- κ B*-dependent apoptosis, in a study by Correa et al.⁶⁰ In accordance with the low *IKK α* -activity of **10f** (see [Table S1](#)), this phenotype was not observed in our experiments. Overall, this leads to the conclusion that the aberrant cystic growth in **10f**-treated zebrafish embryos is unlikely to be mediated by *IKK* cross-reactivity. However, a causative relation to hitherto

H

<https://dx.doi.org/10.1021/acs.jmedchem.0c02118>
J. Med. Chem. XXXX, XXX, XXX–XXX

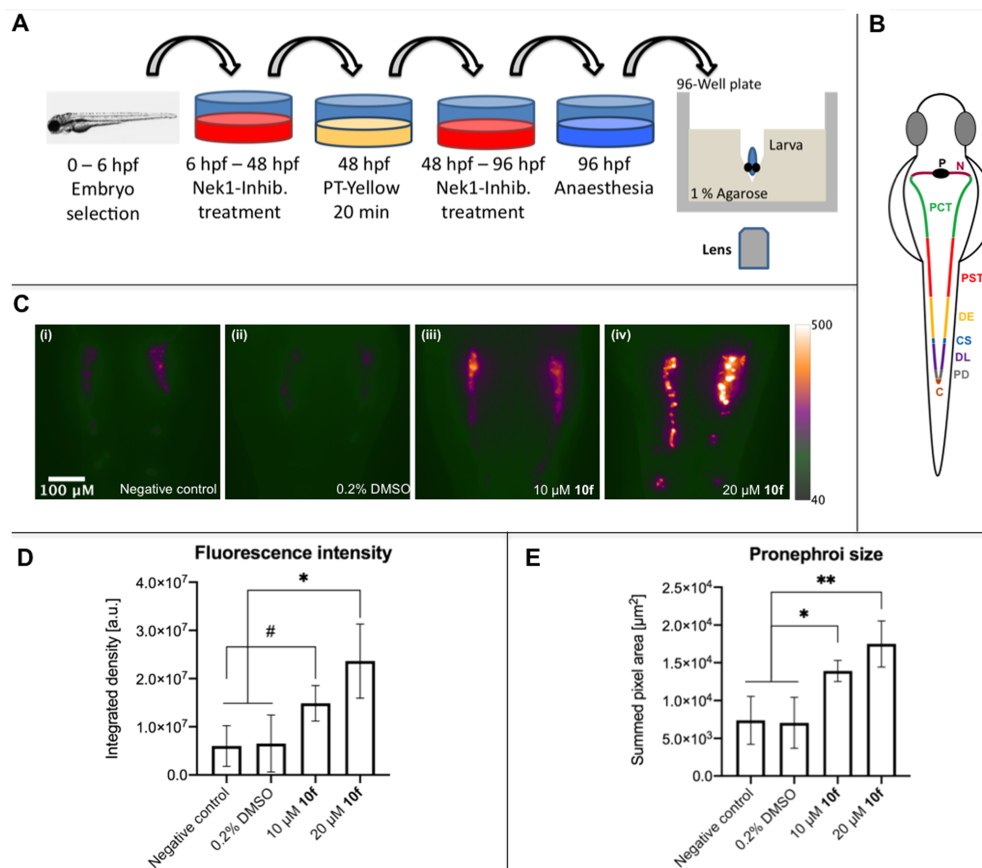


Figure 5. Microscopic imaging of fluorescence-labeled (PT-Yellow) zebrafish pronephroi after treatment with Nek1-inhibitor **10f**. (A) Schematic representation of the workflow, entailing embryo selection, compound treatment, and image acquisition. (B) Schematic representation of the pronephros in the developing zebrafish (28-somite stage). Reprinted with permission from ref 39. Copyright 2018 Gehrig, Pandey and Westhoff. (C) Exemplary maximum intensity projections of deconvolved Z-stacks (15× magnification; 33 Z-slices; dZ = 15 μm). The dotted line indicates the cropped region of interest. (C, i) negative control E3-medium, (C, ii) negative control 0.2% DMSO, (C, iii) 10 μM **10f**, and (C, iv) 20 μM **10f**. (D) Quantification of fluorescence intensity based on summed image projections of deconvolved Z-stacks using ImageJ. $n = 3$ for negative control, 0.2% DMSO, and 10 μM **10f**; $n = 5$ for 20 μM **10f** ($^{\#}P = 0.0516$; $^*P < 0.05$). (E) Quantification of pronephroi size by summed pixel area determination based on summed image projections of deconvolved Z-stacks using ImageJ. $n = 3$ for negative control, 0.2% DMSO, and 10 μM **10f**; $n = 5$ for 20 μM **10f** ($^*P < 0.05$; $^{**}P < 0.01$). Abbreviations: au, arbitrary unit; C, Cloaca; CS, corpuscles of Stannius; DE, distal early tubule; DL, distal late tubule; hpf, hours post fertilization; N, neck region; P, podocytes of the glomerulus; PCT, proximal convoluted tubule; PD, pronephric duct; PST, Proximal straight tubule.

unidentified cross-reactivity cannot be ruled out entirely, due to the aforementioned limitations of the selectivity test panel and the fact that the complex PKD-related molecular pathways and regulatory networks are not yet fully understood.^{61–63}

CONCLUSION

Based on a published chemical starting point, we generated hypotheses for improved interactions with the Nek1 ATP-binding site by molecular docking into the available crystal structures. These hypotheses were challenged by a series of structurally related inhibitors that were based on the same 4-

aryl-7-azaindole scaffold. The most potent compound of this series, **3f**, served as the structural basis of a virtual structure library that encompassed 80 *N*-substituted amino acids and their corresponding alcohols. Seven virtual hits were thereupon identified in an *in silico* virtual library screen in two independent P-loop reconstructed Nek1 3D-structures. This natural product based approach allowed for convenient access to enantiomerically pure starting materials and a straightforward synthetic route and provided the opportunity to exploit nature's own toolkit for protein binding. Our efforts culminated in the ATP-competitive Nek1 inhibitor **10f** that displayed IC₅₀ values in the mid to low nanomolar range.

<https://dx.doi.org/10.1021/acs.jmedchem.0c02118>
J. Med. Chem. XXXX, XXX, XXX–XXX

Moreover, 48 out of 50 kinases were not substantially inhibited by **10f** in a kinase selectivity panel (Figure 4). Ample bioavailability of **10f** was confirmed in a Caco-2 permeability assay, and its toxicity was investigated in wild-type zebrafish embryos. Treatment with **10f** was well tolerated, as full lethality was only observed close to the solubility limit for a concentration of 30 μM . In order to evaluate the *in vivo* efficacy of **10f**, we modified a published procedure for fluorescence microscopy imaging of larval zebrafish pronephroi. As hypothesized, our experiments demonstrated that Nek1 inhibition by **10f** during early organ development causes cystic kidney growth in zebrafish embryos. Our study thus provides the first directed tool compound for a mostly neglected kinase that has been shown to be a key player in numerous forms of cancer and other illnesses, thereby helping to establish Nek1 as a therapeutic target and providing a powerful tool to further elucidate its biological function.

EXPERIMENTAL SECTION

General Information. Unless otherwise noted, starting materials and reagents were purchased from commercial sources and used without further purification. All reactions employing anhydrous conditions were performed in dried glassware with dry solvents under argon atmosphere unless otherwise noted. All cross-coupling reactions were performed with degassed solvents. NMR spectra were recorded on a Bruker Avance II (300 MHz for ^1H and 75 MHz for ^{13}C NMR), a Bruker Avance III spectrometer (300 MHz for ^1H and 75 MHz for ^{13}C NMR), or a Bruker DRX 500 (500 MHz for ^1H and 126 MHz for ^{13}C NMR) spectrometer. Chemical shifts are reported as ppm by frequency downfield of TMS. Coupling constants are reported in Hertz (Hz). Mass spectrometry was performed on a Bruker Daltonik Impact II quadrupol-TOF spectrometer for atmospheric pressure chemical ionization (APCI) and ESI experiments. EI experiments were performed on either a Finnigan MAT95 sector field or a Fisons MD 800 quadrupol spectrometer. HPLC was carried out on an Agilent 1100 system using a Phenomenex Synergi Polar-RP reversed-phase column (4 μm particle size, 150 mm \times 3.0 mm, pore size 80 Å) connected to a variable wavelength detector (VWD) or a Phenomenex Synergi Hydro-RP reversed-phase column (4 μm particle size, 150 mm \times 3.0 mm, pore size 80 Å) connected to a diode array detector (DAD). Solvent gradient = 30% A for 1 min, linear gradient to 10% A for 10 min, 10% A for 1 min; solvent A = 0.1% TFA in water; solvent B = acetonitrile; flow rate 1.0 mL/min. TLC was performed on precoated 0.2 mm silica gel 60 F254 aluminum sheets (Merck) with detection by UV light (254 and 365 nm) or potassium permanganate staining. Flash chromatography was carried out using the specified solvent systems on 40–63 μm NORMASIL 60 silica gel (VWR). All compounds used in biological or biochemical assays had >95% purity as determined in the HPLC method described above.

General Procedure A: Synthesis of Phenylsulfonamides. Procedure A is exemplified by the triethylamine-mediated sulfonamide formation of compound **2a** from 4-bromobenzene-sulfonyl chloride **1** and *N,N*-dimethylethylenediamine. Compounds **2b–h**, **2j**, **9a**, and **9b** were prepared in accordance with procedure A starting from 4-bromobenzene-sulfonyl chloride **1** and the corresponding amine.

General Procedure B: Suzuki–Miyaura Coupling of Aromatic Rings.⁴⁰ Procedure B is exemplified by the Suzuki–Miyaura coupling of 4-bromo-7-azaindole and 4-bromo-*N*-(2-(dimethylamino)ethyl)benzenesulfonamide (**2a**) to give target compound **3a**. Compounds **3b–k**, **10a–f**, and **7** were prepared in accordance with procedure B starting from 4-bromo-7-azaindole and phenylsulfonamides **2b–k** and **9a–f** and benzamide **6**, respectively.

4-Bromo-*N*-(2-(dimethylamino)ethyl)benzenesulfonamide (2a). To a stirred solution of 4-bromobenzene-sulfonyl chloride (**1**, 1.00 g, 3.91 mmol) in 10 mL DCM were added *N,N*-dimethylethylenediamine (414 mg, 4.70 mmol) and triethylamine

(774 mg, 9.78 mmol) at 0 °C under cooling in an ice bath. The cooling bath was removed, and the solution was stirred for 1 h at ambient temperature. The organic layer was washed with water (3 \times 5 mL) and brine (5 mL) and dried over MgSO_4 . The solvent was removed under reduced pressure to give **2a** (1.14 g, 95%) as a light tan solid. ^1H NMR (CDCl_3 , 300 MHz): δ = 7.78–7.71 (m, 2H), 7.69–7.62 (m, 2H), 3.01–2.95 (m, 2H), 2.40–2.33 (m, 2H), 2.11 (s, 6H).

4-Bromo-*N*-(2-(diethylamino)ethyl)benzenesulfonamide (2b). Synthesis of **2b** was performed by following general procedure A using *N,N*-dimethylethylenediamine. Yield 74%, yellow oil. ^1H NMR (CDCl_3 , 300 MHz): δ = 7.77–7.60 (m, 4H), 4.74 (s, 1H), 2.99–2.88 (m, 2H), 2.53–2.45 (m, 2H), 2.39 (q, J = 7.1 Hz, 4H), 0.92 (t, J = 7.1 Hz, 6H). ^{13}C NMR (CDCl_3 , 75 MHz): δ = 139.0, 132.4, 128.8, 127.6, 51.1, 46.5, 40.3, 11.7. m/z (EI): 335 ($[\text{M}]^+$).

4-Bromo-*N*-(2-(piperidin-1-yl)ethyl)benzenesulfonamide (2c). Synthesis of **2c** was performed by following general procedure A using 1-(2-aminoethyl)piperidine. Yield 91%, orange solid. ^1H NMR (CDCl_3 , 300 MHz): δ = 7.78–7.67 (m, 2H), 7.69–7.58 (m, 2H), 5.31 (s, 1H), 2.95 (dd, J = 6.6, 5.1 Hz, 2H), 2.34 (dd, J = 6.6, 5.1 Hz, 2H), 2.19 (t, J = 5.1 Hz, 4H), 1.43 (dp, J = 22.4, 5.7 Hz, 7H). ^{13}C NMR (CDCl_3 , 75 MHz): δ = 138.9, 132.4, 128.8, 127.5, 56.2, 54.0, 39.4, 25.9, 24.3. m/z (APCI): 347.05 ($[\text{M} + \text{H}]^+$).

4-Bromo-*N*-(2-morpholinoethyl)benzenesulfonamide (2d). Synthesis of **2d** was performed by following general procedure A using 4-(2-aminoethyl)morpholine. Yield 87%, colorless solid. ^1H NMR (CDCl_3 , 300 MHz): δ = 7.78–7.70 (m, 2H), 7.70–7.62 (m, 2H), 5.29 (s, 1H), 3.67–3.60 (m, 4H), 3.02 (dd, J = 6.7, 4.9 Hz, 2H), 2.46–2.40 (m, 2H), 2.33–2.27 (m, 4H). ^{13}C NMR (CDCl_3 , 75 MHz): δ = 138.8, 132.4, 128.6, 127.6, 66.7, 56.3, 53.0, 38.9. m/z (APCI): 349.03 ($[\text{M} + \text{H}]^+$).

tert-Butyl (2-(4-bromophenyl)sulfonamido)ethyl)-carbamate (2e). Synthesis of **2e** was performed by following general procedure A using *N*-Boc-ethylenediamine. Yield 78%, colorless solid. ^1H NMR (CDCl_3 , 300 MHz): δ = 7.76–7.59 (m, 4H), 5.05 (s, 1H), 3.24–3.18 (m, 2H), 3.04 (dd, J = 6.3, 4.8 Hz, 2H), 1.41 (s, 9H). ^{13}C NMR (CDCl_3 , 75 MHz): δ = 156.8, 139.2, 132.5, 128.7, 127.6, 52.6, 46.3, 43.9, 42.0, 40.4, 28.54, 28.47, 10.7. m/z (EI): 380 ($[\text{M}]^+$).

4-Bromo-*N*-(2-hydroxyethyl)benzenesulfonamide (2f). Synthesis of **2f** was performed by following general procedure A using 2-aminoethanol. Yield 81%, colorless solid. ^1H NMR ($\text{DMSO}-d_6$, 300 MHz): δ = 7.84–7.70 (m, 4H), 4.67 (t, J = 5.5 Hz, 1H), 3.40–3.32 (m, 2H), 2.80 (q, J = 6.1 Hz, 2H). m/z (APCI): 279.96 ($[\text{M} + \text{H}]^+$).

4-Bromo-*N*-(2-methoxyethyl)benzenesulfonamide (2g). Synthesis of **2g** was performed by following general procedure A using 2-methoxyethylamine. Yield 78%, yellow oil. ^1H NMR ($\text{DMSO}-d_6$, 300 MHz): δ = 7.82–7.78 (m, 2H), 7.75–7.69 (m, 2H), 3.32 (s, 3H), 3.29 (t, J = 5.6 Hz, 2H), 2.92 (q, J = 5.8 Hz, 2H).

4-Bromo-*N*-(2-hydroxyethyl)-*N*-methylbenzenesulfonamide (2h). Synthesis of **2h** was performed by following general procedure A using *N*-methylethanolamine. Yield 90%, colorless oil. ^1H NMR (CDCl_3 , 300 MHz): δ = 7.68 (s, 4H), 3.78 (dd, J = 5.6, 4.9 Hz, 2H), 3.18 (t, J = 5.3 Hz, 2H), 2.85 (s, 3H). m/z (APCI): 293.98 ($[\text{M} + \text{H}]^+$).

2-((4-bromophenyl)sulfonamido)ethyl acetate (2i). To a stirred solution of **2f** (0.77 g, 2.73 mmol) and triethylamine (0.33 g, 3.28 mmol) in 5 mL of DCM, acetic anhydride (0.34 g, 3.28 mmol) was added dropwise at 0 °C under cooling in an ice bath. The cooling bath was removed, and the solution was stirred for 72 h at ambient temperature. The reaction mixture was diluted with 20 mL of DCM and quenched by bringing the pH to 9 through addition of saturated NaHCO_3 (aq). The organic layer was washed with saturated NaHCO_3 (aq, 3 \times 5 mL) and brine (5 mL) and dried over MgSO_4 . The solvent was removed under reduced pressure to give **2i** (0.73 g, 82%) as a yellow oil that was used without further purification. ^1H NMR ($\text{DMSO}-d_6$, 300 MHz): δ = 7.85–7.80 (m, 2H), 7.75–7.69 (m, 2H), 3.95 (t, J = 5.6 Hz, 2H), 3.03 (q, J = 5.6 Hz, 2H), 1.93 (s, 3H). m/z (ESI): 343.96 ($[\text{M} + \text{Na}]^+$).

J

<https://dx.doi.org/10.1021/acs.jmedchem.0c02118>
J. Med. Chem. XXXX, XXX, XXX–XXX

4-Bromo-N-(2-hydroxy-2-methylpropyl)-benzenesulfonamide (2j). Synthesis of 2j was performed by following general procedure A using 1-amino-2-methyl-2-propanol. Yield 64%, yellow solid. $^1\text{H NMR}$ (DMSO- d_6 , 500 MHz): δ = 7.83–7.78 (m, 2H), 7.75–7.71 (m, 2H), 7.59 (t, J = 6.5 Hz, 1H), 4.40 (s, 1H), 2.62 (d, J = 6.5 Hz, 2H), 1.04 (s, 6H). $^{13}\text{C NMR}$ (DMSO- d_6 , 126 MHz): δ = 140.1, 132.1, 128.5, 125.9, 68.7, 53.6, 27.0. $^{13}\text{C NMR}$ (DMSO- d_6 , 126 MHz, DEPT): δ = 132.1, 128.6, 53.6, 45.5, 27.1, 8.5. m/z (APCI): 307.98 ($[\text{M} + \text{H}]^+$).

1-((4-Bromophenyl)sulfonyl)-4-methylpiperazine (2k). To a solution of 4-bromobenzene-sulfonyl chloride (0.40 g, 1.47 mmol) in 9 mL of dry THF, 1-methyl-piperazine (1.41 g, 14.09 mmol) was added, and the mixture was stirred for 16 h at ambient temperature. The solvent was removed under reduced pressure, and the resulting residue was dissolved in 10 mL of DCM. The organic layer was washed with saturated NaHCO_3 (aq, 3×2.5 mL) and dried over MgSO_4 . The solvent was removed under reduced pressure to give 2k (0.37 g, 75%) as a yellow solid. $^1\text{H NMR}$ (CDCl_3 , 500 MHz): δ = 7.69–7.63 (m, 2H), 7.62–7.58 (m, 2H), 3.03 (t, J = 4.9 Hz, 4H), 2.47 (t, J = 5.0 Hz, 4H), 2.26 (s, 3H). $^{13}\text{C NMR}$ (CDCl_3 , 126 MHz): δ = 134.7, 132.4, 129.4, 128.0, 54.1, 46.0, 45.8. m/z (EI): 380 ($[\text{M}]^+$).

((4-Bromophenyl)sulfonyl)-L-phenylalanine (2l). To a stirred solution of L-phenylalanine (194 mg, 1.17 mmol) in 4 mL of water was added sodium bicarbonate (296 mg, 3.52 mmol). The mixture was stirred at ambient temperature for 15 min, and a solution of 4-bromobenzene-sulfonyl chloride (1, 300 mg, 1.17 mmol) in 4 mL of acetone was added at 0 °C under cooling in an ice bath. The cooling bath was removed, and the solution was stirred at ambient temperature for 20 h. After evaporation of the volatile solvent under reduced pressure, the product was precipitated by bringing the pH to 7 using hydrochloric acid (1 N). Filtration and drying under reduced pressure gave 2l (220 mg, 49%) as a yellow solid. $^1\text{H NMR}$ (DMSO- d_6 , 500 MHz): δ = 7.72–7.69 (m, 2H), 7.65–7.61 (m, 2H), 7.18–7.11 (m, 5H), 3.35 (t, J = 5.1 Hz, 1H), 2.98 (dd, J = 13.4, 5.0 Hz, 1H), 2.90 (dd, J = 13.4, 5.2 Hz, 1H). $^{13}\text{C NMR}$ (DMSO- d_6 , 126 MHz): δ = 170.8, 139.7, 138.7, 132.0, 129.9, 128.7, 127.5, 125.9, 125.6, 58.3, 38.5. m/z (ESI): 788.95 ($[\text{2M} + \text{Na}]^+$), 405.97 ($[\text{M} + \text{Na}]^+$), 383.99 ($[\text{M} + \text{H}]^+$).

N-(2-(Dimethylamino)ethyl)-4-(1H-pyrrolo[2,3-b]pyridin-4-yl)benzenesulfonamide (3a). To a solution of sulfonamide 2a (100 mg, 0.33 mmol) in 1.5 mL of DMF were added potassium acetate (97 mg, 0.99 mmol), bis(pinacolato)diboron (100 mg, 0.40 mmol), and $\text{PdCl}_2(\text{dppf})$ (7 mg, 10 μmol), under argon atmosphere. The reaction mixture was stirred at 100 °C for 3 h. After cooling to ambient temperature, 15 mL of ethyl acetate was added, the solution was filtered through Celite, and the organic layer was washed with brine (5×15 mL) before drying over NaSO_4 . The solvent was removed under reduced pressure to give the corresponding boronic acid pinacolester as a crude solid that was dissolved in 1.5 mL of DMF and treated with 4-bromo-7-azaindole (65 mg, 0.33 mmol), 0.5 mL of saturated NaHCO_3 (aq) and $\text{Pd}(\text{PPh}_3)_4$ (38 mg, 36 μmol) under argon atmosphere. The mixture was stirred at 100 °C for 18 h, cooled to ambient temperature, and diluted with 20 mL of EtOAc. After filtration through Celite, the organic layer was washed with brine (5×20 mL) and dried over MgSO_4 , and the solvent was removed under reduced pressure. Purification was performed by column chromatography using a 10:1:0.1 mixture of DCM/MeOH/ NH_3 in MeOH (7 N) to give 3a (47 mg, 42%) as a colorless solid. $^1\text{H NMR}$ (DMSO- d_6 , 300 MHz): δ = 11.89 (s, 1H), 8.33 (d, J = 4.9 Hz, 1H), 7.98 (s, 4H), 7.60 (d, J = 3.5 Hz, 1H), 7.25 (d, J = 4.9 Hz, 1H), 6.64 (d, J = 3.5 Hz, 1H), 2.91 (t, J = 6.8 Hz, 2H), 2.28 (t, J = 6.8 Hz, 2H), 2.07 (s, 6H). $^{13}\text{C NMR}$ (DMSO- d_6 , 75 MHz): δ = 149.2, 142.9, 142.2, 140.3, 138.5, 128.9, 127.2, 127.2, 117.1, 114.4, 98.8, 58.1, 45.0, 40.7. m/z (APCI): 345.13 ($[\text{M} + \text{H}]^+$).

N-(2-(Diethylamino)ethyl)-4-(1H-pyrrolo[2,3-b]pyridin-4-yl)benzenesulfonamide (3b). Starting from 2b, the synthesis of 3b was performed by following general procedure B. Purification was performed by column chromatography using a 10:1:0.1 mixture of DCM/MeOH/ NH_3 in MeOH (7 N). Yield 41%, beige semisolid. $^1\text{H NMR}$ (DMSO- d_6 , 500 MHz): δ = 11.88 (s, 1H), 8.33 (d, J = 4.9 Hz,

1H), 8.04–7.90 (m, 4H), 7.60 (d, J = 3.5 Hz, 1H), 7.25 (d, J = 4.9 Hz, 1H), 6.63 (d, J = 3.5 Hz, 1H), 2.88 (dd, J = 8.1, 6.3 Hz, 2H), 2.43 (t, J = 7.2 Hz, 2H), 2.39 (q, J = 7.1 Hz, 4H), 0.86 (t, J = 7.1 Hz, 6H). $^{13}\text{C NMR}$ (DMSO- d_6 , 126 MHz): δ = 149.2, 142.9, 142.2, 140.3, 138.5, 128.9, 127.2, 127.1, 117.1, 114.3, 98.7, 51.8, 46.5, 41.0, 11.6. m/z (ESI): 373.18 ($[\text{M} + \text{H}]^+$), 187.09 ($[\text{M} + 2\text{H}]^{2+}$). Mp: 143 °C.

N-(2-(Piperidin-1-yl)ethyl)-4-(1H-pyrrolo[2,3-b]pyridin-4-yl)benzenesulfonamide (3c). Starting from 2c, the synthesis of 3c was performed by following general procedure B. Purification was performed by column chromatography using a 15:1:0.1 mixture of DCM/MeOH/ NH_3 in MeOH (7 N). Yield 58%, beige solid. $^1\text{H NMR}$ (DMSO- d_6 , 300 MHz): δ = 11.88 (s, 1H), 8.32 (d, J = 4.8 Hz, 1H), 7.97 (s, 4H), 7.60 (d, J = 3.4 Hz, 1H), 7.25 (d, J = 4.8 Hz, 1H), 6.63 (d, J = 3.4 Hz, 1H), 2.92 (t, J = 6.9 Hz, 2H), 2.29 (t, J = 6.9 Hz, 2H), 2.23 (t, J = 5.0 Hz, 4H), 1.45–1.21 (m, 6H). $^{13}\text{C NMR}$ (DMSO- d_6 , 75 MHz): δ = 149.2, 142.9, 142.1, 140.3, 138.5, 128.9, 127.2, 127.1, 117.1, 114.4, 98.7, 57.6, 53.9, 40.3, 25.4, 23.9. $^{13}\text{C NMR}$ (DMSO- d_6 , 75 MHz, DEPT): δ = 142.9, 128.9, 127.2, 127.1, 114.4, 98.7, 57.6, 53.9, 40.2, 25.34, 23.9. m/z (APCI): 385.18 ($[\text{M} + \text{H}]^+$). Mp: 204 °C.

N-(2-(Morpholinoethyl)-4-(1H-pyrrolo[2,3-b]pyridin-4-yl)benzenesulfonamide (3d). Starting from 2d, the synthesis of 3d was performed by following general procedure B. Purification was performed by column chromatography using a 50:1:0.5 mixture of DCM/MeOH/ NH_3 in MeOH (7 N). Yield 69%, beige solid. $^1\text{H NMR}$ (DMSO- d_6 , 500 MHz): δ = 11.88 (s, 1H), 8.33 (d, J = 4.9 Hz, 1H), 7.98 (s, 4H), 7.65 (t, J = 5.9 Hz, 1H), 7.60 (dd, J = 3.5, 2.5 Hz, 1H), 7.25 (d, J = 4.9 Hz, 1H), 6.64 (dd, J = 3.5, 1.8 Hz, 1H), 3.52–3.46 (m, 4H), 2.95 (q, J = 6.3 Hz, 2H), 2.33 (t, J = 6.8 Hz, 2H), 2.27 (t, J = 4.7 Hz, 4H). $^{13}\text{C NMR}$ (DMSO- d_6 , 126 MHz): δ = 149.2, 142.9, 142.1, 140.3, 138.46, 128.9, 127.2, 127.1, 117.1, 114.4, 98.7, 66.0, 57.2, 53.1, 39.9. $^{13}\text{C NMR}$ (DMSO- d_6 , 126 MHz, DEPT): δ = 142.9, 128.9, 127.2, 127.1, 114.4, 98.7, 66.0, 57.2, 53.1, 39.8. m/z (APCI): 387.16 ($[\text{M} + \text{H}]^+$). Mp: 201 °C.

tert-Butyl(2-((4-(1H-pyrrolo[2,3-b]pyridin-4-yl)phenyl)sulfonamido)ethyl)carbamate (3e). Starting from 2e, the synthesis of 3e was performed by following general procedure B. Purification was performed by column chromatography using a 20:1:0.1 mixture of DCM/MeOH/ NH_3 in MeOH (7 N). Yield 60%, colorless solid. $^1\text{H NMR}$ (DMSO- d_6 , 500 MHz): δ = 11.88 (s, 1H), 8.33 (d, J = 4.9 Hz, 1H), 8.01–7.93 (m, 4H), 7.76 (t, J = 6.0 Hz, 1H), 7.60 (dd, J = 3.5, 2.6 Hz, 1H), 7.26 (d, J = 4.9 Hz, 1H), 6.78 (t, J = 5.9 Hz, 1H), 6.66 (dd, J = 3.5, 1.8 Hz, 1H), 3.01 (q, J = 6.6 Hz, 2H), 2.84 (q, J = 6.4 Hz, 2H), 1.34 (s, 9H). $^{13}\text{C NMR}$ (DMSO- d_6 , 126 MHz): δ = 155.5, 149.2, 142.9, 142.2, 140.0, 138.4, 129.0, 127.2, 127.1, 117.1, 114.4, 98.8, 77.8, 42.3, 28.1. $^{13}\text{C NMR}$ (DMSO- d_6 , 126 MHz, DEPT): δ = 142.9, 129.0, 127.2, 127.1, 114.4, 98.8, 42.3, 39.8, 28.2. m/z (APCI): 417.16 ($[\text{M} + \text{H}]^+$).

N-(2-Hydroxyethyl)-4-(1H-pyrrolo[2,3-b]pyridin-4-yl)benzenesulfonamide (3f). Starting from 2f, the synthesis of 3f was performed by following general procedure B. Purification was performed by column chromatography using a 10:1:0.1 mixture of DCM/MeOH/ NH_3 in MeOH (7 N). Yield 66%, colorless solid. $^1\text{H NMR}$ (DMSO- d_6 , 500 MHz): δ = 11.88 (s, 1H), 8.33 (d, J = 4.9 Hz, 1H), 8.01–7.94 (m, 4H), 7.71 (t, J = 5.9 Hz, 1H), 7.60 (t, J = 3.0 Hz, 1H), 7.26 (d, J = 5.0 Hz, 1H), 6.65 (dd, J = 3.5, 1.8 Hz, 1H), 4.70 (t, J = 5.6 Hz, 1H), 3.42 (q, J = 6.0 Hz, 2H), 2.88 (q, J = 6.2 Hz, 2H). $^{13}\text{C NMR}$ (DMSO- d_6 , 126 MHz): δ = 149.2, 142.9, 142.1, 140.2, 138.5, 128.9, 127.2, 127.12, 117.1, 114.4, 98.8, 59.9, 45.1. $^{13}\text{C NMR}$ (DMSO- d_6 , 126 MHz, DEPT): δ = 142.9, 128.9, 127.2, 127.1, 114.4, 98.8, 60.0, 45.1. m/z (ESI): 318.09 ($[\text{M} + \text{H}]^+$).

N-(2-Methoxyethyl)-4-(1H-pyrrolo[2,3-b]pyridin-4-yl)benzenesulfonamide (3g). Starting from 2g, the synthesis of 3g was performed by following general procedure B. Purification was performed by column chromatography using a 20:1:0.1 mixture of DCM/MeOH/ NH_3 in MeOH (7 N). Yield 65%, colorless solid. $^1\text{H NMR}$ (DMSO- d_6 , 500 MHz): δ = 11.88 (s, 1H), 8.33 (d, J = 4.9 Hz, 1H), 8.02–7.91 (m, 4H), 7.83 (t, J = 6.0 Hz, 1H), 7.60 (dd, J = 3.5,

2.5 Hz, 1H), 7.25 (d, $J = 4.9$ Hz, 1H), 6.65 (dd, $J = 3.6, 1.8$ Hz, 1H), 3.34 (t, $J = 5.7$ Hz, 2H), 2.99 (q, $J = 5.8$ Hz, 2H). ^{13}C NMR (DMSO- d_6 , 126 MHz): $\delta = 149.17, 142.92, 142.15, 140.35, 138.49, 128.87, 127.19, 127.10, 117.13, 114.38, 98.76, 70.56, 57.83, 42.24$. ^{13}C NMR (DMSO- d_6 , 126 MHz, DEPT): $\delta = 142.92, 128.87, 127.19, 127.10, 114.38, 98.76, 70.56, 57.83, 42.24$. m/z (APCI): 332.10 ($[\text{M} + \text{H}]^+$). Mp: 215 °C.

N-(2-Hydroxyethyl)-N-methyl-4-(1H-pyrrolo[2,3-b]pyridin-4-yl)benzenesulfonamide (3h). Starting from 2h, the synthesis of 3h was performed by following general procedure B. Purification was performed by column chromatography using a 20:1:0.1 mixture of DCM/MeOH/NH₃ in MeOH (7 N). Yield 42%, colorless solid. ^1H NMR (DMSO- d_6 , 500 MHz): $\delta = 11.89$ (s, 1H), 8.33 (d, $J = 4.9$ Hz, 1H), 8.01 (d, $J = 8.4$ Hz, 2H), 7.93 (d, $J = 8.4$ Hz, 2H), 7.60 (t, $J = 3.0$ Hz, 1H), 7.27 (d, $J = 5.0$ Hz, 1H), 6.66 (dd, $J = 3.6, 1.8$ Hz, 1H), 4.81 (td, $J = 5.5, 1.3$ Hz, 1H), 3.56 (q, $J = 5.8$ Hz, 2H), 3.10 (t, $J = 6.1$ Hz, 2H), 2.80 (s, 3H). ^{13}C NMR (DMSO- d_6 , 126 MHz): $\delta = 149.2, 142.9, 142.6, 138.25, 136.82, 129.03, 127.71, 127.24, 117.07, 114.36, 98.7, 59.1, 51.94, 35.6$. ^{13}C NMR (DMSO- d_6 , 126 MHz, DEPT): $\delta = 142.9, 142.7, 129.0, 127.7, 127.2, 114.4, 98.7, 59.1, 51.94, 35.6$. m/z (APCI): 332.11 ($[\text{M} + \text{H}]^+$).

2-((4-(1H-pyrrolo[2,3-b]pyridin-4-yl)phenyl)sulfonamido)ethyl Acetate (3i). Starting from 2i, the synthesis of 3i was performed by following general procedure B. Purification was performed by column chromatography using a 15:1:0.1 mixture of DCM/MeOH/NH₃ in MeOH (7 N). Yield 23%, colorless solid. ^1H NMR (DMSO- d_6 , 500 MHz): $\delta = 11.90$ (s, 1H), 8.35 (d, $J = 5.0$ Hz, 1H), 8.03–7.96 (m, 5H), 7.62 (dd, $J = 3.5, 2.5$ Hz, 1H), 7.28 (d, $J = 5.0$ Hz, 1H), 6.67 (dd, $J = 3.5, 1.9$ Hz, 1H), 4.02 (t, $J = 5.6$ Hz, 2H), 3.12 (q, $J = 5.7$ Hz, 2H), 1.96 (s, 3H). ^{13}C NMR (DMSO- d_6 , 126 MHz): $\delta = 170.2, 149.18, 142.94, 142.28, 140.22, 138.45, 128.98, 127.23, 127.1, 117.1, 114.4, 98.8, 62.5, 41.4, 20.6$. m/z (APCI): 360.10 ($[\text{M} + \text{H}]^+$).

N-(2-Hydroxy-2-methylpropyl)-4-(1H-pyrrolo[2,3-b]pyridin-4-yl)benzenesulfonamide (3j). Starting from 2j, the synthesis of 3j was performed by following general procedure B. Purification was performed by column chromatography using a 13:1:0.1 mixture of DCM/MeOH/NH₃ in MeOH (7 N). Yield 11%, colorless solid. ^1H NMR (DMSO- d_6 , 500 MHz): $\delta = 11.87$ (s, 1H), 8.33 (d, $J = 4.9$ Hz, 1H), 8.01–7.94 (m, 4H), 7.62–7.54 (m, 2H), 7.26 (d, $J = 4.9$ Hz, 1H), 6.65 (dd, $J = 3.5, 1.9$ Hz, 1H), 4.42 (s, 1H), 2.70 (d, $J = 6.6$ Hz, 2H), 1.08 (s, 6H). ^{13}C NMR (DMSO- d_6 , 126 MHz): $\delta = 149.2, 142.9, 142.1, 140.4, 138.5, 128.9, 127.18, 127.16, 117.1, 114.4, 98.8, 68.8, 53.7, 27.1$. ^{13}C NMR (DMSO- d_6 , 126 MHz, DEPT): $\delta = 142.9, 128.9, 127.18, 127.16, 114.4, 98.8, 53.7, 27.1$. m/z (EI): 345 ($[\text{M}]^+$).

4-((4-(4-Methylpiperazin-1-yl)sulfonyl)phenyl)-1H-pyrrolo[2,3-b]pyridine (3k). Starting from 2k, the synthesis of 3k was performed by following general procedure B. Purification was performed by column chromatography using a 20:1:0.1 mixture of DCM/MeOH/NH₃ in MeOH (7 N). Yield 58%, colorless solid. ^1H NMR (D₂O, as a TFA salt, 500 MHz): $\delta = 8.39$ (d, $J = 6.0$ Hz, 1H), 8.00–7.87 (m, 4H), 7.72 (d, $J = 3.6$ Hz, 1H), 7.54 (d, $J = 6.0$ Hz, 1H), 6.82 (d, $J = 3.6$ Hz, 1H), 4.02 (d, $J = 13.5$ Hz, 2H), 3.68 (d, $J = 12.7$ Hz, 2H), 3.33 (td, $J = 12.5, 3.3$ Hz, 2H), 2.98 (s, 3H), 2.95–2.86 (m, 2H). ^{13}C NMR (D₂O, as a TFA salt, 126 MHz): $\delta = 146.8, 141.2, 139.6, 135.1, 133.6, 130.2, 130.0, 128.1, 122.9, 114.9, 101.7, 52.7, 43.2, 42.8$. ^{13}C NMR (D₂O, as a TFA salt, 126 MHz, DEPT): $\delta = 133.5, 130.2, 130.0, 128.1, 114.9, 101.7, 52.7, 43.3, 42.8$. m/z (APCI): 357.15 ($[\text{M} + \text{H}]^+$).

((4-(1H-pyrrolo[2,3-b]pyridin-4-yl)phenyl)sulfonyl)-L-phenylalanine (3l). To a solution of sulfonamide 2l (200 mg, 0.52 mmol) in 3 mL of DMF were added potassium acetate (153 mg, 1.56 mmol), bis(pinacolato)diboron (159 mg, 0.62 mmol), and PdCl₂(dppf) (13 mg, 15 μmol) under argon atmosphere. The reaction mixture was stirred at 100 °C for 3 h. After cooling to ambient temperature 20 mL of EtOAc was added, the solution was filtered through Celite, and the organic layer was washed with brine (5 \times 20 mL) before drying over Na₂SO₄. The solvent was removed under reduced pressure to give the corresponding boronic acid pinacolester as a crude solid that was dissolved in 3 mL of DMF and

treated with 4-bromo-7-azaindole (103 mg, 0.52 mmol), 1 mL of saturated NaHCO₃ (aq), and Pd(PPh₃)₄ (60 mg, 52 μmol) under argon atmosphere. The mixture was stirred at 100 °C for 17 h, cooled to ambient temperature, and diluted with 20 mL of EtOAc. After filtration through Celite, the organic layer was washed with brine (5 \times 20 mL), and the product was precipitated by setting the pH to 4 using hydrochloric acid (0.1 N). Filtration and drying under reduced pressure gave 3l (55 mg, 25%) as a colorless solid. ^1H NMR (DMSO- d_6 , 500 MHz): $\delta = 11.89$ (s, 1H), 8.41 (d, $J = 9.0$ Hz, 1H), 8.33 (d, $J = 4.9$ Hz, 1H), 7.80 (d, $J = 8.1$ Hz, 2H), 7.70 (d, $J = 8.3$ Hz, 2H), 7.61 (t, $J = 3.0$ Hz, 1H), 7.22 (d, $J = 4.9$ Hz, 1H), 7.20–7.10 (m, 5H), 6.62 (dd, $J = 3.5, 1.7$ Hz, 1H), 3.95 (dt, $J = 8.8, 4.0$ Hz, 1H), 2.99 (dd, $J = 13.8, 5.5$ Hz, 1H), 2.79–2.72 (m, 1H). ^{13}C NMR (DMSO- d_6 , 126 MHz): $\delta = 172.4, 149.2, 142.9, 141.9, 140.6, 138.6, 136.8, 129.1, 128.5, 128.1, 127.2, 126.8, 126.4, 117.1, 114.3, 98.8, 57.5, 57.5, 37.8$. m/z (APCI): 422.12 ($[\text{M} + \text{H}]^+$).

2-(4-Bromobenzamido)ethyl 4-Bromobenzoate (5). A solution of 4-bromobenzoyl chloride (4, 2.00 g, 9.11 mmol) in 10 mL of DCM was dropwise added to a solution of monoethanolamine (0.67 g, 10.94 mmol) and triethylamine (1.08 g, 6.78 mmol) in 10 mL of DCM over the course of 20 min. The mixture was stirred at ambient temperature for 24 h, diluted with 10 mL DCM, and washed with saturated NaHCO₃ (aq, 3 \times 5 mL). The organic layer was dried over MgSO₄, and the solvent was removed to give a colorless residue that was recrystallized from EtOH to give 5 (0.60 g, 48%) as a colorless solid. ^1H NMR (DMSO- d_6 , 500 MHz): $\delta = 8.76$ (t, $J = 5.6$ Hz, 1H), 7.92–7.87 (m, 2H), 7.81–7.76 (m, 2H), 7.75–7.70 (m, 2H), 7.70–7.64 (m, 2H), 4.40 (t, $J = 5.5$ Hz, 2H), 3.64 (q, $J = 5.6$ Hz, 2H). ^{13}C NMR (DMSO- d_6 , 126 MHz): $\delta = 165.7, 165.1, 133.4, 131.8, 131.3, 131.2, 129.3, 128.9, 127.3, 124.9, 63.6, 38.4$. ^{13}C NMR (DMSO- d_6 , 126 MHz, DEPT): $\delta = 131.8, 131.3, 131.2, 129.3, 63.6, 38.4$. m/z (ESI): 425.93 ($[\text{M} + \text{H}]^+$).

4-Bromo-N-(2-hydroxyethyl)benzamide (6). To a solution of ester 5 (0.50 g, 1.17 mmol) in 20 mL of THF was added 2 mL of 50% w/v aq. KOH solution, and the mixture was stirred at 60 °C for 16 h. The solvent was removed under reduced pressure, and the resulting white residue was taken up in 20 mL of EtOAc and washed with water (3 \times 5 mL) and brine (5 mL). Purification was performed by column chromatography using a 15:1 mixture of DCM/MeOH to give 6 (262 mg, 92%) as a colorless solid. ^1H NMR (DMSO- d_6 , 500 MHz): $\delta = 8.49$ (t, $J = 5.7$ Hz, 1H), 7.82–7.77 (m, 2H), 7.68–7.65 (m, 2H), 4.70 (t, $J = 5.6$ Hz, 1H), 3.51 (q, $J = 5.9$ Hz, 2H), 3.32 (q, $J = 6.1$ Hz, 2H). ^{13}C NMR (DMSO- d_6 , 126 MHz): $\delta = 165.4, 133.7, 131.2, 129.3, 124.73, 59.6, 42.2$. m/z (EI): 243 ($[\text{M}]^+$).

N-(2-Hydroxyethyl)-4-(1H-pyrrolo[2,3-b]pyridin-4-yl)benzamide (7). Starting from 6, the synthesis of 7 was performed by following general procedure B. Purification was performed by column chromatography using a stepwise gradient from a 15:1:0.1 to a 10:1:0.1 mixture of DCM/MeOH/10% aq. NH₄OH (25%) in MeOH. Yield 43%, colorless solid. ^1H NMR (DMSO- d_6 , 500 MHz): $\delta = 11.83$ (s, 1H), 8.53 (t, $J = 5.6$ Hz, 1H), 8.31 (d, $J = 4.9$ Hz, 1H), 8.07–8.00 (m, 2H), 7.89–7.82 (m, 2H), 7.60–7.55 (m, 1H), 7.23 (d, $J = 4.9$ Hz, 1H), 6.63 (dd, $J = 3.6, 1.8$ Hz, 1H), 4.75 (t, $J = 5.6$ Hz, 1H), 3.56 (q, $J = 6.0$ Hz, 2H), 3.39 (q, $J = 6.1$ Hz, 2H). ^{13}C NMR (DMSO- d_6 , 126 MHz): $\delta = 165.9, 149.2, 142.9, 141.0, 139.3, 134.2, 128.0, 127.8, 126.9, 117.2, 114.3, 99.0, 59.8, 42.2$. ^{13}C NMR (DMSO- d_6 , 126 MHz, DEPT): $\delta = 142.9, 128.0, 127.9, 126.9, 114.3, 98.9, 59.8, 42.3$. m/z (ESI): 282.12 ($[\text{M} + \text{H}]^+$).

(R)-4-(2-Amino-3-hydroxypropyl)phenol (8d). To a stirred solution of D-tyrosine methyl ester hydrochloride (2.00 g, 8.63 mmol) in 20 mL of acetonitrile was added potassium carbonate (2.98 g, 21.6 mmol), and the solution was heated to 50 °C for 16 h. Filtration of the formed salt and evaporation of the solvent under reduced pressure gave an orange oil that was taken up in 20 mL of methanol. Under cooling to 0 °C in an ice bath, NaBH₄ (491 mg, 12.99 mmol) was added in small portions over 30 min. The cooling bath was removed, and the solution was stirred at ambient temperature for 5 h. The solvent was removed under reduced pressure, the resulting residue was taken up in 50 mL of water, and the aqueous layer was extracted with ethyl acetate (5 \times 50 mL). The combined organic layers were

L

<https://dx.doi.org/10.1021/acs.jmedchem.0c02118>
J. Med. Chem. XXXX, XXX, XXX–XXXX

dried over MgSO_4 , filtered, and concentrated *in vacuo* to give **8d** (878 mg, 61%) as a crude yellow solid that was used for the next step without further purification. ^1H NMR ($\text{DMSO}-d_6$, 500 MHz): δ = 6.68–6.65 (m, 2H), 6.37–6.34 (m, 2H), 2.97 (dd, J = 10.3, 4.5 Hz, 1H), 2.87–2.83 (m, 1H), 2.24 (dd, J = 13.4, 6.0 Hz, 1H), 2.20–2.09 (m, 1H), 2.02 (dd, J = 13.4, 7.5 Hz, 1H), 1.44 (s, 1H). ^{13}C NMR ($\text{DMSO}-d_6$, 500 MHz): δ = 155.5, 130.0, 129.5, 115.0, 65.5, 54.6, 39.0. m/z (EI): 167 ($[\text{M}]^+$).

(S)-2-Amino-3-(1H-indol-3-yl)propan-1-ol (8e). An oven-dried three-neck flask was charged with L-tryptophan (2.04 g, 10.0 mmol), sodium borohydride (757 mg, 20.0 mmol), and 20 mL of dry THF and equipped with a dropping funnel and a reflux condenser under argon atmosphere. A solution of iodine (2.54 g, 10.0 mmol) in 10 mL dry THF was added dropwise over the course of 30 min at 0 °C under cooling in an ice bath. Once the evolution of gas had stopped, the ice bath was removed, and the mixture was heated to reflux for 20 h. After cooling to ambient temperature, methanol was slowly added under vigorous stirring until the solution became clear. After stirring for another 15 min, removal of the solvents under reduced pressure gave a white residue that was dissolved in 25 mL of aq. KOH solution (20% w/v) and stirred for 16 h at ambient temperature. Adjustment to pH 11 by addition of hydrochloric acid (2 M) was followed by extraction of the aqueous layer with DCM (3 \times 25 mL) and a 1:4 mixture of ethanol/chloroform (5 \times 25 mL). The combined organic layers were washed with water (3 \times 25 mL) and brine (25 mL) and dried over MgSO_4 . The solvent was removed under reduced pressure to give **8e** (1.36 g, 72%) as a crude yellow oil that was used without further purification. ^{13}C NMR (75 MHz, CDCl_3) δ = 136.5, 127.7, 122.9, 122.1, 119.4, 118.9, 112.4, 111.4, 66.6, 53.1, 30.1. m/z (ESI): 191.12 ($[\text{M} + \text{H}]^+$).

(R)-2-Amino-3-(1H-indol-3-yl)propan-1-ol (8f). An oven-dried three-neck flask was charged with D-tryptophan (1.57 g, 7.69 mmol), sodium borohydride (640 mg, 16.91 mmol), and 15 mL of dry THF and equipped with a dropping funnel and a reflux condenser under argon atmosphere. A solution of iodine (1.95 g, 7.69 mmol) in 8 mL of dry THF was added dropwise over the course of 30 min at 0 °C under cooling in an ice bath. Once the evolution of gas had stopped, the ice bath was removed, and the mixture was heated to reflux for 19 h. After the mixture was cooled to ambient temperature, methanol was slowly added under vigorous stirring until the solution became clear. After stirring for another 15 min, removal of the solvents under reduced pressure gave a white residue that was dissolved in 20 mL of aq. KOH solution (20% w/v) and stirred for 15 h at ambient temperature. Adjustment to pH 11 by addition of hydrochloric acid (2 M) was followed by extraction of the aqueous layer with DCM (3 \times 25 mL) and a 1:4 mixture of ethanol/chloroform (5 \times 25 mL). The combined organic layers were washed with water (3 \times 25 mL) and brine (25 mL) and dried over MgSO_4 . The solvent was removed under reduced pressure to give **8f** (1.22 g, 84%) as a crude yellow oil that was used for the next step without further purification. ^1H NMR ($\text{DMSO}-d_6$, 500 MHz): δ = 10.83 (s, 1H), 7.54 (d, J = 7.9 Hz, 1H), 7.34 (d, J = 8.0 Hz, 1H), 7.15 (d, J = 1.8 Hz, 1H), 7.06 (ddt, J = 8.2, 5.0, 1.4 Hz, 1H), 6.99–6.94 (m, 1H), 3.41–3.35 (m, 1H), 3.24 (m, 1H), 3.01 (q, J = 6.1 Hz, 1H), 2.81 (dd, J = 14.2, 6.1 Hz, 1H), 2.60 (dd, J = 14.2, 7.1 Hz, 1H). ^{13}C NMR ($\text{DMSO}-d_6$, 126 MHz): δ = 136.3, 127.58, 123.3, 120.8, 118.4, 118.1, 111.6, 111.3, 65.7, 53.6, 29.4. m/z (ESI): 191.12 ($[\text{M} + \text{H}]^+$).

(S)-4-Bromo-N-(1-hydroxy-3-phenylpropan-2-yl)benzenesulfonamide (9a). Synthesis of **9a** was performed by following general procedure A using L-phenylalaninol (**8a**). Yield 98%, colorless solid. ^1H NMR ($\text{DMSO}-d_6$, 500 MHz) δ = 7.60–7.56 (m, 2H), 7.50–7.46 (m, 2H), 7.12 (dd, J = 5.2, 1.9 Hz, 3H), 7.06–7.00 (m, 2H), 4.80 (s, 1H), 3.33 (dd, J = 10.1, 4.2 Hz, 1H), 3.30–3.24 (m, 1H), 3.21 (dd, J = 9.9, 6.6 Hz, 1H), 2.83 (dd, J = 13.7, 5.3 Hz, 1H), 2.46 (dd, J = 13.7, 8.0 Hz, 1H). ^{13}C NMR ($\text{DMSO}-d_6$, 126 MHz) δ = 140.9, 138.3, 131.8, 129.1, 128.0, 125.7, 125.5, 63.2, 57.3, 37.0. m/z (APCI): 370.01 ($[\text{M} + \text{H}]^+$).

(R)-4-Bromo-N-(1-hydroxy-3-phenylpropan-2-yl)benzenesulfonamide (9b). Synthesis of **9b** was performed by following general procedure A using D-phenylalaninol (**8b**). Yield 99%, colorless

solid. ^1H NMR (CDCl_3 , 300 MHz): δ = 7.48 (s, 4H), 7.21–7.13 (m, 3H), 7.00–6.93 (m, 2H), 3.69 (dd, J = 11.1, 4.1 Hz, 1H), 3.59 (dd, J = 11.1, 4.6 Hz, 1H), 3.53–3.39 (m, 1H), 2.83 (dd, J = 13.9, 6.3 Hz, 1H), 2.68 (dd, J = 14.0, 8.2 Hz, 1H). m/z (ESI): 370.01 ($[\text{M} + \text{H}]^+$).

(S)-4-Bromo-N-(1-hydroxy-3-(4-hydroxyphenyl)propan-2-yl)benzenesulfonamide (9c). To a solution of L-tyrosinol (469 mg, 2.15 mmol) in 10 mL of a 1:1 mixture of water/acetone was added sodium bicarbonate (658 mg, 7.83 mmol), and the mixture was stirred at ambient temperature for 15 min. 4-Bromobenzene-sulfonyl chloride (**1**, 500 mg, 1.96 mmol) was added, and stirring was continued for 17 h. After evaporation of the volatile solvent under reduced pressure, 10 mL of ethyl acetate was added, and the layers were separated. The aqueous layer was extracted with ethyl acetate (3 \times 5 mL), and the combined organic layers were washed with saturated NaHCO_3 (aq, 3 \times 5 mL) and dried over MgSO_4 . The solvent was removed under reduced pressure to give crude crystals that were recrystallized from methanol to give **9c** (455 mg, 60%) as colorless crystals. ^1H NMR ($\text{DMSO}-d_6$, 500 MHz): δ = 9.09 (s, 1H), 7.67 (d, J = 7.3 Hz, 2H), 7.67–7.60 (m, 3H), 7.55–7.49 (m, 2H), 6.87–6.80 (m, 2H), 6.59–6.52 (m, 2H), 4.69 (t, J = 5.1 Hz, 1H), 3.30–3.25 (m, 2H), 3.22–3.14 (m, 2H), 2.69 (dd, J = 13.8, 5.4 Hz, 1H), 2.35 (dd, J = 13.8, 6.9 Hz, 1H). m/z (ESI): 386.01 ($[\text{M} + \text{H}]^+$).

(R)-4-Bromo-N-(1-hydroxy-3-(4-hydroxyphenyl)propan-2-yl)benzenesulfonamide (9d). To a solution of D-tyrosinol (**8d**, 229 mg, 1.37 mmol) in 7 mL of a 1:1 mixture of water/acetone was added sodium bicarbonate (460 mg, 5.48 mmol), and the mixture was stirred at ambient temperature for 15 min. 4-Bromobenzene-sulfonyl chloride (**1**, 350 mg, 1.37 mmol) was added, and the solution was heated to 40 °C for 4 h. After evaporation of the volatile solvent under reduced pressure, 7 mL of ethyl acetate was added, and the layers were separated. The aqueous layer was extracted with ethyl acetate (3 \times 5 mL), and the combined organic layers were washed with saturated NaHCO_3 (aq, 3 \times 5 mL) and dried over MgSO_4 . The solvent was removed under reduced pressure to give **9d** (371 mg, 70%) as a crude yellow solid that was used in the next step without further purification. ^1H NMR ($\text{DMSO}-d_6$, 300 MHz): δ = 7.68–7.58 (m, 2H), 7.52 (d, J = 8.5 Hz, 2H), 6.88–6.78 (m, 2H), 6.60–6.51 (m, 2H), 4.71 (s, 1H), 3.25–3.12 (m, 4H), 2.69 (dd, J = 13.7, 5.5 Hz, 1H), 2.35 (dd, J = 13.9, 6.9 Hz, 1H). ^{13}C NMR ($\text{DMSO}-d_6$, 75 MHz) δ = 155.6, 141.0, 132.9, 131.8, 130.1, 130.0, 128.2, 114.8, 62.8, 57.4, 36.2. m/z (ESI): 386.01 ($[\text{M} + \text{H}]^+$).

(S)-4-Bromo-N-(1-hydroxy-3-(1H-indol-3-yl)propan-2-yl)benzenesulfonamide (9e). To a stirred solution of L-tryptophanol (**8e**, 400 mg, 2.10 mmol) in 40 mL of a 1:2 mixture of DCM/acetonitrile was added N,N' -diisopropylethylamine (326 mg, 2.52 mmol). The mixture was stirred at ambient temperature for 1 h, and 4-bromobenzene-sulfonyl chloride (**1**, 537 mg, 2.10 mmol) was added in small portions over 30 min at 0 °C under cooling in an ice bath. The cooling bath was removed, and the solution was stirred at ambient temperature for 24 h. Removal of the solvent under reduced pressure gave a brown residue that was taken up in 30 mL of DCM, washed with hydrochloric acid (1 N, 3 \times 5 mL), water (3 \times 5 mL), and brine (5 mL) and dried over MgSO_4 . The solvent was removed under reduced pressure to give a crude brown oil that was purified by column chromatography using a 1:1 mixture of ethyl acetate/cyclohexane yielding **9e** (257 mg, 30%) as a yellow oil. ^1H NMR ($\text{DMSO}-d_6$, 500 MHz): δ = 10.70 (s, 1H), 7.73 (d, J = 6.9 Hz, 1H), 7.50–7.43 (m, 4H), 7.28 (dt, J = 7.8, 1.0 Hz, 2H), 7.07–7.01 (m, 2H), 6.91 (tt, J = 6.9, 0.9 Hz, 1H), 4.79 (t, J = 5.3 Hz, 1H), 3.42–3.39 (m, 1H), 3.33–3.25 (m, 2H), 2.95 (dd, J = 14.3, 6.0 Hz, 1H), 2.61 (dd, J = 14.3, 7.0 Hz, 1H). ^{13}C NMR ($\text{DMSO}-d_6$, 126 MHz): δ = 140.6, 136.1, 131.4, 127.9, 127.0, 125.4, 123.7, 120.6, 118.1, 117.9, 111.4, 110.3, 63.2, 56.1, 27.0. m/z (ESI): 409.02 ($[\text{M} + \text{H}]^+$).

(R)-4-Bromo-N-(1-hydroxy-3-(1H-indol-3-yl)propan-2-yl)benzenesulfonamide (9f). To a stirred solution of D-tryptophanol (**8f**, 625 mg, 3.29 mmol) in 60 mL of a 1:2 mixture of DCM/acetonitrile was added N,N' -diisopropylethylamine (510 mg, 3.94 mmol). The mixture was stirred at ambient temperature for 1 h, and 4-bromobenzene-sulfonyl chloride (**1**, 839 mg, 3.29 mmol) was added in small portions over 30 min at 0 °C under cooling in an ice bath.

The cooling bath was removed, and the solution was stirred at ambient temperature for 24 h. Removal of the solvent under reduced pressure gave a brown residue that was taken up in 40 mL of DCM, washed with hydrochloric acid (1 N, 3 × 7 mL), water (3 × 7 mL), and brine (7 mL) and dried over MgSO₄. The solvent was removed under reduced pressure to give a crude brown oil that was purified by column chromatography using a 1:1 mixture of ethyl acetate/cyclohexane yielding **9f** (579 mg, 43%) as a yellow oil. ¹H NMR (DMSO-*d*₆, 500 MHz): δ = 10.66 (s, 1H), 7.69 (d, *J* = 7.0 Hz, 1H), 7.50–7.41 (m, 4H), 7.30–7.23 (m, 2H), 7.05–6.98 (m, 2H), 6.93–6.85 (m, 1H), 4.75 (t, *J* = 5.4 Hz, 1H), 3.40–3.36 (m, 1H), 3.33–3.24 (m, 2H), 2.94 (dd, *J* = 14.4, 6.0 Hz, 1H), 2.60 (dd, *J* = 14.3, 7.0 Hz, 1H). ¹³C NMR (DMSO-*d*₆, 126 MHz): δ = 140.6, 136.1, 131.4, 127.9, 127.0, 125.4, 123.7, 120.6, 118.1, 117.9, 111.4, 110.3, 63.2, 56.1, 27.0. *m/z* (ESI): 409.02 ([M + H]⁺).

(S)-N-(1-Hydroxy-3-phenylpropan-2-yl)-4-(1H-pyrrolo[2,3-*b*]pyridin-4-yl)benzenesulfonamide (10a). Starting from **9a**, the synthesis of **10a** was performed by following general procedure B. Purification was performed by column chromatography using a 20:1:0.1 mixture of DCM/MeOH/10% aq. NH₄OH (25%) in MeOH. Yield 42%, beige solid. ¹H NMR (DMSO-*d*₆, 500 MHz): δ = 11.90 (s, 1H), 8.35 (d, *J* = 14.7, 5.0 Hz, 1H), 7.86–7.67 (m, 4H), 7.59 (t, *J* = 22.3, 3.1 Hz, 1H), 7.28 (d, *J* = 50.0, 4.9 Hz, 1H), 7.16–6.99 (m, 4H), 6.58 (t, 1H), 4.87 (t, *J* = 5.5 Hz, 1H), 3.46–3.40 (m, 1H), 3.35–3.31 (m, 1H), 3.31–3.20 (m, 1H), 2.87 (dd, *J* = 13.6, 5.5 Hz, 1H), 2.47 (d, *J* = 8.4 Hz, 1H). ¹³C NMR (DMSO-*d*₆, 126 MHz): δ = 149.2, 142.9, 141.6, 141.2, 138.6, 138.4, 129.1, 128.6, 128.0, 127.2, 126.8, 125.9, 117.1, 114.31, 98.9, 63.3, 57.3, 37.0. ¹³C NMR (DMSO-*d*₆, 126 MHz, DEPT): δ = 142.9, 129.1, 128.6, 128.0, 127.1, 126.8, 125.8, 114.3, 98.8, 63.3, 57.3, 37.1. *m/z* (ESI): 408.14 ([M + H]⁺). *m/z* (ESI-HRMS): 408.1378 ([M + H]⁺).

(R)-N-(1-Hydroxy-3-phenylpropan-2-yl)-4-(1H-pyrrolo[2,3-*b*]pyridin-4-yl)benzenesulfonamide (10b). Starting from **9b**, the synthesis of **10b** was performed by following general procedure B. Purification was performed by column chromatography using a 20:1:0.1 mixture of DCM/MeOH/10% aq. NH₄OH (25%) in MeOH. Yield 56%, beige solid. ¹H NMR (DMSO-*d*₆, 500 MHz): δ = 11.88 (s, 1H), 8.34 (d, *J* = 4.9 Hz, 1H), 7.80–7.72 (m, 4H), 7.60 (t, *J* = 2.9 Hz, 1H), 7.22 (dd, *J* = 4.9, 1.1 Hz, 1H), 7.15–6.98 (m, 5H), 6.72–6.54 (m, 1H), 4.86 (t, *J* = 5.4 Hz, 1H), 3.44–3.40 (m, 1H), 3.37–3.32 (m, 1H), 3.28 (dt, *J* = 11.1, 6.1 Hz, 1H), 2.88 (dd, *J* = 13.7, 5.4 Hz, 1H), 2.50 (dd, 1H). ¹³C NMR (DMSO-*d*₆, 126 MHz): δ = 149.15, 142.95, 141.64, 141.22, 138.63, 138.37, 129.14, 128.59, 127.97, 127.14, 126.76, 125.85, 117.13, 114.32, 98.80, 63.27, 57.28, 37.07. ¹³C NMR (DMSO-*d*₆, 126 MHz, DEPT): δ = 143.0, 129.2, 128.6, 128.0, 127.2, 126.8, 125.9, 114.4, 98.8, 63.3, 57.3, 37.1. *m/z* (ESI): 815.09 ([2M + H]⁺), 408.14 ([M + H]⁺). *m/z* (ESI-HRMS): 408.1374 ([M + H]⁺).

(S)-N-(1-Hydroxy-3-(4-hydroxyphenyl)propan-2-yl)-4-(1H-pyrrolo[2,3-*b*]pyridin-4-yl)benzenesulfonamide (10c). Starting from **9c**, the synthesis of **10c** was performed by following general procedure B. Purification was performed by column chromatography using a 10:1:0.1 mixture of DCM/MeOH/10% aq. NH₄OH (25%) in MeOH. Yield 51%, colorless solid. ¹H NMR (DMSO-*d*₆, 500 MHz): δ = 11.88 (s, 1H), 9.14 (s, 1H), 8.33 (d, *J* = 4.9 Hz, 1H), 7.86–7.74 (m, 4H), 7.71 (d, *J* = 7.3 Hz, 1H), 7.59 (t, *J* = 3.0 Hz, 1H), 7.26 (d, *J* = 4.9 Hz, 1H), 6.88 (d, *J* = 8.5 Hz, 2H), 6.63 (dd, *J* = 3.6, 1.8 Hz, 1H), 6.58 (d, *J* = 8.4 Hz, 2H), 4.79 (t, *J* = 5.3 Hz, 1H), 3.38–3.33 (m, 1H), 3.25 (p, *J* = 6.1 Hz, 2H), 2.75 (dd, *J* = 13.7, 5.5 Hz, 1H), 2.40 (dd, *J* = 13.7, 6.9 Hz, 1H). ¹³C NMR (DMSO-*d*₆, 126 MHz): δ = 155.7, 149.2, 143.0, 141.8, 141.4, 138.7, 130.1, 128.6, 128.4, 127.2, 126.9, 117.2, 114.9, 114.48, 98.9, 62.9, 57.5, 36.3. *m/z* (ESI): 424.13 ([M + H]⁺). *m/z* (ESI-HRMS): 424.1326 ([M + H]⁺).

(R)-N-(1-Hydroxy-3-(4-hydroxyphenyl)propan-2-yl)-4-(1H-pyrrolo[2,3-*b*]pyridin-4-yl)benzenesulfonamide (10d). Starting from **9d**, the synthesis of **10d** was performed by following general procedure B. Purification was performed by column chromatography using a 10:1:0.1 mixture of DCM/MeOH/10% aq. NH₄OH (25%) in MeOH. Yield 26%, colorless solid. ¹H NMR (DMSO-*d*₆, 500 MHz): δ = 11.87 (s, 1H), 9.10 (d, *J* = 1.3 Hz, 1H), 8.33 (d, *J* = 4.9 Hz, 1H),

7.86–7.80 (m, 2H), 7.79–7.73 (m, 2H), 7.67 (d, *J* = 7.0 Hz, 1H), 7.59 (t, *J* = 2.9 Hz, 1H), 7.26 (dd, *J* = 5.0, 1.4 Hz, 1H), 6.87 (d, *J* = 7.1 Hz, 2H), 6.63 (q, *J* = 3.5, 1.6 Hz, 1H), 6.57 (d, *J* = 8.4 Hz, 2H), 4.75 (t, *J* = 5.2 Hz, 1H), 3.31–3.15 (m, 3H), 2.74 (dd, *J* = 13.7, 5.4 Hz, 1H), 2.40 (dd, *J* = 13.8, 6.8 Hz, 1H). ¹³C NMR (DMSO-*d*₆, 126 MHz): δ = 155.6, 149.1, 142.9, 141.7, 141.3, 138.6, 130.1, 128.6, 128.4, 127.1, 126.9, 117.2, 114.9, 114.4, 98.8, 62.8, 57.4, 36.3. ¹³C NMR (DMSO-*d*₆, 126 MHz, DEPT): δ = 142.9, 130.1, 128.6, 127.1, 126.9, 114.9, 114.4, 98.8, 62.8, 36.3. *m/z* (ESI): 424.13 ([M + H]⁺). *m/z* (ESI-HRMS): 424.1328 ([M + H]⁺).

(S)-N-(1-Hydroxy-3-(1H-indol-3-yl)propan-2-yl)-4-(1H-pyrrolo[2,3-*b*]pyridin-4-yl)benzenesulfonamide (10e). Starting from **9e**, the synthesis of **10e** was performed by following general procedure B. Purification was performed by column chromatography using a 20:1:0.1 mixture of DCM/MeOH/10% aq. NH₄OH (25%) in MeOH. Yield 60%, beige solid. ¹H NMR (DMSO-*d*₆, 500 MHz): δ = 11.85 (s, 1H), 10.69 (s, 1H), 8.32 (d, *J* = 4.9 Hz, 1H), 7.79–7.73 (m, 4H), 7.70 (d, *J* = 6.5 Hz, 1H), 7.57 (t, *J* = 2.9 Hz, 1H), 7.31 (d, *J* = 7.9 Hz, 1H), 7.20 (dd, *J* = 7.0, 5.3 Hz, 2H), 7.07 (d, *J* = 1.8 Hz, 1H), 6.93 (td, *J* = 8.1, 1.3 Hz, 1H), 6.86 (t, *J* = 7.4 Hz, 1H), 6.59 (dd, *J* = 3.4, 1.7 Hz, 1H), 4.74 (s, 1H), 3.42–3.38 (m, 2H), 3.37–3.26 (m, 2H), 2.97 (dd, *J* = 14.3, 6.4 Hz, 1H), 2.67 (dd, *J* = 14.3, 6.0 Hz, 1H). ¹³C NMR (DMSO-*d*₆, 126 MHz): δ = 149.1, 142.8, 141.6, 141.2, 138.6, 136.1, 128.4, 127.2, 127.1, 126.8, 123.8, 120.7, 118.1, 118.0, 117.1, 114.4, 111.3, 110.4, 98.9, 62.9, 56.2, 27.1. ¹³C NMR (DMSO-*d*₆, 126 MHz, DEPT): δ = 142.9, 128.4, 127.1, 126.8, 123.8, 120.7, 118.1, 118.0, 114.4, 111.3, 98.9, 62.9, 56.2, 27.1. *m/z* (ESI): 447.15 ([M + H]⁺). *m/z* (ESI-HRMS): 447.1484 ([M + H]⁺).

(R)-N-(1-Hydroxy-3-(1H-indol-3-yl)propan-2-yl)-4-(1H-pyrrolo[2,3-*b*]pyridin-4-yl)benzenesulfonamide (10f). Starting from **9f**, the synthesis of **10f** was performed by following general procedure B. Purification was performed by column chromatography using a 20:1:0.1 mixture of DCM/MeOH/10% aq. NH₄OH (25%) in MeOH. Yield 62%, beige solid. ¹H NMR (DMSO-*d*₆, 500 MHz): δ = 11.86 (s, 1H), 10.71 (s, 1H), 8.33 (d, *J* = 4.9 Hz, 1H), 7.79–7.74 (m, 4H), 7.71 (d, *J* = 7.0 Hz, 1H), 7.58 (dd, *J* = 3.5, 2.6 Hz, 1H), 7.32 (d, *J* = 7.0 Hz, 1H), 7.22 (d, *J* = 4.9 Hz, 1H), 7.20 (d, *J* = 8.2 Hz, 1H), 7.08 (d, *J* = 2.3 Hz, 1H), 6.94 (ddd, *J* = 8.1, 7.0, 1.1 Hz, 1H), 6.87 (ddd, *J* = 7.9, 7.0, 1.0 Hz, 1H), 6.60 (dd, *J* = 3.5, 1.9 Hz, 1H), 4.76 (t, *J* = 5.4 Hz, 1H), 3.41–3.37 (m, 2H), 3.32–3.29 (m, 1H), 2.98 (dd, *J* = 14.3, 6.5 Hz, 1H), 2.67 (dd, *J* = 14.3, 6.2 Hz, 1H). ¹³C NMR (DMSO-*d*₆, 126 MHz): δ = 149.2, 142.9, 141.6, 141.2, 138.6, 136.1, 128.4, 127.2, 127.1, 126.8, 123.8, 120.7, 118.1, 118.0, 117.1, 114.4, 111.3, 110.4, 98.9, 62.9, 56.2, 27.0. *m/z* (ESI): 893.29 ([2M + H]⁺), 447.15 ([M + H]⁺). *m/z* (ESI-HRMS): 447.1485 ([M + H]⁺).

Molecular Modeling. Molecular modeling was performed using the Molecular Operating Environment (Molecular Operating Environment MOE, 2016.0802; Chemical Computing Group ULC, 1010 Sherbooke St. West, Suite #910, Montreal, QC, Canada, H3A 2R7, 2021) software package, employing an “Amber10” force field.

Isolation of the monomeric kinase domains was achieved by manual deletion of the bridged chain using the “sequence editor”. Superposition of the isolated chains was performed with the “align/superpose” tool of the “sequence editor”.

Reconstruction of the glycine-rich loop (P-Loop) was performed using the “SuperLooper2” web server.⁴⁷ Starting from the crystal structure of Nek1 (PDB code 4B9D.B), the missing loop sequence EGSGF (between G11 and K17) was reconstructed by using the AGPAG loop (between P311 and R317) of the *Mycobacterium tuberculosis* probable periplasmic sugar-binding lipoprotein UspC (PDB code 5K2Y) crystal structure as a template.

The Nek1 kinase domain homology model was created using the “homology model” function and the crystal structure of Nek2 bound to an aminopurine inhibitor (PDB code 5MS3) as the template.⁴⁸

For all docking experiments, residual water molecules were deleted, and the receptors were prepared using the “QuickPrep” function without “automated structure preparation”. Using the respective functions of the “MOE Database Viewer”, all ligands were “washed” before partial charges were determined and the structures underwent energy minimization. The binding sites were designated from the

N

<https://dx.doi.org/10.1021/acs.jmedchem.0c02118>
J. Med. Chem. XXXX, XXX, XXX–XXX

cocrystallized ligand (PDB code 4B9D), which was placed in the binding site by superposition in the case of the apo structure (PDB code 4APC) and the homology model. Docking poses were placed using the "Triangle Matcher" method and scored by a "London dG" function. Refinements of the poses were performed by using the "Rigid Receptor" method and were finally scored using a "GBVI/WSA dG" function. For the docking of **3a** into the apo structure, a hinge binding pharmacophore was defined, based on the cocrystallized ligand.

The sequence homology analysis between the human and zebrafish Nek1 kinase domains was performed using the "MOE protein similarity monitor". Identity and similarity values are equal to the number of matches divided by the number of amino acids in the chain corresponding to the cell column. Residues are considered similar if their BLOSUM62 scores are greater than zero.

In accordance with the author guidelines, all virtual screening hits were filtered for PAINS using the PAINS-remover online application.⁶⁴ All compounds passed the filter.

In Vitro Kinase Activity Assays. Residual kinase inhibition was determined with the commercial Eurofins Discovery KinaseProfiler service at 1 μM compound concentration and either 10 μM ATP or an ATP concentration within 15 μM of the apparent K_m for ATP (see Supporting Information for K_m values). In the case of Nek1 (KinaseProfiler ITEM 15-020KP10 and ITEM 15-020KP), recombinant human Nek1 (1–505) was incubated with 8 mM MOPS (pH 7.0), 0.2 mM EDTA, 250 μM RLRGRDKYKTLRQIRQ, 10 mM magnesium acetate, and [γ -³³P-ATP]. The reaction was initiated by the addition of the Mg/ATP mix. After incubation for 40 min at room temperature, the reaction was stopped by the addition of phosphoric acid to a concentration of 0.5%. Ten microliters of the reaction was then spotted onto a P30 filtermat and washed four times for 4 min in 0.425% phosphoric acid and once in methanol prior to drying and scintillation counting. Values are the mean from two independent experiments.

IC_{50} values for Nek1 and Nek2 were determined in a TR-FRET based activity assays (LANCE Ultra TR-FRET, PerkinElmer) at an ATP concentration within 15 μM of the apparent K_m for ATP in the respective assay format (60 μM for both Nek1 and Nek2). The IC_{50} curves consist of 10 test compound concentrations tested at half-log dilutions from 30 μM to 1 nM with vehicle and inhibitory control wells. For compounds **3j** and **3k**, the maximum concentration was set to 10 μM as a consequence of solubility issues at 30 μM , and the respective IC_{50} curves consist of 9 test compound concentrations tested at half-log dilutions from 10 μM to 1 nM. Values are the mean from two independent experiments. Recombinant human Nek1 (1–505; 0.02 nM) or Nek2 (full length; 0.2 nM) (both from Thermo Fisher Scientific) was incubated with 50 mM HEPES (pH 7.5), 1 mM EGTA, 10 mM MgCl_2 , 0.2 mM DTT, 0.01% Tween20, and 50 nM ULight-p70 S6K (Thr389) peptide (sequence LGFTYVAP; PerkinElmer). The reaction was initiated by the addition of the p70 S6K peptide/ATP mix. After incubation for 30 min at 22 °C, the reaction was stopped by the addition of 10 mM EDTA and 0.3 nM europium-antiphospho-p70 S6K (Thr389) antibody in CR97 detection buffer (both PerkinElmer). After incubation for 1 h at 22 °C for signal development, the plates were analyzed in a plate reader (PHERAstar FSX, BMG LABTECH). For compounds **3g** and **3k**, relative IC_{50} values were provided instead of absolute IC_{50} as the determined IC_{50} values exceeded the employed maximum test concentrations (30 μM for **3g**, 10 μM for **3k**).

For compounds **3a**, **3f**, **10a–f**, IC_{50} values were also determined with the Eurofins Discovery IC50Profiler service at either 10 μM (ITEM 15-020KP10) or an ATP concentration within 15 μM of the apparent K_m for ATP (90 μM , ITEM 15-020KP). The IC_{50} curves consist of 9 test compound concentrations tested at half-log dilutions from 10 μM to 1 nM with vehicle control wells. Values are the mean from two independent experiments.

IC_{50} values and 95% confidence intervals were determined from the raw data provided in the Supporting Information by nonlinear regression (log_inhibitor vs response_variable slope_four parameters) using GraphPad Prism, version 8.4.3 (471) for OS X, (GraphPad

Software, San Diego, California USA, www.graphpad.com). For compounds **3j** and **3k**, the maximum concentration data points were dropped, as a consequence of solubility issues at 30 μM .

Caco-2 Cell Permeability Assay. A–B permeability (Caco-2, pH 6.5/7.4) and percent recovery were determined by HPLC-MS/MS detection of the peak area response in a commercial assay by Eurofins Discovery Services (Item 3318). Propranolol, labetalol, colchicine, and ranitidine were tested concurrently as reference compounds.

Fish Maintenance and Husbandry Protocols. Fish maintenance and husbandry protocols were documented and approved by the Darmstadt administrative authority. All animals were treated humanely in accordance with the German animal protection standards and the EU Directive 2010/63/EU of the European parliament and of the council. Adult wild-type zebrafish (*Danio rerio*) were maintained in 60 L fish tanks in a laboratory with no daylight and a constant temperature of 28 °C. Room light was programmed to a 12 h dark/12 h light cycle. Adult zebrafish were bred in mating containers (2 animals/1 L) or mating tanks (6–8 animals/20 L) that were equipped with plastic grass and a removable sieve at the bottom of the tank. Embryos were collected 2–3 h after a light cycle started, rinsed with E3-medium, and isolated in Petri dishes containing E3-medium. E3-medium was prepared according to the Cold Spring Harbor Protocols recipe for E3 medium for zebrafish embryos (doi: 10.1101/pdb.rec066449).

Zebrafish Developmental Toxicity Assay. The aqueous solubility of **10f** was determined in a shake-flask HPLC solubility assay using the previously described HPLC system connected to a diode array detector (DAD, see General Information). Absorption was measured at 280 nm, and all measurements were performed in triplicate. A saturated solution of **10f** in E3-medium was prepared by shaking for 24 h at 25 °C. A 10 mM stock solution of **10f** in DMSO was diluted to 1, 5, 10, 50, and 100 μM solutions in acetonitrile, and the aqueous solubility of **10f** was determined by interpolation using Prism 8 by GraphPad Software, LLC.

The zebrafish developmental toxicity screen was performed in accordance to guidelines published by M. Haldi et al. in *Zebrafish: Methods for Assessing Drug Safety and Toxicity*.⁶⁵

At 4 hpf (hours postfertilization), 15 embryos per group (0.05, 0.1, 0.5, 1.5, 2.5, 5, 10, 15, 20, 30 μM) that exhibited intact chorion membranes were selected and reexamined after 2 h. A stock solution (10 mM in DMSO) of the test compound was diluted to 10 \times final concentrations, and the embryos were sorted in 180 μL of E3 medium. At 6 hpf, 20 μL of the 10 \times solution was added to give the final concentrations. Survival was monitored every 24 h by observation of the heartbeat. All survival rates were determined at least in triplicate with the controls and the survival rate at 30 μM being determined in 5 replicates.

Stability-Indicating HPLC Assay. The stability-indicating HPLC assay was performed using the previously described HPLC system connected to a diode array detector (DAD, see General Information). A 15 μM solution of **10f** in E3-medium containing 75 μM 2-phenylthiourea (PTU) and a 15 μM solution of **10f** containing 75 μM PTU and 2.5 μM PT-Yellow (BDNCA3-D2) were prepared for HPLC injection. Absorptions were measured every 24 h at 280 nm for compound **10f** and PTU and 548 nm for PT-Yellow over 48 or 120 h, respectively. All measurements were performed in triplicate.

Fluorescence Microscopy Imaging of Zebrafish Pronephroi. The 96-well plate molding tool was manufactured by selective laser melting on an EOS M290 (EOS GmbH Electro Optical Systems, Krailing, Germany) metal 3D-printing system using EOS Stainless-Steel 316L as the material with a layer height of 20 μM . The tool consists of a base plate with 96 perpendicular pins that match the positions of the wells of a microtiter plate. The agarose molds were prepared using 1% NEEQ ultraquality agarose (Carl Roth, Karlsruhe, Germany, Art. No. 2267.1) in black-walled 96-well Nunc polymer optical bottom plates (Thermo Fisher Scientific, Waltham, Massachusetts, USA). The specifications of the molding tool and the preparation of the agarose molds in 96-well microtiter plates followed the procedure published by Westhoff et al.⁵⁵

O

<https://dx.doi.org/10.1021/acs.jmedchem.0c02118>
J. Med. Chem. XXXX, XXX, XXX–XXX

Image Acquisition. Imaging of fluorescently labeled (PT-Yellow) zebrafish embryos was performed on an Olympus IX-81 widefield microscope (Olympus, Shinjuku, Tokyo, Japan), using an Olympus CPlanFL N, 10 \times , NA 0.3 objective in combination with a 1.5 \times tube lens magnification, resulting in a total magnification of 15 \times . Fluorescence was excited using a CoolLED pE300 Ultra (CoolLED Ltd., Andover, NY, USA) and detected on a pco.edge 5.5 (PCO AG, Kelheim, Germany) using appropriate filter sets. The whole setup was controlled using Micromanager 1.4.22.⁵⁶ to record 33 Z-slices with a Z-distance of 15 μ m per embryo after manual orientation in the previously described agarose molds.

Image Processing and Deconvolution. Image processing was performed using ImageJ, version 2.0.0.-rc-69/1.52p. Deconvolution was performed using the DeconvolutionLab2 plugin and a point spread function that was simulated in the PSF Generator plugin. The image stacks are presented as colored maximum Z-projections using the lookup table *blue orange icb* (Figure S14). As it was not possible to remove all out of focus blur with the deconvolution procedure, the sharpest 5 consecutive Z-slices of labeled pronephrons were manually selected in each stack (Figures S15 and S16). Subsequently, the following image analysis steps were applied using ImageJ: (1) subtract background using a 150 pixel rolling ball, (2) sum all 5 images into one, (3) threshold images above 100, (4) convert background to 8-bit mask for the intensity quantification or convert background to NaN for the quantification of the pronephron areas. The pronephron area in the summed stacks was used as the quantity to estimate the size of the pronephron.

■ ASSOCIATED CONTENT

Supporting Information

The Supporting Information is available free of charge at <https://pubs.acs.org/doi/10.1021/acs.jmedchem.0c02118>.

Molecular modeling, homology model coordinates, *in vitro* pharmacology, NMR data, lead compound HPLC traces, bioavailability profile of compound **10f** (PDF)

Molecular formula strings (CSV)

Nek1 homology model (PDB)

Superlooper2 reconstruction model (PDB)

■ AUTHOR INFORMATION

Corresponding Authors

Boris Schmidt – Clemens Schöpf–Institute of Organic Chemistry and Biochemistry, Technische Universität Darmstadt, 64287 Darmstadt, Germany; orcid.org/0000-0003-1662-2392; Phone: +496151-1623745; Email: schmidt_boris@t-online.de; Fax: +496151-163278

Georg Baumann – Clemens Schöpf–Institute of Organic Chemistry and Biochemistry, Technische Universität Darmstadt, 64287 Darmstadt, Germany; Email: georg.baumann@stud.tu-darmstadt.de

Authors

Tobias Meckel – Clemens Schöpf–Institute of Organic Chemistry and Biochemistry, Technische Universität Darmstadt, 64287 Darmstadt, Germany

Kevin Böhm – Clemens Schöpf–Institute of Organic Chemistry and Biochemistry, Technische Universität Darmstadt, 64287 Darmstadt, Germany

Yung-Hsin Shih – Clemens Schöpf–Institute of Organic Chemistry and Biochemistry, Technische Universität Darmstadt, 64287 Darmstadt, Germany

Mirco Dickhaut – Clemens Schöpf–Institute of Organic Chemistry and Biochemistry, Technische Universität Darmstadt, 64287 Darmstadt, Germany

Torben Reichardt – Clemens Schöpf–Institute of Organic Chemistry and Biochemistry, Technische Universität Darmstadt, 64287 Darmstadt, Germany

Johannes Pilakowski – Clemens Schöpf–Institute of Organic Chemistry and Biochemistry, Technische Universität Darmstadt, 64287 Darmstadt, Germany

Ulrich Pehl – Merck Healthcare KGaA, Biopharma R&D, Discovery and Development Technologies, 64293 Darmstadt, Germany

Complete contact information is available at:

<https://pubs.acs.org/doi/10.1021/acs.jmedchem.0c02118>

Author Contributions

G.B., B.S., and T.M. conceived and designed the experiments. G.B., T.M., and B.S. wrote the manuscript. G.B., K.B., Y.S., M.D., U.D., and T.R. performed the experiments. G.B., B.S., U.P., and T.M. analyzed the data. G.B., B.S., T.M., and J.P. gave scientific advice. All authors contributed to the article and approved the submitted version.

Funding

The authors declare that this study received funding from the German Research Foundation (DFG, GRK1657, Project number: 161030019). The funders had no role in study design, data collection and analysis, decision to publish, or preparation of the manuscript.

Notes

The authors declare no competing financial interest.

■ ACKNOWLEDGMENTS

We thank Holger Hermann Merschroth for the design and production of the 96-well plate molding tool and Nadine Herget and Friedrich Baumgärtner for performing the TR-FRET *in vitro* kinase activity assays. We furthermore thank Prof. Markus Löbrich, Julian Spies, and Michael Ensminger for discussions on the biological role of Nek1.

■ ABBREVIATIONS

ALS, amyotrophic lateral sclerosis; CDK, cyclin-dependent kinase; Chk1, checkpoint kinase 1; Chk2, checkpoint kinase 2; cDNA, complementary DNA; DDR, DNA damage response; HR, homologous recombination; IKK, I κ B kinase; JNK, c-Jun N-terminal kinase; DSB, double strand break; HR, homologous recombination; Nek1, NIMA-related kinase 1; NF- κ B, nuclear factor kappa-light-chain-enhancer of activated B-cells; MOE, Molecular Operating Environment; NIMA, never-in-mitosis gene A; PKD, polycystic kidney disease; PSF, point square function; RCC, renal cell carcinoma; SAR, structure–activity relationship; TLC, thin layer chromatography; TPSA, topological polar surface area; Tlk1, touselled-like kinase 1

■ REFERENCES

- (1) van de Kooij, B.; Creixell, P.; van Vlimmeren, A.; Joughin, B. A.; Miller, C. J.; Haider, N.; Simpson, C. D.; Linding, R.; Stambolic, V.; Turk, B. E.; Yaffe, M. B. Comprehensive substrate specificity profiling of the human Nek kinome reveals unexpected signaling outputs. *eLife* **2019**, *8*, No. e44635.
- (2) Letwin, K.; Mizzen, L.; Motro, B.; Ben-David, Y.; Bernstein, A.; Pawson, T. A mammalian dual specificity protein kinase, Nek1, is related to the NIMA cell cycle regulator and highly expressed in meiotic germ cells. *EMBO J.* **1992**, *11*, 3521–3531.
- (3) Meirelles, G. V.; Perez, A. M.; Souza, E. E.; Basei, F. L.; Papa, P. F.; Melo Hanchuk, T. D.; Cardoso, V. B.; Kobarg, J. Stop Ne(c)king around[†]: How interactomics contributes to functionally characterize

P

<https://dx.doi.org/10.1021/acs.jmedchem.0c02118>
J. Med. Chem. XXXX, XXX, XXX–XXX

- Nek family kinases. *World journal of biological chemistry* **2014**, *5*, 141–160.
- (4) Peres de Oliveira, A.; Kazuo Issayama, L.; Betim Pavan, I. C.; Riback Silva, F.; Diniz Melo-Hanchuk, T.; Moreira Simabuco, F.; Kobarg, J. Checking NEKs: Overcoming a Bottleneck in Human Diseases. *Molecules* **2020**, *25*, 1778.
- (5) Janaswami, P. M.; Birkenmeier, E. H.; Cook, S. A.; Rowe, L. B.; Bronson, R. T.; Davison, M. T. Identification and genetic mapping of a new polycystic kidney disease on mouse chromosome 8. *Genomics* **1997**, *40*, 101–107.
- (6) Upadhyay, P.; Birkenmeier, E. H.; Birkenmeier, C. S.; Barker, J. E. Mutations in a NIMA-related kinase gene cause pleiotropic effects including a progressive polycystic kidney disease in mice. *Proc. Natl. Acad. Sci. U. S. A.* **2000**, *97*, 217–221.
- (7) Chebib, F. T.; Torres, V. E. Recent advances in the management of autosomal dominant polycystic kidney disease. *Clin. J. Am. Soc. Nephrol.* **2018**, *13*, 1765–1776.
- (8) Surpili, M. J.; Delben, T. M.; Kobarg, J. Identification of proteins that interact with the central coiled-coil region of the human protein kinase NEK1. *Biochemistry* **2003**, *42*, 15369–15376.
- (9) Chen, Y.; Chiang, H.-C.; Litchfield, P.; Pena, M.; Juang, C.; Riley, D. J. Expression of Nek1 during kidney development and cyst formation in multiple nephron segments in the Nek1-deficient kat2J mouse model of polycystic kidney disease. *J. Biomed. Sci.* **2014**, *21*, 63–65.
- (10) Thiel, C.; Kessler, K.; Giessler, A.; Dimmler, A.; Shalev, S. A.; von der Haar, S.; Zenker, M.; Zahnleiter, D.; Stöss, H.; Beinder, E.; Abou Jamra, R.; Ekici, A. B.; Schröder-Kreß, N.; Aigner, T.; Kirchner, T.; Reis, A.; Brandstätter, J. H.; Rauch, A. NEK1 mutations cause short-rib polydactyly syndrome type Majewski. *Am. J. Hum. Genet.* **2011**, *88*, 106–114.
- (11) Monroe, G. R.; Kappen, I. F. P. M.; Stokman, M. F.; Terhal, P. A.; van den Boogaard, M.-J. H.; Savelberg, S. M. C.; van der Veken, L. T.; van Es, R. J. J.; Lens, S. M.; Hengeveld, R. C.; Creton, M. A.; Janssen, N. G.; Mink van der Molen, A. B.; Ebbeling, M. B.; Giles, R. H.; Knoers, N. V.; van Haften, G. Compound heterozygous NEK1 variants in two siblings with oral-facial-digital syndrome type II (Mohr syndrome). *Eur. J. Hum. Genet.* **2016**, *24*, 1752–1760.
- (12) Brenner, D.; Müller, K.; Wieland, T.; Weydt, P.; Böhm, S.; Lulé, D.; Hübers, A.; Neuwirth, C.; Weber, M.; Borck, G.; Wahlqvist, M.; Danzer, K. M.; Volk, A. E.; Meitinger, T.; Strom, T. M.; Otto, M.; Kassubeck, J.; Ludolph, A. C.; Andersen, P. M.; Weishaupt, J. H. NEK1 mutations in familial amyotrophic lateral sclerosis. *Brain* **2016**, *139*, No. e28.
- (13) Higelin, J.; Catanese, A.; Semelink-Sedlacek, L. L.; Oeztuerk, S.; Lutz, A.-K.; Bausinger, J.; Barbi, G.; Speit, G.; Andersen, P. M.; Ludolph, A. C.; Demestre, M.; Boeckers, T. M. NEK1 loss-of-function mutation induces DNA damage accumulation in ALS patient-derived motoneurons. *Stem Cell Res.* **2018**, *30*, 150–162.
- (14) Fry, A. M.; O'Regan, L.; Sabir, S. R.; Bayliss, R. Cell cycle regulation by the NEK family of protein kinases. *J. Cell Sci.* **2012**, *125*, 4423–4433.
- (15) Polci, R.; Peng, A.; Chen, P.-L.; Riley, D. J.; Chen, Y. NIMA-related protein kinase 1 is involved early in the ionizing radiation-induced DNA damage response. *Cancer Res.* **2004**, *64*, 8800–8803.
- (16) Grudzenski, S.; Raths, A.; Conrad, S.; Rube, C. E.; Löbrich, M. Inducible response required for repair of low-dose radiation damage in human fibroblasts. *Proc. Natl. Acad. Sci. U. S. A.* **2010**, *107*, 14205–14210.
- (17) Spies, J.; Waizenegger, A.; Barton, O.; Surder, M.; Wright, W. D.; Heyer, W.-D.; Löbrich, M. Nek1 regulates Rad54 to orchestrate homologous recombination and replication fork stability. *Mol. Cell* **2016**, *62*, 903–917.
- (18) Chen, Y.; Chen, P.-L.; Chen, C.-F.; Jiang, X.; Riley, D. J. Never-in-mitosis related kinase 1 functions in DNA damage response and checkpoint control. *Cell Cycle* **2008**, *7*, 3194–3201.
- (19) Chen, Y.; Chen, C.-F.; Riley, D. J.; Chen, P.-L. Nek1 kinase functions in DNA damage response and checkpoint control through a pathway independent of ATM and ATR. *Cell Cycle* **2011**, *10*, 655–663.
- (20) Chen, Y.; Craigen, W. J.; Riley, D. J. Nek1 regulates cell death and mitochondrial membrane permeability through phosphorylation of VDAC1. *Cell Cycle* **2009**, *8*, 257–267.
- (21) Chen, Y.; Gaczynska, M.; Osmulski, P.; Polci, R.; Riley, D. J. Phosphorylation by Nek1 regulates opening and closing of voltage dependent anion channel 1. *Biochem. Biophys. Res. Commun.* **2010**, *394*, 798–803.
- (22) Singh, V.; Khalil, M. I.; De Benedetti, A. The TLK1/Nek1 axis contributes to mitochondrial integrity and apoptosis prevention via phosphorylation of VDAC1. *Cell Cycle* **2020**, *19*, 363–375.
- (23) Singh, V.; Jaiswal, P. K.; Ghosh, L.; Koul, H. K.; Yu, X.; De Benedetti, A. The TLK1-Nek1 axis promotes prostate cancer progression. *Cancer Lett.* **2019**, *453*, 131–141.
- (24) Singh, V.; Jaiswal, P. K.; Ghosh, L.; Koul, H. K.; Yu, X.; De Benedetti, A. Targeting the TLK1/NEK1 DDR axis with Thioridazine suppresses outgrowth of androgen independent prostate tumors. *Int. J. Cancer* **2019**, *145*, 1055–1067.
- (25) Singh, V.; Connelly, Z. M.; Shen, X.; De Benedetti, A. Identification of the proteome complement of human TLK1 reveals it binds and phosphorylates NEK1 regulating its activity. *Cell Cycle* **2017**, *16*, 915–926.
- (26) Melo-Hanchuk, T. D.; Martins, M. B.; Cunha, L. L.; Soares, F. A.; Ward, L. S.; Vassallo, J.; Kobarg, J. Expression of the NEK family in normal and cancer tissue: an immunohistochemical study. *BMC Cancer* **2020**, *20*, 23.
- (27) Zhu, J.; Cai, Y.; Liu, P.; Zhao, W. Frequent Nek1 overexpression in human gliomas. *Biochem. Biophys. Res. Commun.* **2016**, *476*, 522–527.
- (28) Chen, Y.; Chen, C.-F.; Polci, R.; Wei, R.; Riley, D. J.; Chen, P.-L. Increased Nek1 expression in renal cell carcinoma cells is associated with decreased sensitivity to DNA-damaging treatment. *Oncotarget* **2014**, *5*, 4283–4294.
- (29) Wei, R. L.; Chen, Y. Overexpression of Nek1 in renal cell carcinoma protects against cell death from ionizing radiation. *Int. J. Radiat. Oncol., Biol., Phys.* **2011**, *81*, S712.
- (30) Freund, I.; Hehlhans, S.; Martin, D.; Ensminger, M.; Fokas, E.; Rödel, C.; Löbrich, M.; Rödel, F. Fractionation-dependent radiosensitization by molecular targeting of Nek1. *Cells* **2020**, *9*, 1235.
- (31) Chen, Y. NEK1 protein kinase as a target for anticancer therapeutics. *Chemotherapy: Open Access* **2012**, *1*, e118.
- (32) Moraes, E.; Meirelles, G.; Honorato, R.; de Souza, T.; de Souza, E.; Murakami, M.; de Oliveira, P.; Kobarg, J. Kinase inhibitor profile for human nek1, nek6, and nek7 and analysis of the structural basis for inhibitor specificity. *Molecules* **2015**, *20*, 1176–1191.
- (33) Melo-Hanchuk, T. D.; Slepicka, P. F.; Meirelles, G. V.; Basei, F. L.; Lovato, D. V.; Granato, D. C.; Pauletti, B. A.; Domingues, R. R.; Leme, A. F. P.; Pelegrini, A. L.; Lenz, G.; Knapp, S.; Elkins, J. M.; Kobarg, J. NEK1 kinase domain structure and its dynamic protein interactome after exposure to Cisplatin. *Sci. Rep.* **2017**, *7*, 5445.
- (34) Wells, C. I.; Kapadia, N. R.; Counago, R. M.; Drewry, D. H. In depth analysis of kinase cross screening data to identify chemical starting points for inhibition of the Nek family of kinases. *MedChemComm* **2018**, *9*, 44–66.
- (35) De Donato, M.; Righino, B.; Filippetti, F.; Battaglia, A.; Petrillo, M.; Pirolli, D.; Scambia, G.; De Rosa, M. C.; Gallo, D. Identification and antitumor activity of a novel inhibitor of the NIMA-related kinase NEK6. *Sci. Rep.* **2018**, *8*, 16047.
- (36) Drewry, D. H.; Wells, C. I.; Andrews, D. M.; Angell, R.; Al-Ali, H.; Axtman, A. D.; Capuzzi, S. J.; Elkins, J. M.; Etmayer, P.; Frederiksen, M.; Gileadi, O.; Gray, N.; Hooper, A.; Knapp, S.; Laufer, S.; Luecking, U.; Michaelides, M.; Müller, S.; Muratov, E.; Denny, R. A.; Saikatendu, K. S.; Treiber, D. K.; Zuercher, W. J.; Willson, T. M. Progress towards a public chemogenomic set for protein kinases and a call for contributions. *PLoS One* **2017**, *12*, No. e0181585.
- (37) Seefeld, M. A.; Rouse, M. B.; McNulty, K. C.; Sun, L.; Wang, J.; Yamashita, D. S.; Luengo, J. I.; Zhang, S.; Minthorn, E. A.; Concha, N. O.; Heerding, D. A. Discovery of 5-pyrrolopyridinyl-2-thiophenecar-

Q

<https://dx.doi.org/10.1021/acs.jmedchem.0c02118>
J. Med. Chem. XXXX, XXX, XXX–XXX

boxamides as potent AKT kinase inhibitors. *Bioorg. Med. Chem. Lett.* **2009**, *19*, 2244–2248.

(38) Liddle, J.; Bamborough, P.; Barker, M. D.; Campos, S.; Cousins, R. P. C.; Cutler, G. J.; Hobbs, H.; Holmes, D. S.; Ioannou, C.; Mellor, G. W.; Morse, M. A.; Payne, J. J.; Pritchard, J. M.; Smith, K. J.; Tape, D. T.; Whitworth, C.; Williamson, R. A. 4-Phenyl-7-azaindoles as potent and selective IKK2 inhibitors. *Bioorg. Med. Chem. Lett.* **2009**, *19*, 2504–2508.

(39) Gehrig, J.; Pandey, G.; Westhoff, J. H. Zebrafish as a model for drug screening in genetic kidney diseases. *Frontiers in Pediatrics* **2018**, *6*, 183.

(40) Bamborough, P.; Barker, M. D.; Campos, S. A.; Cousins, R. P. C.; Faulder, P.; Hobbs, H.; Holmes, D. S.; Johnston, M. J.; Liddle, J.; Payne, J. J.; Pritchard, J. M.; Whitworth, C. Pyrrolo[2,3-b]pyridin-4-yl-benzenesulfonamide compounds as IKK2 inhibitors and their preparation, pharmaceutical compositions and use in the treatment of diseases. WO2008034860A1, 2008.

(41) McKennon, M. J.; Meyers, A. I.; Drauz, K.; Schwarm, M. A convenient reduction of amino acids and their derivatives. *J. Org. Chem.* **1993**, *58*, 3568–3571.

(42) Chong, H.-S.; Song, H. A.; Dadwal, M.; Sun, X.; Sin, I.; Chen, Y. Efficient synthesis of functionalized aziridinium salts. *J. Org. Chem.* **2010**, *75*, 219–221.

(43) Westwood, L.; Cheary, D.-M.; Baxter, J. E.; Richards, M. W.; van Montfort, R. L. M.; Fry, A. M.; Bayliss, R. Insights into the conformational variability and regulation of human Nek2 kinase. *J. Mol. Biol.* **2009**, *386*, 476–485.

(44) Haq, T.; Richards, M. W.; Burgess, S. G.; Gallego, P.; Yeoh, S.; O'Regan, L.; Reverter, D.; Roig, J.; Fry, A. M.; Bayliss, R. Mechanistic basis of Nek7 activation through Nek9 binding and induced dimerization. *Nat. Commun.* **2015**, *6*, 8771.

(45) Irie, T.; Sawa, M. 7-Azaindole: A versatile scaffold for developing kinase inhibitors. *Chem. Pharm. Bull.* **2018**, *66*, 29–36.

(46) Juchum, M.; Günther, M.; Döring, E.; Sievers-Engler, A.; Lämmerhofer, M.; Laufer, S. Trisubstituted imidazoles with a rigidized hinge binding motif act as single digit nM inhibitors of clinically relevant EGFR L858R/T790M and L858R/T790M/C797S mutants: An example of target hopping. *J. Med. Chem.* **2017**, *60*, 4636–4656.

(47) Ismer, J.; Rose, A. S.; Tiemann, J. K. S.; Goede, A.; Preissner, R.; Hildebrand, P. W. SL2: an interactive webtool for modeling of missing segments in proteins. *Nucleic Acids Res.* **2016**, *44*, W390–W394.

(48) Coxon, C. R.; Wong, C.; Bayliss, R.; Boxall, K.; Carr, K. H.; Fry, A. M.; Hardcastle, I. R.; Matheson, C. J.; Newell, D. R.; Sivaprakasam, M.; Thomas, H.; Turner, D.; Yeoh, S.; Wang, L. Z.; Griffin, R. J.; Golding, B. T.; Cano, C. Structure-guided design of purine-based probes for selective Nek2 inhibition. *Oncotarget* **2017**, *8*, 19089–19124.

(49) Roskoski, R. Classification of small molecule protein kinase inhibitors based upon the structures of their drug-enzyme complexes. *Pharmacol. Res.* **2016**, *103*, 26–48.

(50) Smyth, L. A.; Collins, I. Measuring and interpreting the selectivity of protein kinase inhibitors. *Journal of Chemical Biology* **2009**, *2*, 131–151.

(51) Outtandy, P.; Russell, C.; Kleta, R.; Bockenbauer, D. Zebrafish as a model for kidney function and disease. *Pediatr. Nephrol.* **2019**, *34*, 751–762.

(52) Wlodarchak, N.; Tariq, R.; Striker, R. Comparative analysis of the human and zebrafish kinomes: focus on the development of kinase inhibitors. *Trends Cell Mol. Biol.* **2015**, *10*, 49–75.

(53) Knight, Z. A.; Shokat, K. M. Chemical Genetics: Where Genetics and Pharmacology Meet. *Cell* **2007**, *128*, 425–430.

(54) Shalom, O.; Shalva, N.; Altschuler, Y.; Motro, B. The mammalian Nek1 kinase is involved in primary cilium formation. *FEBS Lett.* **2008**, *582*, 1465–1470.

(55) Westhoff, J. H.; Giselbrecht, S.; Schmidts, M.; Schindler, S.; Beales, P. L.; Tönshoff, B.; Liebel, U.; Gehrig, J. Development of an

automated imaging pipeline for the analysis of the zebrafish larval kidney. *PLoS One* **2013**, *8*, No. e82137.

(56) Sander, V.; Patke, S.; Sahu, S.; Teoh, C. L.; Peng, Z.; Chang, Y.-T.; Davidson, A. J. The small molecule probe PT-Yellow labels the renal proximal tubules in zebrafish. *Chem. Commun.* **2015**, *51*, 395–398.

(57) Christou-Savina, S.; Beales, P. L.; Osborn, D. P. S. Evaluation of Zebrafish Kidney Function Using a Fluorescent Clearance Assay. *JoVE (Journal of Visualized Experiments)* **2015**, No. e52540.

(58) Park, E. Y.; Seo, M. J.; Park, J. H. Effects of specific genes activating RAGE on polycystic kidney disease. *Am. J. Nephrol.* **2010**, *32*, 169–178.

(59) Booiij, T. H.; Bange, H.; Leonhard, W. N.; Yan, K.; Fokkelman, M.; Kunnen, S. J.; Dauwerse, J. G.; Qin, Y.; van de Water, B.; van Westen, G. J. P.; Peters, D. J. M.; Price, L. S. High-throughput phenotypic screening of kinase inhibitors to identify drug targets for polycystic kidney disease. *SLAS Discov* **2017**, *22*, 974–984.

(60) Correa, R. G.; Matsui, T.; Tergaonkar, V.; Rodriguez-Esteban, C.; Izpisua-Belmonte, J. C.; Verma, I. M. Zebrafish IκB Kinase 1 Negatively Regulates NF-κB Activity. *Curr. Biol.* **2005**, *15*, 1291–1295.

(61) Li, X. Epigenetics and cell cycle regulation in cystogenesis. *Cell. Signalling* **2020**, *68*, 109509.

(62) Saigusa, T.; Bell, P. D. Molecular pathways and therapies in autosomal-dominant polycystic kidney disease. *Physiology* **2015**, *30*, 195–207.

(63) Song, X.; Di Giovanni, V.; He, N.; Wang, K.; Ingram, A.; Rosenblum, N. D.; Pei, Y. Systems biology of autosomal dominant polycystic kidney disease (ADPKD): computational identification of gene expression pathways and integrated regulatory networks. *Hum. Mol. Genet.* **2009**, *18*, 2328–2343.

(64) Baell, J. B.; Holloway, G. A. New substructure filters for removal of pan assay interference compounds (PAINS) from screening libraries and for their exclusion in bioassays. *J. Med. Chem.* **2010**, *53*, 2719–2740.

(65) Haldi, M.; Harden, M.; D'Amico, L.; DeLise, A.; Seng, W. L. Developmental Toxicity Assessment in Zebrafish. In *Zebrafish: Methods for Assessing Drug Safety and Toxicity*, McGrath, P., Ed.; John Wiley & Sons, Inc.: Hoboken, NJ, 2012; Chapter 2, pp 15–17.

(66) Edelstein, A. D.; Tsuchida, M. A.; Amodaj, N.; Pinkard, H.; Vale, R. D.; Stuurman, N. Advanced methods of microscope control using μManager software. *Journal of Biological Methods* **2014**, No. e10.

R

<https://dx.doi.org/10.1021/acs.jmedchem.0c02118>
J. Med. Chem. XXXX, XXX, XXX–XXX

SUPPORTING INFORMATION

Illuminating a Dark Kinase: Structure-guided Design, Synthesis and Evaluation of a potent Nek1 Inhibitor and its Effects on the Embryonic Zebrafish Pronephros

Georg Baumann[†], Tobias Meckel[†], Kevin Böhm[†], Yung-Hsin Shih[†], Mirco Dickhaut[†], Torben Reichardt[†], Johannes Pilakowski[†], Ulrich Pehl[‡] and Boris Schmidt*[†]*

[†]Clemens Schöpf–Institute of Organic Chemistry and Biochemistry, Technische Universität
Darmstadt, 64287 Darmstadt, Germany

[‡]Merck Healthcare KGaA, Biopharma R&D, Discovery and Development Technologies, 64293
Darmstadt, Germany

*To whom correspondence should be addressed:

Phone: +496151-1623745.

E-Mail: schmidt_boris@t-online.de; georg.baumann@stud.tu-darmstadt.de

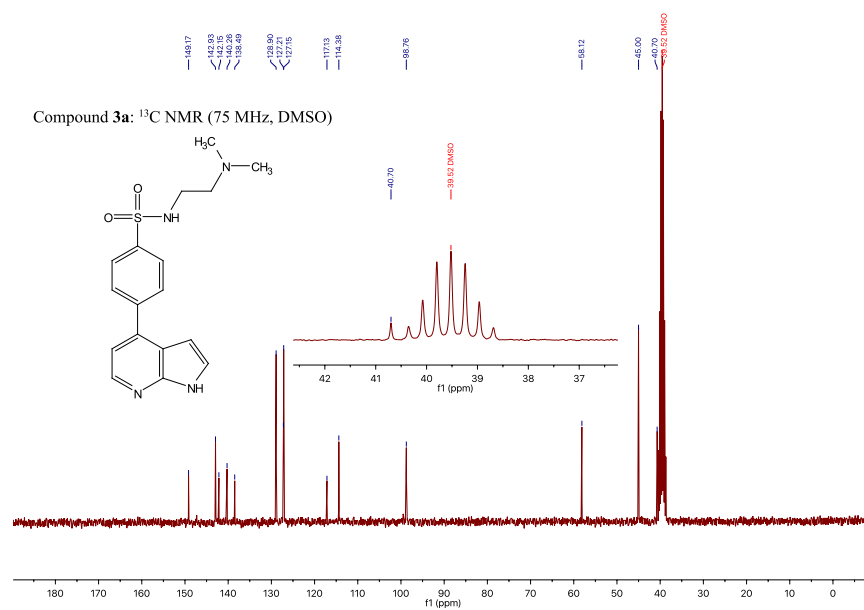
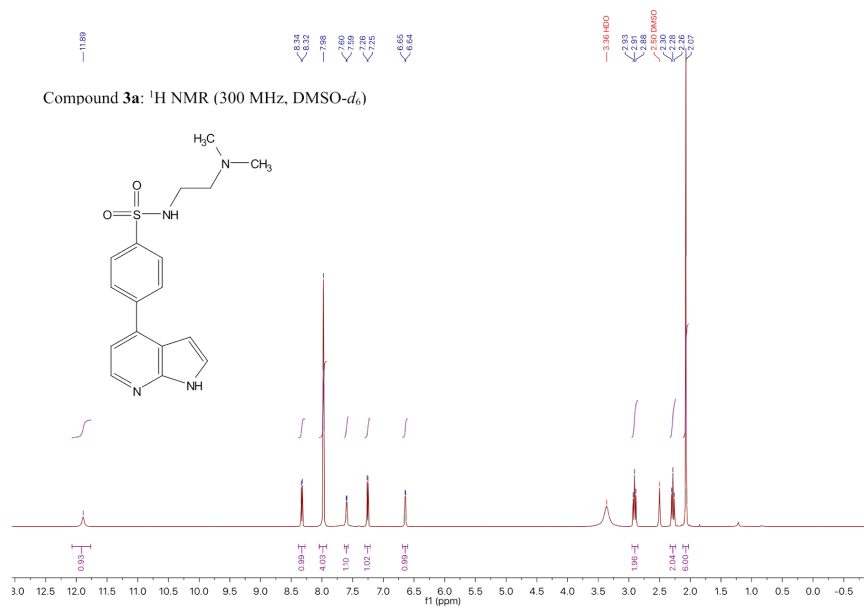
S1

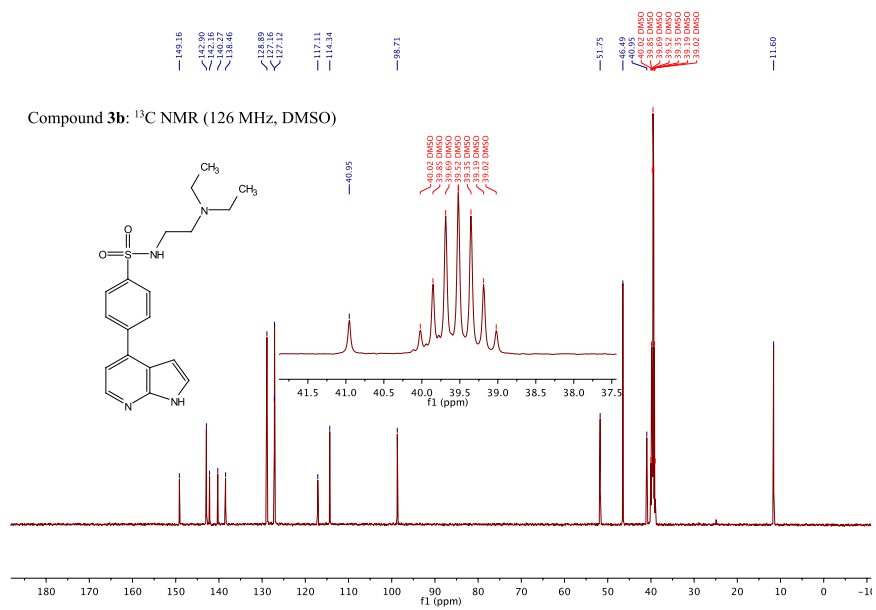
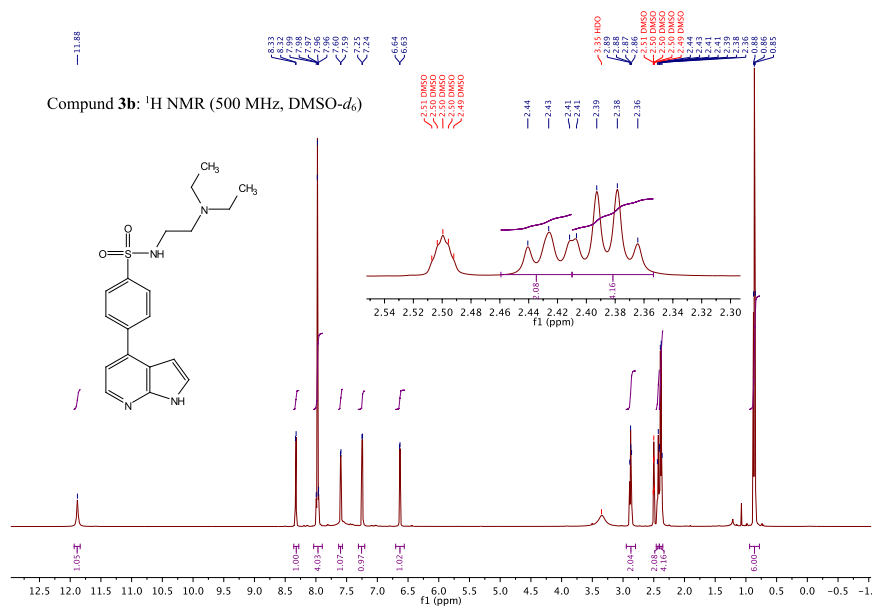
Table of contents

Comparison of Nek1 kinase domain crystal structures	S3
Molecular docking of 3a into the Nek1 ATP-binding site	S4-S6
Molecular docking of 10f into the Nek1 ATP-binding site	S7-8
Nek1/Nek2 Homology Model	S9
Comparison of the human and zebrafish Nek1 kinase domains	S10-11
Kinase selectivity profile for compound 10f	S12-13
Shake-flask aqueous solubility assay	S14
Caco-2 permeability assay	S14
Zebrafish developmental toxicity assay	S15
Stability-indicating HPLC assay	S15
Preparation of agarose molds in 96-well plates	S16
Fluorescence microscopy images of zebrafish pronephroi	S17-19
NMR data of compounds 3a-k, 7 and 10a-f	S20-39
HPLC traces of compounds 3a-k, 7 and 10a-f	S40-55
IC50 determination for compounds 3a-k, 7 and 10a-f	S56-76

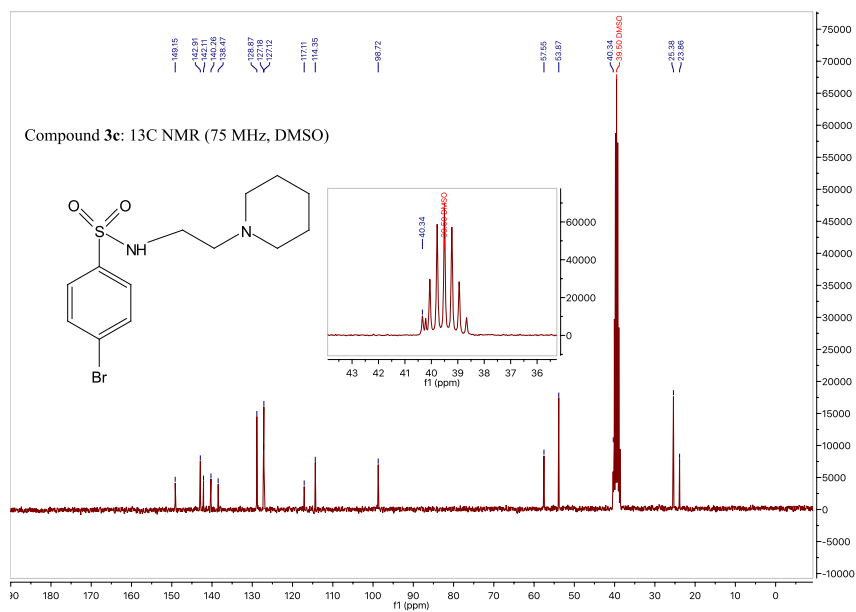
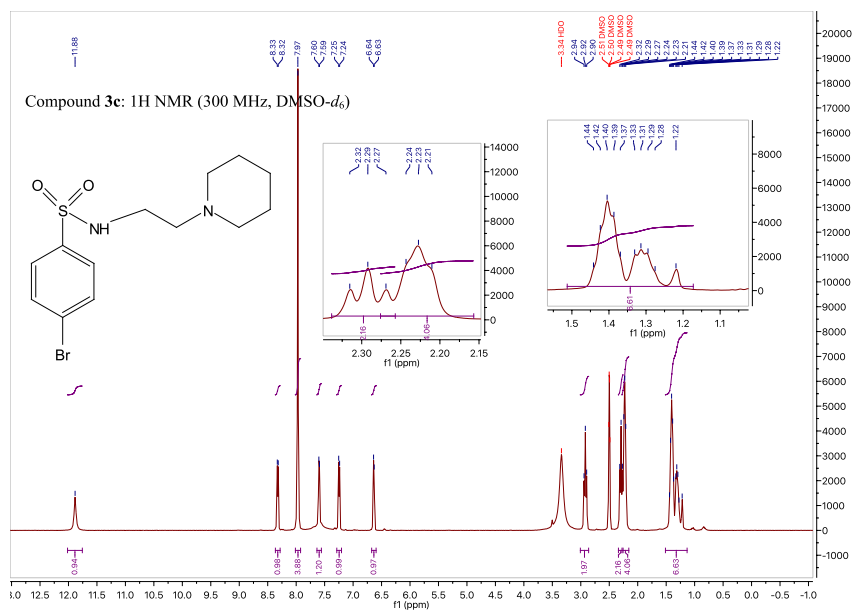
NMR Data of compounds 3a-k, 7 and 10a-f

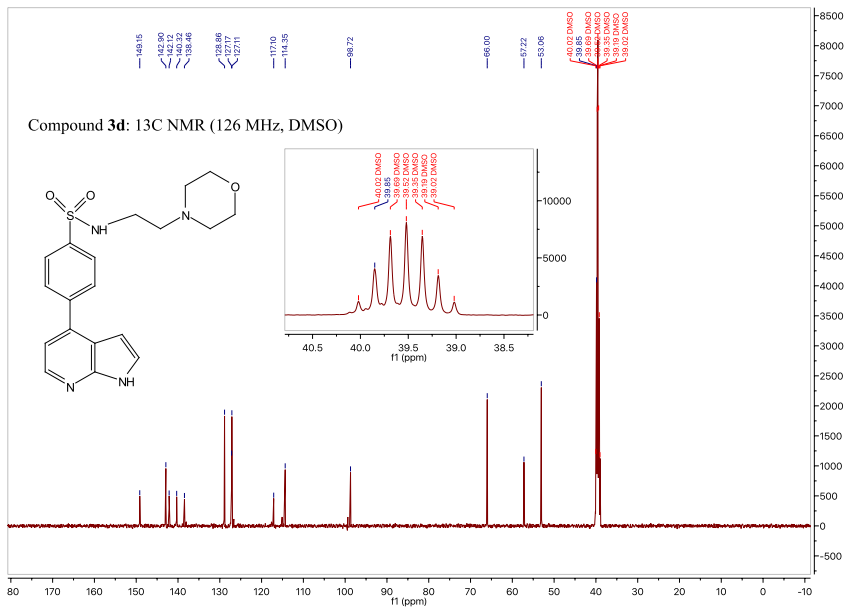
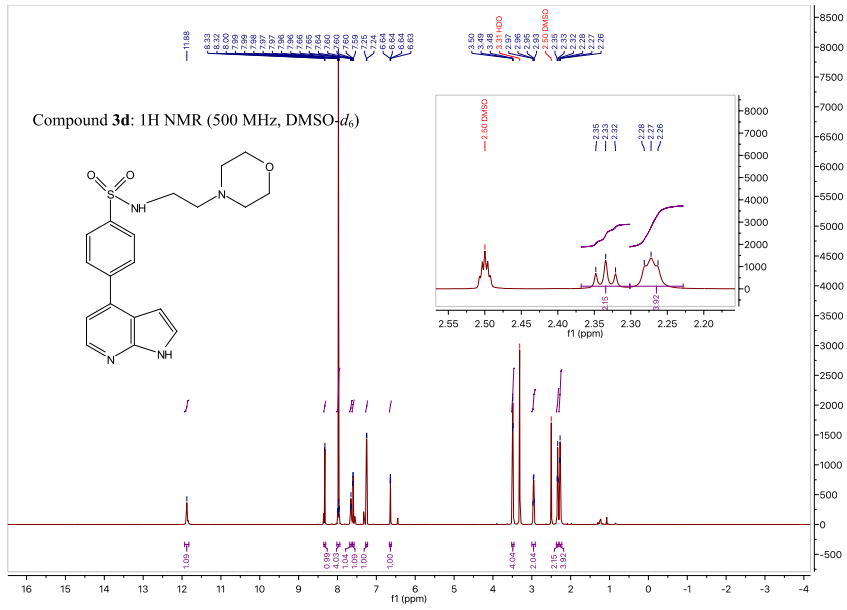
NMR spectra were recorded on a Bruker Avance II (300 MHz for ^1H and 75 MHz for ^{13}C NMR), a Bruker Avance III spectrometer (300 MHz for ^1H and 75 MHz for ^{13}C NMR) or a Bruker DRX 500 (500 MHz for ^1H and 126 MHz for ^{13}C NMR) spectrometer. Chemical shifts are reported as ppm by frequency downfield of TMS. Coupling constants are reported in Hertz (Hz).

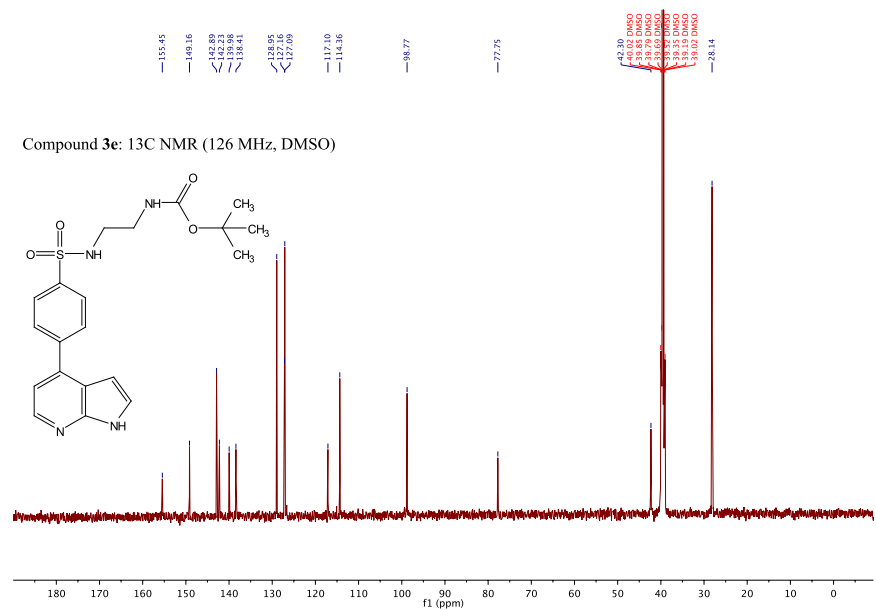
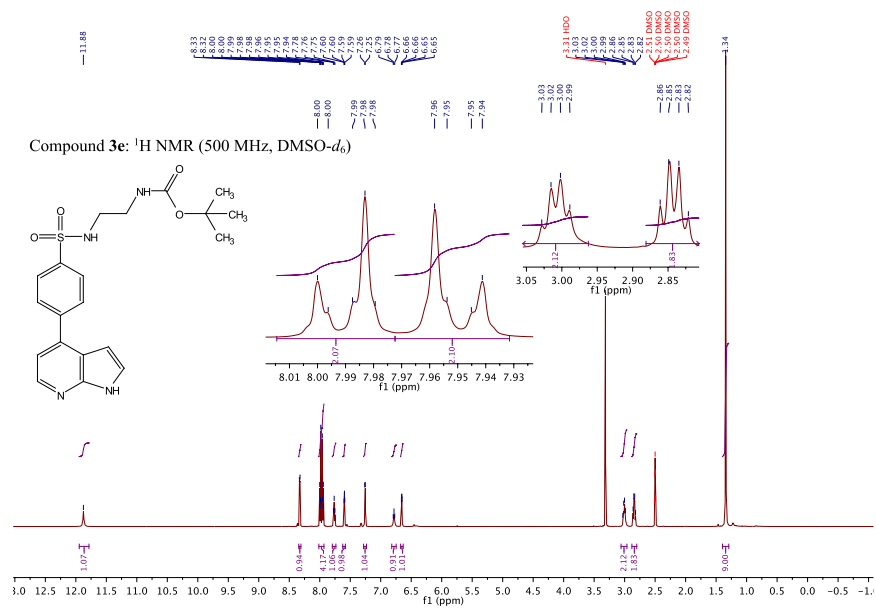




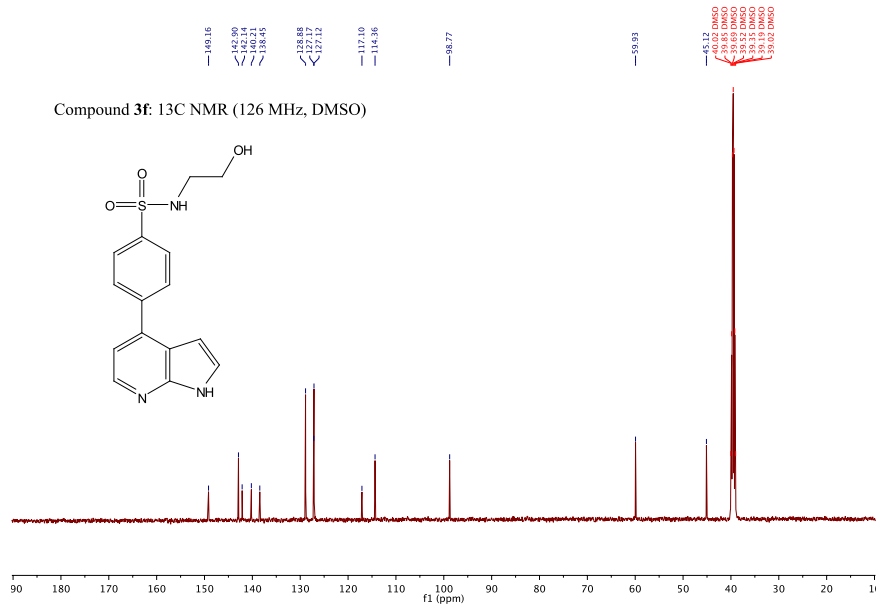
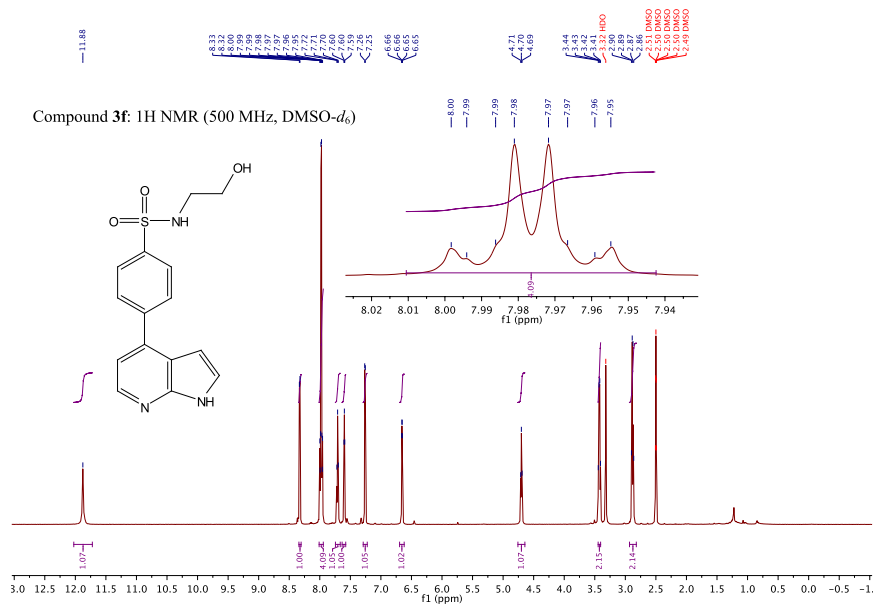
S22



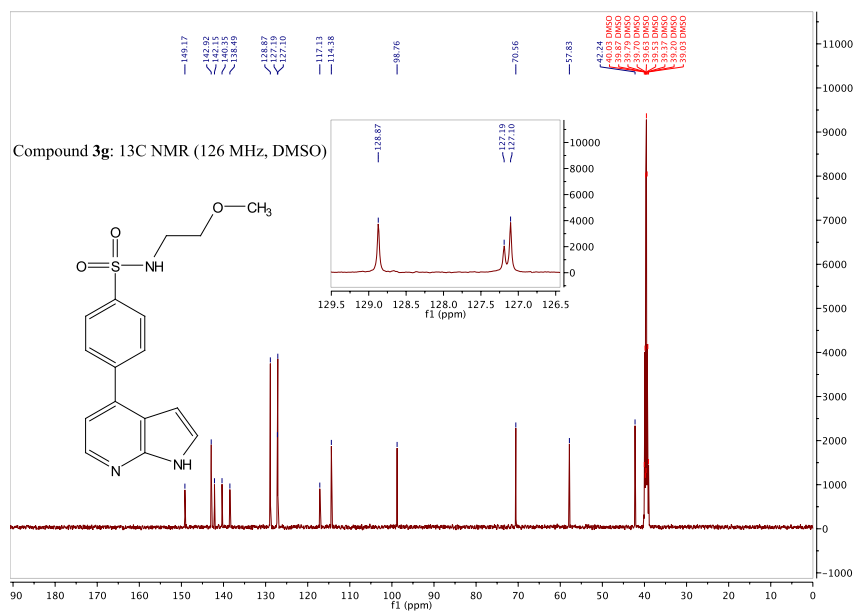
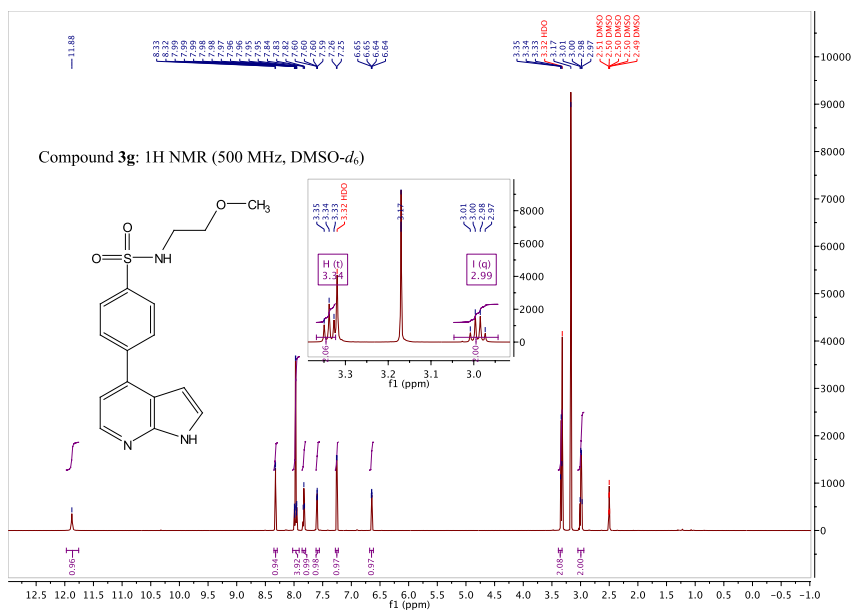


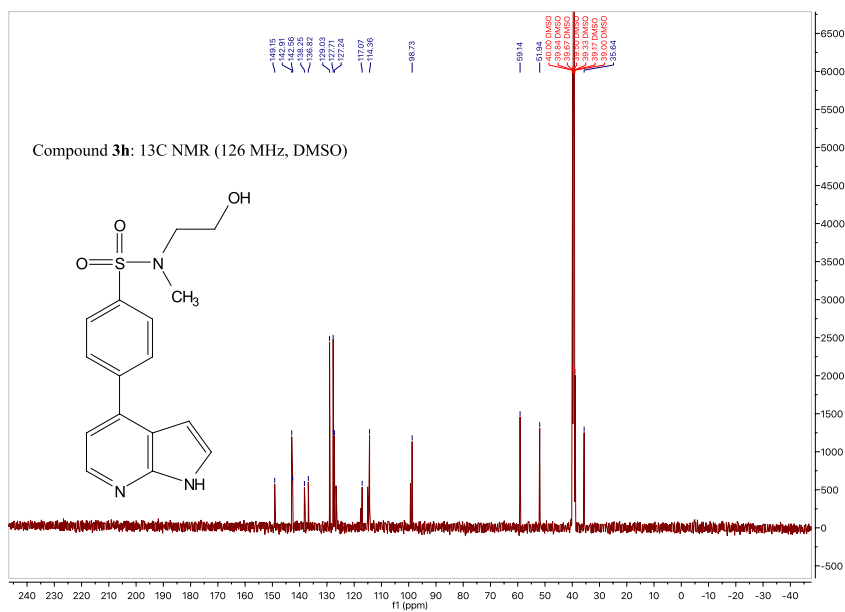
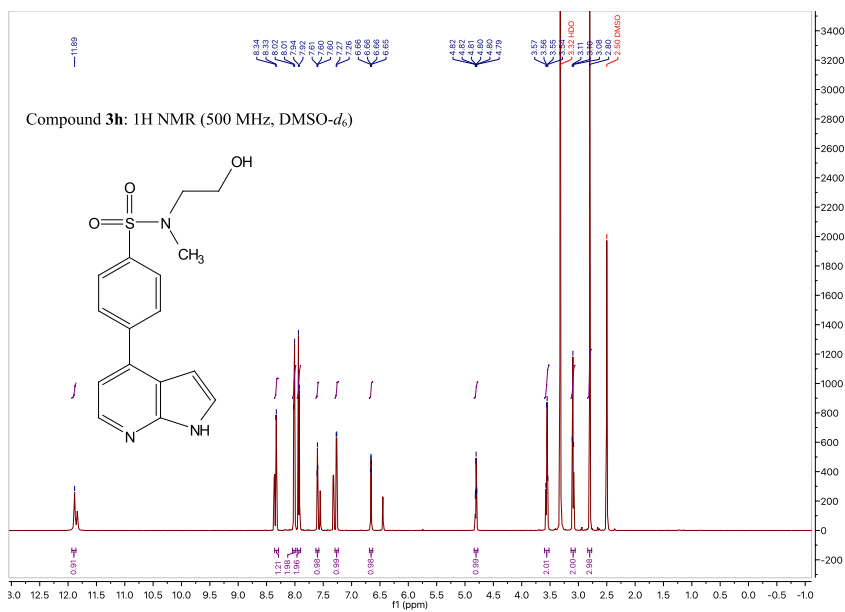


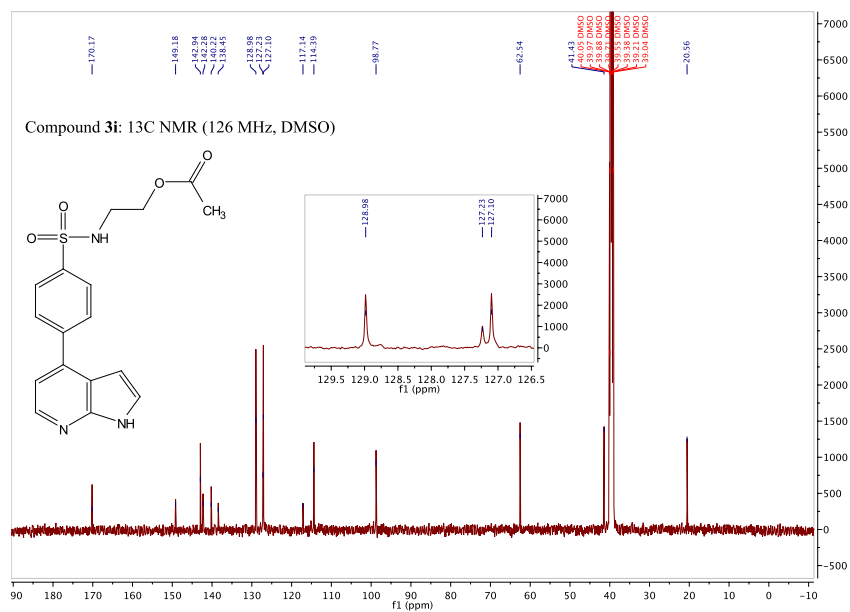
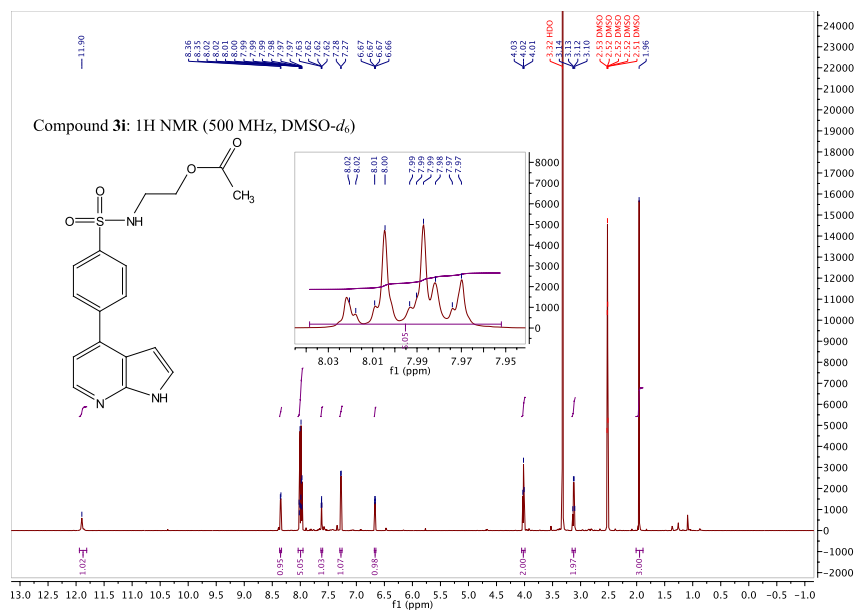
S25

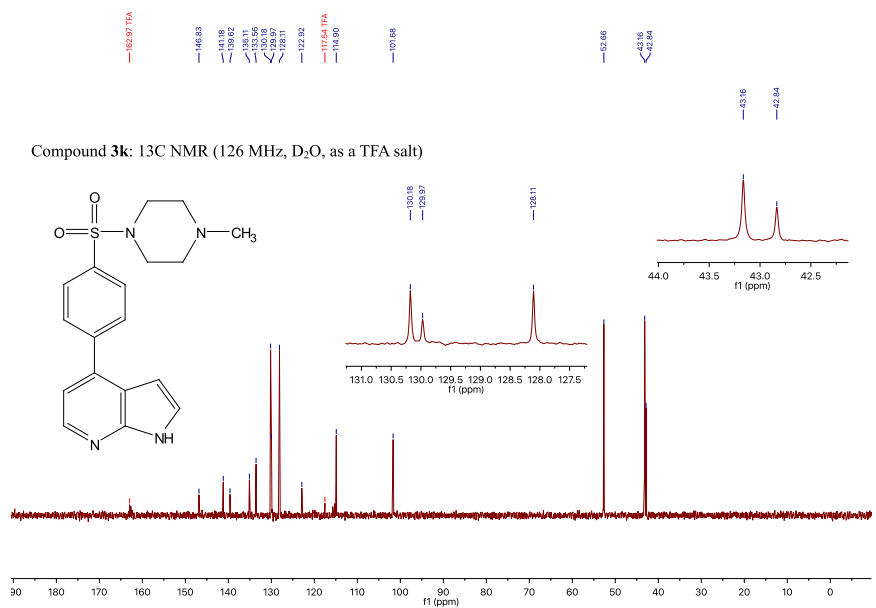
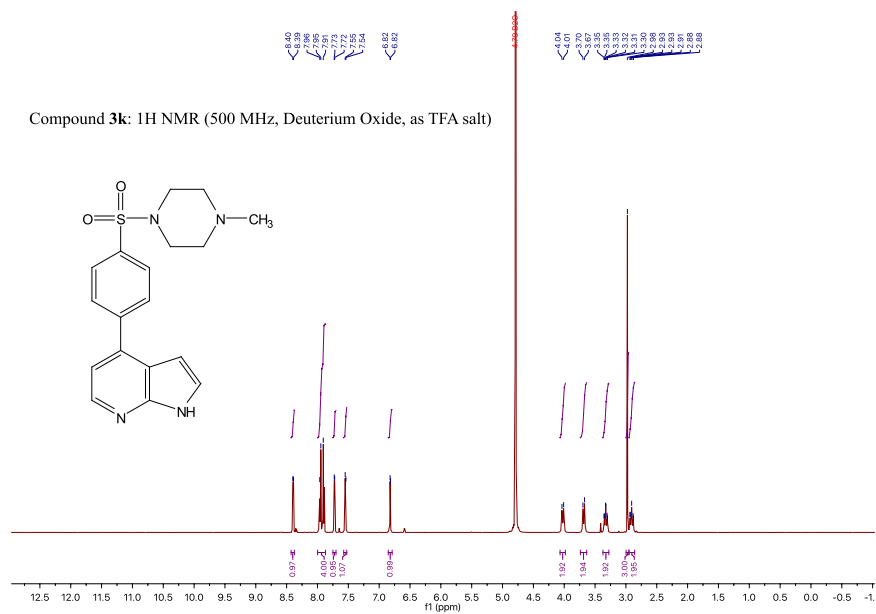


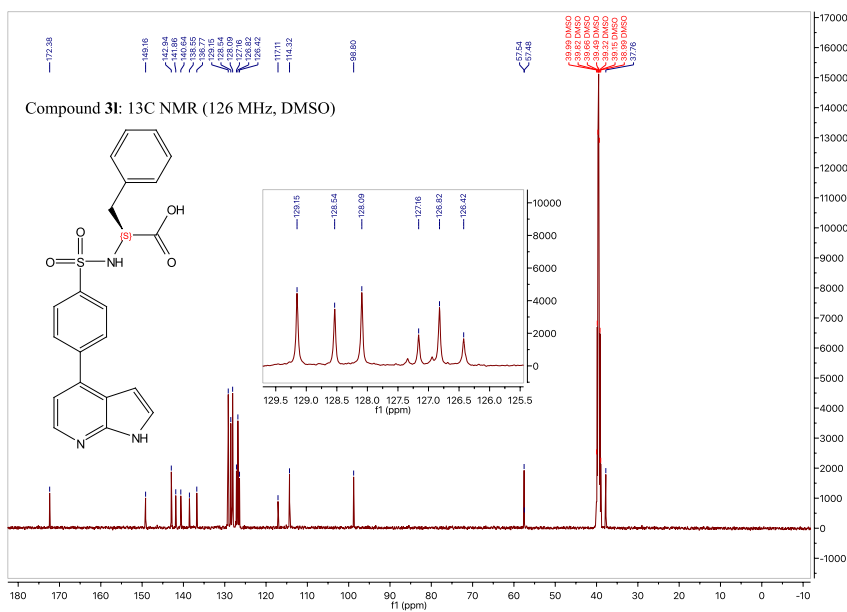
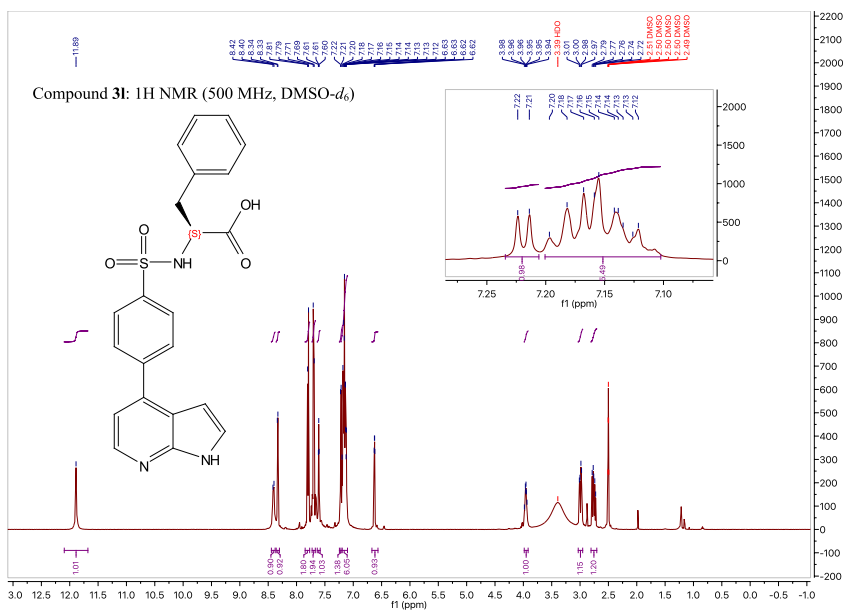
S26



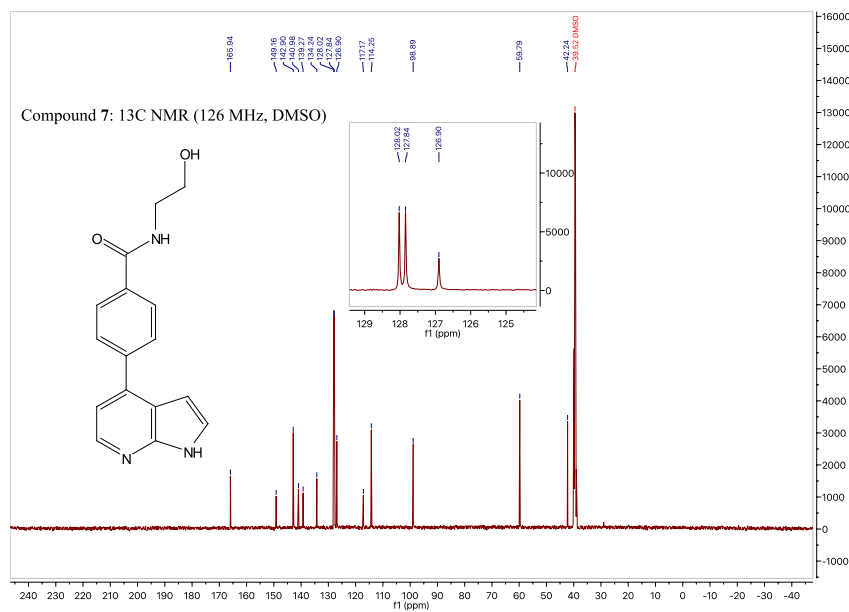
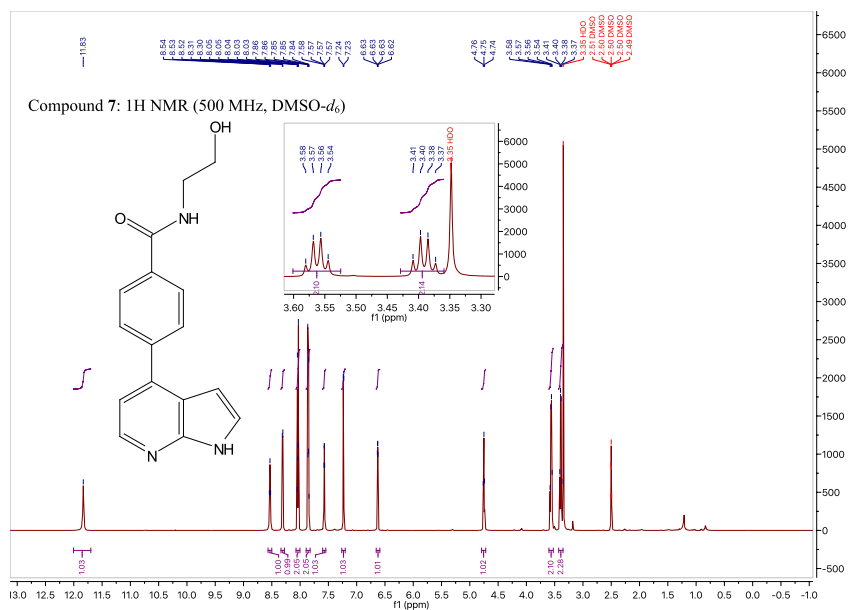


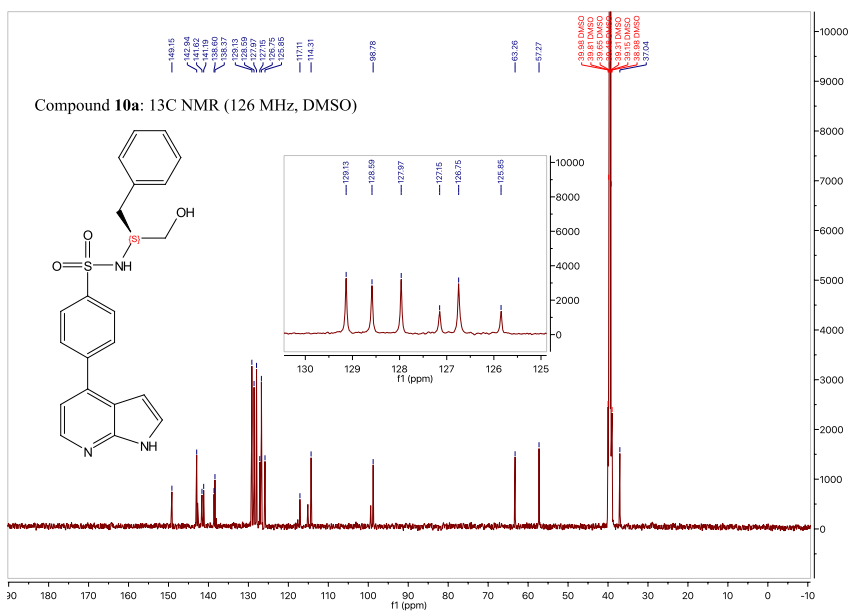
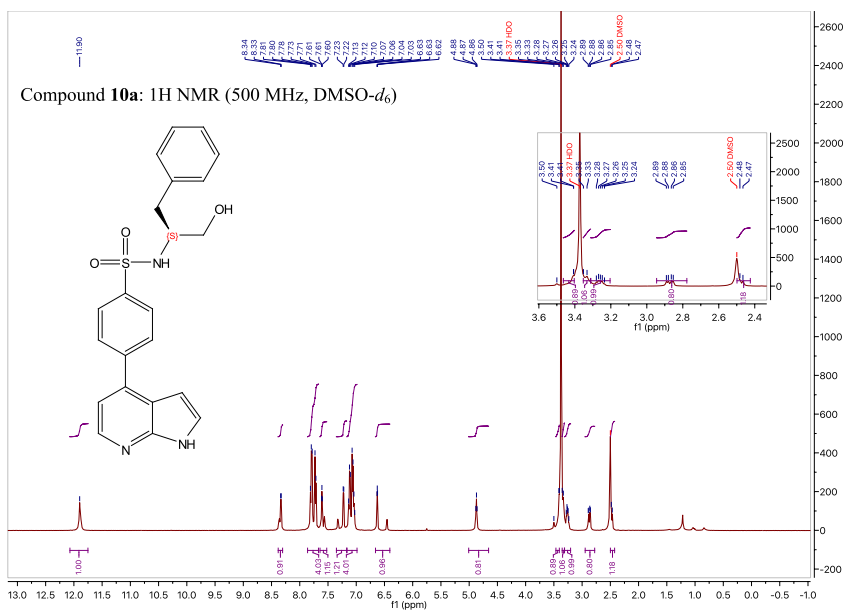


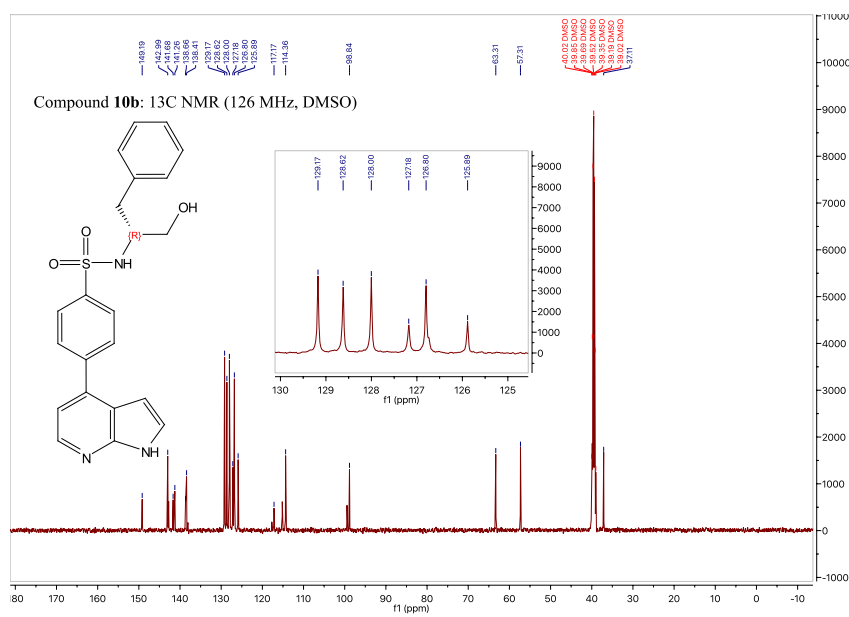
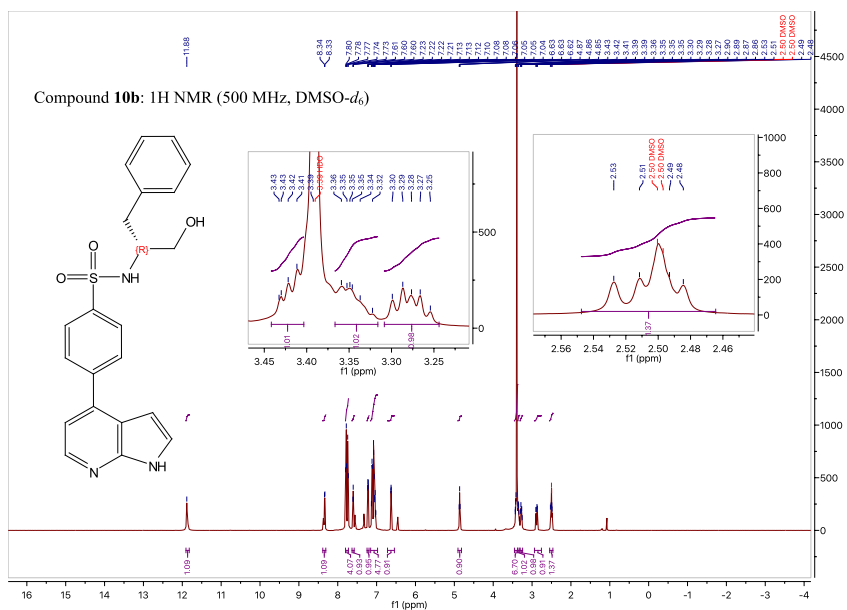


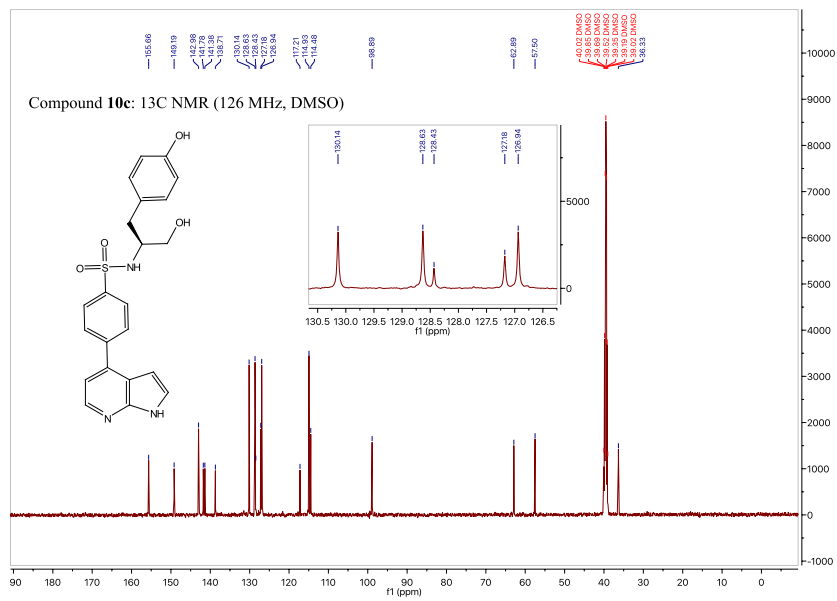
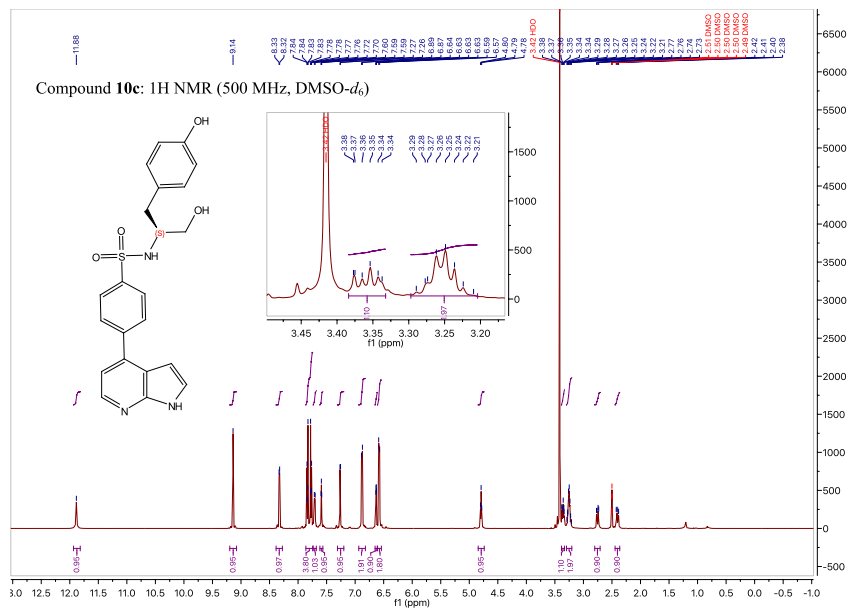


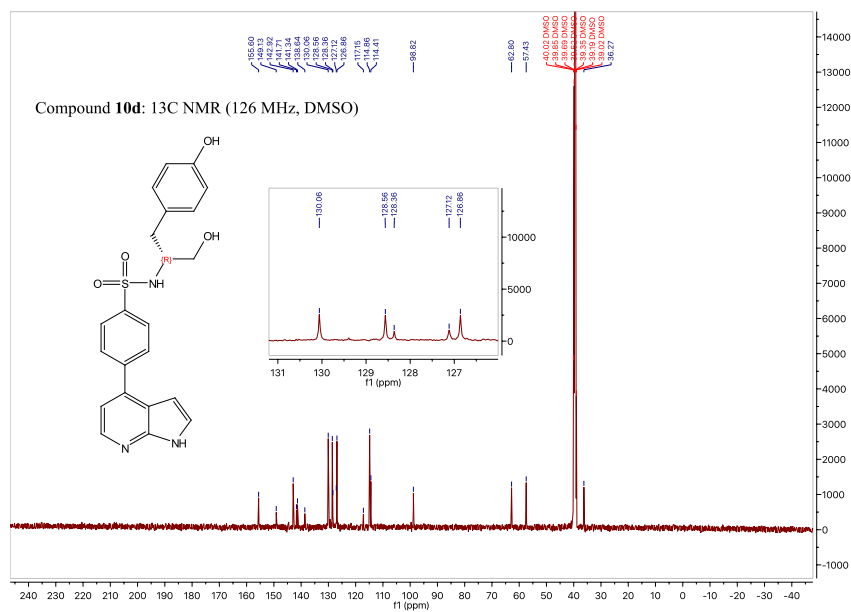
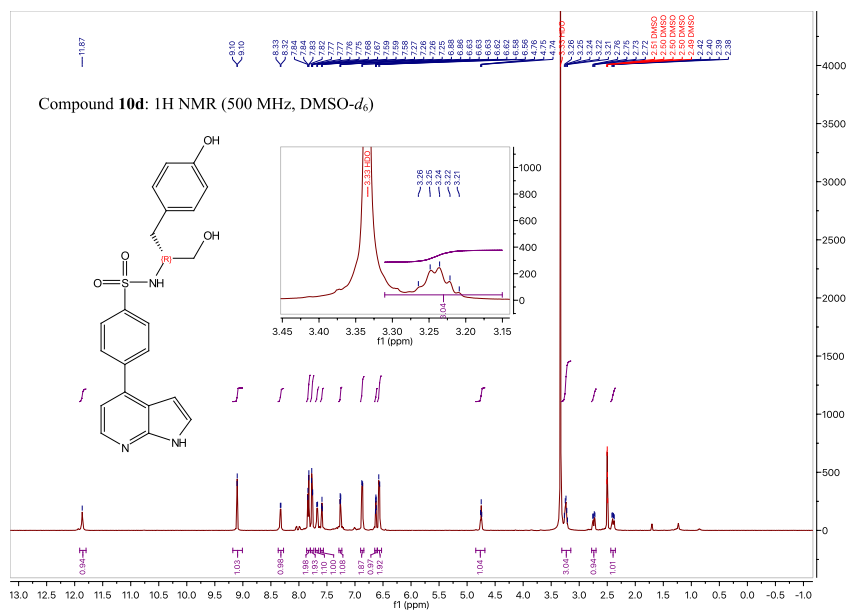
S32

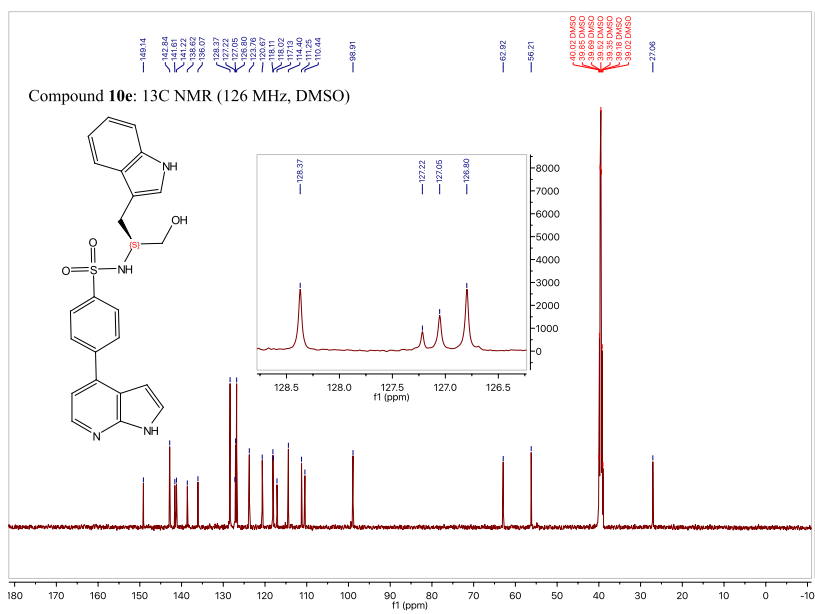
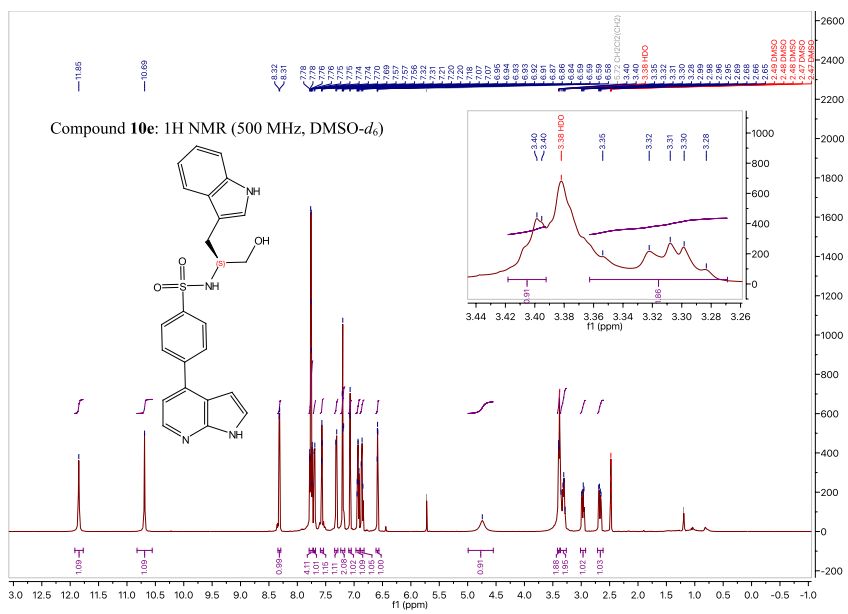










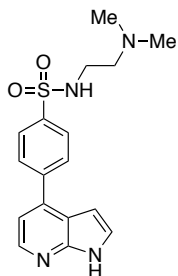


S38

HPLC traces of compounds 3a-k, 7 and 10a-f

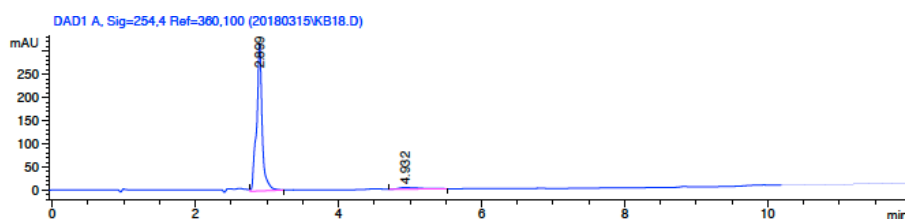
HPLC was carried out on an Agilent 1100 system using a Phenomenex Synergi Polar-RP reversed-phase column (4 μ m particle size, 150 \times 3.0 mm, pore size 80 Å) connected to a variable wavelength detector (VWD) or a Phenomenex Synergi Hydro-RP reversed-phase column (4 μ m particle size, 150 \times 3.0 mm, pore size 80 Å) connected to a diode array detector (DAD). Solvent gradient = 30% A for 1 min, linear gradient to 10% A for 10 min, 10% A for 1 min; solvent A = 0.1% TFA in water; solvent B = acetonitrile; flow rate 1.0 mL/min. All compounds used in biological or biochemical assays had >95% HPLC purity.

Compound 3a

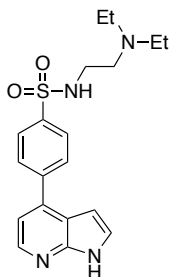


Signal 1: DAD1 A, Sig=254,4 Ref=360,100

Peak #	RetTime [min]	Type	Width [min]	Area [mAU*s]	Height [mAU]	Area %
1	2.899	VB	0.0745	1722.11792	321.50858	95.7960
2	4.932	VB	0.2898	75.57506	3.55808	4.2040

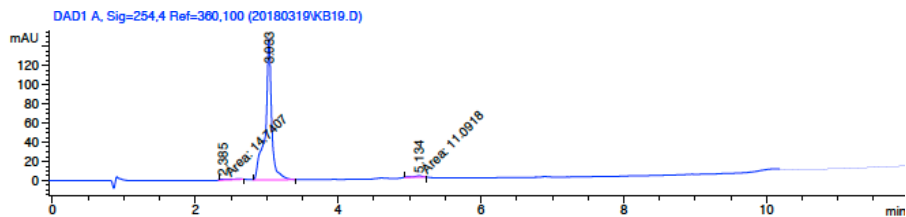


Compound 3b



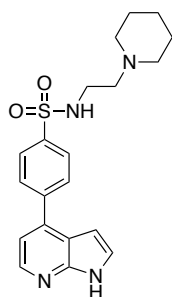
Signal 1: DAD1 A, Sig=254,4 Ref=360,100

Peak #	RetTime [min]	Type	Width [min]	Area [mAU*s]	Height [mAU]	Area %
1	2.385	MM T	0.2138	14.74074	1.14892	1.5436
2	3.033	VB	0.0873	929.13593	147.85735	97.2949
3	5.134	MM	0.1519	11.09181	1.21729	1.1615



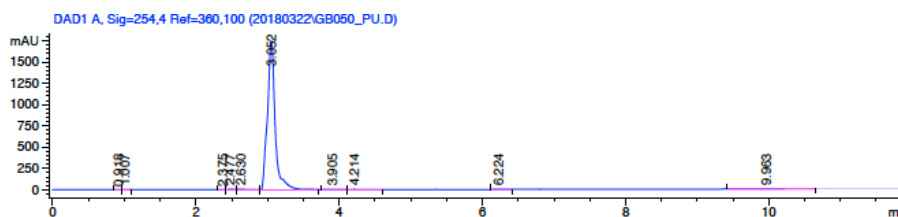
S41

Compound 3c

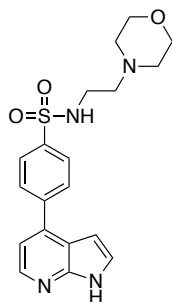


Signal 1: DAD1 A, Sig=254,4 Ref=360,100

Peak #	RetTime [min]	Type	Width [min]	Area [mAU*s]	Height [mAU]	Area %
1	0.918	BP	0.0701	15.17117	3.27132	0.1119
2	1.007	VB	0.0644	25.24015	5.41204	0.1862
3	2.375	BP	0.0626	22.23312	4.74636	0.1640
4	2.477	VV	0.1107	53.16644	7.69064	0.3922
5	2.630	VP	0.1676	108.22440	8.44104	0.7984
6	3.052	VB	0.1077	1.31698e4	1752.92834	97.1606
7	3.905	BV	0.2240	49.70527	2.87020	0.3667
8	4.214	VB	0.1929	30.55477	2.03794	0.2254
9	6.224	PB	0.0956	7.67722	1.18486	0.0566
10	9.963	PP	0.3749	72.89439	2.39637	0.5378

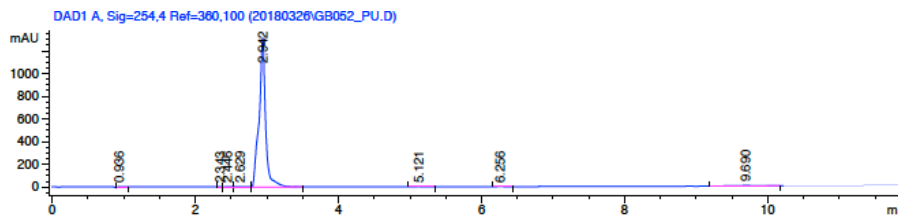


Compound 3d

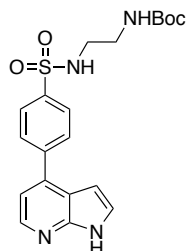


Signal 1: DAD1 A, Sig=254,4 Ref=360,100

Peak #	RetTime [min]	Type	Width [min]	Area [mAU*s]	Height [mAU]	Area %
1	0.936	PB	0.0727	42.79849	7.72055	0.4964
2	2.343	BP	0.0517	13.64645	3.82071	0.1583
3	2.446	VV	0.0919	38.79636	5.96535	0.4500
4	2.629	VV	0.1674	75.88288	5.92618	0.8801
5	2.942	VB	0.0879	8333.64551	1316.03442	96.6598
6	5.121	BB	0.1150	9.29696	1.19164	0.1078
7	6.256	PB	0.1046	7.88513	1.11308	0.0915
8	9.690	PV	0.3696	99.67474	3.50729	1.1561

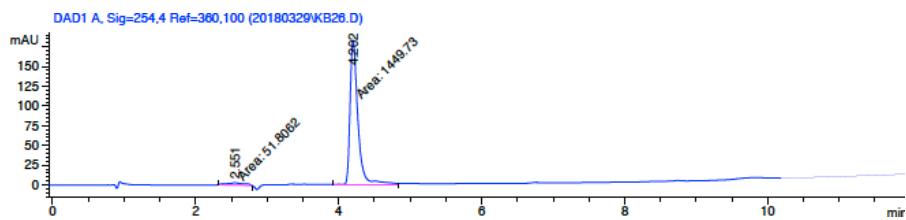


Compound 3e

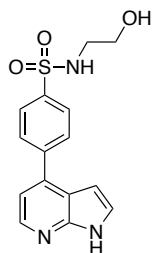


Signal 1: DAD1 A, Sig=254,4 Ref=360,100

Peak #	RetTime [min]	Type	Width [min]	Area [mAU*s]	Height [mAU]	Area %
1	2.551	MM	0.2893	51.80617	2.98493	3.4502
2	4.202	MM	0.1313	1449.72583	184.03851	96.5498

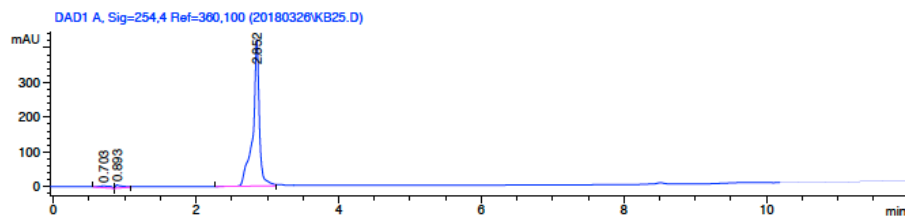


Compound 3f

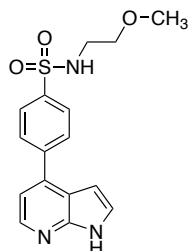


Signal 1: DAD1 A, Sig=254,4 Ref=360,100

Peak #	RetTime [min]	Type	Width [min]	Area [mAU*s]	Height [mAU]	Area %
1	0.703	BP	0.1761	58.69524	4.68796	2.0902
2	0.893	VB	0.0899	61.18455	8.93349	2.1789
3	2.852	PV	0.0880	2688.18823	423.65253	95.7309

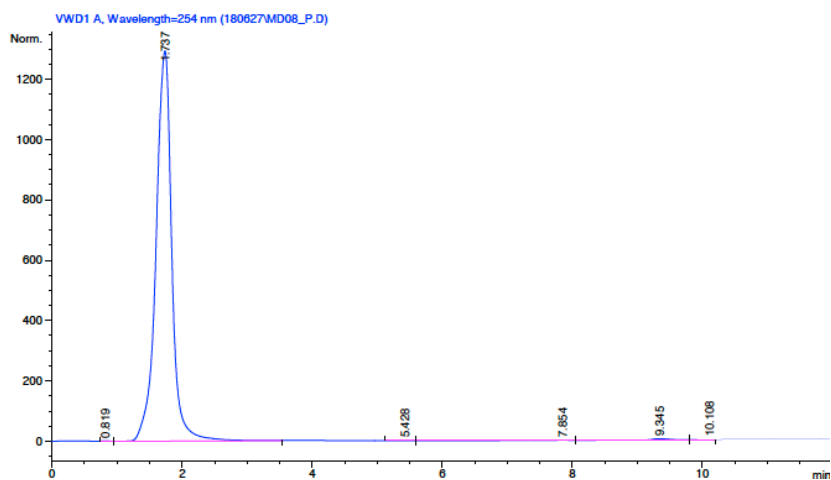


Compound 3g



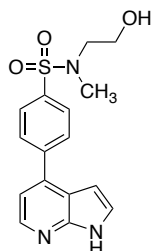
Signal 1: VWD1 A, Wavelength=254 nm

Peak #	RetTime [min]	Type	Width [min]	Area mAU *s	Height [mAU]	Area %
1	0.819	BP	0.0927	11.05829	1.59129	0.0495
2	1.737	VB	0.2610	2.18477e4	1293.97314	97.7271
3	5.428	PV	0.1884	1.74115	1.23000e-1	7.788e-3
4	7.854	VV	0.5299	95.37753	2.20904	0.4266
5	9.345	VV	0.5849	309.87854	6.78901	1.3861
6	10.108	VV	0.2960	90.07392	4.02589	0.4029



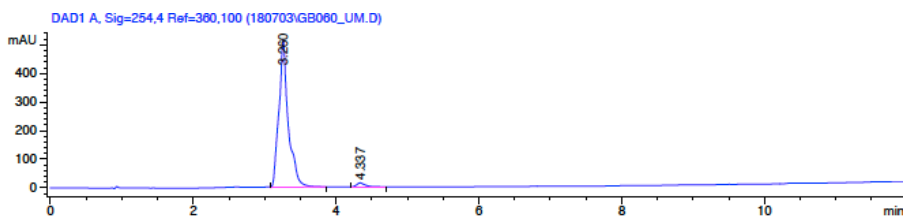
S44

Compound 3h



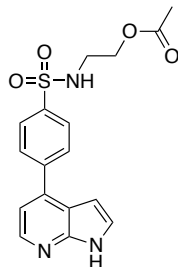
Signal 1: DAD1 A, Sig=254,4 Ref=360,100

Peak #	RetTime [min]	Type	Width [min]	Area [mAU*s]	Height [mAU]	Area %
1	3.260	BP	0.1228	4722.65576	515.68732	97.3659
2	4.337	PB	0.1242	127.76304	14.31060	2.6341



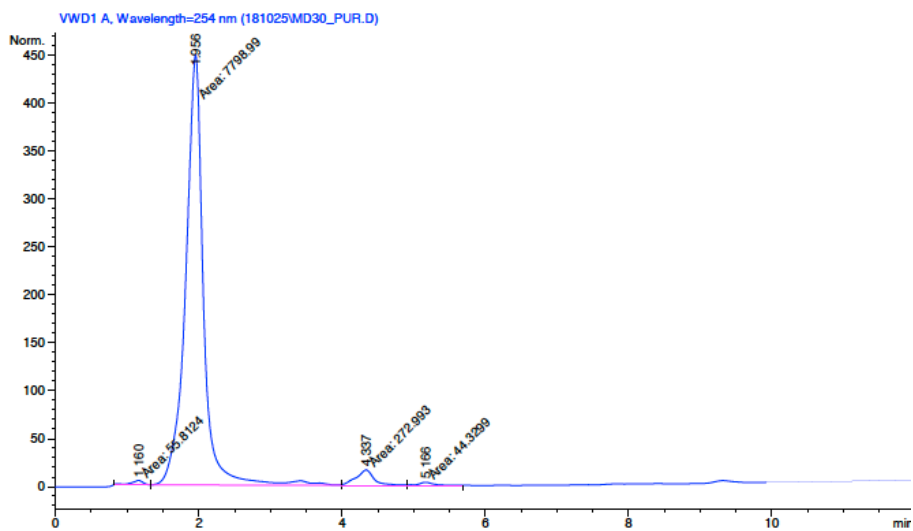
S45

Compound 3i



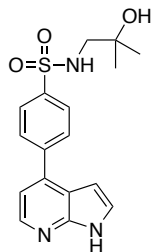
Signal 1: VWD1 A, Wavelength=254 nm

Peak #	RetTime [min]	Type	Width [min]	Area mAU *s	Height [mAU]	Area %
1	1.160	MF	0.2042	55.81241	4.55532	0.6830
2	1.956	FM	0.2894	7798.99268	449.07227	95.4340
3	4.337	MF	0.2845	272.99335	15.99182	3.3405
4	5.166	FM	0.2291	44.32991	3.22450	0.5425



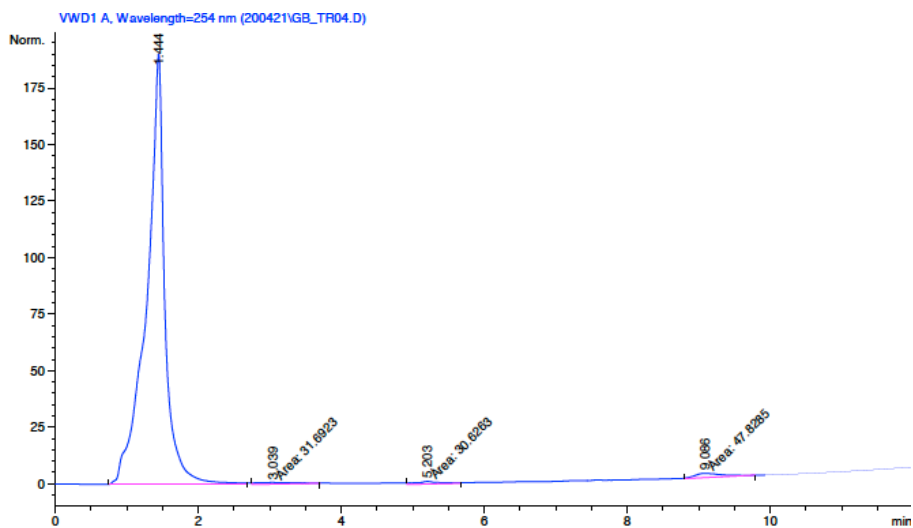
S46

Compound 3j

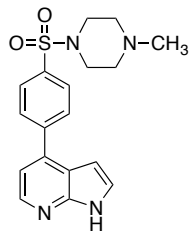


Signal 1: VWD1 A, Wavelength=254 nm

Peak #	RetTime [min]	Type	Width [min]	Area mAU *s	Height [mAU]	Area %
1	1.444	BV	0.2336	3385.48047	190.45901	96.8490
2	3.039	MM	0.4812	31.69227	8.10561e-1	0.9066
3	5.203	MM	0.4227	30.62626	1.20769	0.8761
4	9.086	MM	0.4236	47.82848	1.88171	1.3682

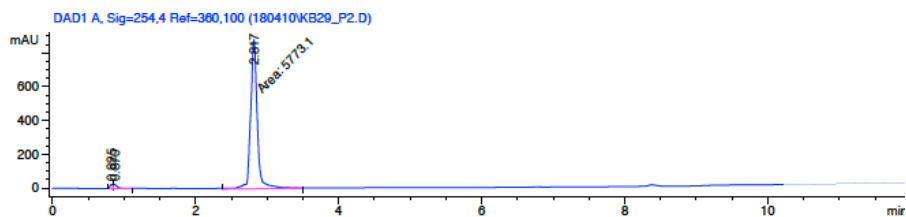


Compound 3k

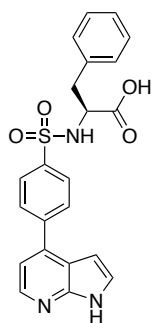


Signal 1: DAD1 A, Sig=254,4 Ref=360,100

Peak #	RetTime [min]	Type	Width [min]	Area [mAU*s]	Height [mAU]	Area %
1	0.825	PV	0.0410	68.34222	25.68645	1.1479
2	0.870	VB	0.0641	112.11481	24.18760	1.8832
3	2.817	MM	0.1089	5773.09619	883.47742	96.9689

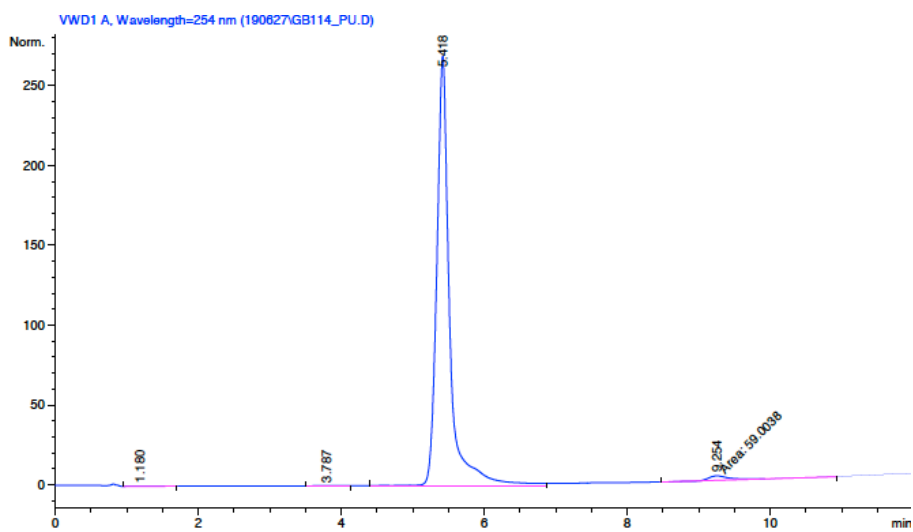


Compound 31

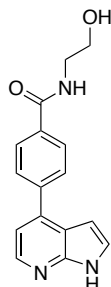


Signal 1: VWD1 A, Wavelength=254 nm

Peak #	RetTime [min]	Type	Width [min]	Area mAU*s	Height [mAU]	Area %
1	1.180	VB	0.3948	9.89864	3.26205e-1	0.2847
2	3.787	BB	0.3234	6.21565	2.56537e-1	0.1788
3	5.418	BB	0.1795	3401.51807	269.11194	97.8393
4	9.254	MM	0.3522	59.00384	2.79253	1.6972

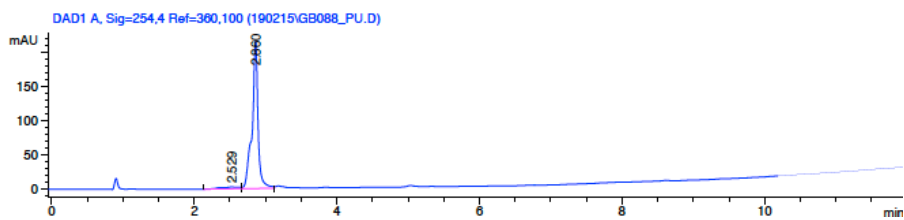


Compound 7

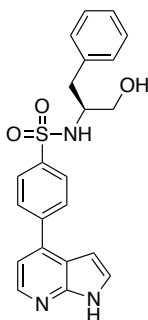


Signal 1: DAD1 A, Sig=254,4 Ref=360,100

Peak #	RetTime [min]	Type	Width [min]	Area [mAU*s]	Height [mAU]	Area %
1	2.529	PV	0.2307	50.86502	2.79007	3.9116
2	2.860	VV	0.0815	1249.49597	216.04950	96.0884

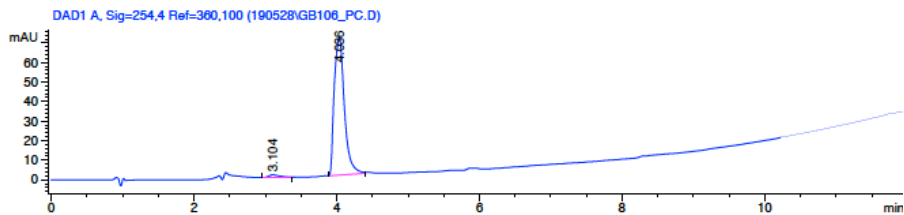


Compound 10a



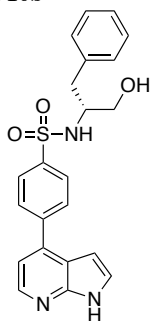
Signal 1: DAD1 A, Sig=254,4 Ref=360,100

Peak #	RetTime [min]	Type	Width [min]	Area [mAU*s]	Height [mAU]	Area %
1	3.104	PB	0.1354	13.43359	1.38164	1.9031
2	4.036	PB	0.1566	692.44995	70.52351	98.0969



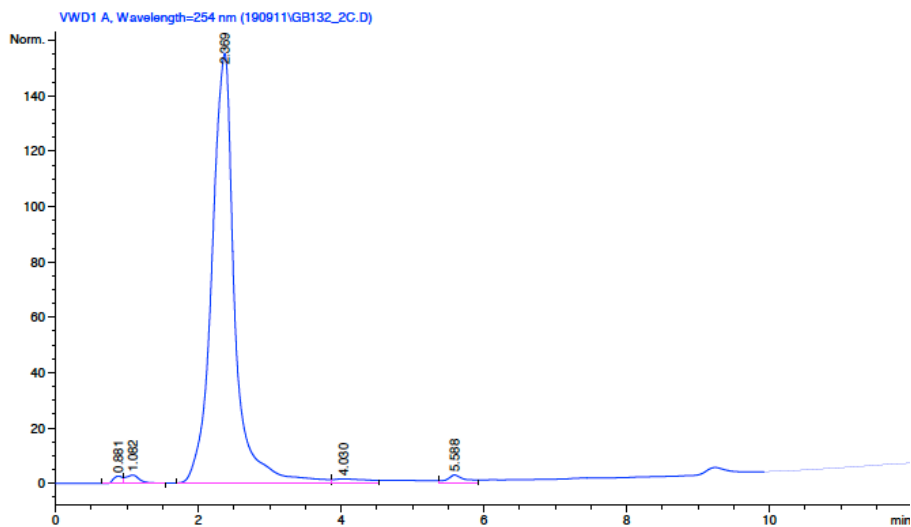
S50

Compound 10b

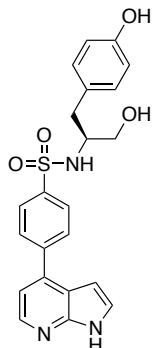


Signal 1: VWD1 A, Wavelength=254 nm

Peak #	RetTime [min]	Type	Width [min]	Area mAU*s	Height [mAU]	Area %
1	0.881	PV	0.1337	22.58297	2.66709	0.6201
2	1.082	VB	0.1951	42.29869	3.02587	1.1615
3	2.369	BV	0.3358	3463.27930	155.37941	95.0992
4	4.030	VV	0.4435	56.49057	1.69790	1.5512
5	5.588	BV	0.2481	57.10468	3.08282	1.5681

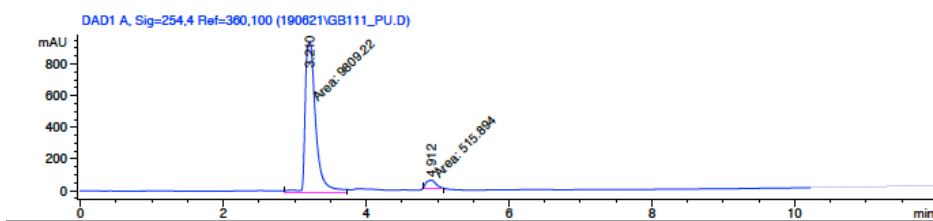


Compound 10c

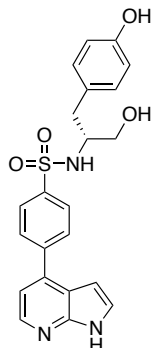


Signal 1: DAD1 A, Sig=254,4 Ref=360,100

Peak #	RetTime [min]	Type	Width [min]	Area [mAU*s]	Height [mAU]	Area %
1	3.210	MM	0.1725	9809.21582	947.50891	95.0035
2	4.912	MM	0.1621	515.89355	53.02645	4.9965

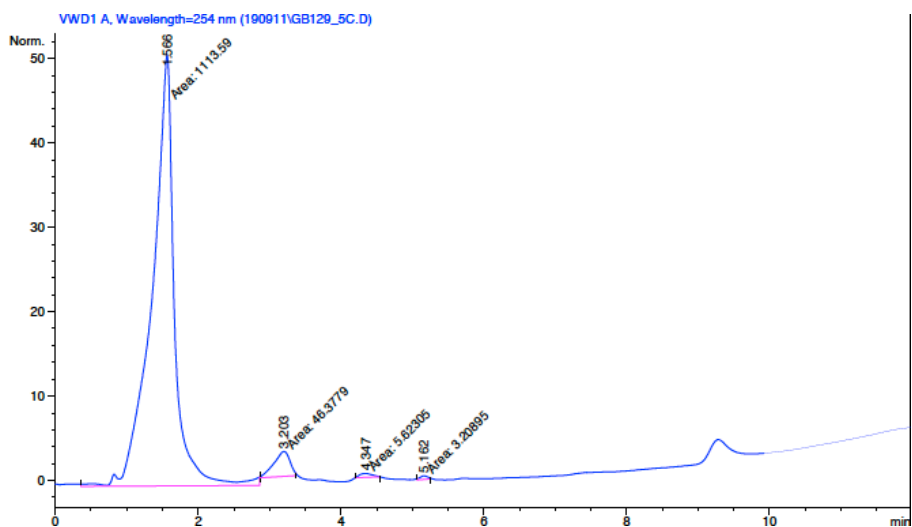


Compound 10d

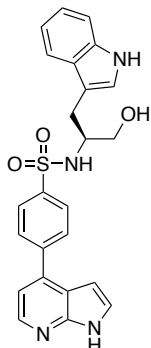


Signal 1: VWD1 A, Wavelength=254 nm

Peak #	RetTime [min]	Type	Width [min]	Area mAU*s	Height [mAU]	Area %
1	1.566	MM	0.3634	1113.58948	51.06890	95.2764
2	3.203	MM	0.2612	46.37790	2.95976	3.9680
3	4.347	MM	0.2058	5.62305	4.55398e-1	0.4811
4	5.162	MM	0.1242	3.20895	4.30565e-1	0.2746

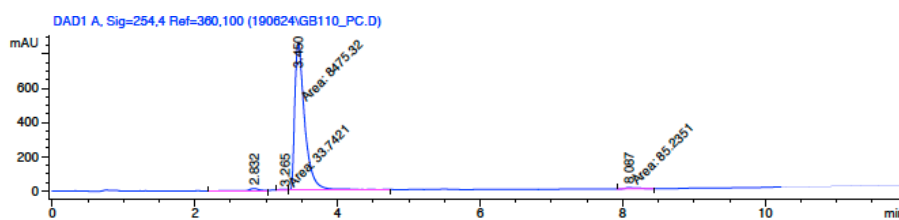


Compound 10e

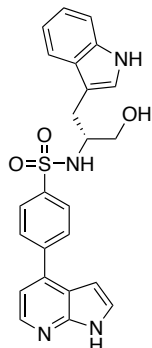


Signal 1: DAD1 A, Sig=254,4 Ref=360,100

Peak #	RetTime [min]	Type	Width [min]	Area [mAU*s]	Height [mAU]	Area %
1	2.832	VV	0.1816	192.88393	15.03968	2.1951
2	3.265	MM	0.1479	33.74209	3.80191	0.3840
3	3.450	MM	0.1637	8475.31641	862.69891	96.4510
4	8.087	MM	0.1793	85.23509	7.92359	0.9700

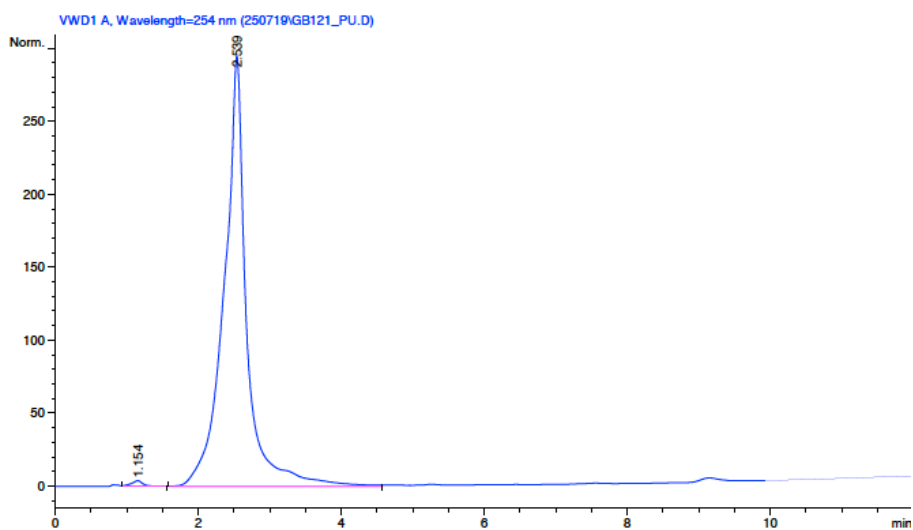


Compound 10f



Signal 1: VWD1 A, Wavelength=254 nm

Peak #	RetTime [min]	Type	Width [min]	Area mAU*s	Height [mAU]	Area %
1	1.154	VB	0.1674	48.16221	3.97992	0.7363
2	2.539	BV	0.2890	6493.06641	294.75516	99.2637



S55

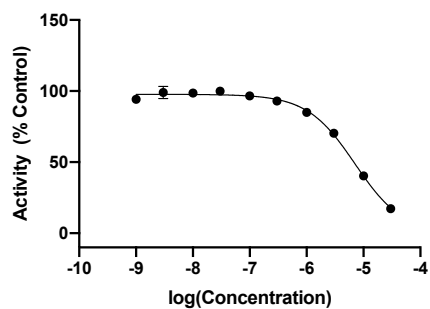
IC₅₀ determination for compounds 3a-k, 7 and 10a-f

IC₅₀ values for Nek1 were determined in a TR-FRET based activity assays (LANCER® Ultra TR-FRET, *PerkinElmer*) at an ATP concentration within 15 μM of the apparent Km for ATP in the respective assay format (60 μM for both Nek1 and Nek2). The IC₅₀ curves consist of 10 test compound concentrations tested at half-log dilutions from 30 μM to 1 nM with vehicle and inhibitory control wells. For compounds **3j** and **3k** the maximum concentration was set to 10 μM as a consequence of solubility issues at 30 μM and the respective IC₅₀ curves consist of 9 test compound concentrations tested at half-log dilutions from 10 μM to 1 nM. Values are the mean from two independent experiments. Recombinant human Nek1 (1-505; 0.02nM) or Nek2 (full length; 0.2nM) (both *Thermo Fisher Scientific*) was incubated with 50 mM HEPES pH 7.5, 1 mM EGTA, 10 mM MgCl₂, 0.2mM DTT, 0.01% Tween20, and 50 nM ULight™-p70 S6K (Thr389) peptide (sequence LGFTYVAP; *PerkinElmer*). The reaction was initiated by the addition of the p70 S6K peptide/ATP mix. After incubation for 30 minutes at 22 °C, the reaction was stopped by the addition of 10mM EDTA and 0.3 nM Europium-anti-phospho-p70 S6K (Thr389) antibody in CR97 detection buffer (both *PerkinElmer*). After incubation for 1 hour at 22 °C for signal development, the plates were analyzed in a plate reader (PHERAstar FSX, *BMG LABTECH*). For compounds **3g** and **3k**, relative IC₅₀ values were provided instead of absolute IC₅₀, as the determined IC₅₀ values exceeded the employed maximum test concentrations (30 μM for 3g, 10 μM for 3k).

For compounds **3a**, **3f**, **10a-f**, IC₅₀ values were also determined with the *Eurofins Discovery* IC₅₀Profiler™ service at either 10 μM (ITEM 15-020KP10) or at an ATP concentration within 15 μM of the apparent Km for ATP (90 μM, ITEM 15-020KP). The IC₅₀ curves consist of 9 test compound concentrations tested at half-log dilutions from 10 μM to 1 nM with vehicle control wells. Values are the mean from two independent experiments.

IC₅₀ values and 95% confidence intervals were determined from the raw data provided in the supporting information by nonlinear regression (log_inhibitor vs. response-variable slope_four parameters) using *GraphPad Prism version 8.4.3 (471) for OS X*, (*GraphPad Software*, San Diego, California USA, www.graphpad.com). For compounds **3j** and **3k** the maximum concentration data points were dropped, as a consequence of solubility issues at 30 μM, and marked red in the data tables and the plots. Results including all data points are provided. No error bars are shown for certain points on plots, where the error bar would be shorter than the size of the symbol.

3a vs Nek1(h) @ KmATP (TR-FRET)



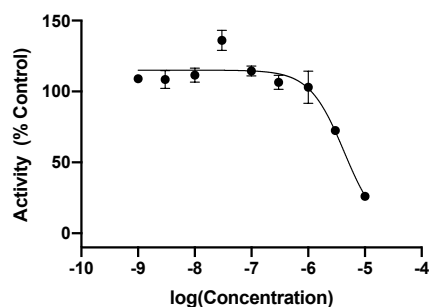
Sample	Activity (% Control)		Mean	SD*
3a @ 0.001 μM	95	94	94	1
3a @ 0.003 μM	102	96	99	4
3a @ 0.01 μM	98	99	99	1
3a @ 0.03 μM	99	101	100	1
3a @ 0.1 μM	96	97	97	1
3a @ 0.3 μM	95	91	93	2
3a @ 1 μM	86	84	85	2
3a @ 3 μM	71	69	70	1
3a @ 10 μM	41	40	40	0
3a @ 30 μM	18	17	17	1
CONTROL	/	/	100	/
	/	/		

* NB. Where n = 2, the value reported here is actually range / $\sqrt{2}$

LogIC50	-5.150
HillSlope	-1.034
IC50	7.080e-006
Span	= 97.69
95% CI (profile likelihood)	
Top	96.21 to 99.19
LogIC50	-5.193 to -5.107
HillSlope	-1.141 to -0.9382
IC50	6.411e-006 to 7.816e-006
Goodness of Fit	
Degrees of Freedom	17
R squared	0.9943
Sum of Squares	84.13
Sy.x	2.225

S57

3a vs Nek1(h) @ KmATP (Eurofins)



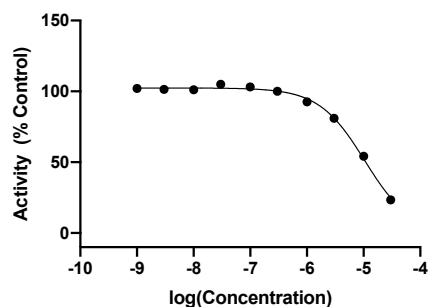
Sample	Counts	Mean (Counts - Blanks)	Activity (% Control)	Mean	SD*
3a @ 0.001µM	6283	5650	107	109	3
	6524		111		
3a @ 0.003µM	6629	5631	113	109	7
	6139		104		
3a @ 0.01µM	6349	5782	108	112	5
	6721		115		
3a @ 0.03µM	7541	7033	131	136	7
	8032		141		
3a @ 0.1µM	6529	5927	112	115	4
	6832		117		
3a @ 0.3µM	6107	5529	103	107	5
	6458		110		
3a @ 1µM	6502	5345	111	103	11
	5694		95		
3a @ 3µM	4498	3753	72	73	0
	4514		73		
3a @ 10µM	2130	1336	27	26	1
	2048		25		
CONTROL	6308	5177	107	100	6
	6018		102		
	5827		98		
	5569		93		
BLANK	753	/	/	/	/
	754	/	/	/	/

* NB. Where n = 2, the value reported here is actually range / $\sqrt{2}$

LogIC50	-5.367
HillSlope	-1.421
IC50	4.296e-006
Span	= 115.1
95% CI (profile likelihood)	
Top	108.8 to 121.6
LogIC50	-5.502 to -5.228
HillSlope	-2.218 to -0.9346
IC50	3.148e-006 to 5.910e-006
Goodness of Fit	
Degrees of Freedom	15
R squared	0.9125
Sum of Squares	1435
Sy.x	9.781

S58

3b vs Nek1(h) @ KmATP (TR-FRET)

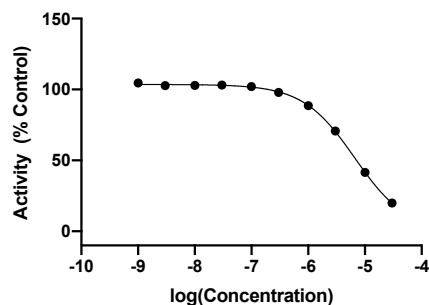


Sample	Activity (% Control)		Mean	SD*
3b @ 0.001µM	101	103	102	1
3b @ 0.003µM	102	100	101	1
3b @ 0.001µM	102	100	101	2
3b @ 0.003µM	107	103	105	3
3b @ 0.1µM	102	104	103	1
3b @ 0.3µM	102	98	100	3
3b @ 1µM	93	92	93	0
3b @ 3µM	83	80	81	2
3b @ 10µM	55	53	54	1
3b @ 30µM	25	22	23	2
CONTROL	/	/	100	/
	/	/		

- NB. Where n = 2, the value reported here is actually range / $\sqrt{2}$

LogIC50	-4.981
HillSlope	-1.074
IC50	1.045e-005
Span	= 102.4
95% CI (profile likelihood)	
Top	101.0 to 103.8
LogIC50	-5.020 to -4.942
HillSlope	-1.185 to -0.9744
IC50	9.558e-006 to 1.143e-005
Goodness of Fit	
Degrees of Freedom	17
R squared	0.9940
Sum of Squares	79.16
Sy,x	2.158

3c vs Nek1(h) @ KmATP (TR-FRET)



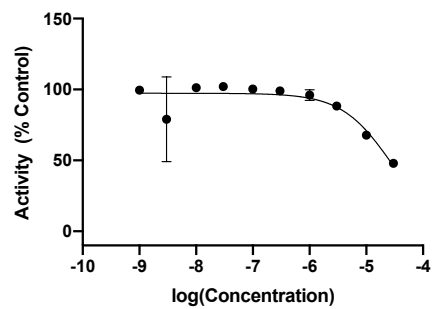
Sample	Activity (% Control)		Mean	SD*
3c @ 0.001 μM	106	103	105	2
3c @ 0.003 μM	103	102	103	1
3c @ 0.001 μM	103	103	103	0
3c @ 0.003 μM	104	102	103	1
3c @ 0.1 μM	103	101	102	2
3c @ 0.3 μM	98	98	98	1
3c @ 1 μM	88	89	89	1
3c @ 3 μM	71	70	71	1
3c @ 10 μM	42	41	42	1
3c @ 30 μM	20	20	20	0
CONTROL	/	/	100	/
	/	/		

• NB. Where n = 2, the value reported here is actually range / $\sqrt{2}$

LogIC50	-5.179
HillSlope	-0.9498
IC50	6.615e-006
Span	= 103.6
95% CI (profile likelihood)	
Top	102.9 to 104.2
LogIC50	-5.199 to -5.160
HillSlope	-0.9887 to -0.9125
IC50	6.331e-006 to 6.911e-006
Goodness of Fit	
Degrees of Freedom	17
R squared	0.9990
Sum of Squares	16.56
Sy.x	0.9869

S60

3d vs Nek1(h) @ KmATP (TR-FRET)



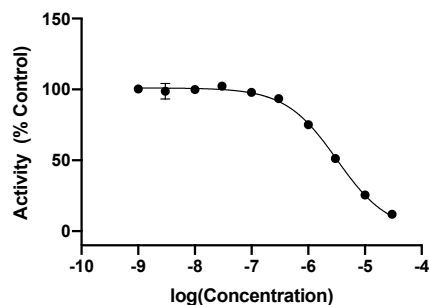
Sample	Activity (% Control)		Mean	SD*
3d @ 0.001 μ M	101	98	100	2
3d @ 0.003 μ M	58	100	79	30
3d @ 0.001 μ M	102	101	101	1
3d @ 0.003 μ M	102	102	102	0
3d @ 0.1 μ M	99	101	100	1
3d @ 0.3 μ M	99	99	99	0
3d @ 1 μ M	93	99	96	4
3d @ 3 μ M	88	89	88	1
3d @ 10 μ M	68	68	68	0
3d @ 30 μ M	46	50	48	3
CONTROL	/	/	100	/
	/	/		

- NB. Where n = 2, the value reported here is actually range / $\sqrt{2}$

LogIC50	-4.566
HillSlope	-0.9942
IC50	2.714e-005
Span	= 97.34
95% CI (profile likelihood)	
Top	91.32 to 103.8
LogIC50	-4.781 to -4.205
HillSlope	-1.826 to -0.5394
IC50	1.654e-005 to 6.239e-005
Goodness of Fit	
Degrees of Freedom	17
R squared	0.7411
Sum of Squares	1759
Sy,x	10.17

S61

3f vs Nek1(h) @ KmATP (TR-FRET)



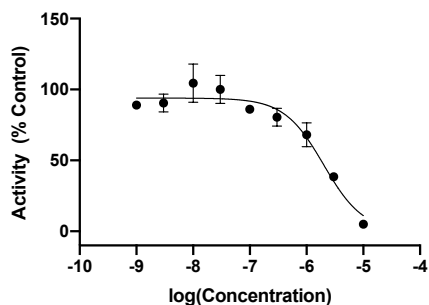
Sample	Activity (% Control)		Mean	SD*
	100	101		
3f @ 0.001µM	100	101	100	1
3f @ 0.003µM	95	103	99	5
3f @ 0.01µM	100	100	100	1
3f @ 0.03µM	104	101	102	2
3f @ 0.1µM	98	98	98	0
3f @ 0.3µM	93	94	94	0
3f @ 1µM	77	73	75	3
3f @ 3µM	52	51	51	0
3f @ 10µM	25	26	25	1
3f @ 30µM	12	12	12	0
CONTROL	/	/	100	/
	/	/		

• NB. Where n = 2, the value reported here is actually range / $\sqrt{2}$

LogIC50	-5.497
HillSlope	-0.9569
IC50	3.188e-006
Span	= 101.1
95% CI (profile likelihood)	
Top	99.51 to 102.7
LogIC50	-5.540 to -5.453
HillSlope	-1.042 to -0.8804
IC50	2.885e-006 to 3.521e-006
Goodness of Fit	
Degrees of Freedom	17
R squared	0.9961
Sum of Squares	82.02
Sy.x	2.197

S62

3f vs Nek1(h) @ KmATP (Eurofins)

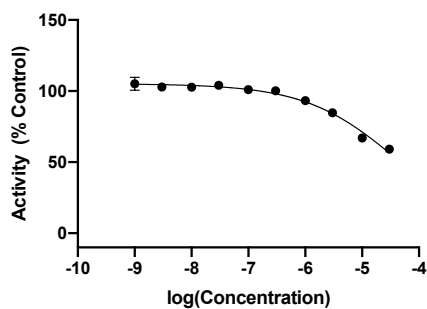


Sample	Counts	Mean (Counts - Blanks)	Activity (% Control)	Mean	SD*
3f @ 0.001µM	4289	3954	89	89	0
	4280		89		
3f @ 0.003µM	4563	4023	95	91	7
	4144		86		
3f @ 0.01µM	5399	4640	114	105	14
	4542		95		
3f @ 0.03µM	4478	4446	93	100	10
	5075		107		
3f @ 0.1µM	4126	3839	85	86	1
	4213		87		
3f @ 0.3µM	4121	3583	85	81	7
	3706		76		
3f @ 1µM	3604	3012	74	68	8
	3081		62		
3f @ 3µM	2022	1721	38	39	1
	2080		39		
3f @ 10µM	617	229	6	5	2
	501		4		
CONTROL	4775	4441	100	100	6
	5154		109		
	4473		93		
	4684		98		
BLANK	281	/	/	/	/
	380		/		

- NB. Where n = 2, the value reported here is actually range / $\sqrt{2}$

LogIC50	-5.699
HillSlope	-1.250
IC50	1.999e-006
Span	= 93.95
95% CI (profile likelihood)	
Top	88.00 to 100.4
LogIC50	-5.865 to -5.546
HillSlope	-1.994 to -0.8403
IC50	1.364e-006 to 2.842e-006
Goodness of Fit	
Degrees of Freedom	15
R squared	0.9388
Sum of Squares	1049
Sy.x	8.361

3g vs Nek1(h) @ KmATP (TR-FRET)



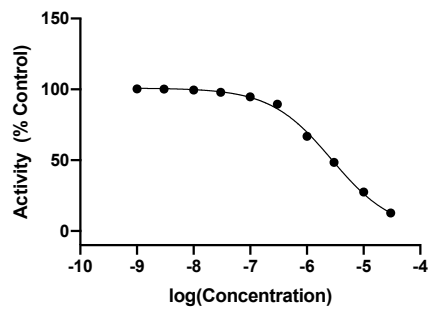
Sample	Activity (% Control)		Mean	SD*
3g @ 0.001μM	108	102	105	4
3g @ 0.003μM	102	104	103	2
3g @ 0.01μM	102	103	103	1
3g @ 0.03μM	105	103	104	1
3g @ 0.1μM	100	102	101	1
3g @ 0.3μM	101	100	100	1
3g @ 1μM	92	94	93	2
3g @ 3μM	84	85	85	1
3g @ 10μM	65	69	67	2
3g @ 30μM	58	60	59	1
CONTROL	/	/	100	/
	/	/		

• NB. Where n = 2, the value reported here is actually range / $\sqrt{2}$

LogIC50	-4.401
HillSlope	-0.5388
IC50	3.971e-005
Span	= 105.1
95% CI (profile likelihood)	
Top	103.0 to 107.5
LogIC50	-4.503 to -4.279
HillSlope	-0.6337 to -0.4537
IC50	3.140e-005 to 5.262e-005
Goodness of Fit	
Degrees of Freedom	17
R squared	0.9778
Sum of Squares	110.0
Sy.x	2.544

S64

3h vs Nek1(h) @ KmATP (TR-FRET)



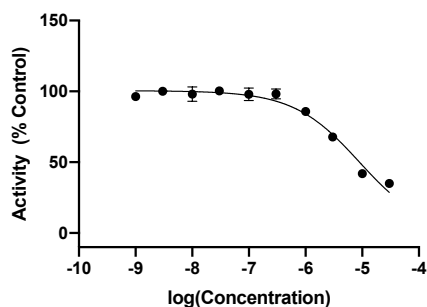
Sample	Activity (% Control)		Mean	SD*
3h @ 0.001µM	100	101	100	0
3h @ 0.003µM	100	101	100	0
3h @ 0.001µM	98	101	99	2
3h @ 0.003µM	100	96	98	3
3h @ 0.1µM	95	94	95	0
3h @ 0.3µM	88	91	90	2
3h @ 1µM	65	68	67	2
3h @ 3µM	49	48	49	1
3h @ 10µM	26	29	28	2
3h @ 30µM	14	12	13	1
CONTROL	/	/	100	/
	/	/		

- NB. Where n = 2, the value reported here is actually range / $\sqrt{2}$

LogIC50	-5.564
HillSlope	-0.8035
IC50	2.732e-006
Span	= 100.9
95% CI (profile likelihood)	
Top	99.30 to 102.6
LogIC50	-5.610 to -5.517
HillSlope	-0.8683 to -0.7438
IC50	2.454e-006 to 3.039e-006
Goodness of Fit	
Degrees of Freedom	17
R squared	0.9964
Sum of Squares	71.35
Sy.x	2.049

S65

3i vs Nek1(h) @ KmATP (TR-FRET)

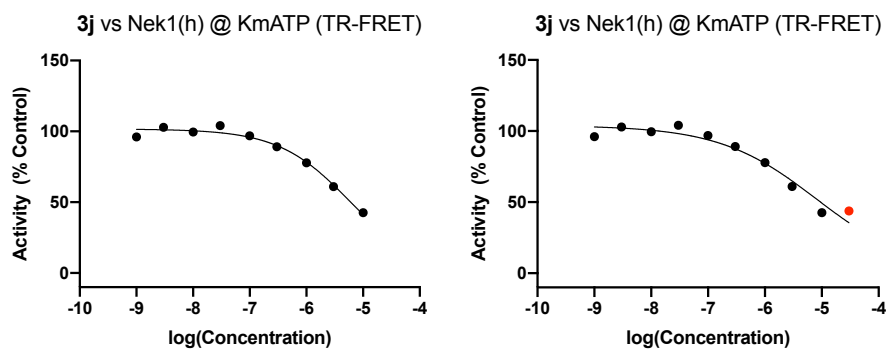


Sample	Activity (% Control)		Mean	SD*
3i @ 0.001 μM	96	97	96	1
3i @ 0.003 μM	101	99	100	2
3i @ 0.001 μM	102	95	98	5
3i @ 0.003 μM	100	101	100	1
3i @ 0.1 μM	101	95	98	4
3i @ 0.3 μM	101	96	98	4
3i @ 1 μM	87	85	86	1
3i @ 3 μM	69	67	68	1
3i @ 10 μM	44	40	42	3
3i @ 30 μM	35	35	35	0
CONTROL	/	/	100	/
	/	/		

- NB. Where n = 2, the value reported here is actually range / $\sqrt{2}$

LogIC50	-5.053
HillSlope	-0.7498
IC50	8.848e-006
Span	= 100.5
95% CI (profile likelihood)	
Top	97.34 to 103.8
LogIC50	-5.157 to -4.945
HillSlope	-0.8997 to -0.6214
IC50	6.961e-006 to 1.136e-005
Goodness of Fit	
Degrees of Freedom	17
R squared	0.9710
Sum of Squares	331.6
Sy.x	4.416

S66



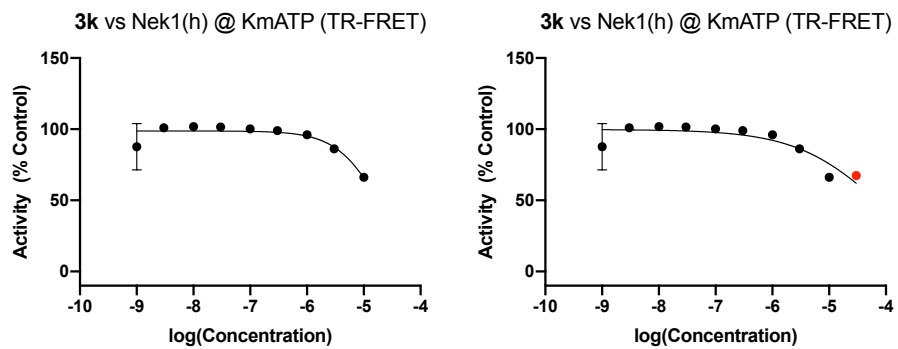
Sample	Activity (% Control)		Mean	SD*
3j @ 0.001µM	97	95	96	2
3j @ 0.003µM	104	102	103	1
3j @ 0.001µM	101	98	100	3
3j @ 0.003µM	104	104	104	1
3j @ 0.1µM	97	97	97	1
3j @ 0.3µM	89	89	89	0
3j @ 1µM	76	80	78	3
3j @ 3µM	61	61	61	1
3j @ 10µM	43	42	43	0
3j @ 30µM	44	44	44	0
CONTROL	/	/	100	/
	/	/		

• NB. Where n = 2, the value reported here is actually range / $\sqrt{2}$

LogIC50	-5.238
HillSlope	-0.6900
IC50	5.781e-006
Span	= 101.7
95% CI (profile likelihood)	
Top	99.07 to 104.5
LogIC50	-5.325 to -5.144
HillSlope	-0.8130 to -0.5824
IC50	4.737e-006 to 7.172e-006
Goodness of Fit	
Degrees of Freedom	15
R squared	0.9795
Sum of Squares	148.2
Sy.x	3.143

LogIC50	-5.085
HillSlope	-0.5058
IC50	8.217e-006
Span	= 103.9
95% CI (profile likelihood)	
Top	99.14 to 109.8
LogIC50	-5.259 to -4.905
HillSlope	-0.6339 to -0.3944
IC50	5.502e-006 to 1.244e-005
Goodness of Fit	
Degrees of Freedom	17
R squared	0.9544
Sum of Squares	472.5
Sy.x	5.272

S67



Sample	Activity (% Control)		Mean	SD*
	1	2		
3k @ 0.001µM	76	99	88	16
3k @ 0.003µM	102	100	101	2
3k @ 0.001µM	104	100	102	3
3k @ 0.003µM	103	100	102	2
3k @ 0.1µM	100	100	100	0
3k @ 0.3µM	99	99	99	0
3k @ 1µM	96	96	96	0
3k @ 3µM	85	87	86	1
3k @ 10µM	64	68	66	3
3k @ 30µM	67	68	67	1
CONTROL	/	/	100	/
	/	/		

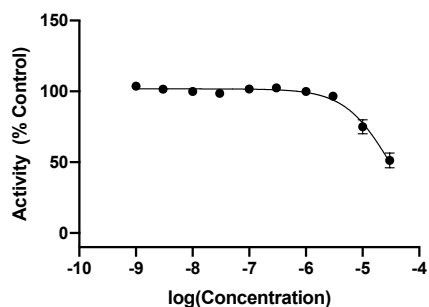
- NB. Where n = 2, the value reported here is actually range / $\sqrt{2}$

LogIC50	-4.731
HillSlope	-1.120
IC50	1.859e-005
Span	= 98.74
95% CI (profile likelihood)	
Top	94.81 to 103.0
LogIC50	-4.916 to -4.288
HillSlope	-2.688 to -0.5942
IC50	1.212e-005 to 5.157e-005
Goodness of Fit	
Degrees of Freedom	15
R squared	0.7596
Sum of Squares	602.2
Sy.x	6.336

LogIC50	-4.155
HillSlope	-0.5873
IC50	7.001e-005
Span	= 99.77
95% CI (profile likelihood)	
Top	94.80 to 105.9
LogIC50	-4.470 to -3.506
HillSlope	-0.9609 to -0.3292
IC50	3.391e-005 to 0.0003116
Goodness of Fit	
Degrees of Freedom	17
R squared	0.7526
Sum of Squares	916.7
Sy.x	7.343

S68

7 vs Nek1(h) @ KmATP (TR-FRET)

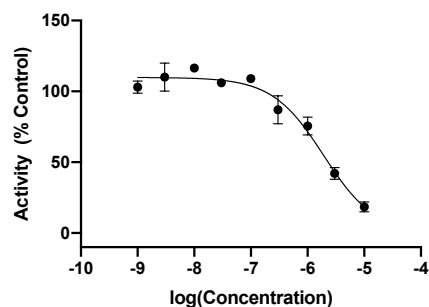


Sample	Activity (% Control)		Mean	SD*
7 @ 0.001µM	106	102	104	3
7 @ 0.003µM	103	100	102	2
7 @ 0.01µM	99	100	100	1
7 @ 0.03µM	100	97	99	2
7 @ 0.1µM	102	101	102	1
7 @ 0.3µM	103	102	103	1
7 @ 1µM	101	99	100	1
7 @ 3µM	95	98	97	3
7 @ 10µM	79	72	75	5
7 @ 30µM	48	55	51	5
CONTROL	/	/	100	/
	/	/		

- NB. Where n = 2, the value reported here is actually range / $\sqrt{2}$

LogIC50	-4.533
HillSlope	-1.090
IC50	2.928e-005
Span	= 101.8
95% CI (profile likelihood)	
Top	100.0 to 103.5
LogIC50	-4.595 to -4.462
HillSlope	-1.305 to -0.9078
IC50	2.543e-005 to 3.455e-005
Goodness of Fit	
Degrees of Freedom	17
R squared	0.9719
Sum of Squares	146.0
Sy.x	2.930

10a vs Nek1(h) @ KmATP (Eurofins)

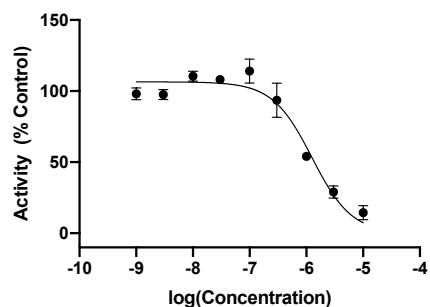


Sample	Counts	Mean (Counts - Blanks)	Activity (% Control)	Mean	SD*
10a @ 0.001 μM	7050	6282	106	103	4
	6685		100		
10a @ 0.003 μM	6820	6663	103	110	10
	7676		117		
10a @ 0.01 μM	7673	7063	117	117	1
	7624		116		
10a @ 0.03 μM	7123	6439	108	106	2
	6926		104		
10a @ 0.1 μM	7144	6609	108	109	1
	7245		110		
10a @ 0.3 μM	5447	5278	80	87	10
	6279		94		
10a @ 1 μM	5418	4582	80	76	6
	4916		71		
10a @ 3 μM	3321	2548	45	42	4
	2945		39		
10a @ 10 μM	1561	1111	16	19	3
	1832		21		
CONTROL	6707	6071	101	100	7
	6440		96		
	7216		109		
	6262		94		
BLANK	684	/	/	/	/
	487		/		

• NB. Where n = 2, the value reported here is actually range / $\sqrt{2}$

5	LogIC50	-5.718
6	HillSlope	-0.9625
7	IC50	1.915e-006
8	Span	= 109.9
9	95% CI (profile likelihood)	
10	Top	104.7 to 115.4
11	LogIC50	-5.847 to -5.592
12	HillSlope	-1.269 to -0.7415
13	IC50	1.423e-006 to 2.561e-006
14	Goodness of Fit	
15	Degrees of Freedom	15
16	R squared	0.9636
17	Sum of Squares	690.3
18	Sy.x	6.784

10b vs Nek1(h) @ KmATP (Eurofins)



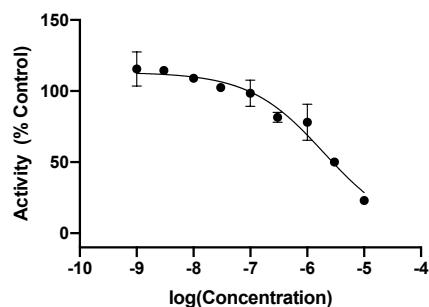
Sample	Counts	Mean (Counts - Blanks)	Activity (% Control)	Mean	SD*
10b @ 0.001µM	6694	5931	101	98	4
	6338		95		
10b @ 0.003µM	6643	5907	100	98	4
	6341		95		
10b @ 0.01µM	7158	6720	108	111	3
	7453		113		
10b @ 0.03µM	7061	6560	107	108	2
	7229		109		
10b @ 0.1µM	7120	6901	108	114	9
	7852		120		
10b @ 0.3µM	6767	5679	102	94	12
	5762		85		
10b @ 1µM	4011	3288	56	54	3
	3735		52		
10b @ 3µM	2513	1756	32	29	4
	2169		26		
10b @ 10µM	1655	876	18	15	5
	1268		11		
CONTROL	6707	6071	101	100	7
	6440		96		
	7216		109		
	6262		94		
BLANK	684	/	/	/	/
	487		/		

- NB. Where n = 2, the value reported here is actually range / $\sqrt{2}$

LogIC50	-5.902
HillSlope	-1.248
IC50	1.255e-006
Span	= 106.5
95% CI (profile likelihood)	
Top	100.4 to 112.8
LogIC50	-6.040 to -5.756
HillSlope	-1.781 to -0.9110
IC50	9.126e-007 to 1.752e-006
Goodness of Fit	
Degrees of Freedom	15
R squared	0.9493
Sum of Squares	1156
Sy.x	8.779

S71

10c vs Nek1(h) @ KmATP (Eurofins)



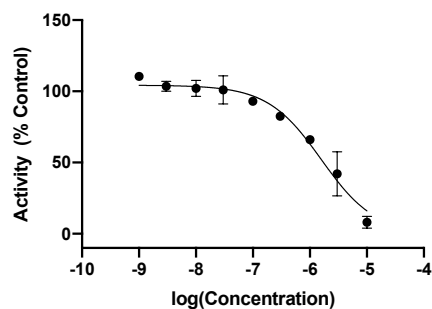
Sample	Counts	Mean (Counts - Blanks)	Activity (% Control)	Mean	SD*
10c @ 0.001µM	8739	7330	124	116	12
	7694		107		
10c @ 0.003µM	8288	7305	116	115	2
	8094		113		
10c @ 0.01µM	7668	6916	107	109	3
	7936		111		
10c @ 0.03µM	7369	6522	102	103	1
	7448		103		
10c @ 0.1µM	7540	6237	105	99	9
	6707		92		
10c @ 0.3µM	6241	5203	84	82	3
	5937		79		
10c @ 1µM	5292	4978	69	78	13
	6437		87		
10c @ 3µM	4190	3182	52	50	3
	3947		48		
10c @ 10µM	2470	1454	25	23	3
	2210		21		
CONTROL	7092	6354	98	100	3
	7173		99		
	7534		105		
	7161		99		
BLANK	974	/	/	/	/
	799	/	/	/	/

• NB. Where n = 2, the value reported here is actually range / $\sqrt{2}$

LogIC50	-5.708
HillSlope	-0.6633
IC50	1.959e-006
Span	= 113.2
95% CI (profile likelihood)	
Top	105.9 to 122.9
LogIC50	-5.921 to -5.524
HillSlope	-0.9329 to -0.4689
IC50	1.199e-006 to 2.992e-006
Goodness of Fit	
Degrees of Freedom	15
R squared	0.9504
Sum of Squares	813.4
Sy.x	7.364

S72

10d vs Nek1(h) @ KmATP (Eurofins)



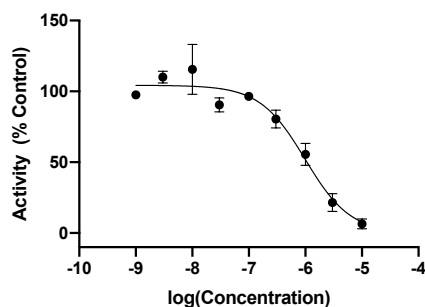
Sample	Counts	Mean (Counts - Blanks)	Activity (% Control)	Mean	SD*
10d @ 0.001µM	8025	7024	112	111	3
	7795		109		
10d @ 0.003µM	7315	6586	101	104	3
	7629		106		
10d @ 0.01µM	7132	6504	98	102	6
	7648		106		
10d @ 0.03µM	7757	6427	108	101	10
	6869		94		
10d @ 0.1µM	6826	5921	93	93	0
	6788		93		
10d @ 0.3µM	6097	5242	82	83	1
	6159		83		
10d @ 1µM	5076	4192	66	66	0
	5080		66		
10d @ 3µM	4283	2687	53	42	16
	2864		31		
10d @ 10µM	1599	530	11	8	4
	1234		5		
CONTROL	7092	6354	98	100	3
	7173		99		
	7534		105		
	7161		99		
BLANK	974	/	/	/	/
	799		/		

• NB. Where n = 2, the value reported here is actually range / $\sqrt{2}$

LogIC50	-5.800
HillSlope	-0.9225
IC50	1.583e-006
Span	= 104.3
95% CI (profile likelihood)	
Top	98.51 to 110.9
LogIC50	-5.959 to -5.655
HillSlope	-1.270 to -0.6805
IC50	1.099e-006 to 2.214e-006
Goodness of Fit	
Degrees of Freedom	15
R squared	0.9616
Sum of Squares	736.9
Sy,x	7.009

S73

10e vs Nek1(h) @ KmATP (Eurofins)



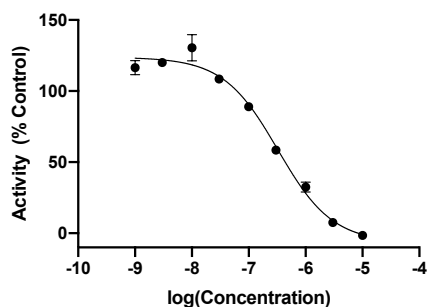
Sample	Counts	Mean (Counts - Blanks)	Activity (% Control)	Mean	SD*
10e @ 0.001µM	7142	6198	98	98	1
	7027		97		
10e @ 0.003µM	8076	6991	113	110	4
	7679		107		
10e @ 0.01µM	7450	7345	103	116	17
	9013		128		
10e @ 0.03µM	6855	5739	94	91	5
	6395		87		
10e @ 0.1µM	6978	6118	96	97	1
	7030		97		
10e @ 0.3µM	5684	5084	76	81	6
	6257		85		
10e @ 1µM	4755	3526	61	56	8
	4070		50		
10e @ 3µM	2526	1376	26	22	6
	1998		17		
10e @ 10µM	1480	413	9	7	4
	1118		4		
CONTROL	7092	6354	98	100	3
	7173		99		
	7534		105		
	7161		99		
BLANK	974	/	/	/	/
	799	/	/	/	/

• NB. Where n = 2, the value reported here is actually range / $\sqrt{2}$

LogIC50	-6.005
HillSlope	-1.086
IC50	9.887e-007
Span	= 104.3
95% CI (profile likelihood)	
Top	97.07 to 112.4
LogIC50	-6.187 to -5.837
HillSlope	-1.673 to -0.7495
IC50	6.504e-007 to 1.455e-006
Goodness of Fit	
Degrees of Freedom	15
R squared	0.9485
Sum of Squares	1266
Sy.x	9.187

S74

10f vs Nek1(h) @ KmATP (Eurofins)

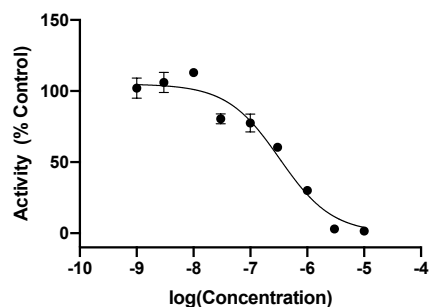


Sample	Counts	Mean (Counts - Blanks)	Activity (% Control)	Mean	SD*
10f @ 0.001µM	6711	6431	113	117	5
	6910		120		
10f @ 0.003µM	7025	6518	122	120	3
	6770		118		
10f @ 0.01µM	7825	7099	137	131	9
	7132		124		
10f @ 0.03µM	6232	5896	108	109	1
	6319		109		
10f @ 0.1µM	5141	4820	88	89	2
	5258		90		
10f @ 0.3µM	3557	3186	58	59	0
	3574		59		
10f @ 1µM	2305	1782	35	33	4
	2017		30		
10f @ 3µM	881	423	9	8	2
	724		6		
10f @ 10µM	271	-69	-2	-2	1
	351		-1		
CONTROL	6104	5438	105	100	4
	5678		97		
	5920		102		
	5566		95		
BLANK	363	/	/	/	/
	396		/		

• NB. Where n = 2, the value reported here is actually range / $\sqrt{2}$

LogIC50	-6.487
HillSlope	-0.9048
IC50	3.258e-007
Span	130.3
95% CI (profile likelihood)	
Top	117.3 to 131.3
LogIC50	-6.649 to -6.286
HillSlope	-1.208 to -0.6646
IC50	2.245e-007 to 5.173e-007
Goodness of Fit	
Degrees of Freedom	14
R squared	0.9858
Sum of Squares	589.2
Sy.x	6.487

10f vs Nek1(h) @ 10 μM ATP (Eurofins)



Sample	Counts	Mean (Counts - Blanks)	Activity (% Control)	Mean	SD*
10f @ 0.001μM	12234	11537	107	102	7
	11089		97		
10f @ 0.003μM	12714	12001	111	106	7
	11538		101		
10f @ 0.01μM	13154	12760	115	113	3
	12616		111		
10f @ 0.03μM	9536	9105	83	81	4
	8924		78		
10f @ 0.1μM	9338	8747	82	78	6
	8406		73		
10f @ 0.3μM	7157	6867	62	61	2
	6827		59		
10f @ 1μM	3595	3379	31	30	1
	3413		29		
10f @ 3μM	507	362	3	3	0
	466		3		
10f @ 10μM	496	206	3	2	2
	166		0		
CONTROL	11514	11292	101	100	4
	11541		101		
	11870		104		
	10743		94		
BLANK	123	/	/	/	/
	127		/		

• NB. Where n = 2, the value reported here is actually range / $\sqrt{2}$

LogIC50	-6.487
HillSlope	-0.9367
IC50	3.260e-007
Span	= 105.0
95% CI (profile likelihood)	
Top	96.36 to 115.4
LogIC50	-6.707 to -6.293
HillSlope	-1.357 to -0.6753
IC50	1.965e-007 to 5.094e-007
Goodness of Fit	
Degrees of Freedom	15
R squared	0.9618
Sum of Squares	1143
Sy.x	8.729

S76

E. Erklärung laut Promotionsordnung

§8 Abs. 1 lit c PromO

Ich versichere hiermit, dass die elektronische Version meiner Dissertation mit der schriftlichen Version übereinstimmt und für die Durchführung des Promotionsverfahrens vorliegt.

§8 Abs. 1 lit d PromO

Ich versichere hiermit, dass zu einem vorherigen Zeitpunkt noch keine Promotion versucht wurde und zu keinem früheren Zeitpunkt an einer in- oder ausländischen Hochschule eingereicht wurde. In diesem Fall sind nähere Angaben über Zeitpunkt, Hochschule, Dissertationsthema und Ergebnis dieses Versuchs mitzuteilen.

§9 Abs. 1 PromO

Ich versichere hiermit, dass die vorliegende Dissertation selbstständig und nur unter Verwendung der angegebenen Quellen verfasst wurde.

§9 Abs. 2 PromO

Die Arbeit hat bisher noch nicht zu Prüfungszwecken gedient.

Darmstadt, den . April 2021

F. Abstract

Despite the impressive accomplishments in the development of small molecule kinase inhibitors over the past 25 years, the majority of human kinases still lack high-quality inhibitors that can be used as chemical probes to investigate their biological function and pharmacology. Many members of the untargeted kinome are known to play a crucial role in the cell cycle and thus represent unexploited cancer drug targets. NIMA-related kinase 1 (Nek1) is one such example, which has lately gained attention for its widespread function in ciliogenesis, apoptosis, and the DNA-damage response and is involved in numerous cancers and several ciliopathies, and neurodegenerative diseases. This work reports the development of the first selective high-quality tool compounds for Nek1 inhibition using structure-guided medicinal chemistry methods. In the first step, two novel 7 azaindole scaffolds were derived from published structural data and reported kinome cross-screening analyses. Iterative steps of computer-assisted design, synthesis, and evaluation of structure-activity-relationships then led to the identification of seven lead compounds, and the top compound was further profiled for its *in vivo* efficacy, toxicity, and bioavailability in a self-established zebrafish polycystic kidney disease model. Administration of the top compound caused the quantifiable expansion of fluorescence-labeled proximal convoluted tubules, thus supporting the hypothesis that Nek1-inhibition causes cystic kidneys in zebrafish embryos. The methods used provide a blueprint for the fast and resource-efficient development of chemical probes for other dark kinases from widely available chemogenomic kinase data sets.

G. Alternative Abstract (German)

Trotz der beeindruckenden Errungenschaften in der Entwicklung niedermolekularer Kinase Inhibitoren, in den vergangenen 25 Jahren, sind für den Großteil der menschlichen Kinasen keine hochwertigen Inhibitoren verfügbar, die als chemische Sonden zur pharmakologischen Untersuchung biologischer Funktionen verwendet werden können. Für viele Vertreter des nicht adressierten Kinoms ist bekannt, dass sie in essenziellen Rollen des Zellzyklus mitwirken und somit ungenutzte Angriffspunkte für Krebstherapien darstellen. NIMA-related Kinase 1 (Nek1) ist eine solche Kinase, welche zuletzt aufgrund ihrer weitreichenden Funktionen in der Ziliogenese, der Apoptoseregulation und der DNA-Schadensantwort Aufmerksamkeit erregt hat, und ist nachweislich an zahlreichen Krebsarten sowie an Ziliopathien und neurodegenerative Erkrankungen beteiligt. Die vorliegende Arbeit beschreibt die auf Struktur-gesteuerten Methoden der Medizinalchemie gestützte Entwicklung der ersten selektiven Werkzeugsubstanzen zur gezielten Hemmung von Nek1. Im ersten Schritt wurden zwei neuartige 7-Azaindol Gerüste aus veröffentlichten Struktur- und Kinase-Cross-Screening-Analysen abgeleitet. Iterative Schritte aus computergestütztem Design, Synthese und Evaluation von Struktur-Aktivitäts-Beziehungen führten zur Identifizierung von sieben Leitstrukturen und die vielversprechendste Verbindung wurde sodann in einem eigenständig entwickelten Zebrafischlebensmodell der polyzystischen Nierenerkrankung hinsichtlich ihrer Wirksamkeit, ihrer Toxizität sowie ihrer Bioverfügbarkeit weiter untersucht. Die Behandlung von Zebrafischembryonen mit der Leitsubstanz führte zu einer messbaren Vergrößerung der fluoreszenzmarkierten Vornieren, wodurch die Hypothese, dass die Inhibition von Nek1 im Entwicklungsstadium zur Ausbildung von renalen Zysten führt, bestätigt werden konnte. Die verwendete Methode stellt zudem ein adaptierbares Konzept für die schnelle und ressourceneffiziente Entwicklung weiterer chemischer Sonden auf Basis breit zugänglicher chemogenomischer Datensätze bereit.